Lithium, Beryllium and Boron in High-Pressure Metamorphic Rocks from Syros (Greece)

Horst R. Marschall

Lithium, Beryllium and Boron in High-Pressure Metamorphic Rocks from Syros (Greece)

INAUGURAL-DISSERTATION

zur Erlangung der Doktorwürde der

Mathematisch-Naturwissenschaftlichen Gesamtfakultät

der Ruprecht-Karls-Universität

Heidelberg

vorgelegt von

Diplom-Mineraloge

Horst R. Marschall

aus Mainz

Heidelberg, im April 2005
Gutachter:
Prof. Dr. Rainer Altherr
Prof. Dr. Angelika Kalt

Tag der mündlichen Prüfung: 01.07.2005

Erfolgsgruppe 2000.
Erfolg ohne Ende.

A rock feels no pain, and an island never cries.*

<div align="right">Simon and Garfunkel</div>

---

*When Paul Simon and Arth Garfunkel wrote the text of "I am a rock" they were probably not aware of rocks being subjected to pressures of 20,000 atmospheres and temperatures of $500\,^{\circ}$C including intense shearing and folding - and they had never seen the dehydration features on the island of Syros. In contrast to J.E. Dixon, who completed his PhD thesis on "The metamorphic rocks of Syros, Greece" in 1968 - the same year when "Sound of Silence" was first released.

Contents

Abstract

Exhumed high-pressure metamorphic rocks in fossil subduction zones include important information on trace-element storage in different lithologies and element transport during devolatilisation of subducting slabs. In this study, high-pressure metamorphic rocks from the island of Syros (Greece) that are interpreted as parts of subducted oceanic crust, equilibrated at about $1.5 - 2.0 \, \mathrm{GPa}$ and $500 \, ^\circ \mathrm{C}$ were analysed. A first group of samples (Group 1) includes serpentinites as well as meta-igneous and meta-sedimentary rocks that preserved the parageneses formed at the pressure peak of metamorphism. In addition, a second group of samples (Group 2) represents metamorphic reaction zones formed at the contacts between contrasting lithologies. These reaction zones formed by rehydration at lower pressures during exhumation of the high-pressure metamorphic unit. Some of them contain abundant tourmaline. The two groups of samples occur in a mélange of blocks of various rock types embedded in a schistose matrix in the northern part of the island.

Bulk rock major and trace elements were analysed using a variety of analytical methods for ~ 50 elements including Li, Be and B. In-situ analyses of Li, Be and B abundances and B isotope ratios were performed using secondary ion mass spectrometry (SIMS). A new method was developed for B analysis at low concentrations using SIMS, which enables a reduction of boron contamination to levels close to or even below the detection limit of $\sim 2 \, \mathrm{ng/g}$, with a lateral resolution of $\sim 30 \, \mu\mathrm{m}$ in a rather short time of $\sim 12 \, \mathrm{min}$ per spot. In addition to the light elements, a number of other trace elements were analysed in situ by laser ablation ICP-MS.

Group-1 samples contribute information on the impact of dehydration of (altered) igneous oceanic crust on whole-rock abundances of different trace elements. In detail, the abundances of Li and Be do not correlate with H_2O contents and are in the same range as in fresh and altered oceanic crust, suggesting that most of the Li and Be remains in the subducting slab and is not released with hydrous fluids. In contrast, B concentrations and B/Be ratios are correlated to the H_2O contents of the rocks. Both decrease in range and value with decreasing H_2O content, suggesting a significant loss of B with hydrous fluids during progressive dehydration. Group-2 samples provide information on the effects of metasomatism of high-pressure metamorphic rocks during exhumation. Li and Be show very high abundances in many samples, suggesting a strong enrichment during metasomatism. The enrichment of B is entirely controlled by the occurrence of tourmaline. Tur-bearing samples display very high B/Be ratios, while Tur-free samples show low B concentrations and B/Be ratios. These results demonstrate that Li is probably a good tool for tracing metasomatic enrichment processes, while B is enriched only in the case of tourmaline formation. The results of bulk-rock analyses suggest that B/Be ratios can be used to trace qualitatively

the progressive dehydration of high-pressure metamorphic rocks, while Li concentrations are more sensitive for metasomatic processes, i.e. the influx of external fluids.

The SIMS study resulted in so far unique sets of inter-mineral partition coefficients for the light elements Li, Be and B for 15 different high-pressure metamorphic minerals, derived on the basis of in-situ analyses of coexisting phases in several different natural rock samples. These sets provide important information on the behaviour of the light elements in different lithologies within subducting slabs, and they are essential for modelling of trace-element and isotope fractionation during subduction and dehydration of oceanic crust. In addition, the important hosts of the light elements were determined and quantified with respect to the whole rock budgets.

Modelling of trace element release from progressively dehydrating rocks was performed for the light elements Li, Be and B, which show contrasting behaviour during fluid/rock interaction processes. Experimentally determined clinopyroxene/fluid partition coefficients for Li, Be and B (Brenan *et al.*, 1998b) were combined with mineral/clinopyroxene partition coefficients for various high-pressure minerals to deduce a set of mineral/fluid partition coefficients. These were combined with the modal compositions of high-pressure metamorphic rocks derived from thermodynamic calculations. The result is a data set of the modal composition of a rock and its whole rock/fluid partition coefficients for the trace elements of interest at any stage of the $P - T$ path, including information on the amount of fluid released at any depth. Based on these data, the concentrations of trace elements in the subducting rocks and in the released fluids along a certain $P - T$ path were modelled. In a second step, the derived information on boron concentrations of rocks and fluids were combined with the temperature dependent isotopic fractionation of B, in order to model the B isotopic evolution of subducting rocks and of the released fluids. In principle, the presented model offers the possibility of a quantification of trace-element release from the slab in any lithology along any reasonable $P - T$ path.

Tourmaline grains of two metasedimentary and one metabasic rock were analysed in-situ for their chemical and B isotopic compositions with high lateral resolution. The δ^{11}B values of prograde and peak metamorphic tourmaline in these samples range from -1.6 to $+2.8\%o$ and are significantly higher than values reported in the literature for high-pressure metasedimentary tourmaline. This demonstrates that the B isotopic composition of metasedimentary rocks from different localities and samples worldwide may differ significantly from one another, and a clear distinction between altered oceanic crust and oceanic sediments is not possible on the basis of B isotopes. The slow volume diffusivity of B in tourmaline allows for a detailed investigation of the evolution of the B isotopes of a tourmaline-bearing rock during its metamorphic and pre-metamorphic history. Samples investigated in this study display heterogeneous sedimentary sources of tourmaline detrital grains with δ^{11}B between $-10.7\%o$ and $+3.6\%o$ in a single sample. Prograde and peak-metamorphic growth zones distinguished by petrographical features and major element chemistry from retrograde overgrowth, also show different signals in their B isotopes.

High-pressure blocks enclosed in the mélange on the island of Syros are rimmed by

reaction zones ("blackwalls") composed of hydrous minerals, such as chlorite, Na- and Ca-amphibole, clinozoisite and phengite in paragenesis with omphacite, albite and dravitic tourmaline. B isotopic composition of tourmaline is unusually heavy with $\delta^{11}B$ values exceeding $+18‰$ in all investigated samples, reaching a unique value of $+28.4‰$ in one sample. Blackwalls formed during exhumation of the high-pressure mélange at a depth of $20-25\,km$. Estimated $P-T$ conditions are $\sim 0.6-0.75\,GPa$ and $400-430\,°C$. They were produced by the influx of external hydrous fluids that probably originated in the subsequently subducting slab. The exceptionally high $\delta^{11}B$ values of the dravite are explained by interaction of the tourmaline-forming fluids with material composing the exhumation channel on their way from the dehydrating slab to the site of tourmaline formation in the blackwalls. The calculated model demonstrates that fluids are rapidly modified in both trace-element and isotopic composition during their migration through the material overlying the subducting slab. Differences in B isotopic composition and concentration are blurred quickly and wiped out after short distances of migration, when the fluid approaches equilibrium with the surrounding wall rock of an exhumation channel. The formation of tourmaline at the contact between mafic or felsic high-pressure blocks and ultramafic matrix by fluids released during dehydration reactions in the subducting slab may also occur on the prograde path, wherever fluids are migrating through such contact zones, i.e. the slab-mantle interface. If this is the case, the formation of blackwall tourmaline has a significant impact on the geochemical cycle of B in subduction zones, as it is fixing heavy B in large quantities in the slab within a highly stable mineral.

Trace elements are only selectively incorporated into the blackwall tourmaline and many elements are excluded from its structure. The light elements Li and Be, the HFSE (Zr, Hf, Nb, Ta, W, Th, U), the REE, Y and the LILE (K, Rb, Ba, Cs) all show very low concentrations and are not incorporated into dravitic tourmaline. First row transition metals (Ti, V, Cr, Mn, Co, Cu, Zn) and Sr, Pb and Ga are incorporated into dravite, demonstrating abundances in the same order as in the respective whole rocks, and in paragenetic rock-forming minerals. Hence, tourmaline is not strongly fractionating these elements in any way.

Kurzfassung

Exhumierte hochdruckmetamorphe Gesteine in fossilen Subduktionszonen enthalten wichtige Informationen zur Spurenelement-Speicherung in unterschiedlichen Lithologien und zum Elementtransport während der Devolatilisierung von subduzierenden Platten. Im Zuge dieser Arbeit wurden hochdruckmetamorphe Gesteine der Insel Syros (Griechenland) analysiert, die als Teile von ehemals subduzierter ozeanischer Kruste interpretiert werden und bei etwa $1.5 - 2.0\,$GPa und $500\,°$C equilibriert haben. Eine Gruppe von Proben (Gruppe 1) umfasst Serpentinite sowie metamagmatische und metasedimentäre Gesteine, die die Paragenesen der Hochdruck-Metamorphose vollständig bewahrt haben. Zusätzlich wurde eine zweite Gruppe von Proben (Gruppe 2) untersucht, die am Kontakt zwischen stark unterschiedlichen Gesteinsarten entstanden sind. Diese Reaktionszonen bildeten sich durch Rehydratation bei niedrigeren Drücken während der Exhumierung der Hochdruck-Einheit. Einige der Gesteine der Gruppe 2 enthalten sehr viel Turmalin. Beide Gesteinsgruppen treten innerhalb einer Mélange von Blöcken in einer schieferigen Matrix auf, die im Norden der Insel Syros ansteht.

Gehalte an Haupt- und Spurenelementen der Gesamtgesteinsproben wurden mittels verschiedener Analysenmethoden bestimmt, wobei etwa 50 verschiedene Elemente einschließlich Li, Be und B analysiert wurden. In-situ-Messungen von Li-, Be- und B-Gehalten und von B-Isotopenverhältnissen wurden mit Hilfe eines Sekundärionen-Massenspektrometers (SIMS) durchgeführt. Für Analysen von B bei niedrigen Konzentrationen am SIMS wurde eine neue Messmethode entwickelt, die es ermöglicht den Beitrag der Kontamination auf das Niveau der Nachweisgrenze von $\sim 2\,$ng/g oder sogar darunter zu reduzieren, bei einer lateralen Auflösung von $\sim 30\,\mu$m und einer Messzeit von nur $\sim 12\,$min pro Analyse. Zusätzlich zu den leichten Elementen wurde eine Reihe von Spurenelementen mittels Laser-Ablations ICP-MS in situ gemessen.

Durch die Untersuchung der Proben der Gruppe 1 erhält man Informationen zum Einfluss der Dehydratation von (alterierter) magmatischer ozeanischer Kruste auf die Gesamtgesteinsgehalte verschiedener Spurenelemente. Die Gehalte von Li und Be korrelieren nicht mit den H_2O-Gehalten und entsprechen in frischer und alterierter Ozeankruste. Daraus lässt sich schließen, dass der größte Teil an Li und Be in der subduzierenden Platte verbleibt und nicht mit den wässrigen Fluiden entweicht. Im Gegensatz dazu korrelieren B-Gehalte und B/Be-Verhältnisse mit den H_2O-Gehalten der Gesteine. Beide sinken, sowohl im Wert als auch in der Streubreite, mit abnehmendem H_2O-Gehalt. Hieraus lässt sich ein signifikanter Verlust von B über wässrige Fluide während fortschreitender Dehydratation ableiten.

Durch die Untersuchung der Proben der Gruppe 2 erhält man Informationen über metasomatische Effekte auf hochdruckmetamorphe Gesteine während ihrer Exhumierung. Viele

dieser Proben zeigen sehr hohe Li- und Be-Gehalte, was auf eine starke Anreicherung während der Metasomatose hindeutet. Die Anreicherung von B wird vollständig durch das Auftreten von Turmalin kontrolliert. Turmalin-führende Proben zeigen sehr hohe B/Be-Verhältnisse, während Turmalin-freie Proben niedrige B-Gehalte und B/Be-Verhältnisse aufweisen. Die Ergebnisse zeigen, dass Li anscheinend ein guter Indikator für metasomatische Anreicherungsprozesse ist, während B nur in den Fällen angereichert wird, in denen sich Turmalin bildet. Die Ergebnisse aus den Gesamtgesteinsuntersuchungen legen nahe, dass B/Be-Verhältnisse benutzt werden können, um die fortschreitende Dehydratation hochdruckmetamorpher Gesteine zumindest qualitativ nachzuvollziehen, während Li-Gehalte viel stärker auf metasomatische Prozesse reagieren, genauer gesagt auf eine Anreicherung durch externe Fluide.

Aus den Untersuchungen am SIMS ergaben sich Mineral/Mineral-Verteilungskoeffizienten für die leichten Elemente Li, Be und B für 15 verschiedene hochdruckmetamorphe Minerale. Diese wurden aus in-situ-Analysen an koexistierenden Phasen in mehreren verschiedenen natürlichen Proben abgeleitet. Die Verteilungskoeffizienten liefern wichtige Informationen zum Verhalten der leichten Elemente in verschiedenen Lithologien innerhalb subduzierender Platten. Sie sind außerdem unentbehrlich für die Modellierung von Spurenelement- und Isotopenfraktionierungen während der Subduktion und Dehydratation ozeanischer Kruste. Zusätzlich wurden die wichtigsten Trägerphasen der leichten Elemente bestimmt und im Hinblick auf die jeweiligen Gesamtgesteins-Budgets quantifiziert.

Die Elemente Li, Be und B zeigen ein stark unterschiedliches Verhalten bei Fluid-Gesteins-Wechselwirkungsprozessen. In dieser Arbeit wurde das Entweichen der leichten Elemente während der fortschreitenden Dehydratation modelliert. Hierzu wurden experimentell bestimmte Klinopyroxen/Fluid-Verteilungskoeffizienten für Li, Be und B (Brenan *et al.*, 1998b) mit Mineral/Klinopyroxen-Verteilungskoeffizienten für verschiedene hochdruckmetamorphe Minerale kombiniert, wodurch sich ein Set von Mineral/Fluid-Verteilungskoeffizienten ergab. Dies wurde mit den Modalzusammensetzungen hochdruckmetamorpher Gesteine kombiniert, die aus thermodynamischen Berechnungen hervorgingen. Das Ergebnis ist ein Datensatz der modalen Zusammensetzung eines Gesteins und seiner Gesamtgesteins/Fluid-Verteilungskoeffizienten für die jeweils interessanten Spurenelemente an jeder Stelle des $P-T$-Pfades, einschließlich der Menge an Fluid, die während zunehmender Tiefe das Gestein verlässt. Ausgehend von dieser Datenbasis wurden die Konzentrationen an Spurenelementen in subduzierenden Gesteinen und der jeweils entweichenden Fluide entlang eines bestimmten $P-T$-Pfades modelliert. In einem zweiten Schritt wurden die so erhaltenen Informationen über die B-Gehalte von Gesteinen und Fluiden mit der Temperaturabhängigen Isotopenfraktionierung kombiniert, um die Entwicklung der B-Isotopie der subduzierenden Gesteine und der entweichenden Fluide zu modellieren. Im Prinzip bietet das vorgestellte Modell die Möglichkeit den Spurenelement-Verlust aus der subduzierenden Platte zu modellieren, und zwar für jedes Gestein und jeden realistischen $P-T$-Pfad.

Turmalinkörner aus zwei metasedimentären und einem metabasischen Gestein wurden in situ mit hoher örtlicher Auflösung auf ihre chemische und B-isotopische Zusammenset-

zung hin analysiert. Die δ^{11}B-Werte der prograden und peakmetamorphen Turmaline in diesen Proben bewegen sich zwischen -1.6 und $+2.8‰$ und liegen damit deutlich über den Werten, die in der Literatur für Turmalin aus hochdruckmetamorphen Sedimenten aufgeführt sind. Die relativ hohen Werte in allen untersuchten Proben zeigen, dass die B-isotopischen Zusammensetzungen von Metasedimenten verschiedener Lokalitäten deutlich variieren können, und dass eine eindeutige Unterscheidung zwischen alterierter ozeanischer Kruste und ozeanischen Sedimenten aufgrund der B-isotopischen Zusammensetzung nicht möglich ist. Die langsame Volumendiffusion von B in Turmalin ermöglicht eine detaillierte Untersuchung der metamorphen und prämetamorphen B-isotopischen Entwicklung Turmalin-führender Gesteine. Eine der hier untersuchten Proben zeigt klar eine heterogene sedimentäre Quelle an; die δ^{11}B-Werte detritischer Turmalinkörner innerhalb der Probe variieren zwischen -10.7 und $+3.6‰$. Prograde und peakmetamorphe Anwachszonen, die aufgrund petrographischer und chemischer Eigenschaften unterschieden werden konnten, zeigen auch charakteristische Unterschiede in der B-Isotopie.

Hochdruckmetamorphe Blöcke in der Mélange von Syros sind häufig von Reaktionszonen umgeben, die man als "Blackwalls" bezeichnet. Sie bestehen aus OH-haltigen Mineralen wie Chlorit, Na- und Ca-Amphibol, Klinozoisit und Phengit, in Paragenese mit Omphazit, Albit und dravitischem Turmalin. Die B-Isotopen-Zusammensetzung des Turmalins ist ungewöhnlich schwer, wobei die δ^{11}B-Werte in allen untersuchten Proben oberhalb von $+18‰$ liegen. In einer Probe erreicht der δ^{11}B-Wert den einmalig hohen Wert von $+28.4‰$. Die Blackwalls bildeten sich während der Exhumierung der Hochdruck-mélange bei Tiefen von $20-25$ km und $P-T$-Bedingungen von etwa $0.6-0.75$ GPa und $400-430\,°C$. Ihre Bildung geht auf die Zufuhr externer Fluide zurück, die wahrscheinlich aus der nachfolgend subduzierten Platte stammen. Die außergewöhnlich hohen δ^{11}B-Werte des Dravit können erklärt werden durch Wechselwirkung der Turmalin-bildenden Fluide mit Material aus dem Exhumierungskanal, das von den Fluiden auf ihrem Weg von der dehydrierenden Platte zu den Blackwalls durchströmt wurde. Das berechnete Modell zeigt, dass sowohl der Spurenelementgehalt als auch die Isotopie von Fluiden sehr schnell verändert werden, während diese das Material oberhalb der subduzierenden Platte durchströmen. Anfängliche Unterschiede in der B-isotopischen Zusammensetzung und der B-Konzentration werden sehr schnell ausgeglichen und verschwinden schon nach einer kurzen Fließstrecke, sobald das Fluid sich dem Gleichgewicht mit dem umgebenden Gestein annähert. Die Bildung von Turmalin am Kontakt zwischen mafischen oder felsischen Blöcken und der ultramafischen Matrix durch Abscheidung aus Fluiden, die bei Dehydratationsreaktionen in der subduzierenden Platte freigesetzt werden, kann wahrscheinlich ebenso bei der Subduktion der Gesteine stattfinden, und zwar immer dann, wenn Fluide durch diese Kontaktzonen migrieren. Eine solche Konzaktzone bildet beispielsweise die Grenzfläche zwischen subduzierender Platte und überlagerndem Mantel. Falls es hier tatsächlich regelmäßig zur Turmalin-Bildung kommt, hat dieser Prozess einen signifikanten Einfluss auf B-Kreislauf in Subduktionszonen, weil er große Mengen an isotopisch schwerem B in einem sehr stabilen Mineral bindet.

Spurenelemente wurden nur sehr selektiv in den Blackwall-Turmalin eingebaut. Die leichten Elemente Li und Be, die HFSE (Zr, Hf, Nb, Ta, W, U, Th), die seltenen Erden, Y und die LILE (K, Rb, Ba, Cs) zeigen durchweg sehr niedrige Konzentrationen und wurden nicht in den dravitischen Turmalin eingebaut. Die erste Reihe der Übergangsmetalle (Ti, V, Cr, Mn, Co, Cu, Zn) und die Elemente Sr, Pb und Ga sind im Dravit enthalten. Die Konzentrationen liegen jedoch im gleichen Bereich wie die Gehalte in den jeweiligen Gesamtgesteinen und wie in koexistierenden gesteinsbildenden Mineralen. Diese Elemente werden also durch Turmalin kaum fraktioniert.

1. Introduction

1.1. Light elements in subduction zones

The Earth   Planet Earth with a radius of approximately 6300 km is composed of four major layers or shells: the crust, the mantle and the outer and inner core (Fig. 1.1). The core consists of a metallic iron and nickel alloy, which is slowly crystallizing from its solid inner part to its liquid outer part. Altogether the core has a radius of approximately 3500 km and has separated from the silicate mantle in the early history of the planet. The third and largest layer ($\sim 83\,\%$ of the Earth's volume, or $2/3$ of its mass) is the silicate mantle, which is composed dominantly of Mg-Fe-silicates and oxides. Its mineralogical composition changes with depth, but is in general relatively simple, with only three to five coexisting phases. The chemical heterogeneities of the mantle are also minor, compared to those of the crust. The outermost shell of the planet – the crust – is a very thin layer of only $5-10$ km thickness beneath the oceans and $20-70$ km at the continents.

The oceanic crust consists mainly of magmatic rocks formed at the ocean floors from magma extracted directly from the underlying mantle, and a sedimentary cover. The compositional variation of rocks in the oceanic crust is also limited. The continental crust on the other hand displays a huge variety of different rock types with different chemical and mineralogical compositions and may range from basalts to granites and from shales and sandstones to marbles and gneisses. Chemical elements that occur at concentration levels of parts per billion in the mantle may be enriched in some rocks within the continental crust to several weight percent and may form deposits of economical interest. The processes that led to such a strong chemical differentiation and to the formation of the continental crust are a matter of scientific research of geoscientists for more than a century. The theory of plate tectonics invented by Alfred Wegener (Wegener, 1912), generally accepted by the scientific community in the 1960s provides a conclusive fundament for the explanation of a number of observations, like distribution of volcanism and earthquakes, and formation of large montain belts, oceans and continents.

Subduction zones   The uppermost layer of the mantle together with the crust form the relatively rigid lithosphere, which is split up into several plates that move relative to each other. At divergent boundaries, where two plates move apart, new
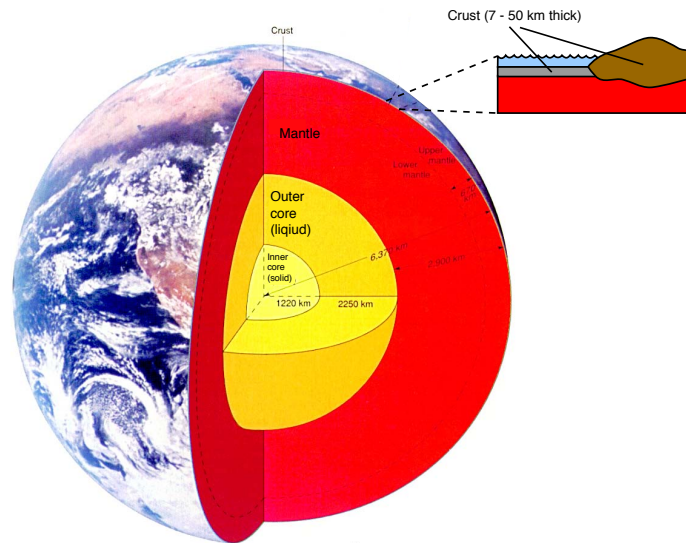
Fig. 1.1. Schematic cross-section of the Earth showing its four major shells, the inner core (bright yellow), the outer core (yellow), the mantle (red) and the crust (blue) in their approximate proportions. The small inset shows a magnification of the crust with the thin oceanic crust (grey) and the thicker continental crust (brown). Note the small thickness of the crust in relation to the mantle, which yields a mass ratio of mantle to crust of $\sim 150:1$. Figure from USGS internet site.

oceanic curst is formed. At convergent plate boundaries on the other hand, one plate is overriding another, which is in turn descending into the mantle. This process of subduction of crustal material into the Earth's mantle leads to large scale recycling and strongly impacts the chemical budgets of the different reservoirs. The boundaries of tectonic plates are places where most of the dynamic activity of the Earth's surface is concentrated. Serious natural hazards, like strong earthquakes that can result in tsunamis and highly explosive volcanic eruptions are generated at these zones. Although processes that occur at divergent and transform plate boundaries all have unique and important consequences, convergent plate boundaries (i.e. subduction zones) are where crustal material is recycled. This modifies the composition of the mantle, and it provides tracers that are fundamental to attempts to model convection processes within the Earth. Most material that composes or attaches to the down-going plate is recycled into the Earth's interior, but this is also where new crust is generated, and where most of the very hazardous active volcanoes on Earth are situated. The reason for the volcanism is the release of fluids and silicate melts from the down-going plate that enable the mantle to melt at lower temperatures.

As the continental crust is not effectively subducted due to its low average density, most subducting plates (or slabs) are oceanic plates. They usually consist of

a large ultramafic layer (the lithospheric mantle), a sequence of magmatic rocks and a sedimentary pile. The magmatic portion can be subdivided into an intrusive mostly gabbroic layer, a subvolcanic layer consisting of basaltic dykes, and an effusive layer consisting of basaltic lava flows and tephra that were rapidly quenched during contact with seawater. Formation of this magmatic sequence occurs at divergent plate boundaries, i.e. the mid-ocean ridges (MOR), which are characterised by high heat flow, as a consequence of upwelling of the asthenosperic mantle and the existence of shallow magma chambers. The high heat flow drives large-scale convection of seawater through the oceanic crust, which leads to a strong hydrothermal alteration of the ultramafic, magmatic and sedimentary rocks. The significant exchange of elements between seawater and the lithosphere at the MOR together with long-term weathering of the rocks exposed to the surface leads to a strong hydration of the upper $\sim 500\,\mathrm{m}$ of the oceanic lithosphere.

Subduction zone element cycle With the slab starting to descend at a convergent plate boundary, pressure and temperature increase continuously and the H_2O (and other volatile components) stored in pores and in minerals is progressively expelled from the slab. This process of dehydration or devolatilisation of subducting slabs starts at the onset of subduction in shallow regions and continues to depths of probably more than $100\,\mathrm{km}$. The fluids expelled from the subducting slab migrate upwards and form hot springs, mud-volcanoes or serpentinite diapirs within the fore-arc system. Fluids or melts released at greater depth will hydrate and metasomatise the mantle rocks of the hanging plate (i.e. the *mantle wedge*). The source of melt for the volcanic arcs located above the subduction zones is this hydrated mantle wedge above the subducted slab. Therefore, deep element cycles occur within subduction zones, where components are enriched in hydrated oceanic lithosphere, subducted to mantle depths, transported to the mantle wedge by fluids or melts derived from the slab and carried back to the surface by arc magmas (Fig. 1.2). However, some fraction of the elements and H_2O will not be released from the subducting rocks, but will stay in the slab and will be dragged down to great depth, maybe as deep as the core-mantle boundary. These fragments of ancient oceanic crust probably form chemical heterogeneities within the Earth's mantle, and are sampled by ocean island volcanoes, many of which are located over deep mantle plumes. This process recycles material on a global scale.

In summary, recycling of material in subduction zones occurs on different scales: (i) return of expelled fluids to the surface or to near-surface levels in the forearc system, (ii) enrichment of the source region of arc magmas by metasomatic agents originating in the subducting slab and eruption of those magmas in the volcanic arc,
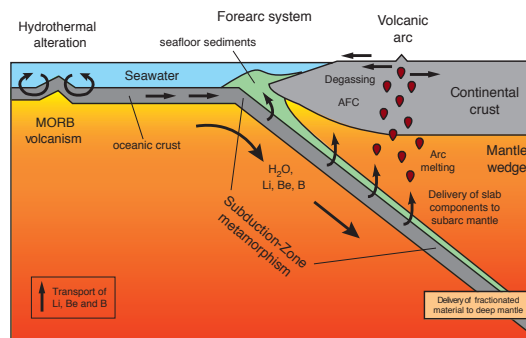
Fig. 1.2. Schematic vertical cross-section through a subduction zone, displaying the geochemical cycle of Li, Be and B in subduction zones. Modified after Bebout (1996).

and (iii) storage of deeply subducted crust in the mantle and later sampling of these heterogeneities by plume-related volcanoes. Subduction zones are therefore the most important sites of chemical interaction between the Earth's crust and mantle and are critical in understanding the long-term evolution of the two geochemical reservoirs.

Investigating the geochemistry of volcanic rocks produced at subduction zones, igneous geochemists have established several element and isotopic ratios as proxies for processes operating within subduction zones to produce the characteristic "subduction zone geochemical fingerprint". Enrichment in fluid-mobile elements (e.g. Cs, Ba, K, Sr, U, Pb), a lack of enrichment in non-fluid-mobile elements (e.g. Nb, Ta, Ti, Zr, Hf) together with specific isotopic signatures (e.g. ^{87}Sr/^{86}Sr, ^{206}Pb/^{204}Pb) are interpreted as a result of metasomatism of the magma source by slab-derived fluids or melts (e.g. Tatsumi & Eggins, 1995; Elliott, 2003). Their detailed investigation has helped to establish the current rather empirical model of slab dehydration and subduction-related melting processes. A key resource, which has enjoyed remarkably little attention, are exhumed high-pressure metamorphic rocks. Containing a large range of rock types (e.g. eclogites, metasediments and serpentinites) they offer a representative cross section through a subducting slab. Therefore, they offer a much more complete picture of the processes and phase changes that govern the release of fluids and the interaction of mantle and recycled crustal material than can be inferred from the chemistry of the erupted volcanic rocks. In particular, the complex effects of the metamorphic history of the subducted slab have been more or less ignored in previous geochemical models, which are based exclusively on arc volcanic rocks.

4

Li, Be and B   Important constraints on the mechanisms of slab-to-mantle transfer can be derived from the abundances and isotopic systematics of the low-atomic mass elements Li, Be and B in subduction-related rocks. The partitioning behaviour of these elements during slab dehydration differs from that during slab melting. Experimentally determined mineral/fluid partition coefficients increase in the order $D_B < D_{Li} \ll D_{Be}$ (Brenan *et al.*, 1998a), while mineral/melt partition coefficients increase in the order $D_B \leq D_{Be} < D_{Li}$ (Brenan *et al.*, 1998b). The use of light elements as tracers in subduction zone geochemistry was also put forward by studies on subduction-related volcanic rocks by various authors starting with J. Ryan and C. H. Langmuir in the late 1980s (Ryan & Langmuir, 1987, 1988, 1993). Element ratios like Li/Yb, B/Be and B/Nb and isotope signatures (^{7}Li/^{6}Li, ^{10}Be/^{9}Be, ^{11}B/^{10}B) have been used over the last ~ 15 years in order to enhance our knowledge on slab dehydration and subduction-related melting processes. In order to fully understand the light-element signatures of arc volcanic rocks, it is necessary to know the behaviour of these elements during subduction-related progressive metamorphism of slab materials.

The light elements lithium and boron both have two stable isotopes (^{6}Li and ^{7}Li, and ^{10}B and ^{11}B). Their high relative mass differences are responsible for variations in their isotopic compositions in nature of about 60‰ for Li and about 100‰ for B (Palmer & Swihart, 2002; Tomascak, 2004). The large B isotopic fractionation at low temperatures has led to the use of the B stable isotope system for studies of processes acting at the Earth's surface (e.g. Hemming & Hanson, 1992; Barth, 1998) and for the detection of subducted material in fluids, serpentinites and subduction-related volcanic rocks (e.g. Ishikawa & Nakamura, 1994; Benton *et al.*, 2001). Li isotopes have attracted increasing attention from geochemists working on metamorphic, igneous and sedimentary rocks (e.g. Chan & Kastner, 2000; Zack *et al.*, 2003; Elliott *et al.*, 2004; Tomascak, 2004). Like B, the strong isotopic fractionation of Li at low temperatures provides a robust tool for tracing hydrous alteration processes at the Earth's surface, and has great potential as a tracer of low-temperature alteration material in subduction zone related fluids, magmas and metamorphic rocks, in mantle xenoliths and ocean island basalts. A key feature is that isotopes of the light elements B and Li have considerable potential as tracers of recycled crust in the Earth's mantle, but such proxies can only be applied once their behaviour during fluid release in subduction zones is better quantified.

Beryllium has only one stable isotope (^{9}Be). However, its cosmogenic radioactive isotopes ^{10}Be with a half live of 1.6 Ma (Pfennig *et al.*, 1998) has been used to trace the subduction of cosmogenic ^{10}Be-bearing sediments by monitoring the output of this nuclide at arc volcanoes, and to place a time frame on these processes.

Summarising the results of previous studies dealing with the behaviour of light

elements in the subduction cycle, some principle conclusions can be made. Li and B are relatively mobile in hydrous fluids and in silicate melts. Be is relatively immobile in normal hydrous fluids but mobile in silicate melts. Li and B concentrations in the slab decrease with increasing depth of subduction, as these elements are released with fluids during dehydration. Therefore, ratios of fluid mobile B and non-mobile elements like Be or Nb (B/Be and B/Nb) also decrease. Concurrently, preferential loss of the heavier isotopes ^{7}Li and ^{11}B results in decreasing δ^7Li and δ^{11}B values in the subducting material. The studies on subduction-related volcanic rocks investigating across-arc profiles show a decrease of B concentrations, decreasing B/Be and B/Nb ratios and δ^{11}B values from trench to back-arc. Within the slab, the most important reservoirs for Li, Be and B are the sediments, the altered oceanic crust (AOC) and serpentinised ultramafic rocks. Fresh mantle and magmatic rocks show very low concentrations and no isotopic anomalies. Sediments, AOC and serpentinites are not only enriched in Li, B and $\pm$Be, but also show δ^7Li and δ^{11}B values higher than MORB (or mantle), due to a preferential enrichment in the heavy isotopes during the interaction with seawater. The hydrous portion of the subducting slab therefore introduces large amounts of heavy Li and B into the subduction zone. Be and especially ^{10}Be are enriched in the sedimentary column of the oceanic crust.

1.2. Framework of the study

The petrology group of the Mineralogisches Institut at Universität Heidelberg has been investigating the geochemical behaviour of the light elements for over five years now. Starting with the investigation of the partitioning of Li in mantle rocks (Seitz & Woodland, 2000; Olker, 2001; Paquin & Altherr, 2002) and in eclogites (Woodland *et al.*, 2002), recently all three elements were analysed for concentrations in mantle rocks (Paquin *et al.*, 2004), and rocks of the continental crust like metapelites (Steppan, 2003) and amphibolites (Hepp, 2003). The secondary ion mass spectrometer (SIMS) installed at the Mineralogisches Institut and operated by Thomas Ludwig is the key instrument to enable the precise in-situ analysis of light elements and their isotopes. Using this facility, light element concentrations can be measured precisely over a concentration range of eight orders of magnitude, i.e. between ~ 1 ng/g and tens of weight percent.

   This thesis is a compilation of a study performed at the Mineralogisches Institut between November 2000 and December 2004. In early 2000, a larger project on the subduction cycle of light elements using the Aegean region as a case study was initiated by Angelika Kalt (now Neuchâtel) and Rainer Altherr and financed dominantly by the Deutsche Forschungsgemeinschaft (DFG). Within this project several
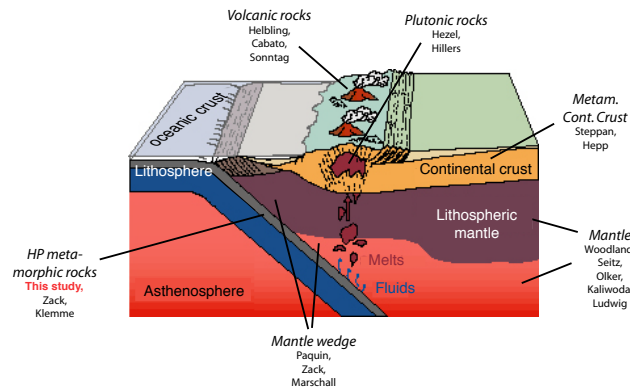
Fig. 1.3. Schematic vertical cross-section through a subduction zone, displaying different studies completed at the Mineralogisches Institut (Heidelberg) investigating the geochemistry of Li, Be and B in different rock types related to subduction zones: *Volcanic rocks* (Helbling *et al.*, 2004; Cabato *et al.*, 2004, and Sonntag, in prep.); *plutonic rocks* (Hezel, 2000; Hillers, 2003); *metamorphic continental crust* (Steppan, 2003; Hepp, 2003); *subcontinental mantle* (Seitz & Woodland, 2000; Olker, 2001; Woodland *et al.*, 2002; Kaliwoda, 2004, and Ludwig, in prep.); *mantle wedge peridotite and serpentinite* (Paquin & Altherr, 2002; Zack & Marschall, 2003; Paquin *et al.*, 2004, and Marschall et al., in prep.); *high-pressure metamorphic rocks* (Klemme *et al.*, 2002; Zack *et al.*, 2003, and this study).

co-workers were (or still are) investigating different rocks related to subduction zone processes for their light element systematics (Fig. 1.3).

1.3. Aim of the study

In this study, high-pressure metamorphic rocks from Syros (Greece) were investigated by petrologic, geochemical and B isotope gechemical means. The geochemical and metamorphic evolutions of the samples are described in this thesis and form a sound basis for the interpretation of abundances, partitioning and budget of Li, Be and B as well as B isotope ratios in the various types of metamorphic rocks. The aim was to better quantify the release of light elements from the subducting slab during progressive subduction and dehydration. High-pressure rocks are ideal objects for the study of trace elements in subduction zones, as they directly represent the subducting slab. The knowledge of partitioning, budget and mobility of elements and their isotopes in these rocks allow for an estimation of the element recycling in subduction zones through the forarc region, the mantle wedge and arc region and to the deeper mantle.

1.4. Structure of this thesis

This thesis is subdivided into 12 chapters, starting with the general introduction presented here. The various chapters contain separate introduction and conclusion sections and should be conclusive without the context of other chapters. They are planned to be published as independent papers. The reader may therefore pick one or more chapters and should be able to follow the conclusions without knowledge of the whole thesis. Literature is considered up to a publication date of November 2004.

Chapter 2 is a detailed description of all analytical methods applied during this study. Furthermore, it includes a manuscript (Marschall & Ludwig, 2004), which presents the analytical improvements of the SIMS for the analysis of B (and Li) at low concentration levels. These improvements were newly developed at the Mineralogisches Institut by Thomas Ludwig (Heidelberg) and me during the course of the PhD project. A second analytical paper (Marschall *et al.*, 2005) is also included, dealing with major and trace-element analysis of high-pressure rocks, using prompt gamma neutron activation (PGNAA). This manuscript resulted from my stay at Budapest Research Center in November 2003 and has been written in cooperation with Zsolt Kasztoszky, Katalin Gméling (both Budapest) and Rainer Altherr (Heidelberg). A detailed description on the modifications of the Heidelberg SIMS, which was performed by Thomas Ludwig in order to enable the precise analysis of B isotope ratios is given in Appendix A.

Chapter 3 provides a brief introduction to the geological setting of Syros and the Cyclades. This chapter is not intended to be a complete review of the geology of the island or of Greece. For more detailed descriptions, the interested reader is referred to the literature in this chapter.

Whole-rock chemistry and major characteristics of the large number of high-pressure metamorphic rocks from Syros are divided into ten different groups on the basis of chemical and petrographic observations. These groups are presented in **Chapter 4**. A detailed petrological discussion of every single sample is given in Appendix B.

Chapter 5 presents a review on the geochemical behaviour of the light elements Li, Be and B and of the B isotope systematics. The emphasis of this review is on processes related to the subduction cycle. Light element abundances and the B isotopic composition of the primitive and depleted mantle are discussed, followed by magmatic and sedimentary rocks of the oceanic crust and the exchange of light elements during hydrothermal metamorphism and weathering at the seafloor. The mobility of the three elements in hydrous fluids at different $P-T$ conditions are reviewed, leading to an overview of the light elements in high-pressure metamorhic

rocks and arc-magmas. The lithium isotope systematics is not discussed here, as no lithium isotope data was obtained on Syros samples in the course of this study.

Whole-rock abundances of light elements in Syros high-pressure metamorphic rocks are discussed in **Chapter 6**. Special emphasis is put on the different processes that led to enrichment and depletion of the three elements during different fluid-rock interaction events, i.e. (i) hydrothermal metamorphism at the ocean floor prior to subduction, (ii) progressive dehydration due to increasing P and T during subduction, and (iii) rehydration during exhumation of the high-pressure unit. In Chapter 6, the effects of rehydration are clearly distinguished from prograde trace element signals.

Partitioning and budget of Li, Be and B in Syros HP rocks are discussed in **Chapter 7**. This chapter includes the results of the detailed in-situ study of light elements by SIMS, and presents the concentrations of all rock-forming silicates (including tourmaline) occurring in the high-pressure rocks. The chapter presents budgets for the three elements, calculated from in-situ and whole-rock analyses. These budgets provide important information on the major hosts of Li, Be and B in greenschists, blueschists, eclogites and other HP-metamorphic rocks. The partitioning of Li, Be and B between the coexisting mineral phases was found to be rather constant and independent from element concentrations. For almost all mineral pairs, apparent partition coefficients vary in a narrow range, while concentrations vary by more than an order of magnitude. Hence, it was possible to establish a set of inter-mineral partition coefficients for Li, Be and B among 15 different high-pressure minerals.

Modelling of Li, Be and B abundances and B isotope ratios in subducting crust is discussed in **Chapter 8**. This chapter contains a model for the quantification of trace element release during dehydration of progressively subducting oceanic crust. The model is based on results from previous work by other authors (e.g. Brenan *et al.*, 1998b; Hervig *et al.*, 2002), and results from studies on natural rocks presented in Chapter 7, combined with phase equilibria calculations performed by Lars Rüpke (Kiel), using the program PerpleX (Conolly, 1990). The results from PerpleX provide modal compositions and H$_2$O contents of progressively metamorphosed rocks along certain P-T paths, calculated from geophysical parameters (Rüpke *et al.*, 2002). The influence of whole-rock chemical composition on the evolution of trace elements and isotopes is demonstrated in this chapter. The presented model is of course afflicted with a number of uncertainties and has to be improved by the input of more sophisticated data. However, in principle it offers the possibility of a quantification of trace element release from the slab in any lithology along any P-T path. Results for the behaviour of Li, Be, B and B isotopes in subducting hydrated MORB are presented in this chapter.

Chapters 9, 10 and 11 discuss the petrographical, chemical and B isotopic char-

acter of tourmaline in Syros high-pressure rocks, and the impact of this boro-silicate on the boron cycle in subduction zones.

Chapter 9 presents boron isotope ratios of detrital and metamorphic tourmaline from metasediments from Syros. The pressure and temperature stability of dravitic tourmaline is very extensive, equivalent to conditions in subducting slabs to depths of ~ 250 km. Therefore, tourmaline growth and stability in subducting metasediments could be responsible for recycling of B with isotopic composition influenced by Earth's surface processes into the deep mantle. Tourmaline can be used for the investigation of the evolution of the B isotopes of a rock during its metamorphic and pre-metamorphic history. In this chapter, it is demonstrated that detrital cores can be distinguished from prograde and retrograde metamorphic growth zones not only by differences in their chemical compositions, but also by their contrasting δ^{11}B values. The δ^{11}B values of prograde and peak metamorphic growth zones of tourmaline will provide information on isotopic composition of the deeply subducting portion of B.

Boron isotope ratios of metasomatic tourmaline, and implications for δ^{11}B values of subduction zone fluids are discussed in **Chapter 10**. High-pressure blocks enclosed in the mélange on the island of Syros are rimmed by reaction zones composed of hydrous minerals in paragenesis with omphacite, albite and dravite. B isotopic composition of tourmaline is uniquely heavy. Tourmaline-bearing blackwalls formed during exhumation of the H*P* mélange by influx of external hydrous fluids, which originated from the subsequent slab that was still subducting as the Syros melange was exhumed. A model providing an explanation of the extremely heavy B isotopic composition of Syros tourmaline will be discussed in this chapter.

Trace element abundances in dravitic tourmaline determined by in-situ methods are presented in **Chapter 11**. Published data on trace element abundances in tourmaline is available from a large number of localities and rock types in literature. However, most of those analyses were performed using bulk powder or solution methods on mineral separates or even whole rocks. Therefore, this data is potentially afflicted with the problem of contamination of the tourmaline by fluid or solid inclusions, which can strongly impact the results of trace element analysis of the tourmaline. This chapter provides high quality in-situ trace element data for Syros tourmaline, determined by Laser-ablation ICP-MS, SIMS and electron microprobe.

Chapter 12 includes a summary of all results and final conclusions of this study.

The **Appendix** includes the description on the technical modifications of the SIMS (Appendix A), a detailed individual description of the investigated samples (Appendix B), tables including whole-rock analyses (Appendix C) and mineral analyses from EPMA (Appendix D) and LA-ICP-MS (Appendix G) and the mathematical formulations used for trace-element and isotope modelling (Appendix H).

Additionally, a list of the Author's publications related to this thesis is given in Appendix I.

2. Analytical methods

2.1. Petrography and sample documentation

Approximately 140 samples of different rock types were collected and studied in thin sections. Out of these, a suite of 43 representative samples were chosen for whole-rock analyses and 22 samples were selected for in-situ analysis by electron probe (EPMA), secondary ion mass spectrometry (SIMS), and laser ablation inductively coupled plasma mass spectrometry (LA-ICP-MS). These samples are characterised by well-preserved mineral assemblages and relatively large grain sizes ($> 100\,\mu$m) for analytical reasons.

Microanalysis by SIMS requires detailed petrographic documentation of the samples. Therefore, optical images were taken from the thin sections using the polarisation microscope in combination with a digital camera, and back-scattered electron (BSE) images were taken using a Leo 440 scanning electron microscope (SEM; Institut für Umweltgeochemie, Heidelberg).

2.2. Electron probe microanalysis

Compositions of mineral phases were determined using a Cameca SX 51 electron microprobe equipped with five wavelength-dispersive spectrometers (Mineralogisches Institut, Heidelberg). Operating conditions were 20 nA beam current and 15 kV acceleration voltage. For analyses of apatite, phengite and paragonite, the electron beam was defocused to 10 μm in order to avoid loss of alkalis and halogens. For analyses of tourmaline it was defocused to 5 μm. For analysed elements, counting times, crystals, standards and detection limits see Table 2.1. PAP correction was applied to the raw data (Pouchou & Pichoir, 1984, 1985).

For tourmaline, a modified matrix correction was applied assuming stoichiometric oxygen and all non-measured components to be B_2O_3. The accuracy of the electron microprobe analyses of tourmaline and the correction procedure was checked by measuring three samples of reference tourmalines (98144: elbaite, 108796: dravite, 112566: schorl; Dyar *et al.* (1998, 2001)). Under the described conditions, analytical errors on all analyses are $\pm 1\,\%$ relative for major elements and $\pm 5\,\%$ relative for minor elements. A detailed description of the applied electron microprobe techniques for tourmaline analysis is given in Kalt *et al.* (2001).

Table 2.1. Analytical setups and parameters used during electron probe microanalysis

Atomic number	Element	Spectral line	Crystal	Analysed minerals	Standard	Concentration in standard	Counting time (s)	Detection limit* at 15 kV/20 nA
9	F	$K\alpha$	PC0	Tur, Ap, Am, Mica	Topaz	20.65 % F	40	0.05 % F
11	Na	$K\alpha$	TAP	all	Albite	8.71 % Na	10	0.04 % Na_2O
12	Mg	$K\alpha$	TAP	all but Tur	MgO	60.31 % Mg	10	0.07 % MgO
		$K\alpha$	TAP	Tur	MgO	60.31 % Mg	20	0.05 % MgO
13	Al	$K\alpha$	TAP	all but Fsp	Al_2O_3	52.93 % Al	10	0.06 % Al_2O_3
		$K\alpha$	TAP	Fsp	Anorthite	19.07 % Al	10	0.04 % Al_2O_3
14	Si	$K\alpha$	TAP	all	Wollastonite	24.08 % Si	10	0.03 % SiO_2
15	P	$K\alpha$	PET	Ap	Apatite	18.43 % P	10	0.18 % P_2O_5
17	Cl	$K\alpha$	PET	Tur, Ap, Am, Mica	Scapolite	1.43 % Cl	30	0.01 % Cl
19	K	$K\alpha$	PET	all	Orthoclase	12.18 % K	10	0.03 % K_2O
20	Ca	$K\alpha$	PET	all but Fsp and Ap	Wollastonite	34.12 % Ca	10	0.04 % CaO
		$K\alpha$	PET	Fsp	Anorthite	13.64 % Ca	10	0.03 % CaO
		$K\alpha$	PET	Ap	Apatite	39.74 % Ca	10	0.05 % CaO
22	Ti	$K\alpha$	PET	all but Tur	TiO_2	59.95 % Ti	10	0.06 % TiO_2
		$K\alpha$	PET	Tur	TiO_2	59.95 % Ti	20	0.04 % TiO_2
24	Cr	$K\alpha$	PET	all but Tur	Cr_2O_3	68.42 % Cr	10	0.07 % Cr_2O_3
		$K\alpha$	PET	Tur	Cr_2O_3	68.42 % Cr	20	0.05 % Cr_2O_3
25	Mn	$K\alpha$	LiF	all but Ap	Rhodonite	33.68 % Mn	10	0.08 % MnO
		$K\alpha$	LiF	Ap	Rhodonite	33.68 % Mn	20	0.06 % MnO
26	Fe	$K\alpha$	LiF	all	Fe_2O_3	69.94 % Fe	10	0.11 % Fe_2O_3
28	Ni	$K\alpha$	LiF	Atg, Am	NiO	78.58 % Ni	30	0.08 % NiO
29	Cu	$K\alpha$	LiF	Chl, Bt	$CuFeS_2$	34.62 % Cu	30	0.09 % CuO
30	Zn	$K\alpha$	LiF	Tur	Gahnite	34.14 % Zn	30	0.09 % ZnO
38	Sr	$L\alpha$	PET	Ep, Ap, Lws	Celestine	47.70 % Sr	20	0.14 % SrO
56	Ba	$L\alpha$	PET	Mica	Baryte	58.84 % Ba	20	0.09 % BaO

*3 RSD (relative standard deviation) of background

14

2.3. Secondary ion mass spectrometry

2.3.1. In-situ analysis of Li, Be and B concentrations

Concentrations of Li, Be and B were measured by secondary ion mass spectrometry (SIMS) with a modified Cameca IMS 3f ion microprobe at the Mineralogisches Institut, Heidelberg, equipped with a primary beam mass filter (Fig. 2.1). Analyses were performed using a $10\,kV/20\,nA$ $^{16}O^-$ primary ion beam. Positive secondary ions were accelerated through a nominal 4.5 kV. The energy window was set to 40 eV. We applied the energy filtering technique with an offset of 75 eV at a mass resolution $m/\Delta m$ (10 %) of ~ 1000 to suppress interfering molecules and to minimise matrix effects (Ottolini $et\ al.$, 1993). For all silicates, secondary ion intensities of ^7Li, ^9Be and ^{11}B were normalised to the count rate of ^{30}Si and calibrated against the NIST SRM 610 glass reference material using the concentrations of Pearce $et\ al.$ (1997). Background near mass 11 was $\leq 10^{-2}$ cps (≤ 1 ng/g). Results are not corrected for background. A 5 min presputtering time was implemented on each spot.
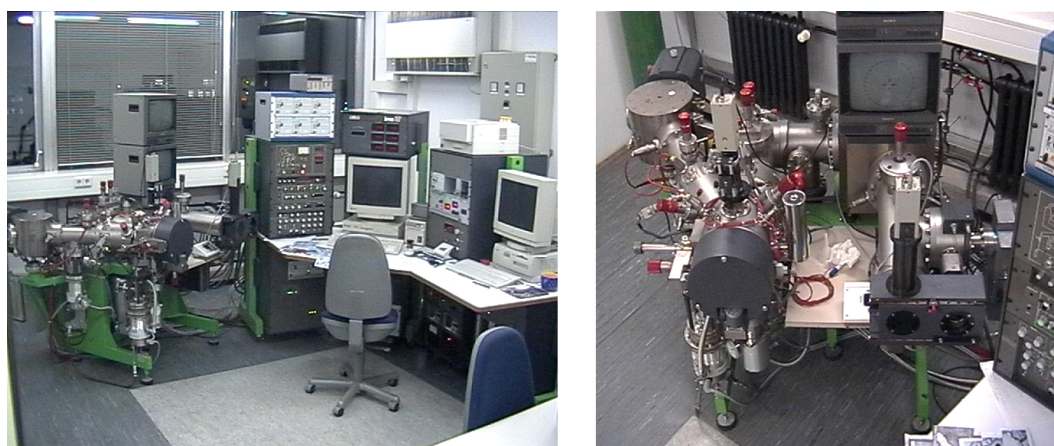
Fig. 2.1. Photographs of secondary ion mass spectrometer Cameca IMS 3f installed at the Mineralogisches Institut, Universität Heidelberg. Left image shows spectrometer and attached computer equipment. Right image shows close-up of spectrometer with oxygen source and primary magnet on the left, sample chamber (round, grey) in the front, electostatic sector, magnetic sector (below monitor) and ion detection device (lower right).

Analyses of trace elements and especially of B at low concentration levels ($<$ $5\,\mu g/g$) are easily influenced by contamination on the surface of thin sections (Shaw $et\ al.$, 1988b; Domanik $et\ al.$, 1993; Marschall & Ludwig, 2004). During this study, contamination was recognised to be a serious problem, as concentrations of B are below $1\,\mu g/g$ in most HP-minerals. Therefore, the developement of a technique to

successfully suppress the effect of contamination on trace element analysis using SIMS was an essential part of this study and is discussed in section 2.4 on "The low-boron contest".

2.3.2. Determination of Li, Be, B and H concentrations in tourmaline

Secondary ions ^{7}Li, ^{9}Be and ^{11}B in tourmaline were collected under an ion-imaged field of 150 μm diameter (Kalt *et al.*, 2001). Secondary ions of ^{1}H were collected by reducing the 25 μm beam spot to an ion-imaged field of 12 μm by using a field aperture in order to minimise the influence of surface contamination (see section on "The Low-Boron contest" and Marschall & Ludwig (2004)). Water contamination was further reduced using a cold-trap cooled with liquid nitrogen attached to the sample chamber of the IMS 3f. The relative ion yields (RIY) for H and B were determined using three different tourmalines as reference material: elbaite (98144), dravite (108796) and schorl (112566). The relative reproducibility (1σ) of the analyses of B was $< 1\%$. For Li and Be the reference material was NIST SRM 610 (Pearce *et al.*, 1997). The relative reproducibility was $< 1\%$ for Li and $< 5\%$ for Be. The accuracy is limited by matrix effects and the uncertainty of the element concentrations in the reference material; the relative uncertainty is estimated to be $< 25\%$ for H, $< 20\%$ for Li and Be and $< 10\%$ for B. Between 10 and 20 Li, Be and B analyses and 5 to 10 H analyses were performed on tourmaline in each sample.

2.4. The Low-Boron Contest: minimising surface contamination and analysing boron concentrations at the ng/g-level by secondary ion mass spectrometry

This section was published in Marschall & Ludwig (2004) in *Mineralogy and Petrology* and resulted from a study performed in cooperation with Thomas Ludwig (Heidelberg). The investigated samples were collected during a contest, which was held at the Mineralogisches Institut, Universität Heidelberg, in order to find a silicate material containing ideally no boron. Samples were donated by people from the institute. The winner of the "Low-Boron Contest" was awarded during a party at the "Tertiärteich".

2.4.1. Introduction

The light element boron has become a useful chemical tracer in both terrestrial and extraterrestrial materials. Despite its growing importance there is still a very restricted number of publications concerning boron in the Earth's mantle or in meteorites. This can be ascribed to the fact that samples – like polished thin sections – are always contaminated with boron on the surface, in cracks and at grain boundaries (Shaw *et al.*, 1988b). This was recognised early (Anders & Ebihara, 1982) and an approximate level of contamination is given in every publication dealing with boron at low concentrations ($<10\,\mu g/g$). These levels depend on the applied techniques of sample preparation and cleaning procedures. Using the SIMS technique, they can vary between $10-50\,ng/g$ (Chaussidon *et al.*, 1997) and $2-5\,\mu g/g$ (Domanik *et al.*, 1993). Recent studies on meteoritic samples report lower contamination levels of $10\,ng/g$ (Kent & Rossman, 2002) or below $10\,ng/g$ (Sugiura *et al.*, 2001). Ottolini (pers. communication, 2003) reported a contamination level of $5\,ng/g$ in peridotite minerals during SIMS analysis. However, a unified method for sample preparation and analyses of boron at low concentrations is still lacking. This has serious implications for the quality of the data, because concentrations of boron in most mantle rocks and meteorites are lower than $1\,\mu g/g$ (Shaw *et al.*, 1988a; Chaussidon & Libourel, 1993). The scope of this work is to compare different analytical setups of SIMS, to present a method to reliably suppress boron contamination and analyse boron concentrations down to the ng/g-level. Furthermore, we wanted to find a silicate material containing ideally no boron at all in order to check the maximum level of contamination.

2.4.2. Surface contamination and its recognition in SIMS analysis

Dynamic SIMS is a method where material is removed from the sample's surface (typical erosion rates: $30\,nm/h$–$10\,\mu m/h$). With a perfectly homogenous and well-defined primary beam at an incidence angle of $0°$ the surface contamination would not contribute to the analytical result once the contamination layer was removed. In reality, the beam current density distribution is not homogeneous, the beam is not perfectly spacially confined, it carries a (hopefully weak) halo of poorly focused neutrals and the incidence angle is $>0°$. Therefore, the bottom of the sputtered crater is not flat, its edge is not perfectly steep and the surface contamination at the crater's edge continues to contribute to the result of the analysis (see Fig. 2.2).

A complete analysis with SIMS usually comprises several acquisition cycles. In each cycle, all unknown isotope(s) (e.g. ^{11}B) and the internal reference isotope (e.g. ^{30}Si) are analysed. Concentrations of the unknown element(s) are calculated by av-
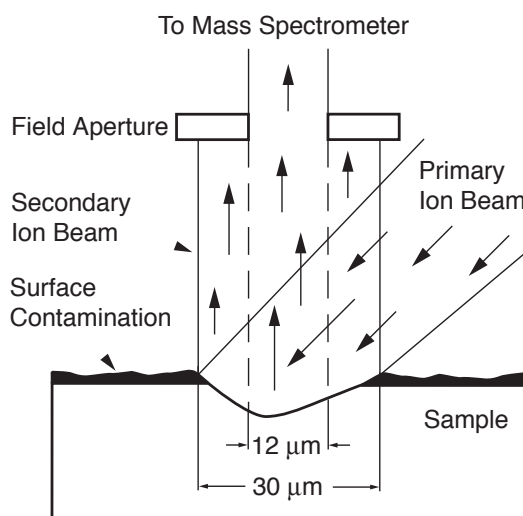
Fig. 2.2. Schematic drawing of the sputtering process. The pure sample (white) is covered with a contamination layer (black). Although most of the contamination is removed during the analysis, there is always some contamination present at the rim of the crater, which will be suppressed by field aperture FA2 (12 μm imaged field). Please note that this is a simplified drawing and that the real layout is more complex.

eraging the results of all measurement cycles, while the (relative) standard deviation of the mean is a measure for the precision of the analysis. Measurements influenced by surface contamination show decreasing unknown-to-reference ratios (or apparent element concentrations) in the course of the analysis. In case of contamination these ratios can decrease by more than one order of magnitude within the first 100 s. This has already been recognised by other authors for B, K and Na (Sugiura *et al.*, 2001; Müller *et al.*, 2003) as an indication of contamination, prohibiting a quantification of these trace elements at low concentration levels.

Quantitative analysis of trace elements with SIMS is usually done with an electron multiplier detector working in a pulse counting mode. In this mode at low concentrations (low count rates), where other sources of random error such as primary beam instability or instability of the mass spectrometer's magnet are negligible, the precision of the result will be dominated by the counting statistics of the trace element.

For the average unknown-to-reference ratio Poisson statistics predict a relative standard error $(1RSD_{mean})$ of $1/\sqrt{N}$, where N is the total number of trace element ions counted. While a stable signal related to the true sample concentration will give a standard error close to $1/\sqrt{N}$, the decreasing count rates of an element in case of contamination will give a $1RSD_{mean} \gg 1/\sqrt{N}$. Thus a much higher standard error

than predicted may be used as an indication of surface contamination.

Another method of recognising contamination is by analysing the same sample with a varying primary beam current I_p. Given the primary beam is always focused, a lower beam current results in a smaller spot. Moreover, since the contribution of the contaminated crater's edge to the total flow of secondary ions increases with a decreasing spot size, the apparent concentration will rise with a falling primary current when contamination is predominant. On clean samples (relative to the trace element concentration), the measured concentration will be independent from I_p.

The last method of evaluating the contamination level is measuring a sample containing extremely low concentrations (ideally zero) of the element of interest, which will be more sensitive towards contamination. The widely used NIST SRM glasses are not suitable for this purpose, as the concentration of boron in SRM 616, nominally containing the lowest trace element concentrations (200 ng/g) of all SRM 61x glasses, is still too high.

2.4.3. Reduction of contamination in sample preparation and of its effect during analysis

Lubricants and cooling liquids ordinarily used in saws and polishing machines for preparation of thin sections may contain several percent of boric acid. These liquids were replaced by pure glycol in our preparation lab. Prior to SIMS analyses, the samples are coated with carbon and investigated by electron microprobe. After microprobe analyses the carbon coating is removed with γ-alumina powder and distilled water. In order to remove boron contamination from the surface and cracks, the samples are first cleaned with acetone, then with distilled water (simple cleaning) and eventually in an ultrasonic cleaner using ultrapure water from a Milli-Q water purification system (Millipore). Ultrasonic cleaning with fresh ultrapure water is performed twice for $\sim$15 min (ultrapure cleaning).

In a simplified model, the contaminated sample may be considered a pure sample covered with a contamination layer. Analysing the pure sample then requires acquiring a depth profile. In depth-profiling, it is common practice to mechanically limit the secondary beam in order to overcome the described negative effects of the crater edge (Benninghoven *et al.*, 1987) as shown schematically in Fig. 2.2. Using an imaged field smaller than the spot size, secondary ions coming from the crater's edge will be suppressed. On Cameca ims 3(4, 5, 6)f instruments this is accomplished by selecting a field aperture of appropriate size in combination with the magnification factor of the selected transfer lens. Typically, depth profiling is performed by rastering the primary beam over an area much larger than the area covered by the imaged field, but this reduces the effective count rates and thus rises the detection

limit. Therefore we chose a setup where the imaged field is only slightly smaller (factor $\sim$0.5) than the primary beam spot, which also allows us to analyse with a lateral resolution $\sim$30 µm. While a small field aperture has the advantage of reducing the contamination signal it also has some disadvantages: the count rate will be lower, resulting in a higher detection limit and the reproducibility will be worse because the beam has to be perfectly centred with respect to the field aperture for each analysis. At low concentration levels both disadvantages are outweighed by the reduced influence of surface contamination. The field aperture was not found to influence significantly the relative ion yield (RIY) of boron, which was 0.55 ± 0.01 for $^{11}\text{B}/^{30}\text{Si}$.

2.4.4. SIMS setup

The boron concentrations presented in Table 2.2 were measured by secondary ion mass spectrometry (SIMS) with a modified Cameca ims 3f ion microprobe (equipped with a primary beam mass filter) at Heidelberg. Analyses were performed using a 10 keV/20 nA $^{16}\text{O}^-$ primary ion beam with a diameter of $\sim$30 µm. Positive secondary ions were accelerated to a nominal energy of 4.5 keV. The mass spectrometer's energy window was set to 40 eV and we employed the energy filtering technique with an offset of 75 eV at a mass resolution m/Δm (10 %) of $\sim$1000 to suppress interfering molecules and to minimise matrix effects (Ottolini *et al.*, 1993). The ims 3f has three field apertures to limit the field imaged by the secondary beam. The influence of contamination was reduced by using the intermediate field aperture FA2 (750 µm) which reduces the imaged field to $\sim$12 µm in the 25 µm imaged field mode. Secondary ion intensities of ^{11}B were normalised to the count rate of ^{30}Si and calibrated against the NIST SRM 610 standard reference material (356.4 µg/g boron; Pearce *et al.* (1997)) for all silicates. One analysis comprised 10 cycles with an integration time of 16 s/*cycle* for boron. Pre-sputtering on every spot lasted $\sim$6 min and analysing time took another 4 min, resulting in $\sim$10 min total analysis time. The mass spectrometer's and the counting system's background near mass 11 u was determined in several analyses with an integration time of 1500 s each (50 cycles; 30 s/*cycle*) at mass 10.8 u with the same setup and Herasil 102 as sample. The background count rate was 0.021 cps and was subtracted from the boron count rates for each cycle of an analysis prior to calculating the mean value and the standard error.

At 20 nA primary current and for the SRM 610, the setup described had an absolute boron sensitivity of 7.2 cps/(µg/g) and an apparent background concentration of 2.9 ng/g (Note that it does not make sense to define a sensitivity normalized to the primary current, because the secondary intensity does not increase further with in-

Table 2.2. Investigated samples with SiO_2 content and measured boron concentrations

Sample	Type	Rock	Locality/Origin	Chemistry	SiO_2 (wt %)	B (ng/g)	2 RSD_{mean} (%)
Meteoritic and mantle minerals							
RFX1	Forsterite	CV3 meteorite	Allende	Mg_2SiO_4	42.8	2.6	208
B5	Olivine	Lherzolite	Eifel/D	$(Mg,Fe)_2SiO_4$	41.2	83.3	19.8
	Amphibole			Mg-Hastingsite	43.3	157	20.2
	Enstatite			$(Mg,Fe)SiO_3$	56.5	78.3	14.1
	Diopside			$Ca(Mg,Fe)Si_2O_6$	52.8	114	13.3
31-C	Enstatite	Harzburgite	Jizan/SA	$(Mg,Fe)SiO_3$	56.7	3.6	127
	Olivine			$(Mg,Fe)_2SiO_4$	41.2	7.8	83.3
1960/5 [1]	Pyrope	Grt-Lherzolite	Marsabit/K	$(Mg,Ca,Fe)_3Al_2Si_3O_{12}$	42.8	6.9	90.4
	Diopside			$Ca(Mg,Fe,Al)Si_2O_6$	53.6	57.5	39.9
	Olivine			$(Mg,Fe)_2SiO_4$	40.8	44.0	41.1
	Enstatite			$(Mg,Fe)SiO_3$	56.1	50.7	24.4
Ch-88-1[2]	Olivine	Dunite	Reunion/F	$(Mg,Fe)_2SiO_4$	38.9	65.9	34.0
ILR-84-4 [2]	Olivine	Dunite	Reunion/F	$(Mg,Fe)_2SiO_4$	40.5	34.4	29.7
Z31/1 [3]	Enstatite	Orthopyroxenite	Zabargad/EG	$(Mg,Fe,Al)SiO_3$	54.7	97.5	19.9
Z104 [3]	Olivine	Olivinite	Zabargad/EG	$(Mg,Fe)_2SiO_4$	41.5	4708	2.0
AA-3P5 [4]	Pyrope	Grt-Lherzolite	Alpe Arami/CH	$(Mg,Ca,Fe)_3Al_2Si_3O_{12}$	41.7	7.8	52.8
84-32	Enstatite	Spl-Lherzolite	Harrat Uwayrid/SA	$(Mg,Fe)SiO_3$	54.8	14.3	55.7
Magmatic minerals							
B3	Acmite	Phonolite	Gran Canaria/E	$NaFeSi_2O_6$	51.9	1249	2.3
B7	Olivine	Basaltic tuff	Hawai'i/USA	$(Mg,Fe)_2SiO_4$	40.9	15.6	69.2
B8	Olivine	Basalt	Hawai'i/USA	$(Mg,Fe)_2SiO_4$	40.8	14.3	59.2
Ro36 [5]	Enstatite	Norite	Romsaas/N	$(Mg,Fe)SiO_3$	55.3	664	8.4
B4 [6]	Beryl	Vein	Adun-Tschilon/RU	$Be_3Al_2Si_6O_{18}$	68.0	117	10.5

Table 2.2. (continued)

Sample	Type	Rock	Locality/Origin	Chemistry	SiO_2 (wt %)	B (ng/g)	2 RSD_{mean} (%)
Metamorphic minerals							
30589-2 [7]	Kyanite	Granulite	Schwarzwald/D	Al_2SiO_5	37.2	28.5	52.1
	Almandine			$(Fe,Ca,Mg)_3Al_2Si_3O_{12}$	36.8	37.2	30.1
SA161	Quartz	Granulite	Granulitgebirge/D	SiO_2	100.0	351	10.0
	Almandine			$(Fe,Ca,Mg)_3Al_2Si_3O_{12}$	36.8	96.6	14.5
ZEH1 [8]	Quartz	Amphibolite	Schwarzwald/D	SiO_2	100.0	206	14.8
B2	Kyanite	Ky-Qtz vein	Prilep/MK	Al_2SiO_5	37.2	17.1	46.1
SY425D	Quartz	Omp-Qtz vein	Syros/GR	SiO_2	100.0	20.3	27.4
80-3 [9]	Quartz	Phe-Qtz vein	Trescolmen/CH	SiO_2	100.0	191	11.0
SY309A	Titanite	Blueschist	Syros/GR	$CaTiSiO_5$	30.2	3.2	171
SY304	Chloritoid	Blueschist	Syros/GR	$(Fe,Mg)_2Al_4Si_{10}(OH)_4$	24.1	6.4	54.4
	Almandine			$(Fe,Ca,Mg)_3Al_2Si_3O_{12}$	37.0	17.6	41.7
B9	Quartz	single crystal	Herkimer/USA	SiO_2	100.0	2.1	119
Synthetic materials							
B1C	Glass	Synth.	Min HD	Nd-Cr-Al-Si-O	27.5	64.1	28.8
B1D	Glass	Synth.	Min HD	Nd-Cr-Al-Si-O	27.3	92.9	27.0
RP1	Glass	Synth.	Min HD	Fe-Ca-Mg-Si-O	47.4	5927	2.0
B11	Forsterite	Synth.	Min HD	Mg_2SiO_4	43.5	6.7	79.0
Herasil 102	Glass	Synth.	Heraeus	SiO_2	100.0	1.0	212
W1	Glass	Synth.	–	SiO_2	100.0	27.4	28.9
W2	Glass	Synth.	–	SiO_2	100.0	29.0	15.8
HD2	Glass	Synth.	Min HD	Ca-Al-Ti-Si-O	37.5	1252	4.1

RSD_{mean} = relative standard deviation of the mean. *Synth.* = synthetic materials. *Min HD* = synthesised at the Mineralogisches Institut Heidelberg. Localities: D = Germany, F = France, GR = Greece, SA = Saudi Arabia, K = Kenya, MK = Macedonia, RU = Russia, CH = Switzerland, N = Norway, E = Spain, EG = Egypt. References for samples: [1] Olker (2001), [2] Staudacher *et al.* (1990), [3] Kurat *et al.* (1993), [4] Paquin *et al.* (2004), [5] Meyer (1989), [6] Kirsten (1964), [7] Marschall *et al.* (2003c), [8] Hepp (2003), [9] Zack *et al.* (2002a).

Table 2.3. Comparison of apparent boron concentrations in Herasil 102 for different virtual analytical setups and cleaning procedures. Data is extracted from the analyses shown in Fig. 2.4

Shown in figure…	Cleaning procedure	Field aperture	Presputtering time (s)	No. of cycles	Integration time (s)	^{11}B/^{30}Si	Apparent Conc. (ng/g)	2 RSD$_{mean}$ (%)	χ_C (ng/g)	χ_D (ng/g)
Virtual setup 1: Very short setup without presputtering (initial contamination)										
2.4a	simple	FA1	<10	1	30	$1.8 \cdot 10^{-4}$	2283	–	1.6	6.7
2.4b	simple	FA2	<10	1	30	$4.9 \cdot 10^{-5}$	635	–	6.0	25
2.4c	ultrapure	FA1	<10	1	30	$8.2 \cdot 10^{-5}$	1053	–	1.6	6.7
2.4d	ultrapure	FA2	<10	1	30	$1.9 \cdot 10^{-5}$	248	–	6.0	25
Virtual setup 2: Normal setup with presputtering for routine work										
2.4a	simple	FA1	400	10	300	$6.7 \cdot 10^{-7}$	8.6	31.9	0.51	1.4
2.4b	simple	FA2	400	10	300	$1.8 \cdot 10^{-7}$	2.4	96.5	1.9	5.1
2.4c	ultrapure	FA1	400	10	300	$3.0 \cdot 10^{-7}$	3.9	28.7	0.51	1.4
2.4d	ultrapure	FA2	400	10	300	$1.4 \cdot 10^{-7}$	1.7	102	1.9	5.1
Virtual setup 3: Setup with long presputtering and long integration time										
2.4a	simple	FA1	2000	50	1500	$1.1 \cdot 10^{-7}$	1.4	26.4	0.23	0.53
2.4b	simple	FA2	2000	50	1500	$1.2 \cdot 10^{-7}$	1.6	77.9	0.9	2.0
2.4c	ultrapure	FA1	2000	50	1500	$8.0 \cdot 10^{-8}$	1.0	33.9	0.23	0.53
2.4d	ultrapure	FA2	2000	50	1500	$8.4 \cdot 10^{-8}$	1.1	93.0	0.9	2.0

RSD$_{mean}$ = relative standard deviation of the mean, χ_C = critical level, χ_D = minimum detectable concentration.

creasing primary beam current once the primary beam spot is larger than the imaged field). The detection limit for boron is calculated using the "working" expressions for radioactivity from Currie (1968). For an integration time of 160 s the average background signal is $\mu_B = 160\,\text{s}\cdot 0.021\,\text{cps} = 3.36$ counts. Since the background signal was analysed separately, not in paired observations, the detection limits are calculated for a well-known blank. For the setup described, the critical value of the net signal is $S_C = 1.64\sqrt{\mu_B} \approx 3.0$ counts and the minimum detectable value is $S_D = 2.71 + 3.29\sqrt{\mu_B} \approx 8.7$ counts, hence for boron concentration the critical value χ_C is 2.6 ng/g and the minimum detectable value χ_D is 7.6 ng/g.

For the data presented in Fig. 2.4 and Table 2.3, some of the analyses were done with the large field aperture FA1 (1.8 mm), resulting in an imaged field of $\sim 32\,\mu\text{m}$, and the same primary beam current (20 nA). Because of the larger field aperture this setup has a higher absolute boron sensitivity of 26.7 cps/µg/g) and while the background count rate remains unchanged, the boron background concentration is lower at 0.8 ng/g. The detection limits for these analyses are presented together with the data.

2.4.5. Experimental results and discussion

We collected a broad variety of 40 different natural and synthetic silicate materials in order to select a material that could be suitable to test the boron contamination level. All analyses were performed after applying the ultrapure cleaning procedure and using the field aperture FA2. The results of all samples are listed in Table 2.2. In some samples, less than 10 ng/g boron was measured and the lowest concentration obtained was 1.0 ng/g in the synthetic SiO_2 glass Herasil 102, which is well below the critical value χ_D for the setup used. Uncertainties, given as relative 2-sigma standard deviation of the mean (standard error), are dominated by counting statistics. The high relative standard deviations (>100 %) for concentrations <10 ng/g are due to the fact that the net boron signal was near or below the critical value S_C.

The relation between measured boron concentration and the relative standard error for all samples listed in Table 2.2 is plotted in Fig. 2.3. Note that here the data is not corrected for background, because the poisson statistics are valid for the gross signal including the background signal. Additionally, in Fig. 2.3 the predicted standard error, valid for an absolute boron sensitivity of 7.2 cps/(µg/g) and an integration time of 160 s, is plotted. The predicted and the actual standard errors are in good agreement, giving no indication of contamination. An example for analyses of a heavily contaminated sample is also shown in Fig. 2.3. For the analyses shown, this sample (Grt SY304) was not prepared using glycol, was not cleaned using the ultrapure procedure and the field aperture was FA1. For these analyses the predicted
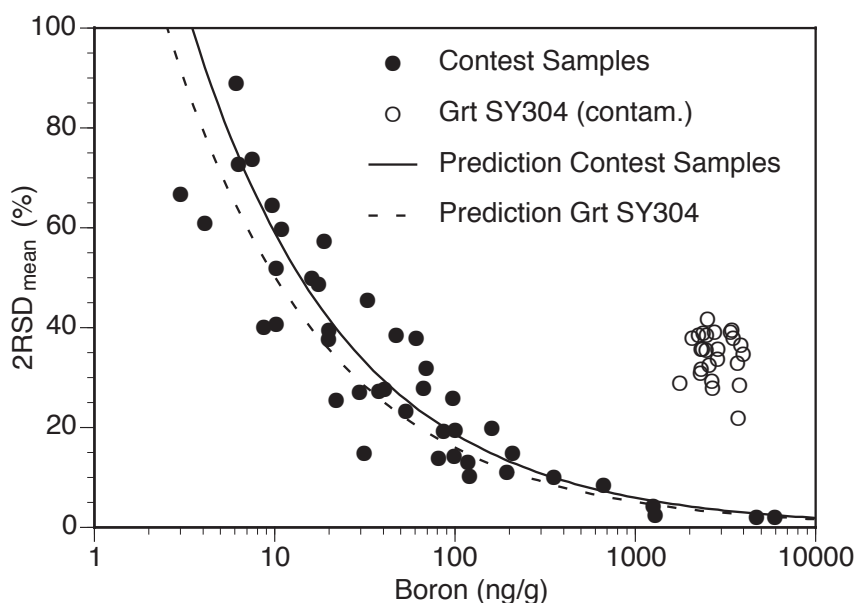
Fig. 2.3. Comparison of the relative standard error $2RSD_{mean}$ of real analyses (Contest Samples, Grt SY304) with the error predicted for the setups used. For the Contest Samples, predicted and measured error are in good agreement whereas for the contaminated sample SY304, the real error is much larger than the predicted

standard error is plotted as well. The difference between prediction and reality is obvious and provides a strong indication of contamination.

To check the efficacy of our analytical method with respect to B contamination, the sample with the lowest boron concentration (Herasil 102) was used. Analyses comprising 100 acquisition cycles with an integration time of 30 s for ^{11}B and 1 s for ^{30}Si per cycle were performed. Prior to each analysis the sample was sputtered for a few seconds – long enough to remove most of the gold layer and to achieve reasonably stable count rates for ^{30}Si. These measurements were performed with field apertures FA1 and FA2 before (simple cleaning) and after the sample was cleaned with ultrapure water (ultrapure cleaning). The results of these analyses are presented in Fig. 2.4, where the ^{11}B$/^{30}$Si ratio is plotted against sputtering time. It is evident that both the ultrapure cleaning and the use of field aperture FA2 make the B count rate decrease more rapidly towards the true value.

By extracting certain acquisition cycles (e.g. cycles No. 11 to 20), virtual analytical setups were simulated. These virtual analyses with their presputtering times, integration times and detection limits χ_C and χ_D are presented in Table 2.3. The detection limits are calculated for the absolute sensitivities (depending on the field

aperture chosen) as given in the analytical setup section and the integration time of each virtual setup.

Virtual setup 1 serves to demonstrate the initial level of boron contamination. Although Herasil 102 is a "perfect" sample (e.g. no pores, no cracks, no inclusions, size > 1 mm, perfectly polished) the surface contamination leads to an apparent boron concentration of 2.3 µg/g for the simple cleaning procedure and 1.1 µg/g for the ultrapure cleaning procedure when analysed with field aperture FA1. Even without any presputtering, the apparent boron concentrations are much lower with field aperture FA2, which proves the efficacy of our method. It is important to note that even a "perfect" sample surface is not safe from contamination.

Virtual setup 2 with a presputtering time of 400 second and an integration time of 300 second represents a typical setup for routine analysis of low boron concentrations. With simple cleaning and field aperture FA1 we get an apparent boron concentration of 8.6 ng/g, which is reduced to 3.9 ng/g by the ultrapure cleaning procedure and to 2.4 ng/g by applying the field aperture FA2. Combining both methods results in 1.7 ng/g in a total analysis time of ~ 12 min per spot. The boron concentration of Herasil 102 is obviously below χ_C and χ_D of this virtual setup, which achieves a contamination level clearly below its detection limits.

Virtual setup 3 is a setup with a presputtering time of 2000 s, an integration time of 1500 s and a total analysis time of ~ 1 h, resulting in very low detection limits. For this virtual setup the size of the field aperture does not make a significant difference, because after 2000 s the contaminated rim of the sputtered crater has moved outside the imaged field of FA1 (32 µm). The ultrapure cleaning procedure still gives boron concentrations lower by ~ 0.5 ng/g. The measured concentration of ~ 1 ng/g is at or above the detection limits. This qualifies Herasil 102 as an excellent sample to test B contamination in SIMS analysis.

2.4.6. Implications for other elements

Our results and the results of other authors show that in-situ analysis of B is impeded by surface contamination, which makes it obligatory to use very elaborate cleaning procedures and analytical setups. This may not be restricted to boron, but is most likely also true for other trace elements. Müller *et al.* (2003) observed surface contamination of Na, K and Fe during trace element analyses of quartz. During our study, we also measured Li and Be. Be did not show any sign of contamination and concentrations in some samples (Grt, Ol, Qtz) were less than 1 ng/g. Lithium, however, was found to be influenced by contamination. This was demonstrated for the minerals garnet and chloritoid in sample SY304, which were analysed with different primary beam currents, after different cleaning procedures and with field
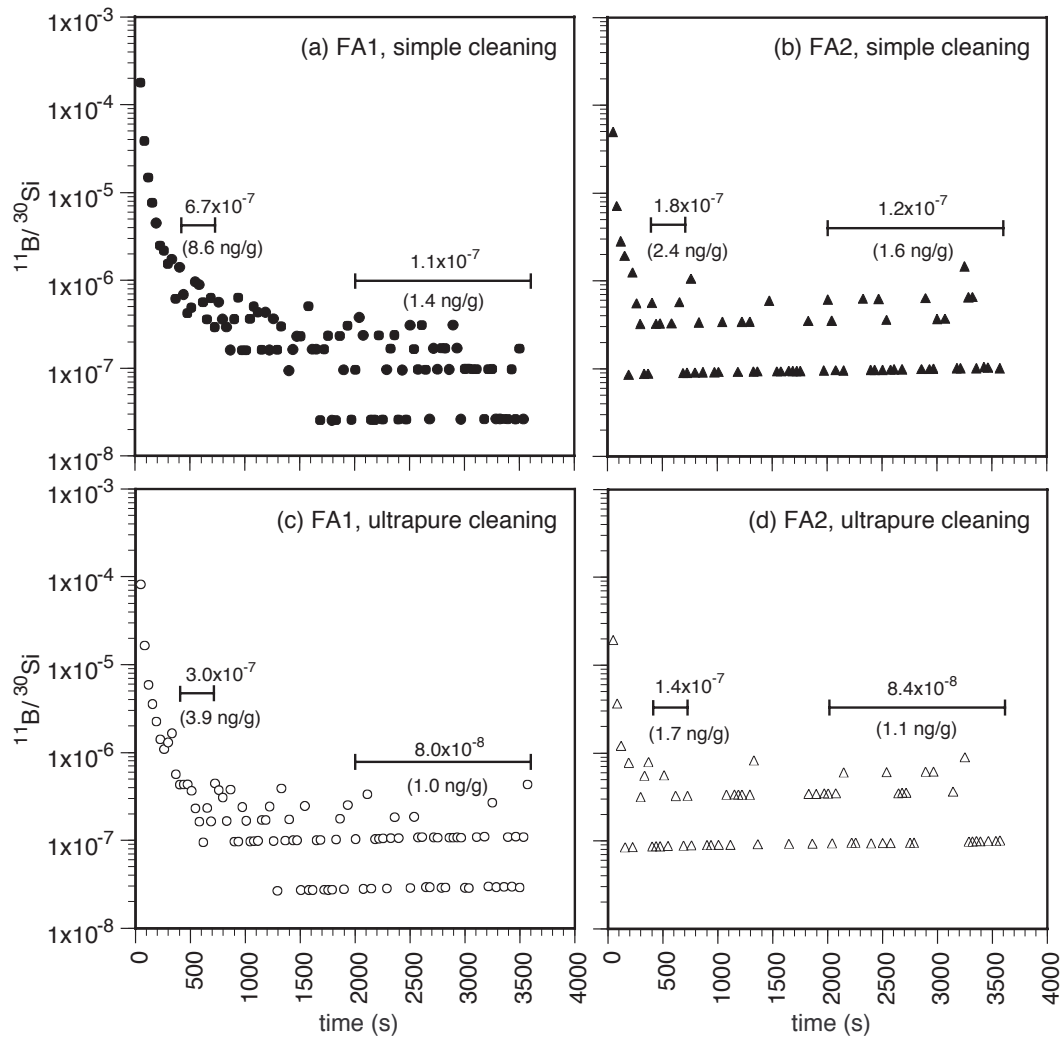
Fig. 2.4. Comparison of different analytical setups and cleaning procedures. **a** imaged field 32 μm (FA1) and simple cleaning procedure, **b** imaged field 12 μm (FA2) and simple cleaning procedure, **c** imaged field 32 μm (FA1) and ultrapure cleaning procedure and **d** imaged field 12 μm (FA2) and ultrapure cleaning procedure. All diagrams show the $^{11}B/^{30}Si$ ratio as a function of sputtering time for the sample Herasil 102. The bars denote the results of the virtual setups described in the text and shown in Table 2.3.
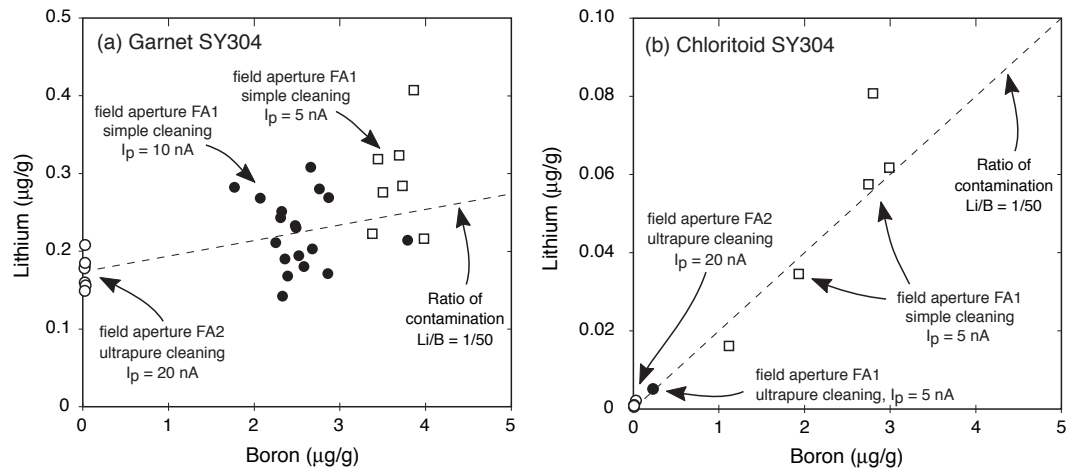
**Fig. 2.5.** Li vs B concentrations of **a** garnet and **b** chloritoid in sample SY304, analysed with different setups and different cleaning procedures. The dotted line shows the approximate Li/B contamination ratio of 1/50 in both samples (Note the different scales for Li). I_p = primary beam current.

aperture FA1 as well as with FA2. The diagrams in Fig. 2.5 show that with field aperture FA1 and the simple cleaning procedure, the contamination of Li on the sample results in a contribution of contamination to the analysed value in the range of 20 to 200 ng/g. Cleaning the thin-section in the ultrasonic cleaner with ultrapure water reduces contamination level to ~ 5 ng/g. An average Li/B contamination ratio of $\sim 1/50$ can be calculated from both garnet and chloritoid in sample SY304. Therefore, in our lab, contamination is 50 times more significant for B than for Li.

2.4.7. Conclusions

Combining an efficient cleaning procedure with a very basic depth-profiling method enables us to reduce boron contamination to levels close to or even below the detection limit of ~ 2 ng/g (critical level χ_C), with a lateral resolution of $\sim 30 \,\mu$m in a rather short time of ~ 12 min per spot. Other methods like pre-sputtering or rastering a larger area prior to analysis may reduce contamination to a level of ~ 10 ng/g (Kent & Rossman, 2002), but require more time and suffer from poor lateral resolution.

The SiO$_2$ glass Herasil 102 from Heraeus Quarzglas GmbH, Germany, is an appropriate material for checking the level of boron contamination of an in-situ analytical method like SIMS. Herasil 102 is an ultrapure, homogeneous material that is available in large quantities. Natural minerals, like olivine, ortho- and clinopyrox-

ene, garnet and quartz are not viable for testing the contamination level, as boron abundances in these minerals vary significantly among different samples and often reach levels of >100 ng/g.

Results for Li, B, Na, K and Fe (this study and Müller *et al.* (2003)) suggest that contamination is a serious problem during in-situ analysis of various trace elements and must be controlled during analysis of materials showing very low concentrations, such as quartz, mantle rocks and meteorites. Contamination of boron, however, is much more significant than e.g. Li contamination.

2.5. In-situ determination of boron isotope ratios by SIMS

Boron isotope ratios of tourmaline were determined using the Cameca IMS 3f ion microprobe at the Mineralogisches Institut, Heidelberg. The machine has been used at the Institut for several years to successfully analyse natural and synthetic samples for concentrations of predominantly light elements, transition metals, and rare earth elements. However, the analysis of isotope ratios required significant changes of both software and hardware of the SIMS. These improvements were developed and installed on the SIMS by Thomas Ludwig (Heidelberg). Most important were changes in the electronic control device of the magnet which allow for faster switches between different masses and better stability of the magnet. The changes are described in detail in appendix A on page 287.

Primary ion beam was $^{16}O^-$ accelerated to 10 keV with a beam current of 1 nA, resulting in count rates for ^{11}B of $\sim 2 \times 10^5 \, s^{-1}$ and $\sim 5 \times 10^4 \, s^{-1}$ for ^{10}B on tourmaline, collected by a single electron multiplier. Diameter of the 1 nA spot was $\leq 5 \, \mu m$. The energy window was set to 50 eV and no offset was applied. 50 cycles were measured on each analysis spot with counting times of 3.307 s and 1.660 s on ^{10}B and ^{11}B, respectively. Presputtering lasted for 5 min and settling time between two different masses was 200 ms, resulting in total analysis time for one spot of approximately 10 min. Internal precision of a single analysis was $\leq 1\%o$ (2σ). Boron isotopic compositions of samples are reported in delta notation ($\delta^{11}B$ in $\%o$) relative to the SRM 951 accepted value (Catanzaro *et al.*, 1970). Instrumental mass fractionation was corrected by using three samples of proposed reference tourmaline (98114: elbaite, 108796: dravite, 112566: schörl; Leeman & Tonarini (2001)). Correction factors α_{inst} for the different tourmalines were 1.0473, 1.0481 and 1.0474 for 98114, 108796 and 112566, respectively, resulting in a mean α_{inst} of 1.0476. Reproducibility of measured isotope ratios during the analytical session (eight days) was $\pm 0.5\%o$.

Boron isotopic compositions of phengite in four different samples with large

($> 200\,\mu m$) phengite grains were measured with a beam current of 30 nA, resulting in a beam diameter of $\sim 40\,\mu m$ and count rates of $\sim 2 \times 10^4\,s^{-1}$ and $\sim 5 \times 10^3\,s^{-1}$ for ^{11}B and ^{10}B, respectively. Boron concentration of phengite in Syros HP-metamorphic rocks is ~ 50 to $150\,\mu g/g$. Offset, energy window, counting and presputtering times were identical to the tourmaline setup. Only the number of acquisition cycles was increased to 200, in order to reach an internal precision of $\leq 2\%o$ (2σ), which increased the total analysis time to $\sim 25\,min$ per spot. Instrumental mass fractionation was corrected by using phengite sample Phe-80-3 provided by T. Zack (Heidelberg), which has a ^{11}B/^{10}B ratio of 3.9879 (δ^{11}B $= -13.77\%o$), determined by S. Tonarini (Pisa) by P-TIMS (see below). The correction factor α_{inst} for Phe-80-3 was 1.0489 to 1.0510 (March to September 2003). SIMS measurements of other materials in the concentration range of $200 - 500\,\mu g/g$ resulted in correction factors of 1.0488 for rhyolitic glass Rocc-3 (Tonarini $et\ al.$, 2003) and 1.0482 for obsidian glass B6 (Gonfiantini $et\ al.$, 2003), when normalised to the P-TIMS measurements of S. Tonarini (Pisa). The results for these three standardisation materials are in good agreement with each other. The determined correction factors are approximately 0.020 higher than the values determined for tourmaline. This discrepancy is due to a dependency of the measured B isotope ratio on the primary beam current (Ludwig $et\ al.$, 2004).

The NIST SRM 610 standard glass is not applicable as a reference material for in-situ B isotope analyses with SIMS, as the secondary ion signals are strongly decreasing at the beginning of the measurements and the measured isotope ratio is not constant (T. Ludwig, personal communication).

Dead time correction Accurate determination of the dead time is essential for the accuracy of measurements of isotope ratios, especially at high concentrations of the element of interest in the sample. The dead time of the counting system used for secondary ion detection in the IMS 3f in Heidelberg was determined by Thomas Ludwig (Heidelberg) by measuring the ^{28}Si/^{30}Si ratio of a pure synthetic SiO_2 glass with different primary beam currents. The count rate of the more abundant isotope ^{28}Si (92.2%) is by far more affected by the dead time than ^{30}Si (3.1%). Correction for an increasing dead time ($0 - 50\,ns$) therefore results in increasing apparent ^{28}Si/^{30}Si ratios. An increase of the primary beam current produces higher secondary ion count rates, with an isotope ratio that is stronger affected by the dead time (Fig. 2.6). For the true dead time, the correction must result in ^{28}Si/^{30}Si ratios which are identical for all primary beam currents. In Fig. 2.6 the ^{28}Si/^{30}Si ratios are plotted as a function of dead time for four different primary beam currents. The intersection of the curves yields the true dead time of $38 \pm 2\,ns$. The uncertainty of
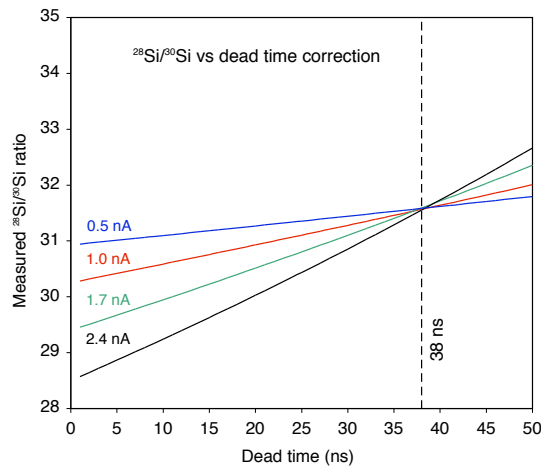
Fig. 2.6. Determination of dead time of the electron multiplier. ^{28}Si/^{30}Si ratio of a pure synthetic SiO$_2$ glass was measured with different primary beam currents, resulting in different secondary ion count rates. The count rate of the more abundant isotope ^{28}Si (92.2 %) is by far more affected by the dead time than ^{30}Si (3.1 %). Correction for different dead times ($0 - 50$ ns) therefore results in curves with a positive slope in the displayed diagram. The slope is increasing with increasing primary beam current. The intersection of the curves gives the true dead time (38 ± 2 ns).

± 2 ns introduces an uncertainty of ± 0.3‰ to the accuracy of the determined δ^{11}B value for a count rate of 2×10^5 cps. The value increases to ± 1.6‰ for a count rate of 1×10^6 cps. For analyses of tourmaline, the primary beam current was 1 nA, in order to keep the count rate of ^{11}B at 2×10^5 cps.

B isotope analysis of tourmaline by P-TIMS During analysis of tourmaline samples by SIMS, traverses through the different grains were measured, in order to check for possible intra-grain variations in δ^{11}B. Between 10 and 50 boron isotope analyses were performed in each sample. SIMS analysis of our samples revealed very high ^{11}B/^{10}B ratios in contrast to the reference tourmalines which range from -12.5‰ to -6.6‰ (Leeman & Tonarini, 2001). In order to ensure consistency, three tourmaline samples from Syros were analysed by positive thermal ion mass spectrometry (P-TIMS). The P-TIMS measurements were performed by Sonia Tonarini at the Istituto di Geocronologia e Geochimica, C.N.R in Pisa, following the method of Tonarini *et al.* (1997). Correlation between SIMS and P-TIMS results for three Syros samples and the three reference tourmalines demonstrate good correlation between the two methods (Fig. 2.7) used in the two laboratories, which proves the instrumental mass fractionation of SIMS to be independent from ^{11}B/^{10}B ratios in the range of δ^{11}B in natural tourmaline.
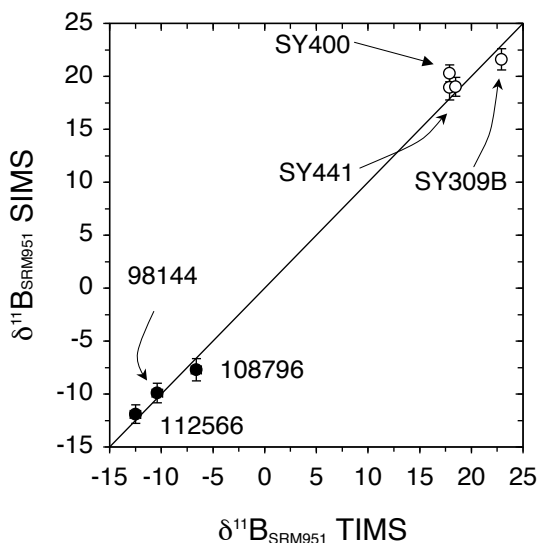
Fig. 2.7. Comparison of B isotope ratios of tourmaline determined by SIMS and TIMS, expressed in the delta notation relative to NIST SRM 951 (Catanzaro *et al.*, 1970). Open circles represent Syros samples, filled circles are standard tourmalines (Leeman & Tonarini, 2001). For sample SY400 core and rim values differ by $\sim 1.3\%_o$, which is displayed by the two data points. Error bars show 2σ errors of SIMS ($\sim 1\%_o$). Errors for TIMS ($\sim 0.5\%_o$) are within the size of the symbols.

2.6. Laser-ablation-ICP-MS

The Laser Ablation ICP-MS technique was used for in-situ analysis of concentrations of several trace elements in several minerals of twelve selected samples. They were performed by myself at the University of Bristol in cooperation with Bruce Paterson (Bristol). The LA-ICP-MS system consisted of a LUV266X laser (New Wave Research Inc., USA) linked to a PlasmaQuad3 with a supplement rotary pump attached to its interface (the so-called S-option, Thermo Elemental, UK). For each analysis 37 to 42 isotopes were repetitively measured in the mass spectrometer for a total time of 90 s. The first 15 seconds of acquisition were used to measure the gas blank followed by about 75 seconds of acquiring a mixture of gases and ablated materials. The gas mixture used during each analysis consisted of pure helium (Grade 5.9 from Air Products, UK), which was used in the sample cell and later mixed downstream with pure argon (Grade 5 from BOC, UK) using a Y-connector located 15 cm away from the sample cell. Tuning of the plasma was set to suppress molecular and double-charged ions. Both ThO/Th ratios (masses 248 and 232) and La^{2+}/La ratios (masses 69.5 and 139) were < 0.010.

The laser beam was condensed with a beam expander and shaped with an ad-
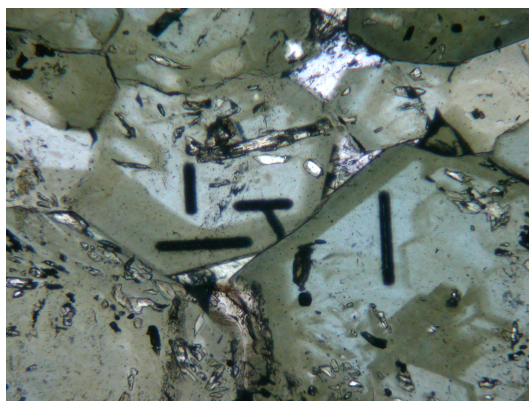
Fig. 2.8. Tracks in tourmaline in a thin section produced by Laser-Ablation during analyses. Maximal length of tracks (black lines) is $100\,\mu m$. In this case three analyses were performed in Tur cores and one in a Tur rim.

justable iris aperture in order to produce a crater size of $\sim 20\,\mu m$ on the sample surface. Paths of $100\,\mu m$ were driven during sample ablation (Fig. 2.8) with a speed of $10\,\mu m/s$ and the laser pulsed at $10\,Hz$. The internal isotope standards used were ^{29}Si for silicates and ^{49}Ti for rutile. Concentrations were calibrated using the NIST SRM 610 glass with the published values from Pearce *et al.* (1997) and controlled by measuring four points on the SRM 612 glass after every tenth analysis point on the samples. Analysed minerals beside tourmaline were garnet, omphacite, glaucophane, phengite, chlorite, epidote, alanite, rutile, titanite, albite, lawsonite and talc. It was not possible to analyse apatite because of its bad absorption for the $266\,nm$ laser (the laser evaporated the epoxy underneath the apatite, which caused the grains to flake off after a few seconds). Analysed elements included Ca, Ga, REE, LILE, HFSE, transition metals, U, Th and Pb.

2.7. Raman spectroscopy

Raman measurements were completed by Lutz Nasdala (Mainz), using a Jobin Yvon (Horiba) LabRam HR 800 at the Institut für Geowissenschaften, Mainz. This notch filter-based Raman system was equipped with an Olympus BX 40 optical microscope, a grating with 1800 grooves per mm, and Si-based, Peltier-cooled charge-coupled device (CCD) detector. Spectra were excited with the $632.8\,nm$ emission of a He-Ne laser (3 mW). The wavenumber accuracy was better than $1\,cm^{-1}$ and the spectral resolution was $0.4\,cm^{-1}$. With the Olympus 100 x objective (numerical aperture 0.9), the lateral resolution was better than $1.5\,\mu m$ and the depth resolution

was $\sim 2\,\mu m$.

Micro-raman spectroscopy was used to distinguish andradite inclusions in almandine garnet in sample SY323 from other Ca-Fe silicates, like vesuvianite.

2.8. Mössbauer spectroscopy

Mössbauer spectroscopy of amphibole was performed by Mario Koch (Heidelberg) at the Mineralogisches Institut, Universität Heidelberg, on Ca-amphibole from sample SY325 in order to check the applicability of the calculation of the oxidation state of Fe, described by Schumacher (1997) in Leake *et al.* (1997). 95 mg of a clean mineral separate of Ca-amphibole (equivalent to 5.5 mg Fe) were mixed $\sim 5:1$ with sugar to avoid preferred orientation, loaded in a 12 mm acryl sample holder, and introduced into a Mössbauer spectrometer working at room temperature (293 K) and in constant acceleration mode with a ~ 50 mCi ^{57}Co source in a Rh matrix. The velocity ramp was ± 5 mm/s. The spectrum was collected over 512 channels calibrated with respect to α-Fe metal, and fitted using the NORMOS software programmes (R. A. Brand, Wissenschaftliche Elektronik GmbH, Germany). The spectrum fitted to one doublet for ferric Fe and two doublets for ferrous Fe. Results revealed $37.5 \pm 2.0\%$ of the Fe being trivalent. The calculation after Schumacher (1997) resulted in a value of $37.0 \pm 4.4\%$. Therefore, the Fe oxidation state of Ca-amphibole calculated by the method of Schumacher (1997) agrees with the results from Mössbauer spectroscopy. For glaucophane, the differences in Fe oxidation state are not significant between the different calculation methods. The calculation of glaucophane formulas was also completed by the method of Schumacher (1997), but not tested by Mössbauer spectroscopy.

Tourmaline from sample SY309 was investigated by Mössbauer spectroscopy at the Bayerisches Geoinstitut (Bayreuth) by Cathrine McCammon, and revealed a $Fe^{3+}/\Sigma Fe$ fraction of $30 \pm 3\%$. The results of Mössbauer spectroscopy and crystal structure determination of tourmaline from sample SY309 are not included in this thesis, but were published in Marschall *et al.* (2004c).

2.9. X-Ray diffraction

A powdered whole-rock aliquot of sample SY347, an almost pure serpentinite, was investigated by x-ray powder diffraction spectrometry (XRD), in order to identify the polymorph(s) of serpentine in the sample (i.e. antigorite and/or chrysotile). Analyses were performed by Stefan Prowatke at the Mineralogisches Institut, Universität Heidelberg, using a Philips PW3710 with monochromatic CuKα radiation,

with the X-ray generator running at 40 kV/30 nA. $2\text{-}\theta$ angle from 10 to 70° was analysed for 0.5 s at each step of 0.02° $2\text{-}\theta$. The resulting XRD pattern was compared with the certified reflexes for the different serpentine polymorphs collected in the JCPDS data base. All reflexes determined for sample SY347 could be related to antigorite, whereas the reflexes of chrysotile were not found in the pattern. It is therefore concluded that sample SY347 consists of at least 95 % antigorite.

2.10. X-ray fluorescence analysis and loss on ignition

To avoid any modification of the primary rock chemistry by late-stage alteration effects, samples were cut with a rock saw to get clean blocks devoid of weathered surfaces and/or crack fillings. 50 to 500 g of each sample were treated in a jaw crusher and powdered in an agate mill. The homogenised rock powders were split into several aliquots that were used for chemical analysis by different techniques.

For XRF analyses, powder tablets of 25 samples were prepared at the Geologisches Institut, Universität Trier, Germany, and analysed by Hans-Peter Meyer (Heidelberg) for 18 different trace elements (including Mn and Cr) and major components TiO_2 and Fe_2O_3 using a SIEMENS SRS3000 X-ray spectrometer at Trier, equipped with a Rh-tube operated at 60 kV/50 mA. Major element compositions (SiO_2, TiO_2, Al_2O_3, Fe_2O_3, MnO, MgO, CaO, Na_2O, K_2O, P_2O_5) of these 25 samples were determined at the Mineralogisches Institut, Universität Tübingen (Germany) by Heinrich Taubald (Tübingen), using fused glass tablets in a SIEMENS SRS303 X-ray spectrometer. The remaining 18 samples were sent to the Institut für Mineralogie und Geochemie, Universität zu Köln (Germany) and analysed by Eberhard Seidel (Köln) for major elements in glass tablets and 13 trace elements in powder press tablets, using a PHILIPS PW2400 X-ray spectrometer. Precision of XRF analyses was $\sim$ 0.5 to 1 % for major elements and between 5 and 10 % for trace elements. Determination of loss on ignition (LOI) of each sample was performed using 1 to 1.5 g of powdered samples weighed in ceramic beakers. These were heated at 900 °C for 30 min, weighed again and subsequently heated for another 60 min at the same temperature and weighed for a third time. Results were corrected for oxidation of FeO to Fe_2O_3, assuming 50 % of the Fe being trivalent in the metamorphic rocks.

2.11. Solution-ICP-MS and -ICP-OES

2.11.1. Preparation of solutions by acid digestion

High-pressure metamorphic rocks frequently contain minor and accessory minerals, that are not easy to dissolve by conventional acid digestion procedures. To increase reactivity, solutions were prepared using a high-temperature microwave autoclave (ultraCLAVE II by MLS GmbH, Germany) at the Institut für Umweltgeochemie, Universität Heidelberg, in cooperation with Michael Krachler and Bernd Kober. The autoclave was operated at 240 °C and 5 to 7 MPa for about 2 h. 200 mg of each powdered sample together with 5 mL HNO_3 (70 %) and 1 mL of HF (48 %) (both acids purified by distillation) were put into a teflon tube located inside a steel pressure vessel. The solutions were transfered to 50 mL teflon beakers and controlled for potential residues of undissolved minerals or precipitated fluorides under a binocular. The beakers were than placed on a hotplate (100 °C) to evaporate the hydrofluoric acid. Teflon beakers containing the dry preparates were transferred to the University of Bristol large-scale geochemical facility to perform ICP-MS and ICP-AES measurements. In Bristol, 19 samples, which showed residual grains (zircon, titanite, tourmaline or opaques) under the binocular, were again digested in a mixture of 3 mL HF (48 %) and 5 mL HNO_3 (70 %) on a hotplate. This second digestion dissolved all residual grains. However, 9 samples showed precipitation of white salts (propably Ca-fluoride). These 9 samples were treated with $HClO_4$ (70 %) on the hotplate overnight. Six of the samples still showed white precipitates in the beakers, which could not be removed. Results of these six samples are therefore doubtful and the impact on certain elements is discussed separately. Finally, all samples were evaporated to incipient dryness, dissolved in 1 % HNO_3, and diluted to 500:1 of the original rocks' concentrations by adding distilled water. For mass calibration the solutions were spiked to contain 10 ng/g of In, Bi, Re and Ru as internal standards. Four rock standards (BHVO2, BEN, GA and Bristol in-house standard 3570) and three repeats of Syros samples were treated in the same way, in order to check for reproducibility.

There are three major problems arising from multi-acid digestion of metamorphic rocks: (i) accessory minerals like zircon, titanite, rutile, tourmaline, allanite and opaques that may control a significant portion of certain trace elements may resist the digestion and are therefore lost from the solutions, (ii) volatile elements and complexes may be lost during evaporation of hydrofluoric acid on the hotplate, and (iii) insoluble salts and complexes may be precipitated from the solutions during digestion. In order to control the qualtiy of the solutions used for ICP analyses, results for several elements were compared to results from XRF. This comparison is a

reliable test for a number of critical elements and provides quantitative information on loss of elements from the solutions by one or several of the above-mentioned mechanisms. Results are discussed below.

2.11.2. Solution ICP-MS measurements at the University of Bristol

ICP-MS analyses were performed on a VG Elemental Plasma Quad II mass spectrometer by Chung Choi and Tony Kemp (Bristol). Solution ICP-MS was used to determine the abundances of Sc, V, Y, Nb, Ta, Zr, Hf, the rare earth elements (REE) and U, Th and Pb. Precision of solution ICP-MS analyses was between 5 and 10 %.

Niobium, Tantalum and Lead.   Nb and Pb are difficult to analyse by XRF at concentrations below $\sim 10\,\mu g/g$. The comparison of ICP-MS results with results from XRF therefore shows a large spread in the range of $1 - 10\,\mu g/g$ for both elements (Fig. 2.9 a, b). However, at higher concentrations the results of both methods demonstrate much better agreement, except for the samples that showed salt precipitation during acid digestion (filled squares in Fig. 2.9), which are depleted in Nb. Consequently, Pb and Nb data from ICP-MS were used, except for Nb of the five problematic samples, for which XRF data were preferred. Ta data of the five problematic samples were rejected, while for all other samples ICP-MS data were taken. The Nb concentrations of the solutions are probably not affected by undissolved accessories, as Nb and Ta in H*P*-rocks are hosted almost exclusively in rutile (Zack *et al.*, 2002b), which was readily dissolved (see section on solution ICP-OES and Fig. 2.10).

Yttrium and the REE.   Rare earth elements were measured by ICP-MS, while Nd, Sm and Gd were also analysed by PGNAA (see section 2.12 on PGNAA, page 43). Additionally Y, which is chemically very similar to the heavy rare earth elements (HREE) was analysed by XRF. Comparison of ICP-MS with XRF results for Y show very good agreement (better than $\pm 10\,\%$ for most samples), except for the samples that showed salt precipitation during acid digestion (Fig. 2.9 c). For Gd the comparison of ICP-MS with PGNAA also reveals very good agreement between the two methods, with the same exceptions of the samples that showed salt precipitation. The results for Nd and Sm of PGNAA had to be corrected by factors of ~ 0.7 and ~ 1.4, respectively, and are therefore not very reliable for an evaluation of the ICP-MS data. However, a comparison of Nd and Sm values of the problematic samples with the corrected PGNAA data show a strong depletion of these elements in the solutions by a factor of ~ 2, consistent with the depletions in Y and Gd. For Y,
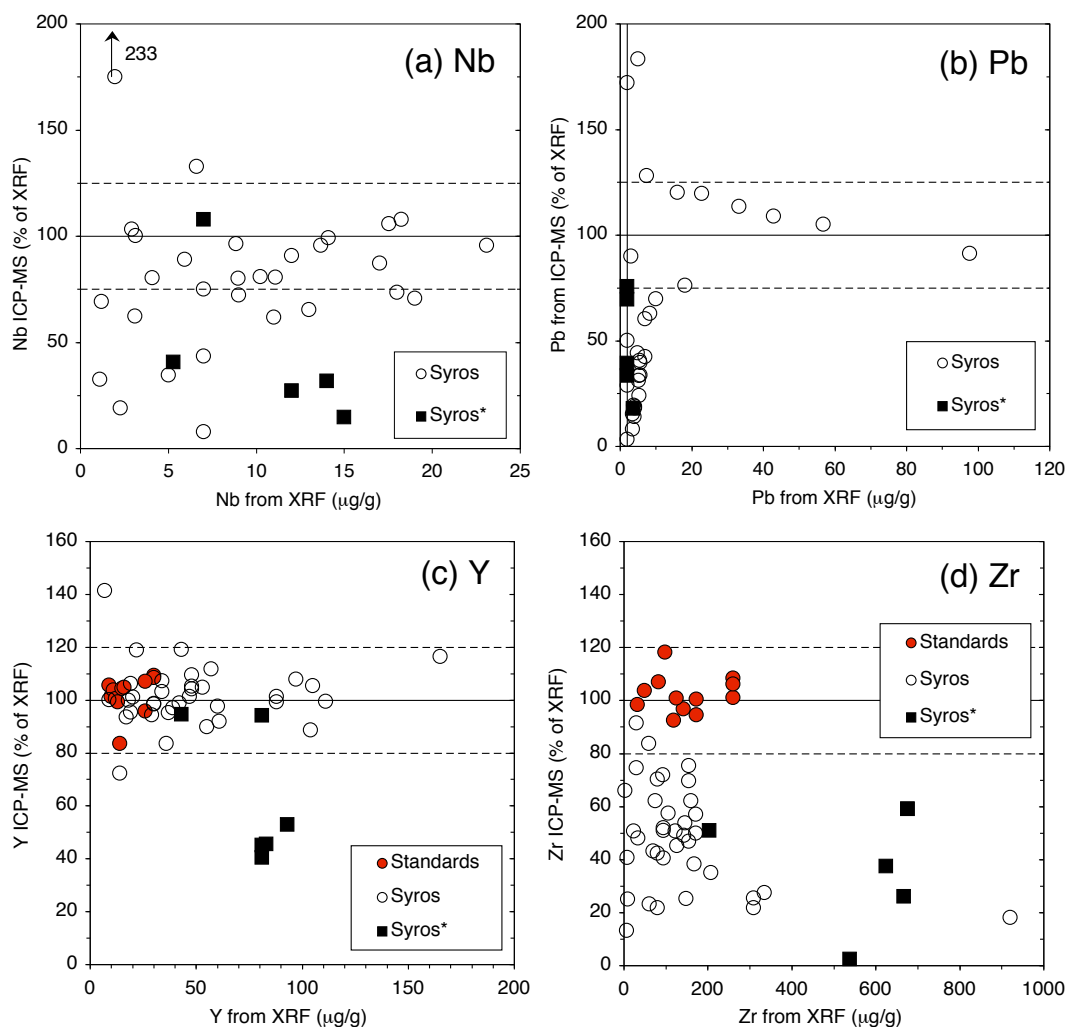
Fig. 2.9. Comparison of solution-ICP-MS data with data from XRF for **a** Nb, **b** Pb, **c** Y and **d** Zr. ICP-MS data are shown in percent of the respective values obtained by XRF. Open circles are Syros samples that dissolved completely during acid digestion, filled squares are Syros samples that showed precipitation of white salts during acid digestion (Syros*), and red circles are standards that were measured parallel to samples. Vertical black line is detection limit of XRF.

the data from XRF were taken, while REE data from ICP-MS were used. For the problematic samples, the REE data from ICP-MS had to be corrected by a factor of ~ 2, based on the discrepancy in Nd, Sm, Gd and Y. Note that this correction procedure possibly decreases the accuracy of REE data for those samples.

Zirconium and Hafnium. Comparison of ICP-MS with XRF results for Zr (Fig. 2.9 d) show that Zr was significantly depleted in the solutions for the whole range of concentrations and for almost all samples. This is most likely due to the high resistance of zircon against hydrofluoric acid. Zircon containing $\sim 60 - 65\%$ ZrO_2 and $\sim 1 - 3\%$ HfO_2 (Tomaschek *et al.*, 2003) is probably the dominant mineral to control the Zr and Hf budgets of the rocks. Therefore, the ICP-MS data for these elements were rejected. For Zr, the XRF data were used, whereas data for Hf are not available. Zircon may also be enriched in Y and the HREEs, but these elements are largely controlled by rock-forming minerals like garnet (Zack *et al.*, 2002a). Therefore, the impact of zircon on Y and HREE in the solutions is insignificant, as is proved by the Y budget (Fig. 2.9 c).

Vanadium, Scandium and Thorium. V and Sc were measured by ICP-MS, PG-NAA and XRF. For V, the three methods show very good agreement for all samples, including those that showed salt precipitation during digestion. The concentrations of Sc are relatively low ($< 50\,\mu g/g$ for most samples), inhibiting analyses by PG-NAA and XRF, since the Sc abundances are below the detection limits of those methods in many samples. ICP-MS data for Sc are available for all samples and agree with the results of the two other methods for samples with high concentrations. Th was analysed by XRF in only 14 samples, three of which were samples that showed salt precipitation during acid digestion. As concentrations are relatively low ($< 5\,\mu g/g$ for most samples), precision of XRF is poor. However, results of ICP-MS and XRF agree well. Even the three problematic samples show no depletion of Th in the solutions. For this study, V data from XRF and Sc and Th data from ICP-MS were used.

2.11.3. Solution ICP-OES measurements at the University of Bristol

The solutions of all samples prepared at the University of Bristol (see section 2.11.1) were used to measure concentrations of Li and Ti by ICP-OES, using a Jobin Yvon Ultima 2 Sequential Spectrometer, operated by Chung Choi (University of Bristol). Ti was measured to compare the concentrations in the solutions with XRF data on the rock powders in order to check for rutile or titanite grains, which might have
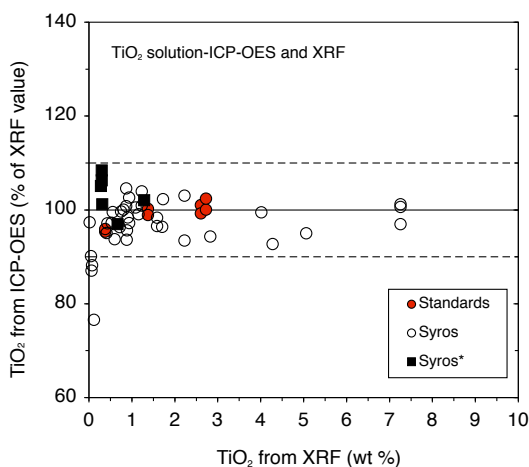
Fig. 2.10. Comparison of solution-ICP-OES data with data from XRF for TiO_2. Open circles are Syros samples that dissolved completely during acid digestion, filled squares are Syros samples that showed precipitation of white salts during acid digestion (Syros*), and red circles are reference materials that were measured parallel to the samples.

resisted acid digestion. Ti was analysed on the 334.941 nm line and calibrated on international rock standards. Li was analysed using the 670.784 nm line and calibrated with 9 international silicate reference materials, ranging from 8.5 to 147 μg/g Li, showing a linear correlation ($R^2 = 0.99954$) of the calibration with recommended values. Several international rock reference materials were measured parallel to the samples. The results for standards are displayed in Fig. 2.10 for Ti and Fig. 2.11 for Li.

Titanium.   Ti data from XRF and ICP-OES agree within $\pm 5\,\%$ for most samples, including the problematic ones that formed white precipitates during acid digestion (Fig. 2.10). These results prove that Ti-minerals (rutile, titanite) were quantitatively dissolved during acid digestion in all samples. This observation is important, as the Ti-minerals are important hosts for a number of trace elements, including Nb, Ta, Th, U, REE (see Zack *et al.*, 2002b, and results from LA-ICP-MS in this study).

2.11.4. Solution ICP-OES measurements by Cavendish (Vancouver, Canada)

Rock powders of 43 samples from Syros together with four international reference materials (ACE, DR-N, BR, W1) and four duplicate samples were sent to Cavendish Analytical Laboratory Ltd., Canada for analysis of Li and Be by ICP-OES. Cavendish used a multi-acid digestion method with a 2:1:1 mixture of HF
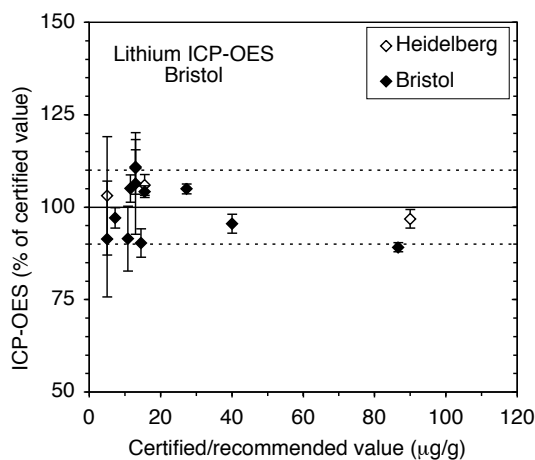
Fig. 2.11. International reference materials measured parallel to the samples during ICP-OES analyses of Li at the University of Bristol plottet vs certified values given in Govindaraju (1994). Filled diamonds: 11 reference materials routinely prepared at Bristol; Open diamonds: 4 reference materials digested at Heidelberg parallel to the samples.

(48 %), HNO_3 (68 %) and $HClO_4$ (70 %) to solubilise the samples. Analysis were performed on a Varian Vista Pro Axial View ICP-OES instrument, equipped with a CCD detector with a high resolution polychromator for "simultaneous" detection of 75 elements. Li concentrations had to be corrected for Ca concentrations of the samples using recommended Li values of the reference materials (Fig. 2.12), because Ca has a strong influence on the background of the ICP-OES signal, which was not considered appropriately by Cavendish.

Lithium. A comparison of the two datasets determined for Li by ICP-OES from Cavendish Analytical Laboratory Ltd. and from the University of Bristol, respectively, is displayed in Fig. 2.13. For most of the samples the (corrected) values from Cavendish agree with the data from Bristol within ±20 %. However, a general trend can be observed for Bristol results overestimating the (corrected) results from Cavendish at low concentrations and underestimating them at high concentrations. This is possibly an effect of the linear correction of the Li data for Ca from Cavendish. Apart from that, the samples that showed salt precipitation during acid digestion in Bristol display a strong depletion in Li in the Bristol data. Therefore, Li must have been quantitatively removed from the solutions by the precipitating salts. Consequently, corrected Li data from Cavendish were used for the samples that showed salt precipitation, whereas Li data determined in Bristol were used for all other samples.

41
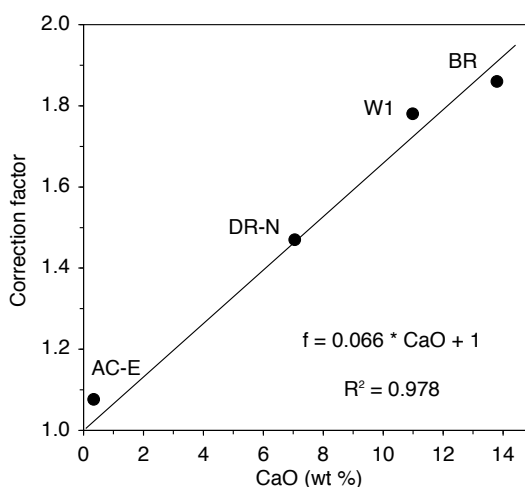
Fig. 2.12. Calibration curve for Li correction for concentrations determined by Cavendish (ICP-OES data). Four international reference materials with different concentrations of CaO and Li were measured parallel to Syros samples and used for correction of measured Li concentrations. The correction factor was calculated by dividing the measured values by the certified values given in Govindaraju (1994).
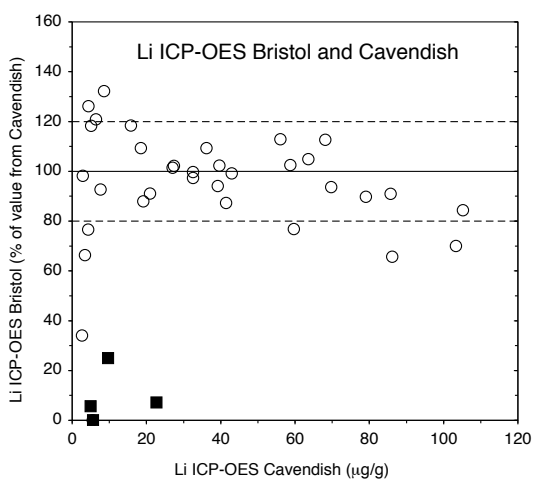
Fig. 2.13. Comparison of solution-ICP-OES data for Li determined at the University of Bristol with the respective data determined by Cavendish (corrected for interfering Ca; see Fig. 2.12) Open circles are Syros samples completely dissolved during acid digestion, filled squares are Syros samples that showed precipitation of white salts during acid digestion.
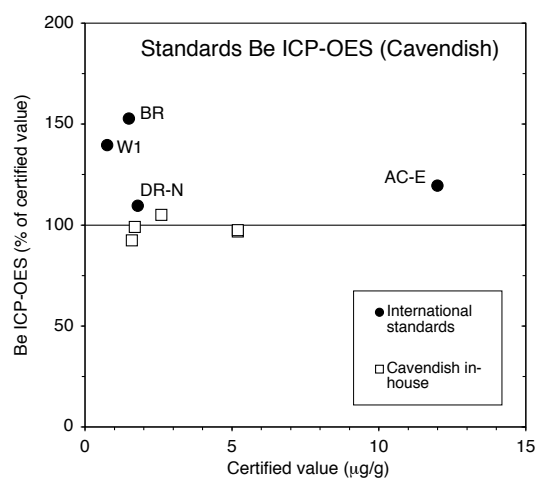
Fig. 2.14. Be concentrations of reference materials determined by Cavendish in comparison to the certified values. Filled squares are international reference materials, open squares are Cavendish in-house standards.

Beryllium. Measured Be concentrations of the reference materials were $\sim 10 - 50\%$ too high (Fig. 2.14) with no correlation to the major element composition. Possibly, there occurred a combination of an increasing background caused by high Ca-concentrations (as was the case for Li) and spectral interferences of e.g. Fe, Ce, V or Th on the Be peak. It is not possible to complete a precise correction of the Be data on the basis of the results provided by Cavendish. Therefore all results for Be had to be corrected by the factor of 0.78 (arythmetic mean of the four standards).

2.12. Prompt Gamma Neutron Activation Analysis

This section is published in Marschall *et al.* (2005) in the *Journal of Radioanalytical and Nuclear Chemistry* and resulted from a study performed in cooperation with Zsolt Kasztovszky (Budapest), Katalin Gméling (Budapest) and Rainer Altherr (Heidelberg).

2.12.1. Introduction

A large part of modern geoscientific research centers on the exact nature of the processes that have led to the chemical differentiation of planet Earth. Apart from the early formation of the metallic core, the ongoing differentiation of the silicate Earth into a Mg-rich mantle and a highly heterogeneous continental crust can only be

understood within the framework of plate tectonics and mantle convection. The formation of new oceanic lithosphere involves the chemical differentiation of mantle material into a basaltic crust and a depleted mantle residue by (i) upward convection of mantle material, (ii) decompression melting, (iii) melt extraction and (iv) crystallization. During cooling and on its way from the oceanic spreading center to a subduction zone, the newly formed lithospheric plate reacts with sea water and becomes covered by sedimentary material. In subduction zones, oceanic lithosphere consisting of water-rich sediments, hydrated magmatic rocks and partially hydrated peridotite is dragged down into the mantle. The concomitant increase in pressure (P) and temperature (T) causes significant changes in the mineralogical and chemical compositions of the subducted materials. Numerous mineral reactions lead to the formation of high-P minerals and rocks. Many of these reactions are dehydration reactions and locally dehydration melting may occur. The aqueous fluids and hydrous melts that are expelled from the subducting slab rise into overlying rock piles and may eventually reach the hot core of the mantle wedge of the hanging plate. At high $P - T$, water can dissolve significant amounts of silicate materials, and the miscibility gap between aqueous solutions and hydrous melts will decrease with increasing P and T (Shen & Keppler, 1997; Bureau & Keppler, 1999; Stalder *et al.*, 1998, 2000, 2001). Addition of H_2O to the hot core of the mantle wedge may cause partial melting leading to subduction-related, often explosive volcanism. Geochemical studies have revealed a strong enrichment of 'water-soluble' elements in subduction-related volcanic rocks as compared to normal oceanic basalts (Ishikawa *et al.*, 2001; Straub & Layne, 2003; Gméling *et al.*, 2005) which is generally explained by transport of these elements in aqueous solutions or hydrous melts from the slab into the hot region of melt formation within the mantle wedge.

Another source of information on element cycling in subduction zones is provided by high-P metamorphic rocks sampled from the subducting plate. Most of these rocks naturally disappear to inaccessible depths within the mantle. In some cases, however, minor volumes of subducted rocks are detached from the slab and are tectonically transported back to the Earth's surface where they can be sampled. The chemical compositions of these rocks, in comparison to their non-subducted equivalents that can be sampled from the present-day oceanic lithosphere offer important information on the nature of chemical transfer within subduction zones.

Major element analyses of rocks are commonly performed by X-ray fluorescence (XRF) analysis where mixtures of rock powder ($< 60\,\mu m$) and a Li-borate flux are fused at $\sim 1250\,^\circ C$ and the melts are quenched to glass tablets that serve as targets for primary X-rays. A number of trace elements are also routinely measured by XRF using tablets pressed from rock powder mixed with minor amounts of an organic binder. Apart from possible problems caused by peak overlap, disadvantages

of XRF methods include (i) eventual loss of volatile components, such as alkali metals during melting, (ii) effects resulting from heterogeneities of powder tablets, and (iii) low sensitivity of XRF for elements with low atomic mass numbers. Hydrogen, lithium and beryllium, for example, cannot be analysed by XRF. Analysis of boron is very difficult and not possible at concentrations below the percent level.

During the last decade, significant progress has been made in the development of inductively-coupled plasma mass spectrometry (ICP-MS) and optical emission spectrometry (ICP-OES). These methods allow rapid analysis of almost all elements. However, the major problem with ICP methods is that samples have to be introduced into the plasma as solutions. Therefore, rock samples have to be dissolved using strong acids which cannot be introduced into the ICP spectrometer without damaging it. So the acids have to be evaporated which may imply a loss of some volatile elements such as silicon, chlorine, and boron. Another problem is caused by accessory mineral grains that resist the dissolution process and contain significant amounts of 'trace' elements. In this case, the analysed solutions are depleted in specific trace elements compared to the bulk rocks. Basaltic volcanic rocks usually do not contain such accessory mineral phases and are therefore readily analysed by solution-ICP methods. High-P metamorphic rocks, however, are fraught with accessory minerals and represent a challenge for successful solution.

Neutron activation-based radio-analytical methods, such as prompt gamma neutron activation analysis (PGNAA) may help to solve many of the analytical problems described above. For analysis with a neutron beam, the samples do not require special treatment, since they can be measured as solid blocks or rock powders. Another advantage of PGNAA is its high sensitivity for the elements boron, chlorine and hydrogen. The analysis of H provides direct information on the degree of dehydration of high-P rocks, while B and Cl are elements of growing importance in subduction-zone geochemistry (Philippot *et al.*, 1998; Brenan *et al.*, 1998b; Ishikawa *et al.*, 2001; Straub & Layne, 2003; Bebout & Nakamura, 2003; Paquin *et al.*, 2004; Gméling *et al.*, 2005).

This section presents the results of a feasibility study on the perspectives of applying PGNAA for the chemical characterization of high-P metamorphic and other crystalline rocks. 41 samples of various high-P rocks from Syros (Greece) were studied by PGNAA using the cold neutron beam at the Budapest Neutron Centre (BNC). The late Gábor Molnár initiated the application of the Budapest PGNAA facility to geological samples. I remember the encouraging discussions during my stay at BNC.

The data are compared with data obtained on the same samples by other techniques such as XRF and solution ICP-MS. In addition, 11 samples of granitoid rocks from various Aegean islands (Greece) were investigated by PGNAA. Major

and trace element data on these latter samples were obtained by XRF and instrumental neutron activation (INA) analyses at the Institute of Mineralogy and Geochemistry, University of Karlsruhe (Altherr & Siebel, 2002).

2.12.2. Experimental techniques

To avoid any modification of the primary rock chemistry by late-stage alteration effects, samples were cut with a rock saw to get clean blocks devoid of weathered surfaces and/or crack fillings. 50 to 500 g of each sample were treated in a jaw crusher and powdered in an agate mill. The homogenised rock powders were split into several aliquots that were used for chemical analysis by different techniques. For analysis of the 11 granitoid samples, aliquots from the same rock powders used by Altherr & Siebel (2002) were taken.

The PGNAA facility installed at the Budapest 10 MW research reactor is equipped with a cold neutron source (20 K). Thermal equivalent neutron flux at the target position is $\sim 5 \cdot 10^7 \, \mathrm{cm}^{-2}\mathrm{s}^{-1}$. The beam area was set to $4 \, \mathrm{cm}^2$, and exposure time was 1 to 4 h for most of the samples. Only samples with very high boron concentrations ($>500 \, \mu\mathrm{g/g}$) were exposed to a smaller beam ($3 \, \mathrm{mm}^2$) for about 10 h, in order to suppress the Compton edge and backscattering in the gamma spectra originating from (n,γ) reaction on $^{10}\mathrm{B}$. Energy spectra ranging from 30 keV to 11 MeV were measured using a high-purity germanium semiconductor (HPGe) – bismuth germanate (BGO) scintillator detector system in Compton-suppressed mode. The data acquisition was performed by a Canberra S100 multichannel analyser. Aliquots from the whole-rock powders were used for analyses in order to allow a proper comparison of PGNAA results with those of the other methods. Prior to analysis, the sample powders ($2 - 4 \, \mathrm{g}$ each) were dried at $105 \, ^\circ\mathrm{C}$ for about 12 h and subsequently sealed in teflon (FEP) bags. Background measurements were done with an empty FEP bag. Analysed elements include all major elements as well as B, Cl and H in all samples. In addition, abundances of the rare earth elements Nd, Sm and Gd, and the transition metals Sc, V, Cr, Co and Ni were quantified in many samples. Gamma spectra were evaluated using the Hypermet PC program (Révay *et al.*, 2001). Concentrations of oxides of all quantified elements were calculated according to the oxidation number of a given element (stoichiometry), and normalised to a total of 100 wt% for quantification. Iron contents were expressed as $\mathrm{Fe_2O_3}$. Sensitivities and precisions of quantified elements are given in 2.4. Detection limits were calculated on the basis of a four-hour measurement of a two-gram sample. Further information on analytical details of the Budapest PGNAA facility is given in Révay *et al.* (2004), Szakmány & Kasztovszky (2004) and Molnár (2004).

For XRF analyses, powder tablets of 25 samples were prepared at the Institute of

Table 2.4. Concentration ranges, precisions and calculated detection limits of cold neutron PGNAA during this study

Oxide	Concentration min	max	Elemental analytical sensitivity (cps/mg)	Precision (%)	Calculated detection limit
	Major oxides (wt %)			Oxides (wt %)	
SiO_2	10	85	0.013	< 2.5	0.90
TiO_2	0.2	7	0.81	< 2.5	0.05
	0.05	0.2		< 4.0	
Al_2O_3	2	25	0.053	< 3.0	0.60
Fe_2O_3	1	17	0.102	< 2.0	0.10
MnO	0.5	3.5	2.54	< 2.5	0.06
	0.06	0.5		< 5.0	
MgO	5	35	0.0186	< 7.0	1.20
	1	5		< 25	
CaO	5	43	0.048	< 3.0	0.80
	0.8	5		< 6.0	
Na_2O	2.5	9	0.368	< 3.0	0.11
	0.2	2.5		< 7.0	
K_2O	0.3	5.8	0.261	< 3.0	0.14
	0.1	0.3		< 10	
P_2O_5		3.2	0.06	25	1.60
CO_2	36	40	0.00075	< 7.5	24
H_2O	3	12	1.68	< 1.5	0.02
	0.5	3		< 2.5	
	Trace elements (µg/g)			Element (µg/g)	
B	5	8750	1054	< 1.3	0.3
	1.9	5		< 1.7	
Cl	100	525	3.13	< 5.0	30
	30	100		< 20	
Sc	50	300	4.47	< 10	30
	30	50		< 20	
V	80	720	1.13	< 10	80
Cr	1000	3000	0.27	< 4	300
	400	1000		< 15	
Co	35	150	3.05	< 15	30
Ni	1000	2000	0.225	< 3.5	300
	300	1000		< 15	
Nd	40	120	2.76	< 10	40
Sm	1	22	684	< 2.5	0.1
	0.3	1		< 4.0	
Gd	0.2	30	1862	< 5.0	0.1

Analytical sensitivities are given in counts per second and milligram for the most intensive prompt-gamma line of the element in the beam line. Note the high sensitivity for boron, being about five orders of magnitude higher than the sensitivity for silicon. Precision was calculated from uncertainty in peak fit of the gamma spectra.

Geology, University of Trier, Germany, and analysed for V, Cr, Co and Ni at Trier using a SIEMENS SRS3000 X-ray spectrometer equipped with a Rh-tube operated at 60 kV/50 mA. Major element compositions (SiO_2, TiO_2, Al_2O_3, Fe_2O_3, MnO, MgO, CaO, Na_2O, K_2O, P_2O_5) of these 25 samples were determined at the Institute of Mineralogy, University of Tübingen (Germany), using fused glass tablets in a SIEMENS SRS303 X-ray spectrometer. The remaining 18 samples were sent to the Institute of Mineralogy and Geochemistry, University of Köln (Germany) and analysed by Eberhard Seidel (Köln) for major elements in glass tablets and Sc, V, Cr and Ni in powder press tablets, using a PHILIPS PW2400 X-ray spectrometer. Precision of XRF analyses was ~ 0.5 to 1% for major elements and between 5 and 10% for V, Cr, Co and Ni. Determination of loss on ignition (LOI) of each sample was performed using 1 to 1.5 g of powdered sample weighed in ceramic beakers. These were heated at $900\,^{\circ}$C for 30 min, weighed again, and subsequently heated for another 60 min at the same temperature and weighed for a third time. Results were corrected for oxidation of FeO to Fe_2O_3, assuming 50% of the Fe being trivalent in the metamorphic rocks.

At the University of Bristol (U.K.) solution ICP-MS was used to determine the abundances of Sc, V and the rare earth elements (REE) including Nd, Sm and Gd. Solutions were prepared at Heidelberg using a high-temperature microwave autoclave (ultraCLAVE II by MLS GmbH, Germany) at the Institute of Environmental Geochemistry, University of Heidelberg, in cooperation with Michael Krachler and Bernd Kober. The autoclave was operated at $240\,^{\circ}$C and $5 \cdot 10^6$ to $7 \cdot 10^6$ Pa for about 2 h. 200 mg of each powdered sample together with 5 mL HNO_3 (70%) and 1 mL of HF (48%) (both acids purified by distillation) were put into a teflon tube located inside a steel pressure vessel. After evaporation of the acids, the samples were dissolved in HNO_3 (1%) and diluted to 500:1 of the original rocks' concentrations by adding distilled water. For mass calibration the solutions were spiked to contain 10 ng/g of In, Bi, Re and Ru as internal standards. Precision of solution ICP-MS analyses was between 5 and 10%. The analyses were performed on a VG Elemental Plasma Quad II mass spectrometer by Chung Choi and Tony Kemp (Bristol).

2.12.3. Results

The contents of major element oxides were measured by both XRF analysis and PG-NAA. As expected, the metamorphic samples display a large compositional range. In Fig. 2.15, PGNAA results are plotted as percent of the respective XRF values versus the XRF value. For SiO_2, Al_2O_3 and Fe_2O_3, the values obtained by both methods generally agree within 5% or better for the whole range of concentrations, and for most samples the results are even consistent within analytical uncertainty

(Fig. 2.15a-c). For TiO_2 concentrations above 1 wt% the values also agree within 5 % (Fig. 2.15d). At concentrations between 0.25 and 1 wt% the agreement is at least within 10 % (Fig. 2.15e).

MnO concentrations measured by PGNAA are systematically higher than those measured by XRF analysis and cluster at around 110 % of the XRF values for concentrations above the calculated detection limit of 0.06 wt% (Fig. 2.15f, g). PGNAA results for MgO are between 90 and 110 % of XRF values at concentrations > 10 wt%, but show larger variations (80 to 120 %) for lower concentrations between 1.2 (detection limit) and 10 wt% (Fig. 2.15h). For CaO, a systematic difference between the values derived from both methods appears: PGNAA values are systematically lower (5 %) than the XRF values (Fig. 2.15i). The offset is very similar for all samples in the entire range of concentrations from 0.8 wt% (detection limit) to more than 40 wt%. The results for Na_2O are more complex. At concentrations < 2 wt%, PGNAA values are within 90 to 180 % of the XRF values (Fig. 2.15j). For a discussion of the results for samples with Na_2O concentrations > 2 wt%, a distinction between the results from the different XRF laboratories is necessary. Between 2 and 5 wt% Na_2O, PGNAA results lie within 100 to 120 % of the XRF data on granitoid rocks (prepared and measured at Karlsruhe) and of those on metamorphic rocks (prepared and measured in Köln). For concentrations above 5 wt%, the agreement with the Köln XRF data is even better (< 10 %). In marked contrast, PGNAA results amount to 125 to 145 % of the XRF values for all samples prepared and measured at Tübingen (Fig. 2.15j). Finally, PGNAA results for K_2O are between 100 and 110 % of XRF values at concentrations above 4 wt% and between 100 and 120 % for concentrations between 0.5 and 4 wt% (Fig. 2.15k).

The abundances of the rare earth elements Nd, Sm and Gd in the metamorphic rocks were measured by PGNAA and solution ICP-MS. For the granitoids, REE data are given in Altherr & Siebel (2002), who analysed the samples by INAA. Values for Nd obtained by PGNAA are systematically higher than ICP-MS and INAA data (120 to 180 %; Fig. 2.16a). For Sm, most of the PGNAA values range from 60 to 80 % of the ICP-MS and INAA values for the whole range of concentrations (Fig. 2.16b). For Gd, PGNAA results for almost all samples agree within 20 % with the results of the other two methods (Fig. 2.16c).

The abundances of Cr, Co and Ni were measured by XRF in all samples of high-*P* metamorphic rocks. Reliable PGNAA results could only be obtained for a few samples characterised by rather high abundances of these elements. For Cr and Ni the results of both methods agree within 10 % (Fig. 2.16d, e). For Co, the results agree within 20 % (Fig. 2.16f).

The transition metals Sc and V were measured by PGNAA, XRF, solution ICP-MS and partly also by INAA. PGNAA results for Sc scatter between 40 and 170 %
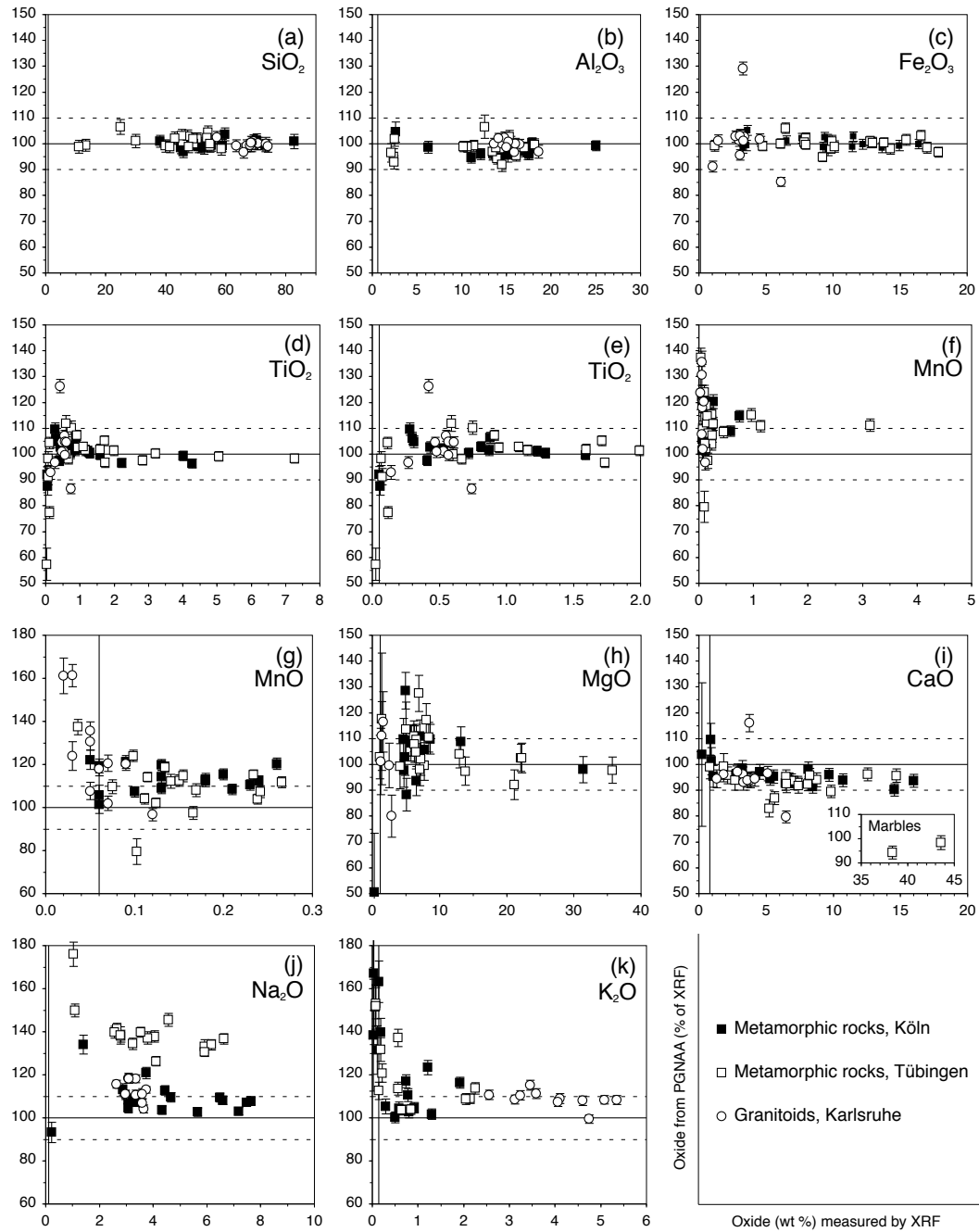
Fig. 2.15. See following page for explanation

Fig. 2.15. (Previous page) Comparison of PGNAA and XRF data for major elements expressed as oxides (wt %). PGNAA values in percent of respective XRF values are plotted versus XRF values. **a** SiO_2, **b** Al_2O_3, **c** Fe_2O_3, **d** TiO_2 for all samples, **e** TiO_2 for samples with less than 2 wt% TiO_2, **f** MnO for all samples, **g** MnO for samples with less than 0.3 wt%, **h** MgO, **i** CaO, inlet showing two marble samples containing $\sim$ 40 wt% CaO, **j** Na_2O, **k** K_2O. Filled squares represent samples of high-*P* metamorphic rocks for which XRF analyses were performed at Köln, while open squares stand for samples prepared and measured at Tübingen. Open circles are data for granitoid rocks from Altherr & Siebel (2002), prepared and measured at Karlsruhe. Vertical lines are the calculated detection limits for PGNAA.
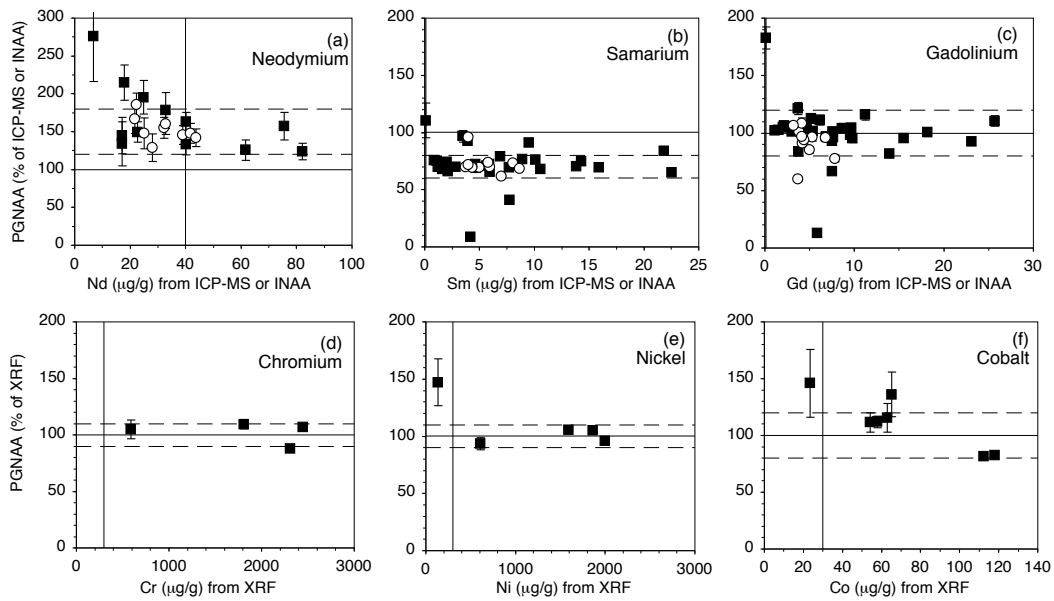
Fig. 2.16. Comparison of PGNAA data with data from solution ICP-MS for high-*P* metamorphic rocks (filled squares), from INAA for granitoids (open circles) and from XRF for metamorphic rocks. PGNAA data are shown in percent of the respective values obtained by other methods. **a** Nd, **b** Sm, **c** Gd. **d** Cr, **e** Ni, **f** Co. Broken lines are for orientation only and include the majority of samples. Vertical lines are the calculated detection limits for PGNAA.

of the XRF values (Fig. 2.17a). In contrast, PGNAA data agree much better with the data obtained from ICP-MS (60 to 140%; Fig. 2.17b). At concentrations $>$ 200 µg/g, PGNAA data for V agree within 40% with data obtained by XRF and ICP-MS, whereby the values for most samples are above the 100% line (cc). At lower concentrations of 80 µg/g (detection limit) to 200 µg/g V, PGNAA results may show stronger deviations from both ICP-MS and XRF data.
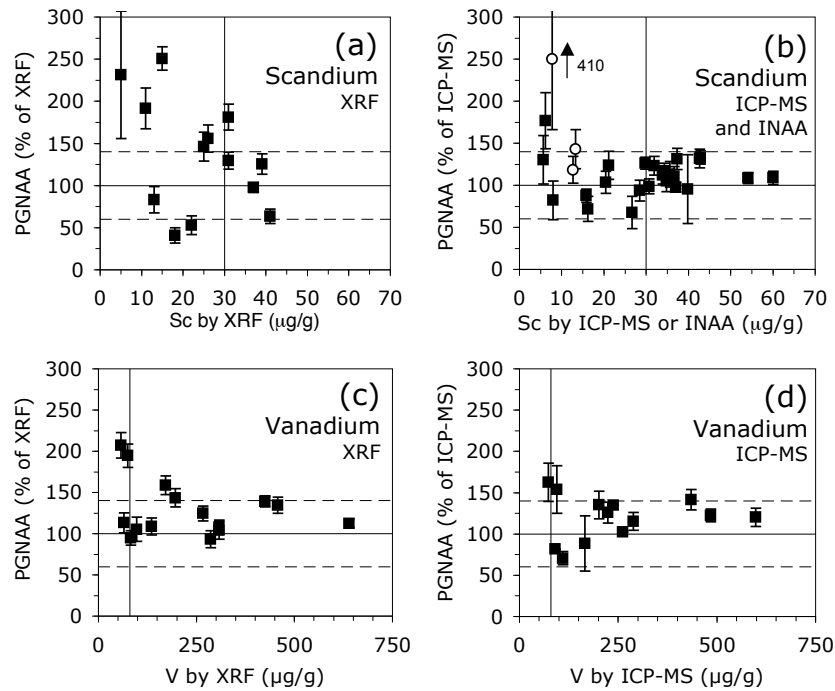
Fig. 2.17. Comparison of PGNAA data for Sc and V with data obtained by other methods. **a** Sc by XRF, **b** Sc by ICP-MS and INAA, **c** V by XRF, **d** V by ICP-MS. Broken lines are for orientation only and include the majority of data points. Vertical lines are the calculated detection limits for PGNAA.

In geochemistry, the determination of H_2O is usually done by (i) Karl-Fischer titration (Behrens, 1995) after thermal decomposition of the sample in a nitrogen atmosphere, (ii) the Penfield method (Penfield, 1894; Jeffrey & Hutchinson, 1981), or (iii) IR gas absorption spectrometry after inductive heating and combustion of the sample in an oxygen atmosphere. The aim is to differentiate between adsorbed moisture and water present as hydroxyl groups within the lattice structure of minerals. If volatile components are not of prime interest, the determination of the loss on ignition (LOI) is preferred. For our samples from high-P metamorphic rocks, only LOI values are available, while H_2O in the samples from granitoids was determined

by Karl Fischer titration (Altherr & Siebel, 2002). LOI values are not very precise at low concentrations (< 0.5 wt%) and represent a total of all volatile species (e.g. H_2O, CO_2), evaporated from the rock powders at $900\,^\circ$C. Furthermore, the oxidation of Fe leads to gain of oxygen during ignition, partially compensating the mass loss by escaping volatile components and decreasing the LOI value. Measured LOI values for the metamorphic rocks were corrected for oxygen gain by assuming that 50 % of the total Fe in the sample powders are present as Fe^{2+} (resulting values are labelled as LOI*). In Fig. 2.18a, a comparison of PGNAA values on H_2O with LOI values (metamorphic rocks) and H_2O values (granitoid rocks) is shown. For LOI*/H_2O values > 0.7 wt%, PGNAA values for most samples are within 60 to 140 % of the LOI* values. For the samples for which H_2O contents were measured by Karl Fischer titration, the PGNAA values tend to be significantly higher. Precision of H_2O measurements was better than 1.5 % at concentrations > 3 wt% and better than 2.5 % for lower concentrations (Fig. 2.18b). For B and Cl, no external data for the metamorphic rocks are available. However, measurements of geological reference materials performed at BNC have shown good agreement of PGNAA results with recommended values (Gméling *et al.*, 2005). For our samples, precisions of Cl measurements were better than 6 % at concentrations $> 100\,\mu$g/g and better than 20 % at concentrations between $30\,\mu$g/g (detection limit) and $100\,\mu$g/g. The majority of high-*P* metamorphic rocks have Cl contents between 25 and $250\,\mu$g/g (Fig. 2.18c). For B, precision is even better (< 1.7 %) in the entire range of concentrations between 2 and $8750\,\mu$g/g (Fig. 2.18d).

CO_2 contents of 36 and 40 wt% were measured in two silicic marbles whereby precisions were 7.5 and 6 %, respectively. P_2O_5 contents of most investigated rocks are below 1 wt% and could not be quantified by PGNAA. For one P-rich sample, however, a P_2O_5 content of 3.2 ± 0.8 wt% was obtained. This value is in good agreement with the value of 3.15 wt% measured by XRF.

2.12.4. Discussion

The contents of the major components SiO_2, Al_2O_3 and Fe_2O_3 (total Fe) can be measured with a precision better than 3 % within the whole compositional range displayed by high-*P* metamorphic rocks. Results are in good agreement with XRF measurements. TiO_2 contents above 0.2 wt% can be measured with similar precision. CaO contents determined by PGNAA are systematically 5 % lower than those obtained from XRF. Systematic differences between PGNAA and XRF data for MnO and K_2O (>0.5 wt%) are minor. Measurements of MgO concentrations were less successful. At concentrations up to 10 wt%, that are typical for most high-*P* metamorphic rocks, the sensitivity of PGNAA is rather poor. Analysis of SiO_2,
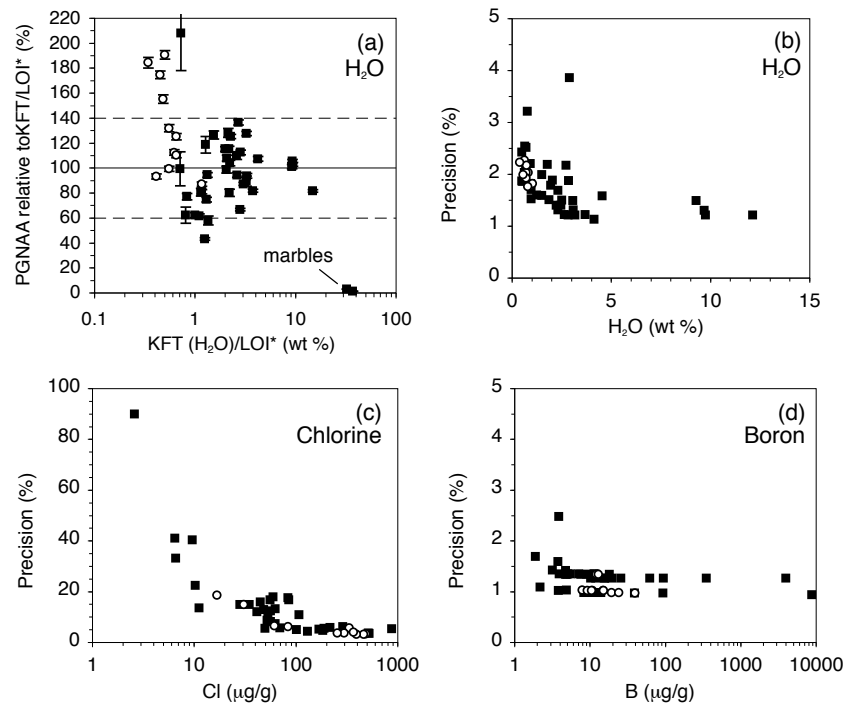
Fig. 2.18. a Comparison of PGNAA data for H_2O contents with H_2O data obtained by Karl Fischer titration after drying and subsquent thermal decomposition of the samples in a nitrogen atmosphere (granitoids: open circles) and with LOI data on metamorphic rocks (filled squares), corrected for the effects of oxygen gain (LOI*). Broken lines are for orientation only and include the majority of data points. **b, c, d** Precision of PGNAA for H_2O **b**, Cl **c** and B **d** for all samples (granitoids: circles; metamorphic rocks: filled squares).

TiO_2, Al_2O_3, Fe_2O_3, MnO, MgO, CaO and K_2O contents are routinely performed by XRF and show precisions of 1% or better and good accuracy within a large range of compositions.

The discrepancies between Na_2O concentrations determined by PGNAA and those determined by XRF need to be discussed in some more detail. During analysis of Na by XRF some problems may arise during both sample preparation and measurement. Na is a volatile element and tends to be evaporated from the sample during fusion of rock powder-flux mixtures and the preparation of glass tablets at about $1250\,°C$. Furthermore, surfaces of repeatedly used glass tablets are easily contaminated by Na implying an increase in Na count rates on standard tablets and consequently, apparent Na_2O concentrations in the sample that are lower than real values. Moreover, XRF measurements on low atomic mass elements are more difficult to quantify, and precision may be lower than for heavier elements. For PGNAA, however, the atomic mass is irrelevant, since sensitivity is determined by the neutron cross-sections and natural abundances of the analysed isotopes.

In this study, preparation of glass tablets and XRF analyses were performed by three different laboratories. Comparison of Na_2O results of PGNAA with XRF analyses reveal significant differences between the various laboratories. For concentrations $> 2\,wt\%$, Köln XRF values lie between 82 and 97% of the PGNAA values. XRF values of the granitoids (Altherr & Siebel, 2002; prepared and measured at Karlsruhe) range from 84 to 96% of the PGNAA values (Fig. 2.19). In marked contrast, XRF values produced at Tübingen are at about 70% of the PG-NAA values, suggesting significant loss of Na during preparation of glass tablets and/or problems during X-ray quantification of Na and/or contamination of reference tablets. PGNAA may therefore be a more reliable method for Na_2O analyses at concentrations $> 2\,wt\%$.

Concentrations of rare earth elements La to Lu of geological samples normalised to CI chondritic values (Boynton, 1985) generally yield continuous patterns with eventual anomalies only for Eu and in some cases Ce, due to redox effects. Since REE may be fractionated between minerals, melts and fluids according to their variable REE^{3+} ionic radii, chondrite-normalised REE patterns may yield important information on both the protolith and the metamorphic evolution of high-P rocks. Chondrite-normalized REE patterns of three samples, measured by solution ICP-MS are shown in Fig. 2.20. Unfortunately, the abundances of REE in most of our samples are below the detection limit of PGNAA. Only Sm and Gd and in some samples also Nd could be quantified. Precisions of Nd, Sm and Gd values were better than 10, 4 and 5%, respectively. However, PGNAA values for Nd and Sm are at about 150% and 70% of the respective ICP-MS values (Fig. 2.20). If the PGNAA values were correct, they would result in rather strange REE patterns that would not
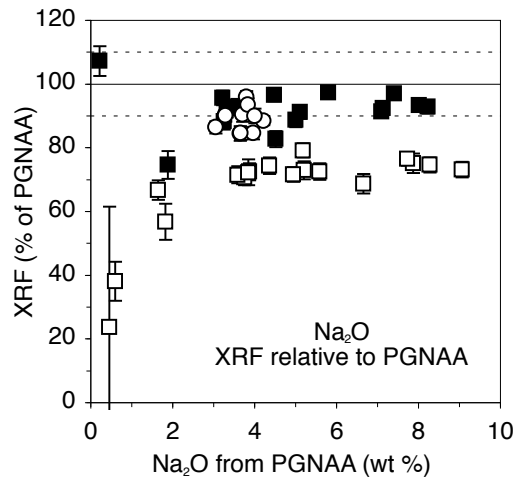
Fig. 2.19. Comparison of XRF data for Na$_2$O on different samples prepared and measured at different laboratories with results obtained by PGNAA. Filled squares represent samples of high-*P* metamorphic rocks for which XRF analyses were performed at Köln, while open squares stand for samples prepared and measured at Tübingen. Open circles are data for granitoid rocks from Altherr & Siebel (2002), prepared and measured at Karlsruhe.

be in accordance with the geochemical behaviour of the REEs. Therefore, it must be stated that PGNAA overestimated the concentrations of Nd by 50 % and underestimated those of Sm by 30 %. Gd values determined by PGNAA, however, are in good agreement with ICP-MS data.

Transition metals Cr, Co and Ni are detectable only at relatively high concentrations, usually occurring in lithologies related to mantle rocks, whereas the abundances of these elements in most metamorphic rocks are too low to be quantified by PGNAA. However, at high concentrations, PGNAA results are in good agreement with XRF. The analysis of Sc and Co by XRF is known to be difficult because of interferences with Ca and Fe peaks, respectively. Therefore, solution ICP-MS data are probably more reliable than XRF data. PGNAA values of Sc agree within 40 % with ICP-MS values, while large discrepancies exist between PGNAA and XRF data (Fig. 2.17a, b). PGNAA is therefore more reliable for the determination of Sc abundances than XRF.

Abundances of V are routinely measured by both XRF and ICP-MS with a precision between 5 and 10 % at concentrations between 10 and 1000 μg/g. Precision of PGNAA values was also better than 10 % for most of the samples. However, agreement of PGNAA data with those obtained by the two other methods varies by 40 % (for concentrations > 200 μg/g) for several samples. The detection limit for V
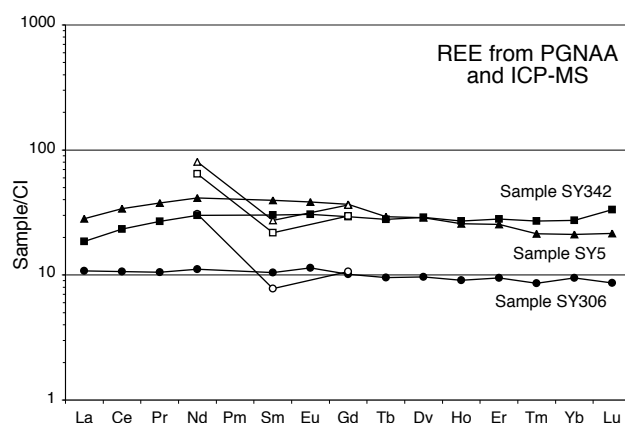
Fig. 2.20. Chondrite-normalized rare earth element patterns of three samples from high-*P* metamorphic rocks determined by ICP-MS (filled symbols). Normalization values were taken from Boynton (1985). Open symbols represent PGNAA results for Nd, Sm and Gd.

in PGNAA is $\sim 80\,\mu g/g$ and, thus, much higher than in XRF analysis ($\sim 2\,\mu g/g$).

For the analysis of H_2O, B and Cl, PGNAA has two major advantages: (i) no sample preparation is required prior to analysis, minimising the risk of sample contamination by impure solutions and the loss of B and Cl by evaporation, and (ii) the high sensitivity of these elements for PGNAA results in high precisions at the concentration levels found in high-*P* metamorphic rocks and other geological materials. Even in strongly dehydrated rocks containing less than $5\,\mu g/g$ B, very precise measurements of B abundances are possible with PGNAA. In order to evaluate the accuracy of H_2O determinations by PGNAA from the data obtained in the course of this study, it is necessary to consider that the sample powders prepared for PGNAA analysis might have adsorbed moisture from the air after they were taken out from the furnace. This problem was avoided during measurement of H_2O contents in the samples from the granitoids by Karl Fischer titration, since the sample powders were dried at $105\,^{\circ}$C in a closed nitrogen atmosphere before thermal decomposition and titration. This may explain why PGNAA values tend to be higher than those obtained by Karl Fischer titration. The problem of moisture adsorption is particularly serious in the case of low H_2O contents as shown by the granitoid samples. A proper evaluation of the data obtained for the samples from the high-*P* metamorphic rocks is not possible, since (i) the correction of measured LOI values for the effects of oxygen gain may have induced additional scatter and (ii) volatile components other than water may have been present.

2.12.5. Summary and Conclusions

41 samples from various high-pressure metamorphic rocks were investigated for their chemical compositions by PGNAA, XRF and solution ICP-MS. In addition, 11 samples from granitoids with published major and trace element concentrations were analysed by PGNAA. Analyses of major components by PGNAA are in good agreement with XRF results. Exceptions are K_2O at concentrations $< 0.5\,\mathrm{wt\%}$ and Na_2O at concentrations $< 2\,\mathrm{wt\%}$. The analysis of MgO contents by PGNAA is not satisfactory. On the other hand, PGNAA may be a superior method for the determination of Na_2O concentrations, since this method avoids the problems that are inherent in XRF analysis.

The abundances of many trace elements of geological interest (e.g. Cs, Ba, Rb, Sr, Nb, Ta, Zr, Hf, Y, U, Th, Pb) are too low in most high-P metamorphic rocks to be quantified by PGNAA. Among the REE, only Nd, Sm and Gd could be quantified. Comparison with results from ICP-MS revealed that Nd and Sm cannot be analysed with sufficient accuracy by PGNAA. Gd abundance values, however, are of good precision and agree well with ICP-MS data. Sc abundances determined by PGNAA are similar to those obtained by ICP-MS. Cr, Co and Ni could be quantified only at high concentration levels that are normally only present in rocks derived from the Earth's mantle. At high concentrations of $> 200\,\mathrm{\mu g/g}$, the precision of V analyses by PGNAA is comparable to those by XRF and ICP-MS, but the detection limits are much higher. Agreement between values obtained by PGNAA and the other two methods is not better than 40 % in the case of V. Generally the accordance of results from PGNAA with those of the other methods becomes poor at low concentrations in agreement with our calculated detection limits.

PGNAA provides very precise measurements of B, Cl and H_2O contents. Knowledge of accurate H_2O contents in high-P metamorphic rocks is of paramount interest, as these values display the degree of rock dehydration. The trace elements B and Cl are of growing importance for the understanding of chemical transfer in subduction zones. The abundances of these elements in geological materials will probably be investigated more extensively in the future, with the improvement of analytical facilities. PGNAA has the capacity to contribute important data to the understanding of the geochemical cycles of B and Cl.

3. Geological setting

3.1. The Hellenides and the Attic-Cycladic Crystalline Complex

The Hellenides form part of a larger collisional belt formed in Mesozoic to Neogene time by continued convergence between Laurasia and Gondwana (e.g. Sengör *et al.*, 1988; Stampfli & Borel, 2002). On the basis of tectonostratigraphic and tectonometamorphic arguments, the Hellenides can be subdivided into five major units (following Jacobshagen, 1986, see Fig. 3.1): the Rhodopes forming an "internal" crystalline belt, the Vardar Zone, the Central Hellenic Nappes, the Pindos Nappe and the External Nappes. In Greece, the stack of the Central Hellenic Nappes includes Variscan basement and Mesozoic to Cenozoic cover series, variably metamorphosed during Mesozoic to Neogene times. The degree of post-Variscan metamorphism decreases from the lower to the upper parts of the nappe pile (e.g. Dürr *et al.*, 1978; Dürr, 1986). The Attic-Cycladic Crystalline Complex (ACCC) including Southern Evvia and Attica, the Cyclades and the Menderes complex in Turkey (Fig. 3.1) forms a large tectonic window exhumed during late Oligocene to Recent extension. In the Cyclades, two groups of tectonic units with contrasting metamorphic histories can be distinguished. Rocks from the lower units were affected by the Eocene period of low-temperature high-pressure metamorphism followed by late Oligocene to early Miocene low- to high-temperature medium- to low-pressure metamorphism and related granitoid plutonism. In marked contrast, the upper units emplaced along normal faults and detachments during back-arc extension are largely unaffected by Tertiary metamorphism. Various klippen comprise Permo-Mesozoic sediments, late Cretaceous granitoids and high-temperature low-pressure metamorphic rocks, Upper Jurassic ophiolite fragments and Paleogene molasse deposits (e.g. Dürr, 1986; Reinecke *et al.*, 1982; Altherr *et al.*, 1994; Altherr & Siebel, 2002, and references therein). It is assumed that the Vardar Zone and its eastern prolongation, the Izmir-Ankara trough represent a Tethyan suture (Jacobshagen, 1986).

3.2. The island of Syros

The island of Syros displays a sequence of rocks of the lower unit of the ACCC. Exposed blueschists and eclogites are very similar in P-T-t history to HP units on the
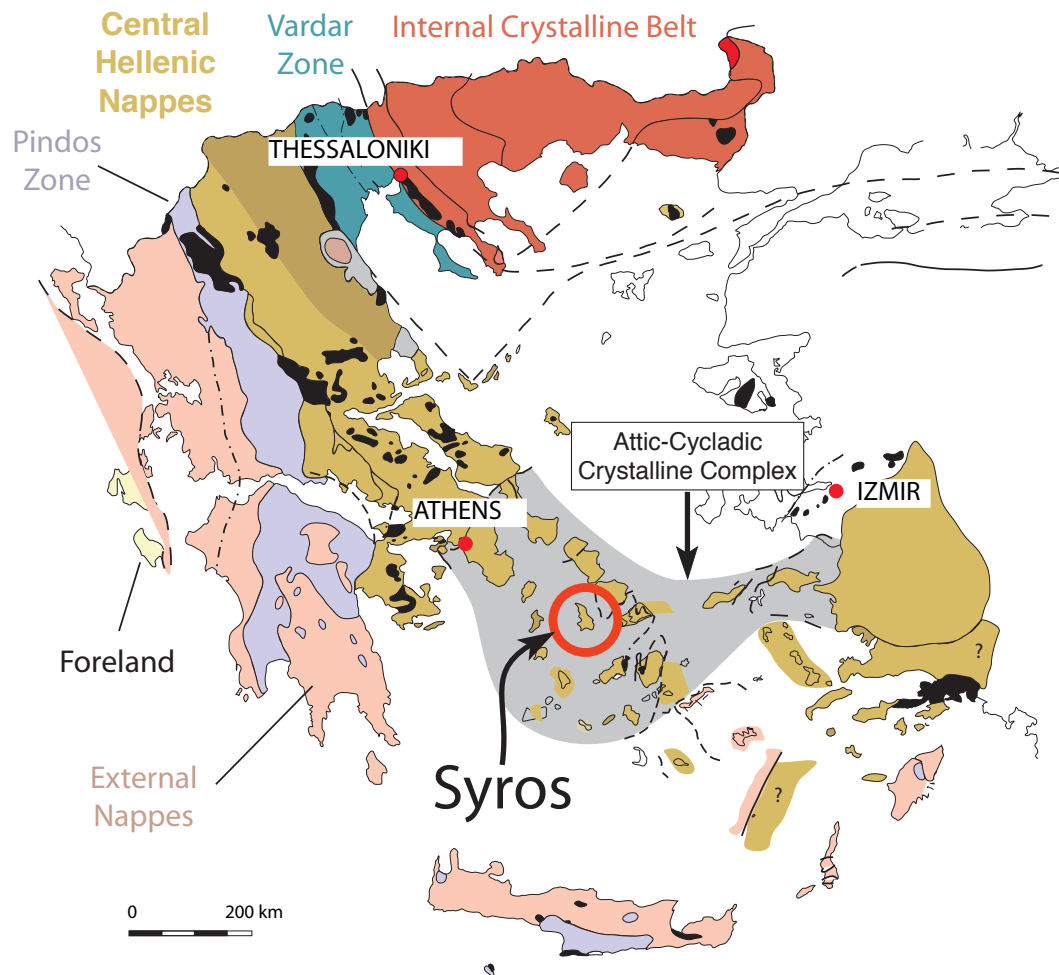
Fig. 3.1. Geological map Greece modified after Jacobshagen (1986) displaying the five major units of the Hellenides. Ophiolites are displayed in black. The island of Syros (red circle) is located in the center of the Attic-Cycladic Crystalline Belt (shaded in grey), which trends from Southern Evia and Attica through the Aegean towards the Menderes massif on the Turkish mainland.

islands of Sifnos (e.g. Altherr *et al.*, 1979; Schliestedt, 1986; Wijbrans *et al.*, 1990; Schmädicke & Will, 2003) and Tinos (e.g. Bröcker, 1990; Bröcker & Franz, 1998; Bröcker & Enders, 2001). The major part of the island is composed of interlayered pelitic schists and marbles (Fig. 3.2) dipping N to NE. The schists are pelitic to psammitic in character with minor intercalations of quarzites, calc-schists and meta-conglomerates (e.g. Hecht, 1984; Dixon & Ridley, 1987; Seck *et al.*, 1996). They are interpreted as metamorphosed flysch sediments by Dixon & Ridley (1987). The sedimentary protoliths of the schists were deposited during the Triassic and Jurassic (up to Cretaceous?), as demonstrated by Keay (1998) by SHRIMP dating of detrital zircon. Marbles are predominantly calcite marbles with minor intercalations of dolomite marbles (Bonneau *et al.*, 1980a). Lower Carboniferous fossils have been described from the marbles (Schumacher *et al.*, 2001), as well as calcite pseudomorphs after aragonite (Dixon, 1968; Brady *et al.*, 2004). In the south-eastern part of the island the $\sim 2 - 3$ km large "Vari Unit" (Fig. 3.2) is regarded as geologically different from the remaining part of the island on the basis of petrological and geochronological evidence. The Vari Unit displays tectonic contacts to the marble-schist sequence and was probably thrusted over these rocks along a basal shear zone (Ridley, 1984; Maluski *et al.*, 1987; Trotet *et al.*, 2001a; Bröcker & Enders, 2001; Tomaschek *et al.*, 2003; Ring *et al.*, 2003). The Vari Unit was suggested to belong to the Upper Unit of the ACCC (Bröcker & Enders, 2001; Rosenbaum *et al.*, 2002). No evidence for a H*P* metamorphic event has yet been found in this unit.

The most interesting formations on the island of Syros are exposed in the northern part near Kámpos and at the coastline around Hermoupolis and Kini (Fig. 3.2). These formations are composed of metagabbros, eclogites, glaucophane schists, meta-plagiogranites, serpentinites and metasediments, which mainly preserved a blueschist- to eclogite-facies metamorphic overprint. Starting in the 1830s by a French expedition to Greece, these rocks have attracted petrological research for almost two centuries now. The abundance of glaucophane in the metabasites were recognised early and led to the first description of this mineral by Hausmann (1845). After several early petrographic and geochemical descriptions of the rocks of Northern Syros, for example by Ktenas (1907), the onset of modern petrology and structural geology can be dated to the late 1960s, when J. E. Dixon completed his PhD thesis on *"The metamorphic rocks of Syros, Greece"* (Dixon, 1968). A geological map (1:50,000) has been published by Hecht (1984, see Fig. 3.2). The structural and tectono-metamorphic evolution of the island of Syros and especially its northern part has been investigated in a large number of studies (Dixon, 1968; Bonneau *et al.*, 1980b; Ridley, 1982, 1984, 1986; Ballhaus & Schumacher, 1995; Trotet *et al.*, 2001a; Rosenbaum *et al.*, 2002; Ring *et al.*, 2003; Brady *et al.*, 2004; Keiter *et al.*, 2004). Most authors distinguish three different ductile deformation phases along a
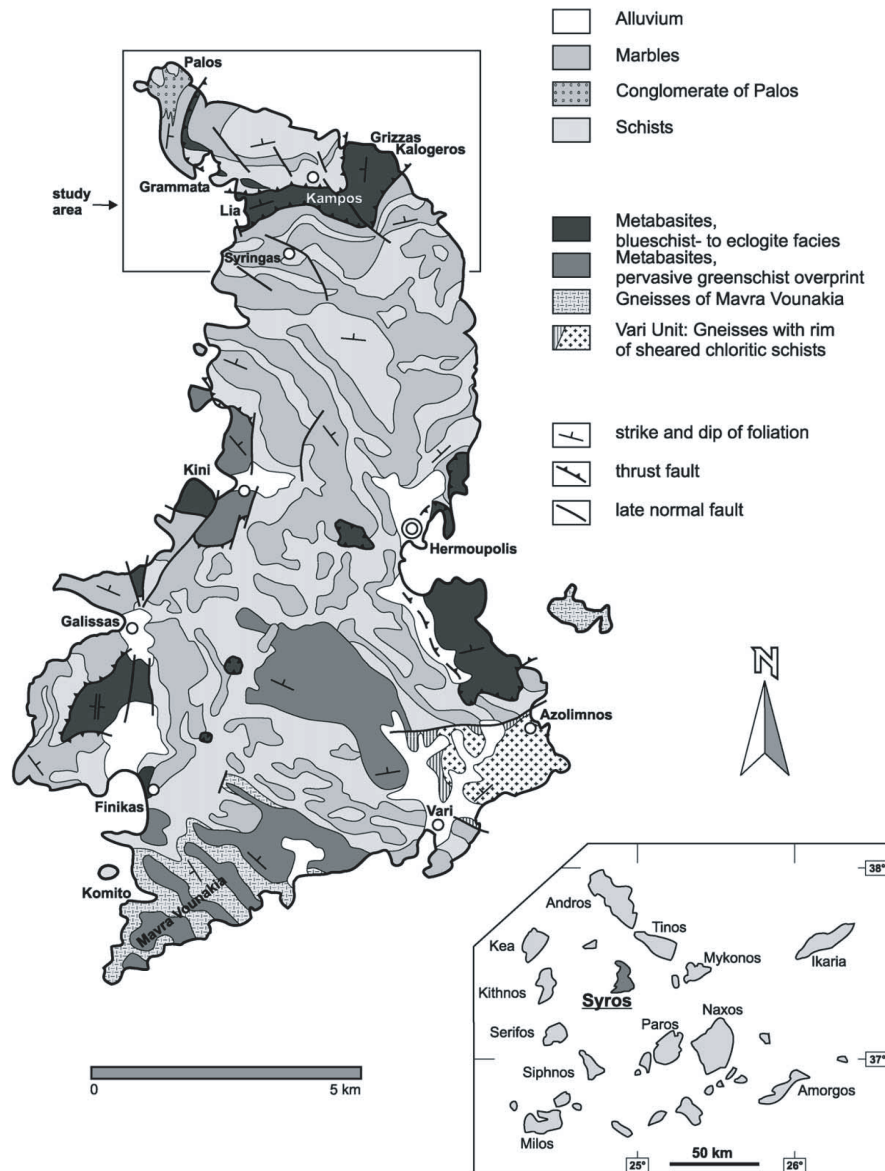
Fig. 3.2. Geological map of Syros from Keiter *et al.* (2004) [in *Journal of Structural Geology*], modified after Hecht (1984). Blueschist to eclogite facies metabasites (dark grey) occur in the northern part and along the eastern and western coasts of the island and display tectonic contacts to the major part of the island, which is composed of interlayerd marbles and schists. The box in the northern part of the island marks the study area, displayed in detail in Fig. 3.3.
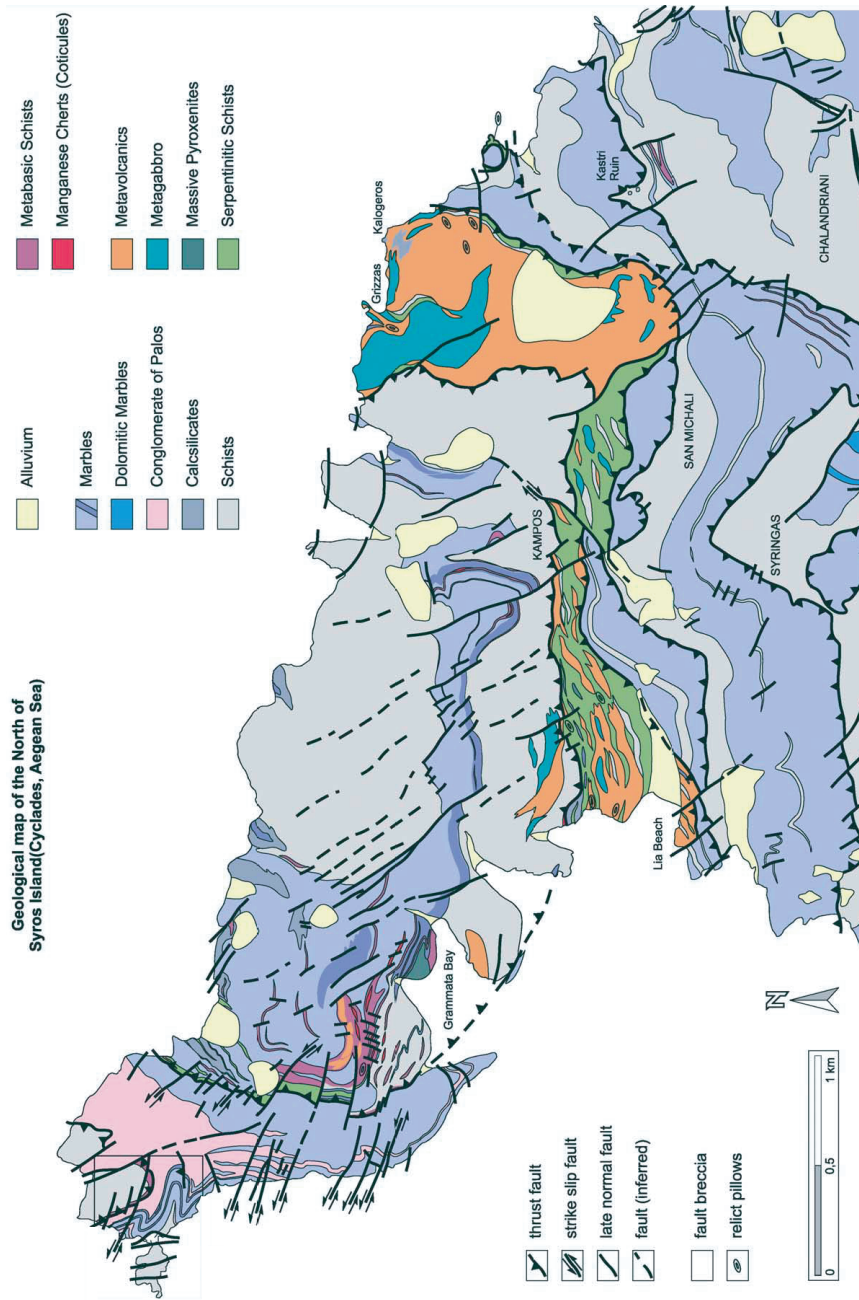
Fig. 3.3. Detailed geological map of Northern Syros from Keiter *et al.* (2004) [in *Journal of Structural Geology*]. The green colours display the Kámpos mélange, composed of several blocks of H*P* rocks embedded in a predominantly ultramafic matrix.

63

single clockwise $P-T$ path: a prograde deformation, a deformation near the pressure peak of metamorphism and a retrograde deformation. The prograde $P-T$ path is characterised by a high P/T ratio, typical for subduction zone metamorphism. Metamorphic peak conditions were estimated to $\sim 470-520\,°C$ and $1.3-2.0\,GPa$ by different authors for different rock types (Dixon, 1968; Ridley, 1984; Okrusch & Bröcker, 1990; Trotet *et al.*, 2001b; Rosenbaum *et al.*, 2002; Keiter *et al.*, 2004). The exhumation path of the rocks is characterised by cooling during decompression, resulting in the preservation of the HP assemblages and minerals. Lawsonite, for example, which is easily decomposed upon heating has been found in some places around the island (Dixon, 1968; Brady *et al.*, 2001, and SY438 in appendix B).

Geochronology of Syros   The geochronology of the HP rocks from Syros (and other islands of the Cyclades) has been until recently a matter of debate. However, a number of U-Pb TIMS and SHRIMP data from zircon, Lu-Hf data from garnet and $^{40}Ar/^{39}Ar$ data from white mica and glaucophane are now available and have been used to date the evolution of Syros HP rocks. Subduction and high-pressure metamorphism occurred in the Eocene ($\sim 54-50\,Ma$; Maluski *et al.*, 1987; Baldwin, 1996; Tomaschek *et al.*, 2003; Lagos *et al.*, 2003). High precision Lu-Hf dating by Lagos *et al.* (2003) demonstrated that any pre-Eocene garnet-forming metamorphic event (i.e. high-pressure metamorphism) must be excluded for Syros. Some geochronometers, like K-Ar in phengite show younger ages of $\sim 40\,Ma$ (Schliestedt *et al.*, 1987) and may display resetting during exumation and cooling. A different interpretation for the younger ages is presented by Putlitz *et al.* (2005). They analysed phengites by a laser-ablation $^{40}Ar/^{39}Ar$ method and revealed ages between 52 and 42 Ma, and argue that the rocks were at high-pressure conditions for $\sim 10\,Ma$. Magmatic protoliths of metabasic rocks and meta-plagiogranites are Cretaceous in age ($\sim 82-74\,Ma$; Keay, 1998; Tomaschek *et al.*, 2003). TIMS U-Pb zircon ages reported by Bröcker & Enders (1999, 2001) demonstrate a concordant age of 78 Ma. After the detailed study by Tomaschek *et al.* (2003) on zircon formation, this date is best interpreted as the protolith age of the investigated sample. Despite the contrasting interpretation by Bröcker & Enders (1999, 2001), the determined age value itself is in perfect agreement with the aforementioned studies.

The Mélange of Kámpos   The above mentioned units of metabasites occur in the upper level of the major marble-schist sequence and are bordered by low-angle thrust faults that are nearly concordant to the dip of this sequence (e.g. Keiter *et al.*, 2004, Fig. 3.2). The internal structure of the northern metabasite unit in the area of Kámpos, which is the best investigated area, is rather complex. A number of

different rock types have been distinguished on the basis of geochemical and petrographic observations within an east-west trending zone. They are interpreted as high-pressure metamorphic equivalents of different parts of ancient oceanic crust (e.g. Seck *et al.*, 1996). West of San Michalis and Kámpos, the different rock types occur as blocks of eclogite, omphacite/jadeite fels, garnet glaucophanite, serpentinite and metagabbro embedded in a matrix of chlorite schist and serpentinite (Dixon, 1968; Hecht, 1984; Dixon & Ridley, 1987; Okrusch & Bröcker, 1990; Seck *et al.*, 1996; Bröcker & Enders, 2001). This association of blocks and matrix has been described as the "Mélange of Kámpos" by most authors. The mélange consists of rigid undeformed blocks of predominantly eclogite surrounded by a schistose matrix, which is characterised by a strong foliation bending around the blocks. Contacts between blocks and chemically and mineralogically contrasting matrix are characterised by reaction zones rich in OH-bearing minerals (see section 4.7, page 81 on hybrid blackwall rocks). The mechanically soft matrix containing abundant chlorite, talc and serpentine is preferentially eroded, while the embedded blocks are more resistant. The eclogite and jadeite fels blocks therefore jut out over the island's western slope (Fig. 3.4). The largest of these blocks ("Monolith 1") with a height of $\sim 20\,\text{m}$ is a dominant marker in the field and a popular photographic motif (see for example Dixon, 1968; Bröcker & Enders, 2001). The eastern part of the metabasite association of Kámpos contains very little serpentinite and is dominated by more continuous lithologies, i.e. metagabbro and metavolcanics (Fig. 3.3).

Geotectonic setting of protoliths   Based on Sr isotopic compositions, REE patterns, major and trace element geochemistry, Seck *et al.* (1996) tried to identify the geodynamic setting of formation of the magmatic protoliths of the metagabbros and metavolcanic rocks of the mélange. They argue for a formation of the rocks in a back-arc basin, rather than at a mid-ocean ridge. Schumacher *et al.* (2001) state that the island of Syros represents a mixture of ocean-floor magmatic rocks and different sediments, i.e. immature volcano-clastic material with an IAB signature and shallow water carbonates. The vicinity of a passive continental margin as source for the (volcano-)clastic detritus has also been proposed by Schliestedt *et al.* (1987). The formation and subduction of small oceans formed in back-arc basins in the Aegean during the late Cretaceous to Eocene is also in accordance with geodynamic/paleogeographic reconstructions (e.g. Robertson & Dixon, 1984; Papanikolaou, 1987).

Seafloor alteration of protoliths   Several of the Syros metagabbros, metavolcanics and metasediments show evidence for interaction with seawater, which must
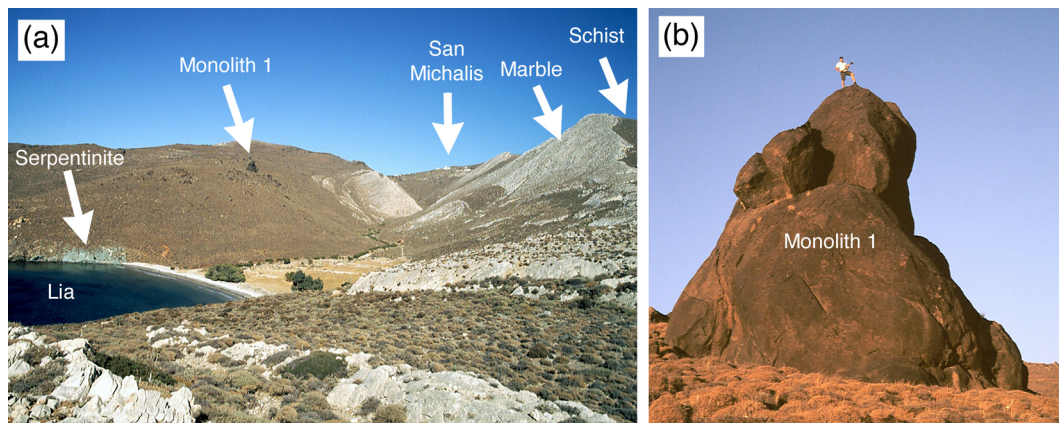
Fig. 3.4. Field views of the study area in the northern part of the island of Syros. **a** View from Lia bay (left) to the East (San Michalis), showing white marble and dark schists on the right, and the Kámbos mélange with serpentinite and eclogite blocks above the valley in the center. The largest eclogite block in the center is Monolith 1 (Dixon, 1968) shown in (b). **b** Monolith 1, a ∼20 m tall HP block, mainly composed of eclogite is a dominant marker in the field. Geologist for scale. The picture was taken during sunset (reddish colours).

have occurred prior to HP metamorphism. Most of the meta-igneous rocks demonstrate high modal abundances of hydrous minerals (e.g. epidote, glaucophane, phengite). Metagabbros display δ^{18}O values typical for gabbros subjected to high-temperature seafloor alteration (Putlitz *et al.*, 2000). Some metagabbros show Fe-rich veins at the outcrop scale, which are best interpreted as hydrothermal vents that were active in the ancient seafloor. Many metasediments are strongly enriched in Mn and Fe, which is typical of ocean-floor sediments interacting with hydrothermal solutions. Some metasediments even contain stratabound sulfide deposits (Melidonis & Constantinides, 1983).

Metasomatism during high-pressure metamorphism The interpretation of the chemical composition of exhumed HP rocks is often ambiguous, as several processes may impact different elements to various degrees. Magmatic protoliths, altered at the seafloor, are dehydrating during subduction and increasing P and T. Metasomatism at high pressures may enrich or leach the rocks in specific components, and rehydration during exhumation leads to the formation of abundant hydrous minerals, incorporating a number of fluid-mobile elements. The rocks of the Kámpos mélange display strong evidence for some of these processes. Bröcker & Enders (2001) have demonstrated that fluid circulation into jadeite felses during peak-metamorphic conditions strongly enriched the HFS elements. Furthermore,

abundant glaucophanite envelopes around eclogite blocks formed during retrograde fluid infiltration. Several HP blocks are rimmed by reaction zones composed of hydrous minerals, such as chlorite, Na- and Ca-amphibole, clinozoisite and phengite in paragenesis with omphacite, albite and tourmaline, which formed by rehydration during exhumation. These blackwall zones are discussed in detail in chapter 10.

Summary and problems   In summary, the island of Syros displays a sequence of metasedimentary and metaigneous rocks, which were subjected to $HP-LT$ metamorphism with peak conditions of $\sim 470-520\,°C$ and $1.3-2.0\,\text{GPa}$ in the Eocene. Magmatic protoliths were probably formed in a small back-arc basin during the Cretaceuos. Sediments were deposited during the Mesozoic and contain continental and island-arc detritus as well as shallow-water carbonates. Some of the magmatic and sedimentary rocks were chemically altered by hydrothermal activity at the seafloor prior to subduction. Metasomatic processes during the subduction zone metamorphic cycle also impacted the major and trace element signatures of many rocks. A more detailed description of the different rock types of Northern Syros is given in chapter 4.

Despite the intense research, one pivotal question on the metamorphic evolution of Syros and especially of the Kámpos mélange is still not satisfactorily answered: Which parts of the metamorphic history do all of the rocks have in common, or when and by which mechanism were they juxtaposed? Different answers have been given in the literature, and several scenarios are possible: **(1 - a high-pressure ophiolite)** The rocks of the Kámpos mélange display different parts of a formerly coherent oceanic lithosphere, which was subducted in one piece. Deformation and shearing during the prograde, peak and retrograde part of the $P-T$ path led to some tectonical mixing of the different lithologies. **(2 - a meta-olistostrome)** The different rock types were juxtaposed by a sedimentation process as large blocks. The large size (meter to kilometer) and large variety of blocks is explained by sedimentation in an olistostrome in this scenario (Dixon, 1968). The mélange has a sedimentary origin and a uniform metamorphic history. **(3 - a pile of thrust sheets)** This model does not directly refer to the mélange itself, but presents a model for the different extent of retrogression observed in the Syros HP rocks. Trotet *et al.* (2001a,b) suggest that the eclogites, blueschists and greenschists of Syros had a uniform subduction history and similar peak $P-T$ conditions, were disrupted at depth by ductile shearing, and exhumed along individual retrograde paths. Their close proximity is explained by late tectonic juxtaposition. **(4 - a tectonic mélange)** Different blocks of the mélange display different origins and prograde $P-T$ paths as well as different peak metamorphic conditions. The juxtaposition of the blocks and

the ultramafic matrix occurred at high pressures within the subduction zone. Results from numerical modeling of subduction processes in general demonstrate that intense mixing of fragments of different parts of the subducting lithosphere with mantle wedge serpentinite may be a common scenario (Gerya *et al.*, 2002). In this model, the premetamorphic history as well as prograde and peak $P - T$ conditions of different blocks should display at least small differences.

Future petrological research may help to exclude one or more of these scenarios.

4. Investigated samples

Approximately 140 different rock samples from the island of Syros were collected by different workers during the last ~ 30 years. Most of these samples are from the northern part of the island. From this collection, 47 representative samples, including all major rock types, were selected for detailed geochemical studies. A first group of samples includes serpentinites as well as meta-igneous and meta-sedimentary rocks. In addition, a second group of samples represents metamorphic reaction zones formed at the contacts between contrasting lithologies within the mélange in the northern part of the island. In this chapter, the chemical and mineralogical characteristics of the various rock types are given. A detailed description and discussion of each sample is given in Appendix B. Major and trace element abundances of all samples are given in Appendix C.

4.1. Meta-igneous glaucophane schists and felses

(8 samples: SY3, SY5, SY304, SY306, SY309A, SY342, SY401A, SY403)

Meta-igneous glaucophane schists and felses are dominated by the paragenesis glaucophane + epidote + white mica (phengite and/or paragonite) $\pm$ Grt $\pm$ Qtz. In addition, rutile and/or titanite and apatite are present. Some samples also contain chloritoid, chlorite and/or magnetite. In a TAS (total alkali vs silica) diagram their bulk chemical compositions plot into the fields of basalt, basaltic andesite and andesite (Fig. 4.1). Chondrite-normalised REE patterns of four samples (SY5, SY304, SY306, SY342) are very flat with $(La/Yb)_{cn}$ (= La/Yb ratio normalised to CI chondritic values of Boynton, 1985) ratios between 0.7 and 1.3 and lack a significant Eu anomaly (Eu/Eu* between 1.0 and 1.2) (Fig. 4.2a). The second group of samples is characterised by significant enrichment of LREE relative to HREE with $(La/Yb)_{cn}$ values between 2.8 and 6.8 and variable Eu anomalies (Eu/Eu* between 0.8 and 1.6). REE abundances for both groups of samples range from 10 to 50 times chondritic, except for sample SY3 that has $La_{cn} \approx 110$.

The flat REE patterns are similar to the patterns of "glaucophanites" from Syros described by Seck *et al.* (1996) and Schumacher *et al.* (2001). Following Dixon & Ridley (1987), these authors interpreted the glaucophanites as high-pressure metamorphic equivalents of basalts produced in different tectonic settings (MOR, BAB,

69
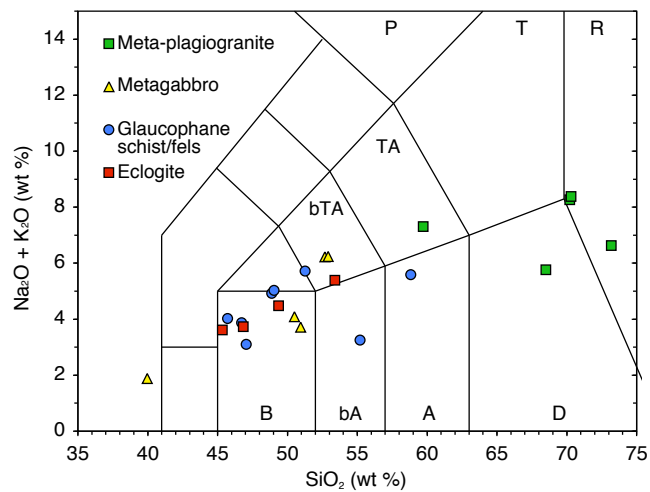
Fig. 4.1. Total alkali vs silica (TAS) diagram displaying investigated meta-igneous samples which do not show significant retrograde rehydration (i.e. no blackwall rocks). Green squares: meta-plagiogranites; yellow triangles: metagabbros; blue circles: glaucophane schists and felses; red squares: eclogites. B = basalt; bA = basaltic andesite; A = andesite; D = dacite; P = phonolite; T = trachyte; R = rhyolite; bTA = basaltic trachy-andesite; TA = trachy-andesite.

IAB). MORB-normalised element abundance patterns are characterised by prominent positive Pb and negative Nb-Ta anomalies (Fig. 4.3a), strongly supporting IAB as protoliths for the glaucophane schists and felses. While Cr and Ni are strongly depleted, (highly) incompatible elements such as Rb, Ba, Th, U, K, Sr and P are enriched in most samples. Among the light elements, B shows an enrichment similar to Ba. In contrast, Be is not significantly fractionated with respect to Nd (nearly constant Be/Nd ratios between ~ 0.03 and 0.06). Li shows a positive anomaly in most samples (except for SY304 and SY306). The observed enrichment of Li and B probably occurred during low-temperature alteration of the former basalts at or beneath the seafloor.

4.2. Metasedimentary glaucophane schists

(2 samples: SY314, SY406)

The meta-sedimentary glaucophane schists contain the assemblage (ferro-)-glaucophane + phengite + fine-grained spessartine-rich garnet $\pm$ Fe-rich jadeite + apatite. In addition, SY314 contains albite and tourmaline. At first glance, major element compositions of these rocks appear similar to that of basalt, with $\sim 50\,\mathrm{wt\%}$ SiO_2, $\sim 15\,\mathrm{wt\%}$ Al_2O_3 and $\sim 5\,\mathrm{wt\%}$ MgO. However, CaO concentrations are low

($< 3\,$wt%), and MnO ($\sim 1-3\,$wt%) and K_2O ($> 2\,$wt%) are too high. REE show high abundances decreasing from La ($200 \times$ CI) to Yb ($20-50 \times$ CI), with negative Eu anomalies (Eu/Eu* between 0.7 and 0.8) and significant negative Ce anomalies with Ce/Ce* between 0.6 and 0.8 (Fig. 4.2b). MORB-normalised element abundance patterns reveal high abundances of LILE accompanied by low abundances of HFSE (Fig. 4.3b). In addition, the samples are characterised by low abundances of Sr and Cr. B abundances are relatively high in sample SY314, but low in SY406. Both samples show an "enrichment" in Li, while Be is "depleted" in sample SY406. The rocks are interpreted as metamorphic equivalents of tuffitic sediments that were exposed to low-temperature seafloor alteration resulting in elevated Mn and K contents due to the formation of Fe-Mn hydroxides and clay minerals. This hypothesis is substantiated by negative Ce anomalies.

4.3. Eclogites

(4 samples: SY109, SY323, SY324, SY411)

Three out of four eclogite samples are very rich in CaO ($\sim 15\,$wt%) and contain abundant epidote together with titanite and apatite, in addition to omphacite and garnet. The fourth sample (SY109) differs from the others by the presence of substantial amounts of K- and Na-bearing hydrous phases, such as phengite, paragonite and glaucophane. Chemically, this sample is characterised by relatively low CaO and high SiO_2 contents. In a TAS diagram, it plots into the trachy-andesite field, while the other three samples plot into the basalt field (Fig. 4.1).

The Ca-rich eclogites are characterised by high abundances of Sr ($\sim 300-880\,\mu$g/g), Pb ($\sim 27-90\,\mu$g/g), Th ($\sim 10-14\,\mu$g/g) and U ($\sim 1.8-2.5\,\mu$g/g), and extremely low contents of K, Rb and Ba, close to or below their respective detection limits. MORB-normalised element abundance patterns display positive anomalies of U-Th and Pb and negative anomalies of Rb-Ba, K, P and Ti (Fig. 4.3c). The eclogites do not display Nb-Ta anomalies. Li shows a positive anomaly, whereas Be/Nd and B/Nb ratios are not fractionated. Chondrite-normalised REE patterns of the three samples are similar, with REE decreasing from La ($150-200 \times$ CI) to Yb ($25-40 \times$ CI) with (La/Yb)$_{\mathrm{cn}}$ ratios of ~ 7 and negative anomalies for Eu (Eu/Eu$^* \approx 0.7$) and Ce (Ce/Ce$^* \approx 0.85$) (Fig. 4.2c).

The high-Ca eclogites are interpreted as the metamorphic equivalent of basalts that were enriched in Ca (and Sr, Pb and Li) during hydrothermal seafloor alteration at elevated temperatures ($> 250\,^{\circ}$C). Products of this rodingitisation are Ca- and Sr-rich (Honnorez & Kirst, 1975; Schandl *et al.*, 1989) and are known to produce Ca-rich eclogites/meta-rodingites during HP metamorphism (e.g. Evans *et al.*, 1979).
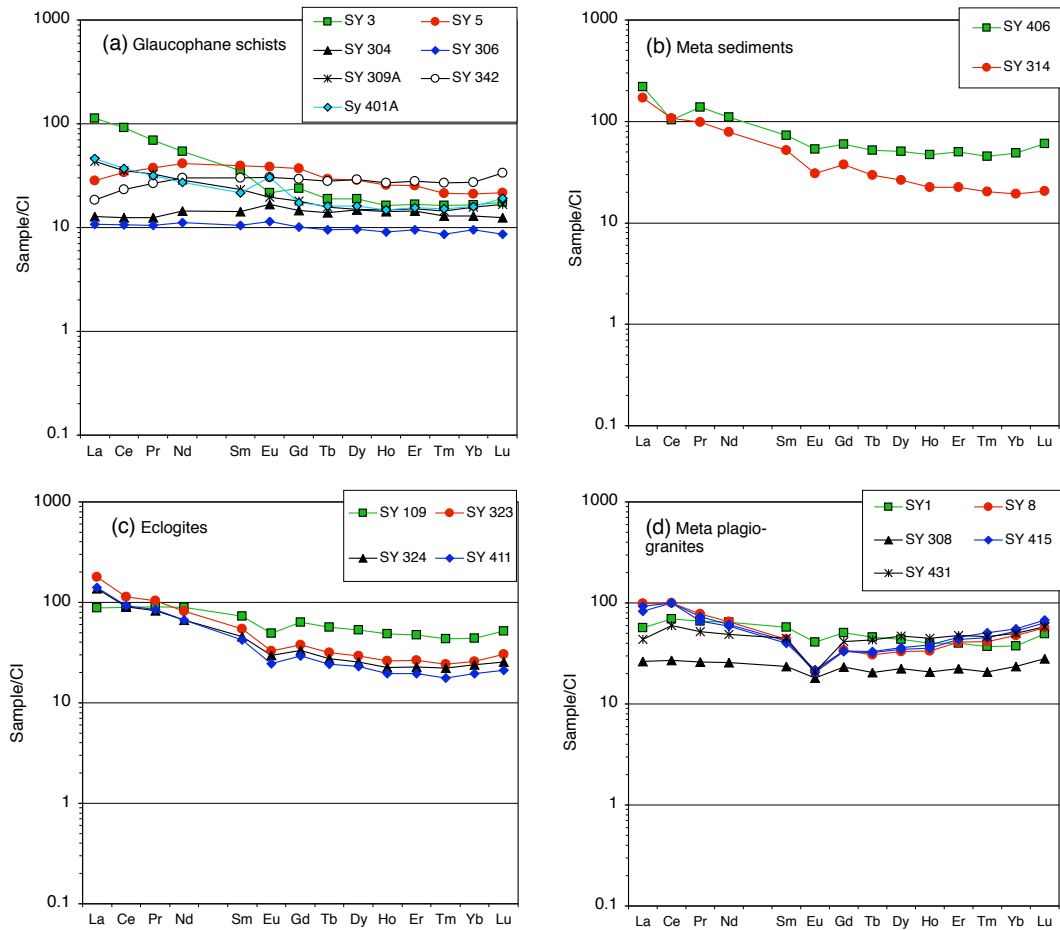
Fig. 4.2. Chondrite-normalised REE patterns of various rock types. **a** Meta-igneous glaucophane schists and felses; **b** meta-sedimentary glaucophane schists; **c** eclogites; **d** meta-plagiogranites (two aliquots of sample SY415); **e** Serpentinites (note the different scale); **f** metagabbros (three aliquots of sample SY112 and two aliquots of SY425); **g** hybrid blackwall rocks without tourmaline; **h** tourmaline-bearing hybrid blackwall rocks (two aliquots of sample SY420). Normalising values from Boynton (1985).
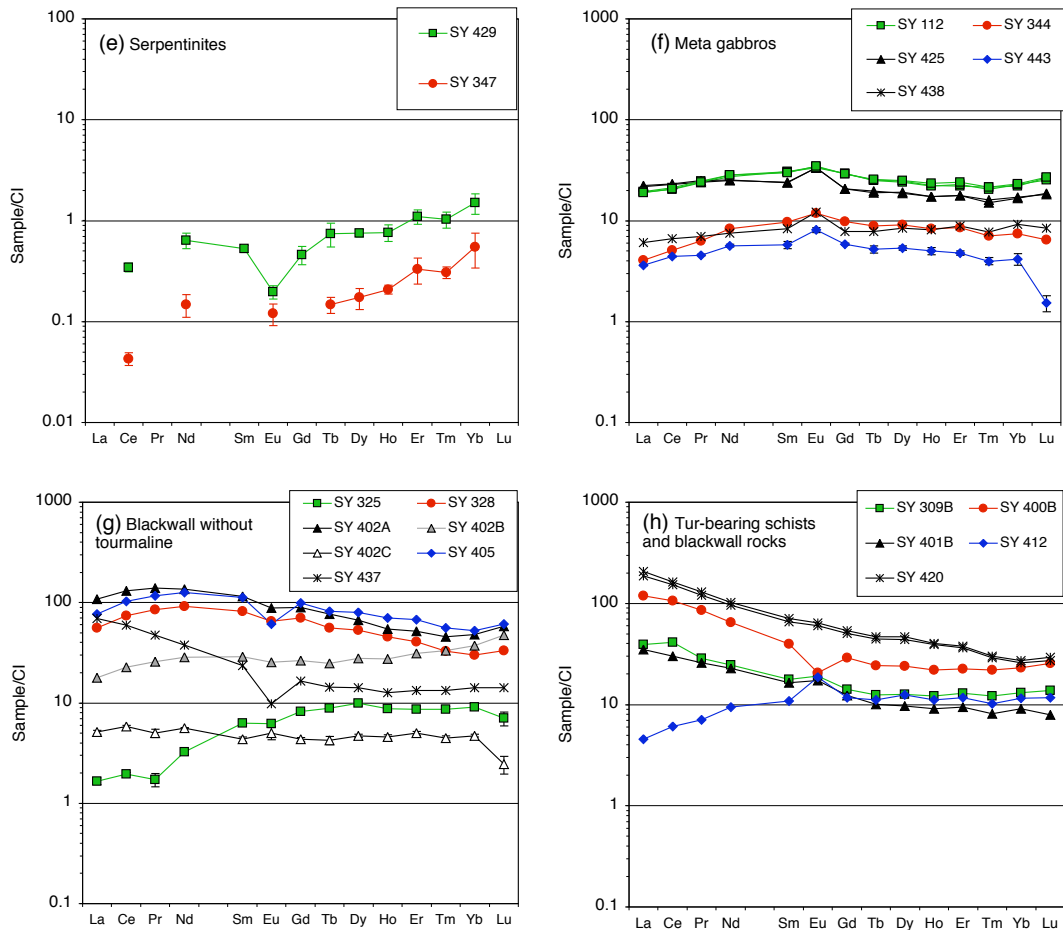
Fig. 4.2. (continued)

Compositions of eclogites SY323, SY324 and SY411 are transitional between those of basalts and rodingites. The enrichment in Th, Pb and Li along with the negative Ce anomaly is possibly related to ocean-floor metamorphism.

The more silica-rich and Ca-poor eclogite (SY109) also shows negative Ti and Eu anomalies (Eu/Eu* ≈ 0.7), but no anomaly in Ce. Furthermore, this rock is less enriched in LREE (La $\sim 90 \times$ CI; (La/Yb)$_{cn} = 2$). The abundances of Sr, Pb and Th are closer to those in MORB, while Ba and Rb are enriched and Li is depleted (Fig. 4.3c). REE patterns of all investigated eclogites are significantly different from those given by Seck *et al.* (1996) for Syros eclogites with moderate concentrations of Ca. The latter patterns are flat or LREE-depleted and show positive Eu anomalies.

4.4. Meta-plagiogranites

(5 samples: SY1, SY8, SY308, SY415, SY431)

Silica-rich, meta-igneous rocks sometimes occur as individual blocks within the mélange, but more often form dyke-like structures (Tomaschek *et al.*, 2003) or net-veined igneous breccias (Dixon, 1968; Dixon & Ridley, 1987; Seck *et al.*, 1996) within eclogites and metagabbros. Their mineralogical composition is dominated by quartz + jadeite + white mica (phengite and/or paragonite) + garnet. Their chemical composition ranges from trachy-andesitic or dacitic to rhyolitic (Fig. 4.1) with up to 73 wt% SiO$_2$, but low K$_2$O contents (< 0.8 wt%). Mg, Fe, Ca as well as compatible trace elements (Ni, Cr, Sc) are also very low, whereas the abundances of Zr are high ($\sim 200 - 670 \, \mu g/g$). MORB-normalised element abundance patterns are characterised by negative anomalies for Sr, P, Ti and Li and positive anomalies for U, Th, Zr. Be is enriched in the three meta-rhyolitic samples. B enrichment was observed in only one sample (Fig. 4.3d). REE patterns are relatively flat (Fig. 4.2d) with (La/Yb)$_{cn}$ values between 0.9 and 2.1, negative Eu anomalies (Eu/Eu* between 0.5 and 0.8) and REE abundances between 25 and 100 $\times$ CI.

The rocks were interpreted as HP metamorphic equivalents of felsic intrusions within former basaltic and gabbroic oceanic crust and were described as "meta-keratophyrs" or "meta-trondhjemites" by Dixon (1968) and Dixon & Ridley (1987), as "meta-plagiogranites" by Tomaschek *et al.* (2003), or with the non-genetic term "jadeite-gneisses" by Okrusch & Bröcker (1990). Major element compositions of these rocks are indeed similar to those of naturally observed plagiogranites from ODP cores (as given in Koepke *et al.*, 2004), and to those of experimentally produced hydrous partial melts from oceanic gabbros (Koepke *et al.*, 2004). It is important to note that the jadeite-quartz gneisses (= meta-plagiogranites) are entirely different from the jadeitites described by Ktenas (1907) and Bröcker & Enders (2001)

that are lower in silica and extremely enriched in Na_2O ($> 10\,wt\%$). These jadeitites with more than $80\,vol\%$ of jadeite are interpreted as products of strong metasomatism of eclogite blocks at high pressures (Bröcker & Enders, 2001), a phenomenon which was also described from other subduction-related mélanges with serpentinite-eclogite juxtapositions, such as Motagua Valley in Guatemala (Harlow, 1994).

4.5. Serpentinites

(2 samples: SY347, SY429)

Serpentinite is a substantial constituent of the mélange of northern Syros. In most places, these rocks are strongly sheared and cut by talc- and/or chlorite-rich veins. Large portions of former serpentinite are replaced by talc- and/or chlorite-rich assemblages, due to reaction of serpentine with adjacent metapelites, metabasites or silica-rich fluid (Dixon, 1968). In the course of this study, only two samples of serpentinite were investigated. Sample SY347 is an almost pure serpentinite with only minor chlorite and Ca-amphibole, while sample SY429 is a talc serpentinite with minor Ca-amphibole. The mesh-like texture of this rock is interpreted as resulting from static hydration and pseudomorphic replacement of a former peridotitic mineral assemblage, without any later deformation (for further details see description on sample SY429 in Appendix B).

Ca-amphibole grains in both samples show edenitic to pargasitic cores with high contents of Al, Na and Cr. The low Si content of $6.54\,cpfu$ translates to a X_{Prg} of 0.73 along the tremolite-pargasite binary join. Schmädicke (2000) calculated the P and T dependence of the pargasite component in Ca-amphibole in peridotitic compositions in the NCMASH system (Na_2O-CaO-MgO-Al_2O_3-SiO_2-H_2O). According to her calculations, Ca-amphibole in a chlorite-peridotite requires pressures in excess of $2.3\,GPa$ at $700\,°C$ in order to stabilise a pargasite component as high as 0.68. The X_{Prg} isopleths have a negative slope in the $P - T$ field, resulting in even higher pressures ($\sim 2.5\,GPa$) at $500\,°C$, and high temperatures of $\sim 800\,°C$ at low pressures ($0.5\,GPa$). If the calculations of Schmädicke (2000) are applicable to the chlorite-amphibole-bearing serpentinites from Syros, the Na-Al-rich amphibole in chlorite serpentinite would require either peak-pressures of the ultramafic rocks significantly higher (i.e. $\sim 2.5\,GPa$) than those derived for the mafic schists and eclogites, or they represent relics of the peridotitic precursor of the serpentinite that formed in excess of $800\,°C$.

Both serpentinite samples have low contents of REE (Fig. 4.2e). Whereas the chondrite-normalised pattern of the pure serpentinite (SY347) is similar to patterns of depleted harzburgites, that of talc serpentinite SY429 shows a negative
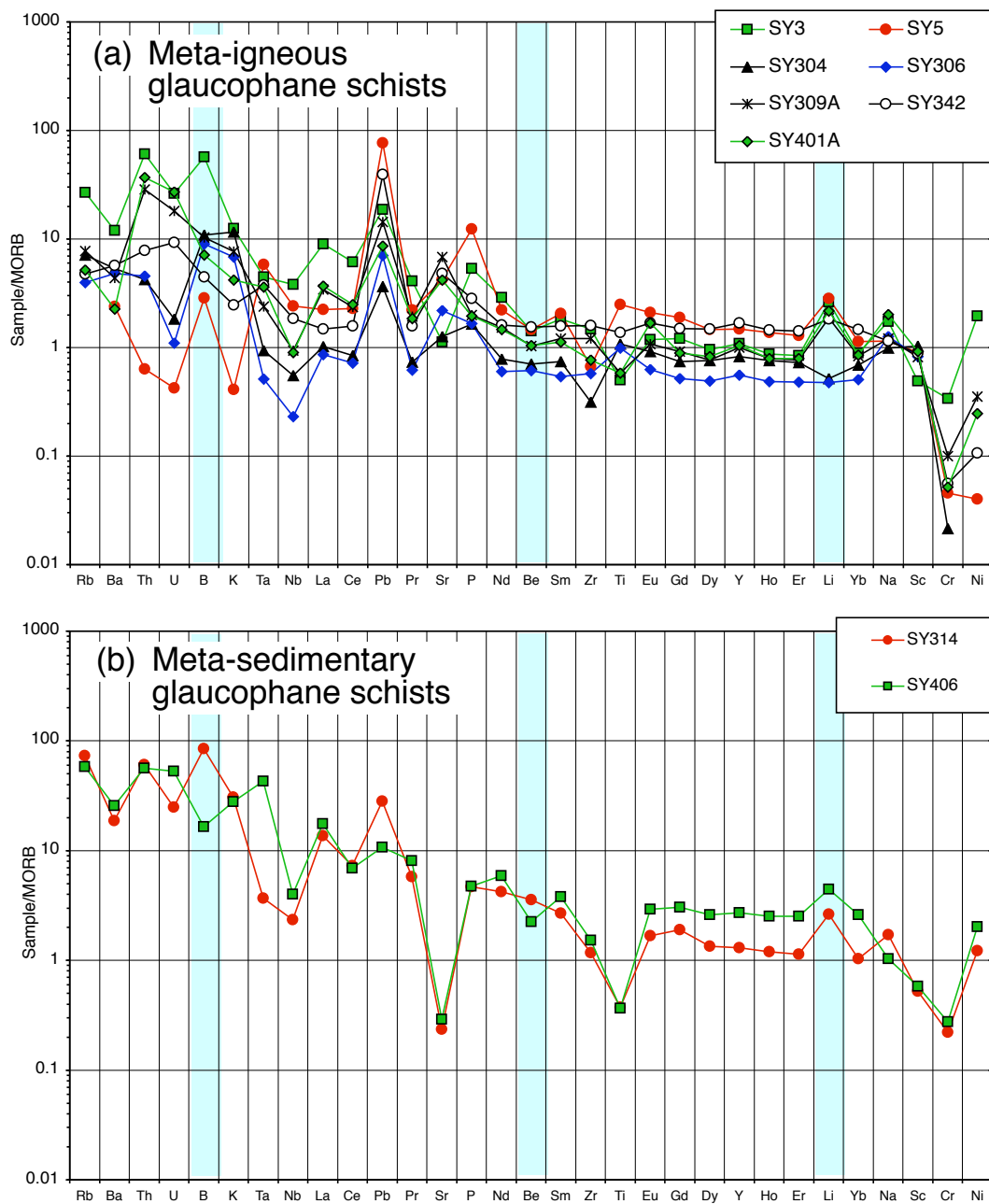
Fig. 4.3. Trace element plots normalised to N-MORB values (Hofmann, 1988). Light elements B, Be and Li are high-lighted. **a** meta-igneous glaucophane schists and felses; **b** metasedimentary glaucophane schists; **c** eclogites; **d** meta-plagiogranites; **e** serpentinites (note different normalisation reservoir: PRIMA = primitive mantle values of McDonough & Sun, 1995); **f** meta-plagiogranites; **g** hybrid blackwall rocks without tourmaline; **h** tourmaline-bearing hybrid blackwall rocks.
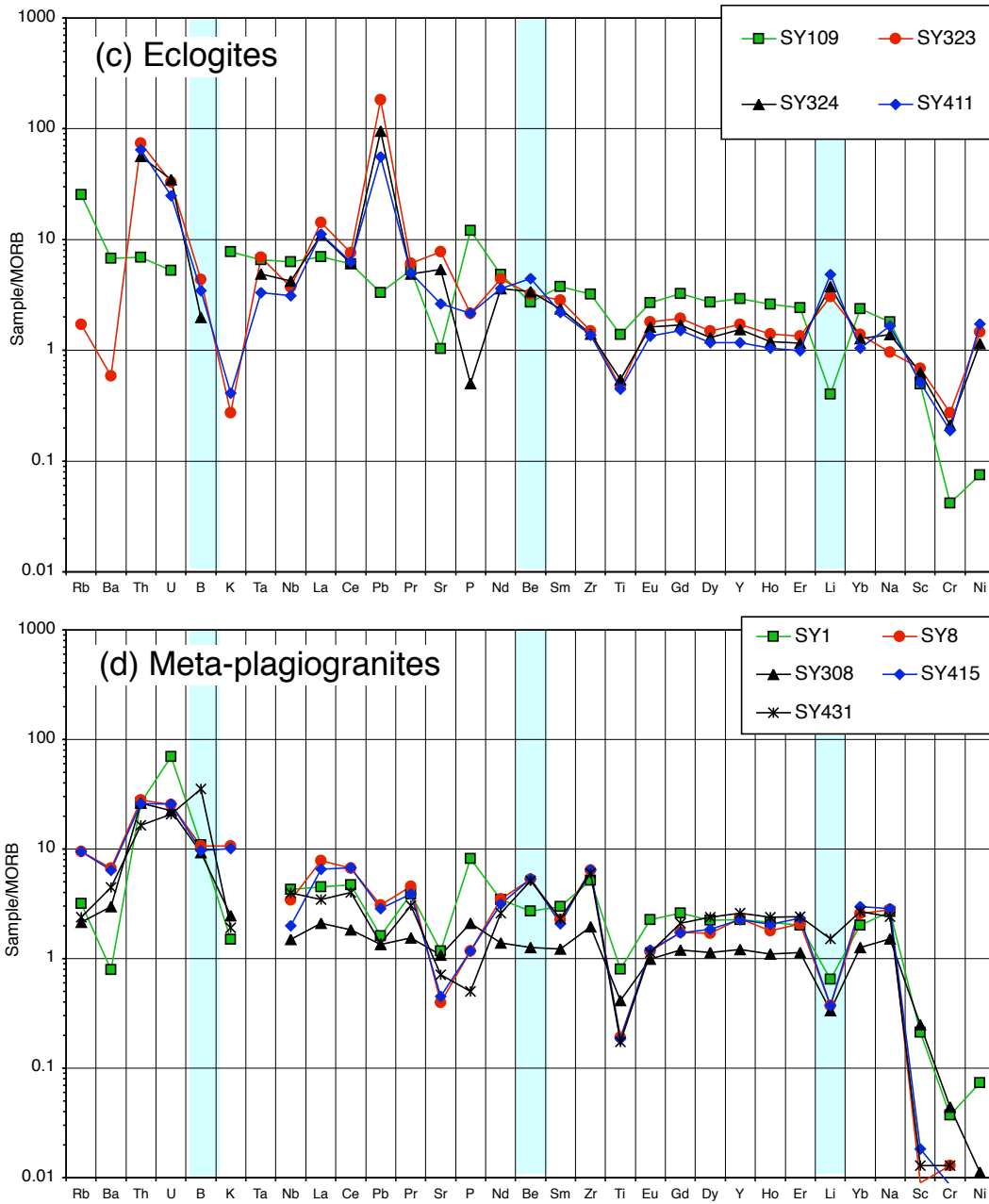
Fig. 4.3. (continued).
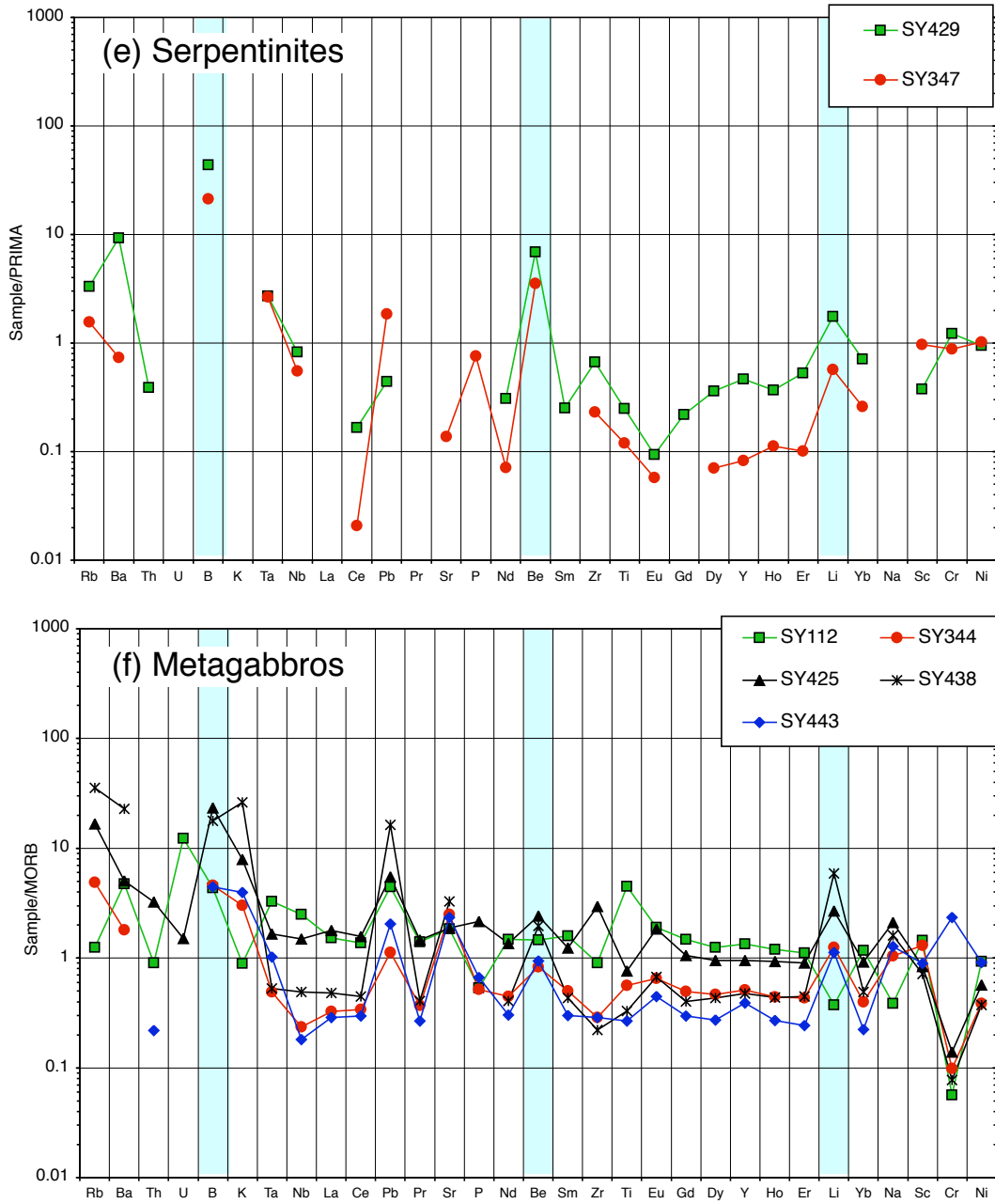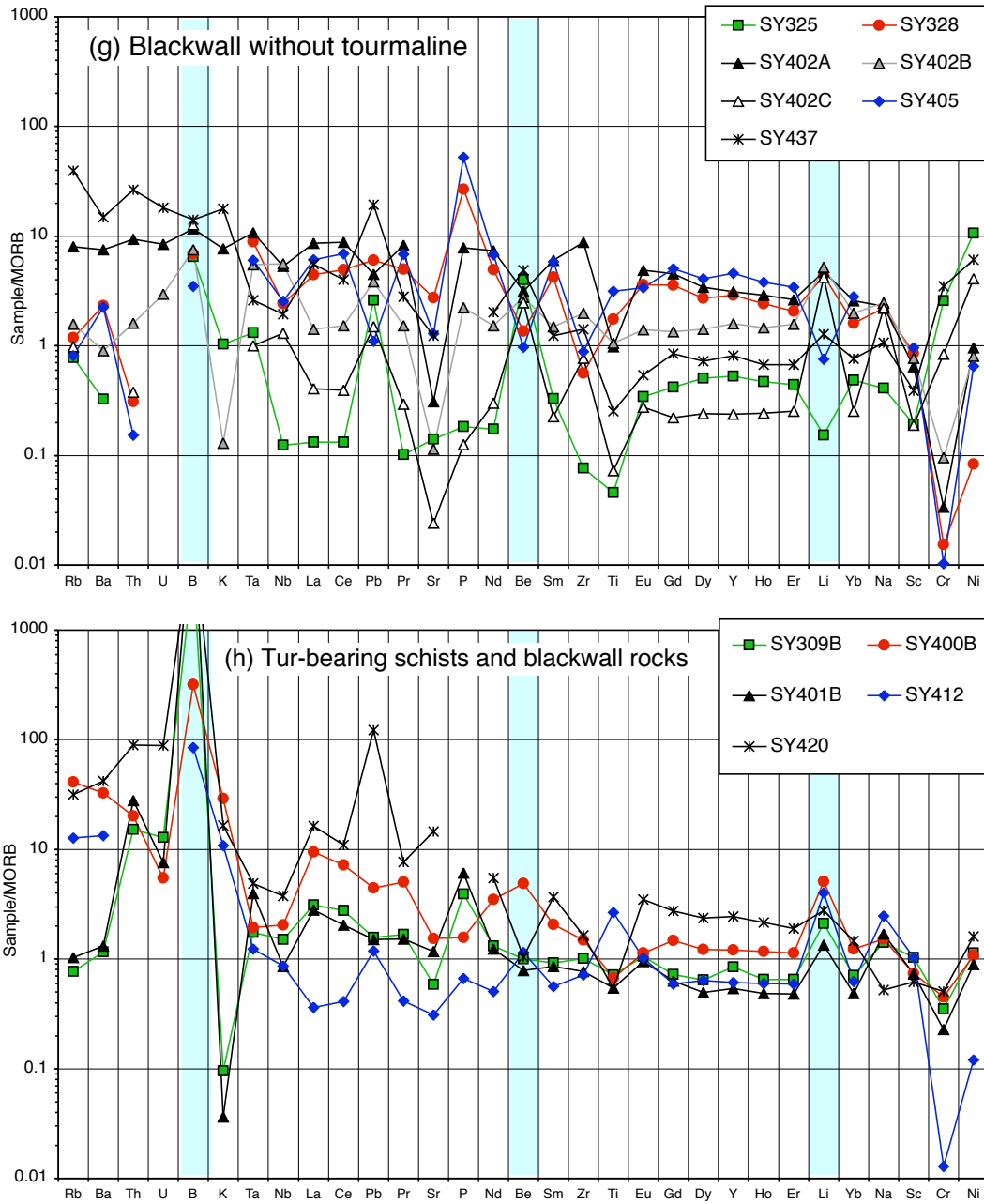
Fig. 4.3. (continued).

Fig. 4.3. (continued).

Eu anomaly (Eu/Eu* = 0.4). Negative Eu anomalies in serpentinites are difficult to explain. Pre-metamorphic processes, such as fractionation of plagioclase in a magmatic precursor rock must be ruled out, as the protolith of the talc-serpentinite was a depleted mantle rock. Therefore, depletion of Eu with respect to other REE in the serpentinite probably occurred during serpentinisation of the former peridotite. Eu, which is partly divalent at low f_{O_2} is expected to differ in fluid/serpentinite partition coefficient from those of the other REE, and probably was selectively leached from the mineral assemblage during serpentinisation.

The abundances of most incompatible trace elements are lower than those of primordial mantle (Fig. 4.3e). It is remarkable that all three light elements, Li, Be and B are enriched.

In principle, there are three possible sources for the peridotitic precursors of the serpentinites: (i) depleted ocean floor (abyssal) peridotites, tectonically emplaced into the magmatic crust and serpentinised at relatively low pressure and temperature at the ocean floor, and subducted together with the magmatic and sedimentary section, or (ii) mantle wedge harzburgites serpentinised at higher $P - T$ conditions by fluids released from the subducted slab and included into the mélange during break-off and exhumation of the meta-igneous/meta-sedimentary blocks, or (iii) they represent ultramafic sections of upper Cretaceous ophiolites that were subducted together with the meta-igneous and meta-sedimentary portions of the Syros mélange (see also Chapter 3 for further discussion).

Dixon & Ridley (1987) argued that the reaction zones (blackwalls) between serpentinites and metapelites are evidence for an early juxtaposition of the two lithologies. In their model, the different rock types of the mélange were deposited in an olistostrome - a turbidite sediment in a trench zone with some blocks reaching kilometer size. However, so far no evidence has been found for a pre-subduction juxtaposition of the different lithologies exposed on Syros.

4.6. Metagabbros

(5 samples: SY112, SY344, SY425G, SY438, SY443)

Coarse-grained epidote-omphacite-glaucophane-Ca-amphibole felses with relic igneous texture have generally been interpreted to represent HP metamorphosed gabbros. Ktenas (1907) already mentioned the similarity of the "saussurite gabbro" from Syros with the Allalin-gabbro in the Central Alps. Dixon (1968), Hecht (1984), Dixon & Ridley (1987), Seck *et al.* (1996), Schumacher *et al.* (2001) and Tomaschek *et al.* (2003) interpreted the large, up to kilometer-sized bodies of these rocks within the mélange as partly undeformed, in some places sheared HP meta-

morphic gabbros. Seck *et al.* (1996) mentioned the observation of relics of magmatic augite by Höpfer (1989). According to Dixon & Ridley (1987), the gabbros were affected by low-*P* hydrothermal metamorphism resulting in "saussurite gabbros" (Czo/Ep + Act + Pg), while glaucophane, garnet and omphacite were formed later during H*P* metamorphism. The saussurite paragenesis can still be observed in the interior of undeformed domains. However, some places also show late-stage assemblages with Ab + Chl + Ep (see description on sample SY443 in Appendix B) that formed by rehydration during exhumation.

Major element compositions of the metagabbros correspond to basalt and basaltic trachy-andesite (Fig. 4.1f), except for sample SY112 that is interpreted as a former Fe-Ti-rich gabbro (see description on sample SY112 in Appendix B). All samples show flat REE patterns [$(La/Yb)_{cn}$ ratios between 0.5 and 1.3] with positive Eu anomalies (Eu/Eu^* between 1.2 and 1.5) (Fig. 4.2f). These patterns are similar to those published by Seck *et al.* (1996) and described by Schumacher *et al.* (2001). They are consistent with a significant accumulation of plagioclase in the gabbroic precursor rocks. MORB-normalised element abundance patterns are characterised by enrichments of highly incompatible LILE and positive anomalies of Pb; only two samples have negative Nb-Ta anomalies (Fig. 4.3f). Li, Be and B are slightly enriched in most samples.

4.7. Hybrid blackwall rocks without tourmaline

(7 samples: SY325, SY328, SY400A, SY402, SY404, SY405, SY437)

The "Glossary of Geology" (Bates & Jackson, 1980) defines the term "blackwall" as *"used in metamorphic petrology for black or dark colored almost monomineralic biotite, chlorite, and amphibole rocks, formed by contact reaction between ultrabasic rock and a rock of contrasting bulk composition"*. Blackwall rocks are hybrids as they have no pre-metamorphic equivalent of comparable chemical composition, but were formed from two different precursor rocks by tectonic mixing and/or metasomatic transfer of matter. This process of blackwall rock formation on Syros was previously described by Dixon (1968) and other workers (Ridley, 1984; Dixon & Ridley, 1987; Okrusch & Bröcker, 1990; Ballhaus & Schumacher, 1995; Seck *et al.*, 1996; Bröcker & Enders, 2001), and is also known from other high-pressure terranes, such as Santa Catalina Island, California/USA (Sorensen & Grossman, 1989; Bebout & Barton, 2002) and NE New Caledonia (Carson *et al.*, 2000; Spandler *et al.*, 2003; Fitzherbert *et al.*, 2004).

Blackwall rocks on Syros comprise a large variety of rock types (Fig. 4.4) generally characterised by parageneses with a limited number of coexisting phases and

low SiO_2 and high Na_2O concentrations. Many are characterised by the absence of quartz. Some of them are even monomineralic, showing the buffering and leaching effects of fluid on different chemical components during metasomatism. Beside chloritites and glaucophanites, there are omphacitites and jadeitites containing $80 - 90\,vol\%$ of Na-rich clinopyroxene. The formation of these blackwall rock types with strongly contrasting compositions are evidence for fluid influx into the mélange at different pressures; omphacitites, jadeitites and glaucophanites formed at blueschist- to eclogite-facies conditions (peak and early retrograde pressures), while albite-chlorite-actinolite assemblages record greenschist facies fluid influx. Transitional lithologies between these different types are also abundant. Therefore, the different products were probably formed by continous fluid influx during exhumation rather than by isolated events. Dixon & Ridley (1987) proposed that some of the reaction zones were even formed during prograde metamorphism before peak pressure was reached.

Major and trace element compositions of blackwall samples are highly variable (Figures 4.2g and 4.3g). Generally, SiO_2 contents decrease from blocks to serpentinite matrix of the mélange, while MgO and Cr contents increase. In some blackwalls, Na_2O and K_2O are strongly enriched and significantly higher than in the interior of the blocks. REE contents generally decrease from blocks to matrix. This is depicted in Fig. 4.2g for sample SY402: REE abundances strongly decrease from SY402A (black triangles) to SY402B (grey triangles) to SY402C (open triangles). Chlorite-talc schist SY325 (green squares in Fig. 4.2g) neighbouring serpentinite matrix shows a LREE-depleted pattern, which is close to the patterns of the serpentinites. Important hosts for REE in the investigated blackwall rocks are accessories such as allanite, titanite, zircon and apatite. MORB-normalised element abundance patterns for most samples display positive anomalies of P, Pb and Li, accompanied by negative anomalies in Sr, Zr and Ti.

4.8. Tourmaline-bearing hybrid blackwall rocks

(10 samples: SY11, SY309B, SY400B, SY401B, SY412, SY413, SY420, SY327, SY441, SY442)

Tourmaline in the blackwall samples occurs in various places within the mélange, forming mm-thick layers on the surface of the high-pressure blocks (Fig. 4.4b and c), or more evenly distributed single crystals or clusters of crystals (Fig. 4.4d) within them. Two samples (SY309B, SY420) are schists from the matrix, that contain tourmaline-rich layers or veins. Tourmaline in all samples is euhedral and black in hand specimen and forms mm- to cm-sized crystals, in paragensis with jadeite-rich
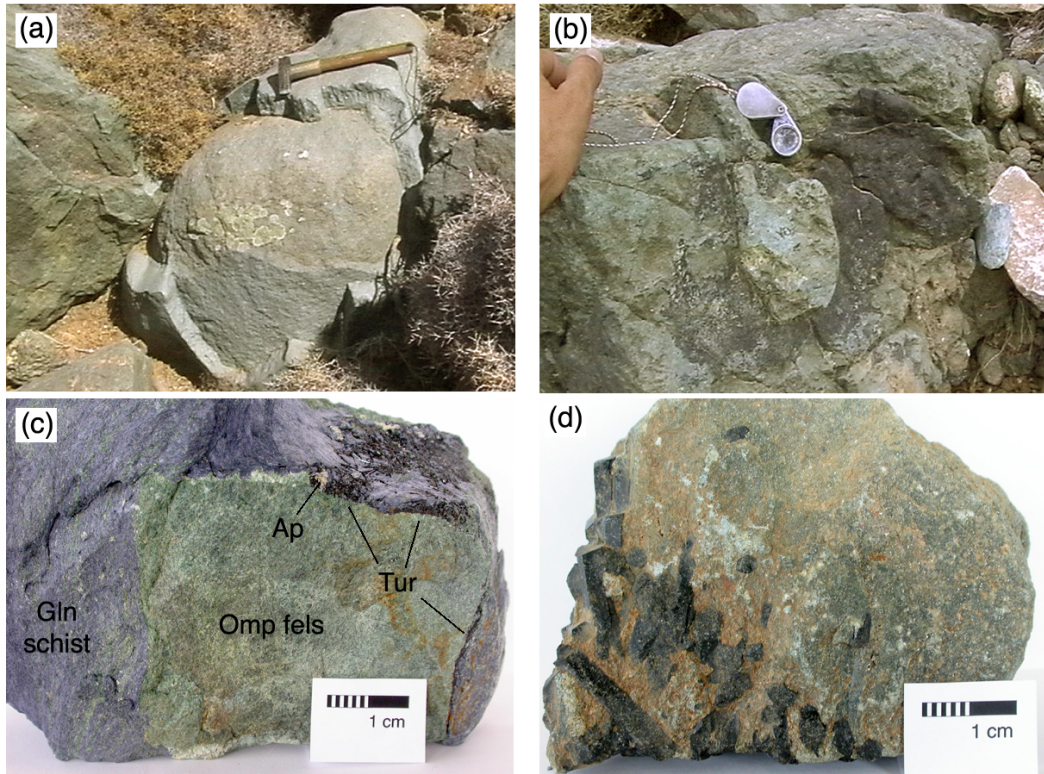
Fig. 4.4. Different varieties of blackwalls in the field and in handspecimen. **a** Jadeite fels enveloped by a ~10 cm thick layer of almost pure chlorite. **b** Tourmaline (black) covering a H*P* block in a dense layer (see also description of sample SY442). **c** Tourmaline and apatite at the contact between an omphacite fels and the sourrounding glaucophanite. **d** Centimeter-sized tourmaline crystals in the outer zone of a jadeite fels (see also description of samples SY11 and SY400).

83

omphacite. Quartz was not observed in any of the samples. Major and trace element composition of the tourmaline-bearing blackwall rocks are highly variable, similar to the variety of the tourmaline-free blackwall samples (Fig. 4.3). Beside B, which is of course strongly enriched in the tourmaline-bearing samples, Li also shows a positive anomaly in all samples. REE patterns of the majority of rock samples show LREE enrichment with $[(La/Yb)_{cn}$ ratios between ~ 3 and ~ 7.5; La up to $200 \times CI]$, with the exception of eclogitic sample SY412, which shows a REE pattern similar to the metagabbros (see Figs. 4.2f and g). All REE concentrations of tourmaline are close to or below CI chondritic values and are strongly depleted with respect to the whole rock concentration (Marschall *et al.*, 2002b; and Chapter 11). A detailed discussion on the $P - T$ conditions and the fluid-rock interaction history related to the formation of tourmaline and tourmaline-bearing blackwalls is given in Chapter 10.

4.9. Silicate marbles

(3 samples: SY2, SY335, SY432)

Siliceous calcite and calcite-dolomite marbles were sampled from the direct vicinity of the mélange. The rocks show different parageneses, like $Cal + Dol + Qtz + Omp$ in SY2, $Cal + Gln + Qtz$ in SY335, or $Cal + Qtz + Ab$ in SY432 (+ white mica, epidote/clinozoisite and accessories). The stability of glaucophane in calcite marble was discussed by Schumacher *et al.* (2000), who showed, that H_2O activity of a fluid in the rock has to be at least 0.97, in order to inhibit the breakdown of glaucophane + calcite (paragensis in sample SY335) to dolomite + omphacite + quartz (displayed in sample SY2). The siliceous marbles are interpreted as carbonate sediments with a contribution of clay and possibly basaltic tuffitic material, as well as ultramafic detritus (see discussion on sample SY2). Schumacher *et al.* (2001) interpreted the Syros former sediments as immature volcano-clastic material interspersed with shallow water carbonates.

4.10. Ep-Qtz vein

(1 sample: SY425D)

High-pressure blocks in the mélange of Syros are in some localities cut by veins consisiting of epidote + quartz ($\pm Grt \pm Omp$) or omphacite + albite or epidote + glaucophane. These veins were probably produced at different $P - T$ conditions by hydrofracturing during dehydration of the host rocks or influx of external fluids. Sample SY425 is a coarse-grained glaucophane-dominated fels truncated by a

quartz vein (SY425D), which is almost exclusively quartz in its center part with individual red euhedral garnet crystals, and green omphacite ($\sim$ Jd$_{38}$) in direct contact to quartz. At the contact between the quartz vein and the host rock, a border zone consisting of large ($\sim$ 1 cm in length) euhedral epidotes formed, which seem to have grown into an open HP fluid-filled crack, in the $P - T$ stability field of omphacite (Jd$_{38}$) + quartz.

5. Geochemistry of Lithium, Beryllium and Boron

5.1. General properties of the light elements

The elements Li, Be and B with the atomic numbers 3, 4 and 5 have very low atomic masses of 6.941 u, 9.012182 u and 10.811 u, respectively (Pfennig *et al.*, 1998), and therefore, have been named "low atomic mass elements" or simply "light elements". The alkali metal Li, the alkaline earth metal Be and the nonmetal B are located in the second period of the periodic system, and form relatively small ions with the electron configuration of He ($1s^2$). Li is exclusively monovalent (Li^+), Be is divalent (Be^{2+}) and B is trivalent (B^{3+}) in nature. Cosmochemically all three elements are lithophile in character, with Be being refractory and Li and B being moderately volatile (McDonough & Sun, 1995).

Lithium   Li is 4-, (4+2)-, 6- or 8-fold coordinated to oxygen, or is found in more distorted and complicated coordination spheres (Wenger & Armbruster, 1991; Olsher *et al.*, 1991). The ionic radius of Li^+ in 6-fold coordination is 76 pm (Shannon, 1976), which is close to the radii of octahedrally coordinated Mg (72 pm) and Fe^{2+} (78 pm). Hence, in most ferro-magnesian minerals Li^+ is substituting for these cations on the octahedral sites. The substitution may be hindered by charge balance limitations. Some minerals like feldspars or amphiboles incorporate Li^+ in sites with larger coordination (7, 8 or 12) for Na^+ or K^+. In hydrous fluids, Li is tetrahedrally coordinated to four H_2O molecules (Olsher *et al.*, 1991). A detailed discussion on the crystal chemistry of Li is given in Wenger & Armbruster (1991) and in Olsher *et al.* (1991).

Lithium has two stable isotopes ^6Li and ^7Li with natural abundances of 7.5 atom% and 92.5 atom%, respectively (Pfennig *et al.*, 1998). Their high relative mass difference ($\sim 17\%$) is responsible for a variation in the Li isotopic composition of $\sim 60\%o$ in nature (Tomascak, 2004). Isotopic fractionation of Li with the heavier isotope enriched in aqueous fluids in contact with silicate rocks is explained by the preference of the heavier isotope for the smaller coordination sphere – the tetrahedron – in the fluid (Tomascak, 2004). Most recently, Li isotopes have attracted more and more attention by geochemists working on metamorphic, igneous and sedimentary rocks (e.g. Chan & Kastner, 2000; Zack *et al.*, 2003; Elliott *et al.*, 2004; Tomascak, 2004). The strong isotopic fractionation at low temperatures pro-

vides a robust tool for tracing hydrous alteration processes at the Earth's surface, and has a great potential to detect low-temperature altered material in subduction zone related fluids, magmas or metamorphic rocks, in mantle xenoliths or ocean island basalts. Detailed discussions on the geochemical applications of the Li stable isotope system are given in Tomascak (2004), Elliott *et al.* (2004) and Bouman (2004). Half lives of all radioactive isotopes of Li (^{8}Li, ^{9}Li and ^{11}Li) are < 1s (Pfennig *et al.*, 1998), and hence have no geological applications.

Beryllium   Be in natural minerals occurs exclusively in tetrahedral coordination to oxygen (Hawthorne & Huminicki, 2002). Be-O bonds are covalent rather than ionic. However, the effective ionic radius of Be^{2+} is determined to be 27 pm, which is very similar to that of Si^{4+} (26 pm; Shannon, 1976). The difference in charge, however, limits the solid solution between the two elements, and a direct substitution of Si^{4+} by Be^{2+} is rare. More commonly, Be^{2+} substitutes for tetrahedral Al^{3+} (39 pm) or tetrahedral B^{3+} (11 pm). Another important mechanism for the incorporation of Be^{2+} into nominally Be-free minerals is into tetrahedrally coordinated sites which are vacant in the Be-free structure. A detailed discussion on the crystal chemistry of Be is given in Hawthorne & Huminicki (2002).

Beryllium has only one stable isotope (^{9}Be). However, there are two cosmogenic radioactive isotopes of Be which are of geochemical interrest. ^{7}Be with a half live of 53 d (Pfennig *et al.*, 1998) has been used for the study of environmental processes on the < 1 year timescale (see Kaste *et al.*, 2002, for a review on ^{7}Be). ^{10}Be with a half live of 1.6 Ma (Pfennig *et al.*, 1998) has been used to trace the subduction of cosmogenic ^{10}Be-bearing sediments by monitoring the output of this nuclide at arc volcanoes, and to put a time frame on these processes. It has also been used for dating of young sediments and for monitoring Milankovitch periodicities in the Pliocene and Quarternary, as its production is dependent on cosmic ray activity (see Morris *et al.*, 2002, for a review on ^{10}Be). Half lives of other radioactive isotopes of Be (^{11}Be, ^{12}Be and ^{14}Be) are in the order of seconds (Pfennig *et al.*, 1998), and hence have no geological applications.

Boron   Boron in minerals, melts and fluids is either trigonally (3-fold) or tetrahedrally (4-fold) coordinated to oxygen (see: Hawthorne *et al.*, 2002). B-O bonds have a strongly covalent character. B does not form isolated B^{3+} ions, but is almost exclusively bonded to O in nature, and occurs as $B(OH)_3$, $B(OH)_4{}^-$ or other complex ions. However, the effective ionic radius of B^{3+} is as small as 11 pm in tetrahedral coordination and only 1 pm in trigonal coordination. Its effective radius is comparable to that of C (^{III}C $= -8$ pm; ^{IV}C $= 15$ pm), which enables an incor-

poration of B into calcite (^{III}B), aragonite and diamond (^{IV}B). In silicate minerals, B^{3+} may substitute for Si^{4+} into the tetrahedral sites, which requires charge balancing and some distortion of the TO_4 units, due to the significantly smaller radius of B^{3+}. On the other hand, it may substitute for tetrahedral Al. A detailed discussion on the crystal chemistry of B is given in Hawthorne *et al.* (2002).

Boron has two stable isotopes ^{10}B and ^{11}B, with natural abundances of 19.9 atom% and 80.1 atom%, respectively (Pfennig *et al.*, 1998). Their high relative mass difference ($\sim 10\%$) is responsible for a variation of $\sim 100\%o$ in nature (Palmer & Swihart, 2002). Similar to Li, the large B isotopic fractionation at low temperatures has led to the use of the B stable isotope system for studies on processes acting on the Earth's surface (e.g. Hemming & Hanson, 1992; Barth, 1998) and for the detection of subducted material in fluids, serpentinites and IABs (e.g. Ishikawa & Nakamura, 1994; Benton *et al.*, 2001). An overview on the B isotope system is given in a seperate section below (Section 5.2), and in Palmer & Swihart (2002). Half lives of all radioactive isotopes of B (^{8}B and ^{12}B to ^{19}B) are < 1 s (Pfennig *et al.*, 1998), and hence have no geological applications.

5.2. Boron isotope fractionation

5.2.1. Theoretical and experimental background and formulation

Fractionation of different isotopes of one element between different phases (minerals or fluids) may be controlled by two different processes: kinetic and equilibrium fractionation. Kinetic fractionation is due to differences in diffusivity of the different isotopes or due to contrasting activation energies during phase transitions of molecules containing different isotopes. During evaporation of H_2O, for example, kinetic fractionation leads to a strong enrichment of $^{1}H_2^{16}O$ in the vapor phase. Equilibrium stable isotope fractionation is based on differences in the structural position in which the element of interest is incorporated in the various phases. Differences in the types of bonding, in oxidation states, and in coordination spheres lead to differences in bond strengths of the element in a crystal lattice, a melt, or in a solution. Fractionation effects are notably large where the coordination polyhedra of the element between the two phases are different. Boron in minerals, melts and fluids is trigonally or tetrahedrally coordinated to oxygen, and therefore, displays large isotopic fractionation between different phases. During stable isotope fractionation, the heavier isotope is preferably incorporated into the substance with higher bond strength (Chacko *et al.*, 2001). In the case of B the higher bond strength of the trigonal coordination leads to a fractionation of ^{11}B into the trigonal sites, and a relative enrichment of the light isotope ^{10}B in the phase with tetrahedrally coor-

dinated B (Palmer & Swihart, 2002). During equilibrium isotope fractionation, the isotopic compositions of different phases can be described by an exchange reaction. For example, the exchange of B isotopes between boro-muscovite and aqueous fluid may be written as:

$$^{11}B(OH)_{3_{fl}} + KAl_2[^{10}BSi_3O_{10}(OH)_2] = ^{10}B(OH)_{3_{fl}} + KAl_2[^{11}BSi_3O_{10}(OH)_2] \tag{5.1}$$
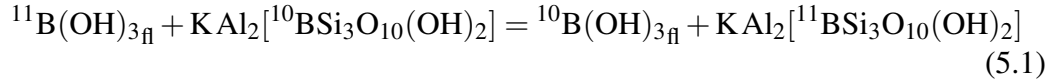
The equilibrium constant K_{Ms-fl} for this exchange reaction is:

$$K_{Ms-fl} = \frac{[^{10}B_{fl}] \cdot [^{11}B_{Ms}]}{[^{11}B_{fl}] \cdot [^{10}B_{Ms}]} = \frac{\left(\frac{^{11}B}{^{10}B}\right)_{Ms}}{\left(\frac{^{11}B}{^{10}B}\right)_{fl}} \tag{5.2}$$

The equilibrium constant K_{Ms-fl} normalised to the exchange of one mole of ^{10}B and one mole of ^{11}B (which is already the case in example 5.2) is defined as the isotope fractionation factor α for this reaction. The B isotope fractionation factor α_{Ms-fl} equals the ratio of the B isotope ratios between muscovite and fluid.

$^{11}B/^{10}B$ ratios in nature are in the order of ~ 4 and vary by $\sim 100‰$. B isotope ratios are commonly expressed in the delta notation, with:

$$\delta^{11}B = \left(\frac{\left(\frac{^{11}B}{^{10}B}\right)_{Sample}}{\left(\frac{^{11}B}{^{10}B}\right)_{Standard}} - 1\right) \cdot 1000. \tag{5.3}$$

The common international isotope standard for B is boric acid NBS-SRM951 with a $^{11}B/^{10}B$ isotope ratio of 4.043627 (Catanzaro *et al.*, 1970). Isotope fractionation between two phases A and B is expressed either by using the fractionation factor as $1000 \ln \alpha_{A-B}$ or simply by the difference between the $\delta^{11}B$ values of the two phases, which is expressed as:

$$\Delta^{11}B_{A-B} = \delta^{11}B_A - \delta^{11}B_B. \tag{5.4}$$

Within the range of natural samples and natural B isotope fractionation, the error introduced by the approximation:

$$\Delta^{11}B \approx 1000 \ln \alpha \tag{5.5}$$

is smaller than the analytical uncertainties and the two terms are often used equivalently.
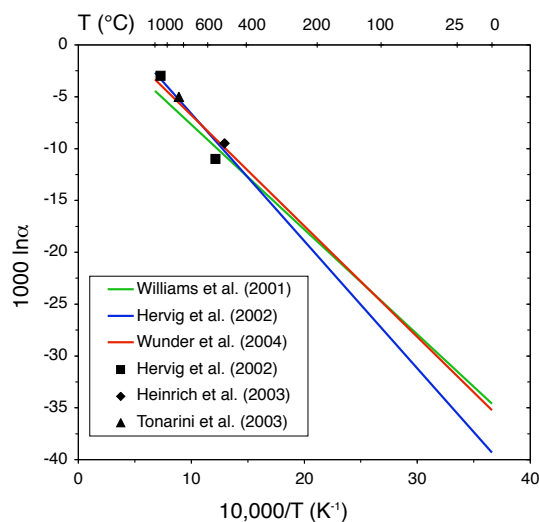
Fig. 5.1. B isotope fractionation ($1000 \ln \alpha$) between silicates and hydrous fluids as a function of reciprocal temperature ($10^4/T$, T in K). Temperature in °C is given on top. B isotope fractionation by Williams *et al.* (2001), Hervig *et al.* (2002) and Wunder *et al.* (2004) are displayed. Additionally some examples of naturally and experimentally observed fractionation pairs are given, as discussed in the text. Several further examples are given in Peacock & Hervig (1999) and Hervig *et al.* (2002).

Equilibrium fractionation of stable isotopes is temperature and pressure dependent; the influence of temperature is much greater than that of pressure. It is largest at Earth's surface conditions and decreases with increasing P and T. Experimental studies (e.g. Hervig *et al.*, 2002, and references therein; Heinrich *et al.*, 2003; Sanchez-Valle *et al.*, 2004; Wunder *et al.*, 2004) have investigated the temperature dependence of B isotopic fractionation between phases of different B coordination (e.g. mica, amphibole, melt, fluid, tourmaline). The results show larger fractionation than predicted by Kakihana *et al.* (1977). Williams *et al.* (2001), Hervig *et al.* (2002) and Wunder *et al.* (2004) demonstrated a systematic decrease of fractionation between silicates and hydrous fluids with increasing temperature, given by the formula

$$\Delta^{11}\text{B} \approx 1000 \ln \alpha = a - b/T \tag{5.6}$$

where α is the fractionation factor, T is the absolute temperature (K) and a and b are constants which are different between the different authors: Williams *et al.* (2001) calculated $a = 2.44$ and $b = 10120$, Hervig *et al.* (2002) calculated $a = 5.68$ and $b = 12290$, and Wunder *et al.* (2004) calculated $a = 3.94$ and $b = 10700$. However, B isotope fractionation ($\Delta^{11}\text{B}$) calculated from the equation by using the three different data sets results in values relatively close to each other ($\pm 1‰$) in the temperature range of 300 to 700 °C (see Fig. 5.1), which is most relevant for

91

subduction zone metamorphic processes.

5.2.2. Coordination of B in different phases

B coordination in H_2O at ambient $P-T$ conditions is strongly dependent on pH. At pH > 9, B is tetrahedrally coordinated in $B(OH)_4^-$ groups. In neutral and acidic (pH < 7) hydrous fluids, it is predominantly trigonally coordinated in $B(OH)_3$ units. Recent experiments have shown that this also holds true at high pressures up to 3.0 GPa (Thomas *et al.*, 2004). Modern seawater has a pH of ~ 8, indicating $\sim 80\%$ of its B in trigonal coordination, with a strong sensitivity to changes in pH (Palmer & Swihart, 2002). B in boro-silicate melts varies between trigonally and tetrahedrally coordinated, depending on silica/B_2O_3 and alkali oxide/B_2O_3 ratios (Dell *et al.*, 1983; Dingwell *et al.*, 2002). For silicate melts containing B at trace levels, Hervig *et al.* (2002) suggested B occupies trigonally coordinated sites. These authors argue on the basis of experimentally observed fluid/melt B isotope fractionation. They also suggest that the B coordination is independent from the chemistry of the silicate melts. In contrast, spectroscopic studies by Tonarini *et al.* (2003) on natural rhyolitic glasses revealed that B at trace levels ($\sim 500\,\mu g/g$) is predominantly in trigonal coordination, with only $\sim 8-26\%$ of the B in occupying tetrahedral sites. Tonarini *et al.* (2003), who investigated only three different samples could not find a correlation of B speciation and melt composition (e.g. $Al/(Al+Si)$).

B in tourmaline, the most wide-spread boro-silicate in natural rocks, is predominantly trigonally coordinated. Only recently has the presence of tetrahedrally coordinated B been demonstrated in natural tourmaline (Ertl *et al.*, 1997; Tagg *et al.*, 1999; Hughes *et al.*, 2000; Kalt *et al.*, 2001; Schreyer *et al.*, 2002; Marschall *et al.*, 2004c). B in calcite is trigonally coordinated, whereas it shows a tetrahedral coordination in aragonite (Sen *et al.*, 1994). White micas (muscovite, phengite and paragonite) have been demonstrated to be the most important hosts of boron in metabasites and metasediments (Domanik *et al.*, 1993; Nakano & Nakamura, 2001). Mica is generally accepted to contain boron in tetrahedral coordination (Werding & Schreyer, 2002; Hervig *et al.*, 2002; Tonarini *et al.*, 2003), and therefore it should preferentially incorporate the lighter isotope ^{10}B in equilibrium with tourmaline or acidic hydrous fluid. Experimental studies by Heinrich *et al.* (2003) show fractionation of 9.5‰ between boro-muscovite and hydrous fluid at 500 °C. A natural muscovite-tourmaline pair investigated by Hervig *et al.* (2002) shows fractionation of 11‰ in rocks equilibrated at about 550 °C. Tonarini *et al.* (2003) observed a B isotope fractionation of ~ 5‰ between rhyolitic glass and its included biotite, formed at magmatic temperatures of ~ 850 °C. Hervig *et al.* (2002) experimentally determined a B isotope fractionation of ~ 3‰ at 1100 °C between hydrous fluid

and basaltic melt.

The strong fractionation of B isotopes at near-surface conditions as well as metamorphic and even magmatic temperatures together with the mobility of B in fluids and melts enhances the value of B as a tracer in geological processes of various kinds. Water-sediment interaction, alteration of oceanic crust, and dehydration processes during diagenesis and metamorphism have been investigated using the B isotope system – and, of course, all other mass-transfer processes operating in the Earth's subduction zones.

5.3. Budgets of Li, Be and B, and variation of δ^{11}B in the mantle

Primitive mantle concentrations are reported to be $1.6 \pm 0.3\,\mu g/g$ Li, $70 \pm 7\,ng/g$ Be and $260 \pm 100\,ng/g$ B (Chaussidon & Jambon, 1994; Chaussidon, 1995; McDonough & Sun, 1995; Palme & O'Neill, 2003). Peridotitic mantle rocks contain $0.6 - 1.9\,\mu g/g$ Li (Jagoutz *et al.*, 1979; Ryan & Langmuir, 1987; McDonough & Sun, 1995; Eggins *et al.*, 1998; Seitz & Woodland, 2000; Seitz *et al.*, 2003; Ottolini *et al.*, 2004), $8 - 70\,ng/g$ Be (McDonough & Sun, 1995; Paquin *et al.*, 2004), and $50 - 800\,ng/g$ B (Agyei & McMullen, 1978; Curtis *et al.*, 1980; Higgins & Shaw, 1984; Shaw *et al.*, 1988a; Chaussidon & Libourel, 1993; Chaussidon & Jambon, 1994; McDonough & Sun, 1995; Paquin *et al.*, 2004; Ottolini *et al.*, 2004). Estimates for the depleted upper mantle suggest B abundances of ~ 10 to $100\,ng/g$ (Chaussidon & Libourel, 1993; Chaussidon & Marty, 1995; Leeman & Sisson, 2002; Ottolini *et al.*, 2004). Li contents reported by Seitz *et al.* (2003) and by Brooker *et al.* (2004) for pyroxenitic and eclogitic mantle rocks range from $2.5 - 9.0\,\mu g/g$. OIB source mantle probably shows higher abundances of B with respect to MORB source mantle (Chaussidon & Marty, 1995). Be contents calculated by Ryan (2002) for OIB source mantle are significantly higher ($80 - 100\,ng/g$) than those of MORB source mantle ($20 - 30\,ng/g$). Ryan (2002) speculates on a global scale recycling of Be-rich oceanic crust to be responsible for the Be enrichment in OIB source mantle.

During mantle melting, all three elements are incompatible with whole rock/melt partition coefficients of $D_{Li} \approx 0.1$ to 0.2 for Li, similar to Yb (Ryan & Langmuir, 1987; Blundy & Wood, 1994; Blundy *et al.*, 1998; Brenan *et al.*, 1998a; Blundy & Dalton, 2000), $D_{Be} \approx 0.02$ to 0.04 for Be, similar to Nd (Tatsumi & Isoyama, 1988; Ryan & Langmuir, 1988; Brenan *et al.*, 1998a), and $D_B \approx 0.01$ to 0.03 for B (Ryan & Langmuir, 1993; Chaussidon & Jambon, 1994; Brenan *et al.*, 1998a). Nearly constant ratios of Li/Yb (~ 1.7), Li/V (~ 0.2), Be/Nd (~ 0.05), Be/Zr (~ 0.005), and B/K (~ 0.001) have been observed in mantle-derived magmas and primitive

Table 5.1. Compilation of literature data on Li concentrations of different geochemical reservoirs.

Material	Lithium	Reference
Solar abundance	57.1 Li per 10^6 Si	Anders & Grevesse (1989)
CI chondrites	1.49 µg/g	Anders & Grevesse (1989); Palme & Jones (2003)
Primitive mantle	1.6 µg/g	McDonough & Sun (1995)
	1.9±2 µg/g	Ryan & Langmuir (1987)
	1.6±0.3 µg/g	Palme & O'Neill (2003)
Depleted mantle	0.7 - 1.9 µg/g	Ryan & Langmuir (1987); Seitz & Woodland (2000); Seitz *et al.* (2003)
MORB source mantle	1.6 - 1.8 µg/g	Ottolini *et al.* (2004)
Continental Crust	11 - 13 µg/g	Rudnick & Fountain (1995); Taylor & McLennan (1995)
	17 - 18 µg/g	Wedepohl (1995); Gao *et al.* (1998)
Upper CC	20 - 22 µg/g	Wedepohl (1995); Taylor & McLennan (1995); Gao *et al.* (1998)
	35±11 µg/g	Teng *et al.* (2004)
Lower CC	6 µg/g	Rudnick & Fountain (1995)
	11 - 13 µg/g	Taylor & McLennan (1995); Wedepohl (1995); Gao *et al.* (1998)
Seawater	0.18 µg/g	e.g. Morozov (1968); Broeker & Peng (1982)
Vent fluids	0.14 - 9.9 µg/g	e.g. Chan *et al.* (1994a); Foustoukos *et al.* (2004)
MOR fresh magmatic rocks		
> 7 % MgO	3 - 8 µg/g	see Fig. 5.2 for references
< 7 % MgO	5 - 30 µg/g	see Fig. 5.2 for references
OIB	3 - 10 µg/g	Ryan & Langmuir (1987); Dostal *et al.* (1996); Chan & Frey (2003)
IAB	1.0 - 46.7 µg/g	e.g. Leeman *et al.* (2004); Bouman (2004) and therein
Forearc		
Serpent. seamounts	0.8 - 26 µg/g	Ryan *et al.* (1996b); Benton *et al.* (2004)
Trench fluids	0.06 - 3.4 µg/g	e.g. You *et al.* (1995a); Chan & Kastner (2000); Kopf *et al.* (2003b)
Hydrothermally altered MORB		
< 150 °C	6 - 37 µg/g	e.g. Kelley *et al.* (2003); Bouman *et al.* (2004)
> 150 °C	2 - 19 µg/g	Chan *et al.* (1992)
Weathered basalt	7 - 75 µg/g	e.g. Stoffyn-Egli & Mackenzie (1984); Chan *et al.* (1992)
Serpentinite	0.6 - 8.2 µg/g	Decitre *et al.* (2002)
Marine sediments		
Clay	0.3 - 118 µg/g	e.g. Chan & Kastner (2000); Bouman (2004) and therein
Carbonates	0.2 - 3.3 µg/g	Hoefs & Sywall (1997)

See also Bouman (2004) and Tomascak (2004) for reviews on Li in terrestrial materials.

Table 5.2. Compilation of literature data on Be concentrations of different geochemical reservoirs.

Material	Beryllium	Reference
Solar abundance	0.73 Be per 10^6 Si	Anders & Grevesse (1989)
CI chondrites	24.9 ng/g	Anders & Grevesse (1989); Palme & Jones (2003)
	27 ng/g	Wasson & Kallemeyn (1988)
Primitive mantle	68 ng/g	McDonough & Sun (1995)
	70 ± 7 ng/g	Palme & O'Neill (2003)
Depleted mantle	8 - 55 ng/g	Paquin & Altherr (2002); Kaliwoda (2004)
Upper mantle	44.2 ng/g	McDonough & Sun (1995)
MORB source mantle	20 - 30 ng/g	Ryan (1989, 2002)
OIB source mantle	80 - 100 ng/g	Ryan (2002)
Continental Crust	1.5 - 2.4 μg/g	Wedepohl (1995); Taylor & McLennan (1995); Gao *et al.* (1998)
Upper CC	1.95 - 3.1 μg/g	Wedepohl (1995); Taylor & McLennan (1995); Gao *et al.* (1998)
Lower CC	0.63 - 1.7 μg/g	Wedepohl (1995); Taylor & McLennan (1995); Gao *et al.* (1998)
Seawater	$0.04 - 0.6$ pg/g	Broeker & Peng (1982); Measures & Edmond (1983)
Marine pore water	~ 2 pg/g	Bourlès *et al.* (1989)
Vent fluids	$90 - 900$ pg/g	e.g. Measures & Edmond (1983); Bourlès *et al.* (1991)
MOR fresh magmatic rocks		
> 7 % MgO	0.1 - 1.0 μg/g	see Fig. 5.3 for references
< 7 % MgO	0.5 - 2.5 μg/g	see Fig. 5.3 for references
OIB	0.5 - 8 μg/g	Ryan & Langmuir (1988); Dostal *et al.* (1996)
Island arc basalts	0.1 - 2.6 μg/g	Ryan & Langmuir (1988); Ryan (2002)
Alkali arc lavas	1 - 10 μg/g	Ryan (2002)
Forearc		
Accretion sediments	1.5 - 2.8 μg/g	You *et al.* (1994)
Pore fluids	$0.3 - 12.6$ pg/g	You *et al.* (1994)
Altered MORB	0.06 - 2.3 μg/g	Bach *et al.* (2001); Kelley *et al.* (2003)
Marine sediments	0.07 - 4 μg/g	Ryan & Langmuir (1988); Bouman *et al.* (2004); Ryan (2002)
Carbonates	0.68 μg/g	Gao *et al.* (1998)
Mn nodules	2 - 15 μg/g	Sharma & Somayajulu (1982); Krishnaswami *et al.* (1982)
Sand-/siltstones	1 - 2 μg/g	Ryan (2002)

See also Ryan (2002) for a review on Be in terrestrial materials.

Table 5.3. Compilation of literature data on B concentrations of different geochemical reservoirs.

Material	Boron	Reference
Solar abundance	21.2 B per 10^6 Si	Anders & Grevesse (1989)
CI chondrites	870 ng/g	Anders & Grevesse (1989)
	690 ng/g	Palme & Jones (2003)
Primitive mantle	250 ± 100 ng/g	Chaussidon & Jambon (1994)
	300 ng/g	McDonough & Sun (1995)
	100 ± 20 ng/g	Chaussidon (1995)
	260 ± 100 ng/g	Palme & O'Neill (2003)
Depleted mantle	≤ 100 ng/g	Leeman & Sisson (2002)
	50 - 300 ng/g	Chaussidon & Libourel (1993)
Upper mantle	75 ± 15 ng/g	Chaussidon (1995)
MORB source mantle	10 - 15 ng/g	Chaussidon & Marty (1995)
	70 - 100 ng/g	Ottolini *et al.* (2004)
OIB source mantle	90 - 110 ng/g	Chaussidon & Marty (1995)
Continental Crust	10 - 11 µg/g	Taylor & McLennan (1995); Wedepohl (1995)
	18 µg/g	Gao *et al.* (1998)
Upper CC	15 - 28 µg/g	Wedepohl (1995); Taylor & McLennan (1995); Gao *et al.* (1998)
Lower CC	5 - 8.3 µg/g	Wedepohl (1995); Taylor & McLennan (1995); Gao *et al.* (1998)
	<1 - 2 µg/g	Shaw *et al.* (1986, 1988c); Leeman *et al.* (1992)
Seawater	4.4 µg/g	Uppstroem (1974); Spivack & Edmont (1987)
Vent fluids	3.8 - 11.5 µg/g	e.g. Spivack & Edmont (1987); Foustoukos *et al.* (2004)
MOR fresh magmatic rocks		
> 7 % MgO	0.4 - 2.3 µg/g	see Fig. 5.4 for references
< 7 % MgO	1 - 11 µg/g	see Fig. 5.4 for references
OIB	0.6 - 11 µg/g	Ryan & Langmuir (1993); Chaussidon & Marty (1995); Dostal *et al.* (1996)
IAB	1 - 90 µg/g	e.g. Ryan & Langmuir (1993); Smith *et al.* (1997); Sano *et al.* (2001)
Forearc		
Serpent. seamounts	1.5 - 126 µg/g	Ryan *et al.* (1996b); Benton *et al.* (2001)
Mud volcanoes	2 - 870 µg/g	Kopf & Deyhle (2002) and therein
Trench fluids	3.6 - 42 µg/g	You *et al.* (1993); Deyhle & Kopf (2002); Kopf *et al.* (2003b)
Hydrothermally altered MORB		
< 150°C	0.7 - 140 µg/g	e.g. Thompson & Melson (1970); Smith *et al.* (1995)
> 150°C	0.17 - 0.52 µg/g	Ishikawa & Nakamura (1992)
Weathered basalt	<290 µg/g	e.g. Bergeron (1989); Ishikawa & Nakamura (1992)
Serpentinite		
< 150°C	50 - 110 µg/g	Bonatti *et al.* (1984); Spivack & Edmont (1987)
> 150°C	24 µg/g	Bonatti *et al.* (1984)
Marine sediments		
Carbonates	0.3 - 22.8 µg/g	Spivack & You (1997); Hoefs & Sywall (1997)
Clay	10 - 160 µg/g	Ishikawa & Nakamura (1993)

See also Leeman & Sisson (2002) for a review on the geochemistry of B.

Table 5.4. Compilation of literature data on B isotopic composition of different reservoirs.

Material	δ^{11}B $_{SRM951}$ (‰)	Reference
Chondrites	-50 to +40	Chaussidon & Robert (1995, 1998)
	-3.3	Zhai *et al.* (1996)
Mantle	-3 ± 1	Spivack & Edmont (1987)
	$+0.2$	Ishikawa & Nakamura (1992)
	-7	Chaussidon & Jambon (1994)
	-10 ± 2	Chaussidon & Marty (1995)
	-4	Ryan *et al.* (1996a)
Continental Crust	-10 ± 3	Chaussidon & Albarède (1992); Kasemann *et al.* (2000)
Seawater	$+39.5 \pm 0.3$	Spivack & Edmont (1987); Nakamura *et al.* (1992); Barth (1993)
Vent fluids	+10 to +39	Spivack & Edmont (1987); Palmer (1991); James *et al.* (1995)
MORB	-6.5 to -1.2	Chaussidon & Jambon (1994)
	-3.7 to -1.6	Spivack & Edmont (1987)
	-7.7 to -6.9	le Roux *et al.* (2004)
OIB	-12 to -8	Chaussidon & Marty (1995)
Island arc volcanic rocks (IAB)		
Lesser Antilles	-5.3 to +1.8	Smith *et al.* (1997)
Kuriles, Kamchatka	-3.8 to +5.9	Ishikawa & Tera (1997); Ishikawa *et al.* (2001)
Aeolian Islands	-6.1 to +2.3	Tonarini *et al.* (2001)
Tonga/Kermadec	-4.4 to +37.6	Clift *et al.* (2001)
Izu	+4.6 to +12.0	Ishikawa & Nakamura (1994); Straub & Layne (2002)
Continental arc volcanic rocks		
Central Andes	-9.7 to +4.2	Schmitt *et al.* (2002); Rosner *et al.* (2003)
Washington Cascades	-9.1 to -0.4	Leeman *et al.* (2004)
Forearc		
Serpentinite seamount	+5.4 to +25.3	Benton *et al.* (2001)
Mud volcanoes	-7.7 to +39.5	Kopf & Deyhle (2002) and therein
Trench fluids	+20 to +50	You *et al.* (1993); Deyhle & Kopf (2002); Kopf *et al.* (2003b)
Altered MORB		
< 150 °C	-4 to + 25	e.g. Spivack & Edmont (1987); Smith *et al.* (1995)
> 150 °C	-0.1 to +1.0	Ishikawa & Nakamura (1992)
Serpentinite	+8.3 to +12.6	Spivack & Edmont (1987)
Marine sediments		
Carbonates	-5.5 to +32	Vengosh *et al.* (1991); Hemming & Hanson (1992); Spivack & You (1997)
Marine clay	-2 to +10	e.g. Spivack *et al.* (1987); Leeman & Sisson (2002)
Terrigeneous clay	-16 to -3	Ishikawa & Nakamura (1993); Leeman & Sisson (2002)
Borates	+15 to +34	Swihart & Moore (1986)
Salts	+10 to +30	Vengosh *et al.* (1992)
Tourmaline		
in metasediments	-23 to +23	Swihart & Moore (1989); Nakano & Nakamura (2001)
in pegmatites	-23 to -1	e.g. Swihart & Moore (1989); Matthews *et al.* (2003)
in massive Sulfide Dep.	-24 to +18	Palmer & Slack (1989); Tourn *et al.* (2004)
in the Lavičky granite	-37 to -21	Jiang *et al.* (2003)
in H*P* rocks	-15 to -6	Bebout & Nakamura (2003)

See also Palmer & Swihart (2002) for a review on the isotope geochemistry of B.

and differentiated MORB (Ryan & Langmuir, 1987, 1988, 1993; Chaussidon & Jambon, 1994; Ryan, 2002).

Abundances of (light) elements in the mantle have been estimated by direct measurements on natural samples of mantle rocks, and by combining partition coefficients with abundances of the elements in primitive mantle magmas. Taking the whole rock/melt partition coefficients for light elements listed above and combining them with typical concentrations in MORB (see Section 5.4) results in concentrations of $0.3 - 1.6 \, \mu g/g$ Li, $2 - 40 \, ng/g$ Be, and $4 - 70 \, ng/g$ B for the mantle after extraction of MORB melt. A re-calculation of abundances in the mantle before extraction of MORB melt results in concentrations of $0.8 - 2.9 \, \mu g/g$ Li, $20 - 230 \, ng/g$ Be, and $80 - 500 \, ng/g$ B, assuming a fraction of partial melting of 20%. The upper values may overestimate the abundances, as the high concentrations of MORB are probably due to magmatic differentiation of the melts and do not represent primitive element abundances. However, the calculated data for mantle concentrations are in good agreement with the literature data cited above and therefore prove the internal consistency of the listed data. On the other hand, Chaussidon & Marty (1995) argue on the basis of global mass balance and of B/K ratios, that MORB source mantle should contain only $10 - 15 \, ng/g$ B, primitive MORB should have $100 - 150 \, ng/g$, and higher concentrations observed in MORB glass are due to assimilation of AOC into the magma chamber.

The determination of the B isotopic composition of mantle rocks is an analytical challenge, due to the very low abundance of this element in primitive and depleted mantle rocks ($< 0.3 \, \mu g/g$; Table 5.3). The data set on B isotope values of the mantle therefore is very limited. Spivack & Edmont (1987) and Chaussidon & Jambon (1994) estimated $\delta^{11}B$ values of the mantle of $-3 \pm 1\%o$ and $-7\%o$, respectively, using analyses of fresh MORB glasses. Chaussidon & Marty (1995) (reviewed in Chaussidon, 1995) analysed volcanic glass from ocean island basalts (OIB) and argued for a $\delta^{11}B$ value of $-10 \pm 2\%o$ for the primitive mantle. The authors explained deviations of MORB and back arc basin basalt (BABB) from the value of $-10\%o$ by assimilation of AOC into the melts, and state that no significant fractionation of B isotopes occurred during differentiation of the mantle. Ryan *et al.* (1996a) analysed intra-plate volcanic rocks and deduced a $\delta^{11}B$ value for the mantle of $-4\%o$. In summary, the B isotopic composition of the Earth's mantle is not defined with high precision, and requires further investigation. However, the data collected so far point to a $\delta^{11}B$ value in the mantle of $-6 \pm 4\%o$.
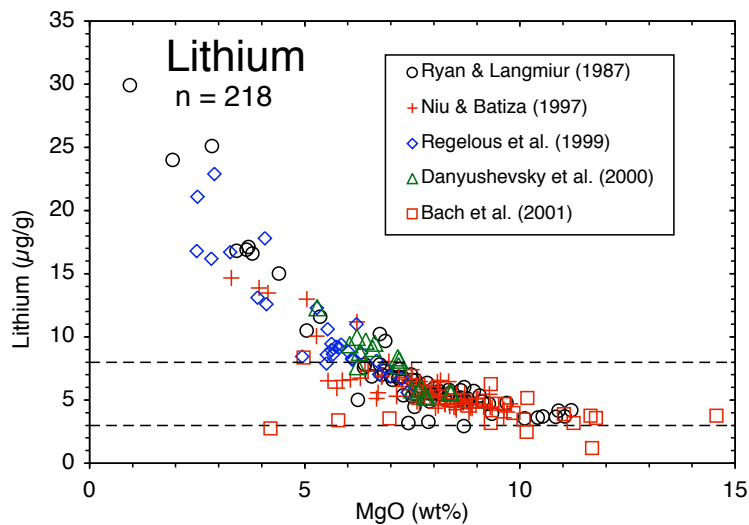
Fig. 5.2. Li vs MgO of various primitive and differentiated fresh volcanic rocks from MOR, ranging from depleted- to enriched-type MORB and from basaltic to dacitic compositions. The dashed lines represent the range of Li concentrations ($3-8 \, \mu g/g$) in relatively primitive basaltic compositions. Localities of samples compiled from literature are: Ryan & Langmuir (1987), Mid Atlantic Ridge (MAR), East Pacific Rise (EPR), SE Indian Ridge (SEIR), Juan de Fuca Ridge (JdFR), Woodlark basin, DSDP Hole 417d; Niu & Batiza (1997) and Regelous *et al.* (1999), EPR; Danyushevsky *et al.* (2000), EPR, SEIR; Bach *et al.* (2001), SWIR.

5.4. Budgets of Li, Be and B, and variations of δ^{11}B in fresh magmatic oceanic crust

Light element concentrations in basalts and differentiated rocks from mid-ocean ridges have been measured by several workers starting in the early 1970s. J.G. Ryan and C.H. Langmuir reviewed the Li, Be and B contents of MORB s.l. in their three papers on the three elements in young volcanic rocks (Ryan & Langmuir, 1987, 1988, 1993). More recently, light element concentrations have been measured more routinely (Chaussidon & Jambon, 1994; Niu & Batiza, 1997; Regelous *et al.*, 1999; Perfit *et al.*, 1999; Danyushevsky *et al.*, 2000; Kamenetsky *et al.*, 2000; Bach *et al.*, 2001).

Figures 5.2, 5.3 and 5.4 display a compilation of the data from fresh volcanic glass from different localities, including the Mid-Atlantic Ridge (MAR), the SE and SW Indian Ridges (SEIR and SWIR), the Juan de Fuca Ridge (JdFR), the East Pacific Rise (EPR), the Red Sea, the Eastern Galapagos Spreading Center, the Gorda Ridge, Macquarie Island and Cretaceous oceanic crust in the western Atlantic (DSDP Hole 417d). Investigated samples range from depleted- to enriched-
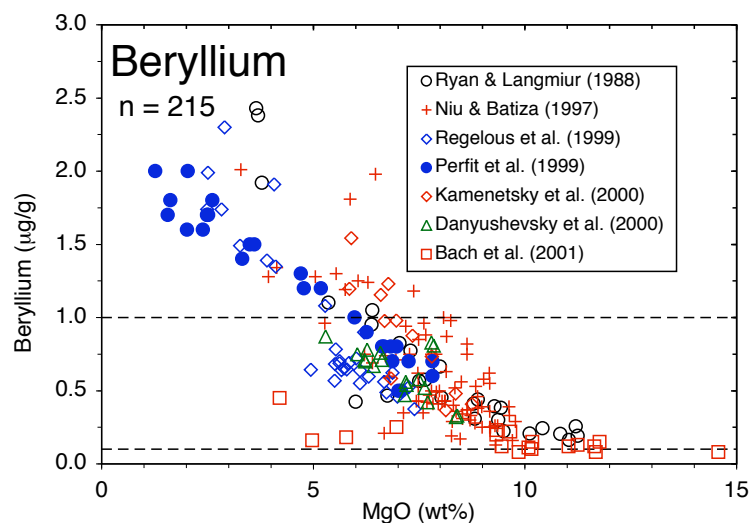
Fig. 5.3. Be vs MgO of various primitive and differentiated fresh volcanic rocks from MOR. The dashed lines represent the range of Be concentrations $(0.1 - 1\,\mu g/g)$ in relatively primitive basaltic compositions. Localities of samples compiled from literature are: Ryan & Langmuir (1988), MAR, EPR, DSDP Hole 417d; Niu & Batiza (1997) and Regelous *et al.* (1999), EPR; Perfit *et al.* (1999), Eastern Galapagos Spreading Center (EGSC); Kamenetsky *et al.* (2000), Macquarie Island; Danyushevsky *et al.* (2000), EPR, SEIR; Bach *et al.* (2001), SWIR.

type MORB and from picritic and basaltic to dacitic compositions. The figures display the concentrations of Li (Fig. 5.2), Be (Fig. 5.3) and B (Fig. 5.4) plotted versus MgO contents. The strong negative correlations in the three diagrams confirm the findings of Ryan & Langmuir (1987, 1988, 1993), and prove the incompatible behaviour of all three elements during magmatic differentiation at mid-ocean ridges. Fresh, relatively undifferentiated (MgO > 7 wt%) MORB glass contains $3 - 8\,\mu g/g$ Li, $0.1 - 1.0\,\mu g/g$ Be, and $0.4 - 2.3\,\mu g/g$ B. Fresh glass of differentiated rocks at MOR show higher concentrations of $5 - 30\,\mu g/g$ Li, $0.5 - 2.5\,\mu g/g$ Be, and $1 - 11\,\mu g/g$ B (Ryan & Langmuir, 1987, 1988, 1993; Niu & Batiza, 1997; Perfit *et al.*, 1999; Regelous *et al.*, 1999).

The determination of B isotopic compositions in fresh basaltic rocks is still difficult – similar to mantle rocks. Precise analytical determinetions are hampered by the low abundances of B, i.e. $< 2\,\mu g/g$ (Table 5.3) and incipient alteration can impact the B budget of such rocks easily. B isotope values obtained on fresh MORB glass were published by Chaussidon & Jambon (1994) [-6.5 to $-1.2‰$] and by Spivack & Edmont (1987) [-3.7 to $-1.6‰$]. Values of $-4.0 \pm 2.0‰$ for $\delta^{11}B$ are given by Chaussidon & Marty (1995) for N-MORB, E-MORB and BABB. le Roux *et al.* (2004) determined $\delta^{11}B$ values of fresh MORB glas samples from northern
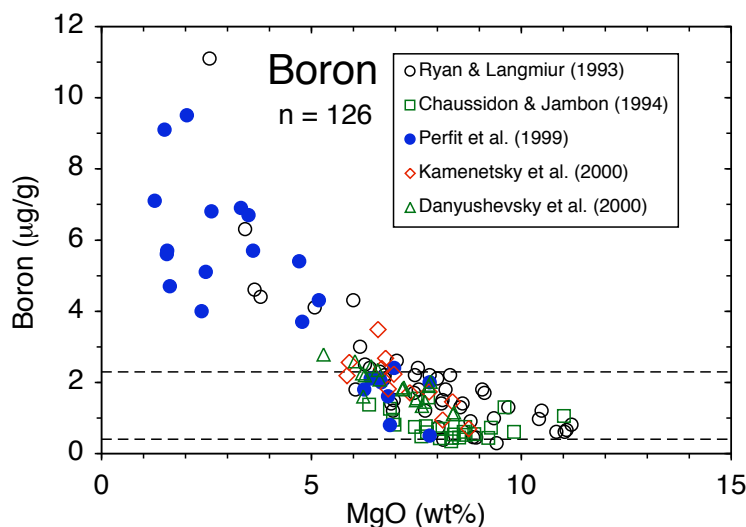
Fig. 5.4. B vs MgO of various primitive and differentiated fresh volcanic rocks from MOR. The dashed lines represent the range of B concentrations ($0.4 - 2.3\,\mu g/g$) in relatively primitive basaltic compositions. Localities of samples compiled from literature are: Ryan & Langmuir (1993), MAR, EPR, JdFR; Chaussidon & Jambon (1994), MAR, Red Sea, EPR, JdFR, Gorda Ridge; Perfit *et al.* (1999), EGSC; Kamenetsky *et al.* (2000), Macquarie Island; Danyushevsky *et al.* (2000), EPR, SEIR.

EPR by multiple-multiplier LA-ICP-MS with a precision better than $\pm 1‰$ (2σ). The analyses resultet in $\delta^{11}B$ values between -7.7 and $-6.9‰$ for all samples, overlapping at the 2σ level. The actual B isotopic composition of MORB is not defined with high precision, but most probably falls within the limits of $\delta^{11}B = -6$ to $-2‰$.

5.5. Mobility of Li, Be and B in hydrous fluids

Lithium   Lithium is generally referred to as mobile in hydrous fluids. It is enriched with respect to seawater in hydrothermal vent fluids and fluids released near the subduction trench (see Table 5.1). Sediments and volcanic rocks show either depletion or enrichment of Li during weathering and interaction with hydrothermal fluids (see Table 5.1). Experiments at high pressure ($2\,GPa$) and temperature ($900\,°C$) by Brenan *et al.* (1998b) revealed partition coefficients of ~ 0.16 between clinopyroxene and hydrous fluid, demonstrating the mobility of Li under upper mantle conditions. In general, Li may be enriched or depleted in rocks and minerals interacting with hydrous fluids, depending on P, T, fluid chemistry and mineralogy of the solids. In any case, hydrous fluids are very effective in transporting Li.

Beryllium Beryllium is generally considered to be immobile in hydrous fluids. This character, of course, is only relative, as it may be true in comparison with highly fluid-mobile elements, like the LILE. The partition coefficient of Be between suspended particles and river water is on the order of $10^5 - 10^6$ (Brown *et al.*, 1992; You *et al.*, 1994). The same values have been found by Chase *et al.* (2002) for the distribution of Be between seawater and solid particles (opal, carbonate, lithogenic particles, organic carbon). Hence, Be is almost insoluble in neutral H_2O at Earth's surface $P - T$ conditions. However, several studies have demonstrated a (limited) mobility of Be in hydrous fluids under different conditions.

In tropical rivers with a pH~ 4 the D_{Be} value of Be is decreased to $\sim 10^4$ (Measures & Edmond, 1983; Brown *et al.*, 1992) and experimental work by You *et al.* (1989) demonstrated a further decrease of D_{Be} to $\sim 60 - 10$ at pH ≈ 1, suggesting a (limited) mobility of Be in acidic water at surface conditions. This solution behaviour is explained by a change of Be speciation in water from neutral $Be(OH)_2$ complexes in neutral solutions to Be^{2+} in acidic (pH< 4) solutions (Brown *et al.*, 1992; Aldahan *et al.*, 1999). This is supported by elevated Be concentrations in pore water of marine sediments and sediments from accretionary wedges with respect to seawater (see Table 5.2). Therefore, You *et al.* (1994) suggested some mobilisation of Be in hydrous fluids during subduction with decreasing pH by increasing P and T.

Analysis of hydrothermal vent fluids (Measures & Edmond, 1983; Bourlès *et al.*, 1991) as well as experimental studies at higher $P - T$ conditions (You *et al.*, 1996; Johnson & Plank, 1999; Tenthorey & Hermann, 2004) demonstrate a further increase of Be mobility with increasing P and T.

Tenthorey & Hermann (2004) completed an experimental study at $3\,GPa/750\,°C$, and revealed a bulk rock/fluid partition coefficient for Be of 0.2 between a chlorite + orthopyroxene + olivine assemblages and siliceous hydrous fluid. This value suggests a strong mobility of Be during breakdown of serpentinite in subducting lithosphere. In contrast, Tatsumi & Isoyama (1988) found whole rock/fluid partition coefficients of > 19 during the hydration of serpentinite. A study by Brenan *et al.* (1998b) at $2\,GPa/900\,°C$ revealed a partition coefficient for Be between clinopyroxene and hydrous fluid of ~ 1.8. The latter study was performed using both pure H_2O and $0.5\,M$ HCl as starting fluid, but did not reveal a difference of Be mobility between the two. Bulk dehydration experiments using natural pelagic clay were performed by Johnson & Plank (1999) and resulted in bulk rock/fluid partition coefficients of Be in the range of 2 to 4.5 at temperatures between $650\,°C$ and $700\,°C$ at $2.0\,GPa$ pressure. Altogether these experiments demonstrate a moderate mobility of Be at elevated P and T during interaction of hydrous fluids with sediments, metabasites and ultramafic assemblages.

Apart from P and T, fluid composition probably has a strong influence on the mobility of Be. The geochemical correlation of Be and F in pegmatites, contact aureoles of granites and Sn-W greisen has led to the suggestion, that Be is transported by complexation with F (e.g. Webster *et al.*, 1987; Reyf, 2004). Be mobilisation by complexes such as BeF_3^-, BeF_4^{2-} and $BeCO_3F^-$ was demonstrated by Wood (1992) to be highly effective in near neutral solutions.

Mobilisation of elements with limited solubility in fluids may also be enhanced by high fluid fluxes, leading to high fluid/rock ratios. Reaction zones between ultramafic lenses and their crustal country rocks for example often display monomineralic reaction zones ("blackwalls") which are formed by intense metasomatic exchange at the contact between the contrasting lithologies. Most of the world's emerald (= Cr-bearing beryl) deposits are located within such blackwalls and demonstrate a mobilisation and concentration of Be by hydrothermal fluids (Franz & Morteani, 2002). Furthermore, the economically most important Be deposits (e.g. Spor Mountain, Utah) are related to hydrothermal/epithermal activity in the aureols of magmatic intrusions, but are not pegmatitic and not directly precipitated by silicate melts (Barton & Young, 2002).

As a conclusion, Be may be treated as a geochemical tracer which is relatively immobile in hydrous fluids. However, fluid-mobility is not absolutely zero and is enhanced at low pH, elevated temperature, elevated pressure and probably by higher halogene contents of the fluids, especially by F contents. In settings with high fluid/rock ratios, Be may be significantly enriched or depleted. London & Evensen (2002) state that the fluid-immobile character *"does not mean that hydrothermal fluids are unimportant in the movement of Be through the Earth's crust, only that they are not as efficient as silicate melts"*.

Boron Boron probably shows the highest mobility in hydrous fluids, compared to Li and Be. Similar to Li, it is enriched with respect to seawater in hydrothermal vent fluids and fluids released near the subduction trench (see Table 5.3). Seawater itself has a relatively high B concentration of $\sim 4.4\,\mu g/g$. Sediments and volcanic rocks show either depletion or enrichment of B during weathering and interaction with hydrothermal fluids (see Table 5.3). Experiments at high pressure (2 GPa) and temperature (900 °C) by Brenan *et al.* (1998b) revealed partition coefficients of ~ 0.016 between clinopyroxene and hydrous fluid (i.e. an order of magnitude lower than for Li), demonstrating the extreme mobility of B under upper mantle conditions. These findings were recently doubted by Tenthorey & Hermann (2004) who performed experiments at $P - T$ conditions of 3 GPa/750 °C and revealed bulk partition coefficients of 0.25 between a chlorite+olivine+orthopyroxene-rich assemblage and

siliceous hydrous fluid, demonstrating a much lower mobility of B during dehydration of serpentinite. Weisbrod *et al.* (1986), Morgan & London (1989) and Fuchs & Lagache (1994) have demonstrated experimentally that tourmaline is formed in chlorite- or amphibole-bearing rocks during interaction with B-bearing fluids. In natural rocks, this process would effectively extract B from fluids in such rocks, limiting the actual mobilisation of the element. In general, B may be enriched or depleted in rocks and minerals interacting with hydrous fluids, depending on P, T, fluid chemistry and mineralogy of the solids. Hydrous fluids, in any case, are very effective in transporting B.

Boron isotopes are strongly fractionated during fluid/rock interaction processes, with a relative enrichment of the heavier isotope ^{11}B into hydrous fluids (see Section 5.2).

5.6. Abundances of Li, Be and B and B isotope fractionation during ocean-floor metamorphism and weathering

Magmatic rocks formed at mid-ocean ridges and peridotites exposed to seafloor by tectonic uplift are strongly affected by hydrothermal metamorphism and weathering (e.g. Alt, 1995). During such processes, chemical and mineralogical compositions of basalt, gabbro and more differentiated rocks are changed to various degrees, depending on parameters like temperature, pressure, water/rock ratio and pH of the hydrothermal fluids (e.g. Alt, 1995; Seyfried & Ding, 1995; Laverne *et al.*, 2001). The rocks are enriched in H_2O up to several percent and form secondary phases, predominantly hydrous minerals, like chlorite, actinolite, smectite, celadonite, zeolites, prehnite, pumpellyite, or epidote. The strongest alteration and enrichment in H_2O together with K_2O and trace elements like Ba, Li and B (see below) is restricted to the uppermost 500 m of the oceanic crust, but may extend to depths of $1000 - 1500$ m in some places, as has been demonstrated on DSDP/ODP drill cores (Bergeron, 1989; Ishikawa & Nakamura, 1992; Spivack & Staudigel, 1994; Smith *et al.*, 1995; Staudigel *et al.*, 1996; Bach *et al.*, 2001; Chan *et al.*, 2002b; Kelley *et al.*, 2003).

Experimental studies on the transfer of major and trace elements between seawater and oceanic lithosphere have shown that Li and B are strongly enriched in the solid phases during low-temperature ($< 150\,^\circ$C) metamorphism, as they are incorporated into the alteration products – predominantly clay minerals (Seyfried & Dibble, 1980; Seyfried *et al.*, 1984, 1998; Berger *et al.*, 1988; You *et al.*, 1995b, 1996; Chan *et al.*, 1996). During high-temperature hydrothermal interaction ($> 150\,^\circ$C) B is leached from the solids and enriched in the fluids (Seyfried *et al.*, 1984; You

et al., 1995b). Li is also leached from basalts and gabbros at high temperatures, in settings with low fluid/rock ratios. Epidote and actinolite, formed as secondary phases under such conditions, are not incorporating significant amounts of Li. At high fluid/rock ratios, however, chlorite may form as the major secondary phase, which incorporates significant amounts of Li. Investigation of submarine basalts (Spivack & Edmont, 1987; Bergeron, 1989; Chan *et al.*, 1992, 1993, 1996; Smith *et al.*, 1995; Dostal *et al.*, 1996; Chan *et al.*, 2002a) and serpentinized peridotites (Thompson & Melson, 1970; Bonatti *et al.*, 1984; Spivack & Edmont, 1987; Decitre *et al.*, 2002) show negative correlation of both Li and B contents with alteration temperature determined by mineral phase assemblages or δ^{18}O thermometry. Trace element concentrations of low-temperature altered or weathered oceanic basalts vary between 1 and 75 µg/g for Li (Holland, 1980; Donnelly *et al.*, 1980; Chan & Edmond, 1988; Chan *et al.*, 1992; Dostal *et al.*, 1996; Kelley *et al.*, 2003), 0.06 and 2.4 µg/g for Be (Bebout *et al.*, 1993; Bach *et al.*, 2001; Kelley *et al.*, 2003), and 0.7 and 290 µg/g for B (Spivack & Edmont, 1987; Bergeron, 1989; Ishikawa & Nakamura, 1992; Moran *et al.*, 1992; Smith *et al.*, 1995; Leeman, 1996). Li and B are adsorbed at or incorporated in clay minerals (smectite, illite), serpentine and chlorite. Similar Be contents of fresh and altered basalt ($0.16 - 2.4$ µg/g; Bebout *et al.*, 1993) suggest a conservative character of this element during water/rock interaction (for a more detailed discussion on Be mobility see Section 5.5). Peridotites serpentinised at low tremperatures show Li contents between 50 and 81 µg/g (Chan *et al.*, 1992), and B contents between 50 and 110 µg/g (Bonatti *et al.*, 1984; Spivack & Edmont, 1987). Be contents of serpentinised peridotites are not reported. Li and B contents of serpentinites decrease with increasing temperatures of metasomatism, and are 0.6 to 8.2 µg/g for Li (Chan *et al.*, 1992; Decitre *et al.*, 2002), and ~ 24 µg/g for B (Bonatti *et al.*, 1984) at $> 150\,°$C. Therefore, serpentinites are moderately (during high-*T* serpentinisation) to strongly (during low-*T* serpentinisation) enriched in Li and B with respect to fresh mantle rocks.

The B isotopic composition of hydrothermally overprinted and weathered rocks is variable and depends on temperature, fluid/rock ratio, pH of the fluid and coordination of B in secondary minerals. Weathering of basalt at the seafloor produces smectite with tetrahedrally coordinated B at low temperature ($\sim 0\,°$C) and very high water/rock ratios with the fluid being seawater (δ^{11}B = +39.5‰, $\sim 80\%$ B in trigonal coordination). B isotope fractionation under these conditions is large and weathered basalts should display low δ^{11}B values relative to seawater. Using equation 5.6 after Hervig *et al.* (2002) results in a δ^{11}B value of +8.0‰ for smectite in equilibrium with seawater at $\sim 0\,°$C. Identical values result from Spivack & Edmont (1987) who determined a B isotope fractionation factor of 1.032 between seawater and alteration products of basalt, with a δ^{11}B value of +8.0‰ for the alteration

products. Alteration at a temperature of $100\,°C$ results in a $\delta^{11}B$ value of $+17.7‰$ in the secondary minerals, calculated after Hervig *et al.* (2002) from equation 5.6. Natural low-temperature altered basalts display a range in $\delta^{11}B$ values from -4 to $+25‰$ (Table 5.4; Leeman & Sisson, 2002), depending on the variables mentioned above. The majority of data on weathered and low-T altered basalts are in the range of ~ 0 to $+10‰$.

During high-T hydrothermal alteration, B is quantitatively leached from basaltic rocks (see above). Data on the B isotope composition of altered basalts are scarce, due to low B concentrations. Relatively low fluid/rock ratios during high-T hydrothermal events may lead to Rayleigh fractionation of B isotopes during leaching of B, resulting in a significant preferential loss of the heavier isotope, and consequently very low $\delta^{11}B$ values. Ishikawa & Nakamura (1992) found $\delta^{11}B$ values between -0.1 and $+1.0‰$ in high-T altered basalts with B concentrations $\leq 0.5\,\mu g/g$ (Tables 5.3 and 5.4).

Serpentinites formed at the ocean floor by hydration of peridotites are strongly enriched in B (Table 5.4), and display $\delta^{11}B$ values between $+8.3$ and $+12.6‰$ (Spivack & Edmont, 1987). Therefore, ultramafic rocks behave very similar to basalts during low-T interaction with seawater. They incorporate high concentrations of B with a heavy isotopic composition.

Further evidence for leaching of Li, B, and also some Be from the rocks at high temperatures is given by the composition of hot vent fluids ($200-400\,°C$), which are enriched in these elements with respect to seawater. Concentrations of Li range from 0.14 to $\sim 10\,\mu g/g$ (Table 5.1 Edmond *et al.*, 1979; Von Damm *et al.*, 1985; Chan *et al.*, 1992, 1993, 1994a; Decitre *et al.*, 2002; Foustoukos *et al.*, 2004) which is an enrichment by a factor of ~ 1 to 50 with respect to seawater ($0.18\,\mu g/g$; Morozov, 1968; Broeker & Peng, 1982). Concentrations of Be in seawater are extremely low and vary from 0.04 to $0.6\,pg/g$ (Broeker & Peng, 1982; Measures & Edmond, 1983). Hot vent fluids also display very low Be concentrations at the sub-ng/g-level ($90-900\,pg/g$; Table 5.2). However, this corresponds to an enrichment of ~ 500 to 1600 with respect to seawater. Note that concentrations of Be in fresh and altered MORB are still ~ 1000 times higher than in vent fluids. The high enrichment of Be in vent fluids with respect to seawater, therefore, is not in contrast to the relative immobile character of Be deduced from the comparison of fresh and altered MORB. B concentrations in seawater are relatively high ($4.4\,\mu g/g$; Uppstroem, 1974; Spivack & Edmont, 1987), but are still surpassed by concentrations in hot vent fluids ($3.8-11.5\,\mu g/g$; Douville *et al.*, 2002; Foustoukos *et al.*, 2004). B in hydrothermal vent fluids is isotopically lighter than in seawater, due to leaching of mantle-derived B from basaltic rocks with negative $\delta^{11}B$ values (Table 5.4). Studies by Spivack & Edmont (1987) and Palmer (1991) have revealed values between $+10‰$ and

$+39‰$.

5.7. Budgets of Li, Be and B, and variations of B isotopes in oceanic sediments

Lithium Lithium concentrations in marine clays vary from $< 1\,\mu g/g$ to $> 100\,\mu g/g$, with most of them ranging from $10\,\mu g/g$ to $70\,\mu g/g$ (Chan *et al.*, 1994a,b; Chan & Kastner, 2000; Bouman, 2004; Bouman *et al.*, 2004; Decitre *et al.*, 2004). Carbonates show low concentrations of Li, ranging from 0.2 to $3.3\,\mu g/g$ (Hoefs & Sywall, 1997). Hydrothermal activity at high temperatures in the vicinity of vent systems probably leaches Li from sediments (Decitre *et al.*, 2004), whereas the formation of clay minerals during weathering leads to an enrichment of Li in the alteration products, as indicated by the high Li contents observed in marine clays.

Beryllium Beryllium concentrations in marine sediments are typically in the range of $0.1 - 2.5\,\mu g/g$, and may reach $4\,\mu g/g$ in areas with a significant contribution of weathered volcaniclastic material (Table 5.2; Ryan & Langmuir, 1988; Bouman *et al.*, 2004; Ryan, 2002). A significant concentration of Be ($2 - 15\,\mu g/g$) has been observed in Mn nodules (Sharma & Somayajulu, 1982; Krishnaswami *et al.*, 1982). Be abundances in continental sand- and siltstones are in the range of $1 - 2\,\mu g/g$ (Ryan, 2002). Limestones and bio-chemical sediments show very low Be concentrations (Ryan, 2002).

^{10}Be concentrations in seafloor sediments prior to subduction decrease from between ~ 1.5 and $3 \cdot 10^9\,\text{atoms/g}$ ($\approx 0.1 - 0.2\,\text{pg/g}$) at the seafloor to almost zero at sediment depths of $\sim 200 - 300\,\text{m}$ (Morris *et al.*, 2002). Concentrations of ^{10}Be in arc magmas are in the range of $10^6 - 10^7\,\text{atoms/g}$ ($\approx 10^{-4} - 10^{-3}\,\text{pg/g}$; Morris *et al.*, 2002). Note that neither the concentration nor the isotope ratio of B of any natural rock are significantly influenced by the contribution of ^{10}B by the decay of ^{10}Be.

Boron The behaviour of B in marine sediments is very similar to that of Li. The concentrations of B in carbonates are relatively low with values between 0.3 and $\sim 20\,\mu g/g$ (Spivack & You, 1997; Hoefs & Sywall, 1997). The high values ($> 5\,\mu g/g$) are probably due to significant amounts of clay within the carbonate samples (Hoefs & Sywall, 1997). Marine clays show high B concentrations of $10 - 200\,\mu g/g$ (Ishikawa & Nakamura, 1993; Leeman & Sisson, 2002).

Boron isotopic compositions of smectite formed by weathering of basalt at the seafloor are different from those of illite which is delivered as detritus from conti-

nents. Submarine smectite displays δ^{11}B values between -2 and $+10\text{‰}$ (Spivack *et al.*, 1987; Ishikawa & Nakamura, 1993; Leeman & Sisson, 2002), whereas terrigeneous clay shows significantly lower δ^{11}B values of -16 to -3‰ (Ishikawa & Nakamura, 1993; Leeman & Sisson, 2002). Carbonates show a large variation of δ^{11}B values ranging from -5.5 to $+32\text{‰}$ (Vengosh *et al.*, 1991; Hemming & Hanson, 1992; Spivack & You, 1997; Leeman & Sisson, 2002). Chemical sediments like salts and marine borates range from $+10$ to $+34\text{‰}$ in δ^{11}B (Swihart & Moore, 1986; Vengosh *et al.*, 1992). A weighted average of B content and B isotopic composition for seafloor sediments on a global scale was estimated by Leeman & Sisson (2002) to be $53\,\mu\text{g/g}$ and δ^{11}B $= -1.6\text{‰}$.

During hydrothermal alteration, sediments behave similar to basaltic rocks. B is leached from the rocks and δ^{11}B values are decreased during high-temperature fluid/rock interaction. Spivack *et al.* (1987), for example, investigated sediments containing $32 - 62\,\mu\text{g/g}$ B with δ^{11}B values between -4.5 and -1.2‰. These sediments were intruded by a basaltic sill generating hydrothermal fluid circulation within the sediments. In the vicinity of the sill the authors observed decreasing B concentrations in the sediments to values of $14 - 33\,\mu\text{g/g}$, and δ^{11}B values of $\sim -8\text{‰}$. In zones of greenschist facies hydrothermal metamorphism, B concentrations were decreased to $\sim 1.3\,\mu\text{g/g}$ (B isotopic compositions of these B-poor samples are not reported).

5.8. Behaviour of Li, Be and B, and B isotope fractionation during subduction

Most of the water incorporated into the oceanic crust as pore water, molecular crystal water or in OH-bearing minerals is released during compaction within the accretionary wedge at the onset of subduction. Analyses of pore waters and vent fluids at seamounts (Benton *et al.*, 2001, 2004) and mud volcanoes at accretionary wedges (Deyhle & Kopf, 2001, 2002; Kopf & Deyhle, 2002) as well as experiments (Johnson & Plank, 1999) show that significant amounts of Li and B are released from the sediments and altered oceanic crust already at shallow depths and temperatures below $200\,^{\circ}$C. Be is not significantly mobilised at this stage and remains in the subducting lithosphere. You *et al.* (1994) investigated sediments and pore fluids in an accretionary wedge and observed Be concentrations in the solids ($1.5 - 2.8\,\mu\text{g/g}$) typical for oceanic sediments (Table 5.2). Be concentration in the pore fluids were higher than seawater but a factor of $\sim 10^6$ ($0.3 - 12.6\,\text{pg/g}$) lower than the host sediments. The mobilities of Li, Be and B in hydrous fluids are discussed in Section 5.5.

The behaviour of Li, Be, and B during progressive high-pressure metamorphism was investigated by whole-rock (WR) studies on metasedimentary and meta-mafic rocks (Moran *et al.*, 1992; Bebout *et al.*, 1993, 1999; You *et al.*, 1995a; Peacock & Hervig, 1999), and by mineral-mineral partition studies (B, Be: Domanik *et al.*, 1993). It has been shown by Bebout *et al.* (1999) that B contents and B/Be and B/Li ratios decrease with increasing metamorphic grade from lawsonite-albite to amphibolite facies. These authors conclude that most of the B is released from the sediments and metabasalts with the escaping fluids at an early stage of subduction, whereas most of the Li and Be remains in the slab. Domanik *et al.* (1993) studied the fractionation of Be and B between minerals of metabasic and metasedimentary lithologies from the Catalina schists (California) and emphasised the importance of white mica stability on the Be and B budgets of subducting rocks. Scambelluri *et al.* (2004) investigated B and Li abundances in natural serpentinites, peridotites and olivine-orthopyroxene whole rocks and demonstrated a limited mobilisation of these elements during dehydration of serpentinite to olivine-orthopyroxene rocks in subducting slabs. Partition coefficients determined by these authors are $D_B^{WR/fluid} \sim 0.2$ and $D_{Li}^{WR/fluid} \sim 0.3$. An experimental study by Tenthorey & Hermann (2004) investigating trace element mobilisation during serpentinite breakdown revealed a similar value for B ($D_B^{WR/fluid} = 0.25$), but a significantly lower value for Li ($D_{Li}^{WR/fluid} \sim 0.01$). Tenthorey & Hermann (2004) also determined a partition coefficient for Be which is almost identical to D_B ($D_{Be}^{WR/fluid} \sim 0.2$). Therefore, B and Be seem to be mobilised moderately during serpentinite dehydration, whereas data for Li suggest either a moderate (Scambelluri *et al.*, 2004) or a significant (Tenthorey & Hermann, 2004) mobilisation of this element. However, results from Tenthorey & Hermann (2004) for Li and Be are in contrast to those of other workers (Brenan *et al.*, 1998b; Scambelluri *et al.*, 2004). Results for B are compatible with the findings of Scambelluri *et al.* (2004), but are in contrast to the generally accepted high fluid mobility of B and the significantly lower $D_B^{WR/fluid}$ values determined by Brenan *et al.* (1998b).

Woodland *et al.* (2002) studied the partitioning of Li between clinopyroxene and garnet in a large variety of eclogites and found that Li is preferentially incorporated in clinopyroxene. Zack *et al.* (2002a) studied eclogites from Trescolmen (Central Swiss Alps) and found that Li and Be budgets are governed by omphacite, while white mica and omphacite control the B budget. Paquin *et al.* (2004) studied the systematics of Li, Be and B in the ultrahigh-pressure garnet peridotite from Alpe Arami that was presumably subjected to a metasomatic overprint by aqueous solutions during exhumation in a supra-subduction zone setting. A detailed study on the partitioning of Li, Be and B between various minerals of high-pressure meta-

morphic rocks from the Greek island of Syros (Cyclades) is presented in Chapter 7.

The formation and stability of minerals that contain specific geochemical tracers as major components, like B in tourmaline, certainly has an enormous impact on trace element budgets, as has been demonstrated by Nakano & Nakamura (2001). Mobility of trace elements, therefore, is not only a function of their solubility in aqueous fluids, but is strongly governed by the solid phases present. The actual trace element content of subducting crust in any specific subduction zone is a function of the minerals that are stable and depends on whole rock chemistry and $P - T$ evolution.

As discussed above (Section 5.2) boron isotopes show a temperature-dependent fractionation between different phases, i.e. phases with B in different coordination to O. Therefore, dehydration of metamorphic rocks is expected to decrease the δ^{11}B values of the rocks, due to the fractionation of the heavier isotope ^{11}B into the released hydrous fluids. Studies on IAB that investigated across-arc profiles show a decrease of δ^{11}B values from trench to back-arc (Ishikawa & Nakamura, 1994; Ishikawa & Tera, 1997; Ishikawa et al., 2001; Benton et al., 2001). Hence, the fluids (or melts) migrating from the slab into the IAB magma sources are transporting a B signal with steadily decreasing ^{11}B/^{10}B ratios with increasing depth of the slab. Matching this hypothesis, Peacock & Hervig (1999) have demonstrated that δ^{11}B values of HP metamorphic rocks are significantly decreased during progressive dehydration. Bebout & Nakamura (2003) have analysed the B isotopic composition of tourmaline from (ultra-) HP metamorphic rocks from the Catalina Schist, California (USA) and from Lago di Cignana (Swiss Alps). They demonstrated decreasing δ^{11}B values during prograde growth (-7 to -15‰ in Catalina tourmaline), very low δ^{11}B values in HP growth zones (-10‰ in coesite-bearing tourmaline from Lago di Cignana) and increasing δ^{11}B values in retrograde growth zones. Intracrystalline isotopic equilibration by diffusion is very limited and different growth zones still display their initial compositions. Tourmaline therefore is a powerful tool to monitor the B isotopic evolution of metamorphic rocks. On the other hand, the presence of tourmaline in a rock strongly controls the B budget and therefore influences the isotopic composition of the rock, as was emphasised by Nakano & Nakamura (2001). Results of chemical and B isotopic investigations on metamorphic (and metasomatic) tourmaline from Syros are discussed in Chapters 9 and 10.

Several authors have modelled light element release (Moran et al., 1992; Bebout et al., 1993; Brenan et al., 1998b) or isotopic fractionation of Li (Zack et al., 2003; Bouman, 2004) and B (Peacock & Hervig, 1999; Bebout & Nakamura, 2003; Rosner et al., 2003) in subduction zones. The aim of all these studies was a more

quantitative estimation of the evolution of trace element content and isotopic composition of both the subducting slab and the released fluids. A more detailed review and a further extension of these models is given in Chapter 8.

6. Lithium, beryllium and boron whole-rock abundances: effects of dehydration and rehydration

6.1. Introduction and investigated samples

In the previous chapter (Chapter 5) the geochemical character of the light elements Li, Be and B has been discussed, with special emphasis on subduction-related processes and element mobility in hydrous fluids. In the following chapter, whole-rock abundances of the light elements in meta-igneous rocks from Syros are discussed. The study was performed in cooperation with Zsolt Kasztoszky, Katalin Gméling (both Budapest) and Rainer Altherr (Heidelberg). First results were presented at the 2004 Goldschmidt Conference in Copenhagen (Marschall *et al.*, 2004a).

The behaviour of Li, Be, and B during progressive high-pressure metamorphism has already been the topic of a few earlier studies, which investigated whole-rock contents of metasedimentary and meta-mafic rocks. Moran *et al.* (1992) investigated whole-rock B abundances of sediments, metasediments, altered basalts and metabasalts. The metamorphic samples display a large range in peak metamorphic temperatures between ~ 200 and $750\,°C$. The authors found a large range in B concentrations for nonmetamorphic rocks and for low-temperature metamorphic samples ($1 - 130\,\mu g/g$ in altered basalts, $3.6 - 370\,\mu g/g$ in sediments). Both metabasalts and metasediments demonstrate a strong decrease of B abundances with increasing metamorphic temperature. Metabasalts of greenschist-facies and higher grade show consistently low concentrations of $< 10\,\mu g/g$ B. Metasediments with peak metamorphic temperatures $> 450\,°C$ typically contain $< 50\,\mu g/g$ B (with a few exceptions), and migmatites and granulites show very low B abundances ($< 3\,\mu g/g$). The authors conclude that B is extracted together with hydrous fluids from sediments and altered basalts from subducting crust with increasing *P* and *T*, but that B is not completely extraced before the slab reaches the depth of arc-magma generation.

Bebout *et al.* (1993, 1999) investigated Li, Be and B whole-rock abundances of metasediments and metamafic rocks from the Catalina Schist, California (USA), which demonstrate a range in metamorphic grade from lawsonite-albite via greenschist and epidote-amphibolite to amphibolite facies. In this suite of samples, Li

and Be abundances and Li/Be ratios show no correlation to metamorphic grade. Concentrations in all investigated samples range from 0.1 to $\sim 5\,\mu g/g$ Be and ~ 6 to $\sim 45\,\mu g/g$ Li. B concentrations and B/Be ratios in metasediments are systematically decreasing with increasing metamorphic grade. The suite of metamafic rocks does not show a significant change with metamorphic grade, but in all samples B/Be ratios are < 30. The authors argue that large amounts of B along with other highly fluid-mobile elements are lost from subducting sediments already at shallow depths. Hence, high B/Be ratios typically found in oceanic sediments and altered oceanic crust are not retained to subarc depths. For high-temperature subduction zones (i.e. during initial subduction) the authors estimate a B content of amphibolite-facies metasediments to be $\sim 25\,\%$ of the protoliths contents.

In this chapter, Li, Be and B whole-rock abundances of basically two different groups of samples are discussed. The first group comprises high-pressure metamorphic rocks that were formed by prograde metamorphism and dehydration and do not show evidence for interaction with fluids during exhumation. This group provides information on the behaviour of (the light) elements during progressive dehydration of different lithologies within the subducting lithosphere. Group 1 is further subdivided on the basis of the respective protoliths (see Chapter 4) and includes *eclogites, glaucophane schists and felses, metagabbros* and *meta-plagiogranites*.

The second group are hybrid blackwall samples that were significantly hydrated during exhumation (see Chapter 4). This group of rocks demonstrates the effects of metasomatism of exhuming HP metamorphic rocks, and may provide information on the trace element composition of fluids that migrate through the exhumation channel. Furthermore, hybrid rocks formed within subduction zones (i.e. at the slab-mantle interface) may contain large amounts of specific trace elements and may therefore impact global trace element budgets (Spandler *et al.*, 2003). Group 2 is further subdivided into tourmaline-bearing and tourmaline-free samples (see Chapter 4).

6.2. Results

Group 1 The analysed meta-igneous rocks display Li concentrations between 5.0 and 88.7 $\mu g/g$, independent from rock type and H$_2$O content. No correlation has been found between Li and any other major or trace element. Whole-rock abundances of Li in most samples are significantly higher than abundances of Li in fresh oceanic igneous rocks ($\sim 3 - 30\,\mu g/g$, Chapter 5). MORB-normalised element abundance patterns (Chapter 4) of most group-1 samples display positive Li anomalies (Li/Yb $\gg 1.7$; see Appendix C). An exception are the meta-plagiogranites

Table 6.1. H_2O concentrations and Li, Be and B abundances of Syros whole-rock samples

Group 1	H_2O	Li	Be	B	B/Be	Group 2	H_2O	Li	Be	B	B/Be
Glaucophane schists and felses						Tur-free blackwall samples					
SY3[T]	2.50	36.9	0.92	62.4	67.9	SY325	3.69	2.3	2.59	7.2	2.8
SY5	1.51	42.6	0.95	3.2	3.3	SY328	2.85	65.3	0.88	7.6	8.6
SY304	3.17	7.8	0.46	12.0	26.1	SY400A	2.34	69.2	3.30	n.a.	
SY306	2.46	7.1	0.40	9.9	24.8	SY402A	0.97	71.0	2.04	12.9	6.3
SY309A	2.32	28.0	0.67	11.4	17.0	SY402B	0.62	78.0	1.81	8.3	4.6
SY342	1.50	27.4	1.00	4.9	4.9	SY402C	2.31	63.3	1.61	13.9	8.7
SY401A	2.53	32.5	0.68	7.9	11.6	SY404	9.69	7.5	0.91	3.8	4.1
SY403	2.90	11.5	1.07	9.1	8.5	SY405	9.28	11.3	0.63	3.9	6.1
Metagabbros						SY437	2.72	19.1	3.18	15.5	4.9
SY112	2.23	5.6	0.95	4.8	5.0	Tur-bearing blackwall samples					
SY344	1.87	18.8	0.54	5.1	9.4	SY309B	4.54	31.7	0.65	3960	6092
SY425	1.94	40.5	1.58	25.6	16.2	SY400B	2.64	76.8	3.17	351	111
SY438	3.08	88.7	1.28	19.6	15.3	SY401B	4.67	20.2	0.51	15308	30016
SY443	2.83	16.9	0.61	4.9	8.0	SY412	3.07	60.2	0.75	93	124
Eclogites						SY420	4.14	36.2	0.68	8760	12882
SY109	0.63	6.1	1.77	n.a.							
SY323[T]	0.78	45.8	2.08	4.8	2.3						
SY324	0.70	56.5	2.20	2.2	1.0	**Other samples**					
SY411	0.50	72.3	2.88	3.8	1.3						
Meta-plagiogranites						Serpentinites					
SY1	0.92	9.7	1.76	12.0	6.8	SY429	9.75	2.8	0.47	11.3	24.1
SY8	1.25	5.6	3.43	11.7	3.4	SY347	12.12	0.9	0.24	5.5	23.0
SY308	1.25	5.0	0.82	10.3	12.5	Metasediments (glaucophane schists)					
SY415	0.68	5.6	3.46	10.6	3.1	SY314[T]	2.03	39.6	2.32	93.9	40.5
SY431	0.95	22.7	3.34	38.8	11.6	SY406	1.77	66.7	1.46	18.2	12.5

n.a. = not analysed. [T]samples SY3, SY314 and SY323 contain accessory tourmaline.

which show low Li concentrations of $\sim 5 - 10\,\mu g/g$ (one outlier), which is low compared to the highly differentiated character of the protoliths of these rocks. The meta-plagiogranites typically display negative Li anomalies in MORB-normalised element abundance patterns (Fig. 4.3, page 76).

Be concentrations of glaucophane schists and metagabbros are between 0.40 and $1.58\,\mu g/g$, i.e. the same range as Be in fresh and altered MORB ($\sim 0.1 - 2.5\,\mu g/g$, see Chapter 5). Concentrations of Be in eclogites ($\sim 1.8 - 2.9\,\mu g/g$) and meta-plagiogranites ($\sim 0.8 - 3.5\,\mu g/g$) are higher than in fresh and altered MORB.

Concentrations of B display a large variation in glaucophane schists and metagabbros ($\sim 3 - 26\,\mu g/g$), and are significantly higher than in fresh MORB ($< 2.3\,\mu g/g$ for MORB with $> 7\%$ MgO; see Chapter 5). Eclogites ($\sim 4 - 6\,wt\%$ MgO) show low B abundances of $\sim 2 - 5\,\mu g/g$. B concentrations in meta-plagiogranites ($\sim 0.3 - 1.6\,wt\%$ MgO) are somewhat higher ($\sim 10 - 12\,\mu g/g$, one outlier). However, the protoliths of these rocks are highly differentiated magmatic rocks, which were probably enriched in incompatible trace elements during magmatic differen-

tiation. B concentrations of $\sim 10 - 12\,\mu g/g$ are typical for ocean floor magmatic rocks with MgO contents below $2\,wt\%$.
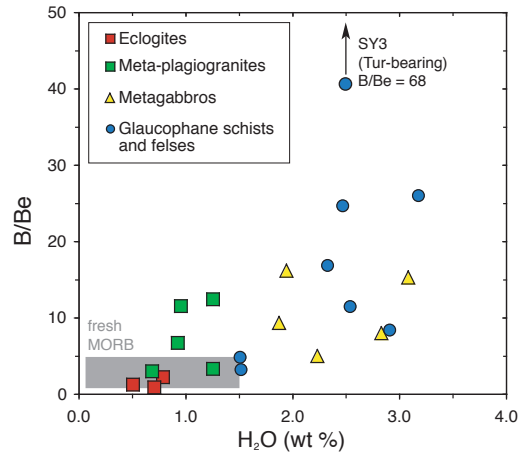

Fig. 6.1. B/Be ratio vs H_2O content of H*P* rocks, which were not rehydrated during exhumation. Range and values of B/Be ratios are decreasing with decreasing H_2O content. Grey field displays data of fresh MORB from literature (Perfit *et al.*, 1999; Danyushevsky *et al.*, 2000; Kamenetsky *et al.*, 2000). Tourmaline-bearing sample SY3 shows a B/Be ratio of ~ 68. Displayed data is summarised in Table 6.1. See Chapter 4 for discussion of different rock types (i.e. Fig. 4.1) and Appendix C for further whole-rock data.

In order to decrease the influence of magmatic differentiation of the precursor rocks on the geochemical signal of B, different authors have discussed B/Be ratios rather than B concentrations. B/Be ratios of all meta-igneous samples are < 30 with the tourmaline-bearing meta-andesite SY3 being the only exception. For Tur-free samples, B/Be ratios are decreasing from glaucophane schists and metagab-bros, which show the largest variation ($\sim 3 - 25$), via meta-plagiogranites ($\sim 3 - 13$) to eclogites (< 2.5). This decrease is correlated with a decrease in H_2O contents of the different rocks from $\sim 3.2\,wt\%$ to $\sim 0.5\,wt\%$ (Fig. 6.1).

Group 2 Li abundances of most Tur-bearing and Tur-free group-2 samples are very high ($\sim 20 - 80\,\mu g/g$), but do not show systematic variation with H_2O content. The same behaviour is observed for Be. Abundances are high ($0.5 - 3.3\,\mu g/g$) in both types of rocks.

B abundances of Tur-bearing and Tur-free samples are of course strongly contrasting. Tur-free rocks have relatively low B contents of $\sim 4 - 15\,\mu g/g$ independent from H_2O content. Tur-bearing samples naturally show a strong enrichment in B. Modal abundances of tourmaline range from $\sim 0.3\,wt\%$ in retrogressed eclogite

SY412 to $\sim 30\,\text{wt\%}$ in phengite-tourmaline schist SY420 and $\sim 50\,\text{wt\%}$ in sample SY401B, which is a tourmaline-rich layer within a glaucophane schist (see description in Appendix B). B/Be ratios of Tur-bearing and Tur-free samples define two discrete trends with increasing H_2O contents as displayed in Fig. 6.2. Tur-bearing samples show a strong increase of B/Be ratios with increasing H_2O content up to values in the order of 10^4. Even relatively low amounts of tourmaline of $\leq 1\,\text{wt\%}$ already increases the B/Be ratios of the whole rocks to > 100. In contrast, Tur-free samples are enriched in H_2O to various degrees ($\sim 0.6 - 9.7\,\text{wt\%}$), but do not show any preferential enrichment in B. All samples show B/Be ratios < 10, which is even lower than the average of the glaucophane schists of group 1.
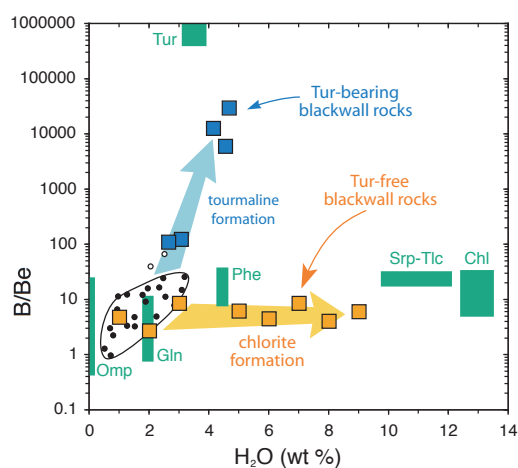

Fig. 6.2. B/Be ratio vs H_2O content of blackwall rocks. Tourmaline-bearing samples (blue squares) show a strong increase in B/Be ratios along a trend marked by the blue arrow. Tourmaline-free blackwall samples (orange squares) show constant B/Be ratios, but a strong increase in H_2O contents, marked by the orange arrow. Samples which were not rehydrated during exhumation (see Fig. 6.1) are shown by small circles (filled = Tur-free; open = Tur-bearing). Compositional variation of different B-Be-bearing minerals (Tur, Omp, Gln, Phe, Chl) from HP rocks are displayed for comparison (data from Chapter 7). Box labelled "Srp-Tlc" represents whole-rock analyses of serpentinite ($\pm$talc-bearing) samples SY347 and SY429. Displayed data is summarised in Table 6.1. See Appendix C for further whole-rock data.

6.3. Discussion

Group 1   Group-1 samples represent a suite of lithologically different rocks with different major and trace element chemistry that developed from different protoliths,

but were overprinted by prograde metamorphism and dehydration probably at similar $P - T$ conditions of $\sim 500\,^{\circ}\mathrm{C}$ and $1.3 - 2.0\,\mathrm{GPa}$ (see Chapter 3). The trace element budget of the rocks is therefore influenced by processes that operated prior to subduction, like magmatic differentiation and hydrothermal alteration, and by fluid release during subduction zone metamorphism. Hence, the interpretation of whole-rock element abundances is difficult in this suite of samples. Low contents of a specific trace element may result from low contents in the protolith, or from effective element loss during dehydration. A quantitative estimation of trace element loss during subduction zone metamorphism of igneous rocks is therefore not possible on the basis of the whole-rock data from Syros samples. However, the evaluation of the whole suite of group-1 samples in relation to their respective H_2O contents provides qualitative information on the behaviour of specific trace elements.

Li concentrations do not correlate with H_2O contents and show high concentrations in many glaucophane schists, metagabbros and eclogites. Whole-rock abundances of several samples are at the upper limit of Li concentrations in altered oceanic crust. This suggests that large portions of Li contained in the hydrothermally altered protoliths are retained within the oceanic crust and are not released with hydrous fluids during HP metamorphism. At least in mafic lithologies, the major part of Li probably stays in the slab and is therefore observed in blueschists and eclogites. Hence, the upper part of the oceanic crust, which is typically enriched in Li during ocean floor metamorphism and weathering (see Chapter 5) probabaly is an important reservoir for deep subduction and recycling of Li into the mantle. This conclusion was also drawn by Woodland *et al.* (2002), who investigated orogenic and xenolithic eclogites from various localities, and proposed that crustal eclogites may be distinguished from mantle eclogites by their significantly higher Li contents.

Be whole-rock abundances do not correlate with H_2O contents, which is in agreement with the low mobility of Be in hydrous fluids (see Chapter 5). Be contents of glaucophane schists and metagabbros are in the same range as in fresh and altered oceanic crust and hence, were probably not influenced by metamorphism or dehydration. High Be concentrations in meta-plagiogranites may be explained by magmatic differentiation of the protoliths (i.e. plagiogranites). The protoliths of the eclogites were not highly differentiated ($\sim 45 - 53\,\mathrm{wt\%}$ SiO_2; up to $5.8\,\mathrm{wt\%}$ MgO; Appendix C), but still show high Be contents. The enrichment of Be in these rocks is accompanied by an enrichment of several other trace elements, like the REE. As a consequence, the eclogites do not display significant Be anomalies in MORB-normalised element abundance plots (Fig. 4.3) and show MORB-like Be/Nd ratios of ~ 0.05 (Appendix C). This overall enrichment in incompatible trace element points to a magmatic rather than a metasomatic process. The eclogite precursors were probabaly enriched basalts.

118

The correlation of B/Be ratios with H_2O contents of group-1 rocks displayed in Fig. 6.1 may be explained by a loss of B together with hydrous fluids during progressive dehydration. However, it has to be considered that the suite of group-1 rocks does not represent different degrees of dehydration of a uniform pre-subduction lithology, but that each of the investigated samples probably has had a different B, Be and H_2O content before the onset of subduction zone metamorphism. Higher B/Be ratios of rocks with higher H_2O contents in principle may be the result of more intense alteration of the protoliths at the seafloor, or it may demonstrate the loss of B during progressive dehydration during subduction. Previous studies (Moran *et al.*, 1992; Bebout *et al.*, 1993, 1999, see above) have interpreted low B abundances in metamorphic rocks as the result of dehydration during metamorphism, i.e. temperature increase. Absolute values of $< 20\,\mu g/g$ B and B/Be ratios of < 30 of metamafic rocks determined in previous studies (Moran *et al.*, 1992; Bebout *et al.*, 1993, 1999) are consistent with the results from Syros. Only tourmaline-bearing meta-andesite SY3 shows a higher B content and a higher B/Be ratio, demonstrating that accessory tourmaline ($B/Be \approx 10^6$) strongly increases the B/Be ratio of a rock.

Group 2 Group-2 samples, representing metamorphic rocks that were strongly metasomatised by hydrous fluids during exhumation may be used to monitor the effects of retrograde metasomatism during exhumation on different elements in general. Li concentrations of $> 50\,\mu g/g$ in many blackwall samples demonstrate an enrichment in Li during fluid infiltration. Be also displays high concentrations of $> 3\,\mu g/g$ in several samples, with some of them also displaying high Be/Nd ratios of > 0.1. The blackwall forming metasomatism therefore led to a selective enrichment in Be with respect to the REE in some samples. B is not enriched in Tur-free blackwall rocks, despite the fact that Tur-free and Tur-bearing blackwalls occur in close vicinity and display very similar lithologies – apart from the tourmaline. They were formed together and hydrating fluids were probably B-rich in both cases. Low B/Be ratios and low B concentrations in Tur-free blackwall rocks may be explained by low partition coefficients of B between silicates and hydrous fluids of $D_B \approx 0.01$ (Brenan *et al.*, 1998b, and Chapter 8). Formation of tourmaline ($\sim 3\,wt\%$ B) by reaction of B-bearing fluids with blackwall silicates (chlorite, glaucophane) led to an effective retention of B in the rocks and strongly increased their B/Be ratios.

6.4. Summary and conclusions

Li, Be and B abundances in whole rocks of two different groups of HP meta-igneous rocks from Syros were measured. Group-1 are samples that preserved the peak metamorphic parageneses and were not rehydrated during exhumation. Their trace element content is controlled by the respective abundances in the (altered) igneous protoliths and by extraction of trace elements by dehydration reactions during prograde metamorphism. Group-2 samples, in contrast were significantly rehydrated during exhumation. Their trace element content is strongly governed by retrograde metasomatism.

Group-1 samples contribute information on the impact of dehydration of (altered) igneous oceanic crust on whole-rock abundances of different trace elements. In detail, the abundances of Li and Be do not correlate with H$_2$O contents and are in the same range as in fresh and altered oceanic crust, suggesting that most of the Li and Be remains in the subducting slab and is not released with hydrous fluids. In contrast, B concentrations and B/Be ratios are correlated to the H$_2$O contents of the rocks. Both are decreasing in range and value with decreasing H$_2$O content, suggesting a significant loss of B with hydrous fluids during progressive dehydration. B/Be ratios of all mafic rocks are < 30, which is in agreement with previous studies (Bebout *et al.*, 1993). Only Tur-bearing samples show much higher ratios.

Group-2 samples provide information on the effects of metasomatism of HP metamorphic rocks during exhumation. Li and Be show very high abundances in many samples, suggesting a strong enrichment during metasomatism. The enrichment of B is entirely controlled by the occurrence of tourmaline. Tur-bearing samples are strongly enriched in B and display very high B/Be ratios ($\gg 100$). Tur-free samples show low B concentrations and B/Be ratios (< 10), which is probably due to low partition coefficients of B between most silicates and hydrous fluids. These results demonstrate that Li is probably a good tool for tracing metasomatic enrichment processes, while B is enriched only in the case of tourmaline formation.

In summary, this study suggests hat B/Be ratios can be used to trace qualitatively the progressive dehydration of HP metamorphic rocks, while Li concentrations are more sensitive for metasomatic processes, i.e. the influx of external fluids. The contrasting behaviour of the three elements is probably due to differences in partition coefficients between silicates and fluids, which are decreasing from B via Li to Be (see Chapter 5). A quantification of the trace element budgets by using the suite of investigated rocks is probably not possible, as the protoliths of the different samples were already entirely different before the onset of subduction. Therefore, in-situ study on element partitioning among different minerals may provide more detailed information on the behaviour of Li, Be and B, as demonstrated in the fol-

lowing chapters.

7. Partitioning and budgets of light elements in high-pressure metamorphic rocks

7.1. Introduction

The light elements Li, Be and B are important tracers for the mass transfer in subduction zones. They are readily mobilised by fluids and melts and display strong isotope fractionation (Li and B) in nature. Concentrations of the three elements in the mantle and in fresh oceanic basalts are very low, whereas they are enriched in sediments, altered oceanic crust and continental crust (see Chapter 5). Therefore, any input of fluid or melt from the subducting slab into the overlying mantle has a strong impact on the light element budget and isotopic composition of the mantle wedge, and the magmas generated there. Island arc volcanic rocks consequently display strong enrichments of Li, Be and B with respect to MORB (see Chapter 5 and Ryan & Langmuir, 1987, 1988, 1993; Smith *et al.*, 1997; Sano *et al.*, 2001; Ryan, 2002) and specific isotopic signatures of light elements (Ishikawa & Nakamura, 1994; Ishikawa & Tera, 1997; Clift *et al.*, 2001; Straub & Layne, 2002; Morris *et al.*, 2002; Palmer & Swihart, 2002; Tomascak, 2004). Detailed knowledge on budget and partitioning of light elements within different materials within the subducting slab are essential for the modelling of Li, Be and B transfer and isotopic evolution in subduction zones. In order to fully understand the light element signatures of arc volcanic rocks, it is necessary to know the behaviour of these elements during subduction-related progressive metamorphism of slab materials.

Recent work has been carried out on the bulk-rock Li, Be and B budgets of metasediments and metabasalts from subduction complexes and it was argued that substantial amounts of B and Li are liberated from the rocks during prograde metamorphism, while Be concentration does not vary significantly with metamorphic grade (see Chapter 5; Moran *et al.*, 1992; Bebout *et al.*, 1993, 1999; You *et al.*, 1994; Peacock & Hervig, 1999). Studies on the partitioning behaviour of Li, Be and B between coexisting metamorphic minerals are scarce. Domanik *et al.* (1993) studied the fractionation of Be and B between minerals of metabasic and metasedimentary lithologies from the Catalina schists (California) and emphasised the importance of white mica stability on the Be and B budgets of subducting rocks. Woodland *et al.* (2002) studied the partitioning of Li between clinopyroxene and garnet in a large

variety of eclogites and found that Li is preferentially incorporated in clinopyroxene. Zack *et al.* (2003) studied eclogites from Trescolmen (Central Swiss Alps) and found that Li and Be budgets are governed by omphacite, while white mica and omphacite control the B budget. Paquin *et al.* (2004) studied the systematics of Li, Be and B in the ultrahigh-pressure garnet peridotite from Alpe Arami that was presumably subjected to a metasomatic overprint by aqueous solutions during exhumation in a supra-subduction zone setting. Scambelluri *et al.* (2004) investigated B and Li concentrations in fluid inclusions and different minerals of serpentinites and olivine-orthopyroxene-chlorite rocks, and estimated the mobility of B and Li during the breakdown of serpentinites during subduction.

In this chapter, abundances and partitioning of Li, Be and B between various minerals of high-pressure metamorphic rocks from the Greek island of Syros (Cyclades) are reported. The major hosts of the light elements are investigated and the whole-rock budgets determined by ICP-AES and PGNAA are compared with estimations from in-situ analyses from SIMS. It will be demonstrated that not only Be, but also considerable amounts of Li may be retained in dehydrated high-pressure metamorphic rocks. The fate of B will mainly depend on the stability of phengite and the formation and stability of tourmaline. If tourmaline is formed, B will be immobilised and will be retained in the subducting slab.

7.2. Investigated samples

Metagabbros (SY344, SY438). Sample SY344 is dominated by garnet and Ca-amphibole, topotactically intergrown with glaucophane, embedded in a matrix of epidote. Sample SY438 is dominated by glaucophane, phengite and lawsonite and a minor omphacite.

Eclogites (SY109, SY323) consisting of garnet and omphacite with minor epidote. SY109 contains additional white mica and glaucophane. SY308 is a *garnet-omphacite-quartz fels* with minor amounts of glaucophane, epidote and paragonite.

Glaucophane schists (SY304, SY314, SY406) are dominated by glaucophane, garnet and phengite that are accompanied by various additional phases such as chloritoid (SY304) or tourmaline (SY314).

Schists from blackwalls (SY309B, SY325, SY328, SY404, SY441), consisting of glaucophane + omphacite + chlorite + epidote + tourmaline (SY309B), chlorite + talc + Ca-amphibole (SY325), omphacite + chlorite + epidote (SY328), chlorite + titanite + apatite (SY404) and chlorite + tourmaline + titanite + omphacite (SY441).

Quartz-rich vein (SY425D) crosscutting a metagabbro. This sample is characterised by euhedral clinozoisite, omphacite and garnet, embedded in a matrix of

quartz.

7.3. Estimation of modal compositions

Mass fractions of minerals in the rocks (Table 7.1) are visual estimates, with the exception that the fractions of phengite, titanite and tourmaline were calculated from bulk-rock concentrations of K_2O, TiO_2 and B_2O_3, respectively. For titanite, this procedure was only possible for rutile-free samples. Calculation of mass fractions of all minerals was not possible, because of major element zonations and similar chemical compositions of glaucophane and omphacite.

7.4. Li, Be and B concentrations in minerals

Mean, minimum and maximum abundances of Li, Be and B in the various minerals are given in Tables 7.2, 7.3 and 7.4. Chloritoid, titanite, epidote/clinozoisite and quartz contain very low amounts of all three low-atomic mass elements. Fresh lawsonite in sample SY438 displays very low abundances of Li and B (0.005 and $0.145\,\mu g/g$, respectively), whereas the concentration of Be is considerable ($1.67\,\mu g/g$).

Garnet displays highly variable concentrations of Li ($0.152 - 5.97\,\mu g/g$), depending on bulk-rock composition, while B concentrations are very low ($0.015 - 0.093\,\mu g/g$) and Be concentrations are generally near the detection limit of $0.001\,\mu g/g$. Small ($<100\,\mu m$) garnet grains in samples SY314 and SY406 show strong zonation in Li with high contents ($6 - 7\,\mu g/g$) in the cores and low contents ($1 - 2\,\mu g/g$) in the rims (Fig. 7.1a). Garnet grains from all other samples are large ($0.5 - 5\,mm$) and show (almost) no zonation in Li (Fig. 7.1b). The concentrations of B are nearly constant within all grains measured.

Type-I tourmaline in sample SY314 shows Li and Be concentrations of 8.6 and $0.37\,\mu g/g$, respectively, whereas concentrations in type-II tourmaline are generally lower ($2.1 - 5.3\,\mu g/g$ Li; $0.041 - 0.055\,\mu g/g$ Be). Profiles measured across large type-II grains show very constant Li and Be concentrations. B_2O_3 contents of $10.5 - 11.3\,wt\%$ result in $3.06 - 3.15\,B\,cpfu$, suggesting small amounts of tetrahedral B (Marschall *et al.*, 2004c).

Clinopyroxene contains very high and variable amounts of Li ($6.81 - 130\,\mu g/g$) and Be ($0.173 - 4.73\,\mu g/g$), but only minor amounts of B ($0.252 - 3.82\,\mu g/g$).

Ca-amphibole has low abundances of Li ($0.976 - 1.30\,\mu g/g$) but relatively high abundances of both Be ($0.662 - 4.34\,\mu g/g$) and B ($2.98 - 9.16\,\mu g/g$). Glaucophane, similar to clinopyroxene, contains very high amounts of Li and Be and only

125

Table 7.1. List of investigated samples with estimated mass fractions of minerals in samples

Sample	Type	Cld	Ttn	Grt	Czo	Lws	Tur	Cpx	Cam	Gln	Chl	Tlc	Phe	Pg	Ab	Qtz	Further minerals
SY109	Eclogite		3	15	0.5			37		25			5.5	1		8	Rt, Zrn, Aln, Ap, Ilm
SY304	Gln schist	12		4	20					38	8		8.5	2nd		3	Rt, Ap
SY308	Meta-plagiogranite			6	4			21		5				25		38	Rt, Zrn, Ap
SY309B	Gln schist		0.3		2		11.8	20		36	25		0.1		2	7	Rt, Zrn, Aln, Ap
SY314	Gln schist		0.5	5	2.5		0.25			34			22		22		Ap, Mag
SY323	Eclogite		2	25	25		0.011	45			20				2nd	1	Rt, Zrn, Ap, Ilm
SY325	Tlc-Chl-Act schist								65		20	15					Rt
SY328	Omp-Chl fels		0.5		6			60			20				2.5		Aln, Ap, Ilm, Mag, Py
SY344	Metagabbro		2	4	12			20	32	28			2.5				Ap
SY404	Chl schist		8	35	2						85						Rt, Aln, Ap, Py
SY406	Gln schist		0.5	5	20		0.2	4		38			19				Rt, Aln, Ap
SY425D	Qtz vein							5								70	
SY438	Gln schist		1.5		5	10		5		59			18.5		2nd	1	
SY441	Chl schist		1.5				40	3			55						Ap

Mass fractions in (*wt%*) were calculated with XRF whole-rock chemical analyses (see section on whole-rock chemistry) and electron microprobe mineral analyses and controlled by using a petrographical microscope. *2nd* = secondary minerals formed during retrograde reactions.

126
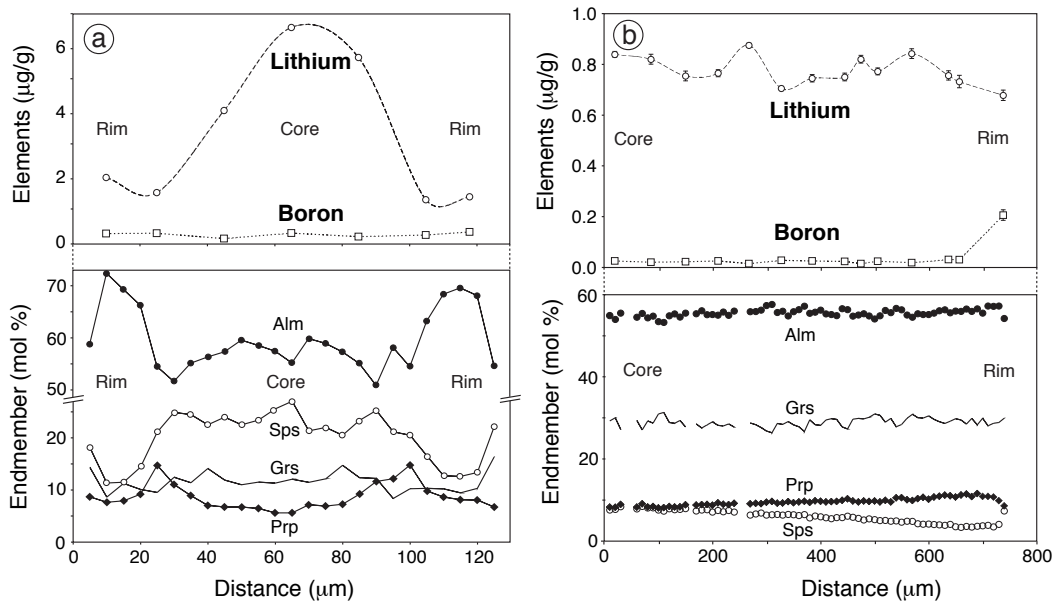
Fig. 7.1. Chemical profile through garnet grains of (a) sample SY406 and (b) sample SY344 showing zonations in Li and B (upper graph) in comparison to major components almandine, spessartine, grossularite and pyrope (lower graph).

minor amounts of B. Li concentrations vary between 5.94 and 115 μg/g and are much higher than those of coexisting Ca-amphibole. On the other hand, the concentrations of Be in glaucophane range from 0.128 to 2.47 μg/g and are thus lower than those of the coexisting Ca-amphibole. B concentrations in glaucophane range from 0.226 to 6.96 μg/g, comparable to coexisting Ca-amphibole.

Phyllosilicates are characterised by highly variable light element abundances. Chlorite shows very high abundances of Li ($3.45 - 115$ μg/g), whereas those of Be and B are low, compared to other sheet silicates (Table 7.2, 7.3 and 7.4). Talc occurring in paragenesis with chlorite and Ca-amphibole (SY325) has relatively low contents of Li (0.433 μg/g) and Be (0.02 μg/g). Phengite contains very high amounts of all three elements ($2.57 - 48.3$ μg/g Li; $1.18 - 5.89$ μg/g Be; $43 - 136$ μg/g B), while paragonite shows very high amounts of Be and B and moderate amounts of Li (Table 7.2, 7.3 and 7.4). Be concentrations in paragonite exceed those of all other silicates, and range from 2.74 to 15.6 μg/g, while B concentrations range from 20.2 to 117 μg/g. Li concentrations vary between 2.77 and 4.91 μg/g, and are higher than Li concentrations in coexisting phengite.

Albite shows very low concentrations of Li ($0.007 - 0.012$ μg/g), moderate abundances of Be ($0.461 - 0.527$ μg/g) and low concentrations of B

Table 7.2. Concentrations of Li in silicates (determined by SIMS) and whole-rock Li concentrations of investigated samples

Sample	Cld	Ttn	Grt	Czo	Lws	Tur	Cpx	Cam	Gln	Chl	Tlc	Phe	Pg	Ab	Qtz	WR_c	WR_m
SY109		n.a.	0.295	n.a.			8.06		7.17			2.57	4.91		<0.001	5.01	6.05
			0.078				0.36		0.28			0.34	1.51			1.00	0.37
			38				15		13			19	11		5		
SY304	<0.001		0.174	n.a.					9.95	11.9		2.71	10.5		0.007	5.50	7.75
			0.020						1.67	2.5		0.41	3.4		0.003	1.10	0.17
	5		7						14	13		9	12		4		
SY308		n.a.	0.152	n.a.			6.81		5.94				2.77		<0.002	2.43	5.02
			0.077				0.32		1.27				1.27			0.49	0.18
			9				5		8				10		7		
SY309B		0.030		0.545		2.10	27.2		41.0	34.7		5.85				29.2	31.7
		0.004		0.092		0.33	3.9		3.1	2.5		1.04				5.8	0.6
		6		5		33	17		19	16		21					
SY314		0.042	5.97	n.a.		8.59			94.0			45.9		0.007	n.a.	42.4	39.6
		0.023	0.92			2.70			16.9			9.3		0.004		8.5	0.8
		3	18			2			27			14		2			
SY323		0.042	3.47	1.11		n.a.	80.6							n.a.	n.a.	37.4	45.8
		0.007	0.81	0.40			18.1									7.5	0.9
		5	52	25			50										
SY325								1.30		3.45	0.433					1.60	2.29
								0.40		0.12	0.128					0.32	0.51
								46		10	11						

Table 7.2. (continued)

Sample	Cld	Ttn	Grt	Czo	Lws	Tur	Cpx	Cam	Gln	Chl	Tlc	Phe	Pg	Ab	Qtz	WR$_c$	WR$_m$
SY328		n.a.		0.436			65.4			115				0.012		62.3	65.3
				0.152			11.7			12				0.009		12.5	2.9
				10			30			21				4			
SY344		n.a.	0.805	n.a.			24.7	0.976	30.6			9.71				14.1	18.8
			0.136				2.3	0.435	7.2			1.32				2.8	0.4
			37				29	26	29			10					
SY404		0.033								9.04						7.69	7.65
		0.006								0.83						1.54	0.14
		3								18							
SY406		n.a.	3.19	n.a.			130		115			49.3				59.4	66.7
			1.52				24		41			12.2				11.9	4.3
			38				17		35			26					
SY425D			1.06	0.220	0.005		59.7								0.067	3.17	3.30
			0.17	0.155	0.002		1.2								0.011	0.63	0.37
			18	5	13		6								7		
SY438		0.048		n.a.			56.4		108			19.9			n.a.	70.2	88.7
		0.037					8.0		13			6.7				14.0	1.9
		2					4		9			8					
SY441		0.057				5.29	49.6			92						54.2	n.a.
		0.001					1.2			4						10.8	
		3				1	2			3							

All concentrations in (μg/g). The first row of each sample is mean concentration; the second row is standard deviation of all analyses; the third row is the number of analyses of this mineral in this sample. WR$_c$ = whole-rock concentrations calculated by using mass fractions of minerals (Table 7.1) and Li concentrations of minerals; standard deviation of 20% assumed due to uncertanties in mineral concentrations and estimation of mass fractions. WR$_m$ = measured whole-rock concentrations and standard deviations (see section on whole-rock chemistry). n.a. = not analysed.

Table 7.3. Concentrations of Be in silicates (determined by SIMS) and whole-rock Be concentrations of investigated samples

Sample	Cld	Ttn	Grt	Czo	Lws	Tur	Cpx	Cam	Gln	Chl	Tlc	Phe	Pg	Ab	Qtz	WR$_c$	WR$_m$
SY109		n.a.	<0.003 6	n.a.			1.31 0.66 15		2.47 1.18 13			5.58 0.94 19	15.6 5.1 11		<0.001 5	1.57 0.31	1.77 0.07
SY304	0.017 0.007 11		<0.001 7	n.a.					0.487 0.151 14	0.234 0.115 13		2.67 0.23 18	2.95 1.52 12		<0.001 4	0.58 0.12	0.46 0.06
SY308		n.a.	<0.001 9	n.a.			0.311 0.046 5		0.128 0.050 8				2.74 0.51 10		<0.001 7	0.76 0.15	0.82 0.01
SY309B		<0.002 6		0.030 0.009 5		0.041 0.006 33	2.38 0.19 17		0.812 0.218 19	0.295 0.055 16		4.11 0.38 21				0.85 0.17	0.65 0.04
SY314		0.028 0.008 3	0.008 0.004 5	n.a.		0.37 0.30 2	4.73 2.38 50		1.59 1.25 27			5.67 0.48 14		0.527 0.342 14	n.a.	1.91 0.38	2.32 0.04
SY323		<0.001 5	<0.004 8	0.046 0.030 13		n.a.								n.a.	n.a.	2.14 0.43	2.08 0.02
SY325								4.34 1.08 46		0.357 0.047 10	<0.021 11					2.89 0.58	2.59 0.03

Table 7.3. (continued)

Sample	Cld	Ttn	Grt	Czo	Lws	Tur	Cpx	Cam	Gln	Chl	Tlc	Phe	Pg	Ab	Qtz	WR$_c$	WR$_m$
SY328		n.a.		0.016			0.173			0.081				0.461		0.13	0.88
				0.010			0.113			0.030				0.057		0.03	0.03
				5			30			21				4			
SY344		n.a.	<0.001	n.a.			0.285	0.662	0.390			1.18				0.41	0.54
							0.148	0.213	0.186			0.39				0.08	0.02
			13				29	26	29			10					
SY404		<0.001		<0.001						0.350						0.3	0.91
										0.030						0.06	0.02
		3								18							
SY406		n.a.	0.012	n.a.			2.89		1.43			5.89				1.78	1.46
			0.013				0.65		0.41			1.55				0.36	0.2
			9				17		35			26					
SY425D			<0.001	0.020			1.25								<0.001	0.07	0.15
				0.007			0.15									0.01	0.02
			18	5			6								7		
SY438		0.008	n.a.		1.67		3.02		1.59			4.74			n.a.	2.13	1.28
		0.003			0.74		0.75		0.95			3.37				0.4	0.03
		2			13		4		9			8					
SY441		<0.002				0.055	1.08			0.315						0.23	n.a.
							0.29			0.022						0.05	
		3				1	2			3							

All concentrations in (μg/g). The first row of each sample is mean concentration; the second row is standard deviation of all analyses; the third row is the number of analyses of this mineral in this sample. WR$_c$ = whole-rock concentrations calculated by using mass fractions of minerals (Table 7.1) and Be concentrations of minerals; standard deviation of 20 % assumed due to uncertanties in mineral concentrations and estimation of mass fractions. WR$_m$ = measured whole-rock concentrations and standard deviations (see section on whole-rock chemistry). n.a. = not analysed.

Table 7.4. Concentrations of B in silicates (determined by SIMS) and whole-rock B concentrations of investigated samples

Sample	Cld	Ttn	Grt	Czo	Lws	Tur	Cpx	Cam	Gln	Chl	Tlc	Phe	Pg	Ab	Qtz	WR$_c$	WR$_m$
SY109		n.a.	0.024 / 0.009 / 6	n.a.			1.60 / 0.42 / 15		1.90 / 0.81 / 13			43.0 / 7.7 / 19	94.2 / 18.0 / 11		0.044 / 0.022 / 5	4.38 / 0.88	n.a.
SY304	0.014 / 0.010 / 5		0.024 / 0.004 / 7	n.a.					1.93 / 0.42 / 6	2.38 / 0.90 / 5		74.9 / 4.9 / 9	117 / 32 / 12		0.040 / 0.033 / 4	13.1 / 2.6	12.0 / 0.2
SY308		n.a.	0.015 / 0.005 / 9	n.a.			0.251 / 0.057 / 5		0.226 / 0.092 / 8				20.2 / 6.3 / 10		0.029 / 0.014 / 7	5.13 / 1.03	10.3 / 0.1
SY309B		0.030 / 0.022 / 4		0.478 / 0.075 / 5		33,623 / 566 / 33	1.92 / 0.25 / 17		5.53 / 0.98 / 19	1.47 / 0.20 / 8		136 / 15 / 14				3960	3960 / 50
SY314		0.408 / 0.134 / 3	0.090 / 0.031 / 5	n.a.		31,496 / 404 / 2			1.43 / 0.96 / 5			66.3 / 6.0 / 14		0.307 / 0.120 / 2	n.a.	93.9	93.9 / 1.2
SY323		0.046 / 0.018 / 5	0.093 / 0.041 / 8	0.273 / 0.097 / 5		n.a.	2.04 / 0.39 / 22							n.a.	n.a.	4.77	4.77 / 0.06
SY325								9.16 / 1.86 / 46		1.92 / 0.28 / 10	4.77 / 1.34 / 11					7.05 / 1.41	7.15 / 0.10

132

Table 7.4. (continued)

Sample	Cld	Ttn	Grt	Czo	Lws	Tur	Cpx	Cam	Gln	Chl	Tlc	Phe	Pg	Ab	Qtz	WR$_c$	WR$_m$
SY328		n.a.		0.609			3.82			2.50				1.35		2.86	7.58
				0.304			0.70			0.52				0.65		0.57	0.10
				5			5			5				4			
SY344		n.a.	0.023	n.a.			1.52	2.98	3.99			48.2				3.58	5.05
			0.005				0.68	0.72	1.88			5.5				0.72	0.07
			13				29	26	29			10					
SY404		0.091								2.51						2.14	3.75
		0.014								0.47						0.43	0.06
		3								18							
SY406		n.a.	0.090	n.a.			2.70		3.92			86.9				18.1	18.2
			0.077				1.07		1.22			13.9				3.6	0.2
			9				17		35			26					
SY425D			0.040	0.221			0.824								0.027	0.11	1.90
			0.009	0.107			0.099								0.005	0.02	0.03
			18	5			6								7		
SY438		0.149	n.a.		0.145		1.29		6.96			79.6			n.a.	18.9	19.6
		0.017			0.071		0.10		2.25			21.2				3.8	0.2
		2			13		4		9			8					
SY441		0.031				34,700	3.28			2.94						13,900	n.a.
		0.007					0.02			0.31						2800	
		3				1	2			3							

All concentrations in (μg/g). The first row of each sample is mean concentration; the second row is standard deviation of all analyses; the third row is the number of analyses of this mineral in this sample. WR$_c$ = whole-rock concentrations calculated by using mass fractions of minerals (Table 7.1) and B concentrations of minerals; standard deviation of 20 % assumed due to uncertanties in mineral concentrations and estimation of mass fractions. WR$_m$ = measured whole-rock concentrations and standard deviations (see section on whole-rock chemistry). n.a. = not analysed.

$(0.307 - 1.35\,\mu g/g)$.

7.5. Budgets of Li, Be and B

The highest concentrations of Li were found in chlorite, glaucophane, omphacite/jadeite, phengite and paragonite. These phases contain more than 95 % of the Li budget of every sample investigated. Garnet, clinozoisite, tourmaline, Ca-amphibole and talc contain only minor amounts of Li, and chloritoid, titanite, lawsonite, quartz and albite are negligible for the Li budgets of the samples.

Be contents are highest in paragonite, phengite, Ca-amphibole, omphacite/jadeite, lawsonite and glaucophane and much lower in albite and chlorite. All other phases are negligible for the Be budgets of the bulk rocks.

Apart from tourmaline, the most important hosts for B are paragonite and phengite with B contents between 20 and $130\,\mu g/g$. All other phases show concentrations below $10\,\mu g/g$, with Ca-amphibole, talc, chlorite, glaucophane, omphacite/jadeite and albite between 0.2 and $9\,\mu g/g$. Nevertheless, these phases are important for the B budget of samples that have very low modal abundances of tourmaline and white micas (e.g. SY325, SY344).

Li, Be and B budgets of the samples were calculated from mineral mass fractions (Table 7.1) and mean element concentrations (Table 7.2, 7.3 and 7.4). In most cases, calculated bulk-rock budgets of Li, Be and B are within 80 to 120 % of the measured bulk-rock concentration values (Fig. 7.2 and 7.3). Only in a few cases are there significant differences between both values. In principle, these discrepancies could be due to (i) incorrect estimates of mineral mass fractions or (ii) incorporation of Li, Be and B in secondary and/or non-silicate minerals or in fluid inclusions.

7.6. Partitioning of Li, Be and B between high-pressure minerals

Equilibrium element partitioning between two phases depends on temperature, pressure and phase compositions. For the investigated samples, peak conditions reached during high-pressure metamorphism are similar and were estimated at $470 - 500\,°C$ and $1.5 - 2.0\,GPa$ (Okrusch & Bröcker, 1990; Trotet *et al.*, 2001b). However, as many mineral grains are chemically zoned, it is clear that equilibrium was not reached. Nevertheless, the partitioning of Li, Be and B between the coexisting mineral phases was found to be rather constant and independent from element concentrations (Tables 7.5, 7.6 and 7.7; Figs 7.4, 7.5 and 7.6). For almost all mineral pairs, apparent partition coefficients vary by less than an order of magnitude and for
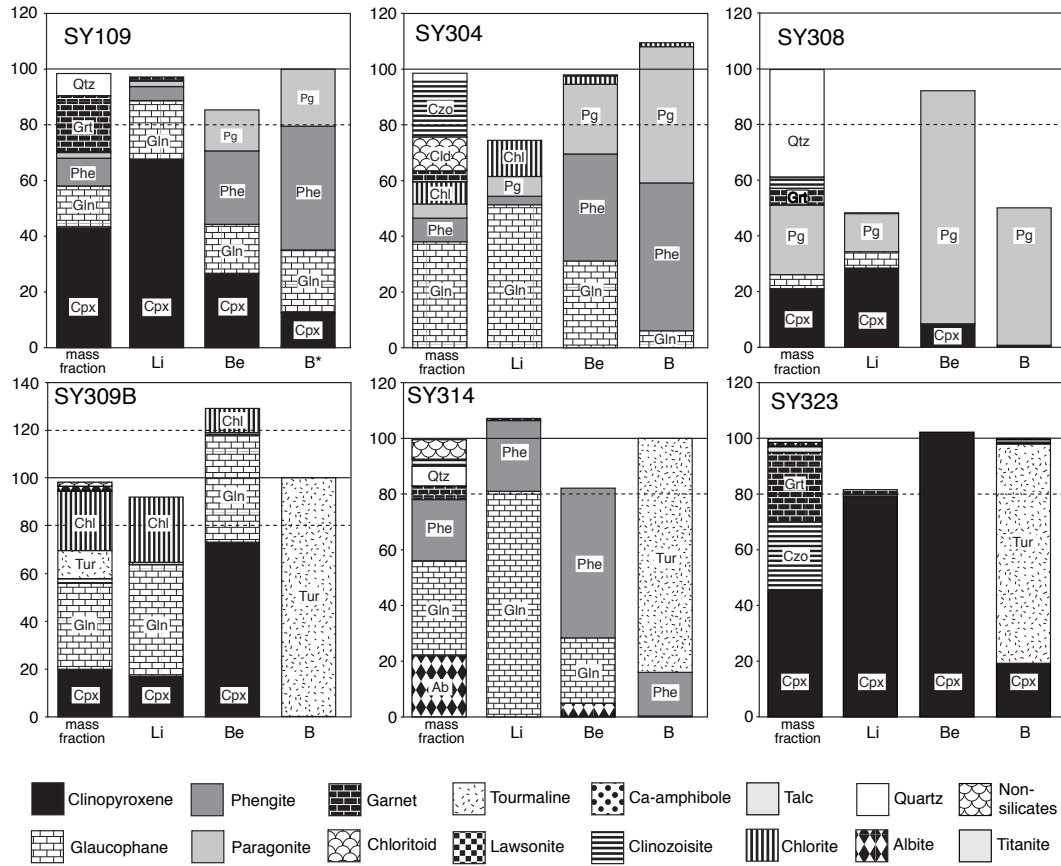
Fig. 7.2. Li, Be and B budgets of 6 samples. Every sample is shown in four columns for mass fraction of minerals, Li, Be and B contents respectively, normalised to 100 % of measured whole-rock contents. Uncertainties in calculation of the budgets are assumed to be 20 % and are marked in all diagrams as dashed lines. *Boron whole-rock data for sample SY109 are not available; B budget for this sample is normalised to the calculated concentration of Table 7.4.
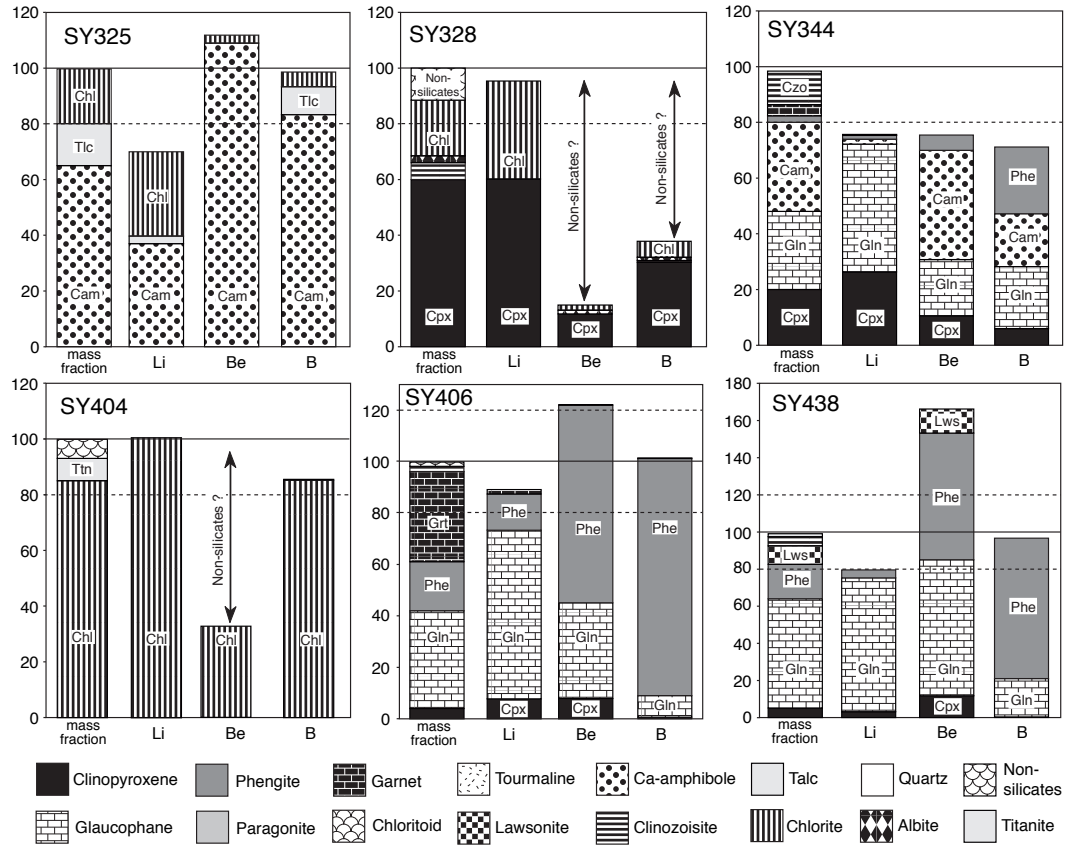
Fig. 7.3. Li, Be and B budgets of 6 samples. Every sample is shown in four columns for mass fraction of minerals, Li, Be and B contents respectively, normalised to 100 % of measured whole-rock contents. Uncertainties in calculation of the budgets are assumed to be 20 % and are marked in all diagrams as dashed lines.

many of them by less than a factor of three, while concentrations vary by more than an order of magnitude.

Partitioning of trace elements between clinopyroxene and garnet is most relevant for eclogites. The partitioning of Li and B between these two phases is shown in Fig 7.4a and b, respectively. Li concentrations range from 6.81 to 80.6 μg/g in clinopyroxene and from 0.152 to 3.47 μg/g in garnets, resulting in Cpx/Grt partition coefficients between 23 and 56 with an average of 37 (Tables 7.2 and 7.5). B concentrations vary between 0.251 and 2.70 μg/g in clinopyroxene and between 0.015 and 0.090 μg/g in garnet. Cpx/Grt partition coefficients for B range from 16 to 67 with an average of 37 (Tables 7.4 and 7.7). Be concentrations in garnet are at or even below detection limit for most of the samples. Therefore, it is only possible to calculate a minimum Cpx/Grt partition coefficient of 250 for Be (Table 7.6). The results show that in eclogitic lithologies, all three elements are strongly fractionated into clinopyroxene.

The partitioning of light elements between glaucophane and garnet (Figs 7.4c and d) is very similar to that between clinopyroxene and garnet. The large variation of Li concentrations shown by glaucophane from various samples is reflected by equivalent variations in coexisting garnet (Table 7.2). Glaucophane/garnet partition coefficients for Li vary between 16 and 57 with an average of 35 (Table 7.5). In the case of B, variations in concentrations are smaller. Apparent partition coefficients show a relative wide range from 15 to 170 (Table 7.7). Be is concentrated in glaucophane, and the minimum partition coefficient is 160. All three elements are strongly fractionated into glaucophane.

Since phengite forms a significant constituent of many blueschists, the partitioning of light elements between glaucophane and phengite is of some importance. Observed Li concentrations in phengite vary between 2.57 and 49.3 μg/g (Table 7.2), resulting in glaucophane/phengite partition coefficients between 2.1 and 7.0 with an average of 3.8 (Table 7.5; Fig. 7.5a). Be concentrations in phengite range from 1.18 to 5.89 μg/g (Table 7.3) and glaucophane/phengite partition coefficients range from 0.18 to 0.44 with an average of 0.29 (Fig. 7.5b; Table 7.6). Measured B concentrations in phengite vary between 43.0 and 136 μg/g B (Table 7.4). The partition coefficient (Gln/Phe) is well defined between 0.022 and 0.088, with an average of 0.050 (Table 7.7; Fig. 7.5c). These results show that Li is partitioned into glaucophane, Be is partitioned into phengite and B is almost exclusively fractionated into phengite.

Partitioning of Li, Be and B between omphacite/jadeite and glaucophane is shown in Figs 7.6a, b and c, respectively. Li concentrations in both minerals show a wide range among different samples, as mentioned above. Clinopyroxene/glaucophane partition coefficients range from 0.52 to 1.15 with an

Table 7.5. Partition coefficients of Li between 15 silicates, calculated from concentrations of Table 7.2

	Cld	Ttn	Grt	Czo	Lws	Tur	Cpx	Cam	Gln	Chl	Tlc	Phe	Pg	Ab	Qtz
Cld	<0.0065 1		>160 1						>8900 1	$>1.1\cdot10^4$ 1		>2400 1			>6.6 1
Ttn			110 2 80 140	22 2 18 26	0.096 1	120 3 70 200	1200 4 800 1900		2000 3 1400 2300	1000 3 300 1600		570 3 200 1090		0.17 1	
Grt		0.0097 2 0.0071 0.0122		0.26 2 0.21 0.32		1.4 1	37 6 23 56	1.2 1	35 6 16 57	69 1		12 5 8 16	17 2 17 18	0.0012 1	0.053 2 0.043 0.064
Czo		0.046 2 0.038 0.055	4.0 2 3.0 4.8			3.9 1	140 4 50 270		75 1	160 2 60 260		11 1		0.027 1	
Lws		10 1					$1.2\cdot10^4$ 1		$2.3\cdot10^4$ 1			4300 1			
Tur		0.010 3 0.005 0.014	0.70 1	0.26 1			11 2 9 13		15 2 11 20	17 2 17 17		4.1 2 2.8 5.3		$8.3\cdot10^{-4}$ 1	
Cpx		$9.1\cdot10^{-4}$ 4 $5.3\cdot10^{-4}$ $11.5\cdot10^{-4}$	0.030 6 0.018 0.043	0.011 4 0.004 0.020	$8.2\cdot10^{-5}$ 1	0.092 2 0.077 0.107		0.040 1	1.2 6 0.9 1.9	1.6 3 1.3 1.9		0.33 5 0.22 0.34	0.51 2 0.41 0.61	$1.8\cdot10^{-4}$ 1	0.0011 1
Cam			0.83 1						31 1	2.7 1	0.33 1	10 1			

Table 7.5. (continued)

	Cld	Ttn	Grt	Czo	Lws	Tur	Cpx	Cam	Gln	Chl	Tlc	Phe	Pg	Ab	Qtz
Gln	$<1.1\cdot10^{-4}$ / 1	$5.4\cdot10^{-4}$ / 3 / $4.5\cdot10^{-4}$ / $7.3\cdot10^{-4}$	0.034 / 6 / 0.018 / 0.064	0.013 / 1	$4.3\cdot10^{-5}$ / 1	0.071 / 2 / 0.051 / 0.091	0.90 / 6 / 0.52 / 1.15	0.032 / 1		1.0 / 2 / 0.8 / 1.2		0.31 / 7 / 0.14 / 0.49	0.58 / 2 / 0.47 / 0.69	$7.6\cdot10^{-5}$ / 1	$7.4\cdot10^{-4}$ / 1
Chl	$<9.4\cdot10^{-5}$ / 1	0.0017 / 3 / 0.0006 / 0.0037	0.015 / 1	0.0098 / 2 / 0.0038 / 0.0157		0.059 / 2 / 0.058 / 0.061	0.63 / 3 / 0.54 / 0.79	0.38 / 1	1.0 / 2 / 0.8 / 1.2		0.13 / 1	0.20 / 2 / 0.17 / 0.23		$1.0\cdot10^{-4}$ / 1	$6.2\cdot10^{-4}$ / 1
Tlc								3.0 / 1		8.0 / 1					
Phe	$<4.2\cdot10^{-4}$ / 1	0.0028 / 3 / 0.0009 / 0.0051	0.091 / 5 / 0.064 / 0.130	0.093 / 1	$2.3\cdot10^{-4}$ / 1	0.27 / 2 / 0.19 / 0.36	3.2 / 5 / 2.6 / 4.7	0.10 / 1	3.8 / 7 / 2.1 / 7.0	5.2 / 2 / 4.4 / 5.9			1.9 / 1	$1.6\cdot10^{-4}$ / 1	0.0027 / 1
Pg			0.058 / 2 / 0.055 / 0.060				2.1 / 2 / 1.6 / 2.5		1.8 / 2 / 1.5 / 2.1			0.52 / 1			$< 6\cdot10^{-4}$ / 2
Ab		5.9 / 1	840 / 1	37 / 1		1200 / 1			$1.3\cdot10^{4}$ / 1	9700 / 1		6400 / 1			
Qtz	<0.15 / 1		44 / 3 / 16 / 92	3.3 / 1			880 / 1		1400 / 1	1600 / 1		370 / 1	>1700 / 2		

Partition coefficients of Li between two minerals are ratios of concentrations (Li in mineral 1 /Li in mineral 2). Mineral 1 is given in the top row, mineral 2 is given in the first column. The first row of each mineral is the mean coefficient; the second row is the number of samples used for calculation of partition coefficients. Maximum or minimum values are given for cases in which one mineral is lying below the detection limit.

139

Table 7.6. Partition coefficients of Be between 15 silicates, calculated from concentrations of Table 7.3

	Cld	Ttn	Grt	Czo	Lws	Tur	Cpx	Cam	Gln	Chl	Tlc	Phe	Pg	Ab	Qtz
Cld									29 1	14 1		160 1		19 1	<0.02 1
Ttn			0.30 1	>10 2	210 1	22 3 13 30	390 1		130 2 60 200	>160 3		400 2 200 610		19 1	
Grt	>30 1	3.4 1		>10 2		44 1	250 1	>900 1	160 2 120 190	>500 1		590 2 510 680	>4000 1	63 1	d.l. 4
Czo			<0.1 2			1.4 1	64 4 11 103		27 1	7.5 2 5.2 9.8		140 1		30 1	<0.02 1
Lws		0.0047 1					1.8 1		0.95 1			2.8 1			
Tur		0.077 1	0.023 1	0.73 1			39 2 20 58		12 2 4 20	6.4 2 5.7 7.2		58 2 15 100		1.4 1	
Cpx		0.0013 4 0.0003 0.0026	0.0020 6 0.0005 0.0024	0.032 4 0.010 0.090	0.55 1	0.034 2 0.017 0.051		2.3 1	0.84 6 0.34 1.89	0.30 3 0.12 0.47		2.8 5 1.6 4.3	10 2 9 12	2.7 1	<0.002 3
Cam			<0.001 1						0.59 1	0.082 1	<0.005 1	1.8 1			

Table 7.6. (continued)

	Cld	Ttn	Grt	Czo	Lws	Tur	Cpx	Cam	Gln	Chl	Tlc	Phe	Pg	Ab	Qtz
Gln	0.035 1	0.0083 3 0.0023 0.0177	0.0037 6 0.0010 0.0081	0.037 1	1.1 1	0.14 2 0.05 0.23	1.8 6 0.5 2.9	1.7 1		0.42 2 0.36 0.48		3.8 7 2.3 5.5	14 2 6 21	0.33 1	<0.005 3
Chl	0.072 1	<0.006 3	<0.002 1	0.15 2 0.10 0.19		0.16 2 0.14 0.18	4.5 3 2.1 8.1	12 1	2.4 2 2.1 2.8		<0.06 1	13 2 11 14		5.7 1	<0.002 1
Tlc								>200 1		>20 1					
Phe	0.0063 1	0.0024 3 0.0005 0.0050	$9.4 \cdot 10^{-4}$ 5 $1.8 \cdot 10^{-4}$ $19.6 \cdot 10^{-4}$	0.0074 1	0.35 1	0.038 2 0.010 0.065	0.44 5 0.23 0.64	0.56 1	0.29 7 0.18 0.44	0.080 2 0.072 0.088					< $1 \cdot 10^{-4}$ 2
Pg			$1.9 \cdot 10^{-4}$ 1				0.099 2 0.084 0.114		0.10 2 0.05 0.16			0.36 1			< $3 \cdot 10^{-4}$ 2
Ab		0.054 1	0.016 1	0.034 1		0.70 1	0.38 1		3.0 1	0.18 1		11 1			
Qtz	>40 1		>1 4	>60 1			>400 3		>200 3	>600 1		>7000 2	>4000 2		

Partition coefficients of Be between two minerals are ratios of concentrations (Be in mineral 1 /Be in mineral 2). Mineral 1 is given in the top row, mineral 2 is given in the first column. The first row of each mineral is the mean coefficient; the second row is the number of samples used for calculation of partition coefficients. Maximum or minimum values are given for cases in which one mineral is lying below the detection limit. d.l. = both minerals below detection limits.

Table 7.7. Partition coefficients of B between 14 silicates, calculated from concentrations of Table 7.4

	Cld	Ttn	Grt	Czo	Lws	Cpx	Cam	Gln	Chl	Tlc	Phe	Pg	Ab	Qtz
Cld	0.60 1		1.7 1					140 1	170 1		5300 1			2.8 1
Ttn			1.1 2 0.2 2.0	11 2 6 16	0.97 1	56 4 9 104	130 1	79 3 35 186	57 3 28 94		1800 3 160 4600		0.75 1	
Grt		2.5 2 0.5 4.5		4.3 2 2.9 5.6		37 6 16 67		68 6 15 170	100 1		1800 5 700 3200	2600 2 1300 4000	3.4 1	1.5 4 0.7 1.9
Czo		0.12 2 0.06 0.17	0.26 2 0.18 0.34			5.4 4 3.7 7.5		12 1	3.6 2 3.1 4.1		280 1		2.2 1	0.12 1
Lws		1.0 1				8.9 1		48 1			550 1			
Cpx		0.041 4 0.010 0.116	0.037 6 0.015 0.061	0.20 4 0.13 0.27	0.11 1		2.0 1	2.4 6 0.9 5.4	0.77 3 0.66 0.90		45 5 27 71	70 2 59 81	0.35 1	0.059 3 0.027 0.116
Cam			0.0079 1					1.3 1	0.21 1	0.52 1	16 1			

Table 7.7. (continued)

	Cld	Ttn	Grt	Czo	Lws	Cpx	Cam	Gln	Chl	Tlc	Phe	Pg	Ab	Qtz
Gln	0.0074 1	0.10 3 0.01 0.29	0.031 6 0.006 0.068	0.087 1	0.021 1	0.59 6 0.19 1.11	0.75 1		0.75 2 0.27 1.23		25 7 11 46	70 2 50 90	0.21 1	0.058 3 0.021 0.129
Chl	0.006 1	0.022 3 0.011 0.036	0.010 1	0.28 2 0.24 0.33		1.3 3 1.1 1.5	4.8 1	2.3 2 0.8 3.8		2.5 1	62 2 32 92		0.54 1	0.017 1
Tlc							1.9 1		0.4 1					
Phe	$1.9 \cdot 10^{-4}$ 1	0.0028 3 0.0002 0.0062	$7.5 \cdot 10^{-4}$ 5 $3.2 \cdot 10^{-4}$ $13.6 \cdot 10^{-4}$	0.0035 1	0.0018 1	0.026 5 0.014 0.037	0.062 1	0.050 7 0.022 0.088	0.021 2 0.011 0.032			2.2 1	0.0046 1	$7.8 \cdot 10^{-4}$ 2 $5.4 \cdot 10^{-4}$ $10.2 \cdot 10^{-4}$
Pg			$5.1 \cdot 10^{-4}$ 2 $2.5 \cdot 10^{-4}$ $7.6 \cdot 10^{-4}$			0.015 2 0.012 0.017		0.016 2 0.011 0.020			0.46 1			$9.5 \cdot 10^{-4}$ 2 $4.7 \cdot 10^{-4}$ $14.4 \cdot 10^{-4}$
Ab		1.3 1	0.30 1	0.45 1				4.7 1	1.9 1		220 1			
Qtz	0.35 1		0.78 4 0.53 1.47	8.2 1		25 3 9 36		33 3 8 48	59 1		1400 2 1000 1900	1400 2 700 2200		

Partition coefficients of B between two minerals are ratios of concentrations (B in mineral 1/B in mineral 2). Mineral 1 is given in the top row, mineral 2 is given in the first column. The first row of each mineral is the mean coefficient; the second row is the number of samples used for calculation of partition coefficients. Maximum or minimum values are given for cases in which one mineral is lying below the detection limit.

143
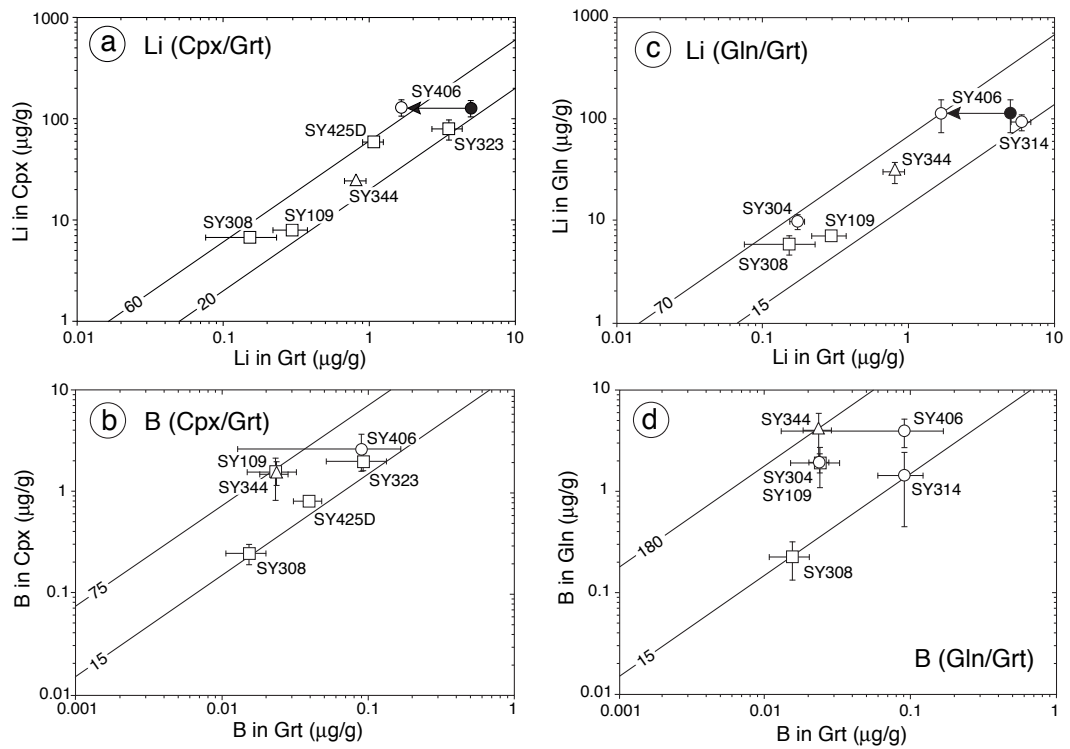
Fig. 7.4. Concentrations of Li (a and c) and B (b and d) in coexisting clinopyroxene-garnet (a and b) and glaucophane-garnet (c and d) pairs. Diagonal lines mark constant partition coefficients (values given on lines). Circles = glaucophane schists; diamonds = black wall schists; squares = eclogites; triangles = meta gabbros. Garnet in sample SY406 is zoned in Li with decreasing concentrations from core (filled cycle) to rim (open cycle), as displayed in Fig. 7.1. See Fig. 7.5 for a legend.
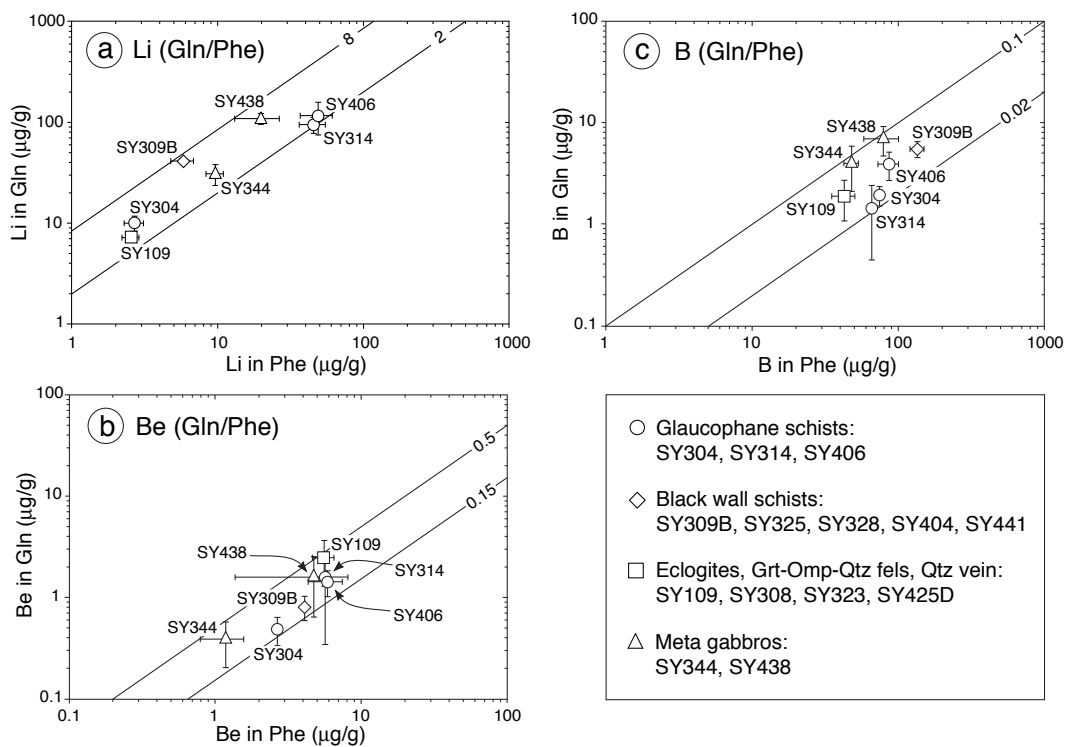
Fig. 7.5. Concentrations of (a) Li, (b) Be and (c) B in coexisting glaucophane-phengite pairs in various samples. Diagonal lines mark constant partition coefficients (values given on lines). (d) Legend for Fig. 7.4, 7.5 and 7.6. Samples were devided into four different groups based on the basis of petrographic observations and geochemistry. Note that not all mineral pairs occur in each samples, and therefore, not all samples are plotted in each diagram.
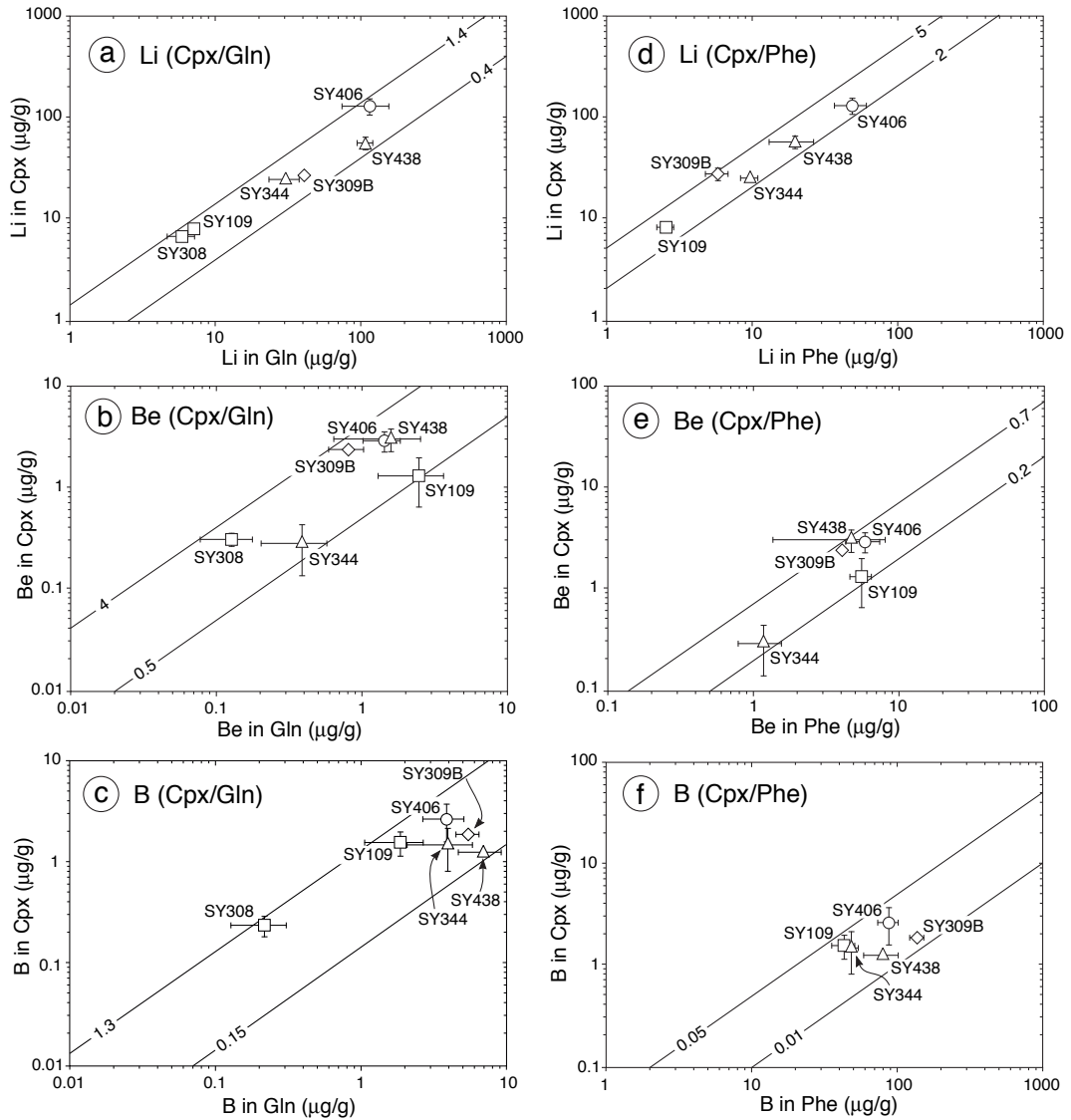
Fig. 7.6. Concentrations of Li, Be and B in coexisting clinopyroxene-glaucophane (a, b and c) and clinopyroxene-phengite (d, e and f) pairs. Diagonal lines mark constant partition coefficients (values given on lines). Circles = glaucophane schists; diamonds = black wall schists; squares = eclogites; triangles = meta gabbros. See Fig. 7.5 for a legend.

average of 0.90 (Table 7.5). The partition coefficients for Be and B range from 0.5 to 2.9 (average 1.8) and from 0.19 to 1.11 (average 0.59), respectively (Tables 7.6 and 7.7). Note that partition coefficients between clinopyroxene and glaucophane of all three elements scatter around unity.

The partitioning of Li, Be and B between clinopyroxene and phengite is shown in Figs 7.6d, e and f, respectively. Fig. 7.6d displays the large spread in Li concentrations in both clinopyroxene and phengite and shows a rather constant partition coefficient ranging from 2.6 to 4.7 with a mean of 3.2 (Table 7.5). The spread in Be concentrations is smaller and partition coefficients for Be vary between 0.23 and 0.64, with an average of 0.44 (Table 7.6). B concentrations in both minerals do not demonstrate much variation. The partition coefficients range from 0.014 to 0.037, with an average of 0.026 (Table 7.7). The results show that Li is fractionated into clinopyroxene, while Be and B are preferentially incorporated into phengite.

The examples discussed above show that in the high-pressure metamorphic rocks from Syros, partitioning of Li, Be and B between coexisting minerals is systematic. Observed partition coefficients vary by a factor of two or three in most examples and they are independent from absolute concentrations. Only in some cases, such as the partitioning of B between garnet and other phases, vary the partition coefficients by more than one order of magnitude. This unusually large variation may be due to uncertainties at very low concentration levels of B in garnet.

In many blueschist- and eclogite-facies high-pressure metamorphic rocks, clinopyroxene is a major host for Li and Be, and it also incorporates some B. The partitioning of Li, Be and B between clinopyroxene and melt and clinopyroxene and aqueous fluid has been studied experimentally (Brenan *et al.*, 1998b,a). Therefore, clinopyroxene is used below as a reference mineral. Mineral/Cpx partition coefficients for Li, Be and B calculated from the observed mineral/mineral partition coefficients (Table 7.5, 7.6 and 7.7) are presented in Figs 7.7, 7.8 and 7.9. The results for Li show that almost all mineral/Cpx partition coefficients are smaller than unity, except for glaucophane (1.2 ± 0.6) and chlorite (1.6 ± 0.3). For Be, actinolite/Cpx and glaucophane/Cpx partition coefficients are near to unity, while the respective partition coefficients of white micas and albite are clearly above unity. For B, phengite/Cpx and paragonite/Cpx partition coefficients are very high (45 and 70, respectively) and those for the amphiboles, chlorite and talc are close to unity.
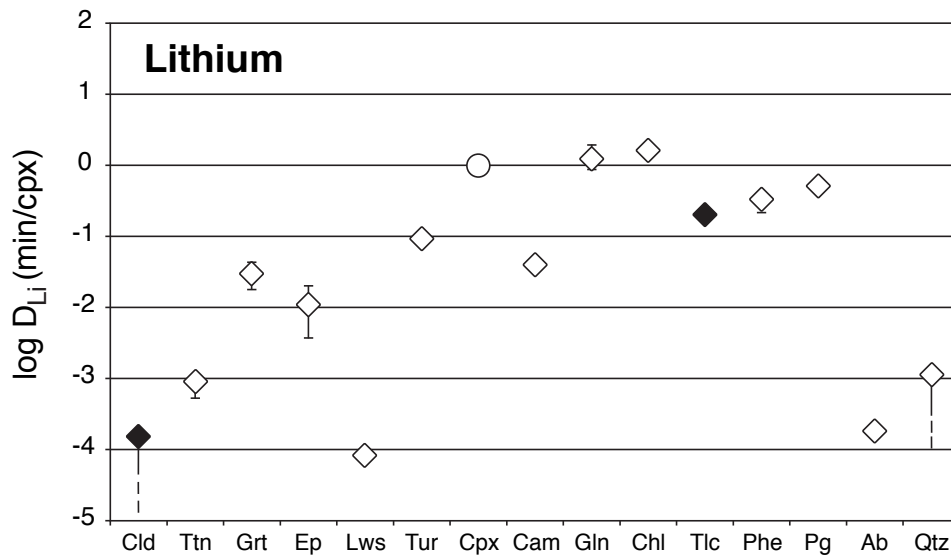
Fig. 7.7. Mineral/Cpx partition coefficients of Li for 15 different HP metamorphic minerals plotted as log $D^{\text{mineral/Cpx}}$. Minerals are arranged in the order of increasing silicate polymerisation. Open diamonds display minerals for which partition coefficients were directly calculated from concentration ratios between the respective mineral and coexisting clinopyroxene. Black diamonds display minerals which were not observed in equilibrium with clinopyroxene. D values for these minerals were calculated by combining Cpx/Chl with mineral/Chl concentration ratios. Open circle represents clinopyroxene.
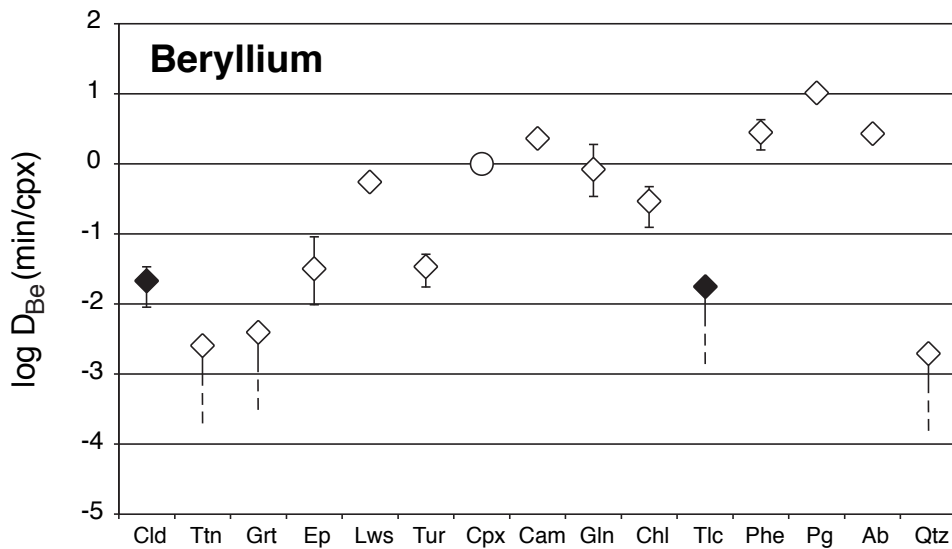
Fig. 7.8. Mineral/Cpx partition coefficients of Be for 15 different HP metamorphic minerals plotted as log $D^{\text{mineral/Cpx}}$. See Fig. 7.7 for further details.
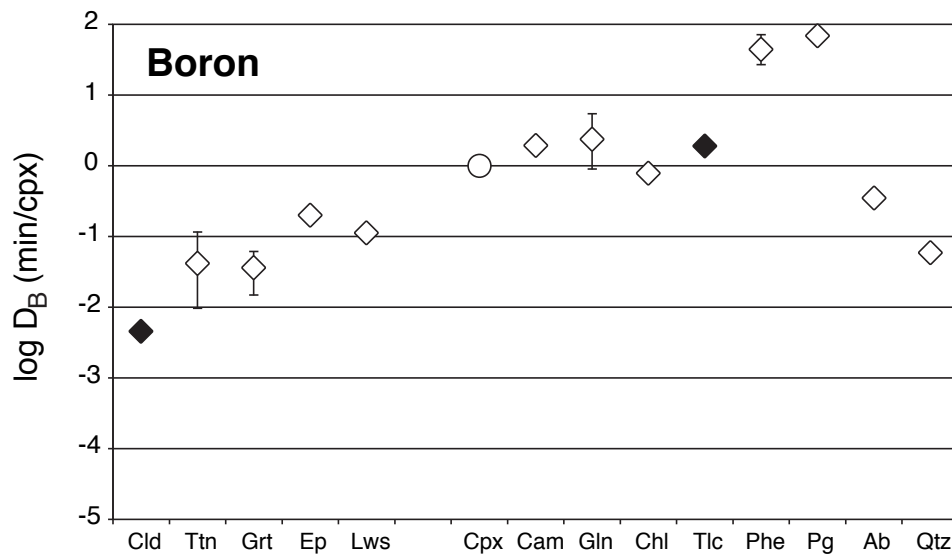
Fig. 7.9. Mineral/Cpx partition coefficients of B for 14 different H*P* metamorphic minerals plotted log $D^{\text{mineral/Cpx}}$. Tourmaline is not displayed. See Fig. 7.7 for further details.

7.7. Discussion and conclusions

All three elements Li, Be and B were found to be strongly fractionated among different minerals. Very high concentrations of lithium were revealed in the major phases of chlorite schists, glaucophane schists, metagabbros and eclogites, namely chlorite, glaucophane and omphacite/jadeite. The budgets of these rocks demonstrate that the major phases are the principal carriers of Li. Obviously, chlorite, glaucophane and clinopyroxene are able to incorporate high amounts of Li into their crystal structures. Therefore, prograde high-pressure metamorphism of altered oceanic crust during progressive subduction should not significantly decrease the amount of Li in these lithologies. At low metamorphic grades, Li can be hosted in chlorite, and during formation of blueschists, it will enter glaucophane. Later on, the blueschist-eclogite transition is characterised by sliding reactions occurring over certain $P - T$ ranges. During this process, the modal abundance of glaucophane is decreasing, while the amount of clinopyroxene increases, until finally an eclogite assemblage dominated by clinopyroxene and garnet will form. As described above, clinopyroxene is able to take in large amounts of Li and, therefore, most of the rock's Li should be retained within the eclogite. Woodland *et al.* (2002) have shown that metabasaltic eclogites from different localities and metamorphic grade show significant whole-rock Li concentrations of up to $31 \, \mu g/g$ most of which is hosted in clinopyroxene. Furthermore, Zack *et al.* (2002a, 2003) report whole-rock Li contents of eclogites

from Trescolmen (Central Alps) reaching $41\,\mu g/g$ and Hermann (2002) reports Li contents of 46 and $102\,\mu g/g$ in two phengite-bearing eclogites from Dora Maira (Western Alps). Therefore, it is clear that most of the Li from altered oceanic crust can be transferred to relatively great depth within eclogitic parageneses.

Tomascak *et al.* (2002) discussed Li, Be and B contents and Li isotopic compositions of basalts and andesites from different island arcs. They found that volcanic rocks enriched in B (high B/Be) neither demonstrate a significant enrichment in Li nor a subduction-related Li isotope signature. The authors emphasise a strong discrepancy between the fluid-mobile character of Li and its lack of enrichment in arc magmas. This apparent contradiction is solved by assuming that Mg-silicates of the mantle wedge may act as a filter. Fluids released from the dehydrating slab are thought to contain high concentrations of Li and B. The partitioning of Li and B between peridotite and hydrous fluid at high pressures and temperatures is significantly different from each other, with $D^{\mathrm{peridotite/fluid}} \approx 0.01$ for B and ≈ 0.1 for Li (Brenan *et al.*, 1998b). Consequently, B will be transported through the mantle wedge to the magma source region, while Li is removed from the fluids by Mg-silicates in the mantle peridotite directly overlying the subducting plate. Paquin *et al.* (2004) have demonstrated that the ultrahigh-pressure garnet peridotite from Alpe Arami (Central Swiss Alps) was subjected to a subduction-related Li metasomatism without a concomittant significant enrichment in B. They argued that clinopyroxene and olivine of the lower and colder parts of the mantle remove slab-derived Li from fluids migrating from the dehydrating slab into the hot regions of sub-arc melting. B, in comparison, is not significantly incorporated by these minerals, due to its low mineral/fluid partition coefficients for mantle minerals (see Chapter 5). The results of the study on Syros H*P* rocks suggest, that large portions of Li may be retained in the subducting oceanic crust itself, and thus may not even be mobilised. Hence, the retainment of Li in eclogitic clinopyroxene probably also contributes to the fractionation of the fluid-mobile elements Li and B. A more quantitative examination of fluid transport and fractionation of the light elements is given in Chapter 8.

Beryllium is mainly hosted in clinopyroxene, glaucophane and white mica; in addition, Ca-amphibole, lawsonite and albite may also contain significant amounts of Be. As discussed above for Li, Be should also be retained in progressively dehydrating rocks of the subducting oceanic crust. It will be hosted by Ca-amphibole and albite in greenschists, by glaucophane and white mica in blueschists and by clinopyroxene in eclogites. Domanik *et al.* (1993) found white mica to contain the highest concentrations of Be in high-pressure rocks, which is in agreement with the results presented here. However, the limited modal abundance of white mica compared to glaucophane and clinopyroxene restricts the importance of phengite

and paragonite for the Be budgets of the rocks. Zack *et al.* (2002a) underlined the importance of clinopyroxene as the principal carrier of Be in eclogites, which is in agreement with the results obtained in this study.

During this study, special emphasis was put on analyses of boron at low concentration levels (see Section 2.4, page 16). This turned out to be very important, as almost all of the investigated minerals contain less than $10 \, \mu g/g$ B and most contain less than $1 \, \mu g/g$. The only minerals (except for tourmaline) showing higher concentrations of B are phengite and paragonite. Previous studies demonstrated that white micas are important carriers of B in high-pressure rocks (Domanik *et al.*, 1993; Zack *et al.*, 2002a; Hermann, 2002). However, these studies were not focused on accuracy of B measurements at low concentration levels and therefore might have overestimated the concentrations of B in minerals coexisting with white mica, namely clinopyroxene, amphibole and garnet. This overestimation of B at low concentration levels led to an underestimation of partition coefficients between white mica and coexisting minerals and belittled the importance of white micas as major carriers of B. The measurements presented here revealed relatively low concentrations in minerals coexisting with B-rich white micas, leading to large partition coefficients ($D^{\text{Phe}/\text{Cpx}} = 45$; $D^{\text{Pg}/\text{Cpx}} = 70$; Table 7.5), and therefore underline the outstanding importance of phengite and paragonite as hosts of B. The contribution of phases other than phengite, paragonite and tourmaline is smaller than formerly thought. In contrast to Domanik *et al.* (1993) who measured 5 to $55 \, \mu g/g$ B in lawsonite, the new measurements of Syros lawsonite reveals only $0.145 \, \mu g/g$ B (SY438; Table 7.4) in equilibrium with B-rich phengite in a B-rich rock (Table 7.4). Therefore, the role of lawsonite as an important carrier of B in high-pressure metamphic rocks has to be negated. Analyses of chlorite during this study showed that surface contamination is a serious problem, especially for sheet silicates. The highest concentrations of B in chlorite from six different samples are only between 2.50 and $2.95 \, \mu g/g$ and are almost two orders of magnitude lower than B concentrations of coexisting paragonite (Table 7.4). Therefore, chlorite must also be recognised as only a minor host of B. Zack *et al.* (2002a) completed a LA-ICP-MS study on hydrous eclogites and report B concentrations in garnet of $2.7 \, \mu g/g$. The calculated B budgets of those rocks revealed a significant amount of B being incorporated into garnet, due to its high modal abundance. Analyses on Syros rocks revealed very low B concentrations in garnet (15 to $93 \, \text{ng/g}$) making garnet insignificant for the B budget of garnet-glaucophanites and eclogites. The significantly higher apparent B concentrations revealed by previous studies using SIMS or LA-ICP-MS techniques may be explained by surface contamination of thin sections (see Section 2.4 on page 16) or by small mineral and fluid inclusions, which have been overlooked during analysis.

Formation and stability of tourmaline during subduction has been demonstrated for rocks of various high-pressure metamorphic terranes by different workers (e.g. Schreyer, 1985; Reinecke, 1998; Peacock & Hervig, 1999; Nakano & Nakamura, 2001; Bebout & Nakamura, 2003; Altherr *et al.*, 2004, see Chapter 9). Tourmaline could form at various $P - T$ conditions, including sedimentary, diagenetic and metamorphic conditions from surface conditions up to very high pressures, exceeding 5 GPa and temperatures of 950 °C (Werding & Schreyer, 2002; Henry & Dutrow, 2002) [see Chapter 9 for a detailed discussion on tourmaline stability]. Nakano & Nakamura (2001) showed that tourmaline can be formed in subducting metasedimentary rocks, and suggested that the B necessary for tourmaline formation was released from white mica within the rock. Hence, the B budgets of the rocks were redistributed during progressive metamorphism, whereas the whole-rock B concentrations were more or less constant. The occurrence of tourmaline, formed early in the metamorphic history of different Syros rocks (eclogites, blueschists) shows that this mechanism may also operate in meta-magmatic rocks. Formation and stability of tourmaline will immobilise B and will cause a quantitative retention of B in the subducting material. Preferential incorporation of B in white mica shows that this element is dominated by the same minerals as K, Rb, Ba, Cs (LILE) in high-pressure metamorphic rocks (Domanik *et al.*, 1993; Sorensen *et al.*, 1997; Melzer & Wunder, 2000; Zack *et al.*, 2001; Schmidt *et al.*, 2004). Formation of tourmaline will lead to a total decoupling of B from LILE (K, Rb, Ba, and Cs), as high-pressure dravite demonstrates very low concentrations of LILE (see Chapter 11 on page 225), whereas B is a major component of this mineral with concentrations of $\sim$ 3wt% B. Occurrence, major and trace element chemistry, B isotopic composition and geological implications of tourmaline in Syros high-pressure rocks are further discussed in Chapters 9, 10 and 11.

The large dataset on Li, Be and B partitioning among HP metamorphic minerals presented in this chapter provides a sound basis for modelling of light element behaviour during subduction, metamorphism and dehydration, which is discussed in Chapter 8.

8. Squeezing out the subducting slab - modelling light element release during progressive high-pressure metamorphism

This chapter contains a model for the quantification of trace element release during dehydration of progressively subducting oceanic crust. The model is based on results from previous work by other authors (e.g. Brenan *et al.*, 1998b; Hervig *et al.*, 2002), and results from studies on natural rocks presented in this thesis (Chapter 7), combined with phase equilibria calculations performed by Lars Rüpke (Kiel), using the program PerpleX (Conolly, 1990). The results from PerpleX provide modal compositions and H_2O contents of progressively metamorphosed rocks along certain *P-T* paths, calculated from geophysical parameters (Rüpke *et al.*, 2002). Modelling of trace element and isotopic fractionation is based on mass balance calculations and was performed by me using an Excel spreadsheet. First results of this study were presented at the International Mineralogical Association's (IMA) general meeting in 2002 in Edinburgh (Marschall *et al.*, 2002a) and the Annual Meeting of the Deutsche Mineralogische Gesellschaft (DMG) in 2004 in Karlsruhe (Marschall *et al.*, 2004d).

8.1. Introduction

Subduction zones are the sites of the most significant material transfer between two major geochemical reservoirs – the Earth's crust and mantle. Recycling of oceanic crust into the upper (and lower) mantle, fluid and melt transport and extensive volcanism have been topics of detailed investigation for several decades. Investigating the geochemistry of island arc basalts (IAB) and continental arc basalts (CAB) – volcanic rocks produced above subduction zones – legions of igneous geochemists have established several element and isotopic ratios as tools to trace processes operating within subduction zones to produce the characteristic "subduction zone geochemical fingerprint". Enrichment in fluid-mobile elements (e.g. Cs, Ba, K, Sr, U, Pb), a lack of enrichment in HFSE (high field-strength elements; e.g. Nb, Ta, Ti, Zr, Hf) together with specific isotopic signatures (e.g. $^{87}Sr/^{86}Sr$, $^{206}Pb/^{204}Pb$) are interpreted as a result of metasomatism of the IAB and CAB source by slab-derived fluids or melts (e.g. Tatsumi & Eggins, 1995). The use of light elements as tracers

in subduction zone geochemistry was also put forward by studies on subduction-related volcanic rocks by various authors starting with J. Ryan and C. H. Langmuir in the late 1980s (Ryan & Langmuir, 1987, 1988, 1993). Recent reviews on the geochemical behaviour of the light elements and their isotopes are given in Bouman (2004), Tomascak (2004) and Elliott *et al.* (2004) for lithium, Ryan (2002) for beryllium and Leeman & Sisson (2002) and Palmer & Swihart (2002) for boron. Element ratios like Li/Yb, B/Be and B/Nb and isotope signatures (^{7}Li/^{6}Li, ^{10}Be/^{9}Be, ^{11}B/^{10}B) have been used over the last ~ 15 years in order to enhance our knowledge on slab dehydration and subduction-related melting processes.

Apart from the volcanic output of subduction zones – the IAB and CAB – information on the light element output has also been deduced from other subduction-related rocks and fluids, like xenoliths from the mantle wedge (Nishio *et al.*, 2004), orogenic peridotites (Paquin & Altherr, 2002; Paquin *et al.*, 2004), mud volcanoes (Deyhle & Kopf, 2002; Kopf & Deyhle, 2002; Kopf *et al.*, 2003a) and serpentinite diapirs (Benton *et al.*, 2001, 2004).

Another important source of information are exhumed high-pressure metamorphic rocks, such as eclogites (Zack *et al.*, 2003), metasedimentary units (Moran *et al.*, 1992; Bebout *et al.*, 1993, 1999) and serpentinites (Scambelluri *et al.*, 2004). In-situ studies on light element partitioning between high-pressure metamorphic minerals allowed for the quantification of the budget of these elements in different lithologies (Chapter 7; Domanik *et al.*, 1993; Woodland *et al.*, 2002). Studies on high-pressure metamorphic tourmaline revealed important insights into B isotope fractionation within dehydrating oceanic crust (Chapter 9; Chapter 10; Nakano & Nakamura, 2001; Bebout & Nakamura, 2003).

Experimental work on light element behaviour during fluid/rock or fluid/mineral interaction has been performed by Seyfried *et al.* (1984), You *et al.* (1995b, 1996), Brenan *et al.* (1998b), Johnson & Plank (1999) and Green & Adam (2003). The temperature dependent boron isotopic fractionation was determined experimentally by Hervig *et al.* (2002) and references therein, and other workers (Wunder *et al.*, 2004; Thomas *et al.*, 2004). Lithium isotope fractionation is less well confirmed. However, several authors report fractionation factors for different temperatures between seafloor conditions ($T = 2\,^\circ$C, Chan *et al.*, 1992) and hydrothermal temperatures of up to 350$\,^\circ$C (Chan *et al.*, 1993; Seyfried *et al.*, 1998; Chan & Kastner, 2000).

Summarising the results of all these studies dealing with the behaviour of light elements in the subduction cycle, some principle conclusions can be made. Li and B are relatively mobile in hydrous fluids and in silicate melts. Be is relatively immobile in hydrous fluids but mobile in silicate melts. Li and B concentrations in the slab are decreasing with increasing depth of subduction, because these elements

are released with fluids during dehydration. Therefore, ratios of fluid-mobile B and non-mobile elements like Be or Nb (B/Be and B/Nb) are also decreasing. Concurrently, preferential loss of the heavier isotopes ^{7}Li and ^{11}B results in decreasing δ^7Li and δ^{11}B values in the subducting material. The studies on subduction-related volcanic rocks investigating across-arc profiles show a decrease of B concentrations, B/Be and B/Nb ratios and δ^{11}B values from trench to back-arc. Li/Yb ratios of IAB are higher than MORB, but across-arc profiles have not shown a systematic trend. δ^7Li of most IAB are MORB-like. This has been explained by equilibration of Li between the fluid and the mantle during the fluid's migration from the slab to the site of melt generation (Tomascak *et al.*, 2002; Bouman, 2004).

Within the slab, the most important reservoirs for Li, Be and B are the sediments, the altered oceanic crust (AOC) and serpentinised ultramafic rocks. Fresh mantle and magmatic rocks show very low concentrations and no isotopic anomalies. Sediments, AOC and serpentinites are not only enriched in Li, B and ±Be, but also show δ^7Li and δ^{11}B values higher than MORB (or mantle), due to a preferential enrichment in the heavy isotopes during the interaction with seawater. The hydrous portion of the subducting slab therefore introduces large amounts of heavy Li and B into the subduction zone. Be (including ^{10}Be) concentrations are especially enriched in the sedimentary column of the oceanic crust.

On the basis of this detailed but only qualitative knowledge on light element behaviour in subduction zones the following chapter presents a model for a quantitative calculation of light element release and B isotope fractionation during dehydration of oceanic crust. The aim is to extract as much information as possible from the data deduced from H*P* metamorphic rocks – to squeeze out the slab.

8.2. Estimating light element release and isotope fractionation

Several authors have modelled light element release (Bebout *et al.*, 1993; Brenan *et al.*, 1998b) or isotopic fractionation of Li (Zack *et al.*, 2003; Bouman, 2004) and B (Peacock & Hervig, 1999; Bebout & Nakamura, 2003; Rosner *et al.*, 2003) in subduction zones. The aim of all these studies was a more quantitative estimation of the evolution of trace element content and isotopic composition of both the subducting slab and the released fluids.

Bebout *et al.* (1993) modelled B/Be ratios of rocks and fluid in subducting sediments during progressive dehydration using Rayleigh fractionation formulations well known from the modelling of trace element distribution during partial melting processes, which have also been used before for modelling fluid/rock interaction processes (Nabelek, 1987).

Brenan *et al.* (1998b) experimentally determined Li, Be and B partition coefficients between clinopyroxene (and garnet) and aqueous fluid (pure water and 0.5 M HCl) at 2.0 GPa and 900 °C. They combined these Cpx /fluid partition coefficients with amphibole/Cpx, lawsonite/Cpx and mica/Cpx partition coefficients determined by Domanik *et al.* (1993) on natural H*P* metamorphic rocks. This resulted in mineral/fluid partition coefficients for five different H*P* minerals (Grt, Cpx, Lws, Am and mica). Brenan *et al.* (1998b) than calculated whole rock/fluid partition coefficients by combining the mineral/fluid partition coefficients with data on the modal composition of MORB + H_2O during progressive subduction from Poli & Schmidt (1995). Both H_2O content and whole rock/fluid partition coefficients are changing due to the change in modal composition of the subducting rock, but can be calculated from the data set. Using this method, Brenan *et al.* (1998b) were able to calculate B /Be ratios of rocks and fluid in subducting hydrous MORB.

Peacock & Hervig (1999) used data on the temperature dependent isotopic fractionation of B from different authors (see Peacock & Hervig, 1999) to calculate the B isotopic composition of rocks and fluids in a system were B is progressively released from the rocks during a temperature increase from 300 to 1000 K. Their model includes neither mineral/fluid partition coefficients nor modal composition of the rocks. Instead it is based on the assumption of boron being steadily released from the rock during increasing temperatures. The same kind of calculation was performed by Bebout & Nakamura (2003). These authors assumed a constant fractionation of 10‰ between silicate rocks and fluid and calculated fluid and rock B isotopic compositions for batch and Rayleigh devolatilisation as a function of B remaining in the rock. The model of Rosner *et al.* (2003) is also similar to that of Peacock & Hervig (1999), and assumes B loss from the slab as a linear function of temperature, decreasing the original B concentration to a value of 20 % at a temperature of 750 °C. The thermal structure of the subducting slab was taken from geophysical data and modelling by Springer (1999). Boron isotope evolution of rocks and fluids were than calculated using the temperature dependent isotope fractionation from Williams *et al.* (2001).

Zack *et al.* (2003) and Bouman (2004) have calculated similar models in order to explain δ^7Li of eclogites and IAB, respectively. In both studies Rayleigh fractionation with constant isotopic fractionation factors and partition coefficients between rocks and fluids are used, together with "typical AOC" Li compositions as starting values for the subducting slab. The results allow for a prediction of Li contents and isotopic compositions of subducting AOC at any stage of dehydration (Bouman, 2004), or for Li contents and isotopic composition of an eclogite's possible protolith (Zack *et al.*, 2003).

8.3. The model

The model presented in this study is based on a combination of the different methods discussed above. A procedure similar to that of Brenan *et al.* (1998b) is used for the calculation of trace element fractionation, which is than combined with a method similar to that of Peacock & Hervig (1999) for the calculation of B isotopic fractionation. Fig. 8.1 displays the principles of this calculation.

It is assumed that a protolith with a certain modal composition, trace element content and isotopic signature is progressively dehydrating with increasing P and T as it is subducting. The H_2O content is calculated from the stoichiometric H_2O contents and weight fractions of all hydrous minerals in the rock. The $P - T$ path, the changing modal composition (metamorphic reactions) and the H_2O contents are calculated using PerpleX (Conolly, 1990; Rüpke *et al.*, 2002). Kerrick & Conolly (2001) and Poli & Schmidt (2002) have estimated the maximum volatile contents of oceanic crust during subduction in the same way. The second set of input data are mineral/clinopyroxene partition coefficients $D_i^{min/\mathrm{Cpx}}$ determined on natural HP metamorphic rocks (from Chapter 7) and are defined as the concentration ratio of an element i in any mineral (c_i^{min}) in equilibrium with clinopyroxene (c_i^{Cpx}):

$$D_i^{min/\mathrm{Cpx}} = \frac{c_i^{min}}{c_i^{\mathrm{Cpx}}} \tag{8.1}$$

For calculating the behaviour of trace elements during dehydration reactions, mineral/fluid partition coefficients are required. Brenan *et al.* (1998b) provide clinopyroxene/fluid partition coefficients $D_i^{\mathrm{Cpx}/fluid}$ for Li, Be and B, determined from experimental studies:

$$D_i^{\mathrm{Cpx}/fluid} = \frac{c_i^{\mathrm{Cpx}}}{c_i^{fluid}} \tag{8.2}$$

These two sets of partition coefficients (8.1 and 8.2) are combined to produce mineral/fluid partition coefficients for the whole set of HP minerals investigated:

$$D_i^{min/fluid} = D_i^{min/\mathrm{Cpx}} \cdot D_i^{\mathrm{Cpx}/fluid} \tag{8.3}$$

Whole rock/fluid partition coefficients are derived from the sum of all mineral/fluid partition coefficients multiplied with the mass fractions X_{min} of the respective minerals in the whole rocks:

$$D_i^{WR/fluid} = \sum_{min} X_{min} \cdot D_i^{min/fluid} \tag{8.4}$$
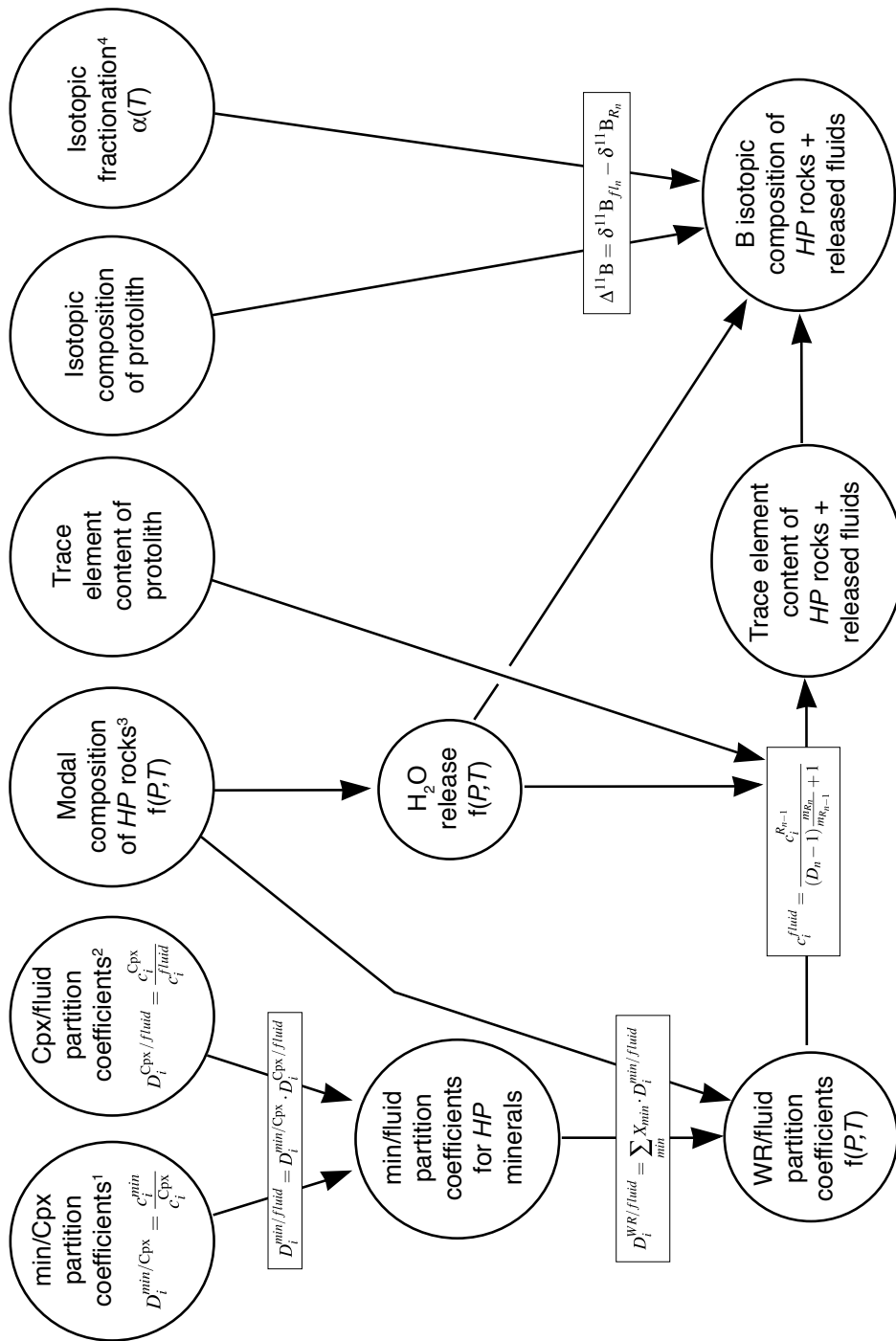
Fig. 8.1. Flowchart of trace element modelling. See following page for explanation.

Fig. 8.1. (Previous page) Flowchart displaying the calculation used for modelling of trace element behaviour and isotope fractionation in dehydrating crust. Input data are: [1]mineral/Cpx partition coefficients from Chapter 7; [2]Cpx/fluid partition coefficients from Brenan *et al.* (1998b); [3]modal composition of the H*P* metamorphic rocks as a function of *P* and *T* from calculations with PerpleX; [4]boron isotopic fractionation as a function of *T* from Hervig *et al.* (2002). Mathematical formulation explained in text and in Appendix H.

Starting with any typical light element content of AOC it is now possible to calculate the evolution of Li, Be and B concentrations in the progressively dehydrating rocks and the released fluids by a mass balance calculation:

$$c_i^{fluid} = \frac{c_i^{R_{n-1}}}{(D_n - 1)\frac{m_{R_n}}{m_{R_{n-1}}} + 1}$$

(8.5)

where $c_i^{R_{n-1}}$ is the concentration of element i in the rock before dehydration step n, D_n is the partition coefficient between dehydrated rock at step n and fluid, and $m_{R_{n-1}}$ and m_{R_n} are the masses of the rock before and after dehydration step n, respectively (see Appendix H for details). The concentration of element i in the rock after dehydration is calculated from the concentration of the element in the fluid and the whole rock/fluid partition coefficient.

In tourmaline-free H*P* metamorphic rocks, B is stored predominantly in mica, amphibole and chlorite (Chapter 7 and Domanik *et al.*, 1993). These minerals are generally assumed to contain B in tetrahedral coordination (Werding & Schreyer, 2002; Hervig *et al.*, 2002; Tonarini *et al.*, 2003). B in acidic hydrous fluids is predominantly trigonally coordinated in $B(OH)_3$ units (Palmer & Swihart, 2002). Recent experiments have shown that this also holds true for high pressures up to 3.0 GPa (Thomas *et al.*, 2004). Experimental studies (e.g. Hervig *et al.*, 2002 and references therein; Heinrich *et al.*, 2003; Sanchez-Valle *et al.*, 2004; Wunder *et al.*, 2004) have investigated the temperature dependence of B isotopic fractionation between phases of different B coordination (e.g. mica, amphibole, melt, fluid, tourmaline). Hervig *et al.* (2002) demonstrated a systematic decrease of fractionation with increasing temperature, given by the formula

$$1000\ln\alpha = 5.68 - 12290/T$$

(8.6)

where α is the fractionation factor and T is absolute temperature (K). Equation 8.6 is used for modelling the B isotopic fractionation of dehydrating H*P* metamorphic rocks containing tetrahedrally coordinated B and released fluid containing B in trigonal coordination. Input parameters for the isotope mass balance calculation (see

Appendix H for details) are (i) the B contents of rocks and fluids, which were calculated before (equation 8.5) and (ii) a value for the B isotopic composition of the protolith, which may be a value for "typical AOC".

Altogether, the model allows for a calculation of light element concentrations and B isotopic compositions of released fluids and restitic rocks for every stage of dehydration with increasing P and T, including changes in modal composition of the rocks. The results include predictions of light element concentrations and B isotopic composition of expelled fluids and high-pressure metamorphic rocks along a specific $P - T$ path.

8.4. Results

8.4.1. $P - T$ path, H_2O content and modal composition

The $P - T$ evolution of the top of the subducted oceanic slab calculated by Lars Rüpke (Kiel) using PerpleX reveals a path of moderately cold subduction, comparable to "path B" of Peacock (1990). The actual T evolution is strongly dependent on the amount of shear heating (frictional heating at the slab-hanging plate interface) introduced into the geophysical model. Fig. 8.2a displays the calculated $P - T$ path on the "basalt + H_2O" diagram of Schmidt & Poli (1998) for orientation. The modal compositions of two slightly different chemical compositions were calculated along the calculated $P - T$ path. Fig. 8.2b displays the modal abundances (by weight) in a H_2O-saturated MORB, while Fig. 8.2c displays the mineral abundances of H_2O-saturated, but K_2O-free MORB. A comparison of the results of trace element modelling for MORB with the phengite-free composition is performed to demonstrate the impact of white mica on B concentrations and its isotope system. The amount of H_2O in the rocks, which is calculated from their modal compositions, is displayed in Fig. 8.2d for the MORB composition, and in Fig. 8.2e for the K_2O-free MORB.

The modal composition in both cases starts with a Lws greenschist, rich in (diopsidic) clinopyroxene, chlorite and lawsonite accompanied by quartz ±phengite, which contains ~ 5.5 wt% H_2O. As temperature increases, garnet is growing at the expense of chlorite and the H_2O content decreases to ~ 3 wt%. The transition from this Lws greenschist to a Lws blueschist is marked by the appearence of glaucophane at the expense of clinopyroxene, while the H_2O content is steadily decreasing to a value of ~ 1.5 wt%. At ~ 520 °C, the amount of omphacitic clinopyroxene starts to increase, while amphibole and lawsonite decrease. The assemblage consisting of garnet + omphacite + barroisitic amphibole + lawsonite + quartz ±phengite can be described as hydrous eclogite or Am-Lws eclogite. The H_2O contents are
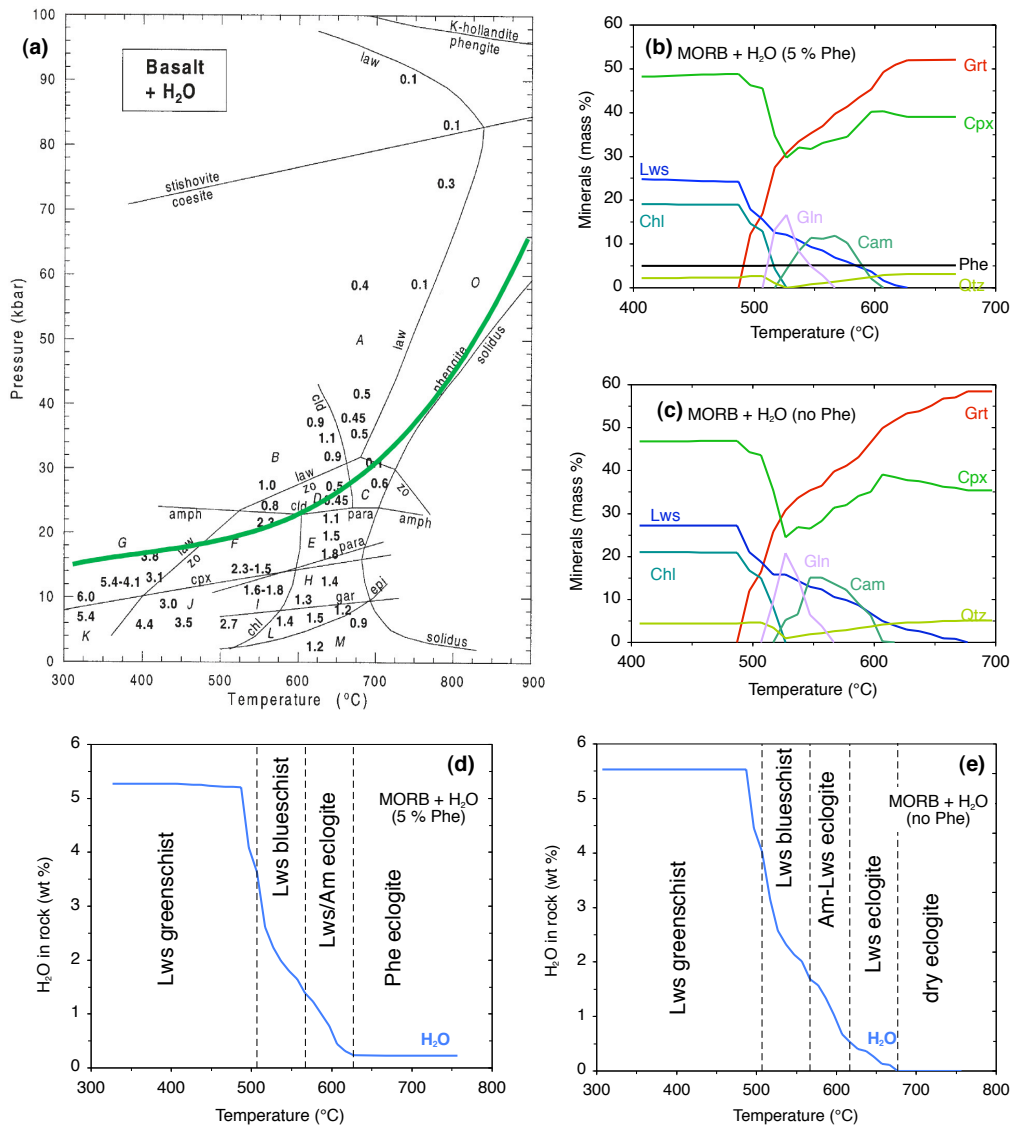
Fig. 8.2. **a** $P-T$ path for the surface of subducting oceanic crust, calculated using PerpleX. The path is plotted on the basalt + H_2O phase diagram from Schmidt & Poli (1998) for orientation. Letters A to M refer to different paragenesis; numbers are H_2O contents (wt%). Details are given in Schmidt & Poli (1998). Note that modelling presented in this chapter is based on calculations performed with PerpleX and are not based on the grid of Schmidt & Poli (1998). Some differences in mineral stabilities (e.g. lawsonite stability) occur between the two data sets. **b** Modal composition of MORB + H_2O as a function of T along the hot $P-T$ path of (a). **c** Same as in (b) for the composition K_2O-free MORB + H_2O which does not contain Phe. **d** H_2O content of rock for which the modal composition is displayed in (b) as a function of T. **e** H_2O content of rock for which the modal composition is displayed in (c) as a function of T.

161
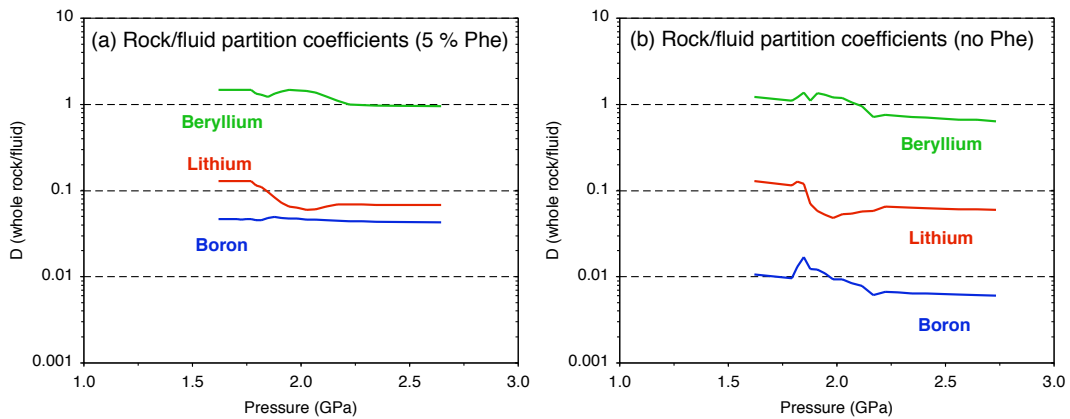
Fig. 8.3. Calculated partition coefficients of light elements between H*P* metamorphic rocks and released fluids as a function of pressure. The diagrams display two different compositions: **a** MORB + H_2O and **b** K_2O-free MORB + H_2O

continously decreasing together with the modal abundances of hydrous minerals. The K_2O-bearing assemblage reaches a limit of ~ 0.25 wt% H_2O as it reaches the stage of Phe eclogite, while in the K_2O-free assemblage no H_2O is left. A dry eclogite is formed in this case.

8.4.2. Calculated whole rock/fluid partition coefficients

Whole rock/fluid partition coefficients, calculated using equation 8.4 are displayed in Fig. 8.3 for the two different compositions discussed above. For both compositions, Be shows a partition coefficient close to unity over the entire pressure range, which is consistent with the relative immobile character of this element. Li shows a decrease of *D* from ~ 0.13 in the chlorite-rich assemblage to values between ~ 0.06 for the blueschists and ~ 0.07 for the eclogites. Partition coefficients for B are the lowest of the three elements and are strongly dependend on the modal abundance of phengite in the rocks. For the Phe-bearing composition they are relatively constant at ~ 0.05, while for the Phe-free composition they are significantly lower and change from ~ 0.010 for the Lws greenschist via ~ 0.012 for the Lws blueschist to ~ 0.006 in the eclogite.

8.4.3. Light element concentrations in rocks and released fluids

Concentrations of Li, Be and B in the rocks and released fluids are displayed in Fig. 8.4 for the two different compositions as a function of pressure. Figs. 8.4a

and b show the light element concentrations in the rocks normalised to the concentrations in the starting rock (100 %). The abundance of Be is very constant from greenschist to eclogite in both compositions. Li concentrations, independent from the abundance of Phe, decrease from greenschist to eclogite to a value of $\sim 55\%$. The amount of B remaining in the rocks is strongly dependent on the modal abundance of phengite. In the first case, containing $\sim 5\%$ phengite, $\sim 37\%$ of the B remains in the eclogite (Fig. 8.4a), while the phengite-free composition is only able to preserve $\sim 1\%$ of the B from the starting composition (Fig. 8.4b).

Absolute values for concentrations of light elements in rocks and fluids can be calculated by refering to typical light element concentrations of AOC as starting values. Keeping in mind the large variability of especially Li and B concentrations in such a reservoir, values from the literature were used for this purpose: $14\,\mu g/g$ Li (Kelley *et al.*, 2003), $0.58\,\mu g/g$ Be (Kelley *et al.*, 2003) and $26\,\mu g/g$ B (Smith *et al.*, 1995). The evolution of the absolute concentrations of the Phe-bearing and the Phe-free compositions are displayed in Figs. 8.4c and d, respectively.

Using the starting values of Smith *et al.* (1995) and Kelley *et al.* (2003) (see above), the concentrations of light elements in the released fluids can be calculated. Figs. 8.4e and f show the concentrations of Li, Be and B in the fluids released from the two different lithologies. The impact of the phengite abundance on the concentrations of Li and Be in the fluids is very limited - as is the case for Li and Be abundances in the rocks. Be concentrations in fluids released from both lithologies range from ~ 0.4 to $\sim 0.9\,\mu g/g$. Li concentrations vary from $\sim 100\,\mu g/g$ released at $\sim 1.6\,GPa$ from the greenschists, to $\sim 200\,\mu g/g$ in fluids released at $\sim 2.0\,GPa$, to $\sim 100\,\mu g/g$ in fluids released at $\sim 2.3\,GPa$ from the eclogites. B concentrations are again strongly dependent on the phengite concentration in the restitic rock. The phengite-bearing assemblage releases fluids with a B concentration decreasing from $\sim 550\,\mu g/g$ to $\sim 200\,\mu g/g$ along the $P-T$ path, while the phengite-free composition releases fluids with $> 1200\,\mu g/g$ B, which rapidly decreases below $100\,\mu g/g$ at $P > 2.2\,GPa$.

8.4.4. B isotopic composition of rocks and released fluids

Depending on fluid/rock ratios, temperature, the extent of alteration and other parameters during sea floor metamorphism of oceanic crust, the B isotopic composition may vary between $-4.3\permil$ to $+24.9\permil$, according to Smith *et al.* (1995). An average $\delta^{11}B$ value of $+0.8\permil$ for layer 2A (uppermost layer) of altered oceanic crust is given by Smith *et al.* (1995) with a boron concentration of $26\,\mu g/g$. This value is used here as the starting $\delta^{11}B$ value for modelling. The results demonstrating the evolution of the B isotopic composition of the two different rocks and
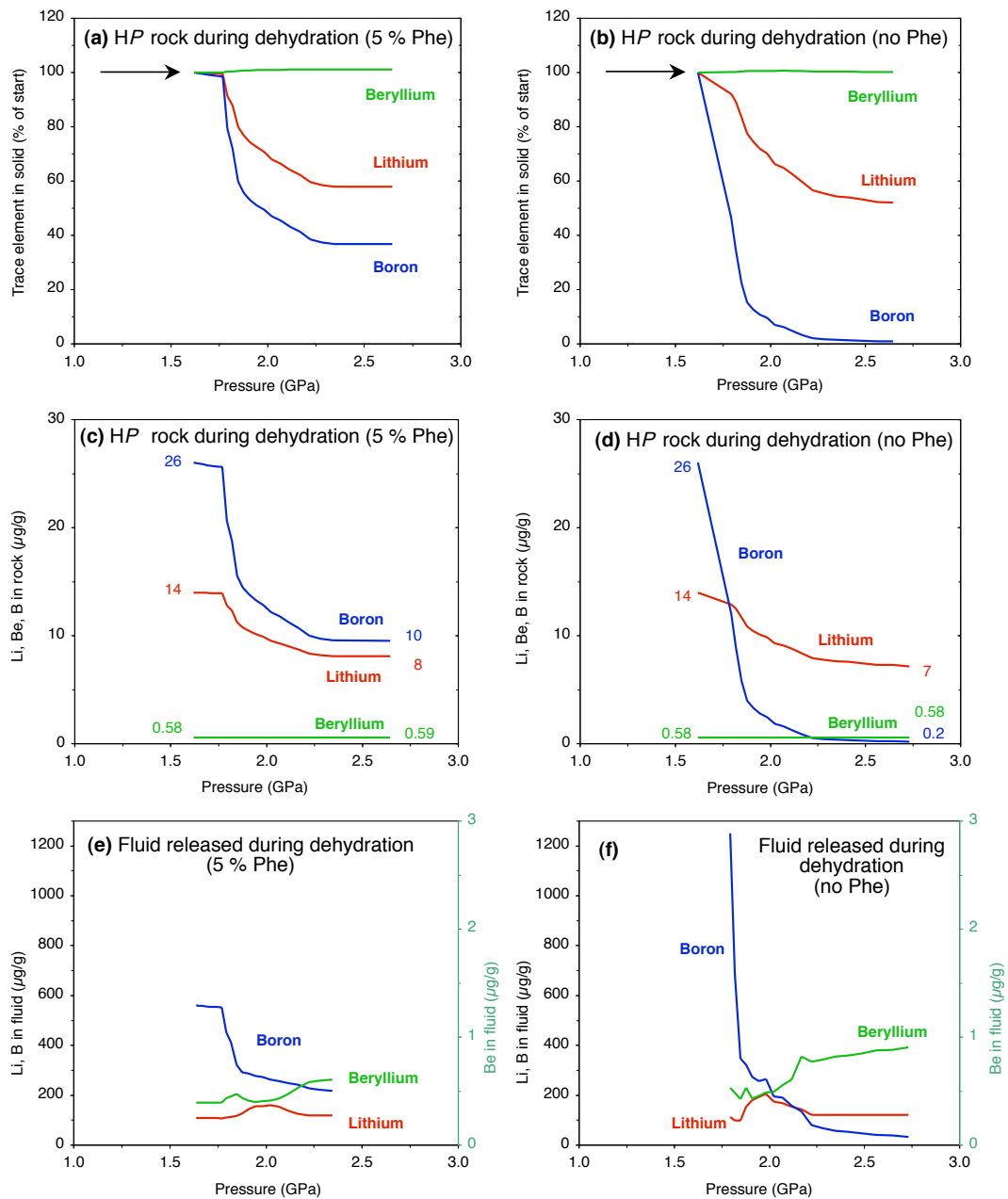
Fig. 8.4. Results of modelling of light element concentrations in H*P* metamorphic rocks and released fluids as a function of pressure. The diagrams display two different compositions: MORB + H_2O in Figs. a, c and e, and K_2O-free MORB + H_2O in Figs. b, d and f. **a, b** Li (red), Be (green) and B (blue) concentrations in the dehydrating rocks normalised to the concentrations in starting rock. **c, d** Li, Be and B absolute concentrations in dehydrating rock. **e, f** Li, Be and B absolute concentrations in released fluids. Note different scale for Be.

164

the respective fluids are displayed in Fig. 8.5. The δ^{11}B evolution of the two different rocks is significantly different. The Phe-bearing composition is lowered to a value of -8.6‰ as it reaches the eclogite stage at ~ 2.2 GPa, whereas the Phe-free composition is shifted to a much lower value of < -30‰ at the same depth. Consequently, the fluids released at the blueschist-eclogite transition at 2.2 GPa show the same difference between $+0.1$‰ and -20.8‰ in the Phe-bearing and the Phe-free composition, respectively. It is important to note, that the δ^{11}B value of the Phe-bearing eclogite is within the δ^{11}B range published for MORB and mantle (Spivack & Edmont, 1987; Ishikawa & Nakamura, 1992; Chaussidon & Jambon, 1994; Chaussidon & Marty, 1995; le Roux *et al.*, 2004). The δ^{11}B value of the Phe-free eclogite on the other hand is significantly lower than the values for MORB and mantle. Correspondingly, the fluid released from the Phe-eclogite carries a positive δ^{11}B signal, whereas the δ^{11}B value of the fluid released from the Phe-free assemblage is extremely negative.

8.5. Discussion

8.5.1. Limits of the presented model

The presented model offers the possibility to calculate the evolution of light elements and their isotopes in progressively dehydrating oceanic crust and the fluids released from it. Parameters used for calculation are mineral/mineral partition coefficients for light elements (Chapter 7), clinopyroxene/fluid partition coefficients (Brenan *et al.*, 1998b), and the temperature-dependent B isotopic fractionation factor (Hervig *et al.*, 2002). The $P-T$ path together with the modal composition of the subducting rocks and their H_2O content are calculated using the program PerpleX (Conolly, 1990). In principle, it is possible to calculate the light element concentrations and isotopic composition for a specific starting material, by determining its modal composition along the $P-T$ path, resulting in Li, Be and B concentrations and B isotopic composition of the rocks and the released fluids along the $P-T$ path.

The universal applicability and significance for nature of the presented model is limited by a number of factors. The whole model is – similar to those of partial melting processes – based on the assumption of equilibrium of all phases in the rocks with respect to the mineral assemblage, the trace element partitioning and the isotope distribution. Furthermore, the trace element and isotopic composition of the generated fluids are assumed to be in equilibrium with the restitic rock and the fluid is extracted from the rock after each step of dehydration (= batch dehydration). Phase equilibrium in metamorphic rocks depends on a number of factors, like grain size, fluid availability, syn-metamorphic deformation and concurrent recrys-
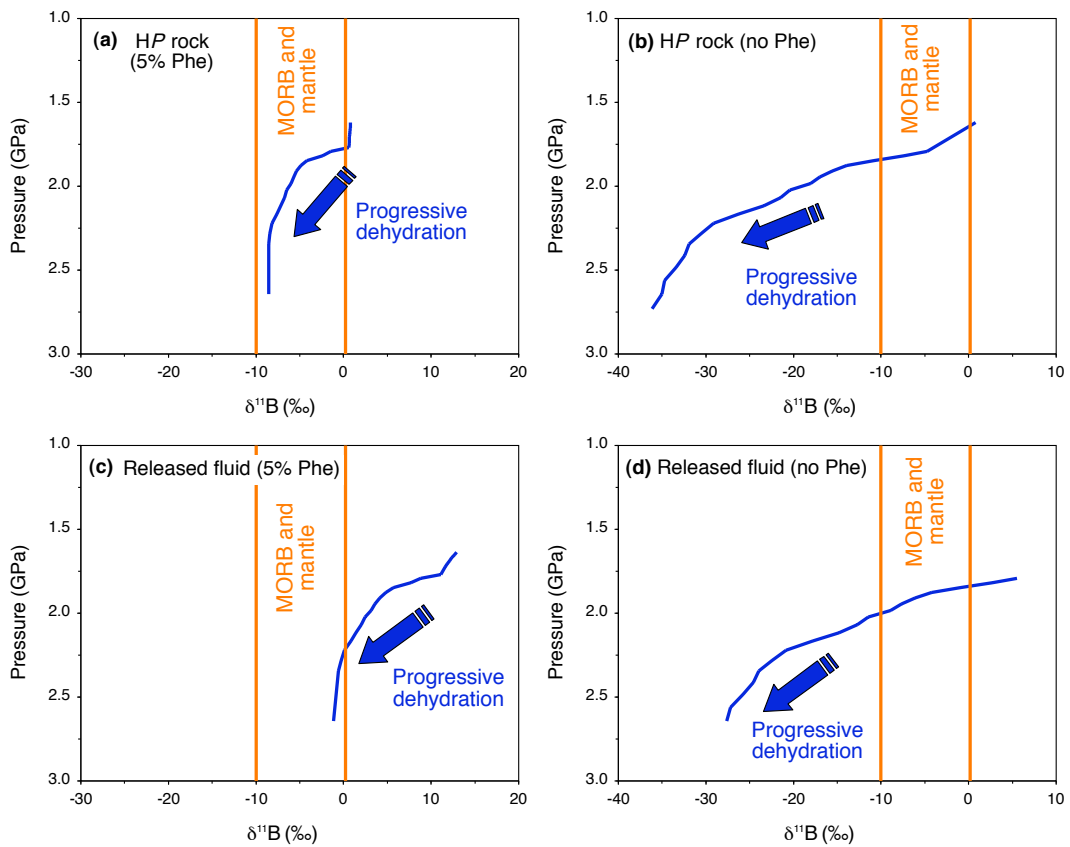
Fig. 8.5. Results of modelling of B isotope ratios in H*P* metamorphic rocks and released fluids as a function of pressure. The diagrams display the two different compositions discussed in the text and in Figs. 8.2, 8.3 and 8.4. Boron isotope composition of MORB and mantle (see Table 5.4, Chapter 5) is shown for comparison. **a** B isotope ratios in the Phe-bearing rock, **b** B isotope ratios in the Phe-free rock, **c** B isotope ratios in the fluids released from the Phe-bearing rock, **d** B isotope ratios in the fluids released from the Phe-free rock.

tallisation, the type of minerals involved and the diffusivity of the trace elements of interest. In the case of Li, Be and B in dehydrating upper oceanic crust during subduction, all these factors are relatively favourable. Firstly, the upper part of the oceanic crust is usually subjected to intense deformation – shearing and isoclinal folding – as is documented in exhumed HP terranes (like Syros). Secondly, increasing temperatures lead to dehydration reactions, providing fluids which in turn accelerate metamorphic reactions within the rocks. Thirdly, the light elements are stored in phases like chlorite, phengite, amphibole and pyroxene which are likely to react relatively fast. Garnet, which might be relatively sluggish especially at low temperatures, is only a minor carrier of Li and does not incorporate Be and B in significant amounts (Chapter 7). Investigation of natural rocks have demonstrated that light element distribution among different metamorphic phases is highly systematic, suggesting a relatively fast adaptation to equilibrium partitioning (Chapter 7).

The preference of modelling batch dehydration instead of Rayleigh dehydration in the individual steps is based on the fact that a certain amount of fluid is required to enable the fluid to escape from the rock. Incremental batch dehydration is therefore assumed to be more realistic and closer to nature.

Another limiting factor for the model is the quality of the partition coefficients used in the calculations. For the present, the data base on light element fractionation among different HP metamorphic minerals and especially between minerals and fluid is rather limited. The detailed investigation on the samples from Syros (Chapter 7) revealed a good basis for inter-mineral partitioning of light elements, but is not able to decipher possible influences of changes in P or T on the coefficients. However, variations in mineral/mineral partitioning of trace elements are not expected to vary extremely, i.e. by more than a factor of 2, as changes in crystallographic parameters (e.g. molar volumes) with P and T of different minerals are relatively close to each other (compared to differences between minerals and fluids). A secondary effect could be generated by a change of the major element composition of a mineral as a consequence of P and T variations, e.g. increasing jadeite content in omphacite as a consequence of increasing pressure. This change in major element composition would affect the crystallographic parameters of the mineral, and could therefore influence trace element partitioning. However, the large variety of compositions investigated in Chapter 7 did not reveal any strong influence of mineral compositions on trace element partitioning. In contrast to inter-mineral partitioning, mineral/fluid partition coefficients, the direct sensitivity to $P-T$ changes may be much more significant. The dataset determined experimentally by Brenan *et al.* (1998b) at relatively high $P-T$ conditions are probably not perfectly transferable to the metamorphic conditions of the calculated $P-T$ path. Therefore, future studies

on fluid/mineral partition coefficients may enhance our knowledge on this aspect and further improve the quality of the results calculated by the presented model.

The modal compositions used in the model do not include the stability of tourmaline. The impact of this boro-silicate on the B budget and δ^{11}B systematics of metamorphic rocks during subduction was already emphasised by Nakano & Nakamura (2001). Tourmaline is probably more frequent in metasediments than in metabasites, but it strongly controlls the B budget and B isotopic composition of rocks, even if it occurs only as an accessory phase (Chapter 7). Nakano & Nakamura (2001) have demonstrated that tourmaline-bearing metasediments are able to retain their entire B budget by incorporating mica-derived boron into newly growing tourmaline. Transferring the presented model to metasediments would therefore require the introduction of tourmaline into the mineral assemblage.

8.5.2. Implications of the results for the subduction cycle of light elements

Lithium The calculations demonstrate that Li concentrations of the eclogites are still approximately half of the starting composition level. Despite the fluid mobile character of this element, the subducting oceanic crust retains more than 50 % of its lithium, even in the H_2O-saturated portion of the crust. This finding has already been proposed by Woodland *et al.* (2002) after investigating Li abundances of natural eclogite samples from several localities. Li concentrations of the released fluids range from ~ 100 to $\sim 200\,\mu g/g$ and are highest at intermediate pressures at the transition from blueschists to hydrous eclogites. The results for the behaviour of Li in subducting AOC provide a good database for modelling of Li isotope fractionation during the same process, as was demonstrated by Zack *et al.* (2003).

Beryllium Be concentrations of the eclogites are almost identical to the concentrations in the starting material. This is because the whole rock/fluid partition coefficients are close to unity. Johnson & Plank (1999) have demonstrated experimentally that whole rock/fluid partition coefficients for Be between progressively metamorphosed clay-rich sediment and the released fluids range from 2 to 4.5, and drop to $0.7 - 0.9$ at the onset of partial melting. Natural HP metamorphic metabasites from Syros also show relatively high concentrations of Be of $0.4 - 3.2\,\mu g/g$ (Appendix C), which is consistent with the conservative behaviour of Be during dehydration as predicted by the presented model. However, concentrations of Be in released fluids is still $\sim 0.5\,\mu g/g$, i.e. as high as the concentration in the rocks. Hence, despite the fact that there is no recognisable change in Be concentrations in the slab, the fluids are rich in Be and may be able to generate anomalies within mantle rocks. Fluids

with a Be concentration of $0.5\,\mu g/g$, corresponding to ~ 10 times primitive mantle ($0.068\,\mu g/g$; McDonough & Sun, 1995) would probably produce a measureable positive Be anomaly in the depleted mantle wedge. Equivalent to the transportation of Be by fluids generated in dehydrating metabasites, fluids from metasediments are expected to transport Be and especially cosmogenic ^{10}Be in concentrations comparable to the dehydrating whole rocks. Therefore, it is not unlikely that ^{10}Be signals in IAB may be generated by metasomatism of the IAB source by hydrous fluids and not exclusively by silicate melts.

Boron The results for B demonstrate the significant influence of phengite on the evolution of B concentration and isotopic composition of rocks and fluids. The hydrous MORB produces a Phe-eclogite (5 wt% Phe) which retains approximately one-third of the original B with an isotopic composition in the range of mantle rocks, while the phengite-free composition produces a dry eclogite with low B concentration (1 wt% of the starting value) and extremely light B. Therefore, deep subduction of Phe-eclogite would produce a B-rich fluid with isotopic composition close to the mantle, as it reaches the pressure stability of phengite ($\sim 10\,$GPa; Schmidt & Poli, 1998). In contrast, deep subduction of dry eclogite would introduce portions of extremely negative δ^{11}B into the deep mantle, but no anomaly in B concentration. Calculated B concentrations for dry eclogite of $0.2\,\mu g/g$ are similar to those of the primitive mantle (Chaussidon & Jambon, 1994; McDonough & Sun, 1995; Palme & O'Neill, 2003).

The results for the two different compositions, containing 5 wt% phengite ($0.5\,$wt% K_2O) and $0.0\,$wt% K_2O (no phengite) demonstrate the strong impact of white mica on the systematics of B and B isotopes in the subduction setting. Low temperature alteration of MORB at the ocean floor may enrich K_2O to concentrations of 2 wt% or even higher (Smith *et al.*, 1995) which would form blueschists and eclogites with higher amounts of phengite ($> 20\,$wt%). These rocks would retain even higher amounts of B and higher δ^{11}B signals to great depths.

Fluids released from the dehydrating AOC show B concentrations in the order of $200-550\,\mu g/g$ from the onset of dehydration to the eclogite stage. In the case of Phe-free rocks, the first fluids show even higher B concentrations of $> 1200\,\mu g/g$. B/Be ratios of fluids are on the order of ~ 1000, reflecting the much higher fluid mobility of B as compared to Be. δ^{11}B values of fluids released at the onset of dehydration are positive and significantly above the ranges of mantle and MORB, while the fluids released at greater depth rapidly reach negative δ^{11}B values, even lower than those of the mantle. Therefore, the high B concentrations and δ^{11}B values of serpentinite diapirs (Benton *et al.*, 2001), mud volcanoes (Kopf & Deyhle, 2002)

169

and trench fluids (Kopf *et al.*, 2000; Deyhle & Kopf, 2002), fed by shallow dehydration of the slab, are well explained by the modelled fluids. In contrast, high δ^{11}B values of various IAB of -3.8 to $+7.3$‰ (Ishikawa & Nakamura, 1994; Ishikawa & Tera, 1997), $+4.6$ to $+12.0$‰ (Straub & Layne, 2002) or even higher (Clift *et al.*, 2001) cannot be explained by fluids extracted from the slab at depths of IAB magma generation (~ 3 GPa). Instead, these high δ^{11}B values may be explained by a multi-stage model: Serpentinite which is infiltrated by high-δ^{11}B slab-derived fluids at shallow depth may be dragged down to sub-arc depth by mechanical coupling to the slab. During serpentinite breakdown B-rich high$-\delta^{11}$B fluids are released and metasomatise the magma source region.

8.5.3. Further applications of the model

The presented model calculates light element and B isotope budgets of dehydrating metabasites and the generated fluids. This model could be in principle extended to other lithologies, like metasediments and serpentinites, as long as the modal compositions of the rocks and the inter-mineral and mineral/fluid partition coefficients are known. The model could also be applied to other elements of geochemical interest, like U, Pb, Rb, Sr, or the REEs. In addition to the B isotopic system, other stable isotope systems, like that of Li may be modelled. In this chapter, only one $P-T$ path was chosen as an example. However, different $P-T$ paths of subducting crust have a strong influence on the modal compositions of the rocks and they vary with subduction angle, age of the lithosphere, convergence rate and other geophysical parameters. Hence, the model could be calculated with different geophysical parameters to demonstrate their impact on the trace element budgets of different rocks and released fluids.

8.6. Summary and conclusions

In this study, modelling of trace element release from progressively dehydrating rocks was performed for the light elements Li, Be and B, which show contrasting behaviour during fluid/rock interaction processes. Clinopyroxene/fluid partition coefficients for Li, Be and B were combined with mineral/clinopyroxene partition coefficients for various HP minerals to deduce a set of mineral/fluid partition coefficients. These were combined with the modal compositions of HP metamorphic rocks derived from thermodynamic calculations using the program PerpleX. The result is a data set of the modal composition of a rock and its whole rock/fluid partition coefficients for the trace elements of interest at any stage of the $P-T$ path,

including information on the amount of fluid released at any depth. Based on these data, the concentrations of trace elements in the subducting rocks and in the released fluids along a certain $P - T$ path were modelled.

In a second step, the derived information on boron concentrations of rocks and fluids were combined with the temperature dependent isotopic fractionation of B, in order to model the B isotopic evolution of subducting rocks and of the released fluids.

Light element budgets of two examples were calculated, (i) MORB + H_2O and (ii) K_2O-free MORB + H_2O. For both compositions, Be concentrations of the dehydrating rocks do not change during dehydration and released fluids also show constant Be concentrations which is similar to that of the rocks. Li concentrations in both assemblages decrease to a level of $\sim 55\%$ between the onset of dehydration and the eclogite stage. Li concentrations of the released fluids range from ~ 100 to $\sim 200\,\mu g/g$ and are highest at intermediate pressures at the transition from blueschists to hydrous eclogites. The behaviour of B and B isotopes is strongly dependent on the amount of white mica in the rock. The first composition, containing $\sim 5\%$ phengite retains $\sim 37\%$ of the original B in the eclogite, while the second, Phe-free assemblage retains only $\sim 1\%$. $^{11}B/^{10}B$ ratios are also significantly different. The Phe-bearing rocks release fluids with positive $\delta^{11}B$ values, reaching the MORB or mantle range as the rocks are transformed to eclogites. The Phe-free assemblage in contrast produces fluids with strongly negative $\delta^{11}B$ values at the blueschist-to-eclogite transition. In both cases, however, fluids with high $\delta^{11}B$ values are released at shallow depth, which may migrate into the accreationary wedge or forearc mantle.

The presented model is of course afflicted with a number of uncertainties and has to be improved by the input of more sophisticated data especially on trace element partitioning. However, in principle this model offers the possibility of a quantification of trace element release from the slab in any lithology along any reasonable $P - T$ path.

9. Boron isotopic composition of tourmaline in metasediments: detrital cores and prograde and retrograde metamorphic overgrowths

9.1. Introduction

In this chapter, in-situ investigation of tourmaline grains from two H*P* metamorphic metasediments and one eclogite from the island of Syros are presented. Chemical compositions were analysed by EPMA, while the B isotopic compositions were analysed by SIMS, completing traverses over several tourmaline grains. Henry & Dutrow (2002) performed a provenance study using chemical composition of tourmaline in a metasedimentary rock and demonstrated a variety of source rocks with contrasting tourmaline compositions for a single sample. In this chapter, it will be demonstrated, that detrital cores can be distinguished from prograde and retrograde metamorphic growth zones not only by differences in their chemical compositions, but also by their contrasting δ^{11}B values. The δ^{11}B values of prograde and peak metamorphic growth zones of tourmaline will provide information on isotopic composition of the deeply subducting portion of B. Several authors (e.g. Peacock & Hervig, 1999; Bebout & Nakamura, 2003) suggest that subducting metasediments display a significantly lower B isotopic composition than metabasalts enriched in B during alteration at the seafloor. This hypothesis will be tested in this study, as tourmaline from three different rocks are investigated: a true metasediment (SY432), a meta-tuffitic rock (SY314) which has been influenced by seafloor alteration prior to subduction, and an eclogite (SY323), which has also been altered by seafloor hydrothermal processes.

Tourmaline Tourmaline is the most wide-spread boro-silicate mineral in natural rocks. It contains ~ 3 wt% B, an element which is of very low abundance in most crustal and mantle rocks (see Chapter 5). Therefore, formation of tourmaline requires effective concentration processes for B, even if it is formed in rocks of the continental crust (average of $\sim 20 \, \mu g/g$ B). This concentration is accomplished either (i) by magmatic differentiation, forming tourmaline in pegmatites enriched in B due to its highly incompatible character, or (ii) by fluid-dominated processes due to its highly fluid-mobile character. The B necessary for tourmaline growth in

fluid-saturated rocks may be supplied by other phases within the rock itself, like clay minerals or mica (Nakano & Nakamura, 2001) or by external fluids during metasomatism. Once formed, tourmaline is highly stable in a large variety of rock types in an exceptionally large $P-T$ range. In addition, tourmaline together with zircon and rutile is one of the most stable minerals during sedimentary processes and is enriched in highly mature sediments (e.g. Thiel, 1941; Hubert, 1962; Henry & Dutrow, 2002). Volume diffusion for major and trace elements and B isotopes within tourmaline up to temperatures of $600\,^{\circ}\mathrm{C}$ is uneffective (Henry & Dutrow, 1994, 2002; Dutrow *et al.*, 1999; Bebout & Nakamura, 2003). Therefore, chemical and isotopic heterogeneities of detrital grains as well as metamorphic growth zones are readily preserved even in high-grade rocks with complex metamorphic and metasomatic histories. Detrital grains preserved in (meta-)sediments were used in several studies to investigate the provenance of the rocks (e.g. Henry & Dutrow, 2002). The development of the SIMS technique for in-situ analyses of B isotope ratios allows for detailed investigations of multiple zoned tourmaline in metamorphic rocks (e.g. Smith & Yardley, 1994; Chaussidon & Appel, 1997; Nakano & Nakamura, 2001; Bebout & Nakamura, 2003; Altherr *et al.*, 2004). Therefore, the B isotopic composition of tourmaline is another potential indicator in provenance studies of sediments and metasediments.

Boron isotopes in H*P*-metamorphic rocks The great potential of B isotopes in tracing processes like metamorphism, metasomatism, dehydration and partial melting, operating in subduction zones, has attracted several studies on various kinds of subduction-related rocks and minerals (see Chapter 5). The strong isotopic fractionation of boron at low temperatures provides a robust tool for tracing hydrous alteration processes at the Earth's surface, and low-temperature altered material in subduction zone related fluids, magmas or metamorphic rocks, in mantle xenoliths or ocean island basalts. The majority of studies on B isotopes in subduction zones has been carried out on volcanic rocks (e.g. Ishikawa & Nakamura, 1994; Ishikawa & Tera, 1997; Smith *et al.*, 1997; Ishikawa *et al.*, 2001; Tonarini *et al.*, 2001; Clift *et al.*, 2001; Straub & Layne, 2002; Schmitt *et al.*, 2002; Rosner *et al.*, 2003; Leeman *et al.*, 2004). However, an important source of information on B isotopes are whole rocks and minerals of exhumed high-pressure metamorphic rocks, like metabasites, metasediments, peridotites and serpentinites. B isotope analyses have been carried out using bulk methods for whole rocks (Nakano & Nakamura, 2001) or in-situ methods for tourmaline (Nakano & Nakamura, 2001; Bebout & Nakamura, 2003) and silicate minerals like phengite and amphibole, which contain B at the trace level (Peacock & Hervig, 1999).

174

Boron isotopes in H*P*-metamorphic tourmaline B isotope studies on high-pressure metamorphic tourmaline revealed important insights into B isotope fractionation within dehydrating subducting crust. Nakano & Nakamura (2001) found nearly constant whole rock B concentrations and δ^{11}B values (-13.4 to $-8.8‰$) in a series of metasediments of increasing metamorphic grade from the Sambagawa belt, SE Japan. In the same samples, B concentrations in mica and chlorite are steadily decreasing, while modal abundance and grain size of tourmaline increases. Tourmaline is strongly zoned with δ^{11}B values decreasing from $-3‰$ in the core to $-10‰$ at the rim of a single grain. Mg contents are steadily inceasing from cores to rims, which is generally interpreted as tourmaline growth during increasing temperatures (Henry & Dutrow, 2002). B isotope zonation patterns are explained by B isotopic fractionation between mica, fluid and tourmaline (see Chapter 5) in the following way: δ^{11}B values of tourmaline cores are higher than δ^{11}B values of surrounding mica. During progressive metamorphism, ^{11}B is preferentially released from mica and transported via fluids along grain boundaries and concentrated in growing tourmaline. The remaining mica is isotopically lighter and releases B with lower δ^{11}B value into the fluid during further heating. Consequently, the growing tourmaline incorporates the lower ^{11}B/^{10}B ratio of the surrounding fluid, without re-equilibrating earlier growth zones. The whole process results in retention of B with initial δ^{11}B values in the metasediments and in subduction of B with an isotopic signature of the Earth's surface into the deep mantle.

A second study by Bebout & Nakamura (2003) investigated $(U)HP$ metamorphic rocks from the Catalina Schist, California (USA) and from Lago di Cignana, Western Alps (Italy). The Catalina Schist metasediments are very similar to the Sambagawa belt samples investigated by Nakano & Nakamura (2001), in that they also display a suite of rocks of progressive metamorphic grade with similar parageneses. Tourmaline grains also display decreasing δ^{11}B values (from -7 to $-15‰$) and increasing X_{Mg} from cores to rims. At the outermost rims ($\sim 30\,\mu$m), δ^{11}B values again increase to $\sim -7‰$ concomitant with a decrease in X_{Mg}. Bebout & Nakamura (2003) accredit the core-to-rim decrease in δ^{11}B values to prograde redistribution of B from mica into tourmaline, similar to Nakano & Nakamura (2001), and the increase of δ^{11}B at the outer rims to growth of tourmaline during influx of B-rich fluids at retrograde metamorphic conditions. Tourmaline grains from Lago di Cignana are 600 μm in diameter and display homogeneous X_{Mg} and B isotopic compositions of $\sim -10‰$ in cores and again a strong increase of δ^{11}B values at the outermost 100 μm accompanied by a decrease in X_{Mg}. According to Bebout & Nakamura (2003), the homogeneous core plateau resulted from diffusive re-equilibration of B isotopes at peak-metamorphic conditions, which were at higher temperatures for these samples ($\sim 620°$C) compared to the aforementioned. Decrease of X_{Mg} and

increase of δ^{11}B values to $+4‰$ again result from retrograde influx of B by fluids. In the case of Lago di Cignana, the interpretation is strongly supported by inclusions of coesite, garnet and rutile in the low δ^{11}B cores and of quartz and epidote in the high δ^{11}B rims.

Stability of tourmaline The mineral group of tourmaline displays a large variation in chemical composition and a huge range of stability in terms of pressure, temperature and host rock composition. Tourmaline is formed as authigenic and epigenic grains and during diagensis in sediments. It is formed and remains stable in metamorphic rocks up to upper amphibolite facies or even granulite facies grade and it is abundant in many pegmatites and granites. Tourmaline is found in metapelites, calc-silicate rocks, marbles, meta-ironstones, massive sulfide deposites, sandstones, metabasites and ultramafic rocks.

Temperature stability extends from surface conditions below $150\,°$C to high-grade metamorphic and magmatic conditions of $> 850\,°$C at pressures between 0.1 and 0.5 GPa (Robbins & Yoder, 1962; Manning & Pichavant, 1983). Similar to the stability of other hydrous phases like amphibole, temperature stability of tourmaline increases with increasing pressure. Werding & Schreyer (2002) report stability of dravite in experiments to temperatures of $> 950\,°$C at pressures between 3 and 5 GPa. The range of tourmaline pressure stability is also surprisingly large. It is surprising because one might expect a breakdown of tourmaline (which contains trigonally coordinated B) to some HP phase(s) with B in tetrahedrally coordinated sites. High- and ultrahigh-pressure stability has been proven both experimentally and in natural samples (Fig. 9.1). Dravite is frequently observed in HP metasediments. Johnson & Oliver (2002) report tourmaline in a talc-kyanite whiteschist from Zimbabwe, equilibrated at $570\,°$C/1.4 GPa. Reinecke (1998) and Bebout & Nakamura (2003) report dravite with coesite inclusions from Lago di Cignana (Western Alps) formed at UHP conditions of ~ 2.8 GPa and $\sim 620\,°$C. Schreyer (1985) report dravite inclusions in coesite-bearing white-schists from Dora Maira (Western Alps), formed at $750 - 800\,°$C and ~ 3.5 GPa (Schertl *et al.*, 1991; Simon *et al.*, 1997). Tourmaline in diamond-bearing metapelites has been described by Hacker *et al.* (2003) from unit II of the Kokchetav massif, Kazakhstan, for which metamorphic peak conditions of $\sim 900\,°$C and ~ 5 GPa have been estimated (Ota *et al.*, 2000; Okamoto *et al.*, 2000; Hacker *et al.*, 2003). Experimental studies by Krosse (1995, cited in Werding & Schreyer, 2002) revealed stability of dravite to pressures in excess of 5 GPa and dravite breakdown between 6 and 8 GPa to a number of Mg-Al phases. EPMA analyses of dravite synthesised at $952\,°$C and 5 GPa were close to ideal dravite composition (Werding & Schreyer, 2002).
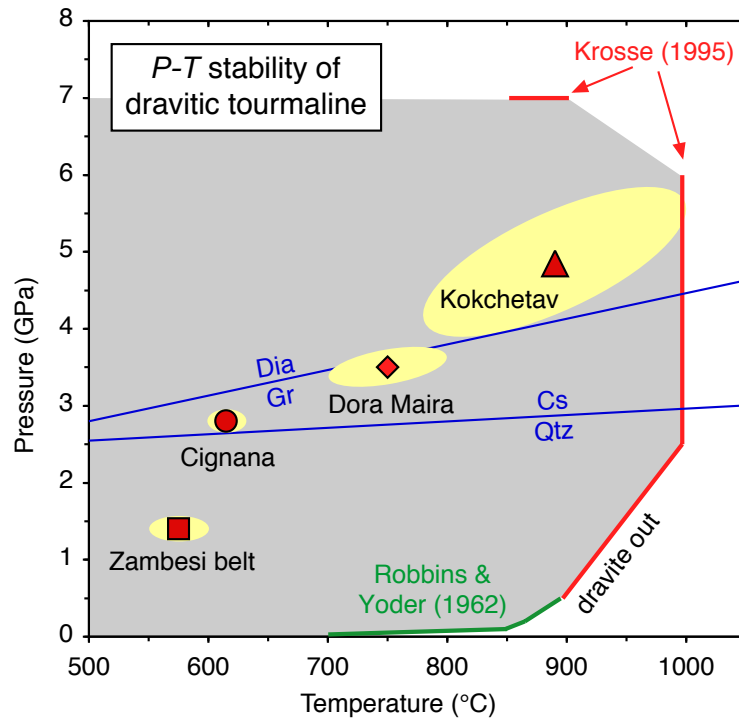
Fig. 9.1. $P - T$ diagram displaying (i) experimentally determined pressure and temperature stability of dravitic tourmaline (grey field) from Robbins & Yoder (1962) [green curve] and Krosse (1995, cited in Werding & Schreyer, 2002) [red lines], and (ii) peak-metamorphic conditions of different tourmaline-bearing natural $(U)HP$ rocks, i.e.: square: Kadunguri talc-kyanite whiteschist from the Chewore Inlier, Zambesi belt, Zimbabwe (Johnson & Oliver, 2002); circle: Coesite-bearing pelagic metasediments from Lago di Cignana, Western Alps, Italy (Reinecke, 1998; Bebout & Nakamura, 2003); diamond: Coesite-kyanite-pyrope-bearing metaesdiments from the Dora Maira massif, Western Alps, Italy (Schreyer, 1985; Werding & Schreyer, 2002); triangle: Diamond-coesite-bearing metapelites from unit II of the Kokchetav massif, Kazakhstan (Hacker *et al.*, 2003). Equilibria of graphite-diamond after Bundy (1980) and quartz-coesite after Bohlen & Boettcher (1982) are displayed for orientation.

Apart from P and T, the most important variable for the growth of tourmaline in metamorphic rocks is the composition of the fluid phase which is transporting the required B. Concentration of B in the fluid and pH of the fluid seem to be the most critical factors controlling tourmaline stability in metamorphic rocks. Experimental studies by Morgan & London (1989) have shown that crystallisation of tourmaline from solutions containing less than $0.2 \, \text{wt\%}$ B_2O_3 ($620 \, \mu g/g$ B) is possible, provided the fluids are low in pH (pH of quenched fluids < 6.5). Weisbrod *et al.* (1986, cited in Dingwell *et al.*, 2002) were able to crystallise dravite from Fe-free chlorite-bearing compositions in equilibrium with fluids containing between $\sim 150 \, \mu g/g$ and $\sim 300 \, \mu g/g$ B, in the temperature range of 350 to $450 \,^{\circ}\text{C}$. At higher temperatures, the critical B concentrations in the fluid required for tourmaline growth steadily increase and are $\sim 9000 \, \mu g/g$ at $750 \,^{\circ}\text{C}$. A more detailed discussion on the *P-T-X* stability of tourmaline is given in Henry & Dutrow (2002) and Werding & Schreyer (2002). Additionally, Henry & Dutrow (2002) give a comprehensive review on the occurrence and chemistry of tourmaline in metamorphic rocks with an extensive list of references.

9.2. Investigated samples

The occurrence of tourmaline in Syros HP metamorphic rocks is related to two entirely different petrographic appearences. Type I is found dominantly within metasedimentary rocks as small ($< 100 \, \mu m$) complexly zoned crystals, often occurring as inclusions in garnet, glaucophane or phengite. Type II appears as aggregates of several large ($0.1 - 15 \, \text{mm}$ in diameter) relatively homogeneous grains and is clearly related to intense metasomtism during exhumation of the Syros mélange. Formation process, chemistry and B isotopic composition of type II tourmaline are discussed in Chapters 10 and 11. This chapter deals with the genesis of type I tourmaline, its chemistry and B isotopic composition.

Two metasedimentary samples (SY314 and SY432) have been recognised to contain abundant type I tourmaline and were analysed in detail for major element composition by EPMA and for B isotopic composition by SIMS. Unfortunately, the different growth zones are too small to allow for meaningful analyses of concentrations of light elements (H, Li, Be and B) by SIMS. Therefore, contents of H_2O and B_2O_3 were calculated stoichiometrically (OH $+$ F $+$ Cl $= 4 \, \text{pfu}$, B $= 3 \, \text{cpfu}$). Li and Be were assumed to be negligible. These assumptions are justified by SIMS analyses, in which averaging whole tourmaline grains of sample SY314 revealed B_2O_3 concentrations of $10.14 \, \text{wt\%}$, and Li and Be concentrations of $8.6 \, \mu g/g$ and $0.37 \, \mu g/g$, respectively (see Chapter 7). Type I tourmaline was also recognised in

two metabasic samples (SY3 and SY323). However, in sample SY323, tourmaline grains are very rare, i.e. less than one grain per thin section, and as small as $\sim 10\,\mu m$ in diameter (see Fig. B.7 on page 305). Therefore, only two SIMS $\delta^{11}B$ analysis were completed for tourmaline in sample SY323. Sample SY3 was not investigated by in-situ methods (see description of sample SY3 in Appendix B).

Phengite-glaucophane schist SY314   Sample SY314 is a glaucophane schist from the matrix of the Syros mélange. Garnet in this rock is abundant, with grain sizes of only $50-100\,\mu m$ (Fig. B.6), with high spessartine contents in the cores ($Alm_{19}Prp_3Sps_{60}Grs_{12}Adr_6$) and high almandine contents in rims I ($Alm_{59}Prp_{14}Sps_{11}Grs_{11}Adr_5$). At the outermost rim many garnet grains show a second rim II of $< 5\mu m$ with a very low pyrope content ($Alm_{66}Prp_4Sps_{17}Grs_7Adr_6$). Additionally, the grains are truncated by a network of fractures, which are annealed by garnet of different composition. These features are less than $1\,\mu m$ in width, but judging from their brightness in BSE images they should have a similar composition as rim II.

Tourmaline occurs as small euhedral grains, $50-100\,\mu m$ in diameter as inclusions in the glaucophane porphyroblasts and in the phengite- and albite-rich matrix (Fig. B.6). In many tourmaline grains, anhedral poikilitic cores are visible, which are overgrown by three zones that differ by colour intensity in optical images from light green near the core to dark green at the edges. Inclusions in poikilitic cores are too small ($< 1\,\mu m$) for a proper EPMA analysis but are opaque in optical images and bright in BSE images and are rich in Fe. Most of the inclusions may therefore be Fe-oxides.

Glaucophane displays a strong chemical zonation with a homogeneous core and oscillatory zoned rim. Cores show a $Ca/(Ca+Na_B)$ ratio of ~ 0.06, a X_{Mg} of ~ 0.58 and a $Al^{VI}/(Al^{VI}+Fe^{3+})$ ratio of ~ 0.80. Rims are lower in Ca and Mg and have compositions tending to ~ 0.01 in $Ca/(Ca+Na_B)$ ratio, a X_{Mg} of ~ 0.27, and a $Al^{VI}/(Al^{VI}+Fe^{3+})$ ratio of ~ 0.64. In some places, rims also show an increase in MnO content to $\sim 0.5\,wt\%$. Cores of Na-amphibole are classified as glaucophane, while rims are ferro-glaucophane after Leake *et al.* (1997) or crossite after older nomenclatures. Phengite is very abundant in the rock and shows a X_{Mg} of ~ 0.50 and $\sim 3.40\,Si\,cpfu$. In some places it is replaced by biotite at its rims. Additionally, the rock contains rare epidote inclusions in glaucophane, zircon, quartz and chlorite inclusions in garnet and apatite and Fe-oxides in the matrix. Fe-oxide forms large ($\sim 1\,mm$), euhedral blasts with inclusions of garnet, and were probably Ti-magnetite, which is now strongly altered and replaced by a fine intergrowth of Fe-oxide or -hydroxide and fine-grained silicate material.

In summary, SY314 displays prograde zonation of minerals like garnet and Na-amphibole, a HP metamorphic assemblage of glaucophane + pyrope-rich garnet + phengite $\pm$ albite, and clear evidence for retrograde reactions forming Fe-rich rims and streaks in garnet, ferro-glaucophane rims at glaucophane and biotite from phengite. Ti-magnetite is decomposed during this retrograde process. However, most parts of the minerals are unaltered and still display their prograde and peak-metamorphic compositions. These observations prove a restricted influx of hydrous fluid into the rock during retrograde metamorphic conditions.

The rock is interpreted as the metamorphic equivalent of basaltic material, probably tuffitic sediments mixed with other detritus. High Mn, K and Si contents are probably due to exposure of the former sediment to seafloor alteration, which typically forms Fe-Mn hydroxides, clay minerals and opal (see description of SY314 in Appendix B).

Eclogite SY323   Sample SY323 is a Ca-rich eclogite containing abundant epidote. The sample is displaying evidence for a complex metamorphic history. Its interpretation is rather ambiguous (see description and discussion on sample SY323 in Appendix B). However, tourmaline grains are included in garnet cores (Fig. B.7 on page 305) and are hence related to the early metamorphic history and the growth of the first generation of garnet.

Siliceous marble SY432   Sample SY432 is a fine-grained siliceous marble, containing quartz, albite, apatite, epidote, phengite, paragonite and small euhedral tourmaline grains of $50 - 100\,\mu$m in diameter. They show anhedral poikilitic cores overgrown by euhedral rims. Tourmaline grains cut parallel to their crystallographic c axis nicely display the polar crystallography of this mineral (Fig. 9.6). Phengite shows Si contents of ~ 3.35 cpfu and X_{Mg} of ~ 0.50. Epidote contains $\sim 0.85 - 0.9\,\text{Fe}^{3+}$pfu. Accessory Fe-oxide is almost pure hematite (Hem$_{97}$).

The rock is interpreted as the metamorphic equivalent of a carbonaceous sediment. Siliceous detritus (probably clay minerals, feldspar and quartz) contributed Na, Mg, Ca, Fe, Si and K, and recrystallised to phengite, paragonite, quartz, albite and epidote under HP metamorphic conditions (see description of SY432 in Appendix B).

9.3. Results

All investigated tourmalines belong to the schorl-dravite solid solution series, with most of them being Mg-rich (dravitic), which is characteristic for tourmaline in HP

metamorphic rocks (see introduction to this chapter). In detail tourmaline grains of the two samples display chemical and B isotopic zonations which are crucial for the inerpretation of the B isotopic history of the rocks.

Phengite-glaucophane schist SY314   Tourmaline in sample SY314 chemically displays significant differences between the four different zones that are visible under the optical microscope. Anhedral poikilitic cores have very low Ca, F and Ti concentrations and relatively high X_{Mg} (Fig. 9.2 and Table 9.1). No differences in chemical composition were observed between poikilitic cores of different grains within sample SY314. Euhedral homogeneous cores, some of which are overgrowing poikilitic cores show relatively high Ca and F contents but are still low in Ti (Fig. 9.2 and Table 9.1). All analysed grains are characterised by strongly decreasing X_{Mg} and Ca contents from homogeneous cores via rim I to rim II at the edge of the crystals, while F contents are constant (Fig. 9.2 and Table 9.1). Most analyses of rims II reveal schorl rather than dravite with X_{Mg} as low as ~ 0.35. Zn and Cr concentrations are below the EPMA detection limits for the majority of analyses (Fig. 9.2c).

Boron isotope analyses of the different zones in tourmaline also revealed systematic differences among the various zones. Poikilitic cores of different grains are indistinguishable from one another with $\delta^{11}B$ values of $-3.3 \pm 1.8\%o$ (Fig. 9.3 and Table 9.1). Euhedral homogeneous cores show $\delta^{11}B$ values of $-1.6 \pm 1.1\%o$ and rims I show values of $+0.7 \pm 1.7\%o$. Within Fe-rich rims II, the $\delta^{11}B$ values of all analysed grains are strongly increasing and reach values as high as $+7.7\%o$ (Fig. 9.3 and Table 9.1). Phengite in sample SY314 displays $\delta^{11}B$ values of $-6.4 \pm 1.5\%o$ (Table 9.2).

Eclogite SY323   Tourmaline in sample SY323 is included in garnet cores and shows poikilitic cores and homogeneous rims in BSE images (see Fig. B.7). One $\delta^{11}B$ analysis of the poikilitic core and one of the rim of a single grain were performed and revealed $\delta^{11}B$ values of $+1.0 \pm 1.1\%o$ for the core and $+2.8 \pm 1.0\%o$ for the rim. Chemical analyses of Tur of sample SY323 are not available.

Siliceous marble SY432   Poikilitic cores of tourmaline grains in sample SY432 display strong chemical differences from one grain to another. Ca, Ti and F contents as well as X_{Mg} are very different among different grains (Fig. 9.4 and Table 9.1). The rims on the other hand, are homgeneous and all chemically similar, with dravitic compositions, containing $\sim 0.35 - 0.50\,F$ pfu, display $Ca/(Ca + Na)$ ratios of ~ 0.09 and X_{Mg} of ~ 0.64 (Fig. 9.4). Cr and Zn contents of most core analyses

Table 9.1. Chemical and B isotopic analyses of tourmaline from metasediments

Sample	SY314				SY432			
Type	PC	core	rim I	rim II	core 1	core 2	core 4	rim
SiO_2	35.90	35.55	34.84	34.53	34.81	35.00	36.28	35.57
TiO_2	0.08	0.23	0.40	0.93	0.28	0.97	0.05	0.24
$B_2O_3{}^*$	10.44	10.29	10.23	10.01	10.25	10.43	10.49	10.35
Al_2O_3	30.55	28.87	29.04	28.14	29.14	31.44	31.72	29.42
Cr_2O_3	0.04	0.06	0.03	0.09	0.09	0.07	0.02	0.09
FeO^t	6.98	8.13	9.08	13.77	7.90	7.23	4.82	8.07
MnO	0.20	0.04	0.03	0.08	0.02	0.00	0.04	0.02
MgO	8.12	8.12	7.50	4.23	7.96	7.46	9.11	8.00
CaO	0.08	0.33	0.25	0.10	1.00	1.32	0.13	0.52
ZnO	0.00	0.07	0.08	0.00	0.16	0.03	0.05	0.15
Na_2O	2.80	2.77	2.89	2.87	2.74	2.12	2.69	2.82
K_2O	0.00	0.04	0.03	0.07	0.01	0.02	0.02	0.03
H_2O^*	3.60	3.55	3.53	3.45	3.11	3.31	3.46	3.12
F	0.27	0.47	0.44	0.42	0.89	0.61	0.33	0.94
Cl	0.00	0.00	0.00	0.00	0.00	0.00	0.00	0.00
-(F+Cl)=O	0.12	0.20	0.19	0.18	0.37	0.26	0.14	0.40
Total	98.93	98.32	98.17	98.51	97.98	99.76	99.08	98.94

Formulas calculated to 31 oxygens, $Fe^{2+} = Fe^t$

Si	5.98	6.01	5.92	6.00	5.91	5.83	6.01	5.97
Ti	0.01	0.03	0.05	0.12	0.04	0.12	0.01	0.03
B	3.00	3.00	3.00	3.00	3.00	3.00	3.00	3.00
Al	5.99	5.75	5.82	5.76	5.83	6.17	6.20	5.82
Cr	0.00	0.01	0.00	0.01	0.01	0.01	0.00	0.01
Fe^{2+}	0.97	1.15	1.29	2.00	1.12	1.01	0.67	1.13
Mn	0.03	0.01	0.00	0.01	0.00	0.00	0.01	0.00
Mg	2.01	2.05	1.90	1.10	2.01	1.85	2.25	2.00
Ca	0.01	0.06	0.04	0.02	0.18	0.24	0.02	0.09
Zn	0.00	0.01	0.01	0.00	0.02	0.00	0.01	0.02
Na	0.90	0.91	0.95	0.97	0.95	0.68	0.87	0.92
K	0.00	0.01	0.01	0.01	0.00	0.01	0.00	0.01
Total	18.92	18.97	18.99	19.00	19.04	18.88	18.99	19.00
X_{Mg}	0.675	0.640	0.596	0.354	0.643	0.648	0.771	0.639
OH	3.86	3.75	3.76	3.77	3.52	3.68	3.83	3.50
F	0.14	0.25	0.24	0.23	0.48	0.32	0.17	0.50
Cl	0.00	0.00	0.00	0.00	0.00	0.00	0.00	0.00

Boron isotope values determined by SIMS

$\delta^{11}B$	−3.3	−1.6	+0.7	+5.4**	−2.8	−10.7†	+3.6	+0.9
$2RSD_{mean}$	1.8	1.1	1.7	3.9**	1.6	1.1†	1.5	1.8
n	6	8	4	4	3	2†	4	23

PC = poikilitic core. *H_2O and B_2O_3 calculated stoichiometrically. All other elements analysed by EPMA. **Rim II of sample SY314 shows B isotopic zonation (see Fig. 9.3) with $\delta^{11}B$ increasing from +3.3 to +7.7‰. †Only analyses of center of core of grain number 4 are listed. n = number of isotope analyses.

Table 9.2. Chemical analyses of mica and B isotopic compositions of phengite from tourmaline-bearing metasediments

Sample	SY314		SY432	
Type	Phe	"Bt"	Phe	Pg
SiO_2	50.34	36.44	51.04	49.18
TiO_2	0.17	0.51	0.14	0.03
Al_2O_3	26.30	12.23	27.86	39.42
Cr_2O_3	0.00	0.00	0.00	0.02
FeO^t	4.63	24.16	4.37	1.33
MnO	0.03	1.16	0.00	0.00
MgO	2.73	9.99	2.50	0.13
CaO	0.00	0.09	0.05	0.29
Na_2O	0.54	0.10	0.52	5.48
K_2O	10.18	8.24	10.04	0.71
H_2O^*	4.43	3.73	4.52	4.78
Total	99.33	96.64	101.05	101.37

Formulas calculated to 11 oxygens

Si	3.409	2.930	3.384	3.083
Ti	0.009	0.031	0.007	0.002
Al	2.099	1.159	2.177	2.912
Cr	0.000	0.000	0.000	0.001
Fe^{2+}	0.262	1.625	0.243	0.070
Mn	0.001	0.079	0.000	0.000
Mg	0.276	1.198	0.247	0.013
Ca	0.000	0.008	0.003	0.019
Na	0.071	0.016	0.067	0.666
K	0.880	0.845	0.849	0.057
OH	2.000	2.000	2.000	2.000
Total	7.008	7.890	6.979	6.821
X_{Mg}	0.513	0.424	0.505	0.152

Boron isotope values determined by SIMS

$\delta^{11}B$	−6.4	*n.a.*	−11.3	*n.a.*
$2RSD_{mean}$	1.5		1.4	
n	2		3	

$^*H_2O$ calculated stoichiometrically. FeO^t = total iron as FeO. $X_{Mg} = Mg/(Mg + Fe^{2+})$. $2RSD_{mean} = 2\times$ relative standard deviation of the mean. n = number of isotope analyses. Note that biotite in sample SY314 is K-deficient and has a low analysis sum, indicating mixed layering with or alteration to chlorite.
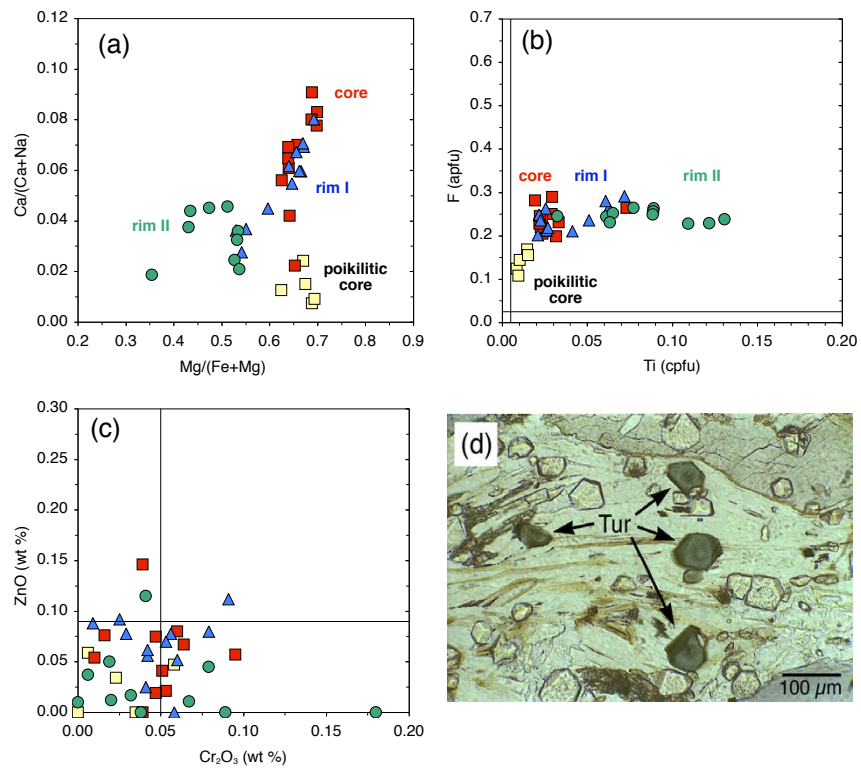
Fig. 9.2. a-c Chemical composition of tourmaline in sample SY314 showing four different zones (poikilitic cores, cores, rims I and rims II) of several grains. **a** $Ca/(Ca + Na)$ vs $Mg/(Mg + Fe)$. **b** F vs Ti. Solid lines refer to detection limits of EPMA. **c** ZnO vs Cr_2O_3. Zn and Cr contents are below detection limit of EPMA (solid lines) for the majority of analyses. **d** Photomicrograph of thin section of SY314 showing four green tourmaline grains with the four different zones visible (poikilitic core = light green with black inclusions; core = dark green; rim I = light green; rim II = dark; polarised light).
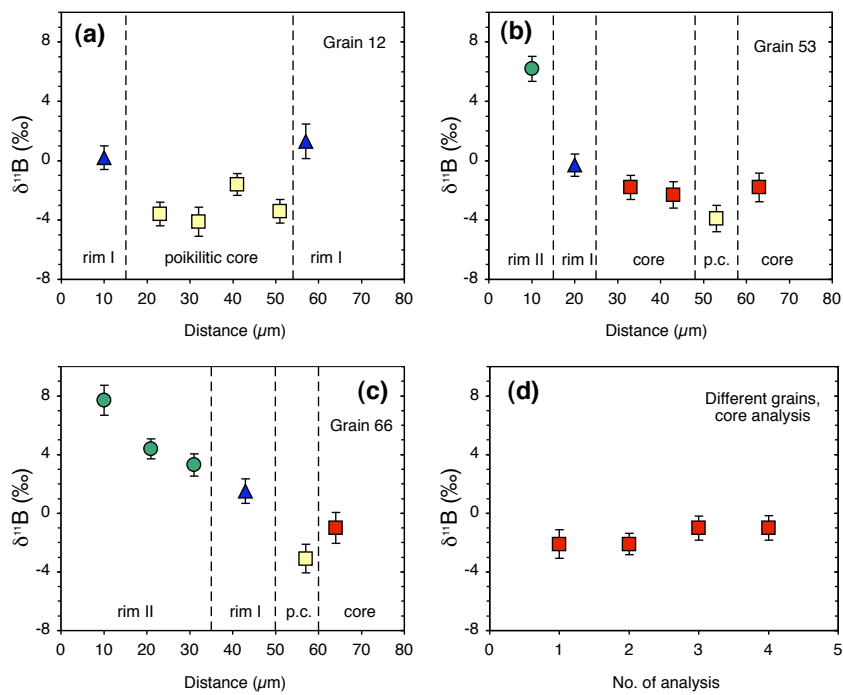
Fig. 9.3. a-d B isotope ratios determined by SIMS of different grains in sample SY314 showing four different zones (poikilitic cores, cores, rims I and rims II) as distinguished by optical and chemical differences (see Fig. 9.2). **a-c** Traverses of δ^{11}B over grains 12, 53 and 66. Note identical colour code to Fig. 9.2. P.c. = poikilitic core. **d** B isotope values of core analyses of different Tur grains of sample SY314.
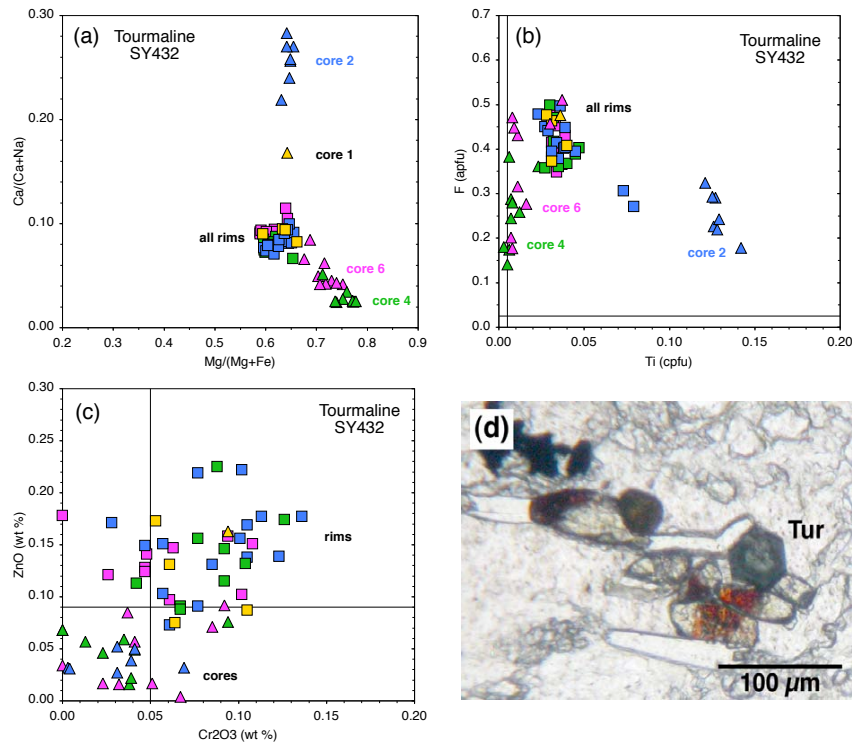
Fig. 9.4. a to c Chemical composition of tourmaline in sample SY432 showing cores and rims of four individual grains (No.1, 2, 4 and 6; grain "C" not shown). Note that rim compositions of all grains are similar, while core compositions differ significantly. **a** $Ca/(Ca + Na)$ vs $Mg/(Mg + Fe)$. **b** F vs Ti. Solid lines refer to detection limits of EPMA. **c** ZnO vs Cr_2O_3. Zn and Cr contents of cores are below detection limit of EPMA (solid lines), while rims show significant amounts of both elements. **d** Photomicrograph of thin section of SY432 showing a euhedral tourmaline grain with light coloured core and dark green rim (polarised light).

are below detection limits of EPMA, while the rims show elevated concentrations of both elements (Fig. 9.4 and Table 9.1). Fe-rich rims were not observed in Tur from sample SY432.

Boron isotope analyses of cores from different tourmaline grains revealed strongly contrasting $\delta^{11}B$ values, ranging from $-10.7 \pm 1.1‰$ via $-2.8 \pm 1.6‰$ to $+3.6 \pm 1.5‰$ (Fig. 9.5 and Table 9.1). The chemically homogeneous and similar rims of all analysed grains display small variations in $\delta^{11}B$ of $+0.9 \pm 1.8‰$ (Fig. 9.5 and Table 9.1). At the boundaries between cores and rims, SIMS analyses revealed $\delta^{11}B$ values intermediate between core and rim. In principle, these could be artefacts of the SIMS spot overlapping the two contrasting zones, or true values which resulted from diffusional re-equilibration between the two zones during
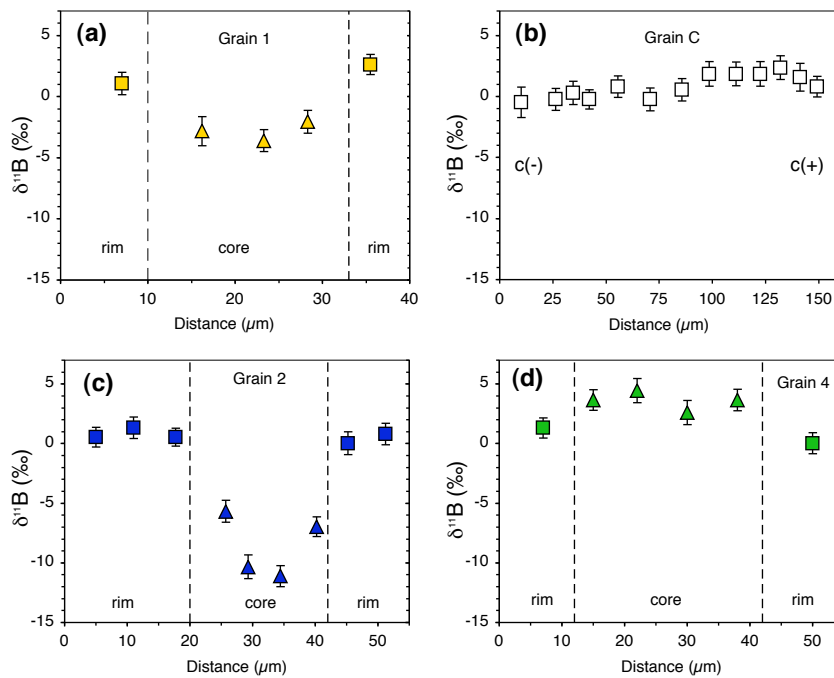
Fig. 9.5. a-d B isotope ratios determined by SIMS of different grains in sample SY432 showing cores and rims of grains 1, "C", 2 and 4. Note identical colour code to Fig. 9.4. Grain "C" is a grain cut parallel to its crystallographic c axis (see Fig. 9.6).
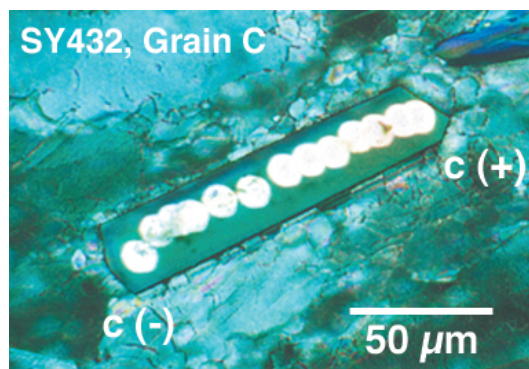
Fig. 9.6. Photomicrograph of gold covered thin section of sample SY432 showing grain "C", a grain cut parallel to its crystallographic c axis displaying the polar crystallography of tourmaline with the antilogous pole c(+) and the analogous pole c(-). Bright circles are spots from SIMS analysis. Results of δ^{11}B analyses are displayed in Fig. 9.5b.

187

metamorphism. The major element profiles determined by EPMA (which provides a higher lateral resolution) do not display diffusional equilibration between cores and rims. Therefore, intermediate δ^{11}B values should be interpreted as analytical artefacts. Increasing δ^{11}B values at the rims of Tur (as in sample SY314) were not observed in sample SY432. Phengite in sample SY432 displays δ^{11}B values of $-11.3 \pm 1.4\%o$ (Table 9.2).

9.4. Discussion

Interpretation of the different growth zones of tourmaline in the two metasedimentary samples (SY314 and SY432) is relatively unambiguous, as major element compositions and B isotope ratios in different growth zones vary highly systematically. Henry & Dutrow (2002) have demonstrated that detrital cores are abundant in many metasediments and act as seeds for the growth of metamorphic tourmaline. These detrital cores are rounded due to sedimentary transport and may display a large range in chemical composition depending on the provenance of the former sediment. HP metamorphic tourmaline reported from different lithologies (metapelites, calc-schists, white schists, graphitic schists) are always Mg-rich and dravitic in composition (see introduction; Reinecke, 1998; Johnson & Oliver, 2002; Hacker *et al.*, 2003; Bebout & Nakamura, 2003). In general, Ca and Mg contents of tourmaline increase with metamorphic grade in all kinds of lithologies (Henry & Dutrow, 2002). However, the actual chemistry of tourmaline is of course still dependent on the chemical composition of the whole rock and may be more Ca-rich in marbles than in metapelites (Henry & Dutrow, 2002). The two studies on HP metamorphic tourmaline by Nakano & Nakamura (2001) and Bebout & Nakamura (2003) have also demonstrated a positive correlation of X_{Mg} of tourmaline and metamorphic temperature. Considering these observations, the tourmaline from Syros metasediments contain detrital cores, and show metamorphic overgrowths formed during prograde or peak metamorphic conditions, while others formed during retrograde influx of B. A more detailed interpretation of the three samples is given below.

Phengite-glaucophane schist SY314 Tourmaline in phengite-glaucophane schist SY314 shows poikilitic rounded cores, which are different in chemical and B isotopic composition from all other zones. They are best interpreted as detrital cores of uniform source with δ^{11}B $= -3.3\%o$. The highest X_{Mg} and Ca contents of tourmaline in this sample are displayed by the euhedral Mg-rich cores and euhedral Mg-rich overgrowths on anhedral poikilitic cores. These core zones are interpreted as grown from mica-derived B during prograde and/or peak metamorphism, simi-

lar to the interpretations by Nakano & Nakamura (2001) and Bebout & Nakamura (2003). A prograde zonation with a core-to-rim decrease in δ^{11}B was not observed in SY314, probably due to analytical restrictions by the limited size of the grains and their individual zones. However, the δ^{11}B value of $-1.6\%o$ in these core zones is characteristic for the peak metamorphic stage of tourmaline in sample SY314.

Towards the rims, Ca and Mg contents are decreasing, while Ti and Fe contents significantly increase, which is interpreted as a result of tourmaline growth during decreasing temperatures. Retrograde growth of tourmaline requires influx of extrenal B, which must have had a very high δ^{11}B value of at least $+7.7\%o$ in the case of sample SY314, as recorded by the Fe-rich rims of tourmaline. The retrograde influx of hydrous fluid is also documented by other petrographic features like Fe-rich rims and streaks in garnet and glaucophane and the formation of biotite/chlorite at the expense of phengite. Phengite in sample SY314 shows a δ^{11}B value of $-6.3\%o$. Hydrous fluid in isotopic equilibrium with this phengite at temperatures of 500, 450 and $400\,^\circ$C (peak and retrograde temperatures for Syros, see Chapters 3 and 10) should show B isotopic compositions of δ^{11}B $= +3.8$, $+4.9$ and $+6.2\%o$, respectively (calculated from equation 5.6 after Hervig *et al.*, 2002, page 91, Chapter 5). Tourmaline, in contact with hydrous fluids at high pressures probably shows no or very little B isotopic fractionation (Chapter 10; Palmer & Swihart, 2002). Therefore, the isotopically heavy B introduced by the retrograde fluids produced Fe-rich tourmaline, but also influenced the B isotopic composition of the phengite.

Eclogite SY323 Rims of tourmaline included in cores of garnet porphyroblasts (see descritption of SY323 in Appendix B) are homogeneous in BSE images and euhedral. For these rims only one B isotopic analysis is available, due to the scarceness and small grain size of tourmaline in this sample. However, the δ^{11}B value of $+2.8 \pm 1.0\%o$ revealed for tourmaline rim is interpreted to represent the B isotopic composition of peak metamorphic tourmaline in this metabasic rock.

Siliceous marble SY432 Tourmaline in sample SY432 also contains rounded cores with chemical compositions different from the surrounding euhedral rims of the grains. In contrast to sample SY314, the chemical and the B isotopic compositions of individual grains are significantly different from one another. Therefore, the heterogeneous provenance of the former sediment is documented not only by the chemistry, but also by the B isotopic composition of detrital tourmaline in the metasediment. Euhedral rims of sample SY432 of all analysed grains are very similar in chemistry and B isotopic composition and show δ^{11}B values of $+0.9 \pm 1.8\%o$. These rims are interpreted as prograde or peak metamorphic overgrowths on the de-

trital cores. Their δ^{11}B value is characteristic for the peak metamorphic stage of tourmaline in sample SY432. Fe-rich rims were not observed on tourmaline in this sample, and no increase in δ^{11}B values has been found. Hence, the rock was not influenced by retrograde influx of B-bearing fluids.

Fluid in B isotopic equilibrium with phengite from sample SY432 (δ^{11}B $=$ $-11.3 \pm 1.4\%_o$) would have a δ^{11}B value of $+1.3$, 0.0 or $-1.1 \pm 1.4\%_o$ for temperatures of 400, 450 and 500 °C, respectively (calculated from equation 5.6 after Hervig *et al.*, 2002). Therefore, phengite was in B isotopic equilibrium with tourmaline rims at metamorphic peak conditions (on the basis of negligible B isotopic fractionation between tourmaline and hydrous fluid at high pressures). Retrograde B influx is documented neither by tourmaline nor by phengite and can therefore be ruled out for sample SY432.

9.5. Summary and Conclusions

Tourmaline grains of two metasedimentary rocks were analysed in-situ for their chemical and B isotopic compositions with high lateral resolution. Sample SY314, a metatuffite displays abundant detrital dravitic tourmaline grains with homogeneous chemical and B isotopic compositions (δ^{11}B $\approx -3.3\%_o$), prograde/peak metamorphic overgrowths with δ^{11}B values of $\sim -1.6\%_o$ in dravite with high Ca and Mg contents. Finally, the influx of B-bearing hydrous fluids is documented not only petrographically in Fe-rich zones of garnet, amphibole and mica, but also in Fe-rich rims of tourmaline, which shows strongly increasing δ^{11}B values towards the grain edges of up to $\sim +7.7\%_o$. The B isotopic composition of phengite ($\sim -6.4\%_o$) is probably also affected by the retrograde fluid.

Sample SY432, a siliceous marble also contains detrital tourmaline. Chemical and B isotopic compositions of different grains are strongly different from one another and point to a heterogeneous provenance of tourmaline in the premetamorphic sediment. δ^{11}B values of detrital cores vary between $\sim -10.7\%_o$ and $\sim +3.6\%_o$. Rims developed during prograde/peak metamorphism are homogeneous and similar among all analysed grains with δ^{11}B values of $\sim +0.9\%_o$. Phengite shows δ^{11}B values of $\sim -11.3\%_o$. Analyses of tourmaline rims and phengite show a fractionation of Δ^{11}B $= 12.2 \pm 2.3\%_o$. For temperatures of $\sim 450 - 500$ °C, which were estimated for peak metamorphic conditions of Syros H*P* metamorphic rocks (Chapter 3; Trotet *et al.*, 2001b), this suggests B isotopic equilibrium between phengite and tourmaline rims in SY432. Fe-rich retrograde rims were not observed in sample SY432. The contrasting δ^{11}B values of detrital cores in sample SY432 demonstrate that in-situ B isotope analysis of tourmaline by SIMS is a potentially powerful tool

for provenance studies in sediments and metasediments.

The δ^{11}B values of prograde and peak metamorphic tourmaline in samples SY314 ($-1.6\%o$), SY323 ($+2.8\%o$) and SY432 ($+0.9\%o$) are significantly higher than values determined by Nakano & Nakamura (2001) for Sambagawa metasedimentary peak metamorphic tourmaline ($-10\%o$) and by Bebout & Nakamura (2003) for samples from the Catalina schists ($-15\%o$) and from Lago di Cignana ($-10\%o$). The relatively high δ^{11}B values of metasedimentary tourmaline from Syros in comparison with the other samples demonstrate that the B isotopic composition of metasedimentary rocks from different localities and samples worldwide may significantly differ from one another. This may not be surprising considering the background of the large compositional heterogeneity of sedimentary rocks in general, but it is an important point to recognise for models of global cycling of B and its isotopes. Additionally, the δ^{11}B values of the metabasic sample and the metasedimentary samples are in the same range. A clear distinction between AOC and oceanic sediments is therefore not possible on the basis of B isotopes.

In summary, dravitic tourmaline is a major carrier of B in a variety of metasedimentary rocks. The pressure and temperature stability of dravitic tourmaline is very extensive, equivalent to conditions in subducting slabs down to depths of $\sim 250\,\mathrm{km}$. Therefore, tourmaline growth and stability in subducting metasediments could be responsible for recycling of B with isotopic composition influenced by Earth's surface processes into the deep mantle. The slow volume diffusivity at temperatures below $600\,^\circ$C allows for a detailed investigation of the evolution of the B isotopes of a tourmaline-bearing rock during its metamorphic and pre-metamorphic history. In addition, variable metamorphic conditions of the rock are recorded by tourmaline itself in changing X_{Mg} and Ca/Na ratios, which allows for a direct correlation of metamorphic history and B isotopic evolution.

10. Syros tourmaline: evidence for very high-δ^{11}B fluids in subduction zones

In this chapter, results of in-situ investigation of tourmaline grains from metasomatic reaction zones (blackwalls) from the island of Syros are presented, with implications for B-rich fluids in subduction zones. The study was completed together with Rainer Altherr and Thomas Ludwig (both Heidelberg). TIMS analyses were performed by Sonia Tonarini (Pisa). First results of this study were presented at the EGS-AGU-EUG Joint Assembly in 2003 in Nice (Marschall *et al.*, 2003a), at the Annual Meeting of the Deutsche Mineralogische Gesellschaft in 2003 in Bochum (Marschall *et al.*, 2003b), at the 2003 Goldschmidt Conference in Kurashiki (Zack & Marschall, 2003), and at the EGU General Assembly in 2004 in Nice (Marschall *et al.*, 2004b).

10.1. Introduction

It is demonstrated in Chapter 9 that dravitic tourmaline is a major carrier of B in a variety of metasedimentary rocks. The pressure and temperature stability of dravitic tourmaline is very extensive, equivalent to conditions in subducting slabs down to depths of ~ 250 km. Therefore, tourmaline growth and stability in subducting metasediments could be responsible for recycling of B with isotopic composition influenced by Earth's surface processes into the deep mantle. The slow volume diffusivity at temperatures below $600\,^{\circ}$C allows for a detailed investigation of the evolution of the B isotopes of a tourmaline-bearing rock during its metamorphic history. The grain size of tourmaline in most HP metamorphic rocks, however, is restricted to $\sim 500\,\mu$m and the modal abundance of tourmaline is small ($\sim 0.1\,\%$). In contrast, blackwall tourmaline from Syros has a large grain size (several cm) and high abundance. It occurs in a large number of different rock types and is widespread especially within the mélange in the northern part of the island. The formation of tourmaline at the contact between mafic or felsic HP blocks and ultramafic matrix probably has a significant impact on the geochemical cycle of B in subduction zones, as it may fix B in large quantities in the slab within a highly stable mineral. The isotopic composition of blackwall tourmaline provides important insights into the B isotope budget of deep metamorphic fluids in subduction zones.

10.2. Selected samples

Eight blackwall samples investigated in this study (Table 10.1) were taken from different places within the melange. They all contain significant amounts of tourmaline, forming mm-thick tourmaline-rich layers on the surface of the high-pressure blocks (Fig. 4.4b and c on page 83), or more evenly distributed single crystals or clusters of crystals (Fig. 4.4d) within them. Two samples (SY309B, SY420) are schists from the matrix, that contain tourmaline-rich layers or veins. Tourmaline in all samples is euhedral and does not show any sign of brittle or ductile deformation. In thin section, the grains commonly show visible zonation. Colours of the pleochroic cores range from colourless to blue, while those of the rims vary from pale pink to green (Fig. B.5d on page 302). Rims of some samples (SY400, SY441, SY442) show two or three zones with different shades of green. Resorption of core regions and replacement by rim material is restricted, while resorption of rim regions was never observed.

Table 10.1. List of tourmaline-bearing blackwall samples investigated for B isotope ratios

Sample	Rock type	Mineral assemblage	Tur diameter[†] (mm)
SY309B	Gln schist*	Omp, Chl, Gln, Phe, Ab, Czo, Ttn	0.1 to 0.5
SY327	Omp-Chl fels	Omp, Chl, Ab, Am, Bt, Ttn	3 to 4
SY400	Omp-Chl fels	Omp, Chl, Phe, Czo	2 to 5
SY412	Eclogite**	Omp, Chl, Phe, Ab, Bt, Rt	1 to 3
SY413	Gln schist	Omp, Chl, Gln, Phe, Ab, Czo, Ttn	4 to 5
SY420	Phe-Ep-Grt schist	Grt, Chl, Phe, Ab, Czo, Ttn, Rt	0.1 to 0.5
SY441	Chl schist	Omp, Chl, Bt, Ttn, Rt	4 to 5
SY442	Omp-Ab fels	Omp, Ab, Ttn	0.5 to 1.5

[†] Diameters of tourmaline are given for sections perpendicular to the c axes. * SY309B is a layer of Tur + Omp + Chl + Ab + Phe, formed within a glaucophane schist consisting of Gln + Czo + Phe + Ttn. ** SY412 is a former eclogite the parageneses of which is partly replaced by the assemblage Tur + Bt + Chl + Ab + Phe.

10.3. *P–T* conditions of formation of blackwalls and tourmaline

Eclogite and jadeite fels blocks from Syros show the parageneses Omp/Jd + Qtz ± Grt with Jd contents of clinopyroxene reaching 90 %. Peak metamorphic $P-T$ conditions for different lithologies were calculated to be approximately 1.5 GPa and 470 °C (Okrusch & Bröcker, 1990). Recently Trotet *et al.* (2001b) showed that at least some of the eclogites had reached conditions of 2.0 GPa at 540 °C, and that
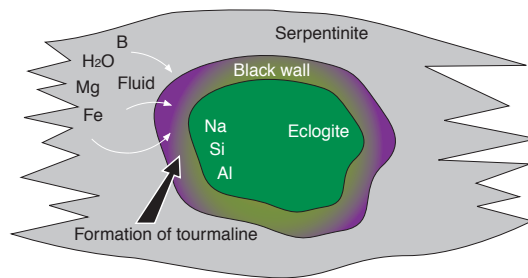
Fig. 10.1. Schematical drawing of an eclogite block embedded in a matrix dominated by serpentinite. At the contact between the contrasting lithologies, hydrous blackwalls formed by mechanical mixing and by the influx of B-rich aqueous fluids. Conditions were probably suitable for tourmaline formation in the contact zones between mafic and ultramafic rocks, as Na, Al and Si were supplied by the eclogites, Mg by the serpentinite and H_2O and B by the fluids.

the rocks from Syros were decompressed at temperatures between 400 and 550 °C to pressures between 1.0 and 0.5 GPa. For a Cpx + Ab + Gln-bearing retrograde assemblage they calculated conditions of 0.78 GPa and 394 °C. The occurrence of fresh lawsonite in different high-pressure rocks (Dixon, 1968; this study: sample SY438), suggests that temperatures during decompression did not exceed the lawsonite stability field. This strongly supports the decompression-cooling retrograde $P − T$ path discussed by Trotet *et al.* (2001b). The tourmaline-bearing samples investigated in this study form envelopes around the high-pressure blocks. Beside tourmaline these reaction zones contain omphacite with jadeite contents between 35 and 53 mole%, chlorite (clinochlore), phengite (3.3 − 3.4 Si per 11 oxygens), and almost pure albite (Ab_{97} - Ab_{100}). Some samples additionally contain biotite (Table 10.1).

Temperature conditions during formation of tourmaline were calculated with the Grt-Cpx Fe-Mg exchange thermometer, using the formulations by Ai (1994) and Krogh Ravna (2000) and by using THERMOCALC (v 3.01; Powell & Holland, 1988; Powell *et al.*, 1998). Only sample SY412 contains garnet in direct contact with omphacite II, i.e. omphacite formed during the fluid influx that precipitated the tourmaline. Therefore, Grt-Cpx thermometry was applied to garnet and omphacite II in contact with one another in sample SY412, in which both are included in tourmaline (Fig. B.23a on page 332). Oxidation states of Fe in garnet and clinopyroxene were estimated by stoichiometric formula calculation. For an assumed pressure of 0.7 GPa, the thermometers of Ai (1994) and Krogh Ravna (2000) both give identical temperatures of 419 °C. This is in agreement with the results from THERMOCALC, which give 429 °C. However, uncertainties may be large (± 50 °C), because the calculated temperature depend on the assumed Fe^{2+}/Fe^{3+}

ratios of garnet and clinopyroxene.

Determining the pressure conditions during formation of the reaction zones is hampered by the fact that the samples are silica undersaturated and quartz is generally absent. The breakdown reaction of albite

$$Ab = Jd + Qtz \tag{10.1}$$

has often been used as a barometer for the calculation of minimum pressures in eclogitic rocks containing omphacitic clinopyroxene and quartz. The paragenesis albite + omphacite in the absence of quartz in a first step provides maximum pressures of equilibration only. However, the reaction

$$Ab = Jd + SiO_2 \tag{10.2}$$

is not only pressure (and temperature) sensitive, but can also act as a buffer reaction for SiO_2 during metasomatic processes. Reaction 10.2 has a positive slope in a $P - \log a(SiO_2)$ diagram (Fig. 10.2). Addition of SiO_2 by a fluid entering a rock containing omphacite + albite at constant pressure would produce more albite by reducing the jadeite component of the coexisting clinopyroxene. Fluids undersaturated in SiO_2 with respect to the rock will remove SiO_2 from the mineral assemblage by decomposing albite and increasing the jadeite component in omphacite, as for example:

$$3\,Jd_{33} + Ab = 4\,Jd_{50} + SiO_2 \tag{10.3}$$

or:

$$2\,CaMgSi_2O_6 + 1\,NaAlSi_2O_6 + NaAlSi_3O_8 =$$
$$2\,CaMgSi_2O_6 + 2\,NaAlSi_2O_6 + SiO_2 \tag{10.4}$$
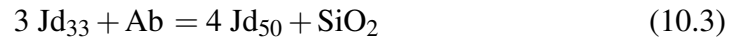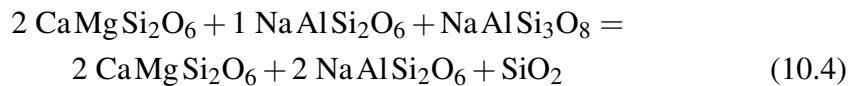
Fig. 10.2 shows the equilibria of albite + omphacite for two different omphacites containing 33 and 50 % jadeite, respectively. At constant temperature, reaction 10.3 could shift an assemblage from point A to point B by reducing $a(SiO_2)$ or proceed to point B' by increasing pressure. Omphacite in sample SY442 shows a two-stage zonation with cores of Jd_{35} and rims of Jd_{53}. Omphacite included in tourmaline rims 1 and 2 (Fig. B.31a, page 344) are relatively low in Na, whereas rims of omphacite included in tourmaline rim 3 are high in Na (Fig. 10.3). Therefore, the two different omphacite generations can be related to different growth stages of tourmaline. The first fluid had a higher silica activity, stabilising $Jd_{35} + Ab$ (point A in Fig. 10.2), whereas the second fluid had a significantly lower $a(SiO_2)$, producing $Jd_{53} + Ab$ (point B in Fig. 10.2). The Ab + Omp equilibrium for a specific omphacite composition is shifted to higher pressures for higher SiO_2 activities and is
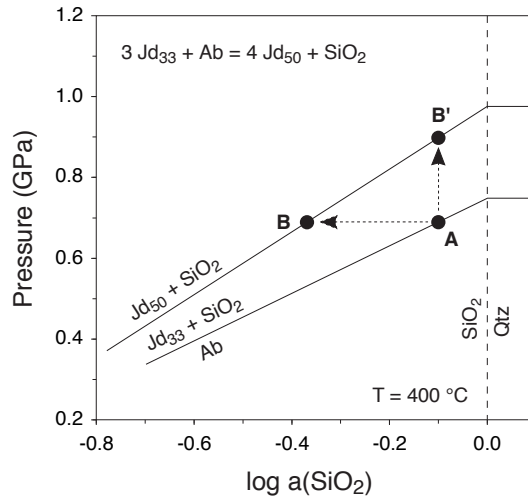
Fig. 10.2. $P - \log a(SiO_2)$ diagram showing the upper pressure breakdown reaction of albite to omphacite + SiO_2 in the SiO_2-undersaturated field for pure albite and omphacite with Jd_{33} and Jd_{50}.

reaching maximum pressures at $a(SiO_2) = 1$, i.e. in the presence of quartz. Therefore, a second, independent equilibrium is needed to determine pressure and silica activity of tourmaline formation.

Samples SY309B, SY413 and SY412 show the mineral assemblage Gln + Phe + Ab + Chl + Omp. The equilibrium of glaucophane, phengite, chlorite and albite or jadeite was calculated by the reactions

$$Gln + Ms + H_2O = Cel + Chl + Ab \tag{10.5}$$

$$Gln + Ms + H_2O = Cel + Chl + Jd + SiO_2 \tag{10.6}$$
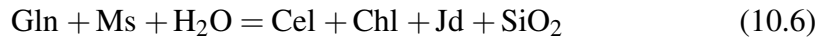
Fig. 10.4a shows the calculated locations of reactions 10.2, 10.5 and 10.6 in a $P - \log a(SiO_2)$ diagram, intersecting at the invariant point *A* at a constant temperature of 400 °C. Fig. 10.4b to d display the shift of point *A* in the $P - T - \log a(SiO_2)$ space. Both *P* and *T* are negatively correlated with the silica activity. Equilibration temperatures are decreasing by ~ 100 °C with $\log a(SiO_2)$ increasing by 0.1. The pressure increase at the same time is ~ 0.1 GPa. For a temperature of 400 °C, point *A* is located at pressures of 0.61, 0.63 and 0.72 GPa for samples SY309B, SY413 and SY412, respectively. Silica activities in the three samples are 0.48 (SY309B; $\log a(SiO_2) = -0.32$), 0.42 (SY413; $\log a(SiO_2) = -0.38$) and 0.51 (SY412; $\log a(SiO_2) = -0.29$).

To summarise, the high-pressure melange of Syros is composed of eclogites, meta-gabbros, high-silica jadeite felses, meta-tuffites and serpentinites, that are in-

197
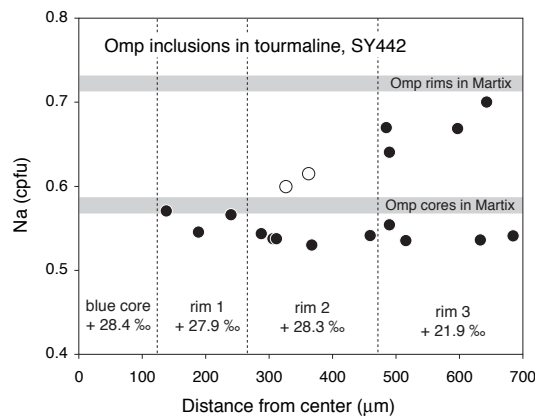
Fig. 10.3. Na content of omphacite included in tourmaline in sample SY442 plotted versus their distance from the tourmaline host's core. Stippled vertical lines mark the boundaries between different growth zones of the tourmaline host (see Fig. B.31a). Omphacite included in rim 3 shows chemical zonation with Na-poor cores and Na-rich rims. Open symbols mark two inclusions that are close to the tourmaline core, but are included in a region, where rim-2 tourmaline was replaced by rim-3 tourmaline. Filled symbols are true inclusions of the respective growth zones. Lower and upper shaded horizontal bars give Na content of omphacite I and omphacite II in the matrix, respectively.

terpreted as different sections of ancient oceanic crust or lithosphere. It was subducted to depths of 50 to 70 km and heated to temperatures of $\sim 500\,^{\circ}$C. During exhumation of the unit, reaction zones formed at contacts between the contrasting lithologies, partly enhanced by mechanical mixing but also triggered by a strong influx of hydrous fluids, which reduced the activity of SiO_2 in the rocks to values between 0.4 and 0.5. Reaction zones (blackwalls) are dominated by hydrous minerals like chlorite, glaucophane, phengite, talc and Ca-amphibole. Some of these blackwalls contain abundant tourmaline that was precipitated during the formation of the blackwalls. $P-T$ conditions of tourmaline formation were $400-430\,^{\circ}$C and $0.62-0.72$ GPa, which corresponds to a depth of ~ 20 to 25 km (Fig. 10.5). Therefore, a major influx of boron-rich hydrous fluid into the Syros melange must have occurred during exhumation of the unit at a depth of 20 to 25 km. The HP melange was probably exhumed by buoyant uplift due to the low density of the serpentinites, marbles and siliceous schists that compose major sections of the rock units exposed on Syros.

10.4. Chemical composition of blackwall tourmaline

Apart from X_{Mg}, variation of tourmaline chemical composition among the different samples is very restricted (Table 10.2). Formula calculations of 31 oxygens
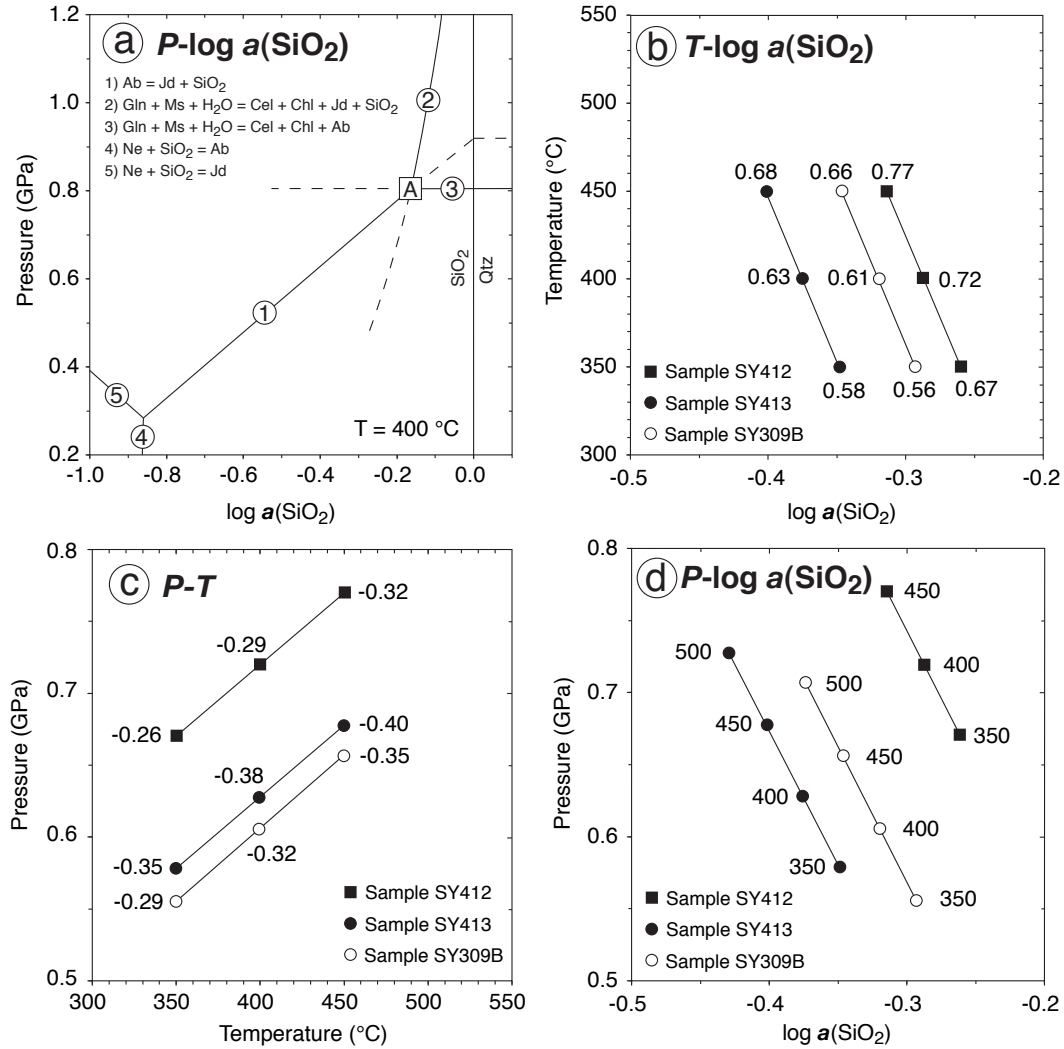
Fig. 10.4. a Schematic $P - \log a(\mathrm{SiO_2})$ diagram showing the intersection of reactions 10.2, 10.5 and 10.6 in invariant point A. Additionally the reactions $\mathrm{Ab} = \mathrm{Ne} + \mathrm{SiO_2}$ and $\mathrm{Jd} = \mathrm{Ne} + \mathrm{SiO_2}$ are shown. **b - d** Location of point A calculated for samples SY309B (open circles), SY412 (filled squares) and SY413 (filled circles) in **b** $T - \log a(\mathrm{SiO_2})$ for different pressures (given as numbers in GPa), **c** $P - T$ for different $\log a(\mathrm{SiO_2})$ (given as numbers) and **d** $P - \log a(\mathrm{SiO_2})$ for different temperatures (given as numbers in °C).

199
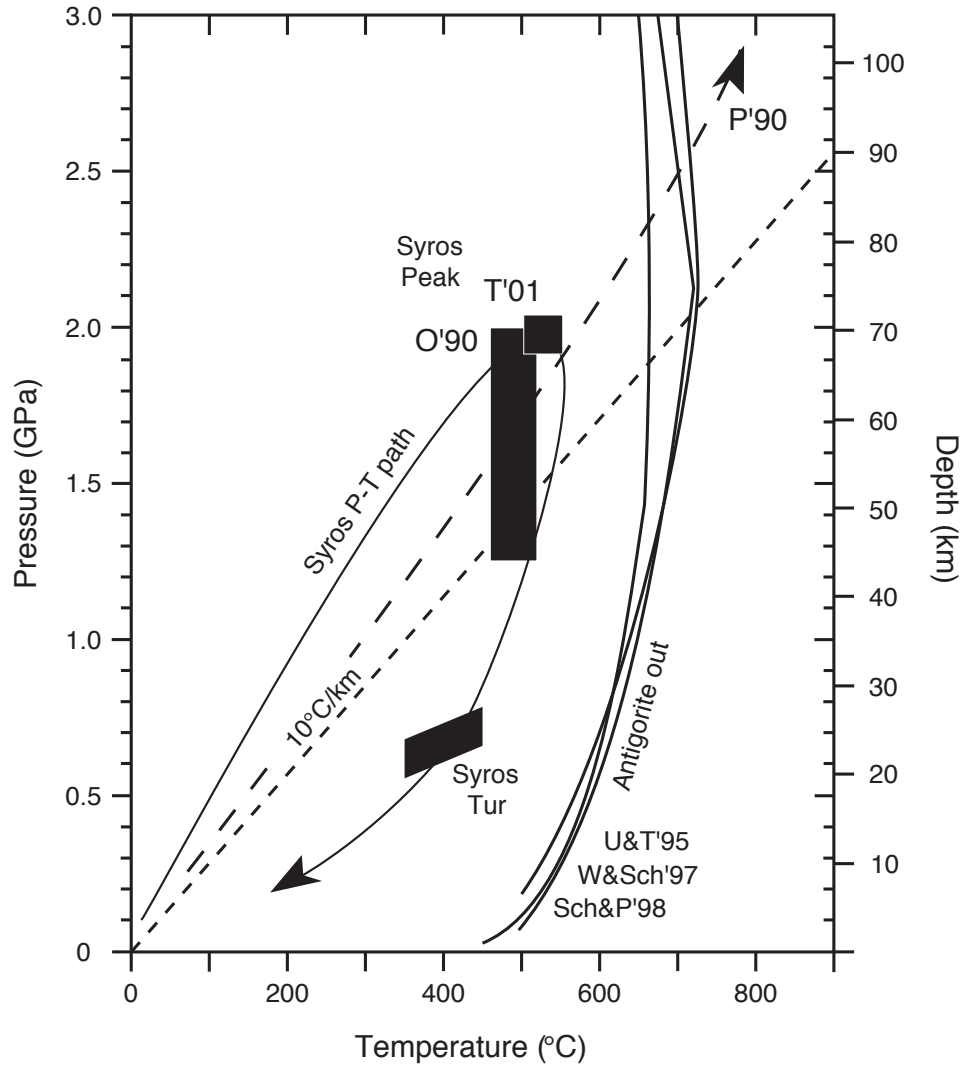
Fig. 10.5. $P - T$ diagram showing the prograde and retrograde $P - T$ path of Syros HP rocks. Peak conditions were taken from Okrusch & Bröcker (1990) and Trotet *et al.* (2001b). Conditions of tourmaline formation were determined during this study. The upper thermal stability limit of antigorite, experimentally determined by different workers (Ulmer & Trommsdorff, 1995; Wunder & Schreyer, 1997; Schmidt & Poli, 1998), was not reached by rocks from Syros. P'90 is $P - T$ path *B* for subducting slabs from Peacock (1990). The fine-dashed line is the 10 °C/km geothermal gradient.

and total Fe as Fe^{2+} result in 5.87 to 5.97 Si, 5.81 to 6.05 Al, 3.06 to 3.15 B and 2.95 to 3.27 $(Mg + Fe + Ti)$ per formula unit. Fe^{2+}/Fe^{3+} ratios in Syros blackwall tourmaline are discussed in Marschall *et al.* (2004c). TiO_2 contents are between 0.12 and 1.05 wt% and vary between the different zones of the crystals that were distinguished by colour in thin section. Ti contents are lowest in the light blue cores and higher in the dark green zones. The X-site is (almost) completely occupied by $(Na + Ca) \geq 0.97$ cpfu, being highly dominated by Na (0.92 to 0.97 cpfu) with only minor Ca (0.02 to 0.08 cpfu). Analyses of F, Cl and H contents revealed no detectable Cl, only minor F (0.04 to 0.10 pfu) and high OH contents, basically > 3.5 OH pfu, in most cases > 3.75 OH pfu. Cr_2O_3 contents range from 0.01 to 0.22 wt% which is translated to ≤ 0.03 Cr cpfu. All other elements measured are of negligible concentrations in the tourmalines, including Mn, Zn, K and Li (see also Chapter 11). Boron contents in excess of 3.00 cpfu in dravite, as well as high Na and OH contents are discussed in Marschall *et al.* (2004c).

The calculated formulae are very close to the ideal schorl-dravite solid solution series and belong to the alkali-dravite group of Hawthorne & Henry (1999) with X_{Mg} between 0.58 and 0.82.

10.5. Boron isotopic composition of blackwall tourmaline

The small size of the SIMS spot during determination of B isotope ratios in tourmaline ($\leq 5 \mu m$) enables us to measure very detailed profiles even in small grains, and to unravel small-scale isotopic heterogeneities. During this study, traverses with 10 to 50 spots each were completed for all eight samples.

The results of these measurements show four important features:

(1) $^{11}B/^{10}B$ isotopic ratios are very high, exceeding $\delta^{11}B$ values of $+18\%o$ in all samples, with an extreme value of $+28.4 \pm 0.7\%o$ in the tourmaline core of sample SY442 (Table 10.2).

(2) In seven out of eight samples intra-grain variation of $\delta^{11}B$ is very limited with profiles showing very little or a lack of internal zonation (Fig. 10.6). Differences between core and rim values are within analytical uncertainties (Table 10.2).

(3) Variation of $\delta^{11}B$ among these seven different samples is also very restricted, i.e. ranging from $+18.8 \pm 0.9\%o$ (sample SY441) to $+22.2 \pm 1.5\%o$ (sample SY413).

(4) Sample SY442 is different from the other seven samples, as it displays a strong zonation in $\delta^{11}B$ (Fig. 10.6h) which correlates with the optically visible zones (Fig. B.31a on page 344). Blue core as well as rims I and II are extremely enriched in the heavy isotope, with $\delta^{11}B$ values of $\sim +28\%o$ (Table 10.2), whereas

rim III is significantly lighter. There is a sharp jump of $\sim$6‰ within 10 µm at the boundary between rims II and III. Rim III itself displays an internal isotopic zonation with δ^{11}B increasing from +21.5‰ in contact to rim II to +24.0‰ in the center of rim III to $\sim$+20.0‰ at the edge of the tourmaline (Fig. 10.6h). A more detailed discussion of the δ^{11}B profile in this sample will follow below.
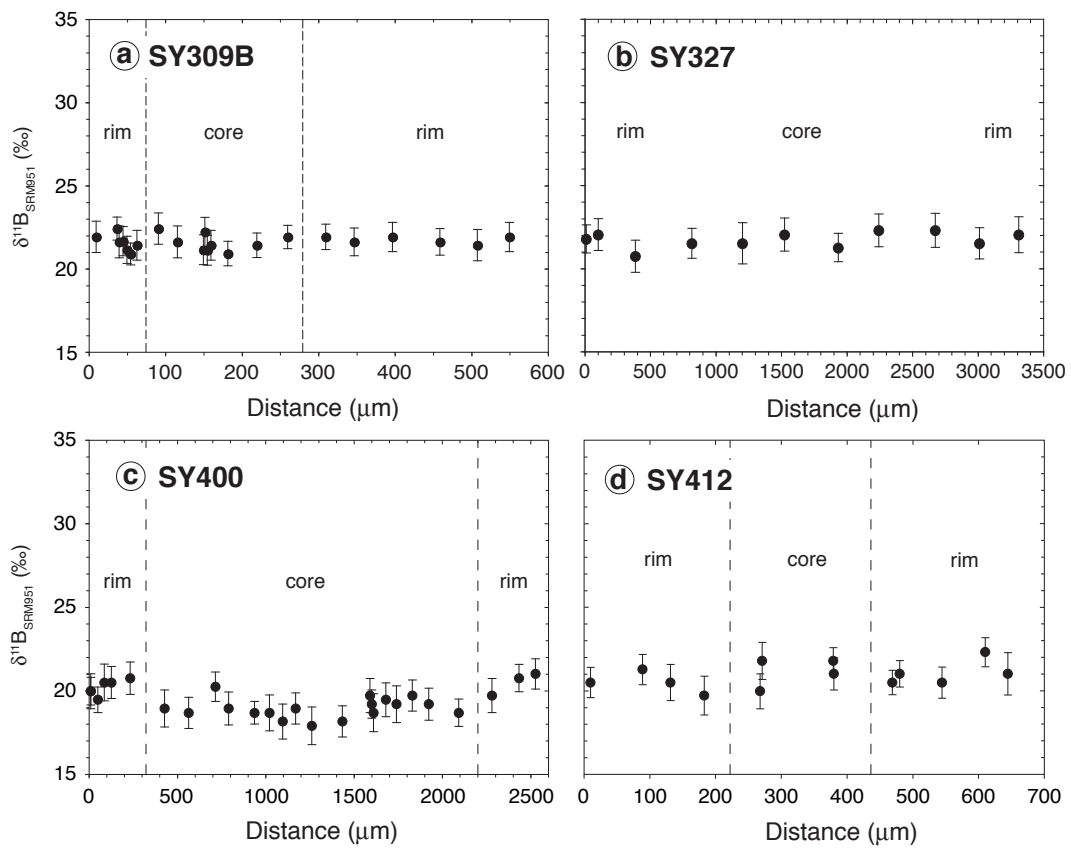
Fig. 10.6. Results of SIMS analyses of B isotopic composition of tourmaline from Syros. For each sample at least one traverse of 10 to 50 single spot analyses was carried out across a grain. Error bars give analytical precision as 2RSD$_{mean}$. **a** Sample SY309B, **b** Sample SY327, **c** Sample SY400, and **d** Sample SY412.
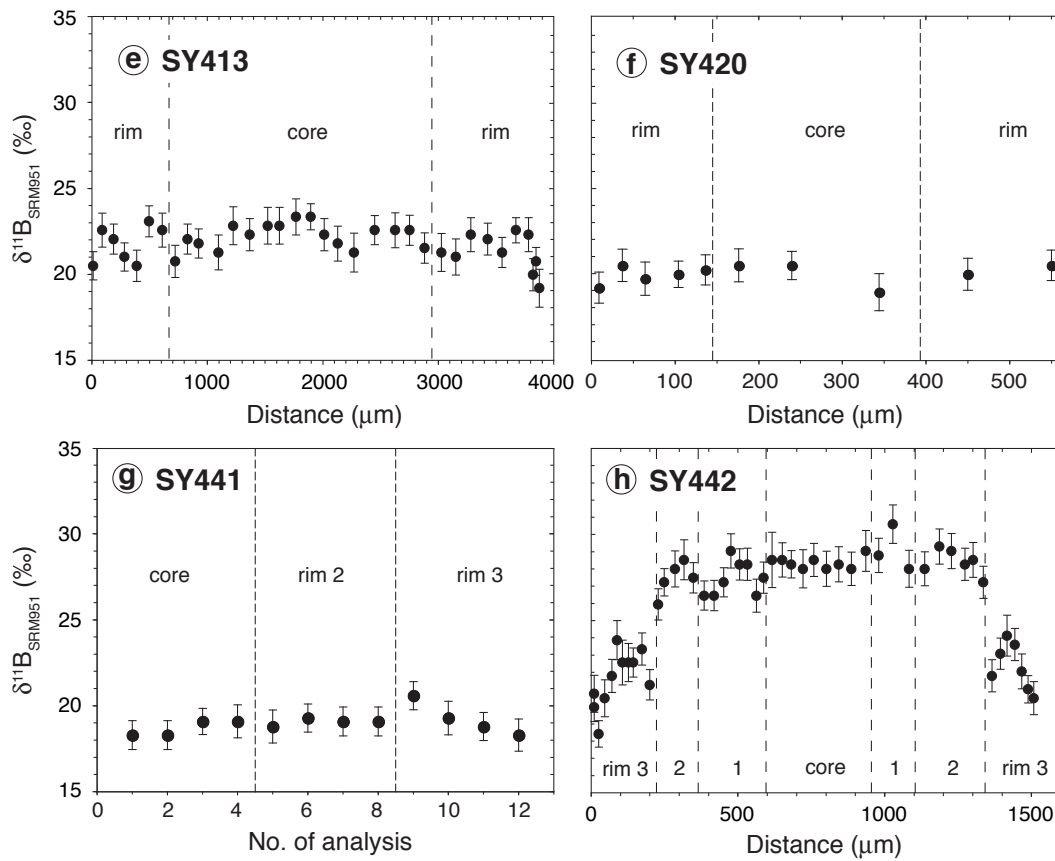
Fig. 10.6. (continued). **e** Sample SY413, **f** Sample SY420, and **g** Sample SY441. In this sample, no profile over one single grain was measured, but analyses from different grains were collected and sorted due to location (core, rim 2, rim 3) within the crystals (rim 1 was not analysed). **h** Sample SY442.

Table 10.2. Chemical and B isotopic analyses of tourmaline (part 1)

Sample	SY309B		SY327		SY400		SY412		SY413	
Type	core	rim	core	rim	core	rim	core	rim	core	rim
SiO_2	36.13	35.73	35.36	35.77	36.27	36.30	35.75	35.60	35.43	35.06
TiO_2	0.15	0.52	1.05	0.53	0.42	0.19	0.38	0.64	0.53	0.71
B_2O_3	11.05	10.75	10.58	10.73	11.18	11.16	10.74	10.64	10.60	10.55
Al_2O_3	31.00	30.24	29.44	30.36	31.37	31.68	30.14	29.41	30.09	29.65
Cr_2O_3	0.11	0.22	0.01	0.01	0.06	0.04	0.02	0.01	0.05	0.06
FeO^t	5.46	6.63	9.27	8.04	4.54	3.97	8.05	9.15	7.84	8.43
MnO	0.02	0.02	0.02	0.02	0.02	0.02	0.01	0.02	0.01	0.02
MgO	9.09	8.65	7.17	7.78	9.59	9.87	8.04	7.55	8.02	7.84
CaO	0.11	0.25	0.45	0.24	0.20	0.11	0.18	0.25	0.24	0.23
ZnO	0.01	0.01	0.02	0.03	0.02	0.02	0.03	0.02	0.02	0.03
Na_2O	3.01	3.01	2.84	2.93	3.04	3.08	2.95	2.90	2.92	2.92
K_2O	0.01	0.01	0.01	0.02	0.02	0.01	0.02	0.02	0.02	0.02
Li (μg/g)	2.0	2.1	8.5	6.9	6.0	6.7	4.0	5.0	4.6	4.4
H_2O	3.78	3.59	3.32	3.39	3.75	3.62	3.41	3.27	3.20	3.17
F	0.14	0.17	0.19	0.18	0.12	0.11	0.15	0.18	0.14	0.19
Cl	0.01	0.00	0.00	0.00	0.00	0.00	0.00	0.00	0.00	0.00
-(F+Cl)=O	0.06	0.07	0.08	0.08	0.05	0.05	0.06	0.08	0.06	0.08
Total	100.04	99.75	99.65	99.95	100.54	100.14	99.80	99.59	99.06	98.81

Formulas calculated to 31 oxygens, $Fe^{2+} = Fe^t$

Si	5.89	5.90	5.93	5.93	5.87	5.88	5.94	5.97	5.94	5.92
Ti	0.02	0.06	0.13	0.07	0.05	0.02	0.05	0.08	0.07	0.09
B	3.11	3.06	3.06	3.07	3.12	3.12	3.08	3.08	3.07	3.07
Al	5.96	5.89	5.82	5.94	5.98	6.05	5.90	5.81	5.95	5.90
Cr	0.01	0.03	0.00	0.00	0.01	0.00	0.00	0.00	0.01	0.01
Fe^{2+}	0.75	0.92	1.30	1.12	0.61	0.54	1.12	1.28	1.10	1.19
Mn	0.00	0.00	0.00	0.00	0.00	0.00	0.00	0.00	0.00	0.00
Mg	2.21	2.13	1.79	1.92	2.31	2.39	1.99	1.89	2.00	1.97
Ca	0.02	0.04	0.08	0.04	0.03	0.02	0.03	0.05	0.04	0.04
Zn	0.00	0.00	0.00	0.00	0.00	0.00	0.00	0.00	0.00	0.00
Na	0.95	0.96	0.92	0.94	0.95	0.97	0.95	0.94	0.95	0.95
K	0.00	0.00	0.00	0.00	0.00	0.00	0.00	0.00	0.00	0.00
Total	18.93	19.01	19.05	19.04	18.95	19.00	19.07	19.10	19.13	19.15
X_{Mg}	0.748	0.699	0.579	0.633	0.790	0.816	0.640	0.595	0.646	0.624
OH	4.11	3.95	3.71	3.75	4.05	3.91	3.78	3.66	3.58	3.57
F	0.07	0.09	0.10	0.09	0.06	0.05	0.08	0.10	0.08	0.10
Cl	0.00	0.00	0.00	0.00	0.00	0.00	0.00	0.00	0.00	0.00
Total	4.18	4.04	3.82	3.84	4.11	3.97	3.86	3.75	3.65	3.67

Boron isotope values determined by SIMS

δ^{11}B	+21.6	+21.6	+21.7	+21.8	+19.0	+20.3	+21.2	+20.8	+22.2	+21.4
$2RSD_{mean}$	0.8	1.0	0.9	1.1	1.2	0.8	1.6	1.5	1.5	2.2
n	12	10	5	6	18	9	4	9	14	18

n = number of isotope analyses. H (H_2O), Li and B measured by SIMS; all other elements by EPMA.

Table 10.2. (continued)

Sample	SY420		SY441				SY442			
Type	core	rim	core	rim 1	rim 2	rim 3	core	rim 1	rim 2	rim 3
SiO_2	36.21	35.72	36.00	36.24	36.34	36.53	35.91	35.90	35.78	35.76
TiO_2	0.12	0.49	0.15	0.62	0.44	0.46	0.25	0.51	0.56	0.65
B_2O_3	11.07	10.84	11.12	11.14	11.15	11.31	11.00	11.01	10.88	10.87
Al_2O_3	30.91	30.11	31.14	30.35	31.07	31.31	30.77	30.20	29.95	29.66
Cr_2O_3	0.05	0.08	0.02	0.01	0.01	0.01	0.11	0.06	0.03	0.01
FeO^t	5.54	6.60	4.51	5.58	4.96	4.31	6.41	7.21	8.14	7.92
MnO	0.04	0.03	0.03	0.02	0.01	0.03	0.01	0.01	0.02	0.02
MgO	9.23	8.76	9.76	9.37	9.33	9.68	8.68	8.32	7.98	8.26
CaO	0.09	0.23	0.11	0.28	0.23	0.18	0.17	0.26	0.26	0.25
ZnO	0.02	0.02	0.02	0.01	0.02	0.02	0.02	0.01	0.03	0.02
Na_2O	3.06	2.97	3.03	2.94	2.97	3.03	2.95	2.94	2.92	2.93
K_2O	0.02	0.02	0.01	0.01	0.01	0.01	0.02	0.02	0.03	0.02
Li ($\mu g/g$)	4.1	4.7	4.6	3.1	3.8	6.0	5.1	5.8	8.0	6.7
H_2O	3.62	3.27	3.66	3.54	3.57	3.64	3.46	3.53	3.32	3.20
F	0.10	0.16	0.08	0.10	0.10	0.09	0.12	0.15	0.17	0.20
Cl	0.01	0.00	0.01	0.00	0.00	0.01	0.01	0.02	0.01	0.01
-(F+Cl)=O	0.04	0.07	0.03	0.04	0.04	0.04	0.06	0.07	0.07	0.09
Total	100.05	99.23	99.59	100.18	100.18	100.59	99.86	100.10	100.02	99.69

Formulas calculated to 31 oxygens, $Fe^{2+} = Fe^t$

Si	5.92	5.94	5.88	5.92	5.92	5.90	5.91	5.91	5.94	5.95
Ti	0.02	0.06	0.02	0.08	0.05	0.06	0.03	0.06	0.07	0.08
B	3.12	3.11	3.14	3.14	3.13	3.15	3.13	3.13	3.12	3.12
Al	5.95	5.90	5.99	5.84	5.96	5.96	5.97	5.86	5.86	5.82
Cr	0.01	0.01	0.00	0.00	0.00	0.00	0.01	0.01	0.00	0.00
Fe^{2+}	0.76	0.92	0.62	0.76	0.68	0.58	0.88	0.99	1.13	1.10
Mn	0.01	0.00	0.00	0.00	0.00	0.00	0.00	0.00	0.00	0.00
Mg	2.25	2.17	2.38	2.28	2.26	2.33	2.13	2.04	1.97	2.05
Ca	0.02	0.04	0.02	0.05	0.04	0.03	0.03	0.05	0.05	0.04
Zn	0.00	0.00	0.00	0.00	0.00	0.00	0.00	0.00	0.00	0.00
Na	0.97	0.96	0.96	0.93	0.94	0.95	0.94	0.94	0.94	0.95
K	0.00	0.00	0.00	0.00	0.00	0.00	0.01	0.01	0.01	0.00
Total	19.02	19.12	19.01	19.02	18.99	18.98	19.04	19.01	19.09	19.14
X_{Mg}	0.748	0.703	0.794	0.749	0.770	0.800	0.707	0.673	0.636	0.650
OH	3.95	3.63	3.99	3.86	3.88	3.92	3.80	3.88	3.68	3.55
F	0.05	0.08	0.04	0.05	0.05	0.05	0.06	0.08	0.09	0.10
Cl	0.00	0.00	0.00	0.00	0.00	0.00	0.00	0.01	0.00	0.00
Total	4.00	3.71	4.03	3.91	3.93	3.97	3.87	3.96	3.77	3.66

Boron isotope values determined by SIMS

$\delta^{11}B$	+20.0	+20.0	+18.8	+18.3	+19.1	+19.3	+28.4	+27.9	+28.3	+21.9
$2RSD_{mean}$	1.8	0.9	0.9	–	0.9	0.9	0.7	2.6	1.4	3.0
n	3	7	3	1	4	4	5	17	8	18

10.6. Discussion

10.6.1. Boron concentration of blackwall-forming fluids

As no data on fluid inclusions related to the tourmaline-forming "event" are available, the concentration of B in the fluids can be estimated only indirectly from B concentrations in minerals. Omphacitic clinopyroxene formed together with tourmaline from different samples within the blackwalls contain between $1.92\,\mu g/g$ (SY309B) and $3.28\,\mu g/g$ (SY441) B (see Chapter 7 on partitioning and budget of light elements, page 123). Combined with clinopyroxene/fluid partition coefficients of 0.016 determined by Brenan *et al.* (1998b), these abundances would imply B concentrations of the fluids in the range of 120 to $205\,\mu g/g$. Experimental studies by Morgan & London (1989) have shown that crystallisation of tourmaline from solutions containing less than $0.2\,wt\%$ B_2O_3 ($620\,\mu g/g$ B) is possible, provided the fluids are low in pH (pH of quenched fluids < 6.5). Weisbrod *et al.* (1986) (cited in Dingwell *et al.*, 2002) were able to crystallise dravite from Fe-free chlorite-bearing compositions in equilibrium with fluids containing between $\sim 150\,\mu g/g$ and $\sim 300\,\mu g/g$ B, in the temperature range of 350 to 450 °C. This may indicate that the calculated B concentrations of $\sim 200\,\mu g/g$ are not too low for the formation of tourmaline.

10.6.2. Fractionation of boron isotopes

Theoretical calculations of isotope fractionation of boron predict preference of ^{10}B for crystallographic sites tetrahedrally coordinated to oxygen, and ^{11}B for trigonal sites. B in acidic hydrous fluids is predominantly trigonally coordinated in $B(OH)_3$ units. Recent experiments have shown that this also holds true for high pressures up to 3.0 GPa (Thomas *et al.*, 2004). Boron in tourmaline is also trigonally coordinated with three BO_3 groups per formula unit. Only small portions of tetrahedral B were observed in tourmaline from Syros (Marschall *et al.*, 2004c), ranging from 0.1 to 0.2 B cpfu. Therefore, at least 95 % of the B in Syros tourmaline is trigonally coordinated.

Experimental studies (e.g. Hervig *et al.*, 2002 and references therein; Heinrich *et al.*, 2003; Sanchez-Valle *et al.*, 2004; Wunder *et al.*, 2004) have investigated the temperature dependence of B isotopic fractionation between phases of different B coordination (e.g. mica, amphibole, melt, fluid, tourmaline). For temperatures above 200 °C, the results show larger fractionation than predicted by Kakihana *et al.* (1977). Hervig *et al.* (2002) demonstrated a systematic decrease of fractionation

with increasing temperature, given by the formula

$$1000 \ln \alpha = 5.68 - 12290/T \qquad (10.7)$$

where α is the fractionation factor and T is absolute temperature (K). For a temperature of $400\,°C$, the assumed temperature for Syros blackwall formation, a fractionation of $12.6‰$ between phengite and fluid or phengite and tourmaline results from this equation. The fractionation between tourmaline ($0.15\,B^{IV}$cpfu) and fluid would be $0.6‰$ applying Equation 10.7, assuming that equilibrium fractionation is exclusively determined by the coordination of B in the phases. However, Palmer *et al.* (1992) have demonstrated experimentally a fractionation between tourmaline and fluid of $\sim 4.5‰$ at $400\,°C$ and $0.2\,GPa$, which was decreasing with both increasing temperature and pressure.

Tourmaline from this study shows very homogeneous $\delta^{11}B$ patterns even in large grains. As these grains were precipitated from hydrous fluid(s) entering the rocks, boron isotopic fractionation processes between the two phases can be monitored using these samples. The formation of tourmaline containing $\sim 30,000\,\mu g/g$ B significantly decreases the B concentration of any coexisting fluid. Isotopic fractionation between tourmaline and fluid, as described by Palmer *et al.* (1992), would lead to an increase of $\delta^{11}B$ in the fluid over time and consequently to an isotopic zonation within the precipitated tourmaline grains, with $\delta^{11}B$ values increasing from cores to rims. Flat $\delta^{11}B$ pattern can be explained either (i) by a very high fluid/rock ratio, flushing the reaction zones with fluid of constant $\delta^{11}B$, or (ii) by weak or absent B isotopic fractionation between tourmaline and hydrous fluid at the $P-T$ conditions of interest. Some of the investigated samples indeed show evidence for high fluid/rock ratios, as they contain large amounts of chlorite and no relics of their primary parageneses. Those samples are located at the outermost parts of the high-pressure blocks (SY441), or in the matrix (SY309B). However, sample SY412 stems from the core of an eclogite block, that showed a gradual transition into blueschist and finally a chlorite-rich assemblage at its rims. SY412 still shows high proportions of its eclogitic paragenesis (Grt + Omp I + Rt), and only restricted hydration. Chloritisation of garnet is not complete. Relics of garnet are found not only as inclusions in tourmaline, but also in the matrix of the rock. Omphacite I is only partly replaced by omphacite II and rutile is replaced by titanite only at its very rims. This sample also contains large tourmaline grains with flat $\delta^{11}B$ patterns (Fig. 10.6d). The blueschist zone of the same block, represented by Sample SY413, shows total replacement of garnet by chlorite, homogeneous omphacite II and titanite instead of rutile. All these observations suggest that (i) fluid/rock ratios strongly decreased from the matrix of the Syros melange to the cores of the high-pressure blocks, and (ii) fluid/rock ratios were rather low during the retrogression of eclogite

SY412, but significantly increased towards the block's rim (SY413). Fluid supply in the eclogitic core of the block was restricted and the growing tourmaline must have had a strong impact on the B concentration of the fluid. Any isotopic fractionation between tourmaline and fluid therfore would have been documented in the precipitated tourmaline grains. Flat δ^{11}B patterns in sample SY412 after all can only be explained by negligible B isotopic fractionation between tourmaline and hydrous fluid. This is in agreement with the fact that B in both tourmaline and acidic hydrous fluids is predominantly in trigonal coordination. However, these observations are in contrast to the experimental study at pressures of 0.2 GPa of Palmer *et al.* (1992).

10.6.3. B isotopic zonation in Tur of sample SY442

The strong B isotopic zonation in tourmaline of sample SY442 can not be explained by fractionation effects between fluid and minerals during formation of the sample or by temperature effects. Instead, the zoning must be due to the precipitation of tourmaline from two different fluids of isotopically different composition entering the rock one after the other. This hypothesis is supported by the two-stage zonation of omphacite in this sample, showing the influx of a second fluid also leading to a drop in SiO_2 activity. Inclusions of omphacite I in tourmaline core, rim I and rim II (high δ^{11}B) and inclusions of omphacite II occurring exclusively in rim III characterised by lower δ^{11}B (Fig. 10.3), support a genetic relationship between the two omphacite generations and the two tourmaline generations. In some places, rim II is corroded and replaced by rim III (Fig. B.31a on page 344), suggesting that parts of the previously grown high-δ^{11}B tourmaline was dissolved during influx of the lower-δ^{11}B second fluid. This must have led to local mixing of B from the early tourmaline and the later fluid with their two contrasting isotopic compositions. The internal isotopic zonation of rim III (Fig. 10.6h) is therefore best explained by mixing between B with $+28\%o$ from early tourmaline and B with $\sim +20\%o$ from the second fluid. Sample SY442 provides evidence for two fluids of different compositions, with a first fluid of δ^{11}B $= +28\%o$ and a second one with δ^{11}B of $\sim +20\%o$.

10.6.4. Phengite - tourmaline B isotope fractionation

White micas (phengite and paragonite) have been demonstrated to be the most important hosts of boron in metabasites (Domanik *et al.*, 1993; and Chapter 7, page 123). Average boron concentrations of phengite in sample SY309B, for example, is 136 µg/g. Phengite is generally accepted to contain boron in tetrahedral coordi-

nation (Werding & Schreyer, 2002; Hervig *et al.*, 2002; Tonarini *et al.*, 2003), and therefore it should preferentially incorporate the lighter isotope ^{10}B in equilibrium with tourmaline or acidic hydrous fluid. Experimental studies by Heinrich *et al.* (2003) show fractionation of 9.5‰ between boro-muscovite and hydrous fluid at 500°C. A natural muscovite-tourmaline pair investigated by Hervig *et al.* (2002) shows fractionation of 11‰ in rocks equilibrated at about 550°C.

In our samples, phengite is characterised by δ^{11}B values that are lighter than those of coexisting tourmalines: 15.0 ± 1.8‰ in sample SY309B, 9.2 ± 4.3‰ in sample SY412, 11.5 ± 2.7‰ in sample SY413, and 13.5 ± 3.4‰ in sample SY420 (Table 10.2 and 10.3). These results are consistent with a difference of 12.6‰ (at 400°C) calculated from Equation 10.7, given in Hervig *et al.* (2002), being aware of the large uncertainties in the δ^{11}B value of the mica, which might be due to some heterogeneities in the minerals.

These results show that crystallising phengite fractionates boron with isotope ratios approximately 12‰ lighter than in coexisting fluid at a temperature of about 400°C. Other silicate minerals (glaucophane, chlorite, actinolite, talc) may also preferentially incorporate ^{10}B, but in contrast to white mica, their boron concentrations are very low in metamorphic rocks (see Chapter 7, page 123), and therefore their impact on the isotopic composition of the fluid is limited.

10.6.5. Possible source of ^{11}B-rich fluid

The formation of cm- to m-sized reaction zones rich in OH-bearing minerals including tourmaline at 20 to 30 km depth during exhumation requires large amounts of H_2O and boron. Within the melange itself, there are no possible sources for significant amounts of H_2O, since the metabasic rocks were dehydrated already on the prograde path, and because OH-bearing minerals in carbonates and schists, such as glaucophane and mica, survived the peak and retrograde metamorphism. Furthermore, the upper thermal stability of antigorite was not reached at Syros. Thus, serpentinite, which is, in principle, an important carrier of H_2O, did not dehydrate. In addition, low δ^{11}B values of minerals from high-pressure rocks not significantly affected by late-stage fluid infiltration rule out that these rocks served as a boron source for tourmaline formation. Phengite (δ^{11}B $= -11.3 \pm 1.4$‰) and metamorphic tourmaline (δ^{11}B $= +0.9 \pm 1.8$‰) in siliceous marble SY432 (see Chapter 9), antigorite (δ^{11}B $= +0.4 \pm 7.8$‰) from serpentinite SY347 (Table E.4), tourmaline from eclogite SY323 (δ^{11}B $= +2.8 \pm 1.0$‰, Chapter 9), metamorphic tourmaline from meta-sedimentary schist SY314 (δ^{11}B $= -1.6 \pm 1.1$‰, Chapter 9) from the Syros melange all show that fluids in equilibrium with these rocks would show δ^{11}B-values between –3 and +3‰ (marble, schist and eclogite) or about +13‰

Table 10.3. Chemical analyses and B isotopic compositions of phengite from tourmaline-bearing samples

Sample	SY309B	SY412	SY413	SY420
SiO_2	53.05	51.28	52.17	49.48
TiO_2	0.05	0.25	0.10	0.10
Al_2O_3	25.48	26.61	24.94	27.38
Cr_2O_3	0.13	0.03	0.10	0.07
FeO^t	2.67	4.03	4.07	3.13
MnO	0.01	0.00	0.08	0.06
MgO	4.05	3.00	3.50	3.28
CaO	0.00	0.01	0.06	0.00
BaO	*n.a.*	*n.a.*	*n.a.*	0.32
Na_2O	0.14	0.59	0.23	0.28
K_2O	10.59	10.41	10.44	10.88
H_2O*	4.54	4.50	4.48	4.43
Total	100.72	100.71	100.16	99.41

Formulas calculated to 11 oxygens

Si	3.504	3.417	3.492	3.350
Ti	0.012	0.005	0.005	0.026
Al	1.983	2.089	1.967	2.185
Cr	0.007	0.002	0.005	0.004
Fe^{2+}	0.148	0.224	0.228	0.177
Mn	0.001	0.000	0.004	0.003
Mg	0.399	0.298	0.349	0.331
Ca	0.000	0.001	0.004	0.000
Ba	*n.a.*	*n.a.*	*n.a.*	0.008
Na	0.018	0.076	0.030	0.037
K	0.892	0.885	0.891	0.940
OH	2.000	2.000	2.000	2.000
Total	6.954	7.005	6.977	7.039
X_{Mg}	0.730	0.570	0.605	0.652

Boron isotope values determined by SIMS

δ^{11}B	+6.6	+11.6	+9.9	+6.5
$2RSD_{mean}$	1.6	4.1	1.5	3.2
n	2	7	5	9

* H_2O calculated stoichiometrically. FeO^t = total iron as FeO. $X_{Mg} = Mg/(Mg + Fe^{2+})$. δ^{11}B values given relative to SRM951 (Catanzaro *et al.*, 1970). $2RSD_{mean} = 2\times$ relative standard deviation of the mean. n = number of isotope analyses. n.a. = not analysed.

(serpentinite), and therefore significantly lower than required for the blackwall formation. Thus, it is concluded that H_2O and boron were introduced into the melange from external sources.

Modern geodynamic models involve a wedge or channel of exhuming rocks, which is located between the subducting and the overriding plate (Liou *et al.*, 1997; Guillot *et al.*, 2001; Engi *et al.*, 2001; Rubatto & Hermann, 2001; Ernst, 2001; Roselle & Engi, 2002; Ring & Fleischmann, 2002; Gerya *et al.*, 2002; Jolivet *et al.*, 2003). Slices of H*P* rocks, sheared off from the subducting plate and tectonically mixed with serpentinites from the hanging plate may be rapidely exhumed in these exhumation channels, while the subduction system is still active. Therefore, fluids released from the subducting plate will enter the overlying exhumation channel and rehydrate H*P* rocks on their way back to the surface. The source of B-rich fluids fluxing into the Syros melange is most likely also located within the plate, which continued to subduct during the exhumation of the Syros melange (Fig. 10.7).

10.6.6. B budget of fluids and rocks during dehydration

As reviewed in the introduction, the major hosts of B in oceanic crust prior to subduction are low-temperature altered basalts, serpentinites that interacted with seawater at low temperatures and sediments, as well as pore water within sediments and altered basalts. B therefore is stored in the uppermost part of the subducting slab, in the same reservoirs that bear the majority of H_2O in the slab. However, among these reservoirs, high $\delta^{11}B$ values ($> +5\%o$) were found only in pore water, low-temperature altered basalts and serpentinites. B in altered basalts is mainly stored in clay minerals, either in their crystal structures or adsorbed on their surfaces. This leads to (i) the loss of B during diagenesis and early metamorphism and (ii) release of major amounts of B during the onset of subduction. Loss of pore water, adsorbed and crystalline water from low-grade minerals (clay minerals) at temperatures below $150\,^{\circ}C$ will strongly fractionate the B isotopes and will lead to a rapid decrease of B concentrations and $\delta^{11}B$ values within the subducting material.

In order to model this fractionation, an average partition coefficient of B between fluid and restitic rock is required, as well as the temperature-dependent B isotopic fractionation, water and B contents and B isotopic composition of the rock prior to subduction. In this study, the isotopic fractionation given by Equation 10.7 is used. For the composition of the starting rock, both high $\delta^{11}B$ values ($+10\%o$) and B concentrations ($200\,\mu g/g$) were used, which are on the high end of the range observed in low-temperature altered oceanic basalts and in clay-rich sediments. Whole rock/fluid partition coefficients for B are not published in the literature and have to be estimated. Fig. 10.8 shows the B concentrations (Fig. 10.8a) and isotopic com-
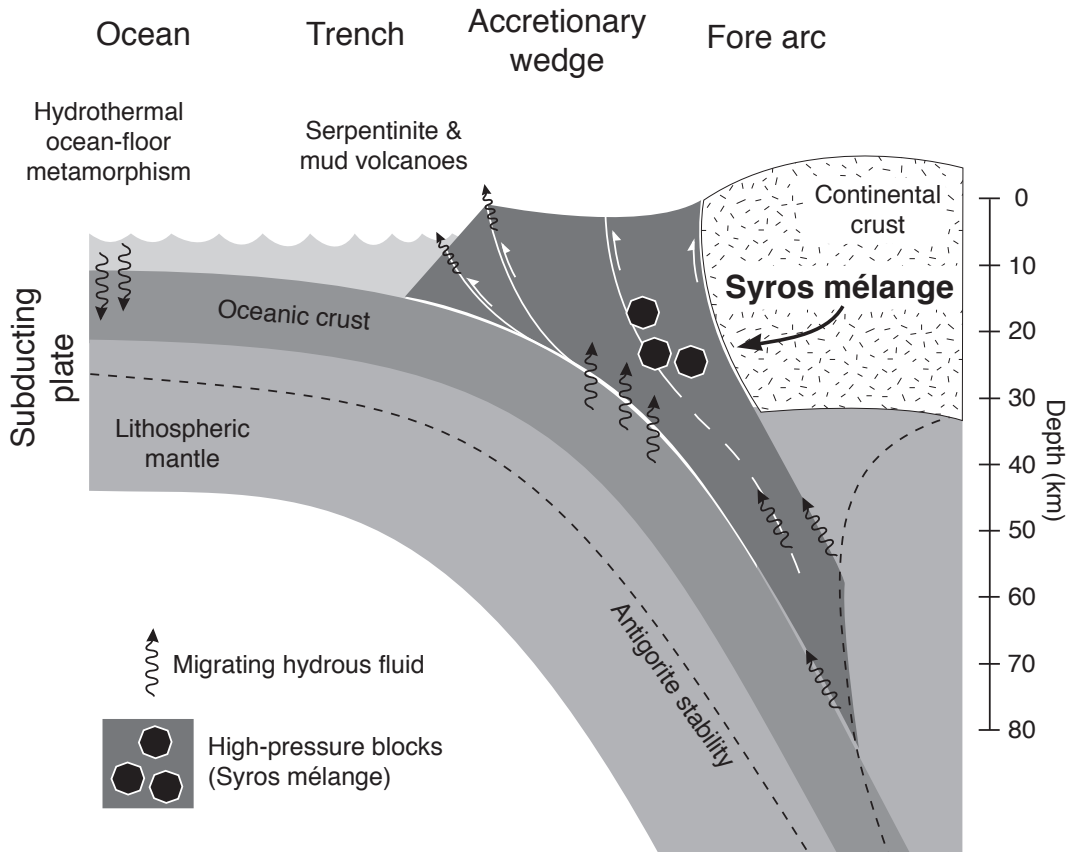
Fig. 10.7. Sketch of vertical cross-section through a subduction zone displaying the exhumation channel located between the subducting slab on the left and the overlying plate on the right. High-pressure rocks, now exposed on the island of Syros were rehydrated during their exhumation by aqueous fluids, probably released from the progressively subducted slab.

Table 10.4. Input parameters and calculated B concentrations and δ^{11}B values for the model dehydration of subducted altered oceanic crust and H_2O-rich sediments

| | Starting rock | after 1st dehydration step $T = 100\,^{\circ}$C | | | | after 2nd dehydration step $T = 200\,^{\circ}$C | | | |
| | | $D_B = 0.1$ | | $D_B = 0.01$ | | $D_B = 0.1$ | | $D_B = 0.01$ | |
		rock	fluid	rock	fluid	rock	fluid	rock	fluid
H_2O (wt %)	20	10		10		5		5	
B (μg/g)	200	100	1000	17	1670	68	680	16	1610
δ^{11}B (‰)	+10.0	-5.0	+22.3	-15.2	+12.1	-12.2	+8.1	-22.2	-1.9

D_B = whole rock/fluid partition coefficient for B. 1st dehydration step calculated for $100\,^{\circ}$C and two different values for D_B. 2nd dehydration step calculated for $200\,^{\circ}$C and two different values for D_B. Starting point for second step are results from $D_B = 0.1$ from 1st step.
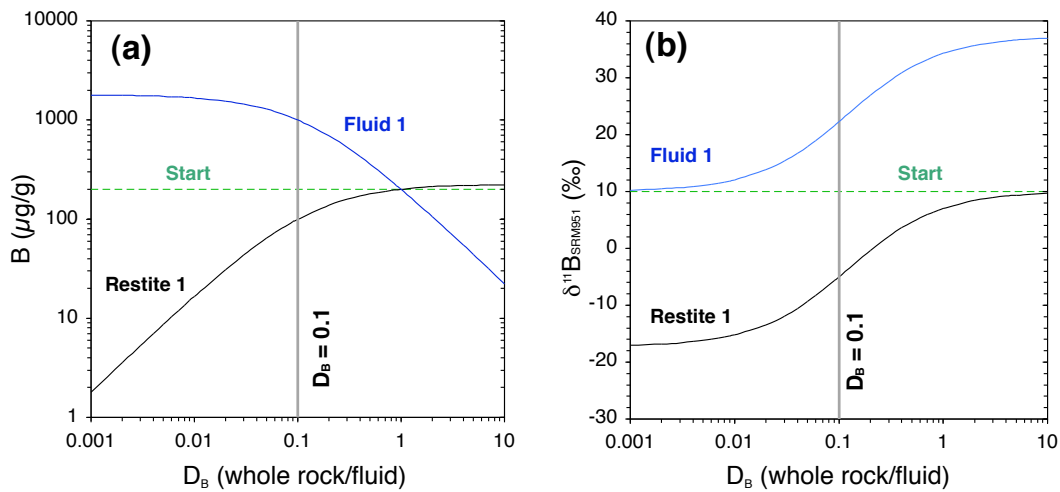
Fig. 10.8. a The diagram displays the calculated B concentrations of starting material (dashed green line), restitic material (black) and escaping fluid (blue) for batch dehydration as a function of whole rock/fluid B partition coefficient D_B. Vertical grey line marks partition coefficient D_B of 0.1. **b** Diagram showing δ^{11}B value vs whole rock/fluid B partition coefficient, displaying the calculated B isotopic composition of starting material (dashed green line), restitic material (black) and escaping fluid (blue). Vertical grey line marks partition coefficient D_B of 0.1. Calculations are based on parameters given in Table 10.4 for first dehydration step.

positions (Fig. 10.8b) of fluid and restitic rock as functions of the whole rock/fluid partition coefficient D_B during dehydration of a starting rock of the above mentioned composition (for parameters see first dehydration step of Table 10.4). In principle, three different areas should be distinguished in Fig. 10.8, with respect to D_B: (i) In the range of high mobility ($D_B \sim 0.001$ to 0.01) almost all B is leaving the rock, producing a B-rich fluid and a nearly B-free restite. B isotopic composition of the fluid is similar to the starting rock ($+10$‰ in this case). (ii) In the range of refractory behaviour ($D_B > 1$), B concentration and isotopic composition of the restite are similar to the starting rock, while the fluid shows a very high δ^{11}B value, but a rather low concentration of B. (iii) The range of moderate mobility between 0.01 and 1 produces a fluid with both high δ^{11}B value and high B content along with a restite with moderate B concentration and a δ^{11}B value, which is significantly lower with respect to the starting rock. It is generally accepted that significant amounts of B are lost during diagenesis and early metamorphism and that B is readily transported by hydrous fluids (Moran *et al.*, 1992; You *et al.*, 1996; Leeman, 1996; Bebout, 1996; Bebout *et al.*, 1999; Deyhle & Kopf, 2002; Kopf & Deyhle, 2002). Therefore, the presented model includes low whole rock/fluid partition coefficients between 0.01 and 0.1. All parameters used and the results of the calculations are shown in Table 10.4 and Fig. 10.9.

The first fluids are characterised by both high B concentrations and δ^{11}B values, as would be expected from a water- and B-rich source. However, subsequently released fluids show δ^{11}B values below $+10$‰ (Fig. 10.9), i.e. significantly lower than those required for tourmaline formation in the blackwalls from Syros. Although the model starts with an "endmember" source (i.e. high B concentration and high δ^{11}B value), the δ^{11}B values of fluids released from this material rapidly decrease after initial dehydration. As the highest B concentration and ^{11}B enrichment is found in low-temperature altered basalts, stored in clay minerals and pore water, the first release of fluid is likely to occur at very low temperatures during recrystallisation below 150 °C. Altogether it seems highly unlikely that the subducting slab is able to release fluids with δ^{11}B values of $+28$‰ or even $+18$‰ at depths of 25 km.

10.6.7. B budget of fluids migrating through the exhumation channel

As shown in the preceding section 10.6.6, the observed extreme enrichment of ^{11}B in the Syros blackwalls rules out any model that assumes tourmaline formation by direct precipitation from unmodified fluids generated by subduction-related dehydration. In order to solve this problem, we have to bear in mind that the exhuming melange most likely was separated from the subducting plate by several kilome-
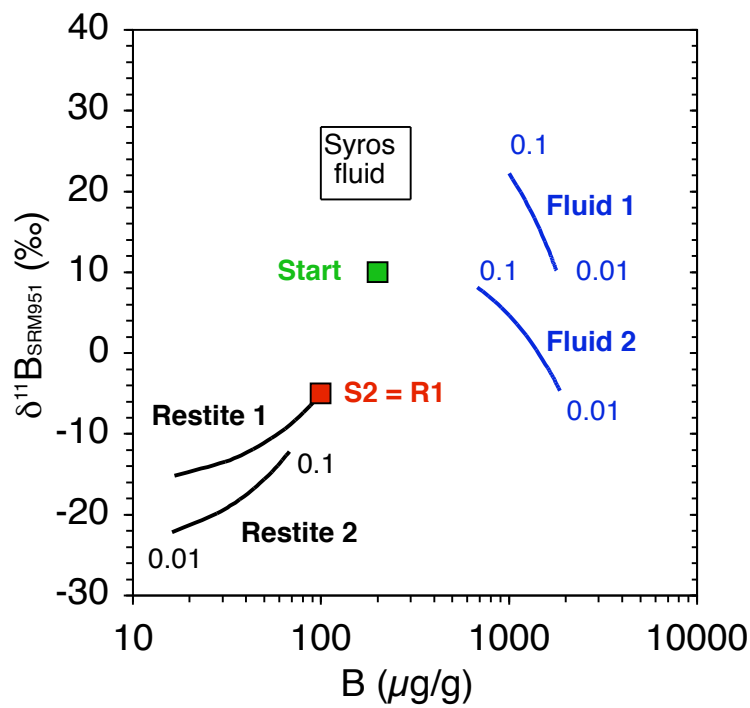
Fig. 10.9. δ^{11}B values and B concentrations reached during modelled dehydration of silicate material in terms of B isotopic composition and concentrations of starting material, restitc material and escaping fluids. Lines define range of results for different rock/fluid partition coefficients D_B between 0.1 and 0.01. Two subsequent stages of dehydration are shown (fluids and restites 1 and 2). S2 marks starting point for second stage, which results as a restite R1 from first dehydration stage with $D_B = 0.1$. Calculations are based on parameters given in Table 10.4.

ters of ductile material (mica-, chlorite- and/or serpentinite-rich rocks forming the "exhumation channel" and the "accretionary wedge"), rather than being in direct contact to it. Therefore, fluids escaping from the upper regions of the subducting slab had to migrate through the a thick pile of rocks before they reached the Syros melánge. On their way, these fluids must have been substantially modified. The model presented below is an approach to predict the changes in both B concentration and B isotopic composition in the fluid during its migration from the slab to the exhuming high-pressure blocks, i.e. the site of tourmaline formation.

The rock materials composing the exhumation channel (hereafter called "filter rock") are assumed to be already saturated in H_2O prior to (further) fluid migation and will thus not remove H_2O from the fluid. H_2O-undersaturated filter rocks could also be included in the model and would result in a passive enrichment of B in the remaining fluid. Significant passive enrichment of B can only occur in cases where H_2O is quantitatively reduced by more than $\sim 80\%$. As such an enrichment has no impact on the isotopic composition of the fluid, it was not considered in the model calculations presented below.

The model comprises a succession of individual steps of fluid-rock interaction with a consecutive change of input parameters for each step. The mass of filter rocks between the fluid source and the site of tourmaline formation is subdivided into a number of volumes and it is assumed that during migration through each rock volume complete equilibration between fluid and rock (with respect to B concentration and isotopic composition) is achieved. The resulting characteristics of the fluid generated through step n serve as starting parameters for step $n+1$. Such a succession of fluid/rock interaction steps is on the one hand easy to calculate and allows for a control of the impact of different parameters, and, on the other hand, it is thought to reasonably represent the actual processes affecting the composition of the migrating fluid.

It is assumed that B in the filter rock is incorporated in minerals – serpentine, mica, amphiboles – in which it is tetrahedrally coordinated, while the fluids are probably acidic and therefore contain B in $B(OH)_3$ groups. B isotopic fractionation between filter rock and fluid was assumed to be determined by a change in coordination from trigonal in the fluid to tedrahedral in the rock and calculated using the formula given by Hervig *et al.* (2002) (Equation 10.7). Other input parameters included in modelling of the distillation process are (i) the temperature of the rocks along the migration path, (ii) the whole rock/fluid partition coefficient for B (D_B), (iii) B concentration and isotopic composition of the filter rock prior to the fluid flux, and (iv) B concentration and isotopic composition of the fluid at its starting point, i.e. when it is leaving the dehydrating slab, and (v) the fluid/rock ratio during interaction of migrating fluids with the filter rock. At first glance, one might

Table 10.5. Parameters used for modelling fluid-rock interaction for fluids ascending through the exhumation channel, and results for B concentrations and $\delta^{11}B$ values of fluids

	Starting fluid	Filter rock	$T = 200\,°C$ after increment No.				$T = 400\,°C$ after increment No.			
			5	25	100	equil.	5	25	100	equil.
B (µg/g)	680	10	460	154	100	100	460	154	100	100
$\delta^{11}B$ (‰)	+8.1	0	+16.4	+31.4	+20.4	+20.3	+13.0	+20.7	+12.6	+12.6

Calculation for $D_B = 0.1$ (whole rock/fluid partition coefficient) and $F/R = 1$ (fluid/rock mass ratio of each increment). Results were calculated for $T = 200\,°C$ and for $T = 400\,°C$. Columns "equil." refer to fluid in equilibrium with the non-influenced filter rock ($\delta^{11}B = 0‰$, $c_B = 10\,µg/g$).

think that the number of unknowns is too high for a meaningful model calculation, but a closer inspection reveals that the reasonable range of variation of some input parameters is rather restricted and the impact of others can be clearly evaluated.

The temperature of the high-pressure blocks was ~400 °C at the time of tourmaline formation, as demonstrated above. They were located at a depth of ~25 km at that time. The subducting slab, releasing the hydrous B-bearing fluids must have been at least at the same depth. However, temperature in the upper part of the slab is lower than in the exhumation channel, as exhuming rocks are transporting heat advectively from greater depth towards the surface, while the slab is cool as it subducts. Isotherms are therefore bended upwards in the exhumation channel, but downwards in the slab. Temperatures during dehydration in the slab might therefore be much lower than during rehydration in the overlying channel. Therefore, the filter model was calculated for a temperature of 400 °C, but also for a lower temperature of 200 °C, and for a fluid that is released at 200 °C and continuously heated to 400 °C as it reaches the H*P* blocks. The results for this heating path are located simply between the 200 °C and the 400 °C paths, and are not shown in the diagrams. The strong temperature dependence of B isotope fractionation results in a significant difference between the two calculations for 200 °C and 400 °C, as is displayed in Fig. 10.10.

Partition coefficients of B between hydrous fluid and rocks were discussed in section 10.6.6. B is enriched in fluids relative to the rocks. The calculations in section 10.6.6 for slab dehydration were performed for D_B between 0.01 and 0.1. For the filter rock, possibly being rich in sheet silicates, a partition coefficient of 0.01 might be too low. Therefore, calculations were performed for $D_B = 0.1$ (Fig. 10.10a) and $D_B = 0.05$ (Fig. 10.10b). A larger partition coefficient will result in a more intense and rapid change of fluid composition. The change in $\delta^{11}B$ and B concentration of the fluid for $D_B = 0.1$ is more pronounced than for $D_B = 0.05$.
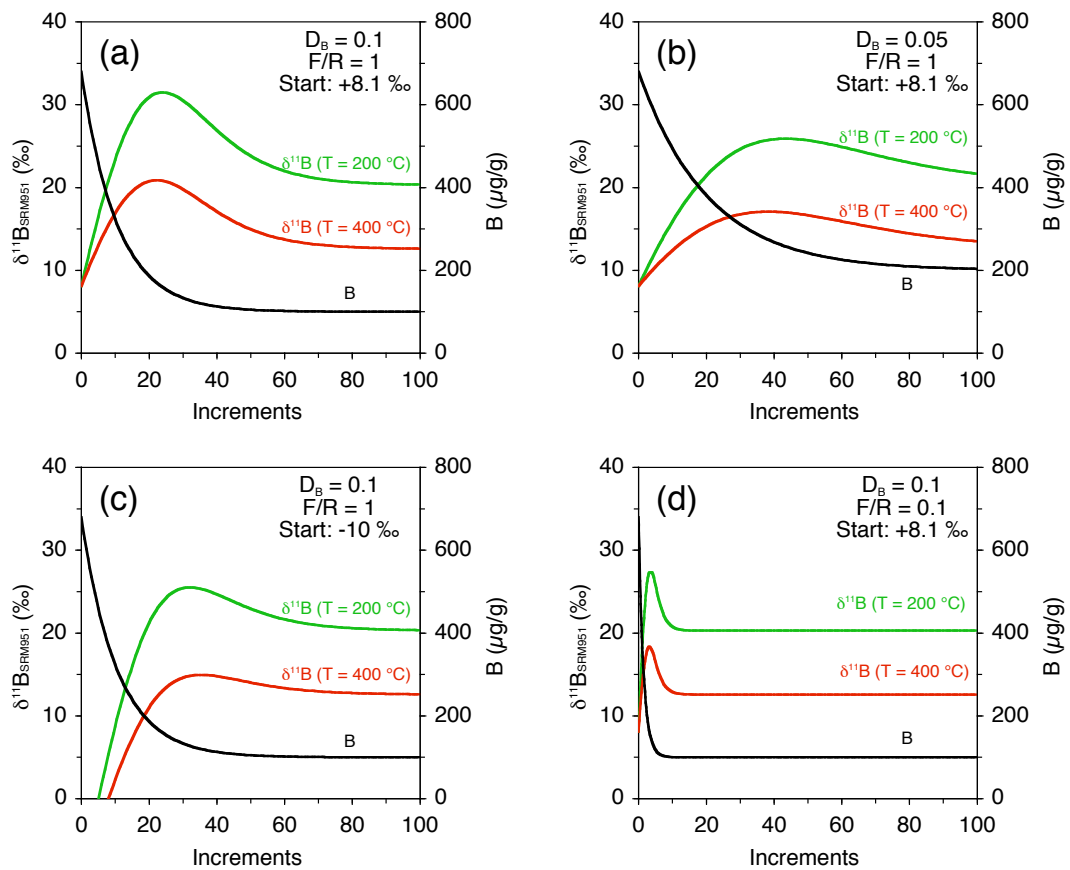
Fig. 10.10. Diagrams displaying results of model on fluid-rock interaction with respect to B isotopic composition (red and green line) and B concentration (black line) of evolving fluids for two different temperatures of 200 °C and 400 °C. Different diagrams are calculated for different input parameters: **a** whole rock/fluid partition coefficient $D_B = 0.1$, fluid/rock mass ratio of each increment $F/R = 1$ and δ^{11}B of starting fluid $= +8.1‰$ **b** $D_B = 0.05$, $F/R = 1$, δ^{11}B $= +8.1‰$ **c** $D_B = 0.1$, $F/R = 1$, δ^{11}B $= -10.0‰$ **d** $D_B = 0.1$, $F/R = 0.1$, δ^{11}B $= +8.1‰$

The B isotopic composition of the filter rock is not known, but its δ^{11}B value is assumed to be above the mantle value ($\sim -6\%o$), as serpentinites or other hydrated rocks are generated by hydrous fluids in the subduction zone. These fluids generally show enrichment in ^{11}B, as was shown in the dehydration calculation above. In order to keep the results of the filter model more transparent, the calculation is performed with δ^{11}B $= 0\%o$ for the filter rock. More realistic, the values may range to much higher values, up to $+15\%o$, as was measured in serpentinites from forearc seamounts at the Mariana island arc by Benton *et al.* (2001). However, starting the calculation with a higher δ^{11}B value in the filter rock, simply shifts the fluid in the same direction. B concentration was assumed to be $10\,\mu$g/g, which is higher than B concentrations in Syros serpentinites, but lower than in the mica-bearing blueschists. Significantly higher B concentrations in the filter rock lead to a very rapid isotopic equilibration of the fluid to the filter rock. The system in this case is controlled by the filter rock from the beginning.

The parameters for the fluid are taken from the dehydration model, described in section 10.6.6. B concentration ($680\,\mu$g/g) and isotopic composition (δ^{11}B $= +8.1\%o$) of the fluid are the values produced after the second dehydration step (Table 10.4) with a D_{B} of 0.1. In order to estimate the impact of a completely different starting composition of the fluid, the calculation was also performed for δ^{11}B $= -10.0\%o$ (Fig. 10.10c).

The incremental fluid/rock ratio is the parameter with the highest uncertainty and may also vary along the migration path of the fluid. Flow along discrete pathways ('veins') causes very high fluid/rock ratios, while percolation through the rock along grain boundaries results in much lower fluid/rock ratios. Due to the lack of detailed information on the mechanisms of fluid transport and fluid/rock ratios, the calculations are performed for a value of 1 (by mass). The influence of this parameter on the results can be estimated from a second calculation for a value of 0.1 (by mass), displayed in Fig. 10.10d.

Independent from the input parameters, the resulting concentrations and isotopic compositions of the fluids show a similar characteristic evolution. During the first increments, B concentration of the fluid is rapidly decreasing, while the ^{11}B/^{10}B ratio rapidly increases to very high values. This peak in δ^{11}B is reached at a point, where the B concentration of the fluid is already low and close to equilibrium with the unaffected filter rock. After the peak in isotopic composition, the δ^{11}B of the fluid is decreasing until it reaches equilibrium with the unaffected filter rock. In the calculation with the standard parameters ($D_{\text{B}\,start} = 0.1$; $F/R = 1$; δ^{11}B$_{start} =$ $+8.1\%o$), the fluid reaches a δ^{11}B of $+31.4\%o$ for $T = 200\,^{\circ}$C and $+20.7\%o$ for $T = 400\,^{\circ}$C after 25 increments (Fig. 10.10a and Table 10.5). After $\sim$70 increments, B isotopic composition and B concentration of the fluid are close to equilibrium

with the unaltered filter rock and any information of the starting composition is lost. During the first increments, the B concentration of the fluid is still high and the B isotopic composition of the system is controlled largely by B from the fluid. Therefore, the δ^{11}B value is steadily increasing. As soon as the B concentration of the fluid is low enough, the B in the filter rock is controlling the system and the isotopic ratio of the fluid decreases towards the equilibrium value. For parameters other than the standard ones (Table 10.5), the peak of the curve is shifted to an earlier or later increment and to higher or lower δ^{11}B value. For a lower fluid/rock ratio of 0.1 the peak is at 18.3‰ (for 400 °C) after the third increment and the fluid values are indistinguishable from equilibrium already after ~10 increments (Fig. 10.10b). For a lower partition coefficient of $D_B = 0.05$ the peak is at 17.1‰ (for 400 °C) after increment #40, but reaches the equilibrium only after more than 100 steps (Fig. 10.10c). For a much lower isotopic starting composition of −10‰, the fluid nevertheless reaches a very high δ^{11}B value of +15.0‰ (for 400 °C) after ~35 increments and a value indistinguishable from equilibrium after ~70 increments (Fig. 10.10d).

Although an exact quantification of fluid modification with respect to B concentration and isotopic composition is by no means possible, the model calculations presented above clearly show that the extraordinarily high δ^{11}B values observed in blackwall tourmaline from Syros can indeed be generated by tourmaline precipitation from slab-derived fluids that were modified during migration through filter rocks in the exhumation channel. The low SiO_2 acitivity of the blackwall rocks as deduced above (section 10.3) may be taken as evidence for an interaction of the fluid with serpentinite on its way through the exhumation channel. Fig. 10.11 displays again the results of the calculation using the standard parameters ($D_B = 0.1$; $F/R = 1$; $B_{start} = 680\,\mu g/g$; $\delta^{11}B_{start} = +8.1‰$). The comparison with the estimated composition of the tourmaline forming fluids from Syros shows, that the modeled fluid composition reaches the Syros tourmaline field after 10 to 15 increments.

10.7. Summary and conclusions

HP blocks enclosed in the melange on the island of Syros are rimmed by reaction zones composed of hydrous minerals, such as chlorite, Na- and Ca-amphibole, clinozoisite and phengite in paragenesis with omphacite, albite and tourmaline. Chemical composition of tourmaline is similar among the different blackwalls and is close to the ideal schorl-dravite series. X_{Mg} ranges from ~ 0.58 to ~ 0.82, which classifies the tourmaline as dravite. B isotopic composition of tourmaline is unusually
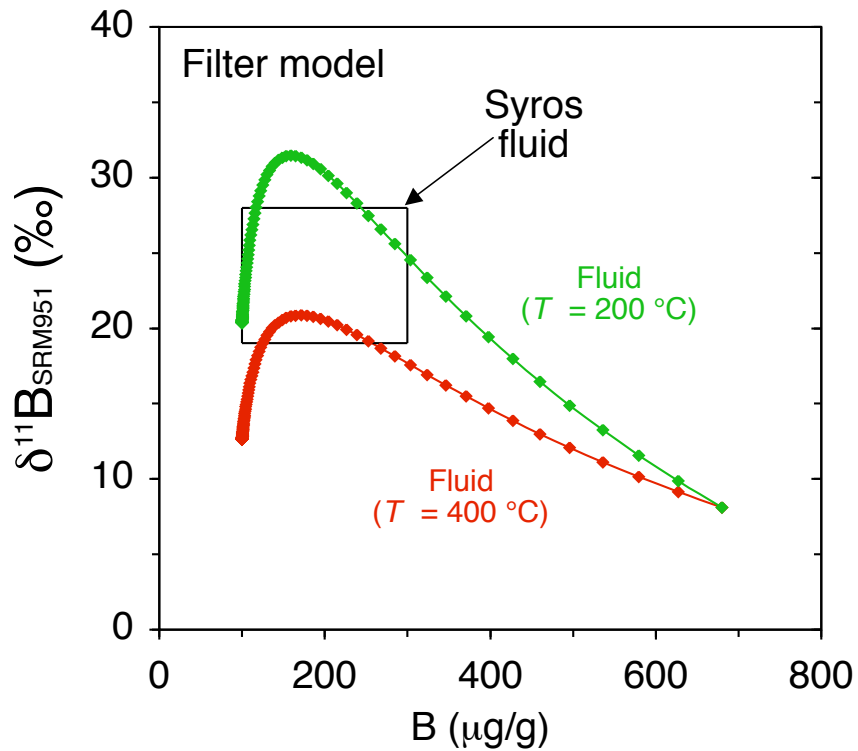
Fig. 10.11. δ^{11}B vs B concentration for fluids interacting with rocks during their ascent from the dehydrating slab through the exhumation channel. Parameters and results are equal to Fig. 10.10a: $D_B = 0.1$, $F/R = 1$, δ^{11}B $= +8.1$‰. The box shows estimated B concentration and B isotopic composition of tourmaline-forming fluids on Syros. Green and red lines show evolution of fluid for temperatures of 200 °C and 400 °C, respectively. Each point on the lines represents one increment of fluid-rock interaction. Lines start on the right side with parameters defined from the dehydration calculation (Table 10.4) and end on the left side at a point where fluid and filter rock are close to equilibrium.

heavy with δ^{11}B values exceeding $+18\permil$ in all investigated samples, reaching a unique value of $+28.4\permil$ in sample SY442, which is extending the range of δ^{11}B values reported from natural tourmalines by more than $5\permil$ (based on a value of $+23\permil$ reported by Swihart & Moore (1989) from meta-sedimentary tourmaline).

Blackwalls formed during exhumation of the HP melange at a depth of $20-25$ km at $P-T$ conditions of $\sim 0.6-0.75$ GPa and $400-430\,°C$, by influx of external hydrous fluids. Tourmaline-bearing blackwall rocks are quartz free and show SiO_2 activities of 0.4 to 0.5, generated during interaction of the rocks with low-SiO_2 fluids. Composition of the fluids are estimated to be in the range of $100-300\,\mu g/g$ B and δ^{11}B values of $+18$ to $+28\permil$.

H_2O and B in the fluids are likely to originate from the subsequent slab that was still subducting as the Syros melange was exhumed. The high δ^{11}B of tourmaline in the blackwalls cannot be explained by tourmaline formation from unmodified slab-derived fluids, because all known reservoirs in subducting slabs would produce a fluid with δ^{11}B below $+10\permil$ at depths exceeding 20 km. Interaction of the fluid with material composing the exhumation channel on its way from the dehydrating slab to the site of tourmaline formation in the blackwalls would produce exceptionally high δ^{11}B values in the fluids. This process is expected to take place within the subduction setting and is therefore favoured in this study to explain the ^{11}B enrichment in Syros tourmaline. The calculated model demonstrates that fluids are rapidly modified in both trace element and isotopic composition during their migration through the material overlying the subducting slab. Differences in B isotopic composition and concentration are blurred quickly and wiped out after short distances of migration, when the fluid is approaching equilibrium with the rock composing the exhumation channel.

The fixation of B, especially with an isotopic composition affected by earth's surface processes, was already emphasised by Nakano & Nakamura (2001), who investigated the B budget of metasedimentary rocks. They claimed, that B is immobilised within the rocks as soon as it is fixed in tourmaline, which results in deep subduction of B into the mantle. However, the isotopic ratio of tourmaline within the meta-sedimentary high-pressure rocks is relatively low. The tourmalines studied so far by Nakano & Nakamura (2001), Bebout & Nakamura (2003) and this study from Syros (see Chapter 9 on tourmaline in meta-sediments, page 173) range from $-16\permil$ to $+2\permil$ for prograde growth zones, and reach a maximum of $+8\permil$ for retrograde growth zones. Furthermore, the grain size of tourmaline in most HP metamorphic rocks is restricted to $\sim 500\,\mu m$ and the modal abundance of tourmaline is small ($\sim 0.1\,\%$). In contrast, blackwall tourmaline from Syros has a large grain size (several cm), high abundance, and an exceptionally high δ^{11}B value, which is significantly different from the mantle value of $\sim -6\permil$. It is important to note that

the blackwall tourmaline formed on the retrograde $P - T$ path during exhumation of the rocks. One might therefore argue that blackwall tourmaline is not relevant for deep subduction processes. However, the formation of tourmaline at the contact between mafic or felsic HP blocks and ultramafic matrix by fluids released during dehydration reactions in the subducting slab may also take place on the prograde path, wherever fluids are migrating through such contact zones, i.e. the slab-mantle interface. If this is the case, the formation of blackwall tourmaline has a significant impact on the geochemical cycle of B in subduction zones, as it is fixing heavy B in large quantities in the slab within a highly stable mineral.

11. Trace element composition of blackwall tourmaline

Tourmaline, produced by metasomatic reactions in high-pressure metamorphic rocks from Syros are described and investigated for their B-isotopic composition in Chapter 10. This chapter contains in-situ trace element data from Syros tourmaline, determined by EPMA and SIMS in Heidelberg and by Laser-ablation ICP-MS at the University of Bristol in cooperation with Bruce Paterson (Bristol). First results of this study were presented at the GEO2002 joint meeting in Würzburg, Germany (Marschall *et al.*, 2002b).

11.1. Introduction

Tourmaline has a large stability with respect to P and T (Chapter 9) and is common in many sedimentary, metamorphic and magmatic rocks (e.g. Henry & Dutrow, 2002; London & Evensen, 2002). Apart from that, the high mobility of B – the critical constituent of tourmaline – in hydrous fluids leads to a widespread formation of this boro-silicate during hydrothermal and metasomatic processes. Especially the occurrence of tourmaline in hydrothermal ore deposits has attracted many workers to investigate its trace element composition, and use it for a prospection on base metal deposits (Griffin *et al.*, 1996; Slack, 2002; Jiang *et al.*, 2004, and references therein). The crystallography of tourmaline is relatively complicated, with various cation and anion sites, expressed in the general formula

$$X_{0-1}Y_3Z_6[Si_6O_{18}](BO_3)_3V_3W. \tag{11.1}$$

This may lead to the suggestion that the tourmaline structure should be tolerant for a large variety of elements, and one might expect high concentrations of trace elements in this mineral. However, a distinction is necessary between the variable mineral group of tourmaline and the much more restricted range of compositions found in high-pressure metamorphic rocks. Equivalent to the mineral group of amphiboles, which also shows a large number of different compositions, the Na-Mg-Al variety – glaucophane – occuring in HP metamorphic rocks is rather restricted in its major and trace element composition. The chemistry of Na-Mg-Al tourmaline – dravite – is to a certain degree comparable to glaucophane. It will be demonstrated

in this chapter that Mg-rich dravite found in Syros rocks is chemically highly selective and excludes a large number of trace elements from its structure.

Despite the potential of tourmaline for economical applications, there is a very limited number of in-situ data on trace element abundances in tourmaline in the literature. Bulk-rock analyses and analyses of mineral separates by wet chemical methods, XRF, INAA, ICP-MS or ICP-OES have been published repeatedly. However, the results of such analyses are burdened with the problem of fluid and solid inclusions. In particular, inclusions of accessory minerals, like monazite, allanite, zircon, rutile, cassiterite and sulphides have been recognized to occur in tourmaline (e.g. Taylor & Slack, 1984; Koval *et al.*, 1991; Jiang *et al.*, 2004), which strongly contaminate the tourmaline analyses with a number of "trace elements". The published values on "trace elements" in tourmaline determined by bulk methods are therefore suitable only as maximum concentration values, as stated by Henry & Dutrow (2002).

In-situ analyses of tourmaline are routinely performed by electron microprobe (EPMA) at a number of laboratories. The disadvantage of EPMA however is its relatively high detection limit for most elements (i.e. several tens to hundreds of $\mu g/g$) and the disability to analyse light elements (Li, Be, B). A combination of EPMA with other in-situ methods is therefore advisable, but has been used only in a very limited number of studies.

Harris *et al.* (1992) analysed tourmaline from anatectic gneisses and leucogranites by SIMS and found very low concentrations of Rb, Ba, Zr, Nb, U, Th, Y and the REE, but higher concentrations of Sr. Griffin *et al.* (1996) analysed tourmaline crystals from massive sulfide deposits and tourmalinites by proton microprobe (PIXE; proton induced X-ray emission). A large number of elements were analysed in situ with high lateral resolution in a large number of samples. The disadvantage of the proton microprobe is its large penetration depth. Griffin *et al.* (1996) had to correct the results from analyses performed on thin sections for the signal contributed by the glass slides. Unfortunately, concentrations of some elements in the glass slides were significantly higher than in tourmaline (e.g. $49\,\mu g/g$ Rb, $426\,\mu g/g$ Ba, $350\,\mu g/g$ Zr) introducing large uncertainties to the analyses of these elements. However, the authors report high abundances of Cr, Ni, Cu, Zn, Ga, Sr, Sn and Pb for many tourmaline samples.

Tourmaline from blackwalls found on the island of Syros frequently occurs as large grains of mm to cm size and shows very limited zonation in major elements and B isotopes (Chapter 10). Many samples contain little or no inclusions. These samples are therefore ideal for in-situ analyses by SIMS and LA-ICP-MS. Tourmaline occurring in different high-pressure rocks from various localities is generally dravitic in composition (Schreyer, 1985; Reinecke, 1998; Bebout & Nakamura,

2003; Altherr *et al.*, 2004, and Chapters 9 and 10). The Syros blackwall tourmaline is therefore thought to be representative for tourmaline in high-pressure metamorphic rocks. The results of analyses of Syros dravite will provide information on the impact of tourmaline on the budget of trace elements in high-pressure metamorphic rocks.

11.2. Investigated samples

11.2.1. Tourmaline-bearing rocks

H*P* blocks enclosed in the mafic-ultramafic mélange on the island of Syros (Chapter 3) are rimmed by reaction zones composed of hydrous minerals, such as chlorite, Na- and Ca-amphibole, clinozoisite and phengite in paragenesis with omphacite, albite and tourmaline. Six blackwall samples investigated in this study (Table 11.1) were taken from different localities within the Syros mélange. They all contain significant amounts of tourmaline, forming mm-thick tourmaline-rich layers on the surface of the high-pressure blocks, or more evenly distributed single crystals or clusters of crystals within them. Three samples (SY309B, SY401B, SY420) are schists from the matrix, that contain tourmaline-rich layers or veins. Tourmaline in all samples is euhedral and does not show any sign of brittle or ductile deformation. In thin section, the grains commonly show visible zonation. Colours of the pleochroic cores range from colourless to blue, while those of the rims vary from pale pink to green (Fig. B.5d on page 302). Resorption of core domains and replacement by rim material is restricted, while resorption of rim domains was never observed. Cores and rims of tourmaline from all samples were analysed for Ti, V, Mn, Co, Cu, Zn, Ga, Rb, Sr, Y, Zr, Nb, Cs, Ba, the REE (La to Lu), Hf, Ta, W, Pb, Th and U by laser-ablation ICP-MS. As described in Chapter 10, the light elements H, Li, Be and B were analysed by SIMS and Si, Ti, Al, Cr, Fe, Mn, Mg, Ca, Zn, Na, F and Cl were determined by EPMA. Minerals occurring in paragenesis with tourmaline like omphacite, glaucophane, phengite, chlorite, epidote, allanite, rutile and titanite were also analysed in some samples in the same way. Analyses of dravite are compared to respective whole-rock abundances, in order to demonstrate which of the trace elements are enriched and which are depleted in dravite.

Blackwalls formed during exhumation of the H*P* mélange at a depth of $20 - 25$ km at $P - T$ conditions of $\sim 0.6 - 0.75$ GPa and $400 - 430$ °C, by influx of external hydrous fluids. H_2O and B in the fluids are likely to originate from the subsequent slab that was still subducting as the Syros melange was exhumed (see Chapter 10).

Table 11.1. List of tourmaline-bearing blackwall samples investigated for trace elements

Sample	Rock type	Mineral assemblage
SY309B	Gln schist*	Omp, Chl, Gln, Phe, Ab, Czo, Ttn, Rt, Ap, Aln
SY400	Omp-Chl fels	Omp, Chl, Phe, Czo, Ttn, Rt, Ap
SY401B	Gln schist*	Omp, Chl, Gln, Phe, Ab, Czo, Ttn, Rt, Ap, Aln
SY412	Eclogite**	Omp, Chl, Phe, Ab, Bt, Ttn, Rt, Ap
SY413	Gln schist	Omp, Chl, Gln, Phe, Ab, Czo, Ttn
SY420	Phe-Ep-Grt schist	Grt, Chl, Phe, Ab, Czo, Ttn, Rt, Aln

* SY309B and SY401B are layers of $Tur + Omp + Chl + Ab + Phe$, formed within a glaucophane schist consisting of $Gln + Czo + Phe + Ttn$. ** SY412 is a former eclogite, the parageneses of which is partly replaced by the assemblage $Tur + Bt + Chl + Ab + Phe$.

11.2.2. Major element composition of tourmaline

Apart from X_{Mg} [$= Mg/(Mg + Fe^{2+})$], variation of tourmaline chemical composition among the different samples is very restricted (Chapter 10). Formula calculations of 31 oxygens and total Fe as Fe^{2+} result in 5.87 to 5.97 Si, 5.81 to 6.05 Al, 3.06 to 3.12 B and 2.95 to 3.27 ($Mg + Fe + Ti$) per formula unit. Fe^{2+}/Fe^{3+} ratios in Syros blackwall tourmaline are discussed in Marschall *et al.* (2004c). TiO_2 contents are between 0.12 and 0.71 wt% and vary between the different zones of the crystals that were distinguished by colour in thin section. Ti contents are lowest in the light blue cores and higher in the dark green zones. The X-site is (almost) completely occupied by $(Na + Ca) \geq 0.97$ cpfu, being highly dominated by Na (0.94 to 0.97 cpfu) with only minor Ca (0.02 to 0.05 cpfu). Analyses of F, Cl and H contents revealed no detectable Cl, only minor F (0.05 to 0.10 pfu) and high OH contents, basically > 3.5 OH pfu, in most cases > 3.75 OH pfu. Boron contents in excess of 3.00 cpfu in dravite, as well as high Na and OH contents are discussed in Marschall *et al.* (2004c). The calculated formulae are very close to the ideal schorl-dravite solid solution series and belong to the alkali-dravite group of Hawthorne & Henry (1999) with X_{Mg} between 0.60 and 0.82. B isotopic composition of tourmaline is unusually heavy with $\delta^{11}B$ values between $+19$ and $+22.2‰$ in all investigated samples (Chapter 10). In all samples, intra-grain variation of $\delta^{11}B$ is very limited with profiles showing very little or a lack of internal zonation. Variation of $\delta^{11}B$ among different samples is also negligible (Chapter 10). A uniform process for the formation of blackwall tourmaline is therefore likely, in terms of *P*, *T*, *t* and fluid composition.

11.3. Results

Comparing the trace-element abundances of all analysed samples with their respective whole-rock abundaces produces very characteristic patterns. Figure 11.1 displays such a pattern for sample SY400 as an example. The figure clearly demonstrates that the elements Cu, Zn, Co, Sr, Pb, Cr, V, Ga and some Ti are incorporated into dravite, whereas all other elements are depleted. In detail, different geochemical groups of elements show the following behaviour:

Large ion lithophile elements (LILE) The elements Cs, Rb and Ba show very low concentrations in all analysed tourmaline samples. Concentrations of the three elements are typically in the range of $0.1 - 3\,\mu g/g$ (Table 11.2). All three elements are highly enriched in phengite with concentrations of 72 to $238\,\mu g/g$ for Rb, 0.7 to $4.9\,\mu g/g$ for Cs, and 199 to $2313\,\mu g/g$ for Ba.
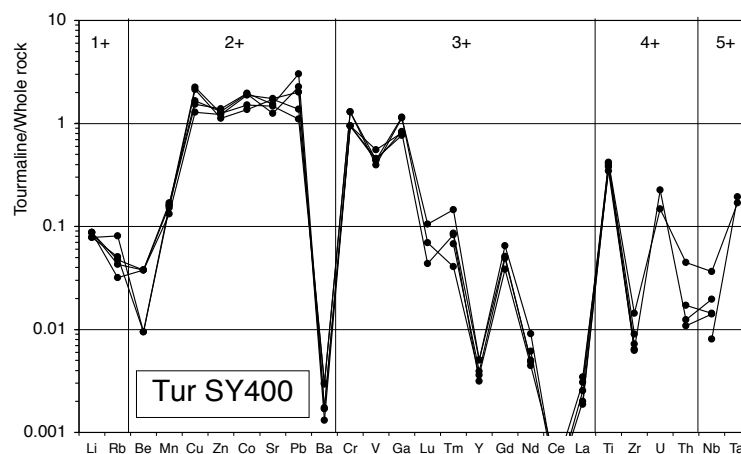
Fig. 11.1. Trace-element composition of tourmaline of sample SY400, normalised to the whole-rock abundances of sample SY400. Elements are grouped by valence state (mono to penta valent) and sorted in order of increasing ionic radii.

High field strength elements (HFSE) The elements Zr, Hf, Nb, Ta, W, Th and U also show very low abundances in tourmaline. The results of most analyses demonstrate concentrations of these elements significantly below $1\,\mu g/g$ (Table 11.2). Zr and Hf in the rocks are probably dominated by accessory zircon. Apart from that rutile shows high abundances of Zr ($50 - 74\,\mu g/g$) and Hf. Rutile and titanite show the highest abundances of Nb of $78 - 144\,\mu g/g$ and $88 - 202\,\mu g/g$, respectively, along with high Ta concentrations. W was detected in high concentrations only

229

Table 11.2. Trace-element abundances of Syros dravite and their respective whole rocks

Sample	SY309B			SY400			SY401B		
Type	core	rim	WR	core	rim	WR	core	rim	WR
Li	2.0	2.1	31.7	6.0	6.7	76.8	n.a.	n.a.	20.2
Be	0.04	0.04	0.65	0.03	0.12	3.2	n.a.	n.a.	0.51
Ti	(900)	(3100)	6950	2714	2423	6530	884	3534	5340
V	180	301	286	66	77	159	231	322	379
Cr	(750)	(1500)	246	(410)	(< 340)	317	n.a.	n.a.	159
Mn	134	130	770	133	130	850	146	141	540
Co	42	40	53	41	54	28	37	38	45
Cu	15	30	13	12	8	6	14	12	18
Zn	68	57	84	45	50	38	53	63	72
Ga	12	15	13	19	13	17	15	18	15
Rb	0.8	0.9	1	3.4	2.1	52	2.3	2.1	1
Sr	97	185	67	280	265	175	40	123	133
Y	0.05	0.08	30	0.05	0.17	43	0.22	0.14	19
Zr	0.44	0.51	105	1.82	1.03	155	1.36	1.34	80
Nb	0.02	0.05	5.28	0.02	0.05	7.18	0.12	0.12	3.01
Cs	0.20	0.23	n.a.	0.84	0.53	n.a.	0.67	0.51	n.a.
Ba	0.39	0.53	16	1.35	0.72	454	0.93	1.11	18
La	0.02	0.02	12.14	0.10	0.09	36.9	0.14	0.05	10.9
Ce	0.01	0.02	33.39	0.03	0.01	86.1	0.04	0.02	24.4
Pr	< 0.01	0.02	3.48	0.06	0.01	10.5	0.03	0.03	3.2
Nd	0.06	0.06	14.70	0.26	0.21	38.9	0.35	0.30	13.8
Sm	0.07	0.05	3.47	0.52	0.17	7.75	0.46	0.23	3.23
Eu	0.03	0.02	1.41	0.02	0.05	1.51	0.07	0.09	1.27
Gd	0.09	0.14	3.68	0.39	0.28	7.51	0.53	0.32	3.19
Tb	< 0.01	0.01	0.59	0.08	0.02	1.16	0.03	0.03	0.48
Dy	0.10	0.07	4.05	0.30	0.08	7.74	0.26	0.16	3.12
Ho	0.01	0.01	0.87	0.04	0.01	1.58	0.05	0.03	0.65
Er	0.04	0.03	2.71	0.17	0.08	4.71	0.10	0.11	1.99
Tm	0.01	0.01	0.39	0.07	0.06	0.71	0.02	0.05	0.26
Yb	0.08	0.08	2.75	0.27	0.07	4.82	0.08	0.14	1.89
Lu	0.01	0.02	0.45	0.07	0.02	0.82	0.07	0.07	0.26
REE	0.52	0.54	84.1	2.39	1.15	211	2.24	1.65	68.6
Hf	0.07	0.05	n.a.	0.38	0.10	n.a.	0.19	0.08	n.a.
Ta	0.01	0.01	0.34	0.07	0.02	0.37	0.04	0.05	0.76
W	0.04	0.04	n.a.	0.20	0.09	n.a.	0.18	0.13	n.a.
Pb	1.16	2.02	0.63	2.71	5.30	2.18	0.99	1.72	0.74
Th	0.03	0.02	2.34	0.08	0.05	3.79	0.16	0.08	5.23
U	0.02	0.03	0.76	0.06	0.03	0.39	0.06	0.04	0.54
n	3	3		2	3		2	5	

Li and Be in tourmaline were determined by SIMS; Ti and Cr in parantheses were analysed by EPMA; all other elements were analysed by LA-ICP-MS; n.a. = not analysed. REE is the sum of all rare earth elements. n = number of LA-ICP-MS analyses. Whole-rock data are taken from Table C. Whole-rock data of sample SY413 are not available.

Table 11.2. (continued)

Sample	SY412			SY413		SY420		
Type	core	rim	WR	core	rim	core	rim	WR
Li	4.0	5.0	60.2	4.6	4.4	4.1	4.7	36.2
Be	0.01	0.01	0.75	0.01	0.02	0.02	0.02	0.68
Ti	3524	4727	25650	3993	4589	1155	2860	5220
V	509	529	639	283	451	116	189	199
Cr	($<$ 340)	($<$ 340)	9	(340)	(410)	(340)	(550)	353
Mn	76	72	1390	151	170	299	282	2010
Co	41	40	44	58	48	74	69	49
Cu	17	15	*n.a.*	32	15	4	8	*n.a.*
Zn	85	83	99	84	70	101	80	81
Ga	27	21	20	18	18	20	28	29
Rb	3.5	3.8	16	4.5	1.8	$<$ 1.2	2.0	40
Sr	48	49	35	91	467	134	261	1640
Y	0.29	0.28	22	1.64	0.30	$<$ 0.06	0.22	88
Zr	1.89	2.03	75	5.97	3.82	0.55	3.08	171
Nb	0.21	0.25	3.05	0.41	0.08	$<$ 0.03	0.11	13.2
Cs	0.55	0.78	*n.a.*	1.48	0.41	$<$ 0.16	0.40	*n.a.*
Ba	0.82	0.77	186	3.10	0.85	1.17	2.41	584
La	0.06	0.09	1.4	0.19	0.44	$<$ 0.02	$<$ 0.02	63.8
Ce	0.02	0.02	4.9	0.11	1.13	$<$ 0.01	$<$ 0.01	131.0
Pr	0.03	0.04	0.9	0.05	0.23	$<$ 0.01	$<$ 0.01	15.9
Nd	0.35	0.18	5.7	0.77	1.00	$<$ 0.05	$<$ 0.06	61.6
Sm	0.23	0.17	2.12	0.09	0.20	0.21	0.22	13.80
Eu	0.03	0.11	1.36	0.15	0.16	0.07	0.06	4.69
Gd	0.76	0.53	3.02	1.86	0.35	0.47	0.59	13.90
Tb	0.07	0.07	0.52	0.13	0.01	0.05	0.05	2.22
Dy	0.06	0.26	4.01	0.61	0.15	$<$ 0.04	0.15	15.00
Ho	0.07	0.04	0.80	0.07	0.04	$<$ 0.01	0.04	2.88
Er	0.19	0.11	2.46	0.39	0.13	$<$ 0.04	0.16	7.90
Tm	0.08	0.02	0.33	0.09	0.04	$<$ 0.02	0.06	0.97
Yb	0.26	0.18	2.43	0.34	0.06	0.17	0.10	5.70
Lu	0.08	0.06	0.38	0.23	0.11	$<$ 0.02	0.03	0.95
REE	2.28	1.88	30.3	5.07	4.05	1.11	1.53	340
Hf	0.26	0.23	*n.a.*	0.07	0.14	$<$ 0.05	0.14	*n.a.*
Ta	0.02	0.05	0.24	0.07	0.03	$<$ 0.03	0.04	0.94
W	0.10	0.21	*n.a.*	0.25	0.10	$<$ 0.05	0.07	*n.a.*
Pb	1.69	1.77	0.58	2.93	4.92	5.08	9.69	59.6
Th	0.05	0.06	*d.l.*	0.39	0.10	0.22	0.13	16.8
U	0.05	0.08	*d.l.*	0.12	0.05	$<$ 0.01	0.09	6.31
n	1	3		3	2	1	3	

in rutile $(6-69\,\mu g/g)$. Th and U are found in high concentrations in epidote and especially allanite. Ti, which also belongs to the HFSE group, is discussed below together with other first row transition metals.

Y and the rare earth elements (REE) Y and the REE also show very low abundances in tourmaline. The sum of all REE together ranges from ~ 0.5 to $5\,\mu g/g$ among the different samples, whereas whole-rock concentrations range from ~ 30 to $340\,\mu g/g$ (Table 11.2). Abundances of light REE in dravite are subchondritic in all samples. Medium to heavy REE (Sm to Lu) are approximately chondritic. Similar patterns were observed for omphacite, phengite and glaucophane. High abundances of LREE and MREE are found in epidote and allanite. MREE and HREE are enriched in titanite, and HREE are enriched in garnet.

First row transition metals and Ga, Sr and Pb The elements Ti, V, Cr, Mn, Co, Cu, Zn, Ga, Sr and Pb show relatively high abundances in dravite in all samples. However, these elements show concentrations in tourmaline in the same range as whole-rock abundances (Table 11.2). They are not extremely fractionated into tourmaline. In Fig. 11.2, the partition behaviour of the transition metals and Ga, Sr and Pb is displayed. Abundances in whole rocks and different minerals are plotted against abundances in tourmaline rims.

Cr was analysed only by EPMA. Concentration in most minerals in most samples are below the detection limit of EPMA for the used setup ($300\,\mu g/g$ Cr in Tur; $360\,\mu g/g$ Cr in other minerals). Only sample SY309B displays significantly higher abundances of Cr in dravite ($\sim 1500\,\mu g/g$) and coexisting minerals. Concentrations in chlorite, glaucophane, omphacite, phengite (all $900-2000\,\mu g/g$) and especially epidote (up to $5000\,\mu g/g$) are in the same range or even higher than in dravite. Ti concentrations in dravite ($\sim 2500-5000\,\mu g/g$) are higher by a factor of ~ 5 than in coexisting omphacite, phengite, glaucophane, epidote and garnet (Fig. 11.2a). Whole rock abundances are still higher than abundances in tourmaline, due to the occurrence of titanite and rutile in the samples. Frequent rutile inclusions in dravite suggest that tourmaline is saturated in Ti. Vanadium concentrations in rutile ($\sim 1200\,\mu g/g$) are significantly higher than in other minerals. Fractionation between tourmaline ($\sim 70-530\,\mu g/g$) and omphacite, glaucophane, epidote and phengite is not significant (Fig. 11.2b). Mn is a major component in garnet. In omphacite, chlorite, epidote, glaucophane and titanite, Mn abundances are 2 to 30 times higher than in coexisiting dravite ($\sim 70-300\,\mu g/g$). Phengite and rutile show similar concentrations of Mn than dravite (Fig. 11.2c). Co is slightly enriched ($1-2\times$) in glaucophane and chlorite relative to dravite ($\sim 40-70\,\mu g/g$). All other minerals
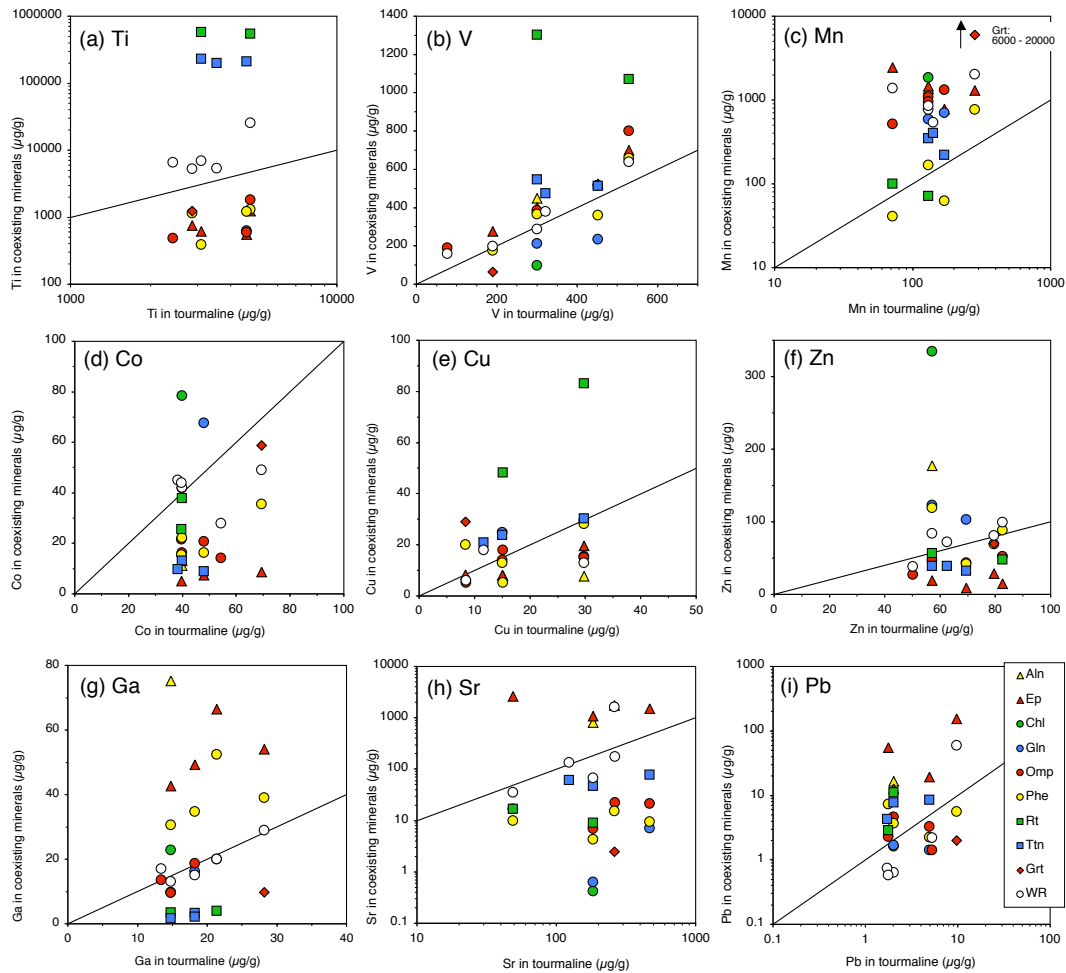
Fig. 11.2. Concentrations of nine different elements (Ti, V, Mn, Co, Cu, Zn, Ga, Sr, Pb) in tourmaline rims in comparison with concentrations in various coexisting minerals and with the respective whole-rock abundances. All concentrations in (μg/g). Symbols above the 1:1 line demonstrate abundances of an element higher than in tourmaline, symbols below the 1:1 line demonstrate depletion with respect to tourmaline.

show concentrations lower than in tourmaline (Fig. 11.2d). Cu is enriched in rutile and garnet by a factor of ~ 2 relative to tourmaline ($\sim 8 - 30\,\mu g/g$), but does not show any significant fractionation among the other silicates (Fig. 11.2e). Zn is strongly enriched in allanite and chlorite and depleted in epidote, omphacite and titanite relative to tourmaline ($\sim 50 - 80\,\mu g/g$). Zn concentrations of phengite and glaucophane are in the same range as in dravite (Fig. 11.2f). Ga is enriched in epidote, allanite and phengite with respect to tourmaline ($\sim 15 - 30\,\mu g/g$) by a factor of $\sim 1.5 - 5$ and strongly depleted in titanite and rutile. Chlorite, glaucophane and omphacite show similar abundances than dravite (Fig. 11.2g). Sr abundances in epidote and allanite are $\sim 3 - 50 \times$ higher than in coexisting dravite ($\sim 50 - 450\,\mu g/g$). However, tourmaline is significantly enriched in Sr with respect to titanite, rutile and especially phengite, omphacite, garnet, glaucophane and chlorite (Fig. 11.2h). Pb concentrations are highest in epidote and allanite, followed by titanite and rutile. Phengite, glaucophane and omphacite show similar concentrations than dravite ($\sim 2 - 10\,\mu g/g$; Fig. 11.2i).

The light elements (Li, Be)　　The partitioning of Li and Be between tourmaline and coexisting minerals is discussed in Chapter 7. Be concentrations are $< 120\,ng/g$ in all samples. High concentrations of this element are found in white mica, omphacite, amphibole and albite. The abundances of Li in dravite from all samples are also relatively low ($\sim 2 - 7\,\mu g/g$; Table 11.2), but are much higher in coexisting omphacite, phengite, glaucophane and chlorite (see Chapter 7).

11.4. Discussion

It has been demonstrated in Chapters 9 and 10 that tourmaline formed in H*P* metamorphic rocks has a strong impact on the geochemical cycle of B. B is an important geochemical tracer which is otherwise enriched in clay minerals during alteration of oceanic crust and in white mica in H*P* metamorphic rocks (Chapters 5 and 7). These mineral phases also dominate the budgets of K and the other LILE (Domanik *et al.*, 1993; Sorensen *et al.*, 1997; Melzer & Wunder, 2000; Zack *et al.*, 2001; Schmidt *et al.*, 2004). The low abundances of Rb, Cs and Ba in dravite, which are consistent with its low K-content (below detection limit of EPMA, $230\,\mu g/g$ in the used setup) demonstrates that LILE are not incorporated in its structure. The crystallographic X-site (see formula 11.1) of the Syros dravite is almost fully occupied by Na and does not allow for the incorporation of larger cations. Therefore, dravite quantitatively separates the LILE from B, a mechanism which is not operating during seafloor alteration, diagenesis, metamorphism, melting and melt fractionation.

The minor occupation of the X-site in dravite by Ca^{2+} (< 0.05 cpfu), which is dominated by Na^+ allows for a substitution of Ca^{2+} by Sr and Pb. A substitution by the trivalent REE and Y is obviously not possible in dravite, as concentrations of these elements are low. The REE patterns of dravite in HP metamorphic rocks are probably determined by type and modal abundance of paragenetic minerals like garnet, epidote, allanite, zircon, apatite and titanite, which strongly impact the budget of the REE. Consequently, the use of dravite REE patterns for a characterisation of tourmaline-forming fluids is limited.

Dravite is enriched in Ti (~ 0.05 cpfu) relative to coexisting omphacite, phengite, glaucophane, epidote and garnet. However, other HFSE like Zr, Hf, Nb, Ta, W, U and Th are not enriched in dravite and show very low concentrations. Tourmaline therefore has no impact on the geochemical cycle of HFSE in subduction zones. The budgets of these elements are governed by rutile, titanite, zircon, epidote, allanite and garnet as has been previously demonstrated (Hermann, 2002; Zack *et al.*, 2002a,b; Spandler *et al.*, 2003).

Very low abundances of K, Rb, Sm, Th and U strongly limit the use of dravite for isotope and fission track dating, which has been applied to other tourmaline (Lal *et al.*, 1977; Altherr *et al.*, 1982; Andriessen *et al.*, 1991; Jiang, 1998; Jiang *et al.*, 1999). On the other hand, the low abundances of the radioactive isotopes together with relatively high concentrations of Sr and Pb qualifies dravite for an investigation of tourmaline-forming fluids by Sr and Pb isotope systematics, as has been demonstrated by King & Kerrich (1989). A comparison of the Sr and Pb isotope ratios of dravite with those of coexisting minerals like carbonates, epidote, apatite or sulfides may be used to distinguish syn-metamorphic from pre-existing tourmaline.

Li is known to occur in high concentrations in pegmatitic tourmaline, and forms a major component in rossmanite and elbaite. Hence, it may be surprising to observe a depletion of Li in dravite with respect to coexisting omphacite, chlorite and glaucophane. The formation of tourmaline in HP metamorphic rocks therefore strongly fractionates B from the light elements Li (and Be) and strongly impacts B/Be and B/Li ratios of the subducting and exhuming material, as discussed in detail in Chapter 6. However, the abundances of Li of $\sim 2 - 7$ µg/g in dravite are still high enough to determine Li isotope ratios by SIMS with high precision. This may be used in future to further develop the genetic model of tourmaline formation presented in Chapter 10 on the basis of B isotope ratios.

First row transition metals Mn, Co, Cu and Zn are probably substituting in dravite for Fe^{2+} and Mg. Fractionation between tourmaline and coexisting Fe-Mg-bearing minerals is therefore limited, but dravite is tolerant for divalent transition metals. Trivalent Cr, V and Ga are probably substituted for Al and Fe^{3+} and are readily

incorporated into dravite. High concentrations of Ga in epidote and phengite and low concentrations in rutile and titanite demonstrate the crystal chemical similarity of Ga and Al. Relatively high abundances of the first row transition metals (Sc to Zn), Sn and Pb in tourmaline has attracted attention by various workers (e.g. Clarke *et al.*, 1989; Griffin *et al.*, 1996; Jiang *et al.*, 2004) to use this mineral group for the prospection on base metal deposits. The chalcophile base metals like Cu, Zn and Pb are usually enriched in sulfides and are found in large massive sulfide deposits. Many of these deposits are associated with tourmalinites, which have been investigated, in order to study the systematics of base metals in tourmaline in relation to ore-forming fluids (s.f. Slack, 2002). In H*P* metamorphic rocks, tourmaline plays only a minor role in the budget of base metals because of the limited fractionation between tourmaline and rockforming Fe-Mg silicates.

11.5. Summary and conclusions

Tourmaline formed at the contact between metabasic or metasedimentary blocks and ultramafic schists in the high-pressure metamorphic mélange of Syros were analysed in situ for a variety of trace elements by LA-ICP-MS, SIMS and EPMA. The major element composition of tourmaline from the different samples is very uniform and is close to the ideal dravite composition with X_{Mg} of $\sim 0.60 - 0.82$. Trace elements are only selectively incorporated into the tourmaline and many elements are excluded from its structure. The light elements Li and Be, the HFSE (Zr, Hf, Nb, Ta, W, Th, U), the REE, Y and the LILE (K, Rb, Ba, Cs) all show very low concentrations and are not incorporated into dravite. First row transition metals (Ti, V, Cr, Mn, Co, Cu, Zn) and Sr, Pb and Ga are incorporated into dravitic tourmaline (Table 11.3), demonstrating abundances in the same order than in the respective whole rocks, and in paragenetic rock-forming minerals. Hence, tourmaline is not strongly fractionating these elements in any way.

The very low abundances of Li, Be, HFSE, LILE and REE in dravite demonstrates that tourmaline is not relevant for the cycle of these elements in subduction zones. The low concentrations of K, Rb, Ba and Cs in dravite demonstrate that the formation of tourmaline in subducting slabs entirely decouples B from the LILE, which are otherwise hosted by the same mineral phases (i.e. clay minerals in AOC and white mica in high-pressure metamorphic rocks) and are all highly mobile in hydrous fluids and highly incompatible during mantle melting.

The use of tourmaline and especially Mg-rich dravite for base metal exploration has been proposed by earlier workers (e.g. Clarke *et al.*, 1989; Griffin *et al.*, 1996; Jiang *et al.*, 2004). Relatively high abundances of the first row transition metals

(Sc to Zn), Sn and Pb in tourmaline predestines this mineral as a monitor of concentrations of these economically interesting elements in hydrothermal and metamorphic fluids, and may be helpful for the understanding of the genesis and for the exploration of ore deposits. However, a detailed petrogenetic understanding of tourmaline is essential for a successful establishment of this mineral for prospection. Detrital and diagenetic tourmaline, or metamorphic tourmaline formed prior to the ore-forming processes may remain unaffected by the fluids and consequently may not show any elevated base metal abundances.

Table 11.3. Summary of trace elements in dravitic tourmaline

Elements moderately enriched in dravite $Tur/WR \geq 1$	Elements moderately depleted in dravite $1 > Tur/WR > 0.1$	Elements strongly depleted in dravite $Tur/WR < 0.1$
V, Cr, Ga Co, Cu, Zn, Pb, Sr (Sc, Ni, Sn)*	Mn, Ti	Nb, Ta, Zr, Hf, W, Th, U REE, Y K, Rb, Cs, Ba Li, Be

*Sc, Ni and Sn not analysed in this study, but reported by Griffin *et al.* (1996) and Jiang *et al.* (2004). WR = whole rock.

High concentrations of Sr and Pb along with low concentrations of Rb, Th and U in tourmaline allow for a characterisation of the sources of tourmaline-forming fluids and for a control of the question on syn-genetic growth of tourmaline and associated minerals, e.g. apatite, carbonates, epidote. Apart from the trace-element isotopes, the isotopic composition of the major elements O, H and B are powerful tools for the characterisation of fluid sources and genesis of tourmaline, as has been demonstrated by Taylor & Slack (1984), Kotzer *et al.* (1993) and in Chapter 10.

12. Summary, conclusions and outlook

12.1. Analytical improvements

12.1.1. Analysis of B and Li by SIMS at low concentrations

In-situ analysis of B is impeded by surface contamination, which makes it obligatory to use very elaborate cleaning procedures and analytical setups. Lithium was also found to be influenced by contamination. In our lab, contamination is 50 times more significant for B than for Li.

Combining an efficient cleaning procedure with a very basic depth-profiling method enables a reduction of boron contamination to levels close to or even below the detection limit of $\sim 2\,\text{ng/g}$, with a lateral resolution of $\sim 30\,\mu\text{m}$ in a rather short time of $\sim 12\,\text{min}$ per spot. Other methods like pre-sputtering or rastering a larger area prior to analysis may reduce contamination to a level of $\sim 10\,\text{ng/g}$ (Kent & Rossman, 2002), but require more time and suffer from poor lateral resolution.

The SiO_2 glass Herasil 102 from Heraeus Quarzglas GmbH, Germany, is an appropriate material for checking the level of boron contamination of an in-situ analytical method like SIMS. Herasil 102 is an ultrapure, homogeneous material that is available in large quantities. Natural minerals, like olivine, ortho- and clinopyroxene, garnet and quartz are not viable for testing the contamination level, as boron abundances in these minerals vary significantly among different samples and often reach levels of >100 ng/g.

Results for Li, B, Na, K and Fe (this study and Müller *et al.*, 2003) suggest that contamination is a serious problem during in-situ analysis of various trace elements and must be controlled during analysis of materials showing very low concentrations, such as quartz, mantle rocks and meteorites. Contamination of boron, however, is much more significant than e.g. Li contamination.

The analytical method established in this study provides the possibility of analysing a large variety of natural rocks and minerals for B (and Li) abundances by SIMS. The method was already applied to the investigation of high-pressure metamorphic rocks in the course of this study, and in several ongoing and completed studies performed at the Mineralogisches Institut (Universität Heidelberg). These include studies on the inter- and intra-mineral partitioning of Li, Be and B in a variety of mantle rocks (Paquin *et al.*, 2004; Kaliwoda, 2004; Kaliwoda *et al.*, 2004),

volcanic rocks (Helbling *et al.*, 2004; Cabato *et al.*, 2004) and granitoids (Hillers, 2003). Without the presented analytical improvements, an investigation of such samples for B abundances would have been impossible.

12.1.2. High-precision whole-rock B analysis by PGNAA

The perspectives of applying prompt gamma neutron activation analysis (PGNAA) for the chemical characterisation of high-P metamorphic and other crystalline rocks was tested in a feasibilty study. The results are presented in the analytical section of this thesis. Samples of various high-P rocks from Syros (Greece) were studied by PGNAA using the cold neutron beam at the Budapest Neutron Centre (BNC). For neutron activation-based radio-analytical methods, such as PGNAA, the samples do not require special treatment, since they can be measured as solid blocks or rock powders. Another advantage of PGNAA is its high sensitivity for the elements boron, chlorine and hydrogen, which are hard or impossible to be analysed by other methods.

41 samples from various high-pressure metamorphic rocks were investigated for their chemical compositions by PGNAA, XRF and solution ICP-MS. In addition, 11 samples from granitoids with published major and trace element concentrations were analysed by PGNAA. Analyses of major components by PGNAA are in good agreement with XRF results. Exceptions are K_2O at concentrations $< 0.5\,wt\%$ and Na_2O at concentrations $< 2\,wt\%$. The analysis of MgO contents by PGNAA is not satisfactory. On the other hand, PGNAA may be a superior method for the determination of Na_2O concentrations, since this method avoids the problems that are inherent in XRF analysis.

The abundances of many trace elements of geological interest (e.g. Cs, Ba, Rb, Sr, Nb, Ta, Zr, Hf, Y, U, Th, Pb) are too low in most high-P metamorphic rocks to be quantified by PGNAA. Among the REE, only Nd, Sm and Gd could be quantified. Comparison with results from ICP-MS revealed that Nd and Sm cannot be analysed with sufficient accuracy by PGNAA. Gd abundance values, however, are of good precision and agree well with ICP-MS data. Sc abundances determined by PGNAA are similar to those obtained by ICP-MS. Cr, Co and Ni could be quantified only at high concentration levels that are normally only present in rocks derived from the Earth's mantle. At high concentrations of $> 200\,\mu g/g$, the precision of V analyses by PGNAA is comparable to those by XRF and ICP-MS, but the detection limits are much higher. Generally the accordance of results from PGNAA with those of the other methods becomes poor at low concentrations, i.e. close to or below our calculated detection limits.

PGNAA provides very precise measurements of B, Cl and H_2O contents. Knowl-

edge of accurate H_2O contents in high-P metamorphic rocks is of paramount interest, as these values display the degree of rock dehydration. The trace elements B and Cl are of growing importance for the understanding of chemical transfer in subduction zones. The abundances of these elements in geological materials will probably be investigated more extensively in the future, with the improvement of analytical facilities. PGNAA has the capacity to contribute important data to the understanding of the geochemical cycles of B and Cl.

12.2. Whole-rock abundances of Li, Be and B in high-pressure metamorphic rocks from Syros

Li, Be and B abundances in whole rocks of two different groups of HP meta-igneous rocks from Syros were measured. Group 1 are samples that preserved the peak metamorphic parageneses and were not rehydrated during exhumation. Their trace element content is controlled by the respective abundances in the (altered) igneous protoliths and by extraction of trace elements by dehydration reactions during prograde metamorphism. Group-2 samples, in contrast were significantly rehydrated during exhumation. Their trace element content is strongly governed by retrograde metasomatism.

Group-1 samples contribute information on the impact of dehydration of (altered) igneous oceanic crust on whole rock abundances of different trace elements. In detail, the abundances of Li and Be do not correlate with H_2O contents and are in the same range as in fresh and altered oceanic crust, suggesting that most of the Li and Be remains in the subducting slab and is not released with hydrous fluids. In contrast, B concentrations and B/Be ratios are correlated to the H_2O contents of the rocks. Both are decreasing in range and value with decreasing H_2O content, suggesting a significant loss of B with hydrous fluids during progressive dehydration. B/Be ratios of all mafic rocks are < 30, which is in agreement with previous studies (Bebout *et al.*, 1993). Only tourmaline-bearing samples show significantly higher ratios.

Group-2 samples provide information on the effects of metasomatism of HP metamorphic rocks during exhumation. Li and Be show very high abundances in many samples, suggesting a strong enrichment during metasomatism. The enrichment of B is entirely controlled by the occurrence of tourmaline. Tourmaline-bearing samples are strongly enriched in B and display very high B/Be ratios ($\gg 100$). Tourmaline-free samples show low B concentrations and B/Be ratios (< 10), which is probably due to low partition coefficients of B between most silicates and hydrous fluids. These results demonstrate that Li is probably a good tool

241

for tracing metasomatic enrichment processes, while B is enriched only in the case of tourmaline formation.

In summary, this study suggests that B/Be ratios can be used to trace qualitatively the progressive dehydration of HP metamorphic rocks, while Li concentrations are more sensitive for metasomatic processes, i.e. the influx of external fluids. The contrasting behaviour of the three elements is probably due to differences in partition coefficients between silicates and fluids, which are decreasing from B via Li to Be (see Chapter 5). A quantification of the trace element budgets of the suite of investigated rocks on the basis of the measured whole-rock abundances is probably not possible, as the protoliths of the different samples were already entirely different before the onset of subduction.

12.3. Partitioning and budget of light elements in HP metamorphic rocks from Syros

All three elements Li, Be and B were found to be strongly fractionated among different minerals in HP metamorphic rocks. Very high concentrations of lithium were revealed in the major phases of chlorite schists, glaucophane schists, metagabbros and eclogites, namely chlorite, glaucophane and omphacite/jadeite. The budgets of these rocks demonstrate that the major phases are the principal carriers of Li. Obviously, chlorite, glaucophane and clinopyroxene are able to incorporate high amounts of Li into their crystal structures. Therefore, prograde high-pressure metamorphism of altered oceanic crust during progressive subduction should not significantly decrease the amount of Li in these lithologies. At low metamorphic grades, Li can be hosted in chlorite, and during formation of blueschists, it will enter glaucophane. As the modal abundance of glaucophane decreases and the amount of clinopyroxene increases, clinopyroxene will take in large amounts of Li and, therefore, most of the rock's Li should be retained within the eclogite. High Li concentrations in crustal eclogites and eclogitic clinopyroxene have been found by other authors as well (Hermann, 2002; Woodland *et al.*, 2002; Zack *et al.*, 2002a, 2003). The results of the study on Syros HP rocks suggest that large portions of Li may be retained in the subducting oceanic crust itself. Hence, the retainment of Li in eclogitic clinopyroxene probably contributes to the fractionation of the fluid-mobile elements Li and B within the subduction cycle.

Beryllium is mainly hosted in clinopyroxene, glaucophane and white mica; in addition, Ca-amphibole, lawsonite and albite may also contain significant amounts of Be. As discussed above for Li, Be should also be retained in progressively dehydrating rocks of the subducting oceanic crust. It will be hosted by Ca-amphibole

242

and albite in greenschists, by glaucophane and white mica in blueschists and by clinopyroxene in eclogites. Domanik *et al.* (1993) found white mica to contain the highest concentrations of Be in high-pressure rocks, which is in agreement with the results presented here. However, the limited modal abundance of white mica compared to glaucophane and clinopyroxene restricts the importance of phengite and paragonite for the Be budgets of the rocks. Zack *et al.* (2002a) underlined the importance of clinopyroxene as the principal carrier of Be in eclogites, which is in agreement with the results obtained in this study.

The special emphasis put on analyses of boron at low concentration levels during this study turned out to be very important, as almost all of the investigated minerals contain less than $10\,\mu g/g$ B and most contain less than $1\,\mu g/g$. The only minerals (except for tourmaline) showing higher concentrations of B are phengite and paragonite. Previous studies demonstrated that white micas are important carriers of B in high-pressure rocks (Domanik *et al.*, 1993; Zack *et al.*, 2002a; Hermann, 2002). However, these studies were not focused on accuracy of B measurements at low concentration levels and therefore might have overestimated the concentrations of B in minerals coexisting with white mica, namely clinopyroxene, amphibole, chlorite, lawsonite and garnet. In this study, the contribution of phases other than phengite, paragonite and tourmaline has been demonstrated to be much smaller than formerly thought. The significantly higher apparent B concentrations revealed by previous studies using SIMS or LA-ICP-MS techniques may be explained by surface contamination of thin sections or by small mineral and fluid inclusions, which have been overlooked during analysis.

This study presents so far unique sets of inter-mineral partition coefficients for the light elements Li, Be and B for 15 different H*P* metamorphic minerals, derived from in-situ analyses of coexisting phases in several different natural rock samples. These sets provide important information on the behaviour of the light elements in different lithologies within subducting slabs, and they are essential for modelling of trace-element and isotope fractionation during subduction and dehydration of oceanic crust.

12.4. Modelling light element release during progressive high-pressure metamorphism

In this study, modelling of trace element release from progressively dehydrating rocks was performed for the light elements Li, Be and B, which show contrasting behaviour during fluid/rock interaction processes. Experimentally determined clinopyroxene/fluid partition coefficients for Li, Be and B (Brenan *et al.*, 1998b)

were combined with mineral/clinopyroxene partition coefficients for various HP minerals (this study) to deduce a set of mineral/fluid partition coefficients. These were combined with the modal compositions of HP metamorphic rocks derived from thermodynamic calculations using the program PerpleX. The result is a data set of the modal composition of a rock and its whole rock/fluid partition coefficients for the trace elements of interest at any stage of the $P - T$ path, including information on the amount of fluid released at any depth. Based on these data, the concentrations of trace elements in the subducting rocks and in the released fluids along a certain $P - T$ path were modelled.

In a second step, the derived information on boron concentrations of rocks and fluids were combined with the temperature dependent isotopic fractionation of B, in order to model the B isotopic evolution of subducting rocks and of the released fluids.

Light element budgets of two examples were calculated, (i) MORB + H$_2$O and (ii) K$_2$O-free MORB + H$_2$O. For both compositions, Be concentrations of the dehydrating rocks do not change during dehydration, and released fluids also show constant Be concentrations which are similar to concentrations of Be in the rocks. Li concentrations in both assemblages decrease to a level of $\sim 55\%$ of the starting value between the onset of dehydration and the eclogite stage. Li concentrations of the released fluids range from ~ 100 to $\sim 200\,\mu g/g$ and are highest at intermediate pressures at the transition from blueschists to hydrous eclogites. The behaviour of B and B isotopes is strongly dependent on the amount of white mica in the rock. The first composition, containing $\sim 5\%$ phengite retains $\sim 37\%$ of the original B in the eclogite, while the second, phengite-free assemblage retains only $\sim 1\%$. ^{11}B/^{10}B ratios are also significantly different. The Phe-bearing rocks release fluids with positive δ^{11}B values, reaching the MORB or mantle range as the rocks are transformed to eclogites. In contrast, the phengite-free assemblage produces fluids with strongly negative δ^{11}B values at the blueschist-to-eclogite transition. In both cases, however, fluids with high δ^{11}B values are released at shallow depth that may migrate into the accretionary wedge or forearc mantle.

The presented model is of course afflicted with a number of uncertainties and has to be improved by the input of more sophisticated data especially on trace element partitioning. However, in principle this model offers the possibility of a quantification of trace element release from the slab in any lithology along any reasonable $P - T$ path.

244

12.5. Boron isotopic composition of tourmaline in metasediments

Tourmaline grains of two metasedimentary and one metabasic rock were analysed in-situ for their chemical and B isotopic compositions with high lateral resolution. Sample SY314, a metatuffite displays abundant detrital dravitic tourmaline grains with homogeneous chemical and B isotopic compositions ($\delta^{11}B \approx -3.3‰$), pro-grade/peak metamorphic overgrowths with $\delta^{11}B$ values of $-1.6‰$ in dravite with high Ca and Mg contents. Finally, the influx of B-bearing hydrous fluids is documented not only petrographically in Fe-rich zones of garnet, amphibole and mica, but also in Fe-rich rims of tourmaline, which demonstrate strongly increasing $\delta^{11}B$ values towards the grain edges of up to $+7.7‰$. The B isotopic composition of phengite ($-6.4‰$) is probably also affected by the retrograde fluid.

Sample SY323 is a Ca-rich eclogite containing abundant epidote, with tourmaline grains included in garnet cores. $\delta^{11}B$ analyses of core and rim of a single grain revealed values of $+1.0 \pm 1.1‰$ and $+2.8 \pm 1.0‰$, respectively. The $\delta^{11}B$ value of $+2.8 \pm 1.0‰$ revealed for the tourmaline rim is interpreted to represent the B isotopic composition of peak metamorphic tourmaline in this metabasic rock.

Sample SY432, a siliceous marble also contains detrital tourmaline. Chemical and B isotopic compositions of different grains are strongly different from one another and point to a heterogeneous provenance of tourmaline in the pre-metamorphic sediment. $\delta^{11}B$ values of detrital cores vary between $-10.7‰$ and $+3.6‰$. Rims developed during prograde/peak metamorphism are homogeneous and similar among all analysed grains with $\delta^{11}B$ values of $+0.9‰$. Phengite shows $\delta^{11}B$ values of $-11.3‰$. Analyses of tourmaline rims and phengite show a fractionation of $\Delta^{11}B = 12.2 \pm 2.3‰$. This suggests B isotopic equilibrium between phengite and tourmaline rims in SY432 for peak metamorphic temperatures of $\sim 450 - 500°C$, which were estimated for Syros HP metamorphic rocks. Fe-rich retrograde rims were not observed in sample SY432. The contrasting $\delta^{11}B$ values of detrital cores in sample SY432 demonstrate that in-situ B isotope analysis of tourmaline by SIMS is a potentially powerful tool for provenance studies in sediments and metasediments.

The $\delta^{11}B$ values of prograde and peak metamorphic tourmaline in samples SY314 ($-1.6‰$), SY323 ($+2.8‰$) and SY432 ($+0.9‰$) are significantly higher than values determined by Nakano & Nakamura (2001) for Sambagawa metasedimentary peak metamorphic tourmaline ($-10‰$) and by Bebout & Nakamura (2003) for samples from the Catalina schists ($-15‰$) and from Lago di Cignana ($-10‰$). The relatively high $\delta^{11}B$ values of "metasedimentary" tourmaline from Syros in

comparison with the other samples demonstrate that the B isotopic composition of metasedimentary rocks from different localities and samples worldwide may significantly differ from one another. This may not be surprising considering the background of the large compositional heterogeneity of sedimentary rocks in general, but it is an important point to recognise for models of global cycling of B and its isotopes. Additionally, the δ^{11}B values of the metabasic sample and the metasedimentary samples are in the same range. A clear distinction between altered oceanic crust and oceanic sediments is therefore not possible on the basis of B isotopes.

In summary, dravitic tourmaline is a major carrier of B in a variety of metasedimentary rocks. The pressure and temperature stability of dravitic tourmaline is very extensive, equivalent to conditions in subducting slabs to depths of ~ 250 km. Therefore, tourmaline growth and stability in subducting metasediments could be responsible for recycling of B with isotopic composition influenced by Earth's surface processes into the deep mantle. The slow volume diffusivity at temperatures below 600 °C allows for a detailed investigation of the evolution of the B isotopes of a tourmaline-bearing rock during its metamorphic and pre-metamorphic history. In addition, variable metamorphic conditions of the rock are recorded by tourmaline itself in changing X_{Mg} and Ca/Na ratios, which allows for a direct correlation of metamorphic history and B isotopic evolution.

12.6. Boron isotopic composition of metasomatic tourmaline formed during exhumation

HP blocks enclosed in the mélange on the island of Syros are rimmed by reaction zones composed of hydrous minerals, such as chlorite, Na- and Ca-amphibole, clinozoisite and phengite in paragenesis with omphacite, albite and tourmaline. Chemical composition of tourmaline is similar among the different blackwalls and is close to the ideal schorl-dravite series. X_{Mg} ranges from ~ 0.58 to ~ 0.82, which classifies the tourmaline as dravite. B isotopic composition of tourmaline is unusually heavy with δ^{11}B values exceeding $+18$‰ in all investigated samples, reaching a unique value of $+28.4$‰ in sample SY442, which is extending the range of δ^{11}B values reported from natural tourmalines by more than 5‰ (based on a value of $+23$‰ reported by Swihart & Moore (1989) from meta-sedimentary tourmaline).

Blackwalls formed during exhumation of the HP mélange at a depth of $20 - 25$ km at $P - T$ conditions of $\sim 0.6 - 0.75$ GPa and $400 - 430$ °C, by influx of external hydrous fluids. Tourmaline-bearing blackwall rocks are quartz free and show SiO_2 activities of 0.4 to 0.5, generated during interaction of the rocks with low-SiO_2 fluids. Composition of the fluids are estimated to be in the range of

$100 - 300\,\mu g/g$ B and δ^{11}B values of $+18$ to $+28‰$.

H_2O and B in the fluids are likely to originate from the subsequent slab that was still subducting as the Syros mélange was exhumed. The high δ^{11}B of tourmaline in the blackwalls cannot be explained by tourmaline formation from unmodified slab-derived fluids, because all known reservoirs in subducting slabs would produce a fluid with δ^{11}B below $+10‰$ at depths exceeding 20 km. Interaction of the fluid with material composing the exhumation channel on its way from the dehydrating slab to the site of tourmaline formation in the blackwalls would produce exceptionally high δ^{11}B values in the fluids. This process is expected to take place within the subduction setting and is therefore favoured in this study to explain the ^{11}B enrichment in Syros tourmaline. The calculated model demonstrates that fluids are rapidly modified in both trace element and isotopic composition during their migration through the material overlying the subducting slab. Differences in B isotopic composition and concentration are blurred quickly and wiped out after short distances of migration, when the fluid is approaching equilibrium with the rock composing the exhumation channel.

The fixation of B in tourmaline, especially with an isotopic composition affected by earth's surface processes, was already emphasised by Nakano & Nakamura (2001), who investigated the B budget of metasedimentary rocks. They claimed, that B is immobilised within the rocks as soon as it is fixed in tourmaline, which results in deep subduction of B into the mantle. However, the isotopic ratio of tourmaline within the meta-sedimentary high-pressure rocks is relatively low. The tourmalines studied so far by Nakano & Nakamura (2001), Bebout & Nakamura (2003) and this study from Syros range from $-16‰$ to $+2‰$ for prograde growth zones, and reach a maximum of $+8‰$ for retrograde growth zones. Furthermore, the grain size of tourmaline in most HP metamorphic rocks is restricted to $\sim 500\,\mu m$ and the modal abundance of tourmaline is small ($\sim 0.1\%$). In contrast, blackwall tourmaline from Syros has a large grain size (several cm), high abundance, and an exceptionally high δ^{11}B value, which is significantly different from the mantle value of $\sim -6‰$. It is important to note that the blackwall tourmaline formed on the retrograde $P - T$ path during exhumation of the rocks. One might therefore argue that blackwall tourmaline is not relevant for deep subduction processes. However, the formation of tourmaline at the contact between mafic or felsic HP blocks and ultramafic matrix by fluids released during dehydration reactions in the subducting slab may also take place on the prograde path, wherever fluids are migrating through such contact zones, i.e. the slab-mantle interface. If this is the case, the formation of blackwall tourmaline has a significant impact on the geochemical cycle of B in subduction zones, as it is fixing heavy B in large quantities in the slab within a highly stable mineral.

12.7. Trace element composition of Syros tourmaline

Tourmaline formed at the contact between metabasic or metasedimentary blocks and ultramafic schists in the high-pressure metamorphic mélange of Syros were analysed in situ for a variety of trace elements by LA-ICP-MS, SIMS and EPMA. The major element composition of tourmaline from the different samples is very uniform and is close to the ideal dravite composition with X_{Mg} of $\sim 0.60 - 0.80$. Trace elements are only selectively incorporated into dravite and many elements are excluded from its structure. The light elements Li and Be, the HFSE (Zr, Hf, Nb, Ta, W, Th, U), the REE, Y and the LILE (K, Rb, Ba, Cs) all show very low concentrations and are not incorporated into dravite. First row transition metals (Ti, V, Cr, Mn, Co, Cu, Zn) and Sr, Pb and Ga are incorporated into dravitic tourmaline (Table 11.3), demonstrating abundances in the same order as in their respective whole rocks, and in paragenetic rock-forming minerals. Hence, tourmaline is not strongly fractionating these elements in any way.

The very low abundances of Li, Be, HFSE, LILE and REE in dravite demonstrates that tourmaline is not relevant for the cycle of these elements in subduction zones. The low concentrations of K, Rb, Ba and Cs in dravite demonstrate that the formation of tourmaline in subducting slabs entirely decouples B from the LILE, which are otherwise hosted by the same mineral phases (i.e. clay minerals in AOC and white mica in high-pressure metamorphic rocks), and are all highly mobile in hydrous fluids and highly incompatible during mantle melting.

The use of tourmaline and especially Mg-rich dravite for base metal exploration has been proposed by earlier workers (e.g. Clarke *et al.*, 1989; Griffin *et al.*, 1996; Jiang *et al.*, 2004). Relatively high abundances of the first row transition metals (Sc to Zn), Sn and Pb in tourmaline predestines this mineral as a monitor of concentrations of these economically interesting elements in hydrothermal and metamorphic fluids. However, in H*P* metamorphic rocks, tourmaline plays only a minor role in the budget of base metals because of the limited fractionation between tourmaline and rockforming Fe-Mg minerals.

High concentrations of Sr and Pb along with low concentrations of Rb, Th and U in tourmaline allow for a characterisation of the sources of tourmaline-forming fluids and for a control of the question on syn-genetic growth of tourmaline and associated minerals, e.g. apatite, carbonates, epidote. Apart from these trace element isotopes, the isotopic composition of the major elements O, H and B are powerful tools for the characterisation of fluid sources and genesis of tourmaline.

12.8. Outlook

The potential of the light elements Li, Be and B and their isotopes as tracers for material transport in subduction zones is now widely recognised. Research performed on various rock types, minerals and fluids in natural and synthetic systems has helped to establish the light elements as important tools in geochemistry. Especially during the last five years, the study on Syros HP metamorphic rocks together with several other studies has helped to establish these tools, and to unravel in detail the behaviour of Li, Be and B during metamorphic and metasomatic processes in subduction zones. However, there are still uncertainties and open questions, some of which may be solved and answered by research in the near future. The investigation presented in this thesis may serve as a basis for further studies, as given below, which may consolidate the relatively new geochemical tools.

Lower- and higher-grade HP metamorphic rocks The rocks investigated in this study equilibrated at $P - T$ conditions of $\sim 1.5 - 2.0$ GPa and $\sim 500\,°$C. Most of them are blueschists or eclogites or a transition between those two. A large variety of HP minerals and paragenesis were observed and investigated for the partitioning and budget of the light elements. However, for a complete investigation of subduction zone metamorphic rocks it would be necessary to include a broader range of rocks. HP metamorphic rocks representing shallower depths of subduction and lower pressures could be used to quantify earlier stages of dehydration, including minerals, such as zeolites, pumpellyite and karpholite. On the other hand, higher-grade rocks (kyanite eclogites, UHP metamorphic rocks and dry eclogites) would provide information on the element loss at sub-arc depths and on deep subduction of Li, Be and B into the mantle. In addition, a set of samples representing a broader range of $P - T$ conditions would enable us to better constrain the influence of P and T on inter-mineral partitioning of the light elements.

Improvement of modelling of light elements in subduction zones In this thesis, the mobilisation of Li, Be and B during progressive dehydration of metamorphic rocks was modelled. It was possible to calculate the concentrations of light elements in both the subducted rocks and the released fluids, on the basis of published fluid/clinopyroxene partition coefficients from Brenan *et al.* (1998b). These partition coefficients, however, were determined for diopsidic clinopyroxene at $P = 900\,°$C and $T = 2.0$ GPa, whereas clinopyroxene in HP metamorphic rocks is enriched in jadeite component and models of $P - T$ conditions suggest much lower temperatures for subducting slabs. Therefore, future experimental studies

should focus on fluid/mineral partition coefficients for a broader range of $P - T$ conditions, i.e. closer to the conditions estimated for subducting slabs. In addition, different fluid compositions, different minerals and minerals with variable major element compositions should be investigated.

Modelling of different $P - T$ paths and different lithologies may culminate in a detailed calculation of light-element behaviour in specific subduction zones, and may allow for a quantitative comparison of the modelled input and the measured output of Li, Be, B and their isotopes in a specific subduction zone.

Trace-element modelling for traditional radiogenic isotope systems   Using the established model on mobilisation of Li, Be and B during progressive dehydration of metamorphic rocks, it was possible to calculate the concentrations of light elements in both the subducted rocks and the released fluids. In future studies, such modelling may be applied to the traditional radiogenic isotope systems of Sr, Nd and Pb. Given how widely these isotope systems are used in models of crustal and mantle evolution, it is surprising how little modelling of the behaviour of the parent and daughter elements during dehydration has been undertaken. Mineral/fluid partition coefficients are available (Stalder *et al.*, 1998; Green & Adam, 2003), and the partitioning of Rb, Sr, Sm, Nd, U, Th and Pb among different minerals could be determined using the well-characterised samples from Syros. The LA-ICP-MS analyses performed in the course of this study serve as a preliminary data set for these rocks, together with the bulk rock analyses for all samples. These are essential for quality control and budget calculations during modelling. The results from trace-element modelling of Rb, Sr, Sm, Nd, U, Th and Pb from high-pressure metamorphic rocks could probably yield new constraints on material transfer in subduction zones and the contributions of different reservoirs (sediment, altered oceanic crust, mantle) in island arc magmas.

Li isotopes in Syros blackwall samples   Li isotopes have attracted increasing attention from geochemists working on metamorphic, igneous and sedimentary rocks (see Tomascak, 2004). Like B, the strong isotopic fractionation of Li at low temperatures provides a robust tool for tracing hydrous alteration processes at the Earth's surface, and has great potential as a tracer of low-temperature alteration material in subduction zone related fluids, magmas and metamorphic rocks, as well as in mantle xenoliths and ocean island basalts. The systematics of isotope fractionation for Li are similar to those of B, in that it fractionates during low-temperature ($< 400\,^{\circ}$C) fluid/rock interaction and the heavier isotope enters the fluid (Zack *et al.*, 2003; Elliott *et al.*, 2004). The main difference is in the partitioning of Li and B into the

fluid phase and among mantle minerals. Thus, there is considerable advantage in the integrated application of Li and B isotopes. The geochemical cycle of Li and its isotopic fractionation during major processes like slab dehydration and metasomatism remain uncertain, and so investigation of the Li isotopic compositions of samples with a well-constrained geological history is necessary to understand the geochemical cycle of this new tracer of crustal recycling.

The blackwall rocks from Syros investigated in this study were intensely overprinted by slab-derived fluids during exhumation. The trace-element and B isotopic composition of these rocks reflect the composition of the fluid overprint, and these rocks potentially record the geochemistry of fluid channels above subducted slabs. The high-pressure metamorphic blocks are rimmed by reaction zones composed of hydrous minerals, such as chlorite, amphibole and phengite that coexist with omphacite, albite and tourmaline. The B isotopic composition of tourmaline is exceptionally heavy. The rocks are also strongly enriched in Li, with whole rock concentrations typically ranging from 30 to 80 µg/g. The most important host minerals for Li are chlorite, omphacite and amphibole. Investigation of Li in-situ isotopic composition of individual mineral grains in Syros blackwall rocks would provide important insights (i) into the behaviour of Li isotopes during fluid/rock interaction, and (ii) into the Li isotope budget of subduction related hydrous fluids.

Tourmaline The importance of tourmaline as a major carrier of B in metasediments and in hybrid rocks has been demonstrated in this study, along with the great potential of this mineral as a monitor for the B isotopic evolution of rocks and interacting fluids. Major element compositions of tourmaline in Syros HP metamorphic rocks are close to dravite, and are similar to tourmaline reported from other HP and UHP metamorphic rocks, such as Lago di Cignana and Dora Maira (e.g. Schreyer, 1985; Reinecke, 1998; Werding & Schreyer, 2002). Most trace elements demonstrate very low abundances in Syros toumaline, except for di- and trivalent base metals and Sr. Future research on (U)HP metamorphic tourmaline from different localities may show, (i) whether it is exclusivley of dravitic composition and (ii) if it always shows strong depletion in Li, Be, REE, HFSE and LILE. Results are important not only for the crystallography and chrystal chemistry of tourmaline itself, but also for budget calculations of trace elements in (U)HP metamorphic rocks, and for characterisation of detrital tourmaline in provenance studies on (meta-)sediments. Investigation of B isotope ratios in (U)HP metamorphic tourmaline using a larger range of samples may complete our knowledge on the δ^{11}B evolution of subducting slabs.

Bibliography

Agyei E, McMullen CC (1978) Determination of the isotopic abundance of boron in meteorites and tektites. *USGS Open File Report* 78: 3–6

Ai Y (1994) A revision of the garnet-clinopyroxene Fe^{2+}-Mg exchange geothermometer. *Contributions to Mineralogy and Petrology* 115: 467–473

Aldahan A, Haiping Y, Possnert G (1999) Distribution of beryllium between solution and minerals (biotite and albite) under atmospheric conditions and variable *pH*. *Chemical Geology* 156: 209–229

Alt JC (1995) Subseafloor Processes in Mid-Ocean Ridge Hydrothermal Systems. In: Humphris SE (ed.) *Seafloor Hydrothermal Systems: Physical, Chemical, Biological, and Geological Interactions*, vol. 91 of *Geophysical Monograph Series*, 85–114, American Geophysical Union, Washington, DC

Altherr R, Siebel W (2002) I-type plutonism in a continental back-arc setting: Miocene granitoids and monzonites from the central Aegean Sea, Greece. *Contributions to Mineralogy and Petrology* 143: 397–415

Altherr R, Schliestedt M, Okrusch M, Seidel E, Kreuzer H, Harre W, Lenz H, Wendt I, Wagner GA (1979) Geochronology of high-pressure rocks on Sifnos (Cyclades, Greece). *Contributions to Mineralogy and Petrology* 70: 245–255

Altherr R, Kreuzer H, Wendt I, Lenz H, Wagner GA, Keller J, Harre W, Höhndorf A (1982) A late Oligocene/early Miocene high temperature belt in the Attic-Cycladic crystalline complex (SE Pelagonian, Greece). *Geologisches Jahrbuch* 23: 97–164

Altherr R, Kreuzer H, Lenz H, Wendt I, Harre W, Dürr S (1994) Further evidence for a late Cretaceous low-pressure/high-temperature terrane in the Cyclades, Greece. *Chemie der Erde* 54: 319–328

Altherr R, Topuz G, Marschall H, Zack T, Ludwig T (2004) Evolution of a tourmaline-bearing lawsonite eclogite from Elekdag area (Central Pontides, N Turkey): evidence for infiltration of slab-derived B-rich fluids during exhumation. *Contributions to Mineralogy and Petrology* 148: 409–425

Anders E, Ebihara M (1982) Solar-system abundances of the elements. *Geochimica et Cosmochimica Acta* 46: 2363–2380

Anders E, Grevesse N (1989) Abundances of the elements; meteoritic and solar. *Geochimica et Cosmochimica Acta* 53: 197–214

Andriessen PAM, Hebeda EH, Simon OJ, Verschure RH (1991) Tourmaline K-Ar ages compared to other radiometric dating systems in Alpine anatectic leucosomes and metamorphic rocks (Cyclades and southern Spain). *Chemical Geology* 91: 33–48

Bach W, Alt JC, Niu Y, Humphris SE, Erzinger J, Dick HJB (2001) The geochemical consequences of late-stage low-grade alteration of lower ocean crust at the SW Indian Ridge: Results from ODP Hole 735B (Leg 176). *Geochimica et Cosmochimica Acta* 65: 3267–3287

Baldwin SL (1996) Contrasting P-T-t histories for blueschists from the Western Baja Terrane and the Aegean: effects of synsubduction exhumation and back arc extension. In: Bebout GE, Scholl DW, Kirby SH, Platt JP (eds.) *Subduction top to bottom*, vol. 96 of *Geophysical Monograph Series*, 135–141, American Geophysical Union, Washington, DC

Ballhaus C, Schumacher JC (1995) Stratigraphy, deformation and high-pressure metamorphism of the island of Syros (Cyclades, Greece). *Bochumer Geologische und Geotechnische Arbeiten* 44: 13–16

Barth S (1993) Boron isotope variations in nature: a synthesis. *Geologische Rundschau* 82: 640–651

Barth S (1998) $^{11}B/^{10}B$ variations of dissolved boron in a freshwater-seawater mixing plume (Elbe Estuary, North Sea). *Marine Chemistry* 62: 1–14

Barton MD, Young S (2002) Non-pegmatitic deposits of beryllium: mineralogy, geology, phase equilibria and origin. In: Grew ES (ed.) *Beryllium: mineralogy, petrology and geochemistry*, vol. 50, chap. 14, 591–691, Mineralogical Society of America, Washington, DC

Bates RL, Jackson JA (1980) *Glossary of Geology*. American Geological Institute, Falls Church, Virginia/USA, 2nd edn.

Bebout GE (1996) Volatile transfer and recycling at convergent margins: mass-balance and insights from high P/T metamorphic rocks (overview). In: Bebout GE, Scholl DW, Kirby SH, Platt JP (eds.) *Subduction top to bottom*, vol. 96 of *Geophysical Monograph Series*, 179–194, American Geophysical Union, Washington, DC

Bebout GE, Barton MD (2002) Tectonic and metasomatic mixing in a high-T, subduction-zone mélange – insights into the geochemical evolution of the slab-mantle interface. *Chemical Geology* 187: 79–106

Bebout GE, Nakamura E (2003) Record in metamorphic tourmaline of subduction-zone devolatilization and boron cycling. *Geology* 31: 407–410

Bebout GE, Ryan JG, Leeman WP (1993) B-Be systematics in subduction-related metamorphic rocks: Characterization of the subducted component. *Geochimica et Cosmochimica Acta* 57: 2227–2237

Bebout GE, Ryan JG, Leeman WP, Bebout AE (1999) Fractionation of trace elements by subduction-zone metamorphism – effect of convergent-margin thermal evolution. *Earth and Planetary Science Letters* 171: 63–81

Behrens H (1995) Determination of water solubilities in high-viscosity melts: an experimental study on $NaAlSi_3O_8$ and $KAlSi_3O_8$. *European Journal of Mineralogy* 73: 905–920

Benninghoven A, Rüdenauer FG, Werner HW (1987) *Secondary Ion Mass Spectrometry*. John Wiley and Sons, New York, Chichester, Brisbane, Toronto, Singapore

Benton LD, Ryan JG, Tera F (2001) Boron isotope systematics of slab fluids as inferred from a serpentine seamount, Mariana forearc. *Earth and Planetary Science Letters* 187: 273–282

Benton LD, Ryan JG, Savov IP (2004) Lithium abundance and isotope systematics of forearc serpentinites, Conical Seamount, Mariana forearc: Insights into the mechanics of slab-mantle exchange during subduction. *Geochemistry, Geophysics, Geosystems* 5, doi: 10.1029/2004GC000708

Berger G, Schott J, Guy C (1988) Behaviour of Li, Rb and Cs during basalt glass and olivine dissolution and chlorite, smectite and zeolite precipitation from seawater: Experimental investigations and modelization between $50\,°C$ and $300\,°C$. *Chemical Geology* 71: 297–312

Bergeron M (1989) Distribution et comportement du bore dans la croûte océanique. *Canadian Journal of Earth Sciences* 26: 782–790

Blundy JD, Dalton J (2000) Experimental comparison of trace element partitioning between clinopyroxene and melt in carbonate and silicate systems, and implications for mantle metasomatism. *Contributions to Mineralogy and Petrology* 139: 356–371

Blundy JD, Wood BJ (1994) Prediction of crystal-melt partition coefficients from elastic moduli. *Nature* 372: 452–454

Blundy JD, Robinson JAC, Wood BJ (1998) Heavy REE are compatible in clinopyroxene on the spinel lherzolite solidus. *Earth and Planetary Science Letters* 160: 493–504

Bohlen SR, Boettcher AL (1982) The quartz-coesite transformation: A pressure determination and the effects of other components. *Journal of Geophysical Research* 87: 7073–7078

Bonatti E, Lawrence JR, Morandi N (1984) Serpentinization of oceanic peridotites: temperature dependence of mineralogy and boron content. *Earth and Planetary Science Letters* 70: 88–94

Bonneau M, Blake MC Jr, Geyssant J, Kienast JR, Lepvrier C, Maluski H, Papanikolaou D (1980a) Sur la signification des séries métamorphiques (schists bleus) des Cyclades (Hellénides, Grèce. L'exemple de l'île de Syros. *Comptes Rendus de l'Académie des Sciences, Paris, Série D* 290: 1463–1466

Bonneau M, Geyssant J, Kienast JR, Lepvrier C, Maluski H (1980b) Tectonique et métamorphisme Haute Pression d'âge éocène dans les Hellénides: exemple de l'île de Syros (Cyclades, Grèce). *Comptes Rendus de l'Académie des Sciences, Paris, Série D* 291: 171–174

Bouman C (2004) *Lithium isotope systematics at subduction zones*. Ph.D. thesis, Vrije Universiteit Amsterdam

Bouman C, Elliott T, Vroon PZ (2004) Lithium inputs to subduction zones. *Chemical Geology* 212: 59–79

Bourlès DL, Klinkhammer G, Campbell AC, Measures CI, Brown ET, Edmond JM (1989) Beryllium in marine pore waters: geochemical and geochronological implications. *Nature* 341: 731–733

Bourlès DL, Raisbeck GM, Brown ET, Yiou F, Edmond JM (1991) Beryllium isotope systematics of submarine hydrothermal systems. *Earth and Planetary Science Letters* 105: 534–542

Boynton WV (1985) *Developments in Geochemistry*, chap. Rare Earth Element Geochemistry, 115. Elsevier, Amsterdam

Brady JB, Able LM, Cheney JT, Sperry AJ, Schumacher JC (2001) Prograde lawsonite pseudomorphs in blueschists from Syros, Greece. *Geological Society of America, Abstracts with Program* 33: 250–251

Brady JB, Markley MJ, Schumacher JC, Cheney JT, Bianciardi GA (2004) Aragonite pseudomorphs in high-pressure marbles of Syros, Greece. *Journal of Structural Geology* 26: 3–9

Brenan JM, Neroda E, Lindstrom CC, Shaw HF, Ryerson FJ, Phinney DL (1998a) Behavior of boron, beryllium and lithium during melting and crystallization: constraints from mineral-melt partitioning experiments. *Geochimica et Cosmochimica Acta* 62: 2129–2141

Brenan JM, Ryerson FJ, Shaw HF (1998b) The role of aqueous fluids in the slab-to-mantle transfer of boron, beryllium, and lithium during subduction: Experiments and models. *Geochimica et Cosmochimica Acta* 62: 3337–3347

Bröcker M (1990) Blueschist-to-greenschist transition in metabasites from Tinos island (Cyclades, Greece): compositional control of fluid infiltration. *Lithos* 25: 25–39

Bröcker M, Enders M (1999) U-Pb zircon geochronology of unusual eclogite-facies rocks from Syros and Tinos (Cyclades, Greece). *Geological Magazine* 136: 111–118

Bröcker M, Enders M (2001) Unusual bulk-rock compositions in eclogite-facies rocks from Syros and Tinos (Cyclades, Greece): implications for U-Pb zircon geochronology. *Chemical Geology* 175: 581–603

Bröcker M, Franz L (1998) Rb-Sr isotope studies on Tinos Island (Cyclades, Greece): additional time constraints from metamorphism, extent of infiltration-controlled overprinting and deformational activity. *Geological Magazine* 135: 369–382

Broeker WS, Peng T-H (1982) *Tracers in the sea*. Lamont-Doherty Geological Observatory, Palisades, New York (USA)

Brooker RA, James RH, Blundy JD (2004) Trace elements and Li isotope systematics in Zabargad peridotites: evidence of ancient subduction processes in the Red Sea mantle. *Chemical Geology* 212: 179–204

Brown ET, Edmond JM, Raisbeck GM, Bourlès DL, Yiou F, Measures CI (1992) Beryllium isotope geochemistry in tropical river basins. *Geochimica et Cosmochimica Acta* 56: 1607–1624

Bryant PJ (1992) Basic theory for magnetic measurements. *CERN* 5: 52–69

Bundy FP (1980) The P,T phase and reaction diagram for elemental carbon. *Journal of Geophysical Research* 88: 6930–6936

Bureau H, Keppler H (1999) Complete miscibility between silicate melts and hydrous fluids in the upper mantle: experimental evidence and geological implications. *Earth and Planetary Science Letters* 165: 187–196

Cabato J, Altherr R, Ludwig T (2004) Li, Be and B in dacite rocks from Nea Kameni, Santorini, Greece. *Supplement issue of Geochimica et Cosmochimica Acta* 68: A56

Carson CJ, Clarke GL, Powell R (2000) Hydration of eclogite from the Pam Peninsula, New Caledonia. *Journal of Metamorphic Geology* 18: 79–90

Catanzaro FJ, Champion CE, Garner EL, Marinenko G, Sappenfield KM, Shields WR (1970) Boric acid: isotopic and assay standard reference materials. *National Bureau of Standards (US) Special Publications* 260: 1–70

Chacko T, Cole DR, Horita J (2001) Equilibrium oxygen, hydrogen and carbon isotope fractionation factors applicable to geologic systems. In: Valley JW, Cole DR (eds.) *Stable Isotope Geochemistry*, vol. 43, chap. 1, 1–81, Mineralogical Society of America, Washington, DC

Chan LH, Edmond JM (1988) Variation of lithium isotope composition in the marine environment: a preliminary report. *Geochimica et Cosmochimica Acta* 52: 1711–1717

Chan LH, Frey FA (2003) Lithium isotope geochemistry of the Hawaiian plume: results from the Hawaii Scientific Drilling Project and Koolau Volcano. *Geochemistry, Geophysics, Geosystems* 4, doi:10.1029/2002GC000365

Chan LH, Kastner M (2000) Lithium isotopic compositions of pore fluids and sediments in the Costa Rica subduction zone: implications for fluid processes and sediment contribution to the arc volcanoes. *Earth and Planetary Science Letters* 183: 275–290

Chan LH, Edmond JM, Thompson G, Gillis K (1992) Lithium isotopic composition of submarine basalts: Implications for the lithium cycle in the ocean. *Earth and Planetary Science Letters* 108: 151–160

Chan LH, Edmond JM, Thompson G (1993) A lithium isotope study of hot springs and metabasalts from mid-ocean ridge hydrothermal systems. *Journal of Geophysical Research* 98: 9653–9659

Chan LH, Gieskes JM, You C-F, Edmond JM (1994a) Lithium isotope geochemistry of sediments and hydrothermal fluids of the Guaymas Basin. *Geochimica et Cosmochimica Acta* 58: 4443–4454

Chan LH, Zhang L, Hein JR (1994b) Lithium isotope characteristics of marine sediments. *EOS Transactions of the American Geophysical Union* 75: 314

Chan LH, Alt JC, Teagle DAH (1996) Alterations of the upper 1.8 kilometers of oceanic crust: A lithium isotope record at ODP site 504B. *EOS Transactions of the American Geophysical Union* 77: F805

Chan LH, Leeman WP, You C-F (2002a) Lithium isotopic composition of Central American volcanic arc lavas: implications for modification of subarc mantle by slab-derived fluids: correction. *Chemical Geology* 182: 293–300

Chan LH, Starinsky A, Katz A (2002b) The behavior of lithium and its isotopes in oilfield brines: evidence from the Heletz-Kokhav field, Israel. *Geochimica et Cosmochimica Acta* 66: 615–623

Chase Z, Anderson RF, Fleisher MQ, Kubik PW (2002) The influence of particle composition and particle flux on scavenging of Th, Pa and Be in the ocean. *Earth and Planetary Science Letters* 204: 215–229

Chaussidon M (1995) Isotope geochemistry of boron in mantle rocks, tektites and meteorites. *Comptes Rendus de l'Académie des Sciences, Paris* 321: 455–472

Chaussidon M, Albarède F (1992) Secular boron isotope variations in the continental crust: an ion microprobe study. *Earth and Planetary Science Letters* 108: 229–241

Chaussidon M, Appel PWU (1997) Boron isotopic composition of tourmalines from the 3.8-Ga-old Isua supracrustals, West Greenland: implications on the Delta[11]B value of early Archean seawater. *Chemical Geology* 136: 171–180

Chaussidon M, Jambon A (1994) Boron content and isotopic composition of oceanic basalts: Geochemical and cosmochemical implications. *Earth and Planetary Science Letters* 121: 277–291

Chaussidon M, Libourel G (1993) Boron partitioning in the upper mantle: an experimental and ion microprobe study. *Geochimica et Cosmochimica Acta* 57: 5053–5062

Chaussidon M, Marty B (1995) Primitive boron isotope composition of the mantle. *Science* 269: 383–386

Chaussidon M, Robert F (1995) Nucleosynthesis of [11]B-rich boron in the pre-solar cloud recorded in meteoritic chondrules. *Nature* 374: 337–339

Chaussidon M, Robert F (1998) ^{7}Li/^{6}Li and ^{11}B/^{10}B variations in chondrules from the Semarkona unequilibrated chondrite. *Earth and Planetary Science Letters* 164: 577–589

Chaussidon M, Robert F, Mangin D, Hanon P, Rose EF (1997) Analytical procedures for the measurement of boron isotope composition by ion microprobe in meteorites and mantle rocks. *Geostandards Newsletter* 21: 7–17

Clarke DB, Reardon NC, Chatterjee AK, Gregoire DC (1989) Tourmaline composition as a guide to mineral exploration: a reconnaissance study from Nova Scotia using discriminant function analysis. *Economic Geology* 84: 1921–1935

Clift PD, Rose EF, Shimizu N, Layne GD, Draut AE, Regelous M (2001) Tracing the evolving flux from the subducting plate in the Tonga-Kermadec arc system using boron in volcanic glass. *Geochimica et Cosmochimica Acta* 65: 3347–3364

Conolly JAD (1990) Multivariable phase diagrams: An algorithm based on generalized thermodynamics. *American Journal of Science* 290: 666–718

Currie LA (1968) Limits for Qualitative Detection and Quantitative Determination. *Analytical Chemistry* 40: 586–593

Curtis D, Gladney E, Jurney E (1980) A revision of the meteorite based cosmic abundance of boron. *Geochimica et Cosmochimica Acta* 44: 1945–1953

Danyushevsky LV, Eggins SM, Falloon TJ, Christie DM (2000) H_2O abundance in depleted to moderately enriched mid-ocean ridge magmas; part I: incompatible behaviour, implications for mantle storage, and origin of regional variations. *Journal of Petrology* 41: 1329–1364

Decitre S, Deloule E, Reisberg L, James R, Agrinier P, Mével C (2002) Behavior of Li and its isotopes during serpentinization of oceanic peridotites. *Geochemistry, Geophysics, Geosystems* 3, doi:10.1029/2001GC000178

Decitre S, Buatier M, James R (2004) Li and Li isotopic composition of hydrothermally altered sediments at Middle Valley, Juan de Fuca. *Chemical Geology* 211: 363–373

Dell WJ, Bray PJ, Xiao SZ (1983) ^{11}B NMR studies and structural modelling of Na_2O-B_2O_3-SiO_2 glasses of high soda content. *Journal of Non-Crystalline Solids* 58: 1–16

Deyhle A, Kopf A (2001) Deep fluids and ancient pore waters at the backstop; stable isotope systematics (B, C, O) of mud-volcano deposits on the Mediterranean Ridge accretionary wedge. *Geology* 29: 1031–1034

Deyhle A, Kopf A (2002) Strong B enrichment and anomalous δ^{11}B in pore fluids from the Japan trench forearc. *Marine Geology* 183: 1–15

Dingwell DB, Pichavant M, Holtz F (2002) Experimental studies of boron in granitic melts. In: Grew ES, Anovitz LM (eds.) *Boron: mineralogy, petrology and geochemistry*, vol. 33 of *Reviews in Mineralogy*, chap. 8, 331–385, Mineralogical Society of America, Washington, DC, 2nd edn.

Dixon JE (1968) *The metamorphic rocks of Syros, Greece*. Ph.D. thesis, St. John's College, Cambridge

Dixon JE, Ridley J (1987) Syros. In: Helgeson HC (ed.) *Chemical transport in metasomatic processes*, vol. 218 of *NATO ASI Series C, Mathematical and Physical Sciences*, 489–501, Reidel, Dordrecht

Domanik KJ, Hervig RL, Peacock SM (1993) Beryllium and boron in subduction zone minerals: an ion microprobe study. *Geochimica et Cosmochimica Acta* 57: 4997–5010

Donnelly TW, Thompson G, Salisbury MH (1980) The chemistry of altered basalts at site 417, Deep Sea Drilling Project Leg 51. *Initial Reports DSDP* 51-53: 1319–1330

Donohue CL, Essene EJ (2000) An oxygen barometer with the assemblage garnet-epidote. *Earth and Planetary Science Letters* 181: 459–472

Dostal J, Dupuy C, Dudoignon P (1996) Distribution of boron, lithium and beryllium in ocean island basalts from French Polynesia; implications for the B/Be and Li/Be ratios as tracers of subducted components. *Mineralogical Magazine* 60: 563–580

Douville E, Charlou JL, Oelkers EH, Bienvenu P, Jove Colon CF, Donval JP, Fouquet Y, Prieur D, Appriou P (2002) The rainbow vent fluids (36°14' N, MAR): the influence of ultramafic rocks and phase separation on trace metal content in Mid-Atlantic Ridge hydrothermal fluids. *Chemical Geology* 184: 37–48

Dürr S (1986) Das Attisch-kykladische Kristallin. In: Jacobshagen V (ed.) *Geologie von Griechenland*, vol. 19 of *Beiträge zur regionalen Geologie der Erde*, 116–148, Gebrüder Bornträger, Stuttgart

Dürr S, Altherr R, Keller J, Okrusch M, Seidel E (1978) The median Aegean crystalline belt: stratigraphy, structure, metamorphism, magmatism. In: Closs H, Roeder DH, Schmidt K (eds.) *Alps, Apennines, Hellenides*, vol. 38 of *Inter-Union Commission on Geodynamics, Scientific Report*, 455–477, Schweizerbart, Stuttgart

Dutrow BL, Foster CT Jr, Henry DJ (1999) Tourmaline-rich pseudomorphs in sillimanite zone metapelites: Demarcation of an infiltration front. *American Mineralogist* 84: 794–805

Dyar MD, Taylor ME, Lutz TM, Francis CA, Guidotti CV, Wise M (1998) Inclusive chemical characterization of tourmaline: Mössbauer study of Fe valence and site occupancy. *American Mineralogist* 83: 848–864

Dyar MD, Wiedenbeck M, Robertson D, Cross LR, Delaney JS, Ferguson K, Francis CA, Grew ES, Guidotti CV, Hervig RL, Hughes JM, Husler J, Leeman W, McGuire AV, Rhede D, Rothe H, Paul RL, Richards I, Yates M (2001) Reference minerals for the microanalysis of light elements. *Geostandards Newsletter* 25: 441–463

Earley D III, Dyar MD, Ilton ES, Granthem AA (1995) The influence of structural fluorine on biotite oxidation in copper-bearing, aqueous solutions at low temperatures and pressures. *Geochimica et Cosmochimica Acta* 59: 2423–2433

Edmond JM, Measures C, McDuff RE, Chan LH, Collier R, Grant B, Gordon LI, Corliss JB (1979) Ridge crest hydrothermal activity and the balances of the major and minor elements in the ocean: The Galapagos data. *Earth and Planetary Science Letters* 46: 1–18

Eggins SM, Rudnick RL, McDonough WF (1998) The composition of peridotites and their minerals: a laser-ablation ICP-MS study. *Earth and Planetary Science Letters* 154: 53–71

Elliott T (2003) Tracers of the Slab. In: Eiler J (ed.) *Inside the Subduction Factory*, vol. 138 of *Geophysical Monograph Series*, 23–45, American Geophysical Union, Washington, DC, 1st edn.

Elliott T, Jeffcoate A, Bouman C (2004) The terrestrial Li isotope cycle: light-weight constraints on mantle convection. *Earth and Planetary Science Letters, Frontiers* 220: 231–245

Engi M, Berger A, Roselle GT (2001) Role of the tectonic accretion channel in collisional orogeny. *Geology* 29: 1143–1146

Ernst WG (2001) Subduction, ultrahigh-pressure metamorphism, and regurgitation of buoyant crustal slices; implications for arcs and continental growth. *Physics of the Earth and Planetary Interiors* 127: 253–275

Ertl A, Pertlik F, Bernhardt HJ (1997) Investigations on olenite with excess boron from Koralpe, Styria, Austria. *Österreichische Akademie der Wissenschaften, Mathematisch-naturwissenschaftliche Kl, Abteilung I, Anzeiger* 134: 3–10

Evans BW, Trommsdorff V, Richter W (1979) Petrology of an eclogite-metarodingite suite at Cima di Gagnone, Ticino, Switzerland. *American Mineralogist* 64: 15–31

Fitzherbert JA, Clarke GL, Marmo B, Powell R (2004) The origin and *P-T* evolution of peridotites and serpentinites of NE New Caledonia: prograde interaction between continental margin and the mantle wedge. *Journal of Metamorphic Geology* 22: 327–344

Foustoukos DI, James RH, Berndt ME, Seyfried WE Jr (2004) Lithium isotopic systematics of hydrothermal vent fluids at the Main Endeavour Field, Northern Juan de Fuca Ridge. *Chemical Geology* 212: 17–26

Franz G, Morteani G (2002) Be-minerals: synthesis, stability, and occurrence in metamorphic rocks. In: Grew ES (ed.) *Beryllium: mineralogy, petrology and geochemistry*, vol. 50 of *Reviews in Mineralogy*, chap. 13, 551–589, Mineralogical Society of America, Washington, DC

Fuchs Y, Lagache M (1994) La transformation chlorite-tourmaline en milieu hydrothermal, exemples naturels et approche expérimentale. *Comptes Rendus de l'Académie des Sciences, Paris, Série II* 2: 907–913

Gao S, Luo T, Zhang B, Zhang H, Han Y, Zhao Z, Hu Y (1998) Chemical composition of the continental crust as revealed by studies in East China. *Geochimica et Cosmochimica Acta* 62: 1959–1975

Gerya TV, Stoeckert B, Perchuk AL (2002) Exhumation of high-pressure metamorphic rocks in a subduction channel; a numerical simulation. *Tectonics* 21: 6–19

Gméling K, Szabolcs H, Kasztovszky Zs (2005) Boron and chlorine concentration of volcanic rocks: an application of prompt gamma activation analysis. *Journal of Radioanalytical and Nuclear Chemistry* 265: 201–214

Gonfiantini R, Tonarini S, Gröning M, Adorni-Braccesi A, Al-Ammar AS, Astner M, Bächler S, Barnes RM, Basset RL, Cocherie A, Deyhle A, Dini A, Ferrara G, Gaillardet J, Grimm J, Guerrot C, Krähenbühl U, Layne G, Lemarchand D, Meixner A, Northington DJ, Pennisi M, Reitznerová E, Rodushkin I, Sugiura N, Surberg R, Tonn S, Wiedenbeck M, Wunderli S, Xiao Y, Zack T (2003) Intercomparison of boron isotope and concentration measurements. Part II: evaluation of results. *Geostandards Newsletter* 27: 41–57

Govindaraju K (1994) 1994 compilation of working values and sample description for 383 geostandards. *Geostandards Newsletter* 18: 1–158

Green TH, Adam J (2003) Experimentally-determined trace element characteristics of aqueous fluid from partially dehydrated mafic oceanic crust at 3.0 GPa, 650 − 700 °C. *European Journal of Mineralogy* 15: 815–830

Griffin WL, Slack JF, Ramsden AR, Win TT, Ryan CG (1996) Trace elements in tourmalines from massive sulfide deposits and tourmalinites: geochemical controls and exploration applications. *Economic Geology* 91: 657–675

Guillot S, Hattori KH, de Sigoyer J, Nägler T, Auzende AL (2001) Evidence of hydration of the mantle wedge and its role in the exhumation of eclogites. *Earth and Planetary Science Letters* 193: 115–127

Hacker BR, Calvert A, Zhang RY, Ernst G, Liou JG (2003) Ultrarapid exhumation of ultrahigh-pressure diamond-bearing metasedimentary rocks of the Kokchetav Massif, Kazakhstan? *Lithos* 70: 61–75

Harlow GE (1994) Jadeitites, albitites and related rocks from the Motagua fault zone, Guatemala. *Journal of Metamorphic Geology* 12: 49–68

Harris NBW, Gravestock P, Inger S (1992) Ion-microprobe determinations of trace-element concentrations in garnets from anatectic assemblages. *Chemical Geology* 100: 41–49

Hausmann JFL (1845) Beiträge zur Oryktographie von Syra und ein neues Mineral, der Glaukophan. *Göttinger Gelehrte Anzeigen* 20: 193–198

Hawthorne FC, Henry DJ (1999) Classification of the minerals of the tourmaline group. *European Journal of Mineralogy* 11: 201–215

Hawthorne FC, Huminicki DMC (2002) The crystal chemistry of beryllium. In: Grew ES (ed.) *Beryllium: mineralogy, petrology and geochemistry*, vol. 50 of *Reviews in Mineralogy*, chap. 9, 333–403, Mineralogical Society of America, Washington, DC

Hawthorne FC, Burns PC, Grice JD (2002) The crystal chemistry of boron. In: Grew E, LM A (eds.) *Boron: mineralogy, petrology and geochemistry*, vol. 33 of *Reviews in Mineralogy*, chap. 2, 41–116, Mineralogical Society of America, Washington, DC, 2nd edn.

Hecht J (1984) *Geological map of Greece 1:50 000, Syros island.* Institut of Geology and Mineral Exploration, Athens

Heinrich W, Wunder B, Romer RL, Meixner A, Wirth R (2003) B-isotope-distribution between boro-muscovite and fluid: first results of an experimental study. *Beiheft 1 zu European Journal of Mineralogy* 15: 79

Helbling A, Marschall HR (2002) Helena Irma Beryl Marschall: When I grow up, I'll also do measurements at the ionprobe (translated title). *Journal of Genetical Reproduction* 7: 24

Helbling A, Marschall HR (2005) Mama's belly is really huge now. *Bulletin of new Babies* in prep.

Helbling A, Altherr R, Ludwig T (2004) Partitioning of Li, Be and B in a K-rich rhyolithic ignimbrite. *Supplement issue of Geochimica et Cosmochimica Acta* 68: A57

Hemming NG, Hanson GN (1992) Boron isotopic composition and concentration in modern marine carbonates. *Geochimica et Cosmochimica Acta* 56: 537–543

Henry DJ, Dutrow BL (1994) Tourmaline in metamorphic rocks: A monitor of boron flux. *Geological Society of America, Abstarcts with Programs* 26: A449

Henry DJ, Dutrow BL (2002) Metamorphic tourmaline and its petrologic applications. In: Grew ES, Anovitz LM (eds.) *Boron: mineralogy, petrology and geochemistry*, vol. 33 of *Reviews in Mineralogy*, chap. 10, 503–557, Mineralogical Society of America, Washington, DC, 2nd edn.

Hepp S (2003) *Amphibolite als Dokumente orogener Prozesse - eine Fallstudie aus dem Schwarzwald (Mitteleuropäische Varisziden).* Dr. rer. nat. thesis, Universität Heidelberg, Germany

Hermann J (2002) Allanite: thorium and light rare earth element carrier in subducted crust. *Chemical Geology* 192: 289–306

Hervig RL, Moore GM, Williams LB, Peacock SM, Holloway JR, Roggensack K (2002) Isotopic and elemental partitioning of boron between hydrous fluid and silicate melt. *American Mineralogist* 87: 769–774

Hezel D (2000) Chemical characterization of tourmaline from magmatic and metamorphic rocks of the island of Ikaria (Aegean Sea). *Beiheft 1 zu European Journal of Mineralogy* 12: 82

Higgins MD, Shaw DM (1984) Boron cosmochemistry interpreted from abundances in mantle xenoliths. *Nature* 308: 172–173

Hillers M (2003) *Die chemische Zusammensetzung der Minerale in miozänen I-Typ-Granitoiden der Ägäis unter besonderer Berücksichtigung von Li, Be und B*. Diploma thesis, Universität Heidelberg, Germany

Hoefs J, Sywall M (1997) Lithium isotope composition of Quarternary and Tertiary biogene carbonates and global lithium isotope balance. *Geochimica et Cosmochimica Acta* 61: 2679–2690

Hofmann AW (1988) Chemical differentiation of the Earth: the relationship between mantle, continental crust, and oceanic crust. *Earth and Planetary Science Letters* 90: 297–314

Holland HD (1980) *The Chemical Evolution of the Atmosphere and the Oceans*. Princeton University Press, Princeton, New Jersey, USA

Honnorez J, Kirst P (1975) Petrology of rodingites from the equatorial Mid-Atlantic fracture zones and their geotectonic significance. *Contributions to Mineralogy and Petrology* 49: 233–257

Höpfer N (1989) *Petrologie der Metagabbros und Eklogite von Syros (Kykladen, Griechenland)*. Diploma thesis, Universität Bonn, Germany

Hubert JF (1962) A zircon-tourmaline-rutile maturity index and the independence of the composition of heavy mineral assemblage with the gross composition and texture of sandstones. *Journal of Sedimentary Petrology* 32: 440–450

Hughes JM, Ertl A, Dyar MD, Grew E, Shearer CK, Yates MG, Giudotti CV (2000) Tetrahedrally coordinated boron in a tourmaline: boron-rich olenite from Stoffhütte, Koralpe, Austria. *Canadian Mineralogist* 38: 861–868

Ishikawa T, Nakamura E (1992) Boron isotope geochemistry of the oceanic crust from DSDP/ODP Hole 504B. *Geochimica et Cosmochimica Acta* 56: 1633–1639

Ishikawa T, Nakamura E (1993) Boron isotope systematics of marine sediments. *Earth and Planetary Science Letters* 117: 567–580

Ishikawa T, Nakamura E (1994) Origin of the slab component in arc lavas from across-arc variation of B and Pb isotopes. *Nature* 370: 205–208

Ishikawa T, Tera F (1997) Source, composition and distribution of the fluid in the Kurile mantle wedge: constraints from across-arc variations of B/Nb and B isotopes. *Earth and Planetary Science Letters* 152: 123–138

Ishikawa T, Tera F, Nakazawa T (2001) Boron isotope and trace element systematics of the three volcanicc zones in the Kamchatka arc. *Geochimica et Cosmochimica Acta* 65: 4523–4537

Jacobshagen V (1986) Bau und Entwicklung der griechischen Gebirge. In: Jacobshagen V (ed.) *Beiträge zur regionalen Geologie der Erde*, vol. 19, 11–53, Gebrüder Bornträger, Berlin, Stuttgart

Jagoutz E, Palme H, Baddenhausen H, Blum K, Cendales M, Dreibus G, Spettel B, Lorenz V, Wänke H (1979) The abundances of major, minor and trace elements in the Earth's mantle as derived from primitive ultramafic nodules. *Proceedings of the 10th Lunar and Planetary Science Conference* 2031–2050

James RH, Elderfield H, Palmer MR (1995) The chemistry of hydrothermal fluids from Broken Spur site, 29°N Mid-Atlantic Ridge. *Geochimica et Cosmochimica Acta* 59: 651–659

Jeffrey PG, Hutchinson D (1981) *Chemical Methods of Rock Analysis*. Pergamon Press, Oxford, 3 edn.

Jiang S (1998) Stable and radiogenic isotope studies of tourmaline: an overview. *Journal of the Czech Geological Society* 43: 75–90

Jiang S-H, Yu J-M, Lu J-J (2004) Trace and rare-earth element geochemistry in tourmaline and cassiterite from the Yunlong tin deposit, Yunnan, China: implication for migmatitic-hydrothermal fluid evolution and ore genesis. *Chemical Geology* 209: 193–213

Jiang S-Y, Yang J-H, Novák M, Selway J (2003) Chemical and boron isotopic compositions of tourmaline from the Lavicky leucogranite, Czech Republic. *Geochemical Journal* 37: 545–556

Jiang SY, Han F, Shen JZ, Palmer MR (1999) Chemical and Rb-Sr, Sm-Nd isotopic systematics of tourmaline from the Dachang Sn-polymetallic ore deposit, Guangxi Province, P.R. China. *Chemical Geology* 157: 49–67

Johnson MC, Plank T (1999) Dehydration and melting experiments constrain the fate of subducted sediments. *Geochemistry, Geophysics, Geosystems* 1, doi:1999GC000014

Johnson SP, Oliver GJH (2002) High f_2 metasomatism during whiteschist metamorphism, Zambezi Belt, Northern Zimbabwe. *Journal of Petrology* 43: 271–290

Jolivet L, Faccenna C, Goffé B, Burov E, Agard P (2003) Subduction tectonics and exhumation of high-pressure metamorphic rocks in the Mediterranean orogens. *American Journal of Science* 303: 353–409

Kakihana H, Kotaka M, Satoh S, Nomura M, Okamoto M (1977) Fundamental studies on the ion exchange separation of boron isotopes. *Bulletin of the Chemical Society of Japan* 50: 158–163

Kaliwoda M (2004) *Petrologie und Li-, Be- und B-Systematik von Mantelxenolithen aus dem Harrat Uwayrid (Saudi Arabien)*. Dr. rer. nat. thesis, Universität Heidelberg, Germany

Kaliwoda M, Altherr R, Ludwig T (2004) Metasomatic phenomena and Li-Be-B characteristics of mantle xenoliths from Harrat Uwayrid, Saudi Arabia. *Supplement issue of Geochimica et Cosmochimica Acta* 68: A53

Kalt A, Schreyer W, Ludwig T, Prowatke S, Bernhardt HJ, Ertl A (2001) Complete solid solution between magnesian schorl and lithian excess-boron olenite in a pegmatite from the Koralpe (eastern Alps, Austria). *European Journal of Mineralogy* 13: 1191–1205

Kamenetsky VS, Everard JL, Crawford AJ, Varne R, Eggins SM, Lanyon R (2000) Enriched end-member of primitive MORB melts: petrology and geochemistry of glasses from Macquarie Island (SW Pacific). *Journal of Petrology* 41: 411–430

Kasemann S, Erzinger J, Franz G (2000) Boron recycling in the continental crust of the central Andes from the Paleozoic to Mesozoic, NW Argentina. *Contributions to Mineralogy and Petrology* 140: 328–343

Kasemann S, Meixner A, Rocholl A, Vennemann T, Rosner M, Schmitt AK, Wiedenbeck M (2001) Boron and oxygen isotopic composition of certified reference materials NIST SRM 610/612 and reference materials JB-2 and JR-2. *Geostandards Newsletter* 25: 405–416

Kaste JM, Norton SA, Hess CT (2002) Environmental chemistry of beryllium-7. In: Grew ES (ed.) *Beryllium: mineralogy, petrology and geochemistry*, vol. 50 of *Reviews in Mineralogy*, chap. 6, 271–289, Mineralogical Society of America, Washington, DC

Keay S (1998) *The geological evolution of the Cyclades, Greece: constraints from SHRIMP U-Pb geochronology*. Ph.D. thesis, Australian National University, Canberra

Keiter M, Piepjohn K, Ballhaus C, Bode M, Lagos M (2004) Structural development of high-pressure metamorphic rocks on Syros island (Cyclades, Greece). *Journal of Structural Geology* 26: 1433–1445

Kelley KA, Plank T, Ludden J, Staudigel H (2003) Composition of altered oceanic crust at ODP Sites 801 and 1149. *Geochemistry, Geophysics, Geosystems* 4, doi:10.1029/2002GC000435

Kent AJR, Rossman GR (2002) Hydrogen, lithium, and boron in mantle-derived olivine: The role of coupled substitutions. *American Mineralogist* 87: 1432–1436

Kerrick DM, Conolly JAD (2001) Metamorphic devolatilization of subducted oceanic metabasalts: implications for seismicity, arc magmatism and volatile recycling. *Earth and Planetary Science Letters* 189: 19–29

King RW, Kerrich R (1989) Strontium isotope composition of tourmaline from gold lode deposits of th Archean Abitibi Greenstone Belt (Ontario-Quebec, Canada): implications for source reservoirs. *Chemical Geology* 79: 225–240

Kirsten T (1964) *Edelgasisotope in irdischen Mineralen und Gesteinen.* Dr. rer. nat. thesis, Universität Heidelberg

Klemme S, Blundy JD, Wood BJ (2002) Experimental constraints on major and trace element partitioning during partial melting of eclogite. *Geochimica et Cosmochimica Acta* 66: 3109–3123

Koepke J, Feig ST, Snow J, Freise M (2004) Petrogenesis of oceanic plagiogranites by partial melting of gabbros: an experimental study. *Contributions to Mineralogy and Petrology* 146: 414–432

Kopf A, Deyhle A (2002) Back to the roots; boron geochemistry of mud volcanoes and its implications for mobilization depth and global B cycling. *Chemical Geology* 192: 195–210

Kopf A, Deyhle A, Zuleger E (2000) Evidence for deep fluid circulation and gas hydrate dissociation using boron and boron isotopes of pore fluids in forearc sediments from Costa Rica (ODP Leg 170). *Marine Geology* 167: 1–28

Kopf A, Behrmann JH, Deyhle A, Roller S, Erlenkeuser H (2003a) Isotopic evidence (B, C, O) of deep fluid processes in fault rocks from the active Woodlark Basin detachment zone. *Earth and Planetary Science Letters* 208: 51–68

Kopf A, Germán M, Deyhle A, Frape S, Hesse R (2003b) Fluid geochemistry in the Japan trench forearc (ODP Leg 186): a synthesis. *Proceedings of the Ocean Drilling Program, Scientific Results* 186: 1–23

Kotzer TG, Kyser TK, King RW, Kerrich R (1993) An empirical oxygen and hydrogen isotope geothermometer for quartz-tourmaline and tourmaline-water. *Geochimica et Cosmochimica Acta* 57: 3421–3426

Koval PV, Zorina LD, Kitajev NA, Spiridonov AM, Ariunbileg S (1991) The use of tourmaline in geochemical prospecting for gold and copper mineralization. *Journal of Geochemical Exploration* 40: 349–360

Krishnaswami S, Mangini A, Thomas JH, Sharma P, Cochran JK, Turekian KK, D PP (1982) ^{10}Be and Th isotopes in manganese nodules and adjacent sediments: nodule growth hiswtories and nuclide behavior. *Earth and Planetary Science Letters* 59: 217–234

Krogh Ravna E (2000) The garnet-clinopyroxene Fe^{2+}-Mg geothermometer: an update calibration. *Journal of Metamorphic Geology* 18: 211–219

Krosse S (1995) *Hochdrucksynthese, Stabilität und Eigenschaften der Borsilikate Dravit und Kornerupin sowie Darstellung und Stabilitätsverhalten eines neuen Mg-Al-borates.* Dr. rer. nat. thesis, Ruhr-Universität Bochum, Germany

Ktenas KA (1907) Die Einlagerungen im krystallinen Gebirge der Kykladen auf Syros und Sifnos. *Tschermak's Mineralogische und Petrographische Mitteilungen* 26: 1–67

Kurat G, Palme H, Embey-Isztin A, Touret J, Ntaflos T, Spettel B, Brandstätter F, Palme C, Dreibus G, Prinz M (1993) Petrology and geochemistry of peridotites and associated vein rocks of Zabargad Island, Red Sea, Egypt. *Mineralogy and Petrology* 48: 309–341

Lagos M, Münker C, Tomaschek F, Ballhaus C, Scherer EE (2003) The age of oceanic crust and of HP/LT-metamorphism on Syros (Cyclades, Greece) based on Lu-Hf geochronology and geochemistry. *Geophysical Research Abstracts* 5: 12 851

Lal N, Parchad R, Nagpaul KK (1977) Fission track etching and annealing of tourmaline. *Nuclear Track Detection* 1: 145–148

Laurent R, Herbert Y (1979) Paragenesis of serpentine assemblages in harzburgite tectonites and dunite cumulate from Quebec Appalachians. *Canadian Mineralogist* 17: 857–869

Laverne C, Agrinier P, Hermitte D, Bohn M (2001) Chemical fluxes during hydrothermal alteration of a 1200 m long section of dikes in the oceanic crust, DSDP/ODP Hole 504B. *Chemical Geology* 181: 73–98

Leake BE, Woolley AR, Arps CES, Birch WD, Gilbert MC, Grice JD, Hawthorne FC, Kato A, Kisch HJ, Krivovichev VG, Linthout K, Laird J, Mandarino J, Maresch WV, Nickel EH, Rock NMS, Schumacher JC, Smith DC, Stephenson NCN, Ungaretti L, Whittaker EJW, Youzhi G (1997) Nomenclature of amphiboles Report of the Subcommittee on Amphiboles of the International Mineralogical Association Commission on New Minerals and Mineral Names. *European Journal of Mineralogy* 9: 623–651

Leeman WP (1996) Boron and other fluid-mobile elements in volcanic ars lavas: implications for subduction processes. In: Bebout GE, Scholl DW, Kirby SH, Platt JP (eds.) *Subduction top to bottom*, vol. 96 of *Geophysical Monograph Series*, 269–276, American Geophysical Union

Leeman WP, Sisson VB (2002) Geochemistry of boron and its implications for crustal and mantle processes. In: Grew ES, Anovitz LM (eds.) *Boron: mineralogy, petrology and geochemistry*, vol. 33, 645–708, Mineralogical Society of America, Washington, DC, 2nd edn.

Leeman WP, Tonarini S (2001) Boron isotopic analysis of proposed borosilicate mineral reference samples. *Geostandards Newsletter* 25: 399–403

Leeman WP, Sisson VB, Reid MD (1992) Boron geochemistry of the lower crust: evidence from granulite terranes and deep crustal xenoliths. *Geochimica et Cosmochimica Acta* 56: 775–788

Leeman WP, Tonarini S, Chan LH, Borg LE (2004) Boron and lithium isotopic variations in a hot subduction zone – the southern Washington Cascades. *Chemical Geology* 212: 101–124

Liou JG, Hacker BR, Zhang RY (1997) Into the forbidden zone. *Science* 287: 1215–1216

London D, Evensen JM (2002) Beryllium in silicic magmas and the origin of beryl-bearing pegmatites. In: Grew ES (ed.) *Beryllium: mineralogy, petrology and geochemistry*, vol. 50 of *Reviews in Mineralogy*, chap. 11, 445–486, Mineralogical Society of America, Washington, DC

Ludwig T, Marschall HR, Altherr R (2004) Is there a matrix effect in SIMS boron isotope analysis? *Supplement Issue to Geochimica et Cosmochimica Acta* 68: A54

Maluski H, Bonneau M, Kienast JR (1987) Dating the metamorphic events in the Cycladic area: ^{40}Ar/^{39}Ar data from metamorphic rocks of the island of Syros (Greece). *Bulletin de la Société de Géologique de France* 8: 833–842

Manning DAC, Pichavant M (1983) The role of fluorine and boron in the generation of granitic melts. In: Atherton MP, Gribble CD (eds.) *Migmatites, Melting and Metamorphism*, chap. 7, 94–109, Shiva Publishing, Cheshire

Marschall HR, Ludwig T (2004) The Low-Boron contest: minimising surface contamination and analysing boron concentrations at the ng/g-level by secondary ion mass spectrometry. *Mineralogy and Petrology* 81: 265–278

Marschall HR, Altherr R, Ludwig T, Kalt A (2002a) Li-Be-B partitioning between high-pressure metamorphic minerals and implications for transfer of these elements in subduction zones. *Abstract Volume of the 18th General Meeting of the IMA 2002, Edinburgh* 206–207

Marschall HR, Altherr R, Ludwig T, Kalt A (2002b) On the occurence and characterization of Tourmaline in high-pressure metamorphic rocks from Syros (Greece). *Schriftenreihe der Deutschen Geologischen Gesellschaft* 21: 233

Marschall HR, Altherr R, Ludwig T, Kalt A (2003a) Boron isotope study of high-pressure metamorphic rocks from Syros (Greece) by secondary ion mass spectrometry (SIMS). *Geophysical Research Abstracts* 5: 05 068

Marschall HR, Altherr R, Ludwig T, Kalt A (2003b) Syros tourmaline: evidence for very high-δ^{11}B fluids in subduction zones. *Beiheft 1 zu European Journal of Mineralogy* 15: 127

Marschall HR, Kalt A, Hanel M (2003c) $P-T$ evolution of a Variscan lower-crustal segment: a study of granulites from the Schwarzwald, Germany. *Journal of Petrology* 44: 227–253

Marschall HR, Altherr R, Gméling K, Kasztovszky Z (2004a) Trace element systematics of high-pressure metamorphic rocks from Syros (Greece). *Supplement Issue to Geochimica et Cosmochimica Acta* 68: A42

Marschall HR, Altherr R, Ludwig T, Kalt A (2004b) Evidence for subduction related fluids and their boron isotopic composition from metasomatic zones in high-pressure metamorphic rocks from Syros (Greece). *Geophysical Research Abstracts* 6: 03 865

Marschall HR, Ertl A, Hughes JM, McCammon C (2004c) Metamorphic Na- and OH-rich disordered dravite with tetrahedral boron, associated with omphacite, from Syros, Greece: chemistry and structure. *European Journal of Mineralogy* 16: 817–823

Marschall HR, Rüpke L, Altherr R (2004d) Squeezing out the slab – modelling trace element transfer in subduction zones by using information deduced from HP-rocks. *Beiheft 1 zu European Journal of Mineralogy* 16: 85

Marschall HR, Kasztovszky Zs, Gméling K, Altherr R (2005) Chemical analysis of high-pressure metamorphic rocks by PGNAA - comparison with results from XRF and solution-ICP-MS. *Journal of Radioanalytical and Nuclear Chemistry* 265: 339–348

Matthews A, Putlitz B, Hamiel Y, Hervig RL (2003) Volatile transport during the crystallization of anatectic melts: Oxygen, boron and hydrogen stable isotope study on the metamorphic complex of Naxos, Greece. *Geochimica et Cosmochimica Acta* 67: 3145–3163

McDonough WF, Sun S-S (1995) The composition of the Earth. *Chemical Geology* 120: 223–253

Measures CI, Edmond JM (1983) The geochemical cycle of ^{9}Be: a reconnaissance. *Earth and Planetary Science Letters* 66: 101–110

Melidonis NG, Constantinides DC (1983) The stratabound sulphide mineralisation of Syros (Cyclades, Greece). *Zeitschrift der Deutschen Geologischen Gesellschaft* 134: 555–575

Melzer S, Wunder B (2000) Island-arc basalts alkali ratios: constraints from phengite-fluid partition experiments. *Geology* 28: 583–586

Meyer H-P (1989) *Zur Petrologie von Orbiculiten*. Ph.D. thesis, Universität Karlsruhe, Germany

Molnár GL (2004) *Handbook of Prompt Gamma Activation Analysis*. Kluwer Academic Publishers, Dordrecht

Moran AE, Sisson VB, Leeman WP (1992) Boron depletion during progressive metamorphism: implications for subduction processes. *Earth and Planetary Science Letters* 111: 331–349

Morgan GB IV, London D (1989) Experimental reactions of amphibolite with boron-bearing aqueous fluids at 200 MPa: implications for tourmaline stability and partial melting in mafic rocks. *Contributions to Mineralogy and Petrology* 102: 281–297

Morozov NP (1968) Geochemistry of rare earth alkali elements in the oceans and seas. *Oceanology* 8: 169–178

Morris JD, Gosse J, Brachfeld S, Tera F (2002) Cosmogenic Be-10 and the solid Earth: studies in geomagnetism, subduction zone processes, and active tectonics. In: Grew ES (ed.) *Beryllium: mineralogy, petrology and geochemistry*, vol. 50 of *Reviews in Mineralogy*, chap. 5, 207–270, Mineralogical Society of America, Washington, DC

Müller A, Wiedenbeck M, van der Kerkhof AM, Kronz A, Simon K (2003) Trace elements in quartz – a combined electron microprobe, secondary ion mass spectrometry, laser-ablation ICP-MS, and cathodoluminescence study. *European Journal of Mineralogy* 15: 747–763

Nabelek PI (1987) General equations for modeling fluid/rock interaction using trace elements and isotopes. *Geochimica et Cosmochimica Acta* 51: 1765–1769

Nakamura E, Ishikawa T, Birck J-L, Allegre CJ (1992) Precise boron isotopic analysis of natural rock samples using a boron-mannitol complex. *Chemical Geology* 94: 193–204

Nakano T, Nakamura E (2001) Boron isotope geochemistry of metasedimentary rocks and tourmalines in a subduction zone metamorphic suite. *Physics of the Earth and Planetary Interiors* 127: 233–252

Nishio Y, Nakai S, Yamamoto J, Sumino H, Matsumoto T, Prikhod'ko VS, Arai S (2004) Lithium isotopic systematics of the mantle-derived ultramafic xenoliths: implications for EM1 origin. *Earth and Planetary Science Letters* 217: 245–261

Niu Y, Batiza R (1997) Trace element evidence from seamounts for recycled oceanic crust in the Eastern Pacific mantle. *Earth and Planetary Science Letters* 148: 471–483

Okamoto K, Liou JG, Ogasawara Y (2000) Petrology of the diamond-bearing eclogite in the Kokchetav Massif, northern Kazakhstan. *The Island Arc* 9: 379–399

Okrusch M, Bröcker M (1990) Eclogites associated with high-grade blueschists in the Cyclades archipelago, Greece: a review. *European Journal of Mineralogy* 2: 451–478

Olker B (2001) *Entwicklung und Anwendung eines Computerprogramms zur numerischen Modellierung von Diffusionsprofilen in Mineralkörnern*. Ph.D. thesis, Universität Heidelberg, Germany

Olsher U, Izatt RM, Bradshaw JS, Dalley NK (1991) Coordination chemistry of lithium ion: a crystal and molecular structure review. *Chemical Reviews* 91: 137–164

Ota T, Terabayashi M, Parkinson CD, Masago H (2000) Thermobaric structure of the Kokchetav ultrahigh-pressure–high-pressure massif deduced from north-south transect in the Kulet and Saldat-Kol regions, Northern Kazakhstan. *The Island Arc* 9: 328–357

Ottolini L, Bottazzi P, Vannucci R (1993) Quantification of Lithium, Beryllium and Boron in silicates by Secondary Ion Mass Spectrometry using conventional energy filtering. *Analytical Chemistry* 65: 1960–1968

Ottolini L, Le Fèvre B, Vannucci R (2004) Direct assessment of mantle boron and lithium contents and distribution by SIMS analyses of peridotite minerals. *Earth and Planetary Science Letters* 228: 19–36

Palme H, Jones A (2003) Solar system abundances of the elements. In: Davis AM (ed.) *Meteorites, Comets and Planets*, vol. 1 of *Treatise in Geochemistry*, chap. 3, 41–61, Elsevier

Palme H, O'Neill HSC (2003) Cosmochemical estimates of mantle composition. In: Carlson RW (ed.) *The Mantle ans Core*, vol. 2 of *Treatise in Geochemistry*, chap. 1, 1–38, Elsevier

Palmer MR (1991) Boron isotope systematics of hydrothermal fluids and tourmalines: A synthesis. *Chemical Geology* 94: 111–121

Palmer MR, Slack JF (1989) Boron isotopic composition of tourmaline from massive sulfide deposits and tourmalinites. *Contributions to Mineralogy and Petrology* 103: 434–451

Palmer MR, Swihart GH (2002) Boron isotope geochemistry: an overview. In: Grew ES, Anovitz LM (eds.) *Boron: mineralogy, petrology and geochemistry*, vol. 33 of *Reviews in Mineralogy*, 709–744, Mineralogical Society of America, Washington, DC, 2nd edn.

Palmer MR, London D, Morgan GB IV, Babb H (1992) Experimental determination of fractionation of $^{11}B/^{10}B$ between tourmaline and aqueous vapor: a temperature- and pressure-dependent isotopic system. *Chemical Geology* 101: 123–129

Papanikolaou D (1987) Tectonic evolution of the Cycladic blueschist belt (Aegean sea, Greece). In: Helgeson HC (ed.) *Chemical transport in metasomatic processes*, vol. 218 of *NATO ASI Series C, Mathematical and Physical Sciences*, 429–450, Reidel, Dordrecht

Paquin J, Altherr R (2002) Subduction-related lithium metasomatism during exhumation of the Alpe Arami ultrahigh-pressure garnet peridotite (Central Alps, Switzerland). *Contributions to Mineralogy and Petrology* 143: 623–640

Paquin J, Altherr R, Ludwig T (2004) Li-Be-B systematics in the ultrahigh-pressure garnet peridotite from Alpe Arami (Central Swiss Alps): implications for slab-to-mantle transfer. *Earth and Planetary Science Letters* 218: 507–519

Peacock SM (1990) Fluid processes in subduction zones. *Science* 248: 329–337

Peacock SM, Hervig RL (1999) Boron isotopic composition of subduction-zone metamorphic rocks. *Chemical Geology* 160: 281–290

Pearce NJG, Perkins WT, Westgate JA, Gorton MP, Jackson SE, Neal CR, Chenery SP (1997) A compilation of new and published major and trace element data for NIST SRM 610 and NIST SRM 612 glass reference materials. *Geostandards Newsletter* 21: 115–144

Penfield SL (1894) Mineralogical notes. *American Journal of Science* 48: 114–118

Perfit MR, Ridley WI, Jonasson IR (1999) Geologic, petrologic, and geochemical relationships between magmatism and massive sulfide mineralization along the eastern Galapagos spreading center. In: Barrie CT, Hannington MD (eds.) *Volcanic-associated massive sulfide deposits; processes and examples in modern and ancient settings*, vol. 8 of *Reviews in Economic Geology*, 75–100, Society of Economic Geologists, Socorro, NM, USA

Pfennig G, Klewe-Nebenius H, Seelmann-Eggebert W (1998) *Chart of the Nuclides*. Forschungszentrum Karlsruhe GmbH, Karlsruhe, Germany, 6th edn.

Philippot P, Agrinier P, Scambelluri M (1998) Chlorine cycling during subduction of altered oceanic crust. *Earth and Planetary Science Letters* 161: 33–44

Poli S, Schmidt MW (1995) H_2O transport and release in subduction zones: Experimental constraints on basaltic and andesitic systems. *Journal of Geophysical Research* 100: 22 299–22 314

Poli S, Schmidt MW (2002) Petrology of subducted slabs. *Annual Reviews in Earth and Planetary Sciences* 30: 207–235

Pouchou JL, Pichoir F (1984) A new model for quantitative analyses. I. Application to the analysis of homogeneous samples. *La Recherche Aérospatiale* 3: 13–38

Pouchou JL, Pichoir F (1985) 'PAP' (ϕ-ρ-Z) correction procedure for improved quantitative microanalysis. In: Armstrong JT (ed.) *Microbeam Analysis*, 104–106, San Francisco Press

Powell R, Holland TJB (1988) An internally consistent dataset with uncertainties and correlations; 3, Applications to geobarometry, worked examples and a computer program. *Journal of Metamorphic Geology* 6: 173–204

Powell R, Holland TJB, Worley B (1998) Calculating phase diagrams involving solid solutions via non-linear equations, with examples using THERMOCALC. *Journal of Metamorphic Geology* 16: 577–588

Putlitz B, Matthews A, Valley JW (2000) Oxygen and hydrogen isotope study of high-pressure metagabbros and metabasalts (Cyclades, Greece): implications for the subduction of oceanic crust. *Contributions to Mineralogy and Petrology* 138: 114–126

Putlitz B, Cosca MA, Schumacher JC (2005) Prograde mica $^{40}Ar/^{39}Ar$ growth ages recorded in high pressure rocks (Syros, Cyclades, Greece). *Chemical Geology* 214: 79–98

Regelous M, Niu Y, Wendt JI, Batiza R, Greig A, Collerson KD (1999) Variations in the geochemistry of magmatism on the East Pacific Rise at 10°30' N since 800 ka. *Earth and Planetary Science Letters* 168: 45–63

Reinecke T (1998) Prograde high- to ultrahigh-pressure metamorphism and exhumation of oceanic sediments at Lago di Cignana, Zermatt-Saas Zone, western Alps. *Lithos* 42: 147–189

Reinecke T, Altherr R, Hartung B, Hatzipanagiotou K, Kreuzer H, Harre W, Klein H, Keller J, Geenen E (1982) Remnants of a Late Cretaceous high temperature belt on the island of Anáfi (Cyclades, Greece). *Neues Jahrbuch für Geologie und Paläontologie Monatshefte* 145: 157–182

Révay Zs, Belgya T, Ember PP, Molnár GL (2001) Recent developments in HYPERMET PC. *Journal of Radioanalytical and Nuclear Chemistry* 248: 401–405

Révay Zs, Belgya T, Kasztovszky Zs, Weil JL, Molnár GL (2004) Cold neutron PGAA facility at Budapest. *Nuclear Instruments and Methods in Physics Research B* 213: 385–388

Reyf FG (2004) Immiscible phases of magmatic fluid and their relation to Be and Mo mineralization at the Yermakovka F–Be deposit, Transbaikalia, Russia. *Chemical Geology* 210: 49–71

Ridley J (1982) Arcuate lineation trends in a deep level, ductile thrust belt, Syros, Greece. *Tectonophysics* 88: 347–360

Ridley J (1984) Evidence for temperature-dependent 'blueschist' to 'eclogite' transformation in high-pressure metamorphism of metabasic rocks. *Journal of Petrology* 25: 852–870

Ridley J (1986) Parallel stretching lineations and fold axes oblique to a shear displacement direction – a model and observations. *Journal of Structural Geology* 8: 647–653

Ring U, Fleischmann T (2002) The weak and superfast Cretan detachement, Greece: exhumation at subduction rates in extruding wedges. *Journal of the Geological Society of London* 159: 225–228

Ring U, Thomson SN, Bröcker M (2003) Fast extension but little exhumation: the Vari detachment in the Cyclades, Greece. *Geological Magazine* 140: 245–252

Robbins CR, Yoder HS Jr (1962) Stability relations of dravite, a tourmaline. *Carnegie Institute Washington Yearbook* 61: 106–108

Robertson AHF, Dixon JE (1984) Introduction: aspects of the geological evolution of the Eastern Mediterranean. In: Dixon JE, Robertson AHF (eds.) *The Geological Evolution of the Eastern Mediterranean*, vol. 17 of *Special Publications*, 1–74, Geological Society of London

Roselle GT, Engi M (2002) Ultra high pressure (UHP) terrains; lessons from thermal modeling. *American Journal of Science* 302: 410–441

Rosenbaum G, Avigad D, Sánchez-Gómez M (2002) Coaxial flattening at deep levels of orogenic belts: evidence from blueschists and eclogites on Syros and Sifnos (Cyclades, Greece). *Journal of Structural Geology* 24: 1451–1462

Rosner M, Erzinger J, Franz G, Trumbull RB (2003) Slab-derived boron isotope signatures in arc volcanic rocks from the Central Andes and evidence for boron isotope fractionation during progrssive slab dehydration. *Geochemistry, Geophysics, Geosystems* 4, doi:10.1029/2002GC000438

le Roux PJ, Shirey SB, Benton L, Hauri EH, Mock TD (2004) In situ, multiple-multiplier, laser ablation ICP-MS measurement of boron isotopic composition (δ^{11}B) at the nanogram level. *Chemical Geology* 203: 123–138

Rubatto D, Hermann J (2001) Exhumation as fast as subduction? *Geology* 29: 3–6

Rudnick RL, Fountain DM (1995) Nature and composition of the continental crust; a lower crustal perspective. *Reviews of Geophysics* 33: 267–309

Rüpke LH, Phipps Morgan J, Hort M, Connolly JAD (2002) Are the regional variations in Central American arc lavas due to differing basaltic versus peridotitic slab sources of fluids? *Geology* 30: 1035–1038

Ryan JG (1989) *The systematics of lithium, beryllium, and boron in young volcanic rocks*. Ph.D. thesis, Columbia University, New York (USA)

Ryan JG (2002) Trace-elements systematics of beryllium in terrestrial materials. In: Grew ES (ed.) *Beryllium: mineralogy, petrology and geochemistry*, vol. 50 of *Reviews in Mineralogy*, 121–145, Mineralogical Society of America

Ryan JG, Langmuir CH (1987) The systematics of lithium abundances in young volcanic rocks. *Geochimica et Cosmochimica Acta* 51: 1727–1741

Ryan JG, Langmuir CH (1988) Be systematics in young volcanic rocks: implications for ^{10}Be. *Geochimica et Cosmochimica Acta* 52: 237–244

Ryan JG, Langmuir CH (1993) The systematics of boron abundances in young volcanic rocks. *Geochimica et Cosmochimica Acta* 57: 1489–1498

Ryan JG, Leeman WP, Morris JD, Langmuir CH (1996a) The boron systematics of intraplate lavas: implications for crustal and mantle evolution. *Geochimica et Cosmochimica Acta* 60: 415–422

Ryan JG, Morris J, Bebout G, Leeman WP (1996b) Describing chemical fluxes in subduction zones: insights from "depth profiling" studies of arc and forearc rocks. In: Bebout GE, Scholl DW, Kirby SH, Platt JP (eds.) *Subduction top to bottom*, vol. 96 of *Geophysical Monograph Series*, 263–268, American Geophysical Union

Sanchez-Valle C, Reynard B, Daniel I, Martinez I, Chervin JC (2004) Boron isotope fractionations in high $P - T$ aqueous fluids from in situ vibrational spectroscopic data. *Supplement issue of Geochimica et Cosmochimica Acta* 68: A50

Sano T, Hasenka T, Shimaoka A, Yonezawa C, Fukuoka T (2001) Boron contents of Japan Trench sediments and Iwate basaltic lavas, Northeastern Japan: estimation of sediment-derived fluid contribution in mantle wedge. *Earth and Planetary Science Letters* 186: 187–198

Scambelluri M, Müntener O, Ottolini L, Pettke TT, Vanucci R (2004) The fate of B, Cl and Li in subducted oceanic mantle and in the antigorite breakdown fluids. *Earth and Planetary Science Letters* 222: 217–234

Schandl ES, O'Hanley DS, Wicks FJ (1989) Rodingites in serpentinized ultramafic rocks of the Abitibi Greenstone Belt, Ontario. *Canadian Mineralogist* 27: 579–591

Schertl HP, Schreyer W, Chopin C (1991) The pyrope-coesite rocks and their country rocks at Parigi, Dora Maira Massif, Western Alps: detailed petrography, mineral chemistry and $P - T$ path. *Contributions to Mineralogy and Petrology* 108: 1–21

Schliestedt M (1986) Eclogite-blueschist relationships as evidenced by mineral equilibria in the high-pressure rocks of Sifnos (Cycladic islands), Greece. *Journal of Petrology* 27: 1437–1459

Schliestedt M, Altherr R, Matthews A (1987) Evolution of the Cycladic crystalline complex: petrology, isotope geochemistry and geochronology. In: Helgeson HC (ed.) *Chemical transport in metasomatic processes*, vol. 218 of *NATO ASI Series C, Mathematical and Physical Sciences*, 389–428, Reidel, Dordrecht

Schmädicke E (2000) Phase relations in peridotitic and pyroxenitic rocks in the model system CMASH and NCMASH. *Journal of Petrology* 41: 69–86

Schmädicke E, Will TM (2003) Pressure-temperature evolution of blueschist facies rocks from Sifnos, Greece, and implications for the exhumation of high-pressure rocks in the Central Aegean. *Journal of Metamorphic Geology* 21: 799–811

Schmidt MW, Poli S (1998) Experimentally based water budgets for dehydrating slabs and consequences for arc magma generation. *Earth and Planetary Science Letters* 163: 361–379

Schmidt MW, Vielzeuf D, Auzanneau E (2004) Melting and dissolution of subducting crust at high pressures: the key role of white mica. *Earth and Planetary Science Letters* 228: 65–84

Schmitt AK, Kasemann S, Meixner A, Rhede D (2002) Boron in central Andean ign-imbrites: implications for crustal boron cycles in an active continental margin. *Chemical Geology* 183: 333–347

Schreyer W (1985) Metamorphism of crustal rocks at mantle depth: high pressure minerals and mineral assemblages in metapelites. *Fortschritte der Mineralogie* 63: 227–261

Schreyer W, Hughes JM, Bernhardt HJ, Kalt A, Prowatke S, Ertl A (2002) Reexamination of olenite from the type locality; detection of boron in tetrahedral coordination. *European Journal of Mineralogy* 14: 935–942

Schumacher JC (1997) The estimation of ferric iron in electron analysis of amphiboles. *European Journal of Mineralogy* 9: 643–651

Schumacher JC, Tonnsen R, Cheney JT, Brady JB (2000) Glaucophane marbles and associ-ated high pressure rocks on the island of Syros, Greece. *Geological Society of America, Abstarcts with Programs* 32: A114

Schumacher JC, Brady JB, Prinkey DR, Walton A, Able L, Sinitsin AG, Cheney JT (2001) Geochemistry and metamorphism of blueschist/eclogite facies rocks on the island of Sy-ros, Cyclades, Greece. *Geological Society of America, Abstarcts with Programs* 33: 250

Seck HA, Kötz J, Okrusch M, Seidel E, Stosch HG (1996) Geochemistry of a meta-ophiolite suite: An association of metagabbros, eclogites and glaucophanites on the island of Sy-ros, Greece. *European Journal of Mineralogy* 8: 607–623

Seitz H-M, Woodland AB (2000) The distribution of lithium in peridotitic and pyroxenitic mantle lithologies – an indicator of magmatic and metasomatic processes. *Chemical Ge-ology* 166: 47–64

Seitz H-M, Brey GP, Stachel T, Harris JW (2003) Li abundances in inclusions in diamonds from the upper and lower mantle. *Chemical Geology* 201: 307–318

Sen S, Stebbins JF, Hemming NG, Gosh B (1994) Coordination environments of B impuri-ties in calcite and aragonite polymorphs: a ^{11}B MAS NMR study. *American Mineralogist* 79: 819–825

Sengör AMC, Altiner D, Cin A, Hsu KJ (1988) Origin and assembly of the Tethyside oro-genic collage at the expense of Gondwanaland. In: Audley-Charles MG, Hallam A (eds.) *Gondwana and Tethys*, vol. 37 of *Special Publications*, 119–181, Geological Society of London

Seyfried WE Jr, Dibble WE Jr (1980) Seawater-peridotite interaction at 300 °C and 500 bar; implications for the origin of oceanic serpentinites. *Geochimica et Cosmochimica Acta* 44: 309–322

Seyfried WE Jr, Ding K (1995) The hydrothermal chemistry of fluoride in seawater. *Geochimica et Cosmochimica Acta* 59: 1063–1071

Seyfried WE Jr, Janecky DR, Mottl MJ (1984) Alteration of the oceanic crust: implications for geochemical cycles of lithium and boron. *Geochimica et Cosmochimica Acta* 48: 557–569

Seyfried WE Jr, Chen X, Chan LH (1998) Trace element mobility and lithium isotope exchange during hydrothermal alteration of seafloor weathered basalts: an experimental study at 350 °C, 500 bars. *Geochimica et Cosmochimica Acta* 62: 959–960

Shannon RD (1976) Revised effective ionic radii in halides and chalcogenides. *Acta Crystallographica* A32: 751–767

Sharma P, Somayajulu BLK (1982) [10]Be dating of large manganese nodules from world oceans. *Earth and Planetary Science Letters* 59: 235–244

Shaw DM, Cramer JJ, Higgins MD, Truscott MG (1986) Composition of the Canadian Precambrian shield and the continental crust of the Earth. In: Dawson JB, Carswell DA, Hall J, Wedepohl KH (eds.) *The Nature of the Lower Continental Crust*, vol. 24 of *Special Publications*, 275–282, Geological Society of London

Shaw DM, Higgins MD, Hinton RW, Truscott MG, Middleton TA (1988a) Boron in chondritic meteorites. *Geochimica et Cosmochimica Acta* 52: 2311–2319

Shaw DM, Higgins MD, Truscott MG, Middleton TA (1988b) Boron contamination in polished thin sections of meteorites: Implications for other trace-element studies by alpha-track image or ion microprobe. *American Mineralogist* 73: 894–900

Shaw DM, Truscott MG, Gray EA, Middleton TA (1988c) Boron and lithium in high-grade rocks and minerals from the Wawa-Kapuskasing region, Ontario. *Canadian Journal of Earth Science* 25: 1485–1502

Shen AH, Keppler H (1997) Direct observation of complete miscibility in the albite-H_2O system. *Nature* 385: 710–712

Simon G, Chopin C, Schenk V (1997) Near-end-member magnesiochloritoid in prograde-zoned pyrope, Dora Maira Massif, Western Alps. *Lithos* 41: 37–57

Slack JF (2002) Tourmaline associations with hydrothermal ore deposits. In: Grew ES, Anovitz LM (eds.) *Boron: mineralogy, petrology and geochemistry*, vol. 33 of *Reviews in Mineralogy*, chap. 11, 559–644, Mineralogical Society of America, Washington, DC, 2nd edn.

Smith HJ, Spivack AJ, Staudigel H, Hart SR (1995) The boron isotopic composition of altered oceanic crust. *Chemical Geology* 126: 119–135

Smith HJ, Leeman WP, Davidson J, Spivack AJ (1997) The B isotopic composition of arc lavas from Martinique, Lesser Antilles. *Earth and Planetary Science Letters* 146: 303–314

Smith M, Yardley BWD (1994) The boron isotopic composition of tourmaline as a guide to fluid processes and boron source in the South-west England orefield: an ion microprobe study. *Mineralogical Magazine* 58A: 856–857

Sorensen SS, Grossman JN (1989) Enrichment of trace elements in garnet amphibolites from a paleo-subduction zone: Catalina Schist, southern California. *Geochimica et Cosmochimica Acta* 53: 3155–3177

Sorensen SS, Grossman JN, Perfit MR (1997) Phengite-hosted LILE enrichment in eclogite and related rocks: implications for fluid-mediated mass transfer in subduction zones and arc magma genesis. *Journal of Petrology* 38: 3–34

Spandler C, Hermann J, Arculus R, Mavrogenes J (2003) Redistribution of trace elements during prograde metamorphism from lawsonite blueschist to eclogite facies; implications for deep subduction-zone processes. *Contributions to Mineralogy and Petrology* 146: 205–222

Spivack AJ, Edmont JM (1987) Boron isotope exchange between seawater and the oceanic crust. *Geochimica et Cosmochimica Acta* 51: 1033–1043

Spivack AJ, Staudigel H (1994) Low-temperature alteration of the upper oceanic crust and the alkalinity budget of seawater. *Chemical Geology* 115: 239–247

Spivack AJ, You CF (1997) Boron isotopic geochemistry of carbonates and pore waters, Ocean Drilling Program Site 851. *Earth and Planetary Science Letters* 152: 113–122

Spivack AJ, Palmer MR, Edmond JM (1987) The sedimentary cycle of the boron isotopes. *Geochimica et Cosmochimica Acta* 51: 1939–1949

Springer M (1999) Interpretation of heat-flow density in the Central Andes. *Tectonophysics* 306: 377–395

Stalder R, Foley SF, Brey GP, Horn I (1998) Mineral-aqueous fluid partitioning of trace elements at $900 - 1200\,^{\circ}$C and $3.0 - 5.7\,$GPa: New experimental data for garnet, clinopyroxene, and rutile, and implications for mantle metasomatism. *Geochimica et Cosmochimica Acta* 62: 1781–1801

Stalder R, Ulmer P, Thompson AB, Günther D (2000) Experimental approach to constrain second critical endpoints in fluid/silicate systems: near solidus fluids and melts in the system albite-H$_2$Ø. *American Mineralogist* 85: 68–77

Stalder R, Ulmer P, Thompson AB, Günther D (2001) High pressure fluids in the system MgO-SiO$_2$-H$_2$O under upper mantle conditions. *Contributions to Mineralogy and Petrology* 140: 607–618

Stampfli GM, Borel GD (2002) A plate tectonic model for the Paleozoic and Mesozoic constrained by dynamic plate boundaries and restored synthetic oceanic isochrons. *Earth and Planetary Science Letters* 196: 17–33

Staudacher T, Sarda P, Allègre CJ (1990) Noble gases systematics of Réunion Island, Indian Ocean. *Chemical Geology* 89: 1–17

Staudigel H, Plank T, White B, Schmincke H-U (1996) Geochemical fluxes during seafloor alteration of basaltic upper oceanic crust; DSDP sites 417 and 418. In: Bebout GE, Scholl DW, Kirby SH, Platt JP (eds.) *Subduction top to bottom*, vol. 96 of *Geophysical Monograph Series*, 19–38, American Geophysical Union, Washington, DC

Steppan N (2003) *Li, Be und B in Mineralen metapelitischer Gesteine: Fallstudien auf der Insel Ikaria, im Kühnischen Gebirge und in den schweizer Alpen.* Dr. rer. nat. thesis, Universität Heidelberg, Germany

Stoffyn-Egli P, Mackenzie FT (1984) Mass balance of dissolved lithium in the oceans. *Geochimica et Cosmochimica Acta* 48: 859–872

Straub SM, Layne GD (2002) The systematics of boron isotopes in Izu arc front volcanic rocks. *Earth and Planetary Science Letters* 198: 26–39

Straub SM, Layne GD (2003) The systematics of chlorine, fluorine, and water in Izu arc volcanic rocks: Implications for volatile recycling in subduction zones. *Geochimica et Cosmochimica Acta* 67: 4179–4203

Sugiura N, Shuzou Y, Ulyanov A (2001) Beryllium-boron and aluminium-magnesium chronology of calcium-aluminium-rich inclusions in CV chondrites. *Meteoritics and Planetary Science* 36: 1397–1408

Swihart GH, Moore PB (1986) Boron isotopic composition of marine and nonmarine evaporite borates. *Geochimica et Cosmochimica Acta* 50: 1297–1301

Swihart GH, Moore PB (1989) A reconnaissance of the boron isotopic composition of tourmaline. *Geochimica et Cosmochimica Acta* 53: 911–916

Szakmány G, Kasztovszky Zs (2004) Prompt Gamma Activation Analysis, a new method in the archeological study of polished stone tools and their raw materials. *European Journal of Mineralogy* 16: 285–295

Tagg SL, Cho H, Dyar MD, Grew ES (1999) Tetrahedral boron in naturally occurring tourmaline. *American Mineralogist* 84: 1451–1455

Tatsumi Y, Eggins S (1995) *Subduction zone magmatism*. Frontiers in earth sciences, Blackwell, Cambridge

Tatsumi Y, Isoyama H (1988) Transportation of beryllium with H_2O at high pressures; implication for magma genesis in subduction zone. *Geophysical Research Letters* 15: 180–183

Taylor BE, Slack JF (1984) Tourmalines from Appalachian-Caledonian massive sulfide deposits: textural, chemical and isotopic relationships. *Economic Geology* 79: 1703–1726

Taylor SR, McLennan SM (1995) The geochemical evolution of the continental crust. *Reviews in Geophysics* 33: 241–265

Teng F-Z, McDonough WF, Rudnick RL, Dalpé C, Tomascak PB, Chappell BW, Gao S (2004) Lithium isotopic composition and concentration of the upper continental crust. *Geochimica et Cosmochimica Acta* 68: 4167–4178

Tenthorey E, Hermann J (2004) Composition of fluids during serpentinite breakdown in subduction zones: evidence for limited boron mobility. *Geology* 32: 865–868

Thiel GA (1941) The relative resistance to abrasion of mineral grains of sand size. *Journal of Sedimentary Petrology* 10: 103–124

Thomas R, Schmidt C, Heinrich W (2004) Boron speciation in aqueous fluids at 22 to 600°C and 0.1 to 3000 MPa. *Supplement 1-2 to Lithos* 73: S110

Thompson G, Melson WG (1970) Boron contents of serpentinites and metabasalts in the oceanic crust: implicatons for the boron cycle in the oceans. *Earth and Planetary Science Letters* 8: 61–65

Tomascak PB (2004) Developments in the understanding and application of lithium isotopes in the earth and planetary sciences. In: Johnson CM, Beard BL, Albarède F (eds.) *Geochemistry of non-traditional stable isotopes*, vol. 55 of *Reviews in Mineralogy*, chap. 5, 153–195, Mineralogical Society of America, Washington, DC

Tomascak PB, Widom E, Benton LD, Goldstein SL, Ryan JG (2002) The control of lithium budgets in island arcs. *Earth and Planetary Science Letters* 196: 227–238

Tomaschek F, Kennedy AK, Villa IM, Lagos M, Ballhaus C (2003) Zircons from Syros, Cyclades, Greece - recrystallization and mobilization of zircon during high-pressure metamorphism. *Journal of Petrology* 44: 1977–2002

Tonarini S, Pennisi M, Leeman WP (1997) Precise boron isotopic analysis of silicate (rock) samples using alkali carbonate fusion and ion-exchange separation. *Chemical Geology* 142: 129–137

Tonarini S, Leeman WP, Ferrara G (2001) Boron isotopic variations in lavas of the Aeolian volcanic arc, South Italy. *Journal of Volcanology and Geothermal Research* 110: 155–170

Tonarini S, Forte C, Petrini R, Ferrara G (2003) Melt/biotite $^{11}B/^{10}B$ isotopic fractionation and the boron local environment in the structure of volcanic glasses. *Geochimica et Cosmochimica Acta* 67: 1863–1873

Tourn SM, Herrmann CJ, Ametrano S, de Brodtkorb MK (2004) Tourmalinites from the Eastern Sierras Pampenas, Argentina. *Ore Geology Reviews* 24: 229–240

Trotet F, Jolivet L, Vidal O (2001a) Tectono-metamorphic evolution of Syros and Sifnos islands (Cyclades, Greece). *Tectonophysics* 338: 179–206

Trotet F, Vidal O, Jolivet L (2001b) Exhumation of Syros and Sifnos metamorphic rocks (Cyclades, Greece). New constraints on the $P-T$ paths. *European Journal of Mineralogy* 13: 901–920

Ulmer P, Trommsdorff V (1995) Serpentinite stability to mantle depths and subduction-related magmatism. *Science* 268: 858–861

Uppstroem LR (1974) The boron/chlorinity ratio of deep seawater from the Pacific Ocean. *Deep Sea Research* 21: 161–162

Vengosh A, Kolodny Y, Starinsky A, Chivas AR, McCulloch MT (1991) Coprecipitation and isotopic fractionation of boron in modern biogenic carbonates. *Geochimica et Cosmochimica Acta* 55: 2901–2910

Vengosh A, Starinsky A, Kolodny Y, Chivas AR, Raab M (1992) Boron variations during fractional evaporation of seawater: new constraints on the marine vs nonmarine debate. *Geology* 20: 799–802

Von Damm KL, Edmond JM, Grant B, Measures CI, Walden B, Weiss RF (1985) Chemistry of submarine hydrothermal solutions at $21°$ N East Pacific Rise. *Geochimica et Cosmochimica Acta* 49: 2197–2220

Wasson JT, Kallemeyn GW (1988) Composition of chondrites. *Philisophical Transactions of the Royal Society of London* A325: 535–544

Webster JD, Holloway JR, Hervig RL (1987) Phase equilibria of a Be, U and F-enriched vitrophere from Spor Mountain, Utah. *Geochimica et Cosmochimica Acta* 51: 389–402

Wedepohl KH (1995) The composition of the continental crust. *Geochimica et Cosmochimica Acta* 59: 1217–1232

Wegener A (1912) Die Entstehung der Kontinente. *Geologische Rundschau* 3: 276–292

Weisbrod A, Polak C, Roy D (1986) Experimental study of tourmaline solubility in the system Na-Mg-Al-Si-B-O-H. Applications to the boron content of natural hydrothermal fluids and tourmalinization processes. *Experimental Mineralogy and Geochemistry International Symposium, Nancy, Abstracts* 140

Wenger M, Armbruster T (1991) Crystal chemistry of lithium; oxygen coordination and bonding. *European Journal of Mineralogy* 3: 387–399

Werding G, Schreyer W (2002) Experimental studies on borosilicates and selected borates. In: Grew ES, Anovitz LM (eds.) *Boron: mineralogy, petrology and geochemistry*, vol. 33 of *Reviews in Mineralogy*, 117–163, Mineralogical Society of America, 2nd edn.

Wijbrans JR, Schliestedt M, York D (1990) Single grain argon laser probe dating of phengites from blueschist to greenschist transition of Sifnos (Cyclades, Greece). *Contributions to Mineralogy and Petrology* 104: 582–593

Williams LB, Hervig RL, Holloway JR, Hutcheon I (2001) B isotope geochemistry during diagenesis. Part I. Experimental determination of fractionation during illitization of smectite. *Geochimica et Cosmochimica Acta* 65: 1769–1782

Wood SA (1992) Theoretical prediction of speciation and solubility of beryllium in hydrothermal solutions to 300°C at saturated vapor pressure: applicaion to bertrandite/phenakite deposits. *Ore Geology Reviews* 7: 249–278

Woodland AB, Seitz H-M, Altherr R, Olker B, Marschall H, Ludwig T (2002) Li abundances in eclogite minerals: a clue to a crustal or mantle origin? *Contributions to Mineralogy and Petrology* 143: 587–601

Wunder B, Schreyer W (1997) Antigorite: High-pressure stability in the system MgO-SiO_2-H_2O (MSH). *Lithos* 41: 213–227

Wunder B, Meixner A, Romer RL, Heinrich W (2004) The geochemical cycle of boron: experiments on boron isotope patitioning between micas and fluids. *Supplement issue of Geochimica et Cosmochimica Acta* 68: A51

You C-F, Castillo PR, Gieskes JM, Chan LH, Spivack AJ (1996) Trace element behavior in hydrothermal experiments: Implications for fluid processes at shallow depth in subduction zones. *Earth and Planetary Science Letters* 140: 41–52

You C-F, Lee T, Li Y-H (1989) The partition of Be between soil and water. *Chemical Geology* 77: 105–118

You C-F, Spivack AJ, Smith JH, Gieskes JM (1993) Mobilization of boron in convergent margins: Implications for the boron geochemical cycle. *Geology* 21: 207–210

You C-F, Morris JD, Gieskes JM, Rosenbauer R, Zheng SH, Xu X, Ku TL, Bischoff JL (1994) Mobilization of beryllium in the sedimentary column at convergent margins. *Geochimica et Cosmochimica Acta* 58: 4887–4897

You C-F, Chan LH, Spivack AJ, Gieskes JM (1995a) Lithium, boron, and their isotopes in sediments and pore waters of Ocean Drilling Program Site 808, Nankai Trough: implications for fluid expulsion in accretionary prisms. *Geology* 23: 37–40

You C-F, Spivack AJ, Gieskes JM, Rosenbauer, R JL Bischoff (1995b) Experimental study of boron geochemistry: Implications for fluid processes in subduction zones. *Geochimica et Cosmochimica Acta* 59: 2435–2442

Zack T, Marschall H (2003) Isotope fractionation during subduction: The case for Li and B. *Supplement issue of Geochimica et Cosmochimica Acta* 67: A573

Zack T, Rivers T, Foley SF (2001) Fluid infiltration at 2.0 GPa in eclogites from Trescolmen, Central Alps: Constraints from Cs-Rb-Ba systematics in phengites and amphiboles. *Contributions to Mineralogy and Petrology* 140: 651–669

Zack T, Foley SF, Rivers T (2002a) Equilibrium and disequilibrium trace element partitioning in hydrous eclogites (Trescolmen, Central Alps). *Journal of Petrology* 43: 1947–1974

Zack T, Kronz A, Foley SF, Rivers T (2002b) Trace element abundance in rutiles from eclogites and associated garnet mica schists. *Chemical Geology* 184: 97–122

Zack T, Tomascak PB, Rudnick RL, Dalpe C, McDonough WF (2003) Extremely light Li in orogenic eclogites: The role of isotope fractionation during dehydration in subducted oceanic crust. *Earth and Planetary Science Letters* 208: 279–290

Zack T, Rivers T, Brumm R, Kronz A (2004) Cold subduction of oceanic crust: Implications from a lawsonite eclogite from the Dominican Republic. *European Journal of Mineralogy* 16: 909–916

Zhai M, Nakamura E, Shaw DM, Nakano T (1996) Boron isotope ratios in meteorites and lunar rocks. *Geochimica et Cosmochimica Acta* 60: 4877–4881

A. Technical modifications of the Heidelberg SIMS for precise analysis of B isotope ratios

Built in 1982 the secondary ion mass spectrometer installed at the Mineralogisches Institut (Heidelberg) is a Cameca IMS 3f. It has been used at the institute for several years to successfully analyse natural and synthetic samples for concentrations of dominantly light elements, transition metals, and rare earth elements. The analysis of isotope ratios, however, required significant changes of both SIMS software and hardware. These improvements were developed by Thomas Ludwig (Heidelberg), and are described in this section, which is an English translation of a German text written by Thomas Ludwig. The text, including results of measurements and diagrams in this section were kindly provided by him.

The precision of measurements of isotope ratios by mass spectrometry is mainly determined by counting statistics and the stability of the different isotope signals. In SIMS, the stability of the isotope signals is governed by the stability of the primary ion beam, as the secondary beam current is proportional to the primary beam current. In the IMS 3f, the stability of the primary beam current is typically $0.1\,\%\,\mathrm{min}^{-1}$, with additional spontaneous changes that can be significantly larger. Slow fluctuations of the isotope signals are generated by charging of the sample or by changes in the secondary ion emission as a result of progressive erosion of the sample.

Ideal setups measure both isotopes simultaneously (as in multi-collector systems), eliminating the influence of fluctuations in the secondary ion intensity. If this is not possible, it is necessary to keep a measurement cycle short with respect to the fluctuation of the isotope signals, in order to diminish the influence of these fluctuations on precision. Therefore, the ability of the mass spectrometer to switch rapidly from one isotope to another is an essential precondition for the precise measurement of isotope ratios.

The Cameca IMS 3f is a magnetic sector field mass spectrometer. The time required for a change between two masses has turned out to be the limiting factor for the precision of the IMS 3f. At high mass resolution ($m/\Delta m > 2000$) the original spectrometer needs up to $10\,\mathrm{s}$ to stabilise the magnetic field. For the analysis of B isotope ratios, the settling time has been $\sim 2\,\mathrm{s}$. Furthermore, the stability of the magnetic field was not adequate for longer measurements ($> 60\,\mathrm{min}$), as required

for samples with low B concentrations. Therefore, an entirely new control device for the magnet was developed and installed at the Heidelberg SIMS. Both the old and the newly developed control devices measure the magnetic field with a temperature stabilised hall-effect probe, and control the magnetic field by regulating the magnet current. The stability of the hall-effect probe therefore is essential for the stability of the magnetic field. The new magnet control device has the following advantages:

(1) Faster change of magnetic field. The primary voltage range of the power supply unit of the magnet was increased from 0 to $+25\,$V to -40 to $+40\,$V, which allows for significantly faster changes in magnet current. Especially changes to lower masses are much faster, due to the negative primary voltage. Furthermore, the new control device (PI controller) is designed to avoid over-shoots in the magnetic field. The results of these improvements are displayed in Fig. A.1.
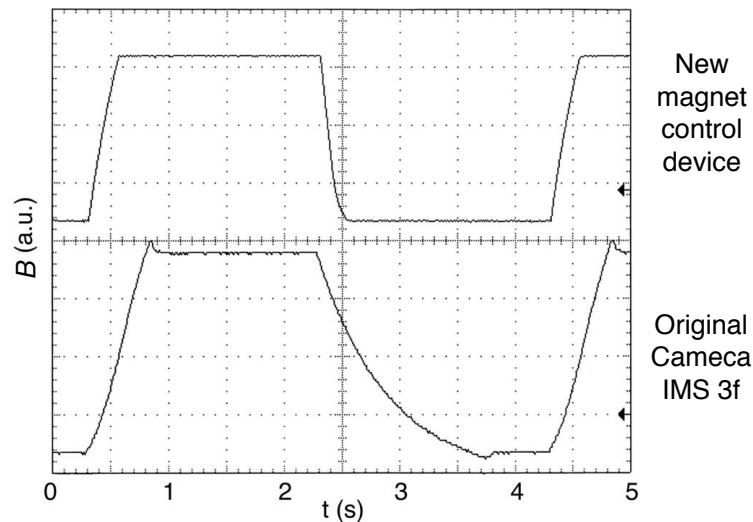
Fig. A.1. Comparison of the original Cameca control with the newly developed magnet control. The diagram shows the magnetic flux density B as a function of time t. In both cases the setting of the magnet was changed from $m = 1\,$u to $m = 100\,$u and back within a period of $4\,$s. The new device is up to five times faster.

(2) Better static temperature stability of the magnetic field. The hall voltage of any hall generator is temperature dependent. The hall generator FC34 (Siemens) used in the IMS 3f, made of InAsP, has a temperature coefficient of $-0.04\,\%\mathrm{K}^{-1}$. For linearisation of the hall voltage it is terminated with a resistor. The internal resistance of the hall-effect probe is also temperature dependent (InAsP: $0.2\,\%\mathrm{K}^{-1}$), which increases the temperature dependence to $-0.067\,\%\mathrm{K}^{-1}$. In order to en-

288
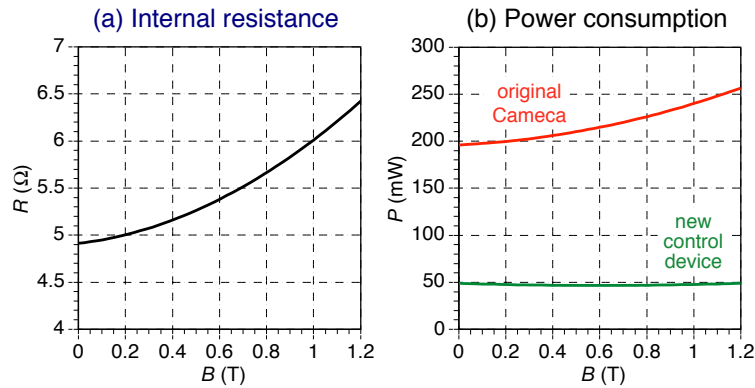
Fig. A.2. a Resistance R of the hall generator as a function of magnetic field B. **b** Power consumption $P = R \cdot I^2$ of the hall generator as a function of magnetic field B. The red line shows the power consumption of the probe with the original Cameca magnet control device. The power consumption increasing with B generates additional internal heat, which has to be compensated by the temperature controller. The green line shows the power consumption being almost independent from B, using the new control device

hance the static temperature stability of the magnetic field, a new temperture controller was developed, which keeps the temperature of the hall generator constant by $\pm 2\,$mK. Additionally, the linearisation resistor was removed. This keeps the temperature dependency of the hall voltage at $-0.04\,\%\mathrm{K}^{-1}$. The linearisation of the hall generator is now controlled by the software.

(3) Better dynamic temperature stability of the magnetic field. The internal resistance R_i of a hall generator increases with increasing magnetic field (Fig. A.2a), while the electric current I through the hall generator is constant. Therefore, the power consumption $P = R_i \cdot I^2$ (Fig. A.2b) increases with an increasing magnetic field B, which generates additional internal heat. The resulting temperature variation has to be compensated by the temperature controller. During fast changes of the magnetic field, the temperature of the hall generator is temporarily shifting, until the temperature control is able to compensate for the extra heat. During that interval, the magnetic field is unstable. Using the original Cameca magnet controller, the magnetic field requires almost 10 s to stabilise after a rapid change. The dynamic temperature stability was improved by reducing the electric current I in the hall generator by 50 %, which reduces the dynamic thermal effects to 25 %. Furthermore, in the new device the current is controlled by the magnetic field in such a way that variations in power consumption are reduced to a minimum (Fig. A.2b). The dynamic thermal effects are almost eliminated.

(4) Improvement of the amplifier for the signal of the hall-effect probe. The low hall voltage requires a differential amplifier. The stability of this amplifier

289

(offset, gain and noise) directly influences the stability of the magnetic field. The maximum hall voltage of the IMS 3f hall probe is $\sim 300\,\text{mV}$. The maximum hall voltage of the new controller is only $\sim 150\,\text{mV}$ because of the lower current in the hall generator. Therefore, low noise and stability of the amplifier in the new setup is even more important. Noise in the important range of 0.1 to $10\,\text{Hz}$ was reduced from $1.2\,\mu\text{V}$ to $60\,\text{nV}$. The offset voltage drift was reduced from $\pm 2\,\mu\text{VK}^{-1}$ to $\pm 0.6\,\mu\text{VK}^{-1}$, and the thermal stability of the gain drift decreased from maximal $25\,\text{ppmK}^{-1}$ to maximal $4\,\text{ppmK}^{-1}$.

(5) Compensation of eddy currents. Any change of the magnetic field induces eddy currents in the core of the magnet, with an intensity proportional to $\mathrm{d}B/\mathrm{d}t$. Modern magnets are laminated in order to inhibit the eddy currents to enter the whole magnet, and therefore enhance their fast decay. The magnet of the IMS 3f, however is made of one piece, producing eddy currents which are additionally amplified by the new magnet controller, being much faster than the original one. Eddy currents introduce an exponentially decreasing inhomogeneity of the magnetic field, which is not correctly analysed by the hall probe, measuring only one spot of the whole magnet. Therefore, after every change of the magnetic field, some time is required to wait for the eddy currents to decay to a certain limit. For this decay the time constant τ is given by (Bryant, 1992):

$$\tau_{m,n} \propto \left(\left(\frac{m\pi}{a} \right)^2 + \left(\frac{n\pi}{b} \right)^2 \right)^{-1} ; m,n = 1,3,5,7...\infty, \tag{A.1}$$

where the shape of the magnet is idealised to be a tetragonal cuboid with a height a and length b. Every time constant $\tau_{m,n}$ is related to an eddy current field $B_{m,n}$ with a specific spacial distribution. Time constant $\tau_{1,1}$ in the magnet of the IMS 3f is $\sim 1.3\,\text{s}$ and $\tau_{1,3} = \tau_{3,1} = 0.27\,\text{s}$. The intensity of the eddy currents rapidly decreases with increasing order m,n. Therefore, it is sufficient to compensate only the fields $B_{1,1}$ and $B_{1,3} = B_{3,1}$. For the new magnet control device, a new electronic compensation was developed, which almost eliminates the effect of the eddy currents. This is obtained by a time dependent correction voltage, which is added to the target voltage controlling the magnet. The correction of B as a function of time is displayed in Fig. A.3.

The new magnet control device allows for significantly faster changes between the masses. Switching from one B isotope to the other, the count rate is stable after $60\,\text{ms}$, at mass resolution $m/\Delta m = 1500$. The stability of the magnetic field is now satisfying for longer measurements ($> 1\,\text{h}$). The precision of B isotope analyses with the modified IMS 3f is exclusively determined by counting statistics. Precision of B isotope analyses using the Heidelberg SIMS is $< \pm 1\,\permil$ for tourmaline with a total analysis time of $10\,\text{min}$, $< \pm 1.7\,\permil$ for NIST SRM610 with a total analysis time
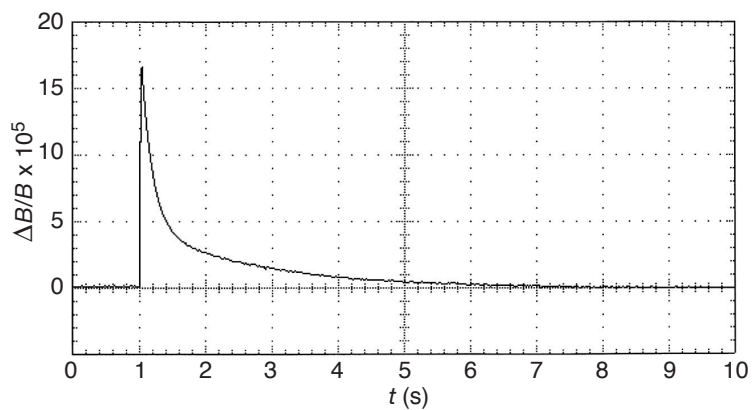
Fig. A.3. Compensation of eddy current fields during the switch from mass $m = 10$ to $m = 11$ at time $t = 1\,\text{s}$. Without the compensation, the eddy current fields need $4\,\text{s}$ to decay to a non-disturbing level.

of $25\,\text{min}$, and $< \pm 2.5\%\!o$ for amphibole containing $5\,\mu\text{g}/\text{g}$ B with a total analysis time of $45\,\text{min}$. In conclusion, the precision of the Heidelberg SIMS is equivalent to ion probes of the newer model with laminated magnet, like Cameca IMS 5f and 6f (Nakano & Nakamura, 2001; Kasemann *et al.*, 2001).

B. Petrology and chemistry of individual samples

For each individual sample a short information is given at the beginning, on the principle rock group of the sample, and when and by whom it was collected. Abbreviations are: A.K. = Angelika Kalt (Neuchâtel); R.A. = Rainer Altherr (Heidelberg); H.M. = Horst Marschall (Heidelberg).

SY1 Collected by A.K. in 1991; Locality: $\sim 500\,\mathrm{m}$ east of San Michalis, lense in marble; Rock type: Garnet-quartz-omphacite fels (meta-plagiogranite).

Sample SY1 is a green, isotropic, fine-grained rock, which is similar to an eclogite in handspecimen. SY1, however, is quartz-rich and is a meta-acidic rock with $\sim 60\,\mathrm{wt\%}$ SiO_2 and only $\sim 1.6\,\mathrm{wt\%}$ MgO. Quartz, garnet and omphacite, the dominant minerals in the rock are in direct contact with each other, accompanied by white mica, glaucophane and rutile. In some parts of the rock, symplectites have developed between quartz and omphacite, which are too small to be characterised by optical microscope. Garnet grains are subhedral to euhedral, $1.0 - 1.5\,\mathrm{mm}$ in diameter and poikiloblastic with inclusions of quartz and rutile. The sample was not analysed by EPMA, but white mica is probably paragonite, as the rock contains very little K_2O (0.11 wt%) and is similar to paragonite-bearing sample SY308. The rock is interpreted as the metamorphic equivalent of a felsic intrusion within the former oceanic crust, e.g. a plagiogranitic dyke with low-K trachyandesitic composition. The rock was equilibrated at HP metamorphic conditions, while retrograde processes are limited to the sporadic thin reaction zones between quartz and omphacite.

SY2 Collected by A.K. in 1991; Locality: $\sim 500\,\mathrm{m}$ east of San Michalis, Rock type: Siliceous dolomite-calcite marble.

Sample SY2 is a siliceuos marble (13.4 wt% SiO_2) dominated by calcite and dolomite. It contains equally dipersed silicate minerals, such as clinozoisite, omphacite, phengite, titanite, quartz and accessory allanite, zircon, rutile and apatite, but also larger ($\sim 1 - 2\,\mathrm{cm}$) elongated pebbles composed of dominantly silicate minerals, i.e. omphacite, chlorite, clinozoisite, actinolite, quartz and phengite. Phengite contains 3.45 Si cpfu, 0.28 wt% BaO, 0.37 wt% Na_2O, and has a X_{Mg} ($= \mathrm{Mg}/(\mathrm{Mg} + \mathrm{Fe}^{2+})$) of 0.79. Chlorite contains 2.15 Al cpfu, 0.25 wt% MnO and has a X_{Mg} of 0.80. Clinozoisite has $0.28 - 0.33$ Fe cpfu, 0.2 wt% Cr_2O_3 and 0.2 wt%

TiO_2. Omphacite contains very little Fe^{3+}, but some Cr_2O_3 ($0.2 - 1.2$ wt%) and has a composition of approximately $Jd_{45}Acm_2Q_{50}$ (with additional Ca-Tschermaks and kosmochlor components). X_{Mg} of omphacite is 0.87. Ca-amphibole has $7.53 - 7.93$ Si cpfu, A-site occupation of $0.03 - 0.26$, X_{Mg} of 0.80 and $Fe^{3+}/\Sigma Fe$ ratio of 0.12. Following the classification of Leake *et al.* (1997), the Ca-amphibole is an actinolite. TiO_2, Cr_2O_3, MnO and K_2O contents are ~ 0.1 wt% each. Carbonates were not quantitatively analysed. The rock is interpreted as a former sediment, composed of mafic detritus embedded in a mixed carbonaceuos-siliceous matrix. All measured phases are rich in Cr, and the whole-rock Cr content is also very high ($1086\,\mu g/g$). Therefore, the former sediment probably contained detritus from ultramafic rocks.

SY3   Collected by A.K. in 1991; Locality: ~ 500 m east of San Michalis, lense in marble; Rock type: Glaucophane schist.

Sample SY3 is a greyish-blue quartz-rich garnet-glaucophane schist with a well-developed foliation, defined by glaucophane and white mica. Garnet grains are subhedral, $\sim 1.0 - 1.5$ mm in diameter and show abundant cracks, but no chloritisation. White mica is probably phengite, according to the whole-rock content of ~ 0.9 wt% K_2O. Accessory minerals are epidote, Fe-oxide (magnetite?), apatite and tourmaline. Rare tourmaline grains are green in thin section and $\sim 100\,\mu m$ in diameter. The sample is interpreted as a former andesitic volcanic rock (59 wt% SiO_2 and 5.6 wt% total alkalis), which formed the blueschist paragenesis during the peak of the HP event. No indications of retrogade overprint were observed in the rock.

SY5   Collected by A.K. in 1991; Locality: Sumit of hill east of San Michalis, (= point 5 of Dixon & Ridley, 1987), lense in metamorphic breccia; Rock type: Garnet-glaucophane fels.

Sample SY5 is an isotropic garnet-glaucophane fels with euhdral garnet poikiloblasts of $\sim 5 - 15$ mm in diameter, and inclusions of rutile, quartz, epidote and minor glaucophane. Formation of secondary chlorite along cracks in garnet is very restricted. Prophyroblasts of Fe-oxide (magnetite?) are $\sim 1 - 4$ mm in diameter and contain inclusions of quartz and rutile. The matrix of the rock consists of glaucophane, epidote and minor quartz, chlorite and titanite. Titanite is anhedral and replaced rutile, which is found as relics in titanite cores. Whole-rock concentrations of TiO_2 (4.0 wt%) and Fe_2O_3 (16.4 wt%) in SY5 are enriched, while alkalis (3.1 wt%) and SiO_2 (47.1 wt%) are relatively low. The rock is interpreted as a former high-Ti basalt, which was transformed to a glaucophane fels during prograde metamorphism. Retrogression is restricted to the formation of titanite from rutile

and very little chlorite in some cracks of garnet.

SY8 Collected by A.K. in 1991; Locality: Sumit of hill east of San Michalis, (= point 5 of Dixon & Ridley, 1987), blocks of different HP-rocks; Rock type: Garnet-quartz-jadeite fels (meta-plagiogranite).

Sample SY8 is a pale green to white, fine-grained quartz-jadeite fels with euhedral red garnet crystals of $200 - 400\,\mu$m in diameter. The rock is SiO_2-rich ($70\,$wt%), and low in MgO ($0.3\,$wt%) and CaO ($0.9\,$wt%). It is composed of jadeite, quartz and minor white mica, which is probably phengite, according for a K_2O content of $\sim 0.8\,$wt% in the bulk rock. Jadeite (colourless in thin section) and quartz are seperated by a very thin symplectite ($\sim 5\,\mu$m). The rock is interpreted as the metamorphic equivalent of a felsic intrusion within the former oceanic crust, e.g. a plagiogranitic dyke of rhyolitic composition. Sample SY8 is very similar to SY415.

SY11 Collected by A.K. in 1991; Locality: $\sim 200\,$m W of Kámbos, block; Rock type: Tourmaline-omphacite-chlorite fels (hybrid blackwall rock).

Sample SY11 is a pale green tourmaline-omphacite-chlorite fels (see Fig. 4.4d), consisting primarily of chlorite and fine-grained omphacite with minor epidote, phengite and accessory rutile, titanite and apatite. Tourmaline crystals are $2 - 5\,$mm in diameter and $10 - 20\,$mm in length and highly poikiloblastic (Fig. B.1a) with inclusions of omphacite, rutile, titanite, apatite and epidote. Omphacite is very Na-rich (Jd_{80}). The sample is interpreted as a hybrid rock, which was formed as a blackwall at the contact between a jadeite fels and the matrix of the Syros mélange, by influx of hydrous fluids during exhumation (see Chapter 10). Whole-rock analyses of this rock are not available, but sample SY11 is very similar to SY400, which is low in SiO_2 ($49.3\,$wt%) and high in K_2O ($2.1\,$wt%), Na_2O and MgO.

SY109 Collected by Eberhard Seidel (Köln) in 1973; Locality: near San Michalis; Rock type: Eclogite.

Sample SY109 is a hydrous eclogite with a higher SiO_2 ($53.4\,$wt%) and alkali ($5.4\,$wt%) contents and lower MgO ($2.5\,$wt%) and Cr ($29\,\mu$g/g) contents, compared to the other eclogite samples (Table C.2). The protolith of eclogite SY109 probably was a differentiated magmatic rock with a composition of basalic andesite to basaltic trachyandesite. The rock contains poikiloblastic, almandine-rich garnet, zoned omphacite (Jd_{80} cores, Jd_{50} rims) and quartz. Quartz mainly occurs around garnet (Fig. B.2a). Hydrous minerals are epidote ($0.70 - 1.00\,$Fe cpfu), phengite ($3.4\,$Si cpfu), paragonite and ferro-glaucophane ($Al^{VI}/(Al^{VI} + Fe^{3+}) = 0.88$, $X_{Mg} = 0.42$). Garnet is chemically zoned, with Mn decreasing from cores ($Alm_{58}Prp_3$-
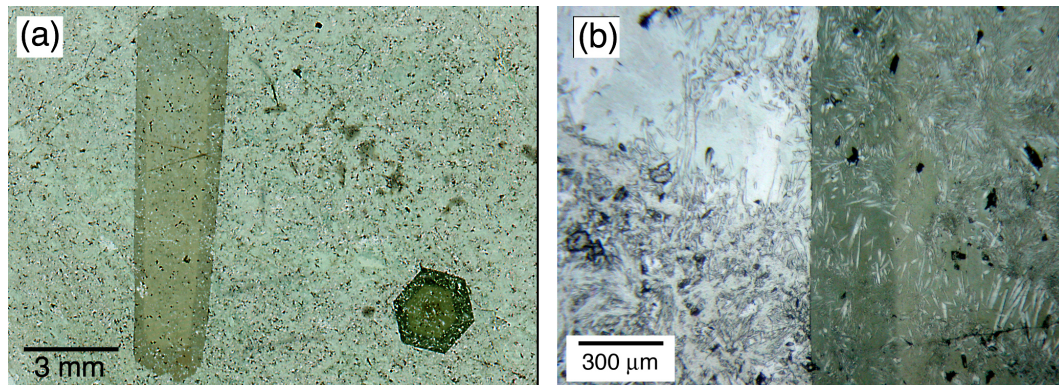
Fig. B.1. a Photomicrograph of sample SY11 in thin section (unpolarised light) showing the tourmaline crystals in different crystallographic orientations (i.e. one parallel and one perpedicular to c-axis) in a fine-grained matrix of omphacite and chlorite. **b** Sample SY400 which is very similar to SY11 shows a crack (horizontal in the image) wich is filled by chlorite and omphacite. The crack was overgrown by a large tourmaline, which replaced the chlorite, but not the omphacite.

$Sps_{13}Grs_{22}Adr_4$) to rim I ($Alm_{66}Prp_{3.5}Sps_{3.5}Grs_{24}Adr_3$), and finally rim II ($Alm_{74}$-$Prp_7Sps_1Grs_{14}Adr_4$). Ca is constant from core to rim I and decreases towards rim II, while Mg and Fe increase from core to rim II. Ti-phases are ilmenite and rutile inclusions in garnet, and rutile rimmed by titanite in the matrix. Other accessory minerals are allanite rimmed by epidote, and apatite in the matrix and as inclusion in garnet. Relics of prograde metamorphism are preserved in the rock, such as ilmenite inclusions in garnet and high Mn-concentrations in garnet cores. HP metamorphism is documented in the paragenesis omphacite cores + garnet (rim II) + quartz + phengite + rutile, while retrogression is recorded in omphacite rims, titanite overgrowths on rutile, Ca-enrichment of glaucophane at its rims in some places together with very rare albite.

Interestingly, SY109 also contains large ($> 300\,\mu m$) grains of zircon, which show oscillatory zoning from cores to rims in cathodoluminescence (CL) images, together with several inclusions of HP minerals, such as omphacite, phengite and glaucophane. These inclusions are connected by a network of cracks in the host zircon, which are annealed by a second generation of zircon (Fig. B.3). It is therefore difficult to recognise these cracks in BSE images. Other zircons show partial or total replacement by zircon with low CL activity together with small inclusions ($< 5\,\mu m$) of Th-silicate, Th-REE-phosphate, U-Th-silicate and xenotime. Zircon from Syros HP rocks was recently dated and interpreted by Tomaschek *et al.* (2003). They interpret the oscillatory zoned large grains to be of magmatic origin, which formed in the late Cretaceous within the magmatic protolith of the eclogites. The replace-

296
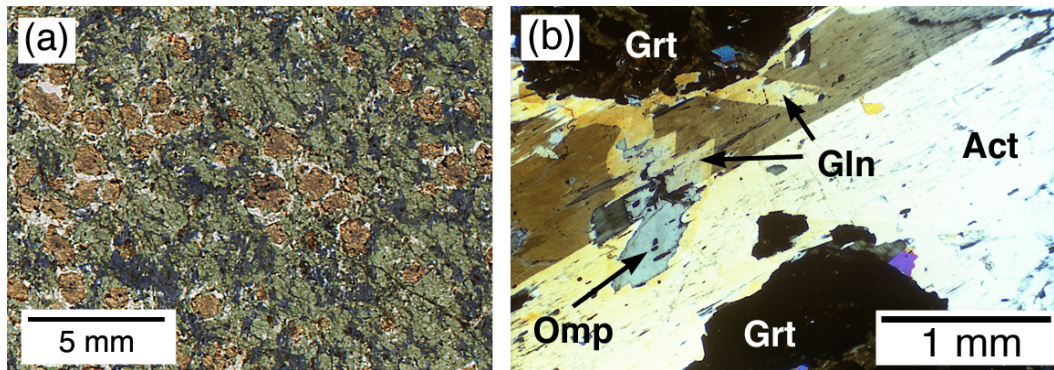
Fig. B.2. a Thick section ($\sim$150 µm) of sample SY109 showing red garnet surrounded by colourless quartz together with blue glaucophane and green omphacite. **b** Thin section of sample SY112 showing large Ca-amphibole (Act) with single twinning surrounded by large garnet grains. Glaucophane is growing topotactically into the actinolite from its rims. In the center, omphacite is grown within glaucophane (crossed polars).

ment of this primary zircon by zircon with lower CL activity, lower REE, Y, Th, U and P content is interpreted to originate from hydrothermal solution-reprecipitation processes of zircon during the Eocene HP event. These results and interpretations from Tomaschek *et al.* (2003) together with the network of secondary zircon, interconnecting all HP mineral inclusions, suggest that the high-pressure minerals were precipitated inside the pre-existing large zircon grains along cracks and newly formed cavities. This result is in conflict with the conclusions of Bröcker & Enders (2001), who took the HP mineral inclusions as evidence for a syn- or post-HP metamorphic origin of the large zircon, and therefore concluded, that subduction in the Cyclades was already active in the Cretaceous (> 75 Ma).

SY112 Collected by R.A. in 1974; Locality: Akros Grizzas; Rock type: Rutile-Glaucophane-actinolite-garnet-epidote fels (metamorphosed Fe-Ti-rich gabbro).

SY112 is a coarse-grained isotropic rock with a dark appearance in hand specimen. Black Ca-amphiboles ($5-10$ mm), redish-brown rutile aggregates ($1-5$ mm), yellow epidote aggregates and partly chloritised garnets ($5-15$ mm) dominate the rock. In thin section, the rock shows two different domains. The first is dominated by coarse-grained Ca-amphibole, garnet and rutile, while the second is dominated by fine-grained epidote aggregates and a pseudomorphic replacement of garnet by an intergrowth of chlorite + glaucophane + epidote + phengite. Rutile in these domains is replaced by titanite. In the first domains glaucophane topotactically replaced Ca-amphibole and in some places is itself replaced by omphacite (Fig. B.2). Garnet contains inclusions of epidote and rutile and is weakly
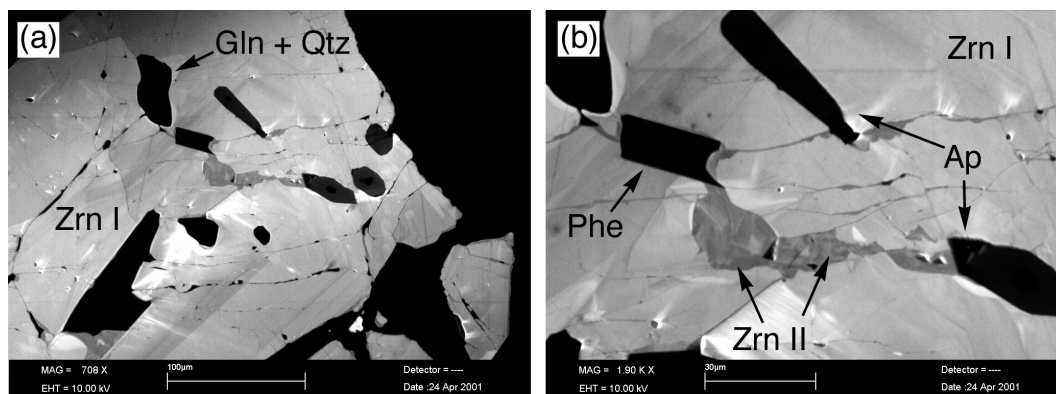
Fig. B.3. Cathodoluminescence (CL) images of zircon in sample SY109. **a** Inclusions of glauco-phane, phengite, apatite and quartz in oscillatory zoned zircon, interconnected by annealed cracks. **b** Close-up of image (a), displaying the crack annealed by secondary zircon with lower CL activity.

zoned, with Mn and Ca decreasing and Fe and Mg slightly increasing from core ($Alm_{60}Prp_{11}Sps_4Grs_{21}Adr_4$) to rim ($Alm_{63}Prp_{15}Sps_{1.5}Grs_{17}Adr_3$). Glaucophane shows a $Ca/(Ca + Na_B)$ ratio of 0.10, a X_{Mg} of 0.63 and a $Al^{VI}/(Al^{VI} + Fe^{3+})$ ratio of 0.85. Ca-amphibole has 7.32 to 7.71 Si cpfu, 0.16 to 0.39 cpfu on the A-site, a $Ca/(Ca + Na_B)$ ratio of ~ 0.66, and a X_{Mg} of 0.69. Following Leake *et al.* (1997), Ca-amphibole ranges from winchite to barroisite. Epidote shows Fe contents ranging from 0.66 to 0.75 cpfu in cores to 0.75 to 0.91 cpfu in rims. Omphacite is in contact with quartz and shows a compositional range from $Jd_{22}Acm_{17}Q_{60}$ to $Jd_{31}Acm_{19}Q_{50}$. Phengite, forming in garnet cracks and pseudomorphs has a X_{Mg} of 0.65 and $3.35 - 3.45$ Si cpfu.

Whole-rock analyses of SY112 revealed a very low SiO_2 content of 40.0 wt% and very high concentrations of TiO_2 (7.3 wt%) and Fe_2O_3 (16.6 wt%). The pro-tolith of the sample probably was a Fe-Ti gabbro. H*P* metamorphism produced garnet, rutile, glaucophane, Ca-amphibole, omphacite + quartz and epidote. During retrogression, garnet was replaced by phengite, chlorite, Fe-rich epidote, and rutile was replaced by titanite. The Ca-amphibole could either have formed during hydrothermal metamorphism of the former gabbro at the ocean floor, or during low-temperature metamorphism at the onset of subduction. A magmatic origin of the Ca-amphibole is unlikely, due to its low TiO_2 content of only 0.10 wt%. Primary magamtic amphibole in Fe-Ti gabbro would be kaersutitic in composition, with TiO_2 contents > 1 wt%.

SY304 Collected by A.K./R.A. in 2000; Locality: Órmos Mégas Lákkos, blocks at the seaside; Rock type: Garnet-chloritoid-epidote-glaucophane schist.

Blueschist sample SY304 shows a well-developed foliation defined by glaucophane and sheet silicates. Porphyroblasts of black chloritoid and red garnet are embedded in a fine-grained matrix of glaucophane, quartz, epidote, phengite, chlorite, and minor rutile and apatite. Chloritoid blasts are $\sim 5\,mm$ in size and contain inclusions of rutile, epidote, quartz and glaucophane. Some grains show formation of paragonite and chlorite at their rims which probably formed by a reaction of chloritoid with glaucophane. Garnet grains are similar in size to chloritoid grains and are very homogeneous in chemical composition ($Alm_{62.5}Prp_{12}Sps_7Grs_{12.5}Adr_6$). Occasionally they show cracks filled by secondary chlorite (Fig. B.4a). Rare inclusions in garnet are glaucophane, apatite, chlorite, quartz and rutile. Phengite and primary chlorite are fine-grained ($\sim 100\,\mu m$) and occur as closely intergrown flakes in some parts of the rock. A clear distinction between the two phases is possible only in BSE images. Glaucophane shows a $Ca/(Ca + Na_B)$ ratio of 0.10, a X_{Mg} of 0.59 and a $Al^{VI}/(Al^{VI} + Fe^{3+})$ ratio of 0.83. The composition of chloritoid is very homogeneous, and was calculated to 14 oxygens and 8 cations, which results in the formula: $(Fe^{2+}_{1.43}Mg_{0.54}Mn_{0.03})(Al_{0.85}Fe^{3+}_{0.15})Al_3O_2[SiO_4]_2(OH)_4$ ($X_{Mg} = 0.27$). Epidote shows Fe contents ranging from 0.74 to 0.82 cpfu. Phengite contains 3.42 Si cpfu, 0.31 wt% Na_2O, and has a X_{Mg} of 0.61. X_{Mg} of chlorite is 0.50.

The whole-rock composition is close to an average MOR basalt, slightly enriched in H_2O (3.2 wt%) and K_2O (0.85 wt%). Therefore, SY304 is interpreted as the HP metamorphic equivalent of a MOR basalt, which was somewhat affected by input of water during seafloor alteration. The rock recrystallised during prograde subduction, to form chloritoid, garnet, rutile, glaucophane and epidote. Large amounts of H_2O were incorporated into the OH-rich HP paragenesis, and probably no fluids were expelled from this blueschist during prograde metamorphism. Retrogression is restricted to little domains within the sample and is documented in the reaction of glaucophane + chloritoid to form paragonite + chlorite and in the chlorite which formed in cracks within garnet.

SY306 Collected by A.K./R.A. in 2000; Locality: Órmos Mégas Lákkos, blocks at the seaside; Rock type: Garnet-chloritoid-epidote-glaucophane schist.

Sample SY306 is very similar to SY304. It is a blueschist with a well-developed foliation, defined by millimeter spaced layers of epidote and glaucophane, and by white mica. Larger porphyroblasts of black chloritoid ($2 - 7\,mm$) and dark red garnet ($1 - 3\,mm$) are abundant. Whole-rock analyses of samples SY304 and SY306 revealed very similar results. Significant differences were observed only in Ca and Sr, for which concentrations in SY306 are higher and for K where the concentration is lower than in SY304. In situ analysis of sample SY306 were not performed.
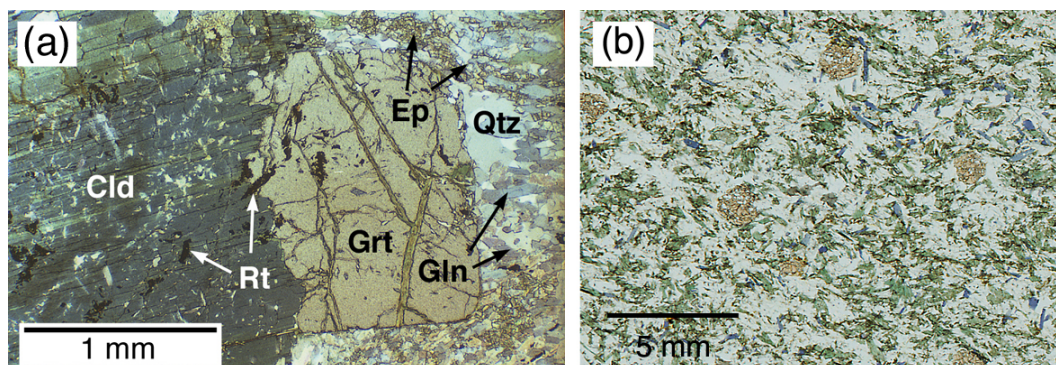
Fig. B.4. a Thin section of sample SY304 showing chloritoid and garnet sourrounded by a matrix of glaucophane, epidote and quartz. Garnet shows chloritisation along cracks. Inclusions in garnet and chloritoid are mainly rutile, epidote and glaucophane. **b** Thin section of sample SY308 showing poikiloblastic, red garnet, green omphacite and blue glaucophane in a colourless quartz-rich matrix with minor paragonite.

SY308 Collected by A.K./R.A. in 2000; Locality: Órmos Mégas Lákkos, blocks at the seaside; Rock type: Garnet-quartz-omphacite fels (meta-plagiogranite).

Sample SY308 is a green, fine-grained quartz-omphacite fels with subhedral red garnet crystals, ~ 1 mm in diameter (Fig. B.4b). The rock is silica-rich (68.5 wt% SiO_2) and is composed of omphacite, quartz, garnet, glaucophane and paragonite with accessory epidote, zircon and apatite. Omphacite and quartz are in direct contact, but omphacite shows compositional zoning in two distinct zones with Ca-rich rims ($Jd_{39}Acm_{17}Q_{43}$) replacing jadeite-rich cores ($Jd_{76}Acm_{10}Q_{13}$). Garnet is poikiloblastic with abundant inclusions of mainly quartz and, shows weak chemical zoning with Mn decreasing and Mg increasing from core ($Alm_{63}Prp_4Sps_7Grs_{22}Adr_4$) to rim ($Alm_{64}Prp_7Sps_2Grs_{23}Adr_4$). Glaucophane shows a $Ca/(Ca + Na_B)$ ratio of 0.02, a X_{Mg} of 0.55 and a $Al^{VI}/(Al^{VI} + Fe^{3+})$ ratio of 0.83. However, in some places it shows strong increase in Ca and Fe at its outer rims, leading to a $Ca/(Ca + Na_B)$ ratio of 0.45 and X_{Mg} of 0.44. Paragonite is abundant in the rock and forms large ($\sim 200\,\mu m$) homogeneous grains, containing little K (~ 0.07 cpfu). Fe contents of epidote range from 0.59 to 0.88 cpfu. The rock is interpreted as the metamorphic equivalent of a felsic intrusion within the former oceanic crust, e.g. a plagiogranitic dyke with low-K dacitic composition. The rock was equilibrated at HP metamorphic conditions, forming garnet, omphacite cores, glaucophane, epidote and paragonite together with quartz. Retrograde processes formed omphacite and glaucophane rims, but did not produce albite or chlorite in the rock.

SY309 Collected by A.K./R.A. in 2000; Locality: Órmos Mégas Lákkos, blocks at the seaside; Rock type: Tourmaline-glaucophane schist.

Sample SY309 is composed of glaucophane schist (SY309A), which is part of the mélange matrix and Tur-rich layers (SY309B), which are concordant to the foliation of the host rock and can be tracked over several meters in the outcrop. Sample SY309B, a $1 - 2$ cm thick layer consisting of tourmaline + omphacite + chlorite + albite + phengite + glaucophane + epidote + apatite + rutile + titanite, is hosted in a glaucophane schist composed of glaucophane + epidote + phengite + titanite (Fig. B.5). Tourmaline crystals are $0.1 - 1.0$ mm in diameter and $1 - 6$ mm in length with some inclusions of titanite, rutile, omphacite, albite ($> 99.7\%$ albite component) and apatite. Compositions of minerals (glucophane, epidote, phengite) in the tourmaline layer and the major rock are almost identical. A significant difference was observed only in Cr content. While Cr_2O_3 contents in the major rock SY309A are below detection limit of the EPMA in all minerals, Tur-rich layer SY309B is characterised by significant Cr_2O_3 contents in phengite (~ 0.14 wt%), omphacite (~ 0.27 wt%), glaucophane (~ 0.10 wt%) and tourmaline (~ 0.22 wt%). This difference is also reflected in the whole-rock Cr concentrations of $70 \, \mu g/g$ in SY309A and $245 \, \mu g/g$ in SY309B.

Glaucophane in both parts of the rock shows a $Ca/(Ca + Na_B)$ ratio of ~ 0.06, a X_{Mg} of 0.69 and a $Al^{VI}/(Al^{VI} + Fe^{3+})$ ratio of ~ 0.88. Epidote ranges from 0.59 to 0.68 Fe cpfu. Omphacite is very homogeneous with a composition of $Jd_{33}Acm_{19}Q_{47}$. Phengite forms large ($> 200 \, \mu m$) grains with a X_{Mg} of 0.69 and ~ 3.45 Si cpfu. Chlorite has a X_{Mg} of 0.73. Tourmaline shows a two-step zonation with concentrations of Ti and Ca being slightly higher in the rims. Tourmaline compositions of SY309 are discussed in detail in Chapter 10 on page 193 and in Marschall *et al.* (2004c).

The whole-rock composition of SY309A shows 48.9 wt% SiO_2 and 7.0 wt% MgO, and is close to an average MOR basalt in both major and trace elements. SY309B, however, is strongly enriched in MgO (13.9 wt%), B and Cr, but depleted in Ca, Sr and Pb. The whole assemblage is interpreted as a former MOR basalt which was strongly sheared and folded during prograde metamorphism. Equilibration at HP conditions formed the paragenesis glaucophane + phengite + rutile + epidote. During exhumation, infiltration of hydrous fluid along the foliation planes introduced B into the rock in restricted domains and led to the formation of tourmaline + omphacite + albite + chlorite + titanite. The fluid was not only rich in B, but also introduced some Cr into the rock and leached Ca, Sr and Pb. For a detailed discussion on the $P - T$ conditions of tourmaline formation, see Chapter 10 on page 193.
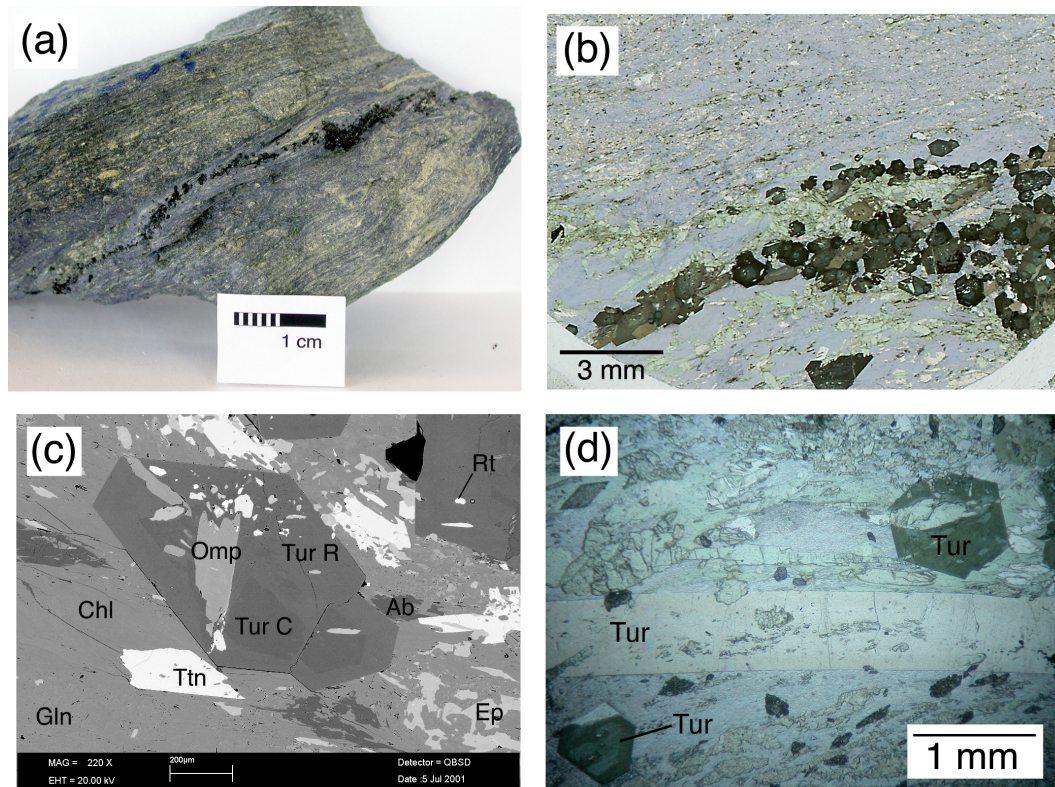
Fig. B.5. Sample SY309 in **a** handspecimen and **b** thin section (unpolarised light) showing the Tur-Omp-Chl layer (SY309B) within an Ep-Phe-Gln-rich blueschist (SY309A). **c** BSE image of tourmaline (C = core; R = rim) intergrown with omphacite, chlorite, albite and glaucophane. **d** Thin section photograph of SY309 showing tourmaline grains in different crystallographic orientation with pleochroism from pale pink to green.

SY314 Collected by A.K./R.A. in 2000; Locality: near Monolithos W of Kámbos; Rock type: Garnet-phengite-albite-glaucophane schist.

Sample SY314 is a glaucophane schist from the matrix of the mélange, consisting of (ferro-)glaucophane, phengite, albite, garnet and accessory apatite, titanite, epidote, quartz, tourmaline and Fe-oxide. Garnet grains in this rock are abundant and small, with grain sizes of $50 - 100\,\mu m$ (Fig. B.6), with high spessartine contents in the cores ($Alm_{19}Prp_{2.5}Sps_{60}Grs_{12}Adr_6$) and high almandine contents in the rims I ($Alm_{59}Prp_{14}Sps_{11}Grs_{11}Adr_5$). Many garnet grains show an outermost rim II of $< 5\,\mu m$ with a very low pyrope content ($Alm_{65}Prp_4Sps_{17}Grs_7Adr_6$). Additionally, the grains are cut by a network of fractures, which are annealed by garnet of different composition. These healed features are less than $1\,\mu m$ in width, but judging from their brightness in BSE images they should have the same composition as rim II. Anhedral apatite grains are $\sim 200\,\mu m$ in size and occur in the matrix and as inclusions in glaucophane. Tourmaline occurs as small euhedral grains, $50 - 100\,\mu m$ in diameter as inclusions in the glaucophane blasts and in the phengite- and albite-rich matrix (Fig. B.6). Zonation is visible in thin section with different shades of green alternating from cores to rims, with compositions changing from dravitic cores to schorl rims. Chemical composition of tourmaline in this sample is discussed in detail in Chapter 9 on page 173. Fe-oxide formes large ($\sim 1\,mm$), euhedral blasts with inclusions of garnet, and were probably Ti-magnetite, which is now strongly altered and replaced by a fine intergrowth of Fe-oxide or -hydroxide and fine-grained silicate material.
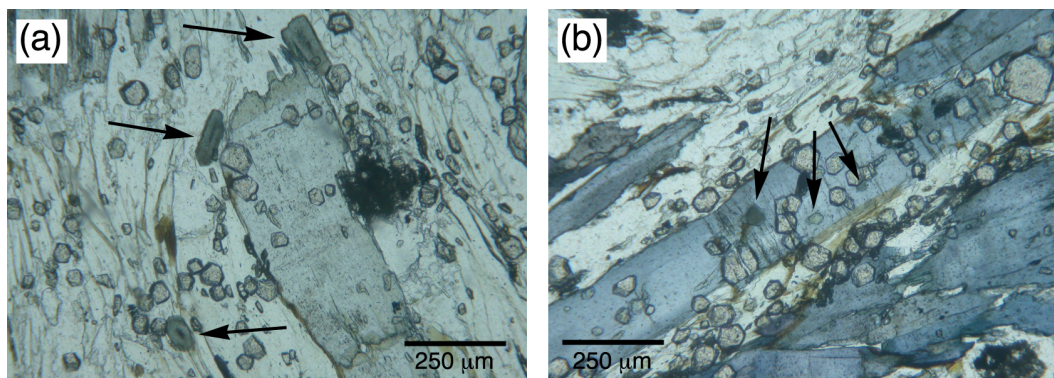
Fig. B.6. Photomicrographs of thin section of sample SY314. **a** Tourmaline grains (arrows) with poikiloblastic cores in a phengite-rich matrix together with a larger glaucophane blast and several small garnet grains (polarised light). **b** Three grains of tourmaline (arrows) included in a glaucophane blast (polarised light).

Glaucophane shows a strong chemical zonation with a homogeneous core and

oscillatory zoned rim. Cores show a $Ca/(Ca + Na_B)$ ratio of ~ 0.06, a X_{Mg} of 0.58 and a $Al^{VI}/(Al^{VI} + Fe^{3+})$ ratio of ~ 0.80. Rims are lower in Ca and Mg and have compositions tending to ~ 0.01 in $Ca/(Ca + Na_B)$ ratio, a X_{Mg} of 0.27, and a $Al^{VI}/(Al^{VI} + Fe^{3+})$ ratio of ~ 0.64. In some places, rims also show an increase in MnO content to $\sim 0.5\,wt\%$. Cores of Na-amphibole are classified as glaucophane, while rims are ferro-glaucophane after Leake *et al.* (1997) or crossite after older nomenclatures. Phengite is very abundant in the rock and shows a X_{Mg} of 0.50 and $\sim 3.40\,Si\,cpfu$. In many places it is replaced by biotite at its rims.

The whole-rock analysis reveals a SiO_2 content of $54.1\,wt\%$, i.e. more silica-rich than MOR basalt. K_2O ($2.3\,wt\%$) and MnO ($\sim 1.0\,wt\%$) are also enriched in SY314. The rock is therefore interpreted as the metamorphic equivalent of basaltic material, probably tuffitic sediments mixed with other detritus, that was exposed to seafloor alteration, increasing Mn, K and Si contents during the typical formation of Fe-Mn hydroxides, clay minerals and opal. The REE pattern of SY314 displays a negative Ce anomaly, which is another argument for seawater alteration. During H*P* metamorphism, the rock recrystallised to form glaucophane, garnet and phengite. Tourmaline probably grew from B, liberated from clay minerals or mica (see Chapter 9 on page 173). The destruction of magnetite, along with the formation of biotite from phengite and the Fe-rich overgrowths on garnet, glaucophane and tourmaline, were probably generated during rehydration of the rock after the metamorphic peak. The occurrence of albite and quartz in the rock without any sign of former omphacite may be interpreted as an upper pressure limit of the metamorphic peak of $\sim 1.3\,GPa$.

SY323 Collected by A.K./R.A. in 2000; Locality: Monolithos west of Kámbos; Rock type: Eclogite.

Sample SY323 is a layered eclogite consisting of Ep-rich and Ep-poor layers, both of which contain $\sim 25\%$ garnet. Ep-poor layers and patches (Fig. B.7a) consist of omphacite, garnet and isolated, euhedral epidote grains ($\sim 100\,\mu m$). Ep-rich layers (Fig. B.7b) consist almost exclusively of epidote and garnet with very little omphacite in some patches. In both layers, titanite occurrs as a minor phase ($\sim 2\%$) and forms large grains (up to $1\,mm$) with small fluid inclusions in some domains and inclusions of euhedral epidote. Accessory phases are quartz, apatite and rutile. Quartz in the matrix is in direct contact to omphacite. Epidote, omphacite and titanite grains do not show any sign of internal deformation. Omphacite is characterised by oscillatory zonation, which is visible both in optical microscope (Fig. B.7c and d) and BSE images.

Garnet grains are $0.5 - 2.0\,mm$ in diameter and poikiloblastic. The inclusions
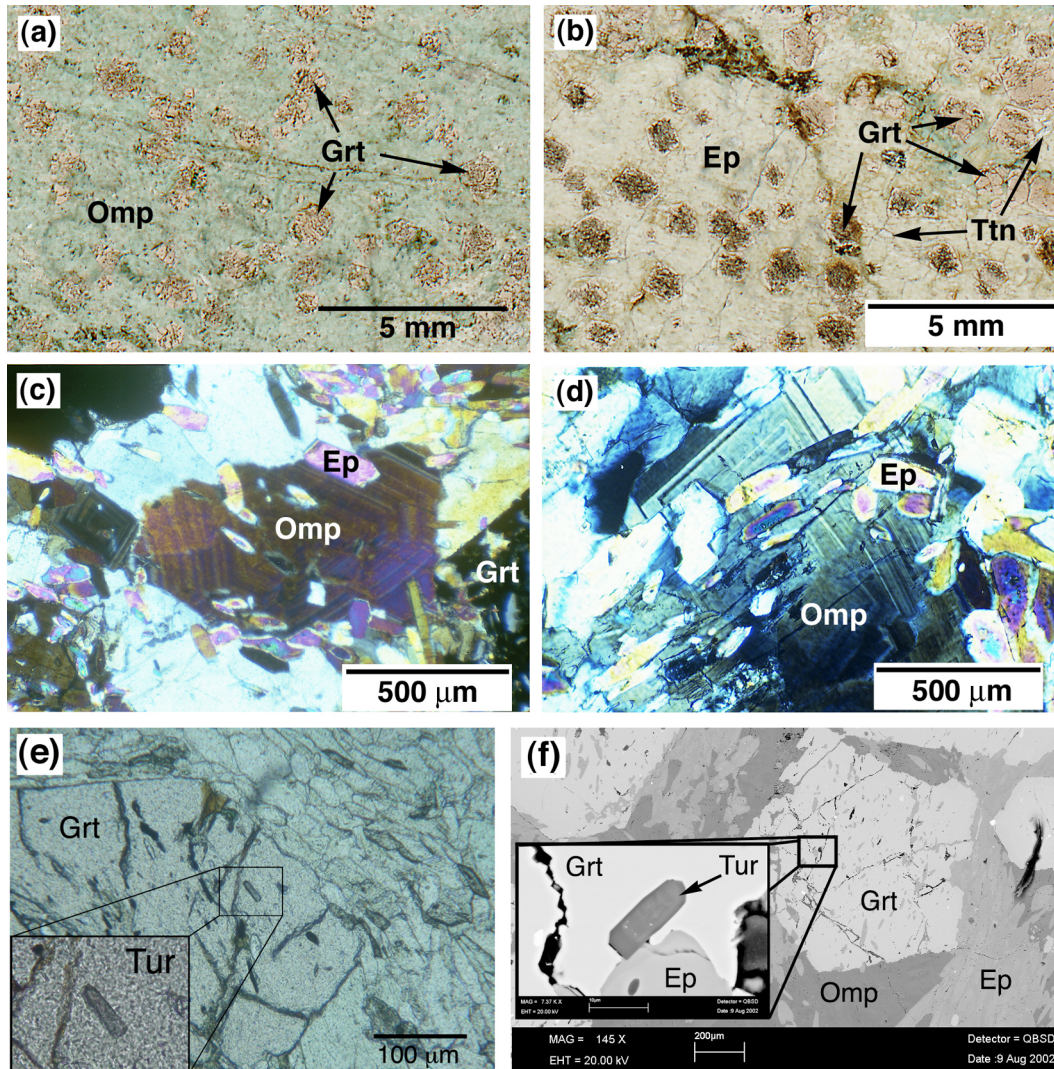
Fig. B.7. a-e Photomicrographs of a thin section of sample SY323. **a** Omp-rich domain with poikiloblastic garnet (unpolarised light). **b** Ep-rich domain with garnet rich in type-II inclusions in the left part of the picture and garnet rich in type-I inclusions in the upper right corner (unpolarised light). **c and d** Omphacite in the matrix showing oscillatory zoning visible under crossed polars. **e** Tourmaline grain included in garnet, which is sourrounded by omphacite and epidote. Inset shows magnification of tourmaline inclusion (both polarised light). **f** BSE image of tourmaline + epidote inclusion in garnet. Garnet shows several partially anealed cracks with different "inclusions" and is surrounded by omphacite and epidote. Inset shows magnification of euhedral tourmaline with poikiloblastic core and homogeneous rim. Scale bar of inset is 10 μm.
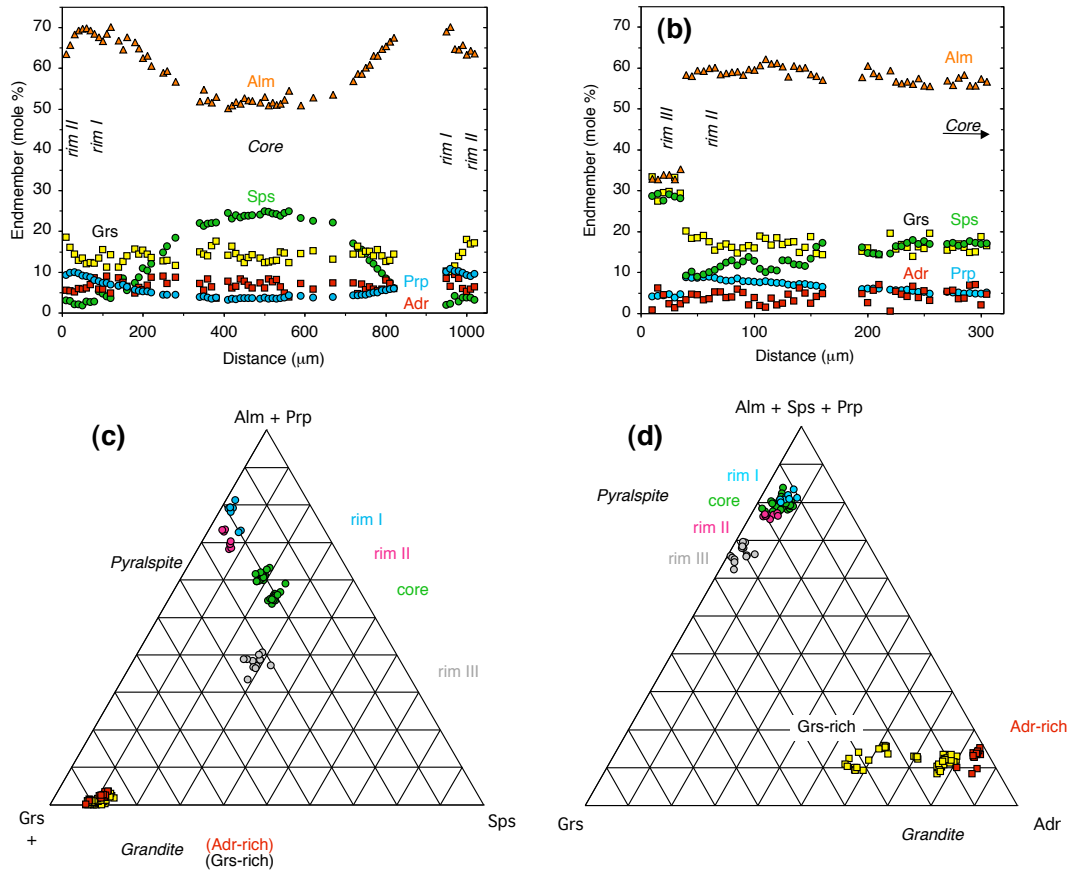
Fig. B.8. Chemical composition of garnet of sample SY323. **a** Rim-core-rim profile over a single garnet grain, showing a typical bell-shaped zonation in spessartine component and increasing pyrope content from core to rim I. Outer rim II is characterised by lower Fe and higher Ca contents. Rim III is not developed in this grain. Gaps in the profile are locations of inclusions of epidote and albite. **b** Profile over the outermost 300 μm of a garnet grain showing the abrupt change in chemistry between rims II and III. **c** (Grs + Adr) - (Alm + Prp) - Sps triangular plot of the six different garnet compositions in SY323. Note that there is a continuous transition from core to rim I, which is not shown for the sake of clarity. **d** Grs - (Alm + Prp + Sps) - Adr triangular plot of the same analyses as in (c).
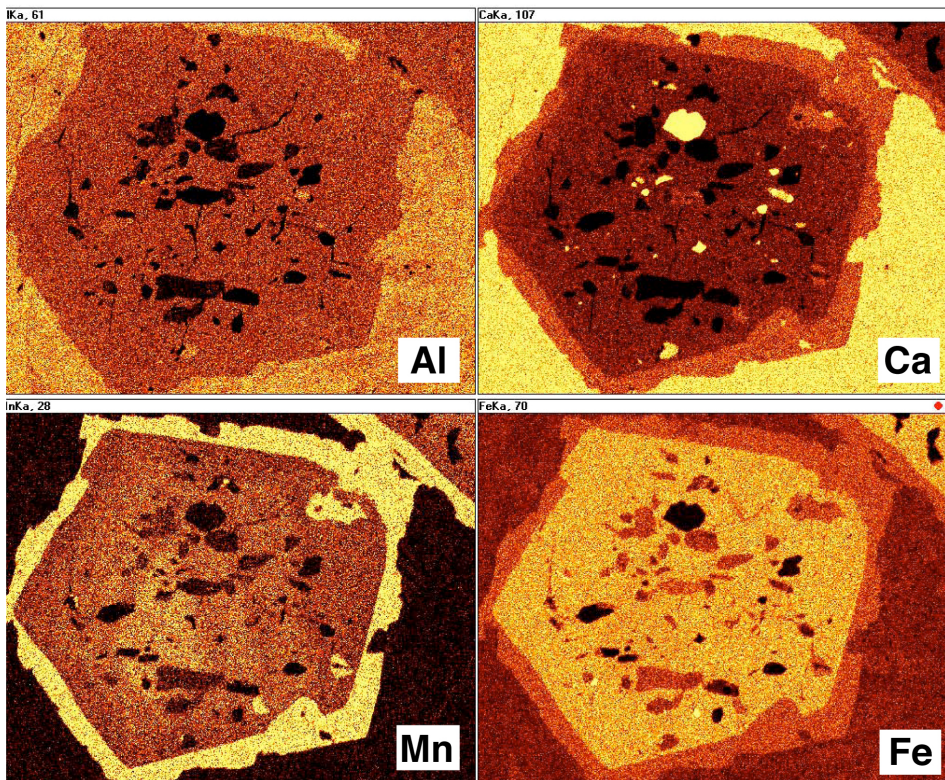
Fig. B.9. EDS chemical mapping of garnet in Ep-rich domain showing Mn-rich core and very Mn-rich rim III with a sharp boundary to rim II. Inclusions are chlorite, epidote and apatite (see also Fig. B.11a for BSE image). Mapped elements are (clockwise from upper left): Al, Ca, Fe and Mn (width of view ∼620 μm).

define S-shaped trails (snowball garnet). Chemically, garnet shows prograde zonation with Mn-rich cores ($Alm_{51}Sps_{25}Grs_{15}Prp_3Adr_6$) and typical bell-shaped Mn-zonations (Fig. B.8a), leading to Fe-rich rims I ($Alm_{70}Sps_2Grs_{12}Prp_{10}Adr_6$) and Ca-rich outer rims II ($Alm_{61}Sps_4Grs_{20}Prp_9Adr_6$). Additionally, garnet grains in the Ep-rich layers may show a $\sim 50\,\mu m$ wide rim III, characterised by a very Ca- and Mn-rich composition ($Alm_{33}Sps_{28}Grs_{32}Prp_4Adr_3$, Fig. B.8b and c and Fig. B.9). Rims II and rims III are free of inclusions, whereas cores and rims I are highly poikiloblastic (Fig. B.11a and b). Included minerals are assigned to two different types. Type-I inclusions are in most cases monomineralic and consist of epidote, omphacite, rutile, apatite, zircon, quartz or tourmaline. Type-II inclusions are composite, consisting of two or three of a large variety of minerals, namely aegirine (Fig. B.11c), hematite, chlorite, biotite, albite, K-feldspar, andradite, epidote and titanite. Most remarkable is the occurrence of andradite-rich garnet, forming small ($10-50\,\mu m$) euhedral grains included in the almandine host (Fig. B.11c, e and f). These andradite inclusions were analysed by micro-Raman spectroscopy (Fig. B.12c) to distinguish them from other Ca-Fe silicates, like vesuvianite. The results show that the inclusions are indeed andradite-rich garnets. It is necessary to note, that host garnet cores, rims I, II and III all contain $\sim 20\,wt\%$ Al_2O_3, equivalent to $\sim 1.95\,Al\,pfu$ and therefore the amount of trivalent Fe is very limited. Chemical mapping of Al concentrations in garnet shows that rim III is indistinguishable from core and rims I and II (Fig. B.9). All host garnet compositions belong to the pyralspite group with different amounts of grossularite component. In contrast, the inclusions range from 9.5 to only $2.5\,wt\%$ Al_2O_3 and belong to the grandite group. Detailed electron-microprobe profiles over grandite and grandite-pyralspite grain boundaries show that hardly any diffusion occurred between the two types of garnet (Fig. B.12a and b). Many grandite inclusions show oscillatory zoning (Fig. B.11f) with grossularite-rich ($Alm_2Sps_{10}Grs_{30}Prp_0Adr_{58}$) and andradite-rich ($Alm_2Sps_{10}Grs_1Prp_0Adr_{87}$) zones (Fig. B.8d).

Chlorite and biotite occur as small ($5-50\,\mu m$) type-II inclusions in garnet (Fig. B.10b). In BSE images fine intergrowth of biotite and chlorite parallel to their cleavage planes is visible. In some grains these intergrowths are to fine to be resolved by the SEM, but EPMA measurements result in K_2O between 0.0 and $9\,wt\%$, extending over the whole compositional range between chlorite and biotite. Surprisingly, lower alkali concentrations are coupled with a strong enrichment in Cu (Fig. B.10a), which reaches concentrations of $3\,wt\%$ in K-poor compositions.

Clinopyroxene in the matrix is omphacite, which is characterised by oscillatory zonation with Ca-rich ($Jd_{23}Acm_{20}Q_{57}$) and Na-rich ($Jd_{38}Acm_{12}Q_{50}$) zones (Fig. B.13a). Concentrations of MnO and TiO_2 are low ($\sim 0.3\,wt\%$ and $\sim 0.03\,wt\%$, respectively, Fig. B.13b). Omphacite in the matrix is in direct contact with acces-
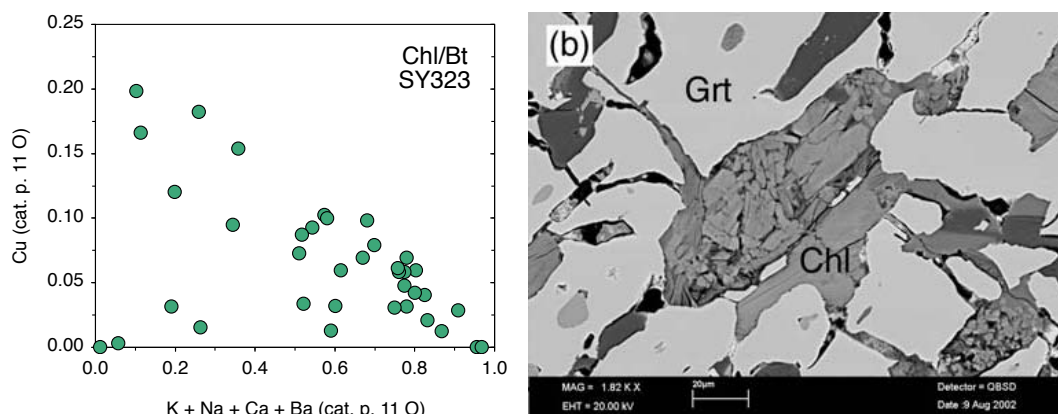
Fig. B.10. a Chemical compositions of type-II inclusions of sheet silicates (biotite/chlorite, calculated to 11 oxygens for comparison) in garnet. Chloritisation of biotite (= decreasing $K + Ba + Na + Ca$) is coupled with a strong increase in Cu (copper!) contents. Analyses of chlorite resulted in concentrations of up to $\sim 3\,wt\%$ CuO. **b** BSE image of type-II inclusions of chlorite in garnet (scale bar is $20\,\mu m$).

sory quartz and garnet rims II. Omphacite is replacing albite which forms type-II inclusions and fills cracks in garnet cores and rims I (Fig. B.11d). Clinopyroxene inclusions in garnet are small grains ($< 100\,\mu m$) intergrown with albite. They are rich in acmite component and show oscillatory zonations (Fig. B.11c) with Al-rich ($Jd_{22}Acm_{31}Q_{46}$), Fe^{3+}-rich ($Jd_6Acm_{83}Q_{11}$) and Ca-rich ($Jd_8Acm_{53}Q_{36}$) zones (Fig. B.13a). Concentrations of MnO and TiO_2 are variable but significantly higher than in matrix omphacite, and reach $3.5\,wt\%$ MnO and $0.75\,wt\%$ TiO_2 (Fig. B.13b). They seem to follow two different trends - a Mn-rich and a Ti-rich trend - which is probably related to the position of the pyroxene with respect to the Mn zonation of the host garnet and to the presence or absence of rutile in the inclusions.

Epidote shows different compositions, depending on its textural position (Fig. B.13c and d). Matrix epidote is homogeneous in Fe ($\sim 0.60\,cpfu$), but zoned in Sr with SrO decreasing from $\sim 1\,wt\%$ in cores to $\sim 0.4\,wt\%$ in rims. In contact to garnet, Fe contents increase, while Sr and Mn contents are still low. Type-I inclusions in garnet contain between 0.80 and $0.90\,Fe^{3+}\,cpfu$, intermediate Mn and low Sr concentrations. Type-II inclusions in garnet are endmember epidotes ($1.00\,Fe\,cpfu$) with high Mn-contents ($0.1\,Mn\,cpfu$). Epidote in stage-4 cracks is also rich in Fe, but poor in Mn.

Fe-Ti oxides forming type-I inclusions in garnet are rutile and ilmenite (Hem_{15}-Ilm_{85}), while type-II inclusions are hematite (Hem_{90} to Hem_{99}). Plagioclase in all textural positions is almost pure albite ($> Ab_{99}$).
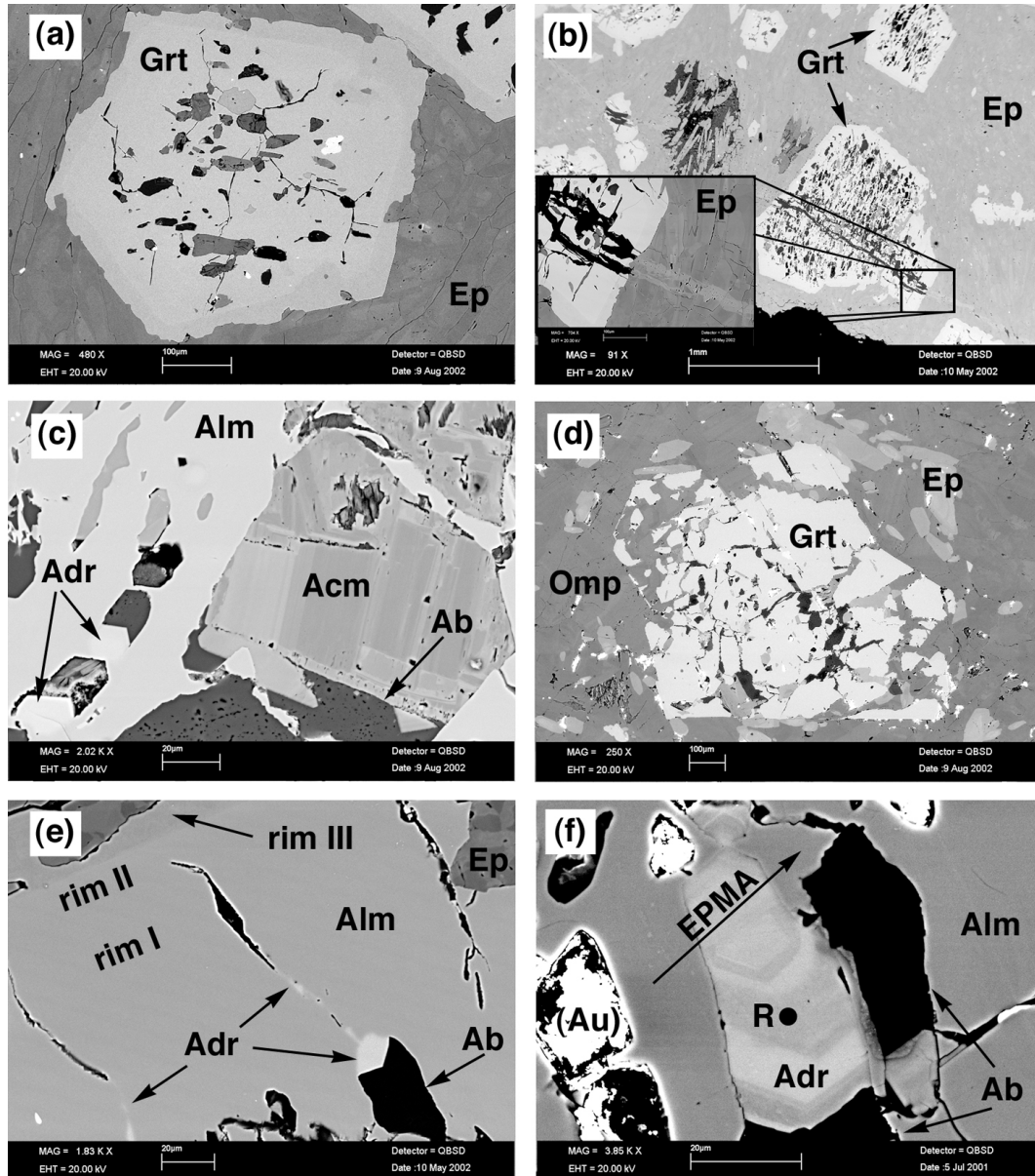
Fig. B.11. BSE images of sample SY323. Description on next page.

Fig. B.11. BSE images of sample SY323 (previous page). **a** Garnet in Ep-rich domain showing type-II inclusions with several cracks. Note that cracks do not reach the rim of the garnet (see also Fig. B.9). **b** Garnet rich in type-II inclusions cut by a late crack which is filled by albite where it cuts the garnet and by Fe-rich epidote where it cuts the matrix epidote. The inset shows a magnification of the garnet rim with the crack. Within the garnet, rim III can be distinguished by a slightly darker colour and by the fact that it is less resorbed by the albite (scale bar of inset corresponds to $100 \, \mu m$). **c** Type-II inclusions in almandine-rich garnet, composed of oscillatory zoned aegirine + albite, small andradite + albite, epidote and chlorite. **d** Garnet in omp-rich domain showing type-II inclusions of albite (black) in its central zone, and cracks filled by omphacite at its rims. **e** Detail of garnet rim showing a crack filled with albite + andradite. Note that andratite (light grey) is found along the crack, which ends within rim II of the host garnet and is not reaching rim III. **f** Oscillatory zoned andradite inclusion in almandine-rich garnet. Arrow marks location of EPMA profile (Fig. B.12a and b). R marks location of Raman spectroscopic analysis (Fig. B.12c). White areas are coverd with gold from SIMS analysis.
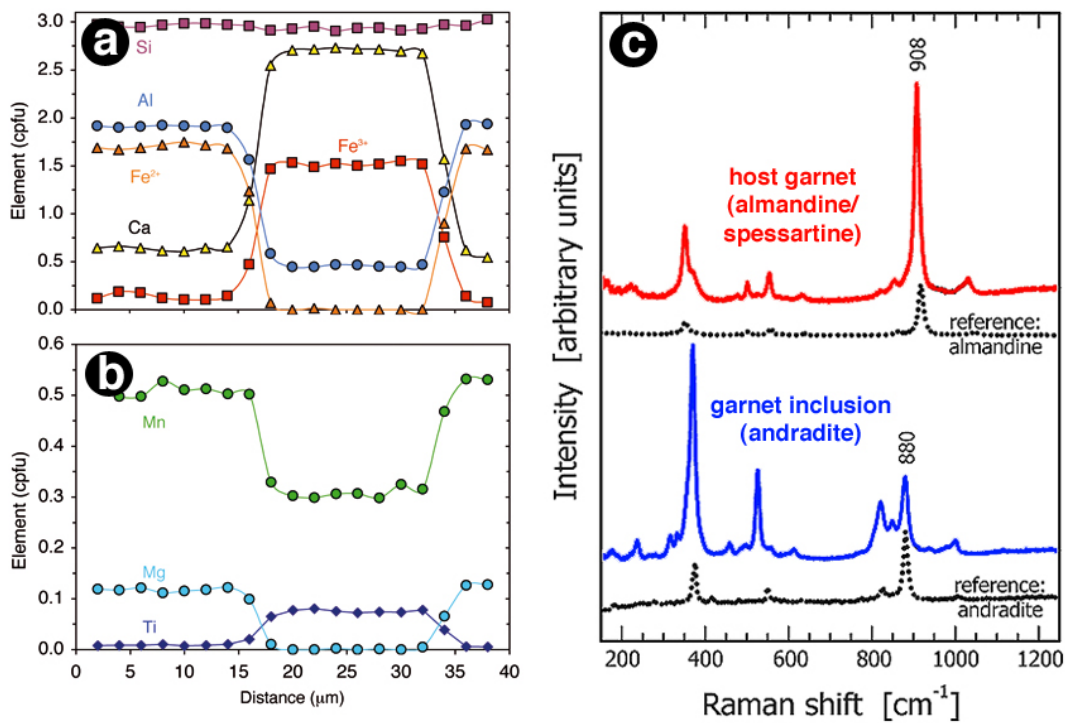
Fig. B.12. a and b EPMA profile over andradite inclusion in almandine-rich garnet (Fig. B.11f). Note the abrupt change in chemistry at the contacts and the low concentrations of Mg and Fe^{2+} in the andradite. **c** Raman spectra of almandine-rich host garnet (red) and andradite inclusion (blue) together with two reference garnets of almandine and andradite, respectively (dotted lines).
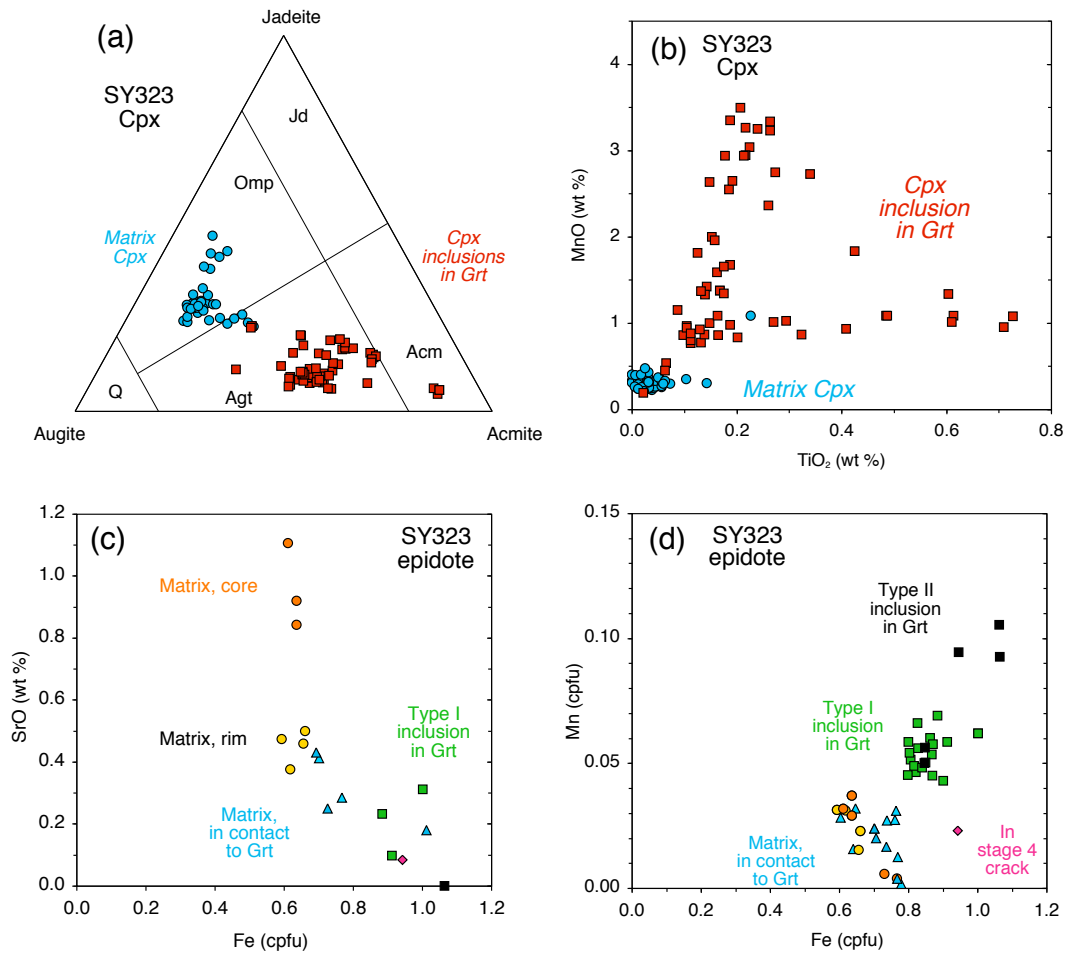
Fig. B.13. (a and b) Composition of clinopyroxene in sample SY323. **a** Augite-jadeite-acmite triangle showing matrix pyroxene (blue circles) plotting into the omphacite field, while type-II inclusions in garnet (red squares) plot into the aegirine field with a trend to pure acmite. **b** MnO vs TiO$_2$ diagram, showing a Ti-rich and a Mn-rich trend for the acmite inclusions, while matrix omphacite is generally low in both elements. **c and d** Epidote compositions of SY323. Red circles = cores of matrix epidotes; yellow circles = rims of matrix epidotes; blue triangles = epidotes in contact to garnet; green squares = type-I inclusions in garnet; black squares = type-II inclusions in garnet; pink diamond = epidote in stage-4 crack. **c** SrO vs Fe. **d** Mn vs Fe.

Several stages of the metamorphic history of eclogite sample SY323 are recorded in the complex microstructures of the rock described above. In this section, I want to present an interpretation of the rock's history, which tries to explain the observed textural and chemical features, and may have implications for the $P-T$ path of the rock. The whole metamorphic history is explained in four major stages, which differ from each other in terms of P, T, f_{O_2}, fluid saturation and/or deformation.

Stage 1 produced garnet poikiloblasts with garnet growing from Mn-rich cores to Mn-poor rims I. Inclusions form S-shaped trails (snowball garnet), proving syn-kinematic garnet growth. This stage was probably characterised by prograde metamorphism (increasing P and T) leading to an increase of Mg and decrease of Mn concentrations from core to rim (Fig. B.14a). Inclusions trapped in garnet are type-I inclusions of epidote, ilmenite, rutile, tourmaline, quartz, apatite and zircon. Additionally garnet must have trapped another species of inclusion, either a hydrous mineral (lawsonite?) or fluid, which dehydrated or decripitated during stage 2 and produced the fractures in the garnet.

Stage 2 produced radial cracks around some inclusions in garnet (Fig. B.11a and Fig. B.14b) and deliberated a highly oxidising fluid. This volume expansion of inclusions is likely to happen either by dehydration of a hydrous mineral reaching its limit of stability, or by decripitation of fluid inclusions trapped by garnet during its growth. Both of these scenarios are most likely to occur during a temperature increase, concerning the steep Clapeyron slopes of both typical dehydration reactions and isochores of H_2O. Type-II fluid inclusions are very rich in trivalent Fe and demonstrate a very high f_{O_2} of the fluid, forming andradite, acmite and hematite. Additionally, the high Cu concentrations in chlorite are probably due to oxidation of Fe-Cu sulfides, which usually host Cu in eclogitic rocks, but are not stable at highly oxidising conditions. Earley et $al.$ (1995) have shown experimentally, that oxidation of biotite in Cu-bearing solutions is leading to Cu-rich sheet silicates with lower K contents. Pressure conditions during stage 2 were within the albite stability field, proved by the occurrence of albite in type-II inclusions and stage-2 cracks.

In stage 3, albite in cracks was replaced by omphacite where it had contact to the matrix and was preserved only where it was shielded by garnet (Fig. B.11d and Fig. B.14a). Cracks formed in stage 2 were also anealed by garnet itself, which formed rims II wich are slightly richer in Ca. This stage is probably characterized by pressure increase, as omphacite and quartz, but no albite was found in the matrix of the rock. Stage 3 was therefore the true eclogite-facies stage, where omphacite rapidly crystallised in presence of a fluid (oscillatory zonation) together with titanite, low-Fe epidote and rims II of garnet.

After pressure release, brittle fractures formed during stage 4. Within these fractures, low-Fe epidote was replaced by high-Fe epidote and garnet was replaced by
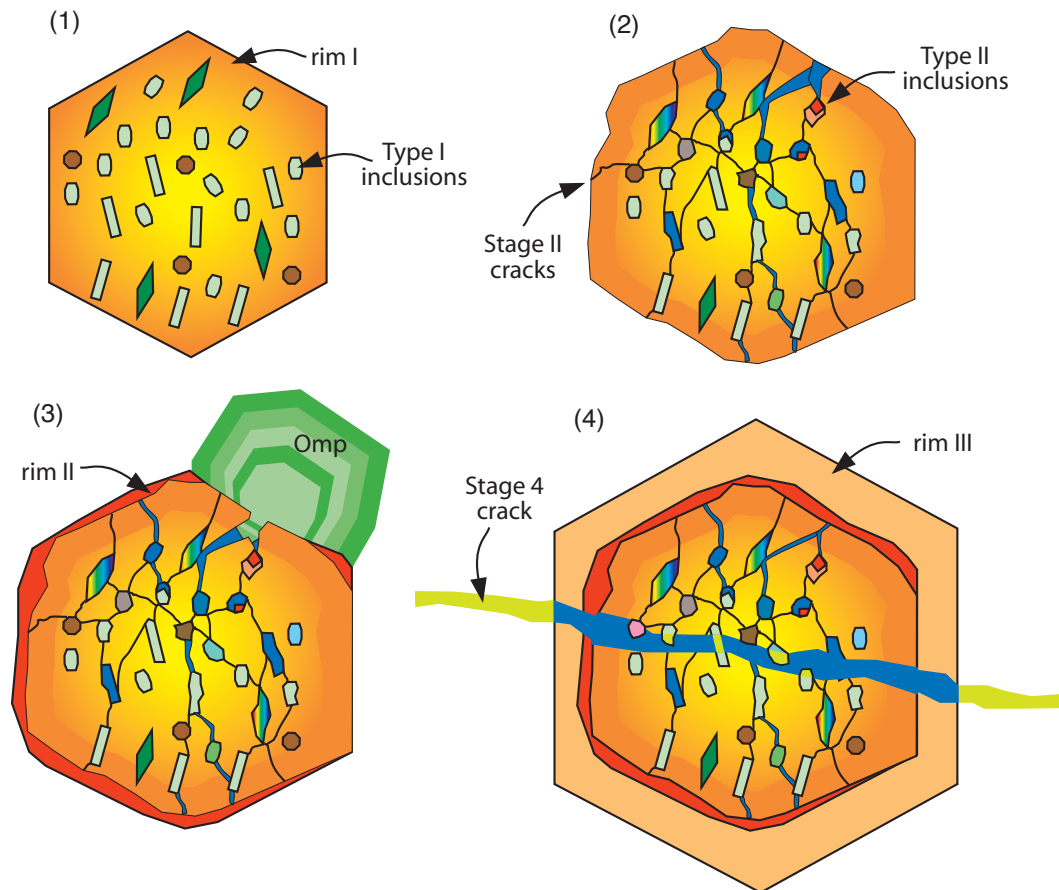
Fig. B.14. Schematic presentation of the evolution of sample SY323. **1** Stage 1: Growth of host garnet with Mg and Fe^{2+} increasing and Mn decreasing from core to rim. Formation of type-I inclusions of epidote, ilmenite, rutile, quartz, apatite, tourmaline and zircon. Possibly, some of the inclusions were also hydrous fluid inclusions. **2** Stage 2: Decripitation of inclusions forming cracks in host garnet. High oxygen fugacity in released fluids form Fe^{3+}-rich minerals like andradite, aegirine and hematite, and titanite, K-feldspar, albite and Cu-rich chlorite. Cu in chlorite was probably derived from oxidation of Fe-Cu-sulfides by the fluid during this stage. **3** Stage 3: Garnet rim II (higher Ca content) partially anealed stage-II cracks. Omphacite in the matrix rapidly crystallised in presence of fluid and established an oscillatory zonation. Omphacite replaced albite within stage-II cracks. **4** Stage 4: Formation of Mn-Ca-rich rim III and large cracks filled with albite and epidote.

albite (Fig. B.11b and Fig. B.14d). In addition, garnet developed high-Mn rims (rim III) which are entirely different to the earlier garnet generations and show sharp boundaries to rims II. The developement of rims III is probably controlled by an equilibrium between grossularite and almandine components in garnet and the stability of epidote, which has been used by Donohue & Essene (2000) for calibrating an oxygen barometer.

Summarising the arguments presented above, the rock first was formed as a garnet-bearing schist (stage 1) under increasing $P - T$ conditions. Then, it was overprinted by significant heating within the stability field of albite (low-P) during stage 2. Afterwards, it was subjected to higher pressure and recrystallised under eclogite-facies conditions in stage 3. In the last stage, it developed several cracks along which the chemistry was significantly changed by fluids. A quantitative evaluation of the history of SY323 requires more detailed calculation of the $P - T$ conditions of the different stages, which was not yet performed. However, the indications presented here point to an anti-clockwise $P - T$ path of this eclogite block, which has not been reported for rocks from Syros, so far. It is important to note that garnet rims II and matrix omphacite crystallised at the same stage at eclogite-facies conditions and were probably in equilibrium. This hypothesis is also supported by textural evidence, as rim-II garnet shows euhedral grain boundaries towards omphacite and is not resorbed (Fig. B.11d). Whole-rock composition and possible protoliths of SY323 are discussed in the next section together with sample SY324.

SY324 Collected by A.K./R.A. in 2000; Locality: Monolithos west of Kámbos; Rock type: Eclogite.

Sample SY324 is a fine-grained eclogite, consisting of small euhedral garnet (100 μm), epidote and omphacite. The rock does not show compositional layering, as is the case for SY323, but shows a well-developed lineation, defined by omphacite. The whole-rock composition is very similar to eclogite samples SY323 and SY411, with high concentrations of CaO (16.0 wt%) and Sr (607 μg/g). The rock is interpreted as the metamorphic equivalent of basalt, that was enriched in Ca (and Sr). This enrichment process probably took place during hydrothermal seafloor-alteration at elevated temperatures ($> 250\,°C$), producing an epidote-rich assemblage. Compositions of eclogites SY323, SY324 and SY411 are between those of basalts and rhodingites.

SY325 Collected by A.K./R.A. in 2000; Locality: Monolithos west of Kámbos; Rock type: Talc-chlorite-actinolite schist (hybrid blackwall rock).

Sample SY325 is part of a blackwall around an eclogite block. Within this black-
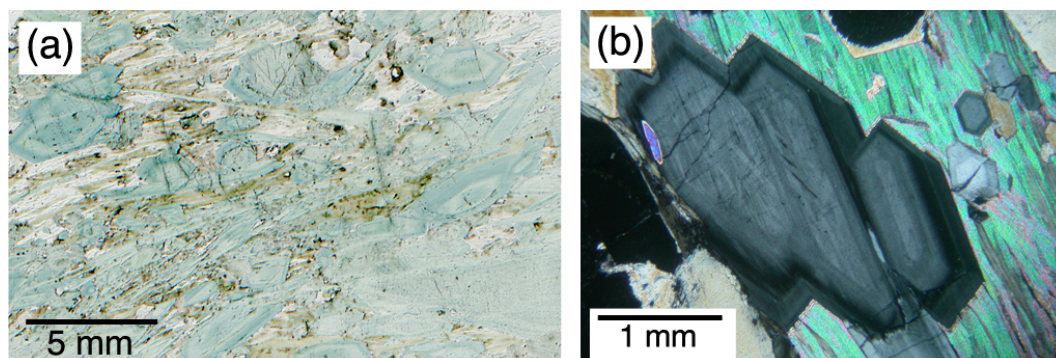
Fig. B.15. a Photomicrograph of a thin section of sample SY325, showing minor chlorite (green), talc (white) and large crystals of Ca-amphibole displaying internal chemical zoning with blue, Cr-rich and colourless, Cr-poor zones (unpolarised light). **b** Euhedral Ca-amphibole in contact with talc (green interference colours). Additional to concentric zonation, amphibole grains show internal structures that were probably inherited from the overgrown talc (crossed polars).

wall, the amount of actinolite is decreases with increasing distance from the eclogite, while the abundance of talc increases. SY325 was sampled from the actinolite-rich domain and contains $\sim 20\%$ chlorite, $\sim 15\%$ talc, accessory Fe-oxides and Cr-bearing rutile (1.9 wt% Cr_2O_3).

Chlorite is also Cr-bearing with concentrations of ~ 0.4 wt% and has a X_{Mg} of 0.82. Talc has a X_{Mg} of 0.93. The dominant Ca-amphibole has a X_{Mg} of 0.80 to 0.85, is Na-, Al- and Cr-rich and shows complex chemical zonation also visible in thin section (Fig. B.15). Cores are inhomogeneous at a small scale. Inner cores, however, show $Ca/(Ca + Na_B)$ ratios of ~ 0.76, occupation of the A-site of 0.22 cpfu, Cr_2O_3 content of 0.3 wt% and 7.81 Si cpfu. Rim I is higher in Ca, Si and Mg and lower in Na, Al and Cr, i.e. it is closer to the actinolite composition. $Ca/(Ca + Na_B)$ ratio of rim I is ~ 0.80, occupation of the A-site of 0.17 cpfu, Cr_2O_3 content is 0.2 wt% and it has 7.91 Si cpfu. Rim II is higher in Na, Al and Cr, with a $Ca/(Ca + Na_B)$ ratio of ~ 0.62, occupation of the A-site of 0.25 cpfu, Cr_2O_3 content of 0.6 wt% and 7.89 Si cpfu. The outer $100 - 200 \mu m$ of the amphibole grains are characterised by a steady decrease in Na, Al and Cr. At the grain boundary, the composition shows a $Ca/(Ca + Na_B)$ ratio of ~ 0.71, occupation of the A-site of 0.28 cpfu, Cr_2O_3 content below detection limit, and 7.95 Si cpfu. The concentrations of the light elements Li, Be and B are correlated to major element concentrations and show low abundances in rims I and III and are highest in rim II (Fig. B.16). Following Leake *et al.* (1997), rim I of Ca-amphibole is actinolite, whereas rims II and III with their higher Na contents are winchite. The core is oscillating between actinolite and winchite.
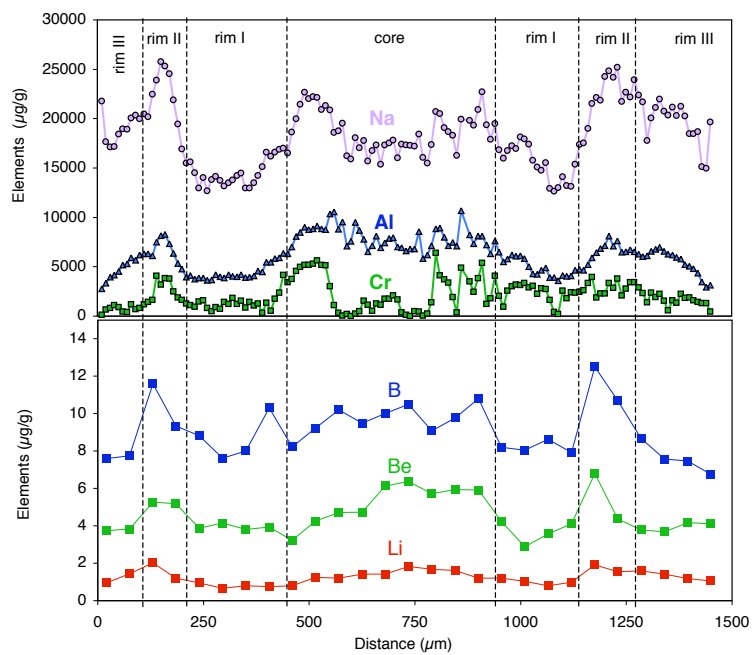
Fig. B.16. Chemical profile over amphibole grain in sample SY325, showing the elements Na, Al and Cr (determined by EPMA), and B, Be and Li (determined by SIMS). Several different zones can be distinguished and correlated with the optical zonation (Fig. B.15). The core is inhomogeneous at a small scale. Rim I shows low concentrations in all displayed elements and is pale blue to colourless in thin section. Rim II shows the highest concentrations of all elements displayed, including Li, Be and B, and is blue in thin section. Within rim III, concentrations of all displayed elements and colour intensity steadily decrease towards the grain boundary.

The whole-rock analysis reveals very low Al_2O_3 concentrations of only 2.1 wt%, but high concentrations of MgO (22.1 wt%), Cr (1812 µg/g) and Ni (1592 µg/g), which result from the tectonic and metasomatic mixing in this blackwall rock, between the eclogite block and the surrounding serpentinite. However, SiO_2 (54.8 wt%) and CaO (7.4 wt%) concentrations are reflecting the influence of the siliceous HP block.

SY327 Collected by A.K./R.A. 2000; Locality: Monolithos west of Kámbos; Rock type: Tourmaline-chlorite-omphacite fels (hybrid blackwall rock).

Sample SY327 is a dark green omphacite-chlorite fels consisting of equal amounts of chlorite and omphacite, making up about 80 % of the rock (Fig. B.17a). Additional phases are abundant apatite ($2 - 3$ mm), albite, ilmenite, titanite, biotite, amphibole and tourmaline. Three compositional types of clinopyroxene were observed in the matrix. The first one are cores of large omphacite grains ($1 - 5$ mm) with intermediate acmite and jadeite contents ($Jd_{37}Acm_{28}Q_{34}$). The second type is found as rims of the same grains with a much higher jadeite content ($Jd_{52}Acm_{27}Q_{19}$). The third type is found in patches composed of small grains (10 µm) closely intergrown with albite (with ~ 97 % albite component). Type 3 clinopyroxene has high acmite and very low jadeite contents ($Jd_{15}Acm_{49}Q_{35}$ = aegirine). Garnet is not preserved in the rock, but was probably present before, as indicated by hexagonal pseudomorphs consisting of fine-grained chlorite (Fig. B.17b). Amphibole occurrs only as small inclusions (< 100 µm) in tourmaline and is zoned from blue in cores to bluish-green at its rims. Composition of blue cores are those of glaucophane, but shows significant occupation of the A-site (~ 0.36 cpfu) and depletion in Si (~ 7.65 Si cpfu). Ca/(Ca $+ Na_B$) ratio is ~ 0.10. Towards the bluish-green rims, the total Na content slightly decreases, the Ca, Al and K contents increase, and the Si content significantly decreases. Following the nomenclature of Leake *et al.* (1997), the compositions change from glaucophane over nyböite to magnesiokataphorite. The most Ca-rich composition has a Ca/(Ca $+ Na_B$) ratio of ~ 0.39, an A-site occupation of ~ 0.88 cpfu and only ~ 6.71 Si cpfu. Tourmaline is close to the ideal schorl-dravite series and has a X_{Mg} of ~ 0.60. Compositions are discussed in detail in Chapter 10 on page 193. Grains are ~ 4 mm in diameter and 3 cm in length and are highly poikiloblastic with inclusions of predominantly omphacite, blue-green amphibole, apatite and chlorite. Whole-rock analyses of sample SY327 are not available. The rock, however is part of a blackwall which formed around an eclogite block. Omphacite I and pseudomorphs after garnet are probably witnesses of the HP eclogite paragenesis. Rehydration during exhumation led to the formation of Ca-Na-amphibole, omphacite II, chlorite, tourmaline, apatite and
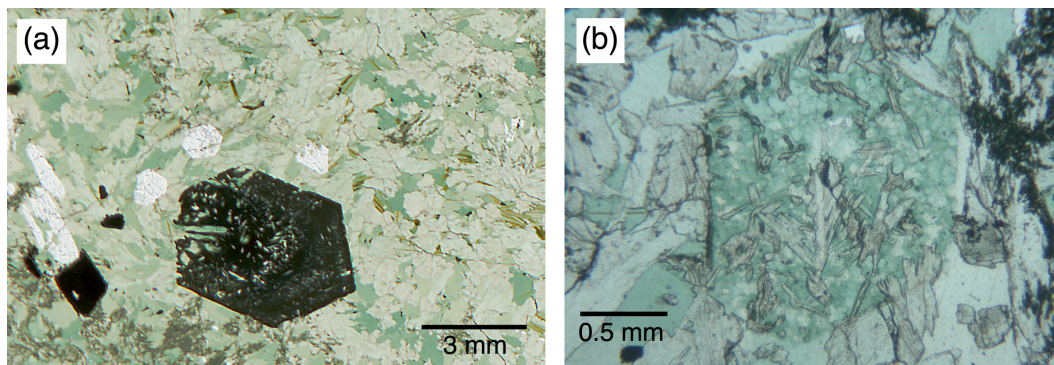
Fig. B.17. Photomicrographs of a thin section of sample SY327. **a** Large apatite (colourless), ilmenite (black) and tourmaline (dark green hexagon in center) blasts enclosed in a matrix of omphacite + chlorite + minor albite and biotite. The greyish assemblage in the lower left corner is a fine-grained intergrowth of aegirine and albite (unpolarised light). **b** Chlorite pseudomorph (probably) after garnet.

finally albite, biotite and aegirine. The retrograde rehydration process with estimation of $P-T$ conditions and silica activity of the hydrous fluids are discussed in Chapter 10 on page 193.

SY328 Collected by A.K./R.A. in 2000; Locality: Monolithos west of Kámbos; Rock type: Omphacite-chlorite fels (hybrid blackwall rock).

Sample SY328 is a dark green omphacite-chlorite fels, similar to sample SY327, but without tourmaline. The rock is composed of large chlorite grains ($1-5\,\mathrm{mm}$, $X_{\mathrm{Mg}} = 0.63$), intergrown with euhedral epidote ($\sim 0.5\,\mathrm{mm}$) and fibrous Na-rich clinopyroxene (Fig. B.18). Additionally, large blasts of apatite, ilmenite and pyrite occur in the rock. More fine-grained parts of the sample show an intergrowth of fibrous jadeite/omphacite with albite (98 % albite component). The fibrous clinopyroxene shows compositional zonation, oscillating between jadeite ($\mathrm{Jd}_{65}\mathrm{Acm}_{25}\mathrm{Q}_{10}$) and omphacite ($\mathrm{Jd}_{47}\mathrm{Acm}_{25}\mathrm{Q}_{27}$). Additionally, small rims of Fe^{3+}-rich pyroxene ($\mathrm{Jd}_{21}\mathrm{Acm}_{59}\mathrm{Q}_{19}$) occur in some places, intergrown with albite. Ilmenite (Ilm_{90}-$\mathrm{Hem}_5\mathrm{Pyrophanite}_4\mathrm{Geikilite}_1$) is rimmed by titanite and shows an intergrowth of rutile + magnetite ($\mathrm{Mag}_{94}\mathrm{Usp}_6$) in its core. Epidote shows Fe contents between 0.72 and $0.80\,\mathrm{cpfu}$, SrO concentrations of up to $2.6\,\mathrm{wt\%}$ and sometimes has inclusions of allanite in its core. Amphibole was found in one place as inclusion in epidote. Its composition is comparable to the Ca-rich blueish-green amphibole of sample SY327. It is, however more depleted in silica ($6.47\,\mathrm{Sicpfu}$) and has an almost fully occupied A-site ($0.95\,\mathrm{cpfu}$). After Leake *et al.* (1997), the amphibole is a magnesio-taramite (close to the boundary to magnesiokataphorite). Apatite is hydroxy-apatite

319
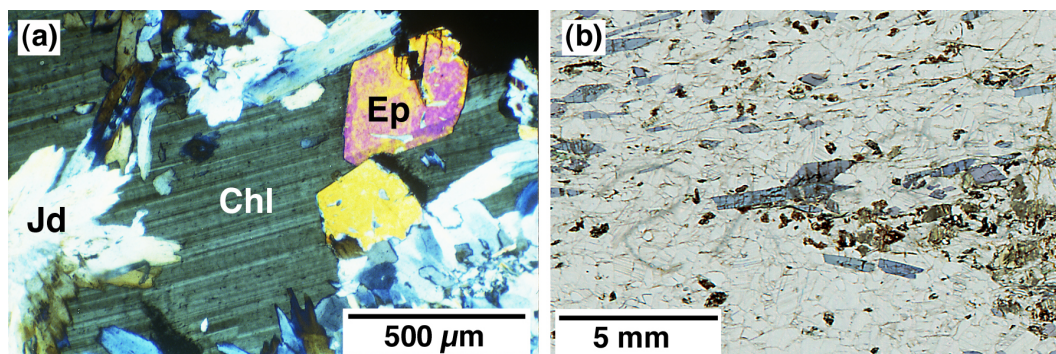
Fig. B.18. Photomicrographs of thin sections. **a** Sample SY328 under crossed polars, showing a large single crystal of chlorite intergrown with euhedral epidote and fibers of jadeite/omphacite. **b** Sample SY335 in unpolarised light, showing a colourless matrix composed of calcite and quartz hosting epidote (pale yellow, high relief) and large euhedral crystals of glaucophane (blue).

with ~ 0.36 F pfu, no detectable Cl and ~ 0.27 wt% SrO.

The whole-rock analysis of blackwall sample SY328 shows low SiO_2 contents (43.0 wt%) and high concentrations of TiO_2 (2.8 wt%), Fe_2O_3 (15.5 wt%), and an enrichment in P_2O_5 to 1.6 wt%. Sulfur was not analysed, but the occurrence of pyrite (~ 1 mm in diameter) suggests also high S contents. Therefore, the blackwall in this place was probably enriched in Ti, Fe, S and P $\pm$ F during its formation within the stability field of albite.

SY335 Collected by A.K./R.A. in 2000; Locality: Monolithos west of Kámbos; Rock type: Glaucophane-bearing marble.

Sample SY335 is a siliceous calcite marble (11.0 wt% SiO_2) containing large ($2-5$ mm), euhedral glaucophane grains (Fig. B.18b). Additional silicates are quartz, phengite ($0.5-1$ mm), epidote and titanite. Hematite ($Hem_{96}Ilm_{3.5}$) is replacing titanite in some parts of the rock. The rock displays a coarse-grained texture with millimeter-sized grains of calcite and silicates, and shows a foliation defined by orientation of glaucophane. Glaucophane grains are large ($2-5$ mm in length), euhedral and chemically homogeneous. They show $Ca/(Ca + Na_B)$ ratio of 0.03, a X_{Mg} of 0.68 and a $Al^{VI}/(Al^{VI} + Fe^{3+})$ ratio of 0.84. Phengite has ~ 3.43 Si cpfu and a X_{Mg} of 0.71. Epidote shows Fe contents between 0.73 and 0.85 cpfu. The stability of glaucophane in calcite marble was discussed by Schumacher *et al.* (2000), who showed that H_2O activity of a fluid in the rock has to be at least 0.97, in order to inhibit the breakdown of glaucophane + calcite to dolomite + omphacite + quartz.

The rock is interpreted as a carbonate sediment with a contribution of clay and possibly tuffitic material, which increased the concentrations of Na, Mg, Ca, Fe,

Si and K, and recrystallised to phengite, glaucophane and epidote under HP metamorphic conditions. In contrast to siliceous marble SY2, the whole-rock analysis of SY335 reveals no enrichment in Cr or Ni. A contribution of ultramafic material in this rock can therefore be excluded. Retrograde reactions in SY335 are restricted to late cracks and to partial replacement of titanite by hematite.

SY342 Collected by A.K./R.A. in 2000; Locality: Ákra Gríza, at the bay; Rock type: Epidote-garnet-glaucophane fels.

Sample SY342 is an isotropic, coarse-grained rock, consisting of glaucophane, epidote, white mica and abundant garnet ($\sim 25\%$). Garnet is dark red, euhedral and up to 5 mm in diameter. In some places, omphacite has crystallised in the rock, marking the transition from a blueschist to an eclogite. Whole-rock analyses show elevated contents of TiO_2 (2.2 wt%), Fe_2O_3 (12.8 wt%) and SiO_2 (55.2 wt%) with respect to MORB. The sample is interpreted as a former Fe-Ti basaltic andesite, which equilibrated at the blueschist-to-eclogite-facies transition during the peak of the HP event.

SY344 Collected by A.K./R.A. in 2000; Locality: Ákra Gríza, at the bay; Rock type: Garnet-glaucophane-epidote fels (metagabbro).

Sample SY344 is a coarse-grained isotropic rock with a gabbroic texture. Dark Ca-amphibole and blue glaucophane are embedded in a fine-grained white matrix of clinozoisite, epidote and isolated red garnet grains. Ca-amphibole shows oriented lamellae of titanite within all grains. At its rims, it shows glaucophane crystals which are topotactically growing from the rims of Ca-amphibole towards the center (Fig. B.19). The titanite lamellae are simply included by the overgrowing glaucophane. Glaucophane shows a $Ca/(Ca + Na_B)$ ratio of 0.08, a X_{Mg} of 0.71 and a $Al^{VI}/(Al^{VI} + Fe^{3+})$ ratio of 0.96. Ca-amphibole ranges from 7.47 to 7.93 cpfu in Si content, 0.02 to 0.23 cpfu at the A-site, and from 0.74 to 0.96 in its $Ca/(Ca + Na_B)$ ratio. Ti content is ~ 0.07 wt%. Following Leake *et al.* (1997), Ca-amphibole ranges from almost pure actinolite towards the field of barroisite, which is hardly reached by a few analyses. X_{Mg} of Ca-amphibole ranges from 0.82 in actinolite to 0.74 in barroisite. Garnet shows weak compositional zoning with Mn slightly decreasing from core ($Alm_{54}Sps_8Grs_{26}Prp_8Adr_4$) to rim I ($Alm_{55}Sps_{3.5}Grs_{26}Prp_{11}Adr_4$) and again increasing within the outermost ~ 30 μm to rim II ($Alm_{52}Sps_7Grs_{26}Prp_9Adr_6$). The fine-grained matrix of the rock consists of clinozoisite ($0.11 - 0.13$ Fe cpfu), which is closely intergrown with epidote ($0.37 - 0.40$ Fe cpfu). Omphacite occurs in the glaucophane-rich domains and as inclusion in garnet, and has a very homogeneous composition of $Jd_{43}Acm_7Q_{49}$. Rare
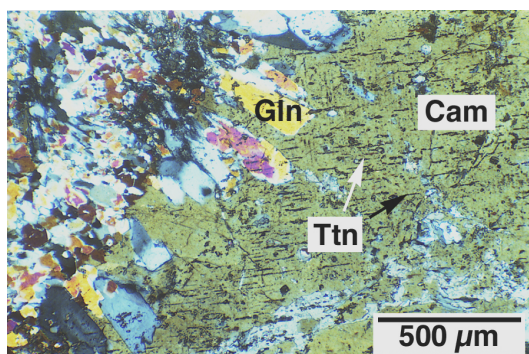
Fig. B.19. Photomicrograph of thin section of sample SY328 under crossed polars, showing a large crystal of actinolite with lamellae of titanite. Ca-amphibole is topotactically replaced by glaucophane at its rims. The surrounding fine-grained mineral assemblage is composed of glaucophane, clinozoisite and omphacite.

phengite has $\sim 3.39\,\mathrm{Si}\,\mathrm{cpfu}$ and a X_{Mg} of 0.79.

The texture of sample SY344 suggests that the protolith was a plutonic rock. Major- and trace-element compositions of whole rock are indeed comparable to unmetamorphosed oceanic gabbro. REE pattern show depletion in LREE $((\mathrm{La}/\mathrm{Yb})_{\mathrm{cn}} = 0.55)$ and a positive Eu anomaly $(\mathrm{Eu}/\mathrm{Eu}^* = 1.22)$, suggesting accumulation of plagioclase during crystallisation of a MORB-type magma. The titanite lamellae in Ca-amphibole probably originated from a Ti-rich precursor mineral from which the Ca-amphibole was formed. Most likely, the former gabbro contained Ti-augite or Ti-rich amphibole (kaersutite) as an igneous phase, which was transformed to actinolite during hydration of the rock. As actinolite is not incorporating large amounts of Ti into its structure, titanite lamellae grew within the newly forming Ca-amphibole. Former plagioclase was replaced by the clinozoisite-epidote intergrowths. During HP metamorphism garnet, glaucophane, phengite and omphacite crystallised in the rock. Retrogression is restricted to very local occurrences of albite, chlorite and calcite, and is recorded in the retrograde zonation in the outermost zones ($\sim 30\,\mu\mathrm{m}$) of garnet.

SY347 Collected by A.K./R.A. in 2000; Locality: Monolithos west of Kámbos; Rock type: Serpentinite.

Sample SY347 is an almost monomineralic serpentinite with very little Ca-amphibole and chlorite. The rock shows a schistose fabric with serpentine clasts $\sim 2\,\mathrm{mm}$ in diameter, surrounded by a sheared serpentine matrix. XRD-pattern of a whole-rock powder aliquot proved SY347 to consist of antigorite only (see section 2.9 on page 34). X_{Mg} of the antigorite is 0.885, $\mathrm{Al_2O_3}$, $\mathrm{Cr_2O_3}$ and NiO

contents are $\sim 2.5\,\text{wt\%}$, $\sim 0.35\,\text{wt\%}$ and $\sim 0.20\,\text{wt\%}$, respectively. Chlorite has a X_{Mg} of ~ 0.90 and contains $\sim 0.6\,\text{wt\%}$ Cr_2O_3 and $\sim 0.3\,\text{wt\%}$ NiO. Ca-amphibole shows chemical zonation with edenitic cores ($\sim 6.64\,\text{Si}\,\text{cpfu}$) to tremolitic rims (8.00 Si cpfu, Fig. B.20a). X_{Mg} is rising from 0.86 in cores to 0.96 in rims, while Cr, Ti (Fig. B.20b), Na and Al decrease. A Si content of only 6.64 cpfu translates to a X_{Prg} of 0.68 in the tremolite-pargasite binary joint. A-site occupation in edenitic cores of 0.82 cpfu translates to even higher X_{Prg} values. Schmädicke (2000) calculated the P and T dependence of the pargasite component in Ca-amphibole in peridotitic compositions in the NCMASH system (Na_2O-CaO-MgO-Al_2O_3-SiO_2-H_2O). According to her calculations, Ca-amphibole in a chlorite-peridotite requires pressures in excess of 2.3 GPa at 700 °C in order to stabilise a pargasite component as high as 0.68. The X_{Prg} isopleths have a negative slope in the $P-T$ field, resulting in even higher pressures (~ 2.5 GPa) at 500 °C, and high temperatures of ~ 800 °C at low pressures (0.5 GPa). If the calculations of Schmädicke (2000) are applicable to the chlorite-amphibole-bearing serpentinites from Syros, the Na-Al-rich amphibole in chlorite serpentinite would require either peak-pressures of the ultramafic rocks significantly higher (i.e. ~ 2.5 GPa) than derived for most of the mafic schists and eclogites, or they represent relics of the peridotitic precursor of the serpentinite, formed in excess of 800 °C. The whole-rock analysis of SY347 shows the expected
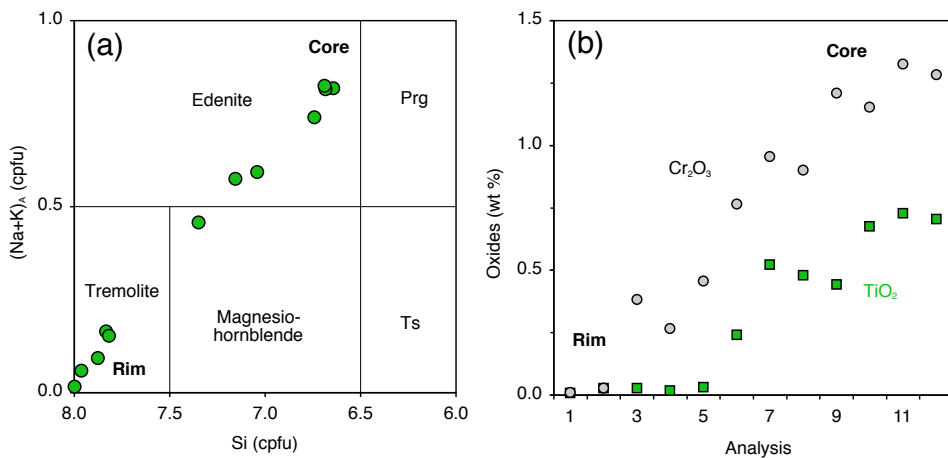
Fig. B.20. Chemical variation of Ca-amphibole in sepentinite sample SY347. **a** Si versus (Na + K) on crystallographic A-site; cores of amphibole are edenitic, while rims are tremolitic. **b** Various analysis (ordered by distance from grain boubdary) show decreasing concentrations of Cr_2O_3 and TiO_2 from cores to rims.

high contents of Ni, Cr and MgO inherited from the ultramafic precursor of the serpentinite and $\sim 12\,\text{wt\%}$ H_2O. Light REEs are strongly depleted, which, together

with the monomineralic charater, point to a depleted mantle rock as precursor, probably a harzburgite. However, it is not obvious, if the serpentinite was formed at the seafloor during hydrothermal overprint of ultramafic portions within the oceanic lithosphere, or if it was introduced into the Syros mélange during exhumation of the HP blocks, and was originally part of the serpentinised mantle wedge.

SY400   Collected by H.M. in 1998; Locality: $\sim 200\,\text{m}$ W of Kámbos, block; Rock type: Tourmaline-omphacite-chlorite fels (hybrid blackwall rock).

Sample SY400 is a pale green tourmaline-omphacite-chlorite fels (Fig. 4.4d), consisting primarily of chlorite and fine-grained omphacite with minor epidote, phengite and accessory rutile, titanite and apatite. Tourmaline crystals are $2 - 5\,\text{mm}$ in diameter and $10 - 20\,\text{mm}$ in length and highly poikiloblastic with inclusions of omphacite, rutile, titanite, apatite and epidote. The rock itself shows healed cracks (about 1 mm wide) filled by chlorite and prismatic omphacite, grown perpendicular to the cracks' elongation. Tourmaline obviously postdates the deformation event, as the cracks can be traced pseudomorphically through the large tourmaline grains by zones of lower inclusion density, but with prismatic omphacite grains, showing the same arrangement as in the cracks outside the tourmaline crystals (Fig. B.1b). Tourmaline itself is not deformed or cracked. Two different portions of whole rock were analysed for major and trace element concentrations, a tourmaline-free part of the rock and a portion containing $\sim 1\,\%$ tourmaline. The composition of the rock is close to an average basalt (49.7 wt% SiO_2, 8.3 wt% MgO), except for K_2O (~ 2 wt%) and Na_2O (~ 5 wt%) and some enriched trace elements, like Ba and Rb. Cr and Ni contents are also relatively high, displaying the influence of the surrounding serpentinite during the generation of the blackwall. $P - T$ conditions, tourmaline composition and fluid history of the tourmaline-bearing blackwall rocks are discussed in detail in Chapter 10 on page 193. Sample SY400 is very similar to SY11.

SY401   Collected by H.M. in 1998; Locality: Órmos Mégas Lákkos, blocks at the seaside; Rock type: Tourmaline-glaucophane schist.

Sample SY401 is composed of an epidote-glaucophane schist (SY401A) which is part of the mélange matrix, and Tur-rich layers (SY401B) which are concordant to the foliation of the host rock, and can be tracked over several meters in the field (see also sample SY309). Sample SY401B is a $1 - 2\,\text{cm}$ thick layer consisting of tourmaline + omphacite + chlorite + albite + phengite + glaucophane + apatite + rutile, hosted in a glaucophane schist composed of glaucophane + epidote + phengite + titanite. Tourmaline crystals are $0.1 - 1.0\,\text{mm}$ in diameter and $1 - 6\,\text{mm}$ in length

with some inclusions of titanite, rutile, omphacite, albite and apatite.

Mineralogy, tourmaline chemistry and whole-rock composition of sample SY401 are similar to SY309, leading to similar interpretations for both samples. They are interpreted as former MOR basalt which was strongly sheared and folded during prograde metamorphism. Equilibration at HP conditions formed the paragenesis glaucophane + phengite + rutile + epidote. During exhumation, infiltration of hydrous fluid along the foliation planes introduced B into the rock in restricted domains and led to the formation of tourmaline + omphacite + albite + chlorite + titanite. For a detailed discussion on the $P-T$ conditions of tourmaline formation, see Chapter 10 on page 193.

SY402   Collected by Stefan Prowatke (Heidelberg) in 1998; Locality: Blocks near Monolithos west of Kámbos; Rock type: Omphacite-glaucophane schist (hybrid blackwall rock).

Sample SY402 was part of a blackwall between an eclogite block and serpentinite. The handspecimen is displaying three different zones and was therefore split into three samples for whole-rock analyses: SY402A (closest to the HP block) is composed of omphacite, glaucophane and phengite; SY402B is a $\sim 1\,\mathrm{cm}$ thick zone consisting of omphacite and rutile; SY402C (close to the matrix of the mélange) is a glaucophanite (Fig. B.21). Both glaucophane and omphacite in SY402A display a two-stage compositional zonation. Cores of omphacite are jadeite-rich ($\mathrm{Jd}_{49}\mathrm{Acm}_{18}\mathrm{Q}_{32}$) and are crowded with small fluid inclusions ($< 5\,\mu\mathrm{m}$). Rims are more acmite-rich ($\mathrm{Jd}_{41}\mathrm{Acm}_{25}\mathrm{Q}_{31}$) and are free of inclusions. Glaucophane cores show a $\mathrm{Ca}/(\mathrm{Ca}+\mathrm{Na_B})$ ratio of ~ 0.06, a X_{Mg} of 0.75, an $\mathrm{Al^{VI}}/(\mathrm{Al^{VI}}+\mathrm{Fe^{3+}})$ ratio of 0.91, and an occupation of the A-site of 0.12 cpfu. Rims are higher in X_{Mg} (0.84), but lower in $\mathrm{Al^{VI}}/(\mathrm{Al^{VI}}+\mathrm{Fe^{3+}})$ ratio (0.86), and also lower in $\mathrm{Ca}/(\mathrm{Ca}+\mathrm{Na_B})$ ratio (0.04) and A-site occupation (0.06 cpfu). Glaucophane rims are in contact with omphacite rims and are intergrown with albite in some places. Apatite is an abundant accessory phase in SY402A. Phengite is visible in handspecimen, but was not analysed by EPMA. The rutile-rich zone, represented by SY402B, also contains omphacite with inclusion-rich cores, and inclusion-free rims. Pyroxene cores are high in jadeite component ($\mathrm{Jd}_{54}\mathrm{Acm}_{21}\mathrm{Q}_{24}$), while rims are more heterogeneous, but generally more Ca-rich ($\mathrm{Jd}_{41}\mathrm{Acm}_{19}\mathrm{Q}_{38}$). Rutile forms large ($\sim 100\,\mu\mathrm{m}$), subhedral grains, surrounded by little titanite in some places. At the contact between SY402B and SY402A, large aggregates ($\sim 1\,\mathrm{mm}$) of titanite are intergrown with glaucophane, which include small grains ($10-50\,\mu\mathrm{m}$) of zircon and allanite. SY402C is an almost monomineralic glaucophanite with large ($\sim 1\,\mathrm{mm}$ in length), inclusion-free glaucophane, showing the same chemical zonation as in SY402A. In a few
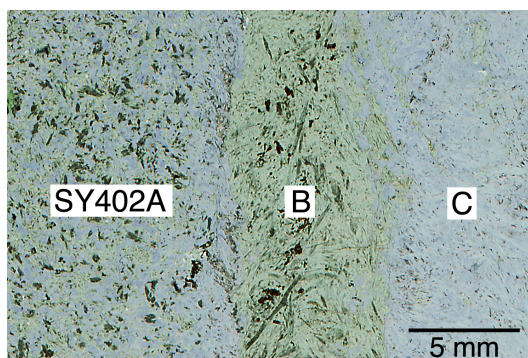
Fig. B.21. Photomicrograph of sample SY402 in thin section (unpolarised light) displaying three distinct zones within this sample, which was part of a blackwall. SY402A was oriented close to the H*P* block, while the pure glaucophanite (SY402C) was oriented towards the matrix of the mélange.

places, small ($\sim 30\,\mu m$) aggregates of bitotite + chlorite occur in contact with glaucophane rims.

Whole-rock composition of SY402A is closest to basalt. However, it is depleted in Al and enriched in Na. Whole-rock analyses of SY402B and SY402C more or less reflect the simple mineralogy of the different zones: SY402B the mix of omphacite and $\sim 1.5\,\%$ rutile; SY402C the average composition of glaucophane. A comparison of the three zones reveals a strong decrease of incompatible trace element contents, including the REE, with distance from the eclogite block, i.e. from A to B to C, and opposed to a strong increase in Cr and Ni.

SY403 Collected by H.M. in 1998; Locality: Ákra Gríza, at the seaside; Rock type: Garnet-glaucophane schist with Lawsonite pseudomorphs.

Sample SY403 is a glaucophane schist with $1-2\,cm$ large fine-grained pseudomorphs after lawsonite. The matrix of the rock consists of glaucophane, garnet, epidote and paragonite, minor titanite and chlorite, and accessory quartz and apatite. In addition to the large lawsonite pseudomorphs, the rock shows elongated domains or vein-like structures of several cm in length, consisting of epidote ($\sim 60\,\%$) + quartz ($\sim 30\,\%$) + minor Fe-oxide, glaucophane and titanite. Within these epidote-quartz veins, large cavities ($100-200\,\mu m$) were observed, which show abundant chlorite crystals ($X_{Mg} = 0.68$) at their rims. Epidote is chemically zoned with Fe-rich cores ($0.72\,cpfu$), which show abundant small ($< 5\,\mu m$) fluid inclusions, and homogeneous, inclusion-free rims, lower in Fe ($0.43\,cpfu$). The lawsonite psudo-morphs consist of epidote + paragonite + titanite + minor albite $\pm$ garnet. Epi-dote in the pseudomorphs is also zoned and shows two compositional types of

subhedral cores. The first type contains $\sim 0.74\,\mathrm{Fe\,cpfu}$, the second type contains $\sim 0.40\,\mathrm{Fe\,cpfu}$. Rims are anhedral and are clinozoisite ($0.12\,\mathrm{Fe\,cpfu}$). Paragonite is the dominant mineral in the pseudomorphs and is rich in fluid inclusions. Garnet forms euhedral blasts of $\sim 1\,\mathrm{mm}$ in diameter and shows some inclusions of titanite, epidote, apatite, glaucophane, quartz and small grains ($< 5\,\mu\mathrm{m}$) of sulfides. Composition changes from Mn-rich cores ($\mathrm{Alm_{47}Sps_{19}Grs_{23}Prp_7Adr_4}$) to Mn-poor rims ($\mathrm{Alm_{56}Sps_7Grs_{25}Prp_8Adr_4}$). Both garnet grains inside the pseudomorphs and in the matrix display a hump in the Mn zonation at a distance of $\sim 100\,\mu\mathrm{m}$ from the rim, where the composition changes to $\mathrm{Alm_{50}Sps_{14}Grs_{27}Prp_6Adr_3}$ in $\sim 30\,\mu\mathrm{m}$ wide zone. Epidote in the matrix and in garnet inclusions is homogeneous with Fe contents between 0.40 and $0.46\,\mathrm{cpfu}$. Glaucophane is also homogeneous and shows a $\mathrm{Ca}/(\mathrm{Ca} + \mathrm{Na_B})$ ratio of ~ 0.07, a X_{Mg} of 0.67, an $\mathrm{Al^{VI}}/(\mathrm{Al^{VI}} + \mathrm{Fe^{3+}})$ ratio of 0.96, and an occupation of the A-site of $0.04\,\mathrm{cpfu}$. Apatite is fluor-apatite with $\sim 0.73\,\mathrm{F\,pfu}$ and detectable Cl ($\sim 0.005\,\mathrm{Cl\,pfu}$). F contents of titanite are $\sim 0.18\,\mathrm{wt\%}$. F contents of glaucophane and paragonite are below detection limit ($0.05\,\mathrm{wt\%}$).

Whole-rock chemistry of SY403 is close to basalt with $49.0\,\mathrm{wt\%}$ $\mathrm{SiO_2}$ and $6.5\,\mathrm{wt\%}$ MgO, but enriched in $\mathrm{TiO_2}$ ($2.0\,\mathrm{wt\%}$) and very low in $\mathrm{K_2O}$ ($< 0.1\,\mathrm{wt\%}$). Analysis of trace elements revealed remarkebly high concentrations of Zn ($640\,\mu\mathrm{g/g}$) and Cu ($343\,\mu\mathrm{g/g}$), probably hosted in the observed sulfides. The rock is interpreted as a metamorphic equivalent of a basaltic rock, which may have been hydrothermally altered at the seafloor, enriching Zn and Cu and leaching K. The HP assemblage was garnet + glaucophane + titanite + Fe-rich epidote + quartz. During heating and/or decompression, lawsonite in the glaucophane schist became unstable and was decomposed by different reactions, one of which was probably the reaction

$$\mathrm{Lws} + \mathrm{Gln} = \mathrm{Pg} + \mathrm{Ep} + \mathrm{Chl} + \mathrm{Qtz} + \mathrm{H_2O} \qquad \text{(B.1)}$$
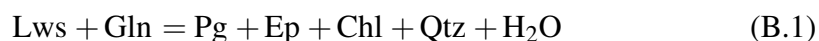
described by Poli & Schmidt (1995) and Brady *et al.* (2001). Lawsonite was replaced by paragonite + clinozoisite + titanite $\pm$ albite, and produced veins of epidote + quartz, which are rich in fluid inclusions. Garnet was stable in the HP lithology and also during and after breakdown of lawsonite. The hump in the compositional profiles of the garnet grains may be due to chemical changes during breakdown of lawsonite. The rock does not show indications of retrograde rehydration.

SY404 Collected by H.M. in 1998; Locality: $\sim 250\,\mathrm{m}$ W of Kámbos, block; Rock type: Pyrite-titanite-apatite-chlorite schist.

Sample SY404 is a chlorite schist from a blackwall, consisting of $\sim 85\,\mathrm{wt\%}$ chlorite , $\sim 4\,\mathrm{wt\%}$ euhedral pyrite crystals, $\sim 8\,\mathrm{wt\%}$ subhedral to euhedral titanite and

3.7 wt% apatite. Chlorite shows a X_{Mg} of 0.77 and a grain size of $\sim 50 - 100\,\mu m$. Pyrite forms large cubes ($0.5 - 1\,cm$), has inclusions of apatite and zircon and is altered to Fe-oxide at its rims and along cracks. Titanite is homogeneously distributed through the rock, shows grain sizes between 50 and $1000\,\mu m$, contains inclusions of allanite, apatite and rutile and shows a very fine oscillatory zonation, with varying Al_2O_3 ($0.1 - 0.9\,wt\%$) and Fe_2O_3 ($0.7 - 1.1\,wt\%$) concentrations. Apatite is anhedral and rounded, also homogeneously distributed through the rock with an average grain size of $\sim 100\,\mu m$ and is found in the matrix, and as inclusion in pyrite and titanite. Chemically, it is hydroxy-apatite with 0.46 F pfu, no detectable Cl and 0.15 wt% SrO.

The whole-rock composition is somehow strange, with low SiO_2 ($29.9\,wt\%$) and high TiO_2 ($3.2\,wt\%$) and P_2O_5 ($1.6\,wt\%$). S was not analysed, but the abundant large pyrite crystals prove a strong enrichment in sulfur. The rock additionally shows significant amounts of MgO ($22.2\,wt\%$), Cr ($384\,\mu g/g$) and Ni ($439\,\mu g/g$), reflecting the influence of the serpentinite matrix in the generation of this blackwall rock.

SY405 Collected by H.M. in 1998; Locality: $\sim$250 m W of Kámbos, block; Rock type: Magnetite-titanite-apatite-chlorite schist.

Sample SY405 is a fine-grained chlorite schist with large euhedral magnetite blasts ($2 - 5\,mm$). Minor components are titanite, apatite and accessory allanite. The sample is very similar to SY404, except for the large blasts of magnetite instead of pyrite. Apatite in SY405 is even more abundant (7.5 wt%) than in SY404, but is also hydroxy-apatite with 0.42 F pfu, no detectable Cl and 0.13 wt% SrO. Magnetite forms idioblasts with abundant inclusions of apatite. Chlorite, magnetite and titanite were not analysed by EPMA. The whole-rock composition is comparable to that of SY404, with a very low SiO_2 content (24.9 wt%) and high concentrations of Mg, Fe, Ti and P. In contrast to SY404, this chlorite schist is not enriched in Cr and Ni. The trace element budget of this blackwall sample therefore seems to be less influenced by the serpentinite.

SY406 Collected by Stefan Hepp (Heidelberg) in 1995; Locality: $\sim 200\,m$ W of Kámbos; Rock type: Jadeite-phengite-glaucophane schist with garnetite layers.

Sample SY406 is a well-foliated and folded rock (Fig. B.22) consisting of glaucophane and phengite with abundant inclusions of small euhedral garnet grains ($50 - 100\,\mu m$), similar to sample SY314. In addition, sample SY406 contains rounded Na-clinopyroxene grains ($\sim 2\,mm$ in diameter), and $0.5 - 5\,cm$ thick layers consisting almost exclusively of small euhedral garnet grains ($50 - 100\,\mu m$
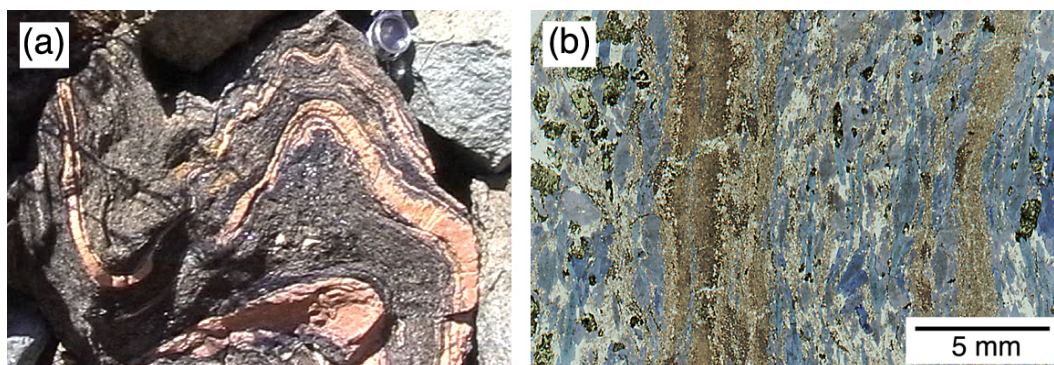
Fig. B.22. a Heavily folded phengite-glaucophane schist with garnetite layers (similar to SY406). Note handlense at the top for scale. **b** Photomicrograph of sample SY406 in thin section (unpolarised light) showing nearly monomineralic layers of garnet between layers of glaucophane + phengite + jadeite (green grains on the left).

in diameter). Garnet in garnet layers is associated with either glaucophane, apatite or phengite, alternating parallel to the layers. Garnet in all layers of the rock displays chemical zonation with cores of homogeneous grossularite and spessartine contents, and pyrope content increase at the expense of almandine, from $Alm_{60}Sps_{25}Grs_{10}Prp_5Adr_4$ to $Alm_{50}Sps_{25}Grs_{10}Prp_{15}Adr_4$. Rims I have a much higher Fe and lower Mn and Mg content with a composition $Alm_{70}Sps_{12}Grs_{10}Prp_8Adr_4$. Rims II are restricted to the outermost $5-10\,\mu m$ with again increasing Mn concentration ($Alm_{60}Sps_{18}Grs_{15}Prp_8Adr_4$). Some of the grains show annealed cracks in cores and rim I, filled by garnet with the same BSE intensity as rim II. The Na-rich clinopyroxene has a composition of $Jd_{43}Acm_{42}Q_{13}$, transitional between jadeite and acmite. At its rims and along $10-100\,\mu m$ thick cracks, it is replaced by the assemblage omphacite ($Jd_{36}Acm_{27}Q_{35}$) + albite (Ab_{99}) + biotite $\pm$ chlorite. In some places, Al-poor clinopyroxene has formed with aegirin composition ($Jd_{14}Acm_{56}Q_{30}$). Glaucophane shows abundant small fluid inclusions ($< 5\,\mu m$) in the core and a chemical zonation with Fe contents increasing from core to rim. Cores show a $Ca/(Ca + Na_B)$ ratio of ~ 0.05, a X_{Mg} of 0.67, and an $Al^{VI}/(Al^{VI} + Fe^{3+})$ ratio of 0.87. Rims are high in Fe and low in Ca, having a $Ca/(Ca + Na_B)$ ratio of ~ 0.02, a X_{Mg} of 0.54, and an $Al^{VI}/(Al^{VI} + Fe^{3+})$ ratio of 0.74. Apatite is accessory in the glaucophane-phengite layers, but forms a major component within the garnetite layers. It shows Sr contents below the detection limit and belongs to the fluor-apatite group with 0.64 F pfu and no detectable Cl. Accessory minerals are allanite, which is more abundant in the garnetite layers, and rutile rimmed by titanite.

The whole-rock analysis of SY406 reveals SiO_2 (47.6 wt%), Al_2O_3 (16.1 wt%)

and MgO (5.0 wt%) concentrations close to an average basalt, but shows significant enrichment in Fe_2O_3 (17.9 wt%), MnO (3.1 wt%) and K, Ba and Rb. The CaO concentration (2.7 wt%) is very low. The rock shows high concentrations in Th, U and REE (220 times CI chondritic La), and a significant negative Ce anomaly ($Ce/Ce^* = 0.59$). The rock is interpreted as a former tuffitic sediment which was significantly altered at low temperatures at the seafloor. The garnetite layers, with almandine-spessartine-rich garnet are interpreted as former Mn-nodules, or Mn-Fe-rich mineralisation horizons within the former sediment, as described by Alt (1995). Enrichment in K, Rb and Ba occurred probably due to formation of abundant clay minerals, which recrystallised to phengite during HP metamorphism. The negative Ce anomaly is further evidence for strong interaction with seawater. Evidence for a significant portion of basaltic material in the sedimentary source rock of SY406 is provided by the relatively high Mg, Cr (194 µg/g) and Ni (304 µg/g) contents. During HP metamorphism, the rock was folded and formed the assemblage garnet (cores) + glaucophane (cores) + phengite + jadeite/acmite and formed garnet rims I. In a second stage, glaucophane rims I formed. During decompression, very little fluid fluxed some parts of the rock, leading to the fromation of omphacite + albite + biotite from jadeite, and the annealed cracks and rims II of garnet. Glaucophane probably also developed its Fe-rich rim at this stage.

SY411   Collected by H.M. in 2001; Locality: ~ 50 m W of Kámbos; Rock type: Eclogite.

Sample SY411 is an eclogite, consisting of ~ 5 mm large poikiltic garnet, omphacite, ~ 8 mm in length, epidote and abundant titanite and apatite. Similar to eclogite sample SY323, garnet shows highly poikiloblastic cores and inclusion-free rims. Inclusions can also be subdivided into a group of subhedral solitary grains of epidote, omphacite and rutile, and a second group of composite inclusions of chlorite/biotite, albite, hematite, epidote, which are connected by cracks in the garnet host. EPMA analyses were not performed on this sample, but the microstructures are very similar to ecclogite SY323. The major difference between the two samples is the compositional layering between epidote-rich and omphacite-rich domains in SY323. In contrast, SY411 shows a homogeneous distribution of epidote, garnet and omphacite and a well-developed lineation, defined by omphacite.

Whole-rock composition of SY411 is very similar to eclogite samples SY323 and SY324, with a high concentration of CaO (14.6 wt%). The rock is interpreted as the metamorphic equivalent of basalt, that was enriched in Ca during hydrothermal seafloor-alteration at elevated temperatures ($> 250 °C$), producing an epidote-rich assemblage. Compositions of eclogites SY323, SY324 and SY411 are between

those of basalts and rodingites. For a discussion on the metamorphic evolution of this sample see description of SY323.

SY412 Collected by H.M. in 2001; Locality: $\sim 50\,\text{m}$ W of Kámbos; Rock type: Retrogressed eclogite.

Sample SY412 was taken from an interior part of an eclogite block, which shows a transition into a glaucophane-rich assemblage at its margins (see SY413 below). Eclogitic paragenesis of SY412 is garnet + omphacite I + rutile + phengite + glaucophane + epidote ($\pm$ quartz?). This primary assemblage is partly replaced by a secondary assemblage of dominantly hydrous minerals which form small, closely intergrown aggregates between the larger primary phases. The secondary assemblage is composed of phengite + glaucophane + albite + chlorite + omphacite III + tourmaline. In some patches, biotite formed at the expense of phengite. The $P-T$ conditions of the secondary fluid infiltration process are discussed in detail in Chapter 10 on page 193 together with the tourmaline chemistry. The eclogitic garnet contains inclusions of glaucophane and is partly pseudomorphosed by chlorite. It shows chemical zonation with decreasing Mn content and increasing Fe and Mg contents from core ($\text{Alm}_{52}\text{Sps}_{15}\text{Grs}_{20}\text{Prp}_5\text{Adr}_8$) to rim ($\text{Alm}_{64}\text{Sps}_1\text{Grs}_{21}\text{Prp}_{10}\text{Adr}_4$). Omphacite is chemically zoned with omphacite-I cores ($\text{Jd}_{43}\text{Acm}_{16}\text{Q}_{39}$), omphacite II zones richer in Fe^{3+} ($\text{Jd}_{34}\text{Acm}_{31}\text{Q}_{34}$) and omphacite-III rims ($\text{Jd}_{52}\text{Acm}_{32}\text{Q}_{14}$). Omphacite-II zones are not developed in all grains. Rutile is still abundant and shows only a thin overgrowth of titanite ($< 5\,\mu\text{m}$). Phengite shows a X_{Mg} of 0.56 and 3.42 Si cpfu. Epidote is Fe-rich ($0.62-0.86\,\text{cpfu}$). Chlorite has a X_{Mg} of 0.62, which is lower at the contact to garnet (~ 56). Glaucophane shows a $\text{Ca}/(\text{Ca}+\text{Na}_{\text{B}})$ ratio of ~ 0.11, a X_{Mg} of 0.57, an $\text{Al}^{\text{VI}}/(\text{Al}^{\text{VI}}+\text{Fe}^{3+})$ ratio of 0.90, and 7.81 Si cpfu. In biotite-rich zones, it shows increasing Ca, Al and Fe contents, rising the $\text{Ca}/(\text{Ca}+\text{Na}_{\text{B}})$ ratio to ~ 0.26, and decrease the X_{Mg} to 0.53 and the Si content to 7.48 cpfu, shifting the composition from glaucophane to barroisite. Tourmaline forms large grains of $1-3\,\text{mm}$ in diameter and $5-15\,\text{mm}$ in length, with inclusions of omphacite, glaucophane, garnet, phengite, epidote, albite and rutile (Fig. B.23a). Garnet grains includuded in tourmaline show incipient chloritisation along cracks, that was probably stopped by the shielding tourmaline (Fig. B.23a). Furthermore, tourmaline locally grew into the chlorite-filled cracks of garnet. Therefore, it is obvious, that tourmaline replaced chlorite, but did not interact with garnet. Garnet rims are in direct contact with tourmaline and omphacite III. The replacement of chlorite by tourmaline during the infiltration of B-rich fluid was observed in natural rocks and performed experimentally by Fuchs & Lagache (1994) and Weisbrod *et al.* (1986) (cited in Dingwell *et al.*, 2002) and also

observed in retrogressed eclogites by Altherr *et al.* (2004). The petrographic relationship of the different minerals, i. e. tourmaline, chlorite and garnet described by Altherr *et al.* (2004) are very similar to those of sample SY412.
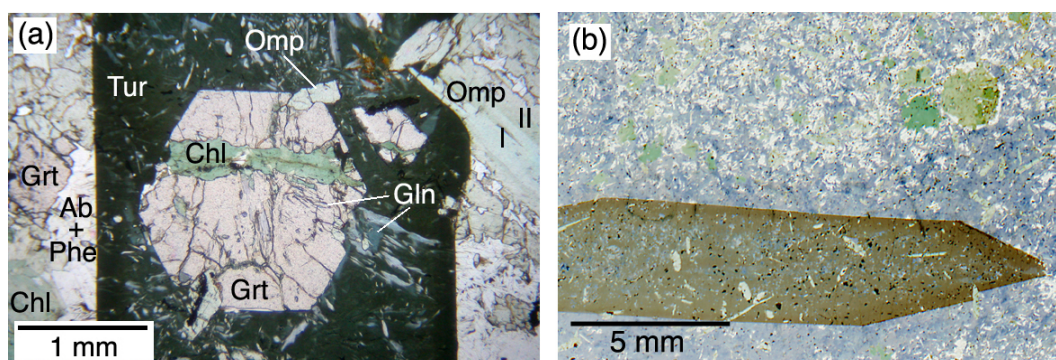
Fig. B.23. Photomicrograph of thin sections. **a** Sample SY412 showing an idioblast of garnet, truncated by a chlorite-filled crack and enclosed in a large tourmaline crystal. Outside tourmaline, garnet is strongly resorbed and replaced by chlorite in paragenesis with albite, omphacite, phengite and glaucophane. **b** Sample SY413 dominated by glaucophane, chlorite pseudomorphs after garnet and large poikiloblastic tourmaline crystals. Needle-shaped, pale green omphacite crystals occur both in the matrix and as inclusions in tourmaline.

The whole-rock analysis of SY412 reveals major element concentrations close to those of other high-Ti sample (SY5, SY112). It shows relatively low concentrations of SiO_2 (45.8 wt%) and Al_2O_3 (13.5 wt%) and high concentrations of TiO_2 (4.3 wt%) and Fe_2O_3 (15.0 wt%). The REE pattern is very similar to the investigated metagabbros. It shows a strong positive Eu anomaly ($Eu/Eu^* = 1.65$) and a depletion in LREE ($(La/Yb)_{cn} = 0.39$). Therefore, the rock is interpreted as a HP metamorphic Fe-Ti-rich gabbro, which formed the eclogitic paragensis at high pressures. During exhumation, it was rehydrated by boron-rich hydrous fluids and formed tourmaline and other hydrous minerals (see Chapter 10 for details).

SY413   Collected: H.M. 2001; Locality: ~ 50 m W of Kámbos; Rock type: Tourmaline-glaucophane schist/retrogressed eclogite (blackwall rock).

Sample SY413 is part of the glaucophane-rich envelope of the above-desribed block of sample SY412. The rock is dominated by glaucophane and chlorite pseudomorphs after garnet, accompanied by phengite, omphacite, albite, titanite, tourmaline and epidote. Long-prismatic omphacite grains occur throughout the rock and also inside the large, poikiloblastic tourmaline grains (Fig. B.23b). Further inclusions in tourmaline are glaucophane, rutile, titanite, albite, chlorite and epidote. Tourmaline grains are about 5 mm in diameter and $20-30$ mm in length.

Tourmaline compositions of SY413 are discussed in detail in Chapter 10 on page 193. Omphacite is homogeneous with the composition $Jd_{42}Acm_{15}Q_{41}$. Epidote contains $\sim 0.62\,Fe\,cpfu$. Phengite and chlorite have X_{Mg} of 0.60 and 0.62, respectively. Phengite has $3.46\,Si\,cpfu$. Albite has almost pure endmember composition ($Ab_{99.8}$). Glaucophane shows a $Ca/(Ca+Na_B)$ ratio of ~ 0.05, a X_{Mg} of 0.58, an $Al^{VI}/(Al^{VI}+Fe^{3+})$ ratio of 0.89, and $7.95\,Si\,cpfu$. In contact to epidote, it shows increasing Ca and Fe contents, rising the $Ca/(Ca+Na_B)$ ratio of ~ 0.10, and decreasing the X_{Mg} to 0.51 and the Si content to $7.60\,cpfu$.

SY413 originated from a similar protolith as SY412, but was stronger influenced by rehydration during exhumation by the tourmaline-forming fluid. The paragenesis glaucophane + chlorite + albite + phengite + tourmaline, which is found in some places in the core of the eclogite block (represented by sample SY412) is the dominating assemblage of sample SY413. Garnet is entirely transformed to chlorite, and rutile is replaced by titanite. Whole-rock analysis of this sample were not performed.

SY415   Collected by H.M. in 2001; Locality: Hill above San Michalis at OTE station; Rock type: Garnet-quartz-jadeite fels (meta-plagiogranite).

Sample SY415 is a high-silica fels ($70.3\,wt\%$ SiO_2), showing a pale green to white colour in handspecimen, with small ($< 0.5\,mm$) red garnet grains. The rock consists of jadeite, quartz and phengite with little garnet and epidote. Albite ($Ab_{99.7}$) forms small ($\sim 10\,\mu m$) coronas around jadeite at the contact to quartz. Jadeite is poor in Ca, Mg and Fe, with a composition of $Jd_{90}Acm_5Q_4$ ($\sim 22\,wt\%$ Al_2O_3). Phengite shows a Si content of $3.30\,cpfu$ and a low X_{Mg} of 0.37. Garnet is homogeneous in Ca, has very low Mg contents ($< 0.4\,wt\%$) and is zoned with Mn decreasing and Fe increasing from core ($Alm_{40}Sps_{33}Grs_{25}Prp_1Adr_4$) to rim ($Alm_{67}Sps_{2.5}Grs_{26}Prp_{1.5}Adr_3$). At a distance of $\sim 50\,\mu m$ from rims, garnet shows a small plateau with a composition of $Alm_{52}Sps_{21}Grs_{20}Prp_1Adr_6$. Epidote is Fe-rich ($0.88-0.92\,cpfu$).

The chemical analysis of the whole rock reveals a rhyolitic composition with high SiO_2 and Na_2O ($7.6\,wt\%$) contents and very low abundances of CaO and MgO (both $< 1\,wt\%$). The rock is interpreted as the metamorphic equivalent of a felsic intrusion within the oceanic crust, e. g. a plagiogranitic dyke. During HP metamorphism, the rock recrystallised to jadeite + quartz + phengite + garnet + epidote. During decompression, albite formed at the contact of jadeite and quartz. Further indications of retrogression or rehydration of the rock were not observed.

SY420 Collected by H.M. in 2001; Locality: $\sim$50 m W of Kámbos; Rock type: Phengite-epidote-tourmaline schist.

Sample SY420 is a schist from the matrix surrounding the blocks of the Syros mélange. The rock is foliated and folded and shows layering with alternating epidote- and chlorite-rich layers, both of which contain abundant tourmaline, phengite, garnet and albite (Fig. B.24a). Accessories are allanite cores in epidote, rutile and titanite. Rutile forms large inclusions (500 µm) in garnet. Garnet has developed a chemical zonation with Mn-rich core ($Alm_{57}Sps_7Grs_{28}Prp_4Adr_4$) and Fe-rich rim I ($Alm_{63}Sps_2Grs_{26}Prp_5Adr_4$). Rim I is partially resorbed and replaced by chlorite + albite. However, some grains show newly grown rims II with Ca- and Mn-rich composition ($Alm_{26}Sps_{34}Grs_{31}Prp_5Adr_4$). They show a sharp contrast to Fe-rich rim I without diffusional equilibration. Albite is close to the endmember composition ($Ab_{99.4}$). Epidote shows two to four different zones with Fe contents alternating between 0.47 and 0.61 cpfu. Some grains show Fe-rich rims with 0.79 to 0.84 Fe cpfu. Chlorite has a X_{Mg} of 0.71. Phengite forms large grains of $0.5 - 2$ mm in lenght (Fig. B.24b), has a X_{Mg} of 0.65 and contains ~ 3.35 Si cpfu and 0.68 wt% BaO. $10 - 50$ µm wide rims of phengite show strong increase in Fe content and therefore a decrease in X_{Mg} to 0.52. Tourmaline grains are $0.1 - 0.5$ mm in diameter, $1 - 3$ mm in length. They are dravitic in composition with X_{Mg} of 0.75 in cores and 0.70 in rims. Details of tourmaline composition are discussed in Chapter 10 on page 193.
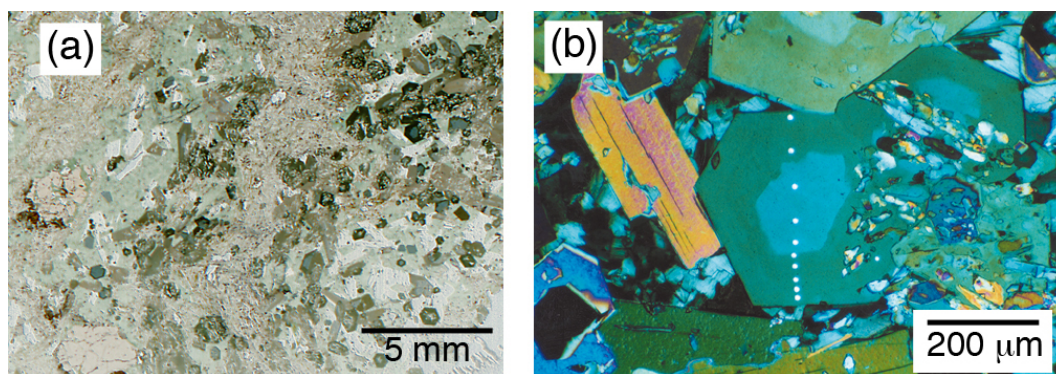
Fig. B.24. Photomicrographs of thin section of sample SY420. **a** Unpolarised light showing garnet, phengite, chlorite, epidote and zoned tourmaline crystals with blue cores and green rims. **b** Tourmaline, chlorite (dark blue) and phengite (yellow) under crossed polars. The thin section was covered with a gold layer prior to SIMS analysis, producing the dark blue colours of the picture. The measurement spots of the ion probe are visible as white dots.

The whole-rock composition of SY420 is characterised by very low concentrations of SiO_2 (38.1 wt%) and Na_2O (1.4 wt%) and high concentrations of Al_2O_3

(25.0 wt%) and B_2O_3 (2.8 wt%). Additionally, the LILE are strongly enriched, especially Sr (1640 µg/g), Ba (584 µg/g) and Pb (60 µg/g). REE, Th and U show high abundances, but Cr (353 µg/g) amd Ni (240 µg/g) are also enriched. The geochemistry of this rock underlines the hybrid character of this sample. It is interpreted as a former sedimentary schist which has been strongly overprinted during the influx of hydrous B-rich fluids. The $P-T$ conditions are disccussed in Chapter 10 on page 193 together with the chemistry of fluid and tourmaline.

SY425 Collected by H.M. in 2001; Locality: ~ 50 m W of Kámbos; Rock type: Phengite-garnet-epidote-glaucophane fels (metagabbro) with omphacite-epidote-quartz vein.

Sample SY425 is a coarse-grained glaucophane-dominated fels veined by a network of sub-millimeter wide epidote-rich veinlets, which give the rock a weak foliation (Fig. B.25a). Additionally, the glaucophane fels is truncated by a ~ 3 cm wide quartz vein, which is bordered to both sides by aggregates of euhedral epidote (Fig. B.25). Two whole-rock aliquots were taken from this rock: SY425G from the main body of the glaucophane fels and SY425D from the quartz vein, including the epidote-rich rims. SY425G consists of large ($1-2$ cm) glaucophane blasts, epidote, phengite and abundant red subhedral garnet (~ 2 mm in diameter) and rutile aggregates of up to 1 cm in size. A network of epidote- and phengite-rich veinlets is anastamoising around the glaucophane and garnet blasts. Omphacite formed along the veinlets, especially around glaucophane. The large quartz vein (SY425D) is almost exclusively quartz in its central part with individual red euhedral garnet crystals (~ 500 µm in diameter) and green omphacite. At the contact to the host rock, the vein developed a border zone consisting of large (~ 1 cm in length) euhedral epidotes, which obviously grew into the vein (Fig. B.25). Omphacite in the vein is in direct contact to quartz, without any retrograde albite. It shows abundant small (< 5 µm) fluid inclusions, but a relatively homogeneous composition of $Jd_{38}Acm_{21}Q_{37}$. Epidote occurs as anhedral inclusions in omphacite, where it also contains small fluid inclusions and is Fe-rich ($0.77-0.84$ cpfu), and as large euhedral grains intergrown with quartz. Fe contents of these large crystals vary between 0.56 and 0.63 cpfu. Garnet shows only small chemical variations, e. g. between 4 and 8 % in spessartine content. In general it is almost homogeneous with a composition of $Alm_{61}Sps_6Grs_{25}Prp_8Adr_4$. In the glaucophane fels, garnet is not only larger, but also chemically zoned, from Mn-rich cores ($Alm_{54}Sps_{12}Grs_{22}Prp_7Adr_5$) to Mn-poor rims ($Alm_{62}Sps_3Grs_{18}Prp_{11}Adr_5$). Epidote again shows two different compositions with the majority ranging in Fe content from 0.59 to 0.67 cpfu, and some rims incresing to values between 0.95 and 0.98 Fe cpfu. Glaucophane is very

homogeneous and shows a $Ca/(Ca + Na_B)$ ratio of ~ 0.04, a X_{Mg} of 0.62, and an $Al^{VI}/(Al^{VI} + Fe^{3+})$ ratio of 0.92. Phengite was not analysed.
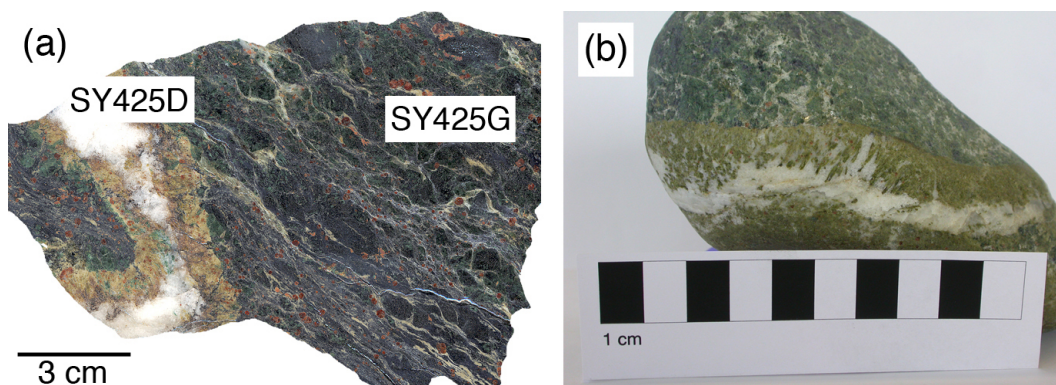
Fig. B.25. Photographs of epidote-quartz vein cutting through a phengite-garnet-epidote-glaucophane fels (metagabbro). **a** polished handspecimen of sample SY425, showing yellowish green epidote, green omphacite and red garnet within the white quartz vein. Sample SY425D was taken from the vein, while SY425G represents the metagabbro. **b** naturally rounded handspecimen displaying the sharp contact between vein and metagabbro with euhedral epidote crystals oriented sub-perpendicular to the contact.

The results of the whole-rock analysis of glaucophane fels SY425G is consistent with the interpretation of the rock being a metagabbro. Starting from an average basaltic composition, the magma which formed the gabbro seems to have been slightly differentiated, showing higher SiO_2 (52.7 wt%) and total alkali (6.2 wt%) and lower MgO (4.9 wt%) and CaO (6.4 wt%) contents. In addition, the accumulation of plagioclase in the gabbro is witnessed by a positive Eu anomaly (Eu/Eu* = 1.51). During H*P* metamorphism, glaucophane, epidote, phengite and garnet were formed. The dehydration from glaucophane to omphacite, representing the blueschist-eclogite transition can be directly observed in the epidote-phengite-rich veinlets, along which glaucophane is replaced by omphacite. These veinlets are interpreted as the pathways of the metamorphic fluid deliberated by glaucophane dehydration. They are connected to the large quartz vein (SY425D) which is interpreted as a large H*P* fluid vein, in which euhedral epidote was able to grow into the open crack in the stability field of omphacite (Jd_{38}) + quartz.

The quartz vein is composed of epidote, which grew from components derived directly from the glaucophane fels and from components filtered from the surrounding fluid. The quartz was probably precipitated directly from the fluid in a late stage, because the precipitation of quartz is obviously sealing the vein. Garnet probably grew inside the vein, as its chemical composition is distinctly different from gar-

net in the glaucophane fels. Omphacite may have grown inside the vein, or being entrapped as a solid by breaking off from the vein's country rock. The major and trace element composition of the quartz vein therefore does not represent the fluid composition. $P - T$ conditions of formation of the quartz vein were calculated using THERMOCALC (v 3.01; Powell & Holland, 1988; Powell $et\ al.$, 1998). For calculation of temperatures, the garnet-clinopyroxene Fe-Mg exchange reaction was used, yielding 428 °C at a minimum pressure of 0.96 GPa, estimated from the stability of $Jd_{38} + Qtz$. For an assumed pressure of 1.5 GPa, the Grt-Cpx thermometer yields a temperature of 450 °C, which is consistent with the $P - T$ estimation of other authors (Dixon, 1968; Okrusch & Bröcker, 1990) for the peak of metamorphism of Syros metabasites. Hence, the quartz vein is interpreted as a result of dehydration of the metagabbro (SY425G) during peak-pressure conditions, but it just represents a left-over of the fluid, and not the trace-element composition of the fluid itself.

SY429   Collected by H.M. in 2001; Locality: Kámbos; Rock type: Talc serpentinite.

Sample SY429 is a serpentinite with large talc blasts (~ 5 mm) embedded in a matrix of talc + serpentine + magnetite. The matrix shows a polygonal texture with serpentine + talc intergrowths sourrounded by fine-grained magnetite (Fig. B.26). The microstructure of this rock suggests static serpentinisation of a former peridotite without any deformation. The same mesh-texture was observed in serpentinites from other localities (e. g. New Caledonia and Quebec) by other authors and interpreted as pseudomorphs after olivine as a result of static hydration (Laurent & Herbert, 1979; Fitzherbert $et\ al.$, 2004). Larger oxide blasts consist of magnetite ($Fe^{2+}Fe^{3+}_{1.9}Cr_{0.1}O_4$), hematite ($Hem_{72}Ilm_{25}Pyr_2Esc_1$) and ilmenite ($Hem_7Ilm_{82}Pyr_9Gei_1$). Talc contains $2 - 3$ wt% FeO ($X_{Mg} = 0.96$). Serpentine has a X_{Mg} of 0.87 and contains 0.5 wt% Cr_2O_3 and 1.9 wt% Al_2O_3. Ca-amphibole shows chemical zonation from edenitic cores (~ 6.54 Si cpfu, $X_{Mg} = 0.86$) to tremolitic rims (7.99 Si cpfu, $X_{Mg} = 0.97$). A Si content of only 6.54 cpfu translates to a X_{Prg} of 0.73 in the tremolite-pargasite binary joint. A-site occupation of edenitic cores of 0.85 cpfu translates to even higher X_{Prg} values. For a discussion of edenitic/pargasitic amphibole in serpentinite see section on sample SY347.

The whole-rock analysis of SY429 shows high contents of Ni, Cr and MgO typical for derivates of ultramafic rocks and ~ 9.8 wt% H_2O. Light REEs are depleted, but concentrations are significantly higher than in serpentinite SY347. Together with the talc-rich and amphibole-bearing mineralogy, SY429 therefore shows a less depleted character, compared to SY347. It probably contained significant orthopy-
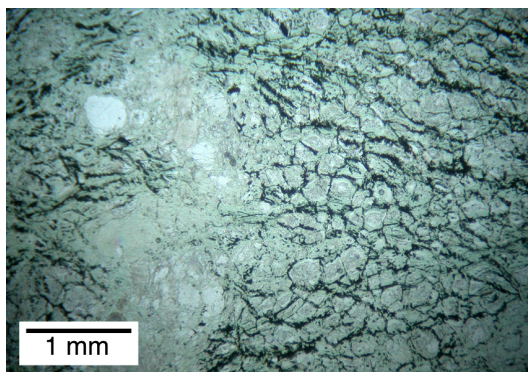
Fig. B.26. Photomicrograph of sample SY429 in thin section (polarised light). Greenish serpentine, colourless talc and black magnetite form a network that is probably pseudomorph after a granoblastic peridotite. The network is interrupted by talc blasts - former large orthopyroxene (?).

roxene and also clinopyroxene, before it was hydrated and serpentinised. Most interesting is the absence of deformation in this talc-serpentine rock, which may be taken as an argument for a relatively late incorporation of the serpentinite into the mélange, and therefore an origin of the serpentinite in the mantle wedge.

SY431 Collected by H.M. in 2001; Locality: Ákra Gríza; Rock type: Garnet-quartz-jadeite fels (meta-plagiogranite).

Sample SY431 shows highest silica content of all investigated samples (73.2 wt% SiO_2). It is green to white in handspecimen, with small (< 0.5 mm) red garnet grains. The rock consists of jadeite, quartz, white mica, little garnet and acessory epidote and titanite, and shows a weak foliation defined by relatively coarse-grained mica ($\sim 1 - 2$ mm). At the contact between jadeite and quartz, small (< 5 µm) coronas have formed which probably consist of albite and an opaque phase. The sample was not analysed by EPMA, but white mica is probably paragonite, as the rock contains very little K_2O (0.14 wt%), similar to paragonite-bearing sample SY308. The chemical analysis of the whole rock reveals a rhyolitic composition with high SiO_2 and Na_2O (6.5 wt%) contents and very low abundances of Ca and Mg. The rock is interpreted as the metamorphic equivalent of a felsic intrusion within the oceanic crust, e. g. a plagiogranitic dyke. HP metmorphism produced jadeite + quartz + paragonite + garnet. During decompression, thin coronas of albite (?) formed at the contact between jadeite and quartz.

SY432 Collected by H.M. in 2001; Locality: ~ 250 m E of Kámbos; Rock type: Tourmaline-bearing siliceous marble.

Sample SY432 is a fine-grained siliceous marble, containing quartz, albite, apatite, epidote, phengite, paragonite and small euhedral tourmaline grains, $50-100\,\mu$m in diameter, which are very similar in appearance to those of sample SY314. They show anhedral, poikiloblastic cores, overgrown by euhedral rims. While the cores are inhomogeneous and different from one another, the rims are homgeneous and all chemically similar, with dravitic composition, containing $\sim 0.4-0.5$ F pfu, ~ 0.09 Ca cpfu and a X_{Mg} of 0.60. Epidote contains $\sim 0.85-0.90\,Fe^{3+}$ cpfu. Phengite shows Si contents of ~ 3.35 cpfu and BaO concentrations of ~ 0.25 wt%. Accessory Fe-oxide is almost pure hematite (Hem$_{97}$). Whole-rock analysis of this sample are not available.
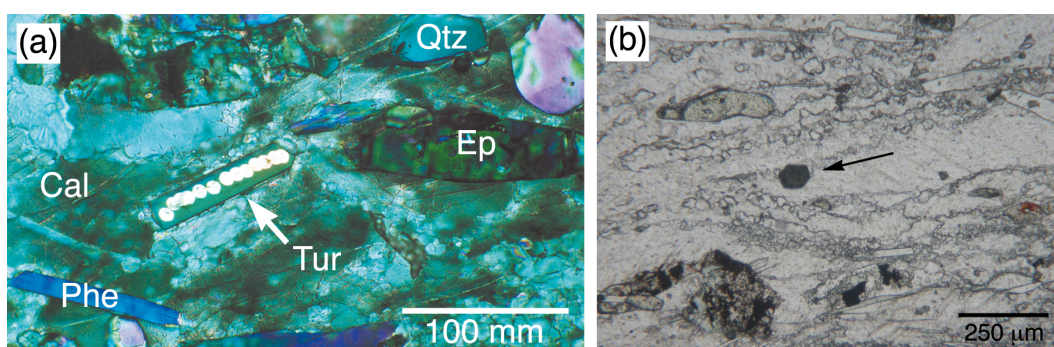
Fig. B.27. Siliceous marble SY432 in thin section. **a** Euhedral tourmaline in calcite + epidote + quartz + phengite matrix. Dark blue colours are due to gold cover. Analysis spots from SIMS are visible as bright spots (diameter $\sim 5\,\mu$m) in tourmaline (crossed polars). **b** Euhedral tourmaline (arrow) sourrounded by calcite, quartz, epidote (high relief), paragonite and phengite (polarised light).

The rock is interpreted as a carbonate sediment with a contribution of siliceous detritus, which contributed Na, Mg, Ca, Fe, Si and K as clay minerals and quartz, and recrystallised to phengite, paragonite, quartz, albite and epidote under HP metamorphic conditions. The history of tourmaline in this sample is discussed in detail in Chapter 9 on page 173.

SY437 Collected by H.M. in 2001; Locality: Ákra Gríza; Rock type: Cr-phengite glaucophanite (hybrid blackwall rock).

Sample SY437 is a schist from a blackwall, which is dominated by glaucophane, and contains large amounts of green Cr-phengite (formerly known as "fuchsite") and minor epidote. The whole-rock analysis shows strong enrichment of MgO (13.2 wt%), Cr (2448 μg/g) and Ni (915 μg/g), but also K$_2$O (1.3 wt%) and CaO (6.7 wt%), showing the influence of both the eclogite block and the surrounding

serpentinite in the generation of this hybrid rock.

SY438   Collected by H.M. in 2001; Locality: $\sim 150\,\text{m}$ uphill Órmos Grammata; Rock type: Phengite-epidote-lawsonite-glaucophane fels (metagabbro).

Sample SY438 is a glaucophane-rich fels with $\sim 10\,\text{mm}$ large lawsonite blasts that are partly replaced by albite-clinozoisite-muscovite assemblages. Some lawsonite has been preserved and could be measured by in-situ methods. The matrix of the rock is composed of phengite, glaucophane and epidote. Glaucophane shows a $\text{Ca}/(\text{Ca}+\text{Na}_\text{B})$ ratio of 0.04, a X_{Mg} of 0.70, a $\text{Al}^{\text{VI}}/(\text{Al}^{\text{VI}}+\text{Fe}^{3+})$ ratio of 0.93 and $7.98\,\text{Si}\,\text{cpfu}$. Phengite in the glaucophane-rich matrix has a X_{Mg} of 0.75 and $\sim 3.42\,\text{Si}\,\text{cpfu}$. At the contact to lawsonite it is intergrown with quartz and shows decreasing Si, Mg and Fe contents which reach a composition of almost pure muscovite ($\sim 3.12\,\text{Si}\,\text{cpfu}$) in direct contact to the decomposing rims of lawsonite (Fig. B.28a). Lawsonite itself shows inclusions of omphacite, epidote and glaucophane. It has a low content of SrO ($< 0.27\,\text{wt\%}$) and Fe_2O_3 ($\sim 0.54\,\text{wt\%}$). Fe content increases towards the rim (Fig. B.28b). Lawsonite shows several indications of breakdown: (i) some of the omphacite inclusions in lawsonite show breakdown to albite + clinozoisite (Fig. B.28c); (ii) the celadonite content of phengite decreases towards the contact to lawsonite, which is probably a result of the reaction

$$\text{Lws} + \text{Cel} = \text{Czo} + \text{Ms} + \text{Tr} + \text{Qtz} + \text{H}_2\text{O} \qquad \text{(B.2)}$$
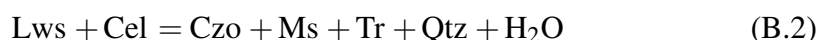
which was also suggested by Brady *et al.* (2001) to be responsible for lawsonite breakdown in Syros H*P* rocks; (iii) subhedral epidote inclusions with Fe contents between 0.67 and $0.77\,\text{cpfu}$ in lawsonite are surrounded by abundant epidote with different, but lower Fe content with Fe content ranging from 0.48 to $0.56\,\text{cpfu}$ (Fig. B.28d). This secondary low-Fe epidote is intergrown with albite + quartz $\pm$ phengite, includes several cavities (black spots in Fig. B.28d), and is interpreted as a product of lawsonite decomposition, forming epidote, albite, quartz, muscovite and fluid. Stability and breakdown of the assemblage omphacite + lawsonite are discussed in detail in Zack *et al.* (2004).

The whole-rock analysis of SY438 shows a composition of basaltic trachyandesite with $52.9\,\text{wt\%}$ SiO_2, $6.2\,\text{wt\%}$ total alkalis and $7.7\,\text{wt\%}$ MgO. Among the trace elements Rb ($45\,\mu\text{g/g}$) and Ba ($318\,\mu\text{g/g}$) are strongly enriched, which is concordant to the relatively high K_2O contents of $1.9\,\text{wt\%}$. The REE pattern shows a depletion in LREE ($(\text{La}/\text{Yb})_{\text{cn}} = 0.66$) and a positive Eu anomaly ($\text{Eu}/\text{Eu}^* = 1.51$). The rock is interpreted as a former gabbro, which was enriched in K, Rb and Ba probably during alteration at the seafloor. H*P* metamorphism produced epidote, lawsonite, glaucophane, omphacite and phengite. The decomposition of lawsonite
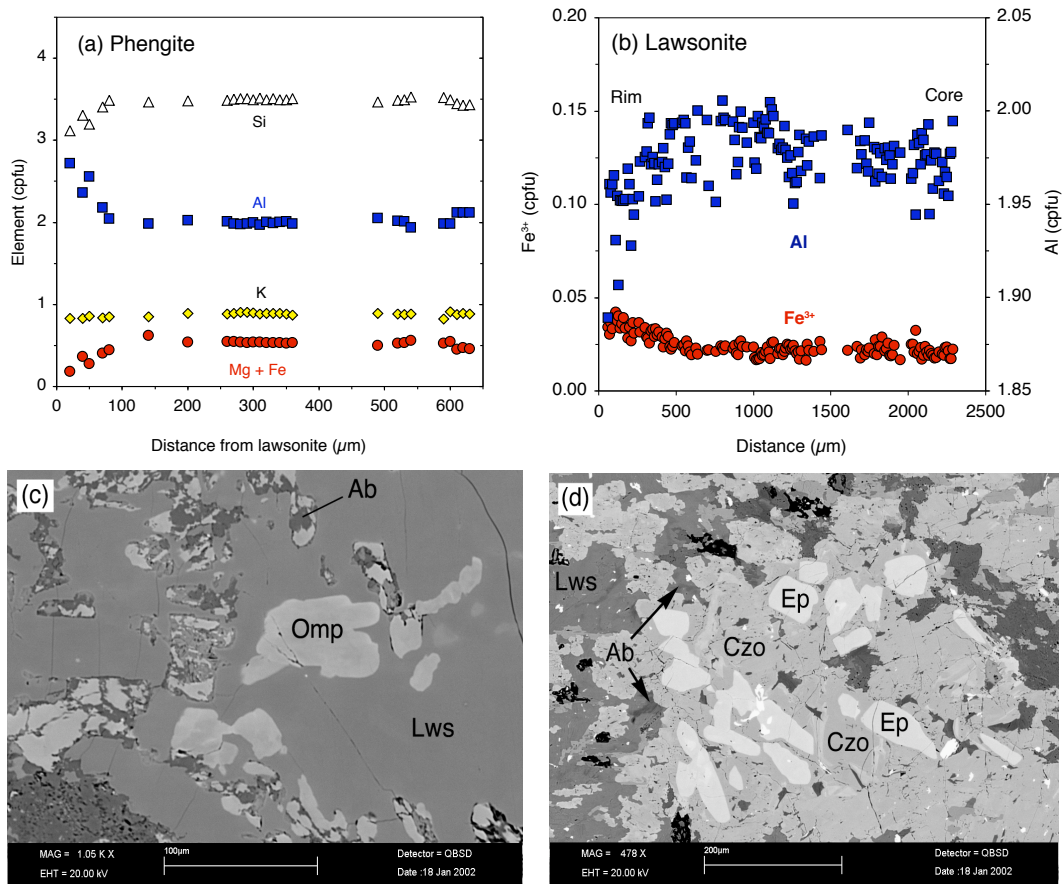
Fig. B.28. Sample SY438. **a** Chemical composition of phengite in contact to lawsonite. The celadonite component decreases towards the contact to lawsonite. **b** Al and Fe^{3+} in a profile from rim to core of lawsonite. Fe content increases within the outermost 500 μm towards the rim, while Al decreases. **c** BSE image of omphacite inclusions in lawsonite. Some inclusions show breakdown of omphacite + lawsonite to clinozoisite + albite. **d** BSE image of inclusions of subhedral Fe-rich epidote, surrounded by low-Fe epidote (Czo), albite and cavities (black).
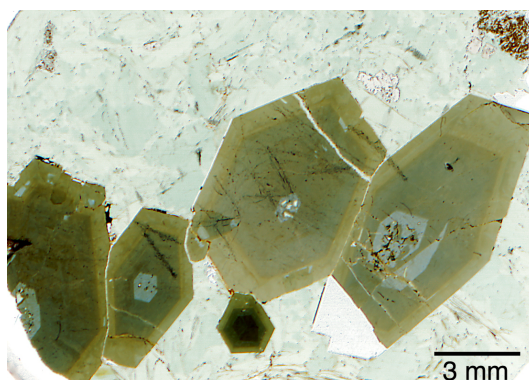
Fig. B.29. Photomicrograph of thin section of sample SY441 showing large zoned tourmaline crystals with very few colourless inclusions of chlorite in cores (unpolarised light).

is probably related to the decompression history, as is indicated by the occurrence of albite in the reaction products. Signs for retrograde rehydration were nor found in the sample.

SY441 Collected by H.M. in 2001; Locality: between Kámbos and Órmos Mégas Lákkos; Rock type: Tourmaline-chlorite schist (hybrid blackwall rock).

Sample SY441 is part of a blackwall that almost exclusively consists of coarse-grained chlorite and clusters of large tourmaline crystals (Fig. B.29), with only little omphacite and titanite and accessory allanite and rutile. Omphacite has the composition $Jd_{42}Acm_{14}Q_{43}$. The rock is rich in MgO, as shown by high X_{Mg} of chlorite (0.82), biotite (0.78) and tourmaline (0.75-0.80). Tourmaline crystals are about 5 mm in diameter and $30 - 50$ mm in length and show four different zones in thin section. The cores are light blue and sometimes contain inclusions of chlorite. The outer zones (rim I to rim III) are free of inclusions and show green colours. Rim I is almost black and not developed in all grains. Rim II is dark green and the outermost rim III is pale green. Tourmaline chemistry is discussed in detail in Chapter 10 on page 193. Whole-rock analysis of this sample was not performed.

SY442 Collected by H.M. in 2001; Locality: Small river bed between Kámbos and Órmos Mégas Lákkos; Rock type: Tourmaline-albite-omphacite fels (hybrid blackwall rock).

Sample SY442 was taken from a blackwall wrapping an eclogite block with a thin black layer of tourmaline, covering its surface (Fig. 4.4b). The blackwall is mineralogically zoned with relatively sharp boundaries between the different zones, changing with distance from the HP block. Sample SY442 displays four different

zones (Fig. B.30). Zone I, closest to the ecclogite is composed of omphacite + titanite + albite. Zone II is dominated by omphacite with rutile aggregates, which form pseudomorphs most probably after titanite. Zon III is formed of large omphacite crystals embedded in a matrix of albite. Zone IV shows abundant tourmaline in a matrix of fine-grained omphacite and albite. Tourmaline grains are $0.5 - 1.5\,\mathrm{mm}$ in diameter and $2 - 3\,\mathrm{mm}$ in length and are concentrated in a layer of a few millimeters in thickness. They display four different colour zones in thin section, with a light blue core, a green rim I, gradually fading into a dark, almost black rim II, which is sharply marked off from green rim III (colours in unpolarized light perpendicular to the c-axis; Fig. B.31a).
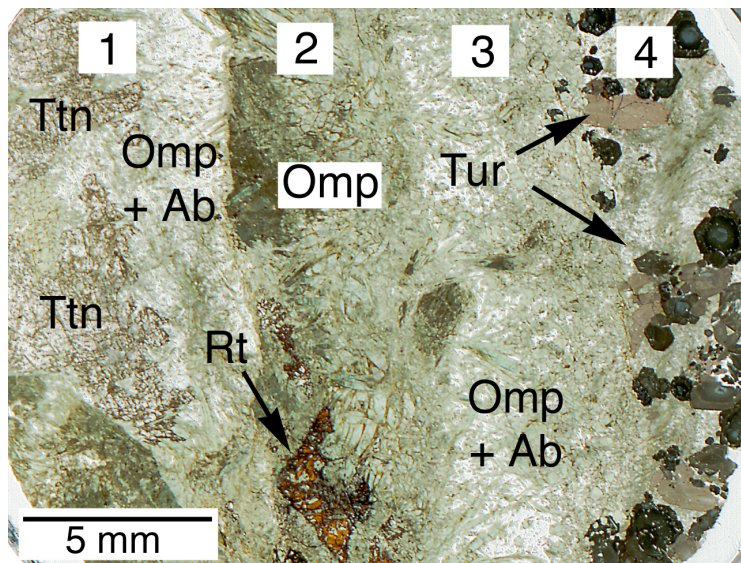
Fig. B.30. Photomicrograph of thick section ($\sim 100\,\mathrm{\mu m}$) of sample SY442 displaying the different zones within the blackwall. The HP block is located to the left, the serpentinite matrix is located to the right. Zone 1 consists of large titanite poikiloblasts intergrown with omphacite and albite. Zone 2 is built of omphacite with large rutile pseudomorphs after titanite. Zone 3 is composed of large euhedral omphacite intergrown with albite (see also Fig. B.31b). Zone 4 shows fine-grained omphacite in paragenesis with albite and tourmaline. (unpolarised light).

Omphacite included in rims I and II has low Na content ($Jd_{36}Acm_{21}Q_{41}$), whereas omphacite included in rim III shows rims with higher Na content ($Jd_{45}Acm_{25}Q_{27}$). Omphacite and albite ($An_{99.2}$) in the rock matrix are closely intergrown and show petrographic equilibrium in thin section, suggested by sharp and euhedral grainboundaries (Fig. B.31b). Omphacite is chemically zoned with cores showing low jadeite contents ($Jd_{36}Acm_{22}Q_{39}$) and rims with high jadeite contents ($Jd_{51}Acm_{20}Q_{26}$). Tourmaline chemistry is discussed in detail in Chapter 10 on page

193. Whole-rock analysis of this sample was not performed. The sample is part of a blackwall which formed during the influx of hydrous fluid during exhumation of the mélange, and displays the chemical gradients in different elements within the reaction zone. The replacement of titanite by rutile, for example, is probably a result of decreasing activities of Si and Ca in zone II with respect to zone I. Precipitation of tourmaline is also restricted to a specific layer.
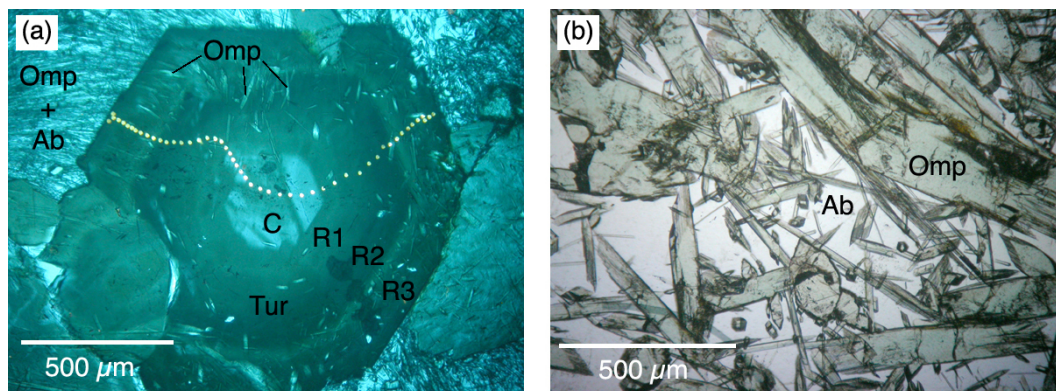
Fig. B.31. Photomicrographs of thick section ($\sim 100\,\mu m$) of sample SY442. **a** Zoned tourmaline crystal with small omphacite inclusions, sourronded by a matrix of omphacite + albite. The thin section was covered with a gold layer prior to SIMS analysis, producing the dark blue colours of the picture. The spots generated during SIMS analyses are visible as white dots (polarised light). **b** Detail of the matrix sourrounding tourmaline consisting of euhedral and subhedral omphacite intergrown with albite (polarised light).

SY443   Collected by R.A. in 2001; Locality: between Kámbos and Ákra Gríza; Rock type: Phengite-omphacite-glaucophane-epidote fels (metagabbro).

Sample SY443 was taken from a large outcrop interpreted as metagabbro. The major part of the outcrop is displaying a coarse-grained, isotropic rock with mm- to cm-sized dark glaucophane and omphacite grains embedded in a fine-grained white clinozoisite-rich matrix. Garnet is rare and forms isolated grains included in omphacite. Some restricted parts of the metagabbro are more leucocratic and are characterised by very large omphacite crystals ($> 5\,cm$). These domains may be interpreted as residual melt pockets of the former gabbro. At other places syn-metamorphic shear zones are crosscutting the metagabbro, displaying strongly reduced grain sizes and a well-defined foliation. Sample SY443 was taken from a relatively undeformed part of the outcrop and shows only weak foliation in hand-specimen. The rock consists of $\sim 1\,cm$ large blasts of glaucophane, Ca-amphibole and omphacite, embedded in a fine-grained matrix composed of colourless clino-

zoisite and phengite. Garnet is rare and occurs anly as inclusion in omphacite. Some of the amphibole blasts show deformation features in thin section, like undulatory extinction and subgrain boundaries. The major part of the rock shows a replacement of Ca-amphibole and omphacite by chlorite + albite + glaucophane + epidote + Cr-phengite ("fuchsite"). This secondary epidote forms large ($\sim 100\,\mu m$) euhedral grains with pleochroism from pale to dark yellow. The secondary mineral assemblage is undeformed.

The chemical whole-rock analysis revealed 51.0 wt% SiO_2, 8.6 wt% MgO and 3.7 wt% total alkalis, which is consistent with the interpretation of the rock being a metagabbro. High concentrations of Ca and a positive Eu anomaly (Eu $/Eu^* = 1.39$) point to a cumulation of plagioclase during the magmatic generation of the former gabbro. Very high abundance of Cr ($1645\,\mu g/g$) may be interpreted as a result of chromite accumulation at the same time. However, the late hydrothermal overprint of the HP assemblage together with the occurrence of Cr-phengite, which was also observed in the blackwall samples (e. g. SY437) suggests the enrichment in Cr was caused by hydrothermal alteration during deformation and decompression. During HP metamorphism, glaucophane, clinozoisite/epidote and garnet were formed. Retrograde fluid influx produced Cr-phengite, epidote, albite and chlorite after deformation of the HP minerals.

C. Major- and trace-element abundances in Syros high-pressure metamorphic rocks

Appendix C includes five tables with major and trace element whole rock analyses of the 43 samples that were analysed by different analytical methods. The rocks are grouped according to their geological character as discussed in chapter 4 on page 69 (each of the tables is divided into two parts, due to the large number of elements measured):

    Table C.1: Glaucophane schists and -felses

    Table C.2: Eclogites and meta-plagiogranites

    Table C.3: Serpentinites, marbles and metagabbros

    Table C.4: Blackwall rocks without tourmalin

    Table C.5: Tourmaline-bearing blackwall rocks

Analyses of major elements (SiO_2 to P_2O_5) were performed by XRF with the exception of Na_2O in samples marked by (*), where PGNAA values were preferred. CO_2 and H_2O were analysed by PGNAA, except for samples marked by (*), where only L.O.I. values were obtained. The trace elements V to Ba were analysed by XRF. Sc, Nb, Ta and the rare earth elements (REE) were analysed by solution-ICP-MS, except for samples marked by (*), where Sc and Gd values from PGNAA and Nb values from XRF were preferred. Trace elements Pb, Th and U were analysed by solution-ICP-MS, except for samples marked by (*), where Pb and Th values of XRF were preferred. Li was analysed by solution-ICP-AES at the University of Bristol, except for samples marked by (†), where values from Cavendish Analytical Laboratory Ltd. (Vancouver) were preferred. Be was analysed by solution-ICP-AES. B and Cl were analysed by PGNAA. A detailed discussion on the analytical methods and the data quality is given in chapter 2.

Letters K and T in the third line of the tables are: K = XRF analyses performed at the Universität Köln. T = XRF analyses of major elements performed at Universität Tübingen, and of trace elements performed at Universität Trier. Mg# were calculated from molar $MgO/(MgO + FeO^{tot})$ ratio, where FeO^{tot} is total Fe as FeO. Mass ratios of selected elements are given at the end of each table. $(La/Yb)_{cn}$ is the La/Yb ratio normalised to CI chondritic values (Boynton, 1985). Eu/Eu^* and Ce/Ce^* are also CI chrondrite normalised ratios, whereby $Eu^* = \sqrt{Sm_{cn} \cdot Gd_{cn}}$ and $Ce^* = \sqrt{La_{cn} \cdot Pr_{cn}}$.

Table C.1. Whole rock analyses of glaucophane schists and felses

Type	Andesitic	Metabasic							Metasedimentary	
Sample	SY3 K	SY5 K	SY304 T	SY306 K	SY342 K	SY309A T	SY401A T	SY403 T	SY406 T	SY314 T
Major elements (wt%), XRF										
SiO_2	58.85	47.06	45.74	46.74	55.21	48.88	51.27	49.05	47.60	54.14
TiO_2	0.81	4.02	1.73	1.59	2.23	0.94	0.94	1.99	0.59	0.60
Al_2O_3	17.21	13.70	18.16	16.99	13.81	15.93	14.25	16.97	16.10	15.32
Fe_2O_3	7.69	16.38	14.28	13.67	12.82	9.85	10.15	10.11	17.86	12.76
MnO	0.06	0.23	0.24	0.20	0.21	0.15	0.13	0.27	3.14	0.96
MgO	4.71	5.10	6.52	5.79	4.89	6.95	8.67	6.47	5.00	3.95
CaO	2.79	8.14	5.62	8.48	7.08	8.77	6.17	6.49	2.70	1.83
Na_2O	4.66	3.07	3.17*	3.37	3.07	4.36*	5.40*	4.95*	3.84*	6.66*
K_2O	0.92	0.03	0.85	0.50	0.18	0.56	0.31	0.08	2.05	2.25
P_2O_5	0.32	0.74	0.10	0.10	0.17	0.12	0.12	0.31	0.29	0.28
H_2O	2.50	1.51	3.17	2.46	1.50	2.32	2.53	2.90	1.77	2.03
Summe	100.52	99.98	99.58	99.89	101.17	98.84	99.94	99.58	100.94	100.79
Mg#	61.0	44.3	53.8	52.0	49.3	64.3	68.6	62.0	41.7	44.2
TA	5.58	3.10	4.02	3.87	3.25	4.92	4.37	5.03	5.89	8.91
Trace elements (µg/g), XRF										
V	116	457	306	334	251	307	325	266	263	308
Cr	238	32	15	*d.l.*	39	70	36	182	194	155
Co	47	37	32	26	26	30	35	33	54	72
Ni	291	6	*d.l.*	*d.l.*	16	53	37	81	304	183
Cu	*n.a.*	*n.a.*	15	*n.a.*	*n.a.*	27	30	343	60	13
Zn	123	114	104	77	78	77	73	640	179	184
Ga	19	16	19	19	24	20	17	21	18	19
Rb	34	*d.l.*	9	5	6	10	7	2	74	93
Sr	127	477	144	249	544	774	474	236	33	27
Y	39	53	30	20	60	36	37	37	97	47
Zr	154	70	33	60	167	126	80	182	159	122
Ba	166	33	74	67	79	61	31	34	355	260
Trace elements (µg/g), ICP-MS										
Sc	20.4	37.3	42.8	34.3	36.6	33.8	38.2	*n.a.*	24.0	21.6
Nb	13.4	8.50	1.93	0.81	6.50	3.28	3.15	9.69*	14.0	8.27
Ta	0.86	1.12	0.18	0.10	0.72	0.46	0.69	*n.a.*	8.23	0.70

Table C.1. (continued)

Type	Andesitic	Metabasic							Metasedimentary	
Sample	SY3	SY5	SY304	SY306	SY342	SY309A	SY401A	SY403	SY406	SY314
Rare earth elements (μg/g), ICP-MS										
La	35.0	8.75	3.98	3.34	5.74	13.4	14.3	*n.a.*	68.4	53.0
Ce	73.8	27.4	10.1	8.64	18.9	28.5	30.0	*n.a.*	83.1	87.2
Pr	8.47	4.60	1.53	1.28	3.27	3.98	3.86	*n.a.*	16.8	12.0
Nd	32.5	24.8	8.71	6.69	18.0	17.1	16.4	*n.a.*	65.7	47.2
Sm	6.88	7.71	2.79	2.04	5.90	4.52	4.24	*n.a.*	14.3	10.1
Eu	1.59	2.81	1.23	0.84	2.24	1.43	2.24	*n.a.*	3.90	2.25
Gd	6.16	9.55	3.78	2.63	7.58	4.68	4.50	*n.a.*	15.5	9.68
Tb	0.90	1.39	0.66	0.45	1.32	0.74	0.76	*n.a.*	2.48	1.41
Dy	6.05	9.26	4.76	3.11	9.30	4.84	5.19	*n.a.*	16.4	8.47
Ho	1.17	1.84	1.02	0.65	1.94	1.06	1.06	*n.a.*	3.39	1.61
Er	3.50	5.35	3.02	2.00	5.89	3.17	3.27	*n.a.*	10.4	4.72
Tm	0.53	0.69	0.42	0.28	0.88	0.47	0.49	*n.a.*	1.47	0.66
Yb	3.47	4.42	2.70	1.98	5.73	3.27	3.34	*n.a.*	10.2	4.02
Lu	0.56	0.69	0.40	0.28	1.08	0.54	0.61	*n.a.*	1.95	0.66
Pb, Th, U (μg/g), ICP-MS										
Pb	9.16	37.7	1.78	3.44	19.2	6.98	4.20	7.*	5.25	13.8
Th	11.4	0.12	0.79	0.86	1.47	5.35	6.87	0.5*	10.6	11.3
U	1.87	0.03	0.13	0.08	0.66	1.29	1.93	*n.a.*	3.76	1.77
Li, Be (μg/g), ICP-AES										
Li	36.9	42.6	7.75	7.14	27.4	28.0	32.5	11.5†	66.7	39.6
Be	0.92	1.0	0.46	0.40	1.0	0.67	0.68	1.1	1.5	2.3
B, Cl (μg/g), PGNAA										
B	62.4	3.16	12.0	9.91	4.92	11.4	7.86	9.11	18.2	93.9
Cl	169	63	217	300	63	516	308	290	85	83
B/Be	67.9	3.3	26.1	24.8	4.9	17.0	11.6	8.5	12.5	40.5
B/Nb	4.7	0.4	6.2	12.3	0.8	3.5	2.5	0.9	1.3	11.4
Li/Yb	10.61	9.63	2.87	3.60	4.79	8.56	9.73		6.56	9.85
Be/Nd	0.028	0.038	0.053	0.060	0.056	0.039	0.041		0.022	0.049
Cl/K	0.022	0.25	0.031	0.072	0.042	0.11	0.12	0.46	0.005	0.004
Ce/Pb	8.1	0.73	5.7	2.5	1.0	4.1	7.1		16	6.3
La/Yb$_{cn}$	6.8	1.3	0.99	1.1	0.67	2.8	2.9		4.5	8.9
Ce/Ce*	1.03	1.04	0.99	1.00	1.05	0.94	0.97		0.59	0.83
Eu/Eu*	0.75	1.00	1.16	1.11	1.03	0.95	1.57		0.80	0.69

Table C.2. Whole rock analyses of eclogites and meta-plagiogranites

Type	Eclogites				Meta-plagiogranites				
Sample	SY323 T	SY324 K	SY411 K	SY109 T	SY1 K	SY308 T	SY8 K	SY415 K	SY431 K
Major elements (wt%), XRF									
SiO_2	45.35	46.85	49.39	53.40	59.72	68.52	70.23	70.32	73.20
TiO_2	0.75	0.88	0.72	2.23	1.29	0.67	0.31	0.30	0.28
Al_2O_3	15.51	14.27	12.10	14.04	15.17	14.30	15.18	15.34	14.86
Fe_2O_3	12.95	11.50	12.22	12.94	9.39	4.75	3.54	3.29	3.13
MnO	1.14	0.74	0.58	0.25	0.18	0.08	0.06	0.05	0.06
MgO	4.12	4.62	5.77	2.45	1.58	1.43	0.31	0.28	0.38
CaO	14.70	15.97	14.56	5.40	3.24	3.84	0.93	0.89	1.08
Na_2O	3.59*	3.73	4.44	4.82	7.19	5.58*	7.48	7.64	6.48
K_2O	0.02	0.00	0.03	0.57	0.11	0.18	0.78	0.74	0.14
P_2O_5	0.13	0.03	0.13	0.73	0.49	0.13	0.07	0.07	0.03
H_2O	0.78	0.70	0.50	0.63*	0.92	1.25	1.25	0.68	0.95
Summe	99.03	99.29	100.44	97.46	99.28	100.72	100.14	99.60	100.59
Mg#	44.8	50.6	54.7	32.6	30.1	43.5	18.3	17.9	23.7
TA	3.61	3.73	4.47	5.39	7.30	5.76	8.26	8.38	6.62
Trace elements ($\mu g/g$), XRF									
V	196	176	171	125	24	97	18	11	13
Cr	190	149	132	29	26	31	9	6	9
Co	47	50	63	28	14	10	*d.l.*	6	*d.l.*
Ni	219	172	259	11	11	2	*d.l.*	*d.l.*	*d.l.*
Cu	134	*n.a.*	*n.a.*	24	*n.a.*	6	*n.a.*	*n.a.*	*n.a.*
Zn	93	121	148	166	104	26	37	36	37
Ga	22	16	16	25	30	16	27	25	28
Rb	2	*d.l.*	*d.l.*	32	4	3	12	12	3
Sr	881	607	299	117	133	121	45	51	81
Y	61	55	42	105	81	43	83	81	93
Zr	155	146	143	334	538	203	667	676	624
Ba	8	*d.l.*	*d.l.*	94	11	41	93	89	62
Trace elements ($\mu g/g$), ICP-MS									
Sc	28.4	26.0	21.1	20.5	8.83	10.3	0.37	0.76	0.54
Nb	13.1	14.8	10.9	22.1	15.*	5.*	12.*	7.*	14.*
Ta	1.33	0.94	0.64	1.26	*n.a.*	*n.a.*	*n.a.*	*n.a.*	*n.a.*

Table C.2. (continued)

Type	Eclogites				Meta-plagiogranites				
Sample	SY323	SY324	SY411	SY109	SY1	SY308	SY8	SY415	SY431
Rare earth elements (µg/g), ICP-MS									
La	55.4	42.7	43.4	27.2	14.9	6.99	14.3	8.60	6.15
Ce	91.6	73.3	75.3	72.4	47.9	18.7	37.7	27.4	22.0
Pr	12.7	10.1	10.4	11.1	6.83	2.73	4.44	2.72	2.89
Nd	49.0	40.1	40.2	53.8	32.8	13.3	18.3	11.9	13.3
Sm	10.6	8.91	8.28	14.2	9.50	3.93	3.96	2.62	3.94
Eu	2.41	2.17	1.80	3.60	2.55	1.13	0.72	0.54	0.69
Gd	9.82	8.62	7.63	16.4	11.2	5.18	4.13	2.93	4.86
Tb	1.49	1.31	1.14	2.68	1.85	0.83	0.68	0.53	0.93
Dy	9.39	8.25	7.41	17.1	12.0	6.15	5.00	3.93	6.86
Ho	1.88	1.60	1.41	3.49	2.44	1.27	1.13	0.93	1.46
Er	5.58	4.81	4.13	10.0	7.08	4.01	4.03	3.25	4.55
Tm	0.78	0.71	0.57	1.40	1.02	0.58	0.63	0.55	0.68
Yb	5.39	4.99	4.09	9.20	6.64	4.22	4.68	3.91	4.77
Lu	0.98	0.82	0.68	1.67	1.35	0.77	0.85	0.73	0.86
Pb, Th, U (µg/g), ICP-MS									
Pb	89.1	46.7	27.3	1.62	0.79	0.66	1.51	1.39	0.67
Th	13.9	10.6	12.1	1.29	4.98	4.92	5.23	4.87	3.09
U	2.34	2.48	1.76	0.38	1.81	1.59	1.81	1.82	1.47
Li, Be (µg/g), ICP-AES									
Li	45.8	56.5	72.3	6.05	9.68[†]	5.02[†]	5.58[†]	5.62[†]	22.7[†]
Be	2.1	2.2	2.9	1.8	1.8	0.82	3.4	3.5	3.3
B, Cl (µg/g), PGNAA									
B	4.77	2.18	3.80	*n.a.*	12.0	10.3	11.7	10.6	38.8
Cl	60	28	35	*n.a.*	53	69	45	52	101
B/Be	2.3	1.0	1.3		6.8	13	3.4	3.1	12
B/Nb	0.4	0.1	0.35		0.80	1.9	1.0	1.5	2.8
Li/Yb	8.50	11.33	18	0.66	1.5	1.2	1.2	1.4	4.8
Be/Nd	0.042	0.055	0.072	0.033	0.054	0.062	0.19	0.29	0.25
Cl/K	0.36		0.14		0.058	0.046	0.007	0.008	0.087
Ce/Pb	1.0	1.6	2.8	45	61	28	25	20	33
La/Yb$_{cn}$	6.9	5.8	7.2	2.0	1.5	1.1	2.1	1.5	0.87
Ce/Ce*	0.83	0.85	0.85	1.01	1.14	1.03	1.14	1.36	1.26
Eu/Eu*	0.72	0.76	0.69	0.72	0.76	0.77	0.55	0.59	0.48

Table C.3. Whole rock analyses of serpentinites, marbles and metagabbros

Type	Serpentinites		Marbles		Metagabbros					Qtz vein
Sample	SY429 K	SY347 K	SY2 T	SY335 T	SY112 T	SY344 T	SY425G K	SY438 K	SY443 K	SY425D K
Major elements (wt%), XRF										
SiO$_2$	45.03	41.41	13.38	11.00	39.97	50.50	52.69	52.92	50.96	82.80
TiO$_2$	0.05	0.02	0.07	0.12	7.26	0.91	1.23	0.53	0.43	0.06
Al$_2$O$_3$	2.60	2.48	2.41	2.42	13.93	14.55	17.53	17.38	17.88	6.25
Fe$_2$O$_3$	11.43	9.22	3.13	1.17	16.58	6.45	9.28	6.53	4.60	3.62
MnO	0.10	0.12	0.10	0.04	0.45	0.13	0.24	0.09	0.13	0.13
MgO	31.39	35.70	6.16	1.09	8.05	7.70	4.91	7.70	8.64	0.32
CaO	0.21	0.16	38.35	43.56	9.83	12.54	6.45	5.31	10.73	5.57
Na$_2$O	0.00	0.00	0.60*	0.33*	1.82*	3.87*	5.65	4.32	3.43	0.23
K$_2$O	0.00	0.00	0.14	0.64	0.07	0.22	0.58	1.92	0.29	0.02
P$_2$O$_5$	0.00	0.02	0.10	0.06	0.03	0.03	0.13	0.00	0.04	0.07
CO$_2$	*d.l.*	*d.l.*	36.25	40.10	*d.l.*	*d.l.*	*d.l.*	*d.l.*	*d.l.*	*d.l.*
H$_2$O	9.75	12.12	0.97	0.48	2.23	1.87	1.94	3.08	2.83	0.54
Summe	100.56	101.26	101.64	101.02	100.21	98.79	100.63	99.78	99.96	99.61
Mg#	87.5	90.8	83.4	70.5	55.4	75.3	57.5	75.1	82.7	18.4
TA	0.00	0.00	0.74	0.98	1.89	4.09	6.23	6.24	3.72	0.25
Trace elements (μg/g), XRF										
V	135	82	48	31	425	274	103	160	91	75
Cr	3203	2308	1086	27	40	69	98	54	1645	*d.l.*
Co	118	112	24	2	44	30	25	33	30	*d.l.*
Ni	1865	1997	488	9	139	58	85	56	136	*d.l.*
Cu	*n.a.*	2	50	20	14	62	*n.a.*	*n.a.*	*n.a.*	*n.a.*
Zn	64	49	65	18	77	46	94	68	52	6
Ga	7	6	6	4	16	13	18	16	15	11
Rb	2	1	7	12	2	6	21	45	*d.l.*	4
Sr	*d.l.*	3	398	276	209	282	214	372	266	310
Y	*d.l.*	*d.l.*	24	8	48	18	34	17	14	7
Zr	7	2	46	19	94	30	309	23	30	9
Ba	61	5	*d.l.*	*d.l.*	66	25	70	318	*d.l.*	*d.l.*
Trace elements (μg/g), ICP-MS										
Sc	6.11	15.8	*d.l.**	*d.l.**	60.1	54.2	34.8	29.7	37.0	5.65
Nb	0.55	0.36	3.*	3.*	8.78	0.83	5.25	1.73	0.64	0.08
Ta	0.10	0.10	*n.a.*	*n.a.*	0.63	0.09	0.32	0.10	0.20	0.02

Table C.3. (continued)

Type	Serpentinites		Marbles		Metagabbros					Qtz vein
Sample	SY429	SY347	SY2	SY335	SY112	SY344	SY425G	SY438	SY443	SY425D

Rare earth elements (µg/g), ICP-MS

La	*d.l.*	*d.l.*	*n.a.*	*n.a.*	5.92	1.26	6.94	1.88	1.12	4.97
Ce	0.28	0.03	*n.a.*	*n.a.*	16.5	4.09	18.81	5.34	3.56	13.3
Pr	*d.l.*	*d.l.*	*n.a.*	*n.a.*	2.91	0.77	3.04	0.85	0.55	1.97
Nd	0.38	0.09	*n.a.*	*n.a.*	16.5	5.00	15.15	4.53	3.38	12.9
Sm	0.10	*d.l.*	*n.a.*	*n.a.*	5.95	1.88	4.66	1.62	1.13	4.15
Eu	0.01	0.01	*n.a.*	*n.a.*	2.53	0.87	2.47	0.89	0.59	2.89
Gd	0.12	*d.l.*	2.35*	0.95*	7.52	2.53	5.35	2.03	1.51	5.86
Tb	0.04	0.01	*n.a.*	*n.a.*	1.21	0.42	0.94	0.37	0.25	1.27
Dy	0.24	0.06	*n.a.*	*n.a.*	7.91	2.94	6.00	2.72	1.72	12.3
Ho	0.05	0.01	*n.a.*	*n.a.*	1.61	0.59	1.24	0.59	0.36	3.02
Er	0.23	0.07	*n.a.*	*n.a.*	4.61	1.79	3.72	1.85	1.00	11.0
Tm	0.03	0.01	*n.a.*	*n.a.*	0.70	0.23	0.52	0.25	0.13	1.62
Yb	0.31	0.11	*n.a.*	*n.a.*	4.60	1.55	3.58	1.92	0.87	12.2
Lu	*d.l.*	*d.l.*	*n.a.*	*n.a.*	0.86	0.21	0.59	0.27	0.05	1.32

Pb, Th, U (µg/g), ICP-MS

Pb	0.07	0.28	24.*	6.*	2.17	0.55	2.68	8.01	1.00	52.2
Th	0.03	*d.l.*	*d.l.**	0.5*	0.17	*d.l.*	0.61	*d.l.*	0.04	*d.l.*
U	*d.l.*	*d.l.*	*n.a.*	*n.a.*	0.87	*d.l.*	0.11	*d.l.*	*d.l.*	*d.l.*

Li, Be (µg/g), ICP-AES

Li	2.81	0.91	*n.a.*	*n.a.*	5.61	18.8	40.5	88.7	16.9	3.30
Be	0.47	0.24	*n.a.*	*n.a.*	1.0	0.54	1.6	1.3	0.61	0.15

B, Cl (µg/g), PGNAA

B	11.3	5.52	3.92	15.8	4.78	5.05	25.6	19.6	4.88	1.90
Cl	6	11	50	*d.l.*	189	56	57	10	130	7

B/Be	24	23			5.0	9.4	16	15	8.0	13
B/Nb	21	15	1.5	4.6	0.54	6.1	4.9	11	7.7	24
Li/Yb	9.0	7.9			1.2	12	11	46	19	0.27
Be/Nd	1.22	2.70			0.058	0.11	0.10	0.28	0.18	0.012
Cl/K			0.042		0.35	0.030	0.012	0.001	0.054	0.040
Ce/Pb	4.2	0.13			7.6	7.4	7.0	0.67	3.6	0.26
La/Yb$_{cn}$					0.87	0.55	1.31	0.66	0.87	0.27
Ce/Ce*					0.96	1.00	0.99	1.02	1.09	1.02
Eu/Eu*	0.40				1.16	1.22	1.51	1.51	1.39	1.79

353

Table C.4. Whole rock analyses of blackwall rocks without tourmaline

Type	Blackwall rocks without tourmaline								
Sample	SY325 T	SY328 T	SY400A T	SY402A T	SY402B T	SY402C T	SY404 T	SY405 K	SY437 K
Major elements (wt%), XRF									
SiO_2	54.75	43.02	49.66	53.76	54.67	58.49	29.93	24.91	51.81
TiO_2	0.07	2.83	1.06	1.59	1.71	0.12	3.21	5.06	0.41
Al_2O_3	2.08	13.45	15.55	11.34	10.63	10.16	13.81	12.55	11.07
Fe_2O_3	7.87	15.47	5.94	7.99	7.87	7.95	13.79	17.02	9.64
MnO	0.23	0.17	0.11	0.14	0.15	0.11	0.17	0.24	0.13
MgO	22.10	6.28	8.25	7.10	7.19	12.99	22.24	21.15	13.18
CaO	7.38	6.88	8.51	7.39	8.24	0.80	5.24	6.51	6.70
Na_2O	1.64*	7.87*	4.35	8.28*	9.07*	7.72*	0.45*	0.00	2.87
K_2O	0.08	0.00	1.93	0.56	0.01	0.00	0.00	0.00	1.30
P_2O_5	0.01	1.61	0.10	0.47	0.13	0.01	1.58	3.15	0.00
H_2O	3.69	2.85	2.34*	0.97	0.62	2.31	9.69	9.28	2.72
Summe	99.91	100.43	97.80	99.59	100.30	100.65	100.11	99.88	99.83
Mg#	87.8	50.9	78.0	69.4	70.0	80.7	80.5	76.0	77.7
TA	1.72	7.87	6.28	8.84	9.08	7.72	0.45	0.00	4.17
Trace elements ($\mu g/g$), XRF									
V	58	62	167	118	123	65	54	174	138
Cr	1812	11	333	24	67	590	384	7	2448
Co	54	34	26	29	23	58	65	52	53
Ni	1592	12	146	143	120	612	439	97	915
Cu	2	15	6	13	13	2	27	43	n.a.
Zn	67	139	34	32	28	55	137	148	138
Ga	6	20	17	23	25	17	21	19	14
Rb	1	1	47	10	2	1	1	1	50
Sr	16	312	158	35	13	3	68	146	140
Y	19	104	40	111	57	9	137	165	29
Zr	8	59	129	920	207	80	481	93	148
Ba	5	32	349	104	13	d.l.	23	31	207
Trace elements ($\mu g/g$), ICP-MS									
Sc	7.97	35.6	n.a.	26.6	31.9	7.81	n.a.	39.8	16.2
Nb	0.43	8.52	7.*	18.6	19.7	4.57	22.*	8.95	6.79
Ta	0.25	1.71	n.a.	2.06	1.05	0.19	n.a.	1.16	0.50

Table C.4. (continued)

Type	Blackwall rocks without tourmaline								
Sample	SY325	SY328	SY400A	SY402A	SY402B	SY402C	SY404	SY405	SY437

Rare earth elements (μg/g), ICP-MS

La	0.52	17.2	*n.a.*	33.7	5.52	1.58	*n.a.*	23.8	21.5
Ce	1.59	59.5	*n.a.*	106	18.3	4.72	*n.a.*	82.7	47.9
Pr	0.21	10.4	*n.a.*	17.1	3.15	0.61	*n.a.*	14.2	5.80
Nd	1.94	55.4	*n.a.*	82.0	17.0	3.36	*n.a.*	75.6	22.7
Sm	1.23	15.9	*n.a.*	22.5	5.63	0.84	*n.a.*	21.8	4.62
Eu	0.46	4.79	*n.a.*	6.50	1.87	0.37	*n.a.*	4.51	0.72
Gd	2.14	18.2	*n.a.*	23.1	6.82	1.12	30.0*	25.7	4.29
Tb	0.42	2.64	*n.a.*	3.62	1.18	0.20	*n.a.*	3.86	0.68
Dy	3.20	17.0	*n.a.*	21.6	8.97	1.51	*n.a.*	25.8	4.54
Ho	0.63	3.26	*n.a.*	3.89	1.97	0.33	*n.a.*	5.08	0.90
Er	1.82	8.53	*n.a.*	10.9	6.51	1.05	*n.a.*	14.2	2.78
Tm	0.28	1.06	*n.a.*	1.47	1.07	0.15	*n.a.*	1.82	0.43
Yb	1.90	6.28	*n.a.*	10.0	7.75	0.99	*n.a.*	11.0	2.97
Lu	0.23	1.07	*n.a.*	1.87	1.53	0.08	*n.a.*	1.97	0.46

Pb, Th, U (μg/g), ICP-MS

Pb	1.28	2.94	5.*	2.21	1.88	0.73	4.*	0.54	9.43
Th	*d.l.*	0.06	*n.a.*	1.74	0.30	0.07	0.2*	0.03	4.96
U	*d.l.*	*d.l.*	*n.a.*	0.60	0.21	*d.l.*	*n.a.*	*d.l.*	1.29

Li, Be (μg/g), ICP-AES

Li	2.29	65.3	69.2[†]	71.0	78.0	63.3	7.5[†]	11.3	19.1
Be	2.6	0.88	3.3	2.0	1.8	1.6	0.91	0.63	3.2

B, Cl (μg/g), PGNAA

B	7.15	7.58	*n.a.*	12.9	8.28	13.9	3.75	3.85	15.5
Cl	3	107	*n.a.*	48	41	*d.l.*	*d.l.*	871	184

B/Be	2.8	8.6		6.3	4.6	8.7	4.1	6.1	4.9
B/Nb	16	0.89		0.69	0.42	3.0	0.17	0.43	2.3
Li/Yb	1.2	10		7.1	10	64		1.0	6.4
Be/Nd	1.33	0.016		0.025	0.11	0.48		0.008	0.14
Cl/K	0.004			0.010	0.53				0.017
Ce/Pb	1.2	20		48	9.8	6.5		153	5.1
La/Yb$_{cn}$	0.18	1.9		2.3	0.48	1.1		1.5	4.9
Ce/Ce*	1.16	1.07		1.06	1.06	1.16		1.08	1.03
Eu/Eu*	0.86	0.86		0.87	0.92	1.15		0.58	0.49

C. Whole-rock analyses

Table C.5. Whole rock analyses of tourmaline-bearing blackwall rocks

Type	Tur bearing blackwall rocks				
Sample	SY309B T	SY400B T	SY401B T	SY412 K	SY420 K
Major elements (wt%), XRF					
SiO_2	47.29	49.34	43.21	45.82	38.06
TiO_2	1.16	1.09	0.89	4.28	0.87
$B_2O_3{}^P$	1.28	0.11	4.93	0.03	2.82
Al_2O_3	14.47	16.57	20.91	13.53	25.03
Fe_2O_3	9.93	6.11	8.35	14.96	9.59
MnO	0.10	0.11	0.07	0.18	0.26
MgO	13.87	8.38	11.22	7.04	6.54
CaO	2.15	8.11	1.66	4.52	9.69
Na_2O	5.20*	5.18*	4.55*	6.59	1.40
K_2O	0.01	2.14	0.00	0.80	1.21
P_2O_5	0.24	0.09	0.37	0.04	0.00
H_2O	4.54	2.64	4.67	3.07	4.14
Total	100.23	99.87	100.82	100.86	99.61
Mg#	78.1	77.8	77.4	54.6	63.5
TA	5.21	7.32	4.55	7.39	2.61
Trace elements (µg/g), XRF					
V	286	159	379	639	199
Cr	246	317	159	9	353
Co	53	28	45	44	49
Ni	170	161	134	18	240
Cu	13	6	18	*n.a.*	*n.a.*
Zn	84	38	72	99	81
Ga	13	17	15	20	29
Rb	1	52	1	16	40
Sr	67	175	133	35	1640
Y	30	43	19	22	88
Zr	105	155	80	75	171
Ba	16	454	18	186	584
Trace elements (µg/g), ICP-MS					
Sc	43.0	30.6	30.3	42.6	25.6
Nb	5.28	7.18	3.01	3.05	13.2
Ta	0.34	0.37	0.76	0.24	0.94

Table C.5. (continued)

Type	Tur bearing blackwall rocks				
Sample	SY309B	SY400B	SY401B	SY412	SY420

Rare earth elements (μg/g), ICP-MS

La	12.1	36.9	10.9	1.41	63.8
Ce	33.4	86.1	24.4	4.92	131
Pr	3.48	10.5	3.16	0.86	15.9
Nd	14.7	38.9	13.8	5.66	61.6
Sm	3.47	7.75	3.23	2.12	13.8
Eu	1.41	1.51	1.27	1.36	4.69
Gd	3.68	7.51	3.19	3.02	13.9
Tb	0.59	1.16	0.48	0.52	2.22
Dy	4.05	7.74	3.12	4.01	15.0
Ho	0.87	1.58	0.65	0.80	2.88
Er	2.71	4.71	1.99	2.46	7.90
Tm	0.39	0.71	0.26	0.33	0.97
Yb	2.75	4.82	1.89	2.43	5.70
Lu	0.45	0.82	0.26	0.38	0.95

Pb, Th, U (μg/g), ICP-MS

Pb	0.77	2.18	0.74	0.58	59.6
Th	2.83	3.79	5.23	*d.l.*	16.8
U	0.91	0.39	0.54	*d.l.*	6.31

Li, Be (μg/g), ICP-AES

Li	31.7	76.8	20.2	60.2	36.2
Be	0.65	3.2	0.51	0.75	0.68

B, Cl (μg/g), PGNAA

B	3,960	351	15,308	93.4	8,760
Cl	524	10	*n.a.*	56	*d.l.*

B /Be	6,092	111	30,015	124	12,882
B /Nb	750	49	5,091	31	663
Li /Yb	12	16	11	25	6.4
Be /Nd	0.044	0.082	0.037	0.13	0.011
Cl /K	9.01	0.001		0.008	
Ce /Pb	44	39	33	8.5	2.2
La /Yb$_{cn}$	3.0	5.2	3.9	0.39	7.6
Ce /Ce*	1.24	1.05	1.00	1.07	0.99
Eu /Eu*	1.21	0.61	1.21	1.65	1.03

D. Representative mineral analyses determined by electron probe micro analysis (EPMA)

The following tables include representative mineral analyses from EPMA. For minerals that show relatively homogeneous chemical compositions only one representative analysis is given. In case of zoned minerals, two or more analyses are given. For each analysis, the oxide analysis from EPMA and the calculated formulas are given. The analyses are grouped by minerals as follows:

Table D.1: Garnet
Table D.2: Clinopyroxene
Table D.3: Phengite, paragonite and biotite
Table D.4: Na-, Ca- and Na-Ca-amphibole
Table D.5: Chlorite
Table D.6: Epidote and clinozoisite
Table D.7: Albite
Table D.8: Talc, antigorite, lawsonite and chloritoid
Table D.9: Rutile
Table D.10: Hematite, magnetite and ilmenite
Table D.11: Apatite
Table D.12: Titanite

Table D.1. Garnet

Sample	SY109			SY112		SY304	SY308		SY314			SY323					
Mineral Type	Grt core	Grt rim I	Grt rim II	Grt core	Grt rim	Grt	Grt core	Grt rim	Grt core	Grt rim I	Grt rim II	Grt core	Grt rim I	Grt rim II	Grt rim III	Adr type II	Grs type II
SiO_2	37.20	37.24	37.44	37.81	37.97	37.19	37.26	37.29	36.70	37.49	36.87	36.45	36.76	36.89	37.75	33.82	36.30
TiO_2	0.31	0.15	0.04	0.12	0.07	0.09	0.13	0.01	0.21	0.00	0.02	0.16	0.09	0.10	0.12	3.12	0.84
Al_2O_3	20.12	20.34	20.67	20.50	20.20	20.80	20.42	20.75	19.15	20.77	20.29	20.06	20.11	20.46	20.74	2.78	9.05
Cr_2O_3	0.00	0.03	0.01	0.02	0.01	0.04	0.00	0.02	0.01	0.00	0.01	0.03	0.00	0.00	0.07	0.02	0.05
Fe_2O_3	1.42	0.84	1.30	1.41	1.08	1.61	1.42	1.32	2.17	1.73	2.26	2.29	1.94	1.88	0.45	25.27	17.75
FeO	25.67	29.38	32.90	28.71	28.57	28.00	28.35	28.36	8.13	26.46	28.26	22.83	30.69	28.02	14.78	0.00	0.41
MnO	5.68	1.72	0.29	1.43	0.66	2.85	2.98	1.18	25.95	4.94	7.50	10.26	0.77	1.34	12.70	3.51	0.00
MgO	0.78	0.83	1.84	3.38	3.91	2.89	0.98	1.79	0.58	3.52	1.00	0.87	2.27	2.30	0.97	0.01	4.03
CaO	9.10	9.31	6.41	6.92	7.07	6.63	9.00	9.14	6.65	5.53	4.75	6.99	6.62	8.27	12.27	30.88	30.91
Na_2O	0.06	0.03	0.02	0.06	0.04	0.00	0.00	0.02	0.02	0.00	0.04	0.00	0.01	0.03	0.02	0.03	0.02
K_2O	0.00	0.00	0.01	0.00	0.00	0.00	0.00	0.02	0.00	0.00	0.06	0.01	0.00	0.00	0.02	0.00	0.00
Total	100.34	99.85	100.93	100.36	99.59	100.10	100.56	99.89	99.56	100.43	101.06	99.93	99.27	99.29	99.89	99.43	99.34

Formulas calculated to 12 oxygens and 8 cations

Si	2.990	3.002	2.988	2.997	3.020	2.967	2.986	2.983	2.999	2.977	2.972	2.960	2.976	2.969	3.006	2.860	2.967
Ti	0.019	0.009	0.003	0.007	0.004	0.005	0.008	0.001	0.013	0.000	0.001	0.010	0.006	0.006	0.007	0.198	0.051
Al	1.906	1.932	1.944	1.915	1.893	1.956	1.928	1.957	1.844	1.944	1.928	1.919	1.919	1.940	1.946	0.277	0.872
Cr	0.000	0.002	0.001	0.001	0.001	0.003	0.000	0.001	0.001	0.000	0.001	0.002	0.000	0.000	0.005	0.001	0.003
Fe^{3+}	0.086	0.051	0.078	0.084	0.065	0.097	0.086	0.079	0.134	0.103	0.137	0.140	0.118	0.114	0.027	1.608	1.091
Fe^{2+}	1.726	1.980	2.196	1.903	1.900	1.868	1.900	1.897	0.556	1.757	1.905	1.550	2.078	1.886	0.984	0.000	0.028
Mn	0.387	0.118	0.020	0.096	0.044	0.192	0.202	0.080	1.797	0.332	0.512	0.705	0.053	0.091	0.857	0.251	0.279
Mg	0.094	0.099	0.219	0.399	0.463	0.344	0.117	0.213	0.071	0.417	0.120	0.105	0.274	0.276	0.115	0.002	0.000
Ca	0.784	0.804	0.548	0.588	0.603	0.567	0.773	0.783	0.582	0.470	0.410	0.608	0.574	0.713	1.047	2.798	2.706
Na	0.010	0.005	0.003	0.009	0.006	0.001	0.000	0.003	0.003	0.000	0.007	0.000	0.001	0.004	0.003	0.005	0.003
K	0.000	0.000	0.001	0.000	0.000	0.000	0.000	0.002	0.000	0.000	0.006	0.001	0.000	0.000	0.002	0.000	0.000
X_{Mg}	0.052	0.048	0.091	0.173	0.196	0.156	0.058	0.101	0.113	0.192	0.059	0.063	0.116	0.128	0.104	n.n.	n.n.
Prp	3.1	3.3	7.3	13.4	15.4	11.6	3.9	7.2	2.4	14.0	4.1	3.5	9.2	9.3	3.8	0.0	0.0
Alm	57.7	66.0	73.6	63.7	63.1	62.9	63.5	63.8	18.5	59.0	64.6	52.2	69.8	63.6	32.8	0.0	0.9
Sps	12.9	3.9	0.7	3.2	1.5	6.5	6.8	2.7	59.8	11.2	17.4	23.8	1.8	3.1	28.5	8.2	9.3
Grs	21.9	24.2	14.5	15.5	16.7	14.4	21.6	22.4	12.6	10.8	7.3	13.7	13.5	18.5	33.5	6.5	34.3
Adr	4.3	2.6	3.9	4.2	3.3	4.7	4.3	3.9	6.8	5.0	6.6	6.8	5.8	5.6	1.4	85.3	55.5

Table D.1. Garnet continued

Sample	SY344		SY403			SY406			SY412		SY415		SY420			SY425D		SY425G	
Mineral Type	Grt core	Grt rim	Grt core	Grt 2	Grt rim	Grt core	Grt rim I	Grt rim II	Grt core	Grt rim	Grt 2	Grt rim	Grt 1	Grt 2	Grt 3	Grt core	Grt rim	Grt core	Grt rim
SiO_2	37.50	37.52	37.28	37.31	37.14	36.61	36.77	37.32	37.49	37.84	36.54	37.06	37.32	37.44	37.76	36.68	37.18	37.17	37.63
TiO_2	0.15	0.06	0.15	0.13	0.06	0.12	0.03	0.00	0.20	0.08	0.08	0.13	0.24	0.21	0.16	0.15	0.07	0.17	0.08
Al_2O_3	20.54	20.93	20.76	21.02	20.86	19.38	20.08	20.30	20.41	20.92	19.71	20.33	20.79	20.95	20.35	20.47	21.23	20.47	20.74
Cr_2O_3	0.02	0.01	0.01	0.03	0.07	0.00	0.07	0.03	0.02	0.01	0.05	0.00	0.04	0.04	0.05	0.00	0.00	0.00	0.03
Fe_2O_3	1.79	1.74	1.31	0.79	1.65	2.92	2.26	1.27	1.11	0.75	2.20	0.88	1.38	1.23	1.36	2.97	1.65	0.93	1.12
FeO	24.17	25.04	20.79	22.35	24.68	24.62	29.98	23.44	24.02	26.29	22.59	29.68	25.58	28.59	11.85	25.44	26.08	24.98	27.86
MnO	3.44	1.86	8.39	6.23	2.98	10.04	5.73	9.85	5.19	4.22	8.93	1.05	2.89	0.93	15.30	2.63	1.97	5.14	1.27
MgO	2.25	2.57	1.70	1.64	1.91	1.79	2.10	1.70	1.40	1.73	0.22	0.39	0.99	1.24	1.11	1.67	2.83	1.67	2.80
CaO	10.29	10.45	9.51	10.21	10.40	4.38	3.47	5.77	10.23	9.10	9.05	9.92	11.29	10.31	12.36	10.01	8.82	8.82	8.40
Na_2O	0.02	0.00	0.04	0.01	0.00	0.06	0.00	0.06	0.03	0.00	0.03	0.06	0.02	0.00	0.02	0.02	0.02	0.03	0.03
K_2O	0.01	0.01	0.00	0.00	0.01	0.00	0.00	0.16	0.00	0.00	0.00	0.01	0.00	0.01	0.02	0.00	0.01	0.00	0.01
Total	100.18	100.18	99.94	99.73	99.75	99.93	100.49	99.90	100.10	100.94	99.40	99.48	100.55	100.93	100.32	100.03	99.85	99.38	99.96

Formulas calculated to 12 oxygens and 8 cations

	SY344		SY403			SY406			SY412		SY415		SY420			SY425D		SY425G	
Si	2.978	2.969	2.978	2.980	2.965	2.979	2.971	3.009	2.995	2.996	2.981	3.001	2.970	2.970	2.998	2.937	2.954	2.993	2.992
Ti	0.009	0.003	0.009	0.008	0.003	0.007	0.002	0.000	0.012	0.005	0.005	0.008	0.014	0.013	0.009	0.009	0.004	0.010	0.005
Al	1.922	1.952	1.954	1.979	1.962	1.858	1.913	1.929	1.922	1.953	1.895	1.940	1.950	1.959	1.905	1.932	1.988	1.943	1.943
Cr	0.001	0.001	0.001	0.002	0.004	0.000	0.004	0.002	0.001	0.001	0.003	0.000	0.002	0.003	0.003	0.000	0.000	0.000	0.002
Fe^{3+}	0.107	0.104	0.079	0.048	0.099	0.179	0.137	0.077	0.067	0.045	0.135	0.054	0.083	0.074	0.081	0.179	0.099	0.056	0.067
Fe^{2+}	1.605	1.657	1.389	1.493	1.647	1.675	2.026	1.581	1.605	1.741	1.541	2.010	1.702	1.897	0.787	1.704	1.733	1.682	1.853
Mn	0.231	0.124	0.567	0.422	0.201	0.692	0.392	0.673	0.351	0.283	0.617	0.072	0.195	0.062	1.029	0.178	0.133	0.351	0.086
Mg	0.266	0.303	0.203	0.195	0.227	0.218	0.253	0.204	0.167	0.204	0.026	0.047	0.118	0.146	0.132	0.199	0.335	0.200	0.332
Ca	0.876	0.886	0.814	0.873	0.889	0.382	0.301	0.499	0.876	0.772	0.791	0.860	0.963	0.876	1.051	0.859	0.751	0.760	0.715
Na	0.003	0.000	0.002	0.000	0.000	0.009	0.001	0.010	0.004	0.000	0.005	0.009	0.003	0.000	0.002	0.003	0.003	0.000	0.004
K	0.001	0.001	0.000	0.000	0.001	0.000	0.000	0.017	0.000	0.000	0.000	0.001	0.000	0.001	0.002	0.000	0.001	0.000	0.001
X_{Mg}	0.142	0.155	0.127	0.116	0.121	0.115	0.111	0.114	0.094	0.105	0.017	0.023	0.065	0.072	0.144	0.105	0.162	0.106	0.152
Prp	8.9	10.2	6.8	6.5	7.7	7.3	8.5	6.9	5.6	6.8	0.9	1.6	4.0	4.9	4.4	6.8	11.3	6.7	11.1
Alm	53.9	55.8	46.7	50.0	55.6	56.5	68.2	53.5	53.5	58.0	51.8	67.3	57.2	63.6	26.2	58.0	58.7	56.2	62.1
Sps	7.8	4.2	19.1	14.1	6.8	23.3	13.2	22.7	11.7	9.4	20.7	2.4	6.5	2.1	34.3	6.1	4.5	11.7	2.9
Grs	24.1	24.8	23.5	26.9	25.2	4.1	3.4	13.0	25.8	23.5	19.9	26.1	28.3	25.8	31.0	20.8	20.7	22.6	20.6
Adr	5.3	5.1	3.9	2.4	4.8	8.8	6.7	3.8	3.4	2.2	6.7	2.7	4.1	3.6	4.1	8.5	4.7	2.8	3.3

Table D.2. Clinopyroxene

Sample	SY2	SY109		SY112		SY308	SY309B	SY323	SY327					SY328					
Mineral Type	Omp	Jd core	Omp rim	Omp	Omp	Jd core	Omp rim	Omp	Omp Na-rich	Omp Ca-rich	Acm Ca-rich	Acm Al-rich	Acm Fe^{3+}-rich	Omp core	Jd rim	Agt	Jd	Omp	Acm
SiO_2	56.17	57.21	55.43	54.76	54.88	57.84	55.43	55.46	55.75	54.22	50.94	52.86	52.05	55.55	56.49	53.96	57.91	55.51	53.66
TiO_2	0.07	0.05	0.07	0.06	0.25	0.03	0.07	0.08	0.03	0.02	0.26	0.20	0.15	0.09	0.03	0.06	0.27	0.13	0.16
Al_2O_3	10.92	16.24	10.85	5.70	8.02	18.72	10.16	8.90	9.04	6.09	2.42	4.62	1.24	8.65	12.47	3.43	19.08	11.65	5.25
Cr_2O_3	0.34	0.03	0.00	0.00	0.00	0.00	0.00	0.15	0.00	0.09	0.00	0.03	0.02	0.00	0.00	0.00	0.01	0.00	0.02
Fe_2O_3	1.20	4.13	8.40	6.64	7.66	3.70	6.43	6.60	4.40	8.02	17.99	15.12	28.83	9.83	9.40	17.12	5.11	9.13	20.86
FeO	2.06	4.24	3.86	1.72	1.04	2.46	3.52	1.91	3.21	1.65	7.61	6.36	0.42	2.85	2.57	3.10	1.01	1.29	1.09
MnO	0.03	0.06	0.03	0.05	0.12	0.08	0.23	0.15	0.30	0.40	3.23	0.83	2.00	0.09	0.03	0.09	0.05	0.05	0.00
MgO	8.60	1.71	3.92	9.90	8.08	1.58	5.47	7.31	7.78	8.86	0.56	2.46	0.95	5.26	2.98	5.00	1.04	4.46	2.83
CaO	13.50	3.73	7.93	15.75	13.27	3.31	10.85	11.53	12.84	14.59	9.21	8.87	2.83	8.81	4.92	8.86	1.70	7.11	5.02
Na_2O	7.01	12.15	9.76	5.59	7.17	12.85	8.39	7.87	12.84	6.11	9.21	8.72	11.78	9.25	11.49	8.86	13.89	10.37	11.16
K_2O	0.00	0.00	0.02	0.01	0.01	0.00	0.01	0.01	0.01	0.00	0.01	0.01	0.00	0.00	0.02	0.00	0.00	0.00	0.00
Total	99.89	99.55	100.26	100.18	100.50	100.56	100.57	99.95	100.44	100.05	100.31	100.08	100.27	100.38	100.42	100.49	100.05	99.69	100.06

Formulas calculated to 6 oxygens and 4 cations

	SY2	SY109		SY112		SY308	SY309B	SY323	SY327					SY328					
Si	1.990	2.021	1.995	1.983	1.970	2.001	1.988	1.993	1.995	1.973	1.978	1.995	1.989	2.004	2.009	2.003	2.003	1.988	1.991
Ti	0.002	0.001	0.002	0.002	0.007	0.001	0.002	0.002	0.001	0.000	0.008	0.006	0.004	0.002	0.001	0.002	0.007	0.003	0.005
Al	0.456	0.676	0.460	0.243	0.339	0.763	0.430	0.377	0.381	0.261	0.111	0.206	0.056	0.368	0.523	0.150	0.778	0.491	0.229
Cr	0.009	0.001	0.000	0.000	0.000	0.000	0.000	0.004	0.000	0.003	0.000	0.001	0.001	0.000	0.000	0.000	0.000	0.000	0.001
Fe^{3+}	0.032	0.110	0.227	0.181	0.207	0.096	0.174	0.178	0.118	0.220	0.526	0.429	0.829	0.267	0.252	0.478	0.133	0.246	0.582
Fe^{2+}	0.061	0.125	0.116	0.052	0.031	0.071	0.106	0.057	0.096	0.050	0.247	0.201	0.013	0.086	0.076	0.096	0.029	0.039	0.034
Mn	0.001	0.002	0.001	0.001	0.004	0.002	0.007	0.004	0.009	0.012	0.106	0.027	0.065	0.003	0.001	0.003	0.001	0.001	0.000
Mg	0.454	0.090	0.210	0.534	0.432	0.081	0.293	0.391	0.415	0.480	0.032	0.139	0.054	0.283	0.158	0.277	0.054	0.238	0.156
Ca	0.513	0.141	0.306	0.611	0.510	0.123	0.417	0.444	0.492	0.569	0.383	0.359	0.116	0.341	0.188	0.352	0.063	0.273	0.200
Na	0.482	0.832	0.681	0.392	0.499	0.862	0.584	0.548	0.491	0.431	0.608	0.638	0.873	0.647	0.792	0.638	0.932	0.720	0.803
K	0.000	0.000	0.001	0.000	0.000	0.000	0.000	0.001	0.000	0.000	0.001	0.000	0.000	0.000	0.001	0.000	0.000	0.000	0.000
X_{Mg}	0.882	0.418	0.644	0.911	0.932	0.533	0.735	0.872	0.812	0.905	0.116	0.409	0.802	0.767	0.674	0.742	0.647	0.860	0.823
Jd	45.0	72.2	45.4	21.1	29.2	76.6	41.0	37.0	37.3	21.1	8.2	20.9	4.4	38.0	54.1	16.0	79.9	47.4	22.0
Acm	3.2	11.0	22.7	18.1	20.7	9.6	17.4	17.8	11.8	22.0	52.6	42.9	82.9	26.7	25.2	47.8	13.3	24.6	58.2
Aug	50.3	14.1	30.1	59.3	48.0	12.3	40.5	43.7	48.8	54.2	36.2	35.4	10.5	34.1	18.8	35.2	6.3	26.0	19.0
Cat	1.0	0.0	0.5	1.7	3.0	0.0	1.2	0.7	0.5	2.7	2.2	0.5	1.1	0.0	0.0	0.0	0.0	1.2	0.9

Mineral abbriviations are: Acm = acmite; Agt = aegirin-augite; Jd = jadeite; Omp = omphacite.

Table D.2. Clinopyroxene continued

Sample	SY344	SY402A		SY402B		SY406			SY412			SY413	SY415	SY425D	SY438	SY441	SY442	
Mineral Type	Omp	Omp core	Omp rim	Omp core	Omp rim	Jd core	Omp at crack	Agt	Omp core I	Omp core II	Jd rim	Omp	Jd	Omp	Omp	Omp	Omp core	Omp rim
SiO$_2$	55.86	56.43	55.46	56.40	55.78	55.22	55.22	52.88	55.67	55.22	56.25	55.80	58.88	54.35	56.20	56.17	55.21	56.03
TiO$_2$	0.12	0.10	0.10	0.24	0.07	0.01	0.04	0.01	0.20	0.03	0.06	0.16	0.01	0.10	0.01	0.08	0.08	0.05
Al$_2$O$_3$	11.04	12.28	10.17	13.62	10.86	10.40	9.45	3.43	10.20	7.88	12.29	10.54	21.32	10.27	10.57	10.62	8.34	12.41
Cr$_2$O$_3$	0.00	0.00	0.00	0.06	0.06	0.00	0.00	0.05	0.00	0.02	0.02	0.07	0.00	0.02	0.00	0.00	0.00	0.01
Fe$_2$O$_3$	3.61	6.67	7.96	6.67	5.74	15.29	9.57	19.68	5.50	11.76	11.33	4.37	0.49	7.11	3.20	3.85	8.14	7.00
FeO	3.21	1.44	2.35	2.20	1.92	1.91	0.90	4.13	3.98	2.88	2.97	3.43	4.06	2.80	1.88	2.70	3.86	3.86
MnO	0.16	0.20	0.22	0.15	0.17	0.11	0.26	0.69	0.00	0.10	0.06	0.13	0.03	0.10	0.20	0.21	0.16	0.08
MgO	6.63	5.36	5.69	3.82	6.66	1.88	6.13	2.70	6.17	4.79	1.97	6.33	0.31	6.08	7.72	6.88	6.00	3.64
CaO	12.13	8.06	9.37	6.20	10.43	3.34	9.77	7.42	10.90	8.67	3.56	11.26	0.87	10.40	12.16	10.83	10.28	6.41
Na$_2$O	7.80	9.93	8.99	10.90	8.49	12.16	8.94	9.50	8.14	9.37	12.12	8.11	13.94	8.19	7.71	8.24	8.24	10.44
K$_2$O	0.01	0.00	0.00	0.00	0.02	0.00	0.00	0.01	0.01	0.00	0.01	0.00	0.01	0.01	0.00	0.00	0.00	0.00
Total	100.56	100.47	100.30	100.26	100.20	100.33	100.27	100.50	100.77	100.70	100.63	100.19	99.92	99.43	99.65	99.58	100.30	99.93

Formulas calculated to 6 oxygens and 4 cations

Si	1.986	1.993	1.988	1.994	1.986	1.996	1.981	1.991	1.989	1.999	2.007	1.995	2.026	1.969	2.002	2.008	1.998	2.005
Ti	0.003	0.003	0.003	0.006	0.002	0.000	0.001	0.000	0.005	0.001	0.002	0.004	0.000	0.003	0.000	0.002	0.002	0.001
Al	0.463	0.511	0.429	0.568	0.456	0.443	0.399	0.152	0.429	0.336	0.517	0.444	0.864	0.439	0.444	0.447	0.356	0.523
Cr	0.000	0.000	0.000	0.002	0.002	0.000	0.000	0.001	0.000	0.000	0.001	0.002	0.000	0.000	0.000	0.000	0.000	0.000
Fe^{3+}	0.097	0.177	0.215	0.177	0.154	0.416	0.258	0.558	0.148	0.320	0.304	0.117	0.013	0.194	0.086	0.104	0.222	0.189
Fe^{2+}	0.095	0.043	0.070	0.065	0.057	0.058	0.027	0.130	0.119	0.087	0.089	0.103	0.117	0.085	0.056	0.081	0.117	0.116
Mn	0.005	0.006	0.007	0.005	0.005	0.003	0.008	0.022	0.000	0.003	0.002	0.004	0.001	0.003	0.006	0.006	0.005	0.003
Mg	0.351	0.282	0.304	0.202	0.354	0.102	0.328	0.151	0.329	0.258	0.105	0.337	0.016	0.328	0.410	0.367	0.324	0.194
Ca	0.462	0.305	0.360	0.235	0.398	0.129	0.375	0.299	0.417	0.336	0.136	0.431	0.032	0.404	0.464	0.415	0.399	0.246
Na	0.537	0.680	0.625	0.747	0.586	0.852	0.622	0.694	0.564	0.658	0.838	0.562	0.930	0.575	0.533	0.571	0.578	0.724
K	0.000	0.000	0.000	0.000	0.001	0.000	0.000	0.001	0.001	0.000	0.000	0.000	0.000	0.001	0.000	0.000	0.000	0.000
X$_{Mg}$	0.786	0.869	0.812	0.756	0.861	0.638	0.924	0.538	0.735	0.747	0.542	0.767	0.120	0.795	0.880	0.819	0.735	0.627
Jd	44.1	50.3	41.0	57.0	43.2	43.6	36.3	13.6	41.6	33.7	53.4	44.5	91.7	38.2	44.7	46.7	35.7	53.5
Acm	9.7	17.7	21.5	17.7	15.4	41.6	25.8	55.8	14.8	32.0	30.4	11.7	1.3	19.4	8.6	10.4	22.2	18.9
Aug	44.8	29.8	34.7	22.9	38.4	12.6	35.6	29.1	40.6	33.6	13.6	42.6	3.2	37.3	46.4	41.5	39.7	24.6
Cat	1.4	0.7	1.2	0.6	1.4	0.4	1.9	0.9	1.1	0.1	0.0	0.5	0.0	3.1	0.0	0.0	0.2	0.0

Table D.3. Phengite, paragonite and biotite

Sample	Sy2		SY109		SY112	SY304		SY308	SY309A	SY309B	SY314		SY323	SY327	SY335	SY344
Mineral Type	Phe core	Phe rim	Phe	Pg	Phe	Phe	Pg	Pg	Phe	Phe	Phe	Bt-Chl	Bt-Chl	Bt-Chl	Phe	Phe
SiO_2	50.66	51.97	50.29	47.97	50.96	51.45	46.63	48.35	51.73	53.05	50.34	36.44	37.37	35.52	51.29	52.35
TiO_2	0.16	0.06	0.47	0.05	0.25	0.16	0.06	0.03	0.19	0.05	0.17	0.51	0.05	0.43	0.17	0.17
Al_2O_3	26.45	25.17	27.78	39.13	25.61	27.18	36.74	39.04	26.38	25.48	26.30	12.23	12.15	14.33	25.69	28.79
Cr_2O_3	0.07	0.15	0.00	0.03	0.04	0.02	0.00	0.00	0.00	0.13	0.00	0.00	0.00	0.00	0.06	0.00
FeO	1.89	1.45	3.28	0.91	3.28	3.63	1.67	0.67	2.97	2.67	4.63	24.16	18.70	23.84	2.50	1.65
MnO	0.00	0.03	0.00	0.01	0.00	0.00	0.02	0.00	0.02	0.01	0.03	1.16	1.54	0.16	0.00	0.02
MgO	3.76	4.25	2.54	0.18	3.53	3.21	0.38	0.17	3.62	4.05	2.73	9.99	13.83	9.86	3.87	3.41
BaO	0.28	0.23														
CaO	0.00	0.01	0.05	0.31	0.00	0.01	0.10	0.13	0.07	0.00	0.00	0.09	0.28	0.11	0.10	0.04
Na_2O	0.41	0.32	0.84	5.36	0.37	0.31	5.91	6.17	0.36	0.14	0.54	0.10	0.16	0.11	0.37	0.52
K_2O	10.28	10.32	9.67	0.63	10.66	9.82	2.27	0.78	10.57	10.59	10.18	8.24	9.18	9.14	10.79	9.27
H_2O	4.43	4.45	4.47	4.69	4.44	4.51	4.57	4.72	4.51	4.54	4.43	3.73	3.50	3.76	4.46	4.60
Total	98.38	98.39	99.39	99.25	99.13	100.30	98.35	100.05	100.41	100.72	99.33	96.64	96.77	97.24	99.28	100.81

Formulas calculated to 10 oxygens + 2 OH; $Fe^{2+} = Fe^t$

Si	3.426	3.502	3.374	3.065	3.444	3.418	3.061	3.071	3.440	3.504	3.409	2.930	3.199	2.835	3.450	3.412
Ti	0.008	0.003	0.024	0.002	0.013	0.008	0.003	0.001	0.009	0.002	0.009	0.031	0.003	0.026	0.009	0.008
Al	2.108	1.999	2.196	2.946	2.040	2.128	2.843	2.922	2.067	1.983	2.099	1.159	1.225	1.348	2.036	2.211
Cr	0.004	0.008	0.000	0.001	0.002	0.001	0.000	0.000	0.000	0.007	0.000	0.000	0.000	0.000	0.003	0.000
Fe^{2+}	0.107	0.082	0.184	0.049	0.186	0.202	0.000	0.035	0.165	0.148	0.262	1.625	1.339	1.591	0.141	0.090
Mn	0.000	0.001	0.000	0.000	0.000	0.000	0.001	0.000	0.001	0.001	0.001	0.079	0.112	0.010	0.000	0.001
Mg	0.379	0.427	0.254	0.017	0.355	0.318	0.037	0.016	0.359	0.399	0.276	1.198	1.765	1.173	0.388	0.331
Ba	0.008	0.006														
Ca	0.000	0.000	0.004	0.021	0.000	0.000	0.007	0.009	0.005	0.000	0.000	0.008	0.026	0.009	0.007	0.002
Na	0.053	0.041	0.110	0.664	0.048	0.040	0.752	0.760	0.046	0.018	0.071	0.016	0.027	0.017	0.048	0.066
K	0.887	0.887	0.828	0.051	0.919	0.832	0.190	0.064	0.897	0.892	0.880	0.845	1.003	0.930	0.926	0.771
Total	6.980	6.956	6.973	6.817	7.006	6.946	6.986	6.878	6.989	6.954	7.008	7.890	8.700	7.939	7.008	6.893
X_{Mg}	0.780	0.839	0.580	0.257	0.657	0.612	0.288	0.311	0.685	0.730	0.513	0.424	0.569	0.424	0.734	0.787

Table D.3. Phengite, paragonite and biotite continued

Sample	SY402C	SY403	SY406		SY412		SY413	SY415	SY420		SY432		SY438		SY441	SY442
Mineral Type	Bt-Chl	Pg	Phe	Bt	Phe	Bt	Phe	Phe	Phe core	Phe rim	Phe	Pg	Phe core	Ms at Lws	Bt	Bt-Chl
SiO$_2$	40.12	48.58	53.44	35.08	51.28	38.37	52.17	50.90	49.48	47.57	48.95	49.18	51.12	46.63	39.43	36.38
TiO$_2$	0.14	0.13	0.13	0.88	0.25	0.31	0.10	0.10	0.10	0.12	0.14	0.03	0.13	0.01	0.79	0.76
Al$_2$O$_3$	14.04	38.51	24.83	13.32	26.61	15.68	24.94	28.11	27.38	27.42	26.99	39.42	26.78	38.29	16.48	13.63
Cr$_2$O$_3$	0.00	0.00	0.08	0.07	0.03	0.00	0.10	0.00	0.07	0.08	0.08	0.02	0.01	0.02	0.02	0.00
FeO	9.62	0.86	4.43	28.50	4.03	18.16	4.07	3.52	3.13	4.66	4.40	1.33	1.99	0.17	9.40	22.87
MnO	0.20	0.04	0.09	1.17	0.00	0.34	0.08	0.09	0.06	0.09	0.00	0.00	0.00	0.01	0.18	0.24
MgO	19.20	0.49	3.71	6.58	3.00	12.96	3.50	2.38	3.28	2.99	2.59	0.13	3.62	0.22	18.66	10.53
BaO									0.32	0.78	0.30		0.21	0.03		
CaO	0.23	0.04	0.00	0.04	0.01	0.01	0.06	0.01	0.00	0.01	0.06	0.29	0.00	0.24	0.16	0.10
Na$_2$O	0.08	6.06	0.18	0.02	0.59	0.10	0.23	0.30	0.28	0.21	0.66	5.48	0.50	2.24	0.15	0.16
K$_2$O	8.16	1.24	9.49	8.75	10.41	9.65	10.44	10.05	10.88	10.63	10.23	0.71	10.62	7.63	9.63	7.99
H$_2$O	4.02	4.73	4.54	3.69	4.50	3.98	4.48	4.50	4.43	4.35	4.38	4.78	4.48	4.60	4.13	3.77
Total	95.80	100.69	100.92	98.10	100.71	99.55	100.16	99.97	99.41	98.90	98.78	101.37	99.47	100.08	99.01	96.42
Formulas calculated to 10 oxygens + 2 OH; $Fe^{2+} = Fe^t$																
Si	2.990	3.078	3.529	2.850	3.417	2.891	3.492	3.395	3.350	3.278	3.349	3.083	3.425	3.040	2.863	2.892
Ti	0.008	0.006	0.006	0.054	0.012	0.018	0.005	0.005	0.005	0.006	0.007	0.002	0.006	0.000	0.043	0.045
Al	1.233	2.875	1.932	1.275	2.089	1.392	1.967	2.210	2.185	2.227	2.176	2.912	2.114	2.941	1.410	1.277
Cr	0.000	0.000	0.004	0.004	0.002	0.000	0.005	0.000	0.004	0.004	0.004	0.001	0.001	0.001	0.001	0.000
Fe^{2+}	0.599	0.046	0.245	1.937	0.224	1.144	0.228	0.197	0.177	0.268	0.252	0.070	0.111	0.009	0.571	1.520
Mn	0.013	0.002	0.005	0.081	0.000	0.021	0.004	0.005	0.003	0.005	0.000	0.000	0.000	0.000	0.011	0.016
Mg	2.133	0.046	0.365	0.797	0.298	1.456	0.349	0.236	0.331	0.307	0.264	0.013	0.361	0.021	2.020	1.248
Ba									0.008	0.021	0.008		0.005	0.001		
Ca	0.018	0.003	0.000	0.004	0.001	0.001	0.004	0.001	0.000	0.000	0.005	0.019	0.000	0.017	0.012	0.009
Na	0.012	0.745	0.023	0.003	0.076	0.014	0.030	0.039	0.037	0.028	0.087	0.666	0.065	0.283	0.021	0.024
K	0.776	0.100	0.799	0.907	0.885	0.928	0.891	0.855	0.940	0.935	0.893	0.057	0.907	0.634	0.892	0.810
Total	7.780	6.901	6.908	7.911	7.005	7.866	6.977	6.942	7.039	7.081	7.044	6.821	6.998	6.948	7.844	7.841
X_{Mg}	0.781	0.503	0.599	0.292	0.570	0.560	0.605	0.546	0.652	0.534	0.512	0.152	0.765	0.689	0.780	0.451

Table D.4. Amphibole

Sample	SY2		SY109		SY112			SY304	SY308		SY309A	SY309B	SY314		
Mineral Type	Act	Act	Fgl core	Fgl rim	Bar	Win	Gln	Gln	Gln	Win	Gln	Gln	Gln core	Fgl rim I	Gln rim II
SiO$_2$	56.17	52.93	56.76	54.34	51.29	53.81	57.26	56.73	57.86	51.93	57.87	57.89	56.88	54.81	56.79
TiO$_2$	0.02	0.11	0.02	0.14	0.09	0.07	0.03	0.01	0.03	0.04	0.04	0.02	0.04	0.05	0.03
Al$_2$O$_3$	1.86	5.80	10.14	11.25	7.64	4.76	9.23	8.62	10.32	2.71	10.21	9.99	8.88	7.18	7.60
Cr$_2$O$_3$	0.02	0.07	0.00	0.00	0.05	0.00	0.03	0.02	0.03	0.01	0.00	0.11	0.03	0.06	0.00
Fe$_2$O$_3$	0.75	0.63	2.51	1.72	2.70	2.03	2.14	2.63	2.80	5.99	2.38	2.79	3.32	6.34	6.92
FeO	7.02	8.24	13.31	13.85	9.29	8.97	9.00	10.63	10.49	16.53	7.57	7.35	9.92	16.61	9.76
MnO	0.12	0.07	0.00	0.00	0.13	0.16	0.06	0.07	0.09	0.20	0.03	0.11	0.12	0.07	0.35
MgO	18.57	16.24	7.19	6.86	13.76	14.93	11.18	10.48	8.82	9.56	11.27	11.56	10.09	4.74	8.68
CaO	11.64	10.60	0.16	1.16	8.32	8.81	1.36	1.59	0.21	5.03	0.23	0.45	0.71	0.13	0.09
Na$_2$O	1.00	2.19	7.36	6.93	3.42	2.79	6.72	6.67	7.31	4.47	7.48	7.36	7.12	7.16	7.27
K$_2$O	0.07	0.17	0.01	0.10	0.36	0.15	0.05	0.02	0.00	0.03	0.02	0.01	0.02	0.03	0.00
H$_2$O	2.15	2.12	2.15	2.11	2.10	2.11	2.17	2.16	2.19	2.01	2.20	2.20	2.16	2.07	2.15
Total	99.39	99.16	99.61	98.48	99.20	98.67	99.22	99.65	100.14	98.55	99.33	99.87	99.30	99.28	99.66

Formulas calculated to 22 oxygens + 2 OH; Fe^{2+}/Fe^{3+} calculated after Schumacher (1997)

T-site															
Si	7.895	7.525	7.990	7.791	7.374	7.716	7.954	7.935	7.998	7.787	7.964	7.936	7.961	7.997	7.997
Al	0.105	0.475	0.010	0.209	0.626	0.284	0.046	0.065	0.002	0.213	0.036	0.064	0.039	0.003	0.003
C-site															
Al	0.203	0.498	1.672	1.693	0.668	0.521	1.465	1.356	1.679	0.266	1.619	1.551	1.426	1.231	1.259
Ti	0.002	0.011	0.002	0.015	0.009	0.007	0.003	0.001	0.003	0.004	0.004	0.002	0.004	0.005	0.003
Fe^{3+}	0.079	0.067	0.265	0.186	0.292	0.219	0.223	0.277	0.291	0.676	0.247	0.288	0.350	0.696	0.733
Cr	0.002	0.007	0.000	0.000	0.005	0.000	0.004	0.002	0.000	0.002	0.000	0.011	0.003	0.007	0.000
Mg	3.891	3.442	1.510	1.467	2.948	3.192	2.316	2.186	1.817	2.137	2.313	2.363	2.106	1.031	1.823
Fe^{2+}	0.823	0.975	1.551	1.639	1.078	1.061	0.989	1.178	1.210	1.915	0.817	0.785	1.111	2.026	1.150
Mn	0.000	0.000	0.000	0.000	0.000	0.000	0.000	0.000	0.000	0.000	0.000	0.000	0.000	0.003	0.034
B-site															
Mg	0.000	0.000	0.000	0.000	0.000	0.000	0.000	0.000	0.000	0.000	0.000	0.000	0.000	0.000	0.000
Fe^{2+}	0.003	0.005	0.016	0.022	0.038	0.015	0.057	0.065	0.002	0.157	0.054	0.058	0.050	0.000	0.000
Mn	0.014	0.009	0.000	0.003	0.016	0.019	0.007	0.009	0.011	0.026	0.003	0.012	0.014	0.005	0.008
Ca	1.753	1.614	0.025	0.178	1.281	1.354	0.202	0.238	0.031	0.808	0.034	0.066	0.106	0.020	0.014
Na	0.230	0.372	1.960	1.797	0.664	0.612	1.734	1.688	1.956	1.009	1.908	1.864	1.830	1.974	1.978
A-site															
Na	0.043	0.230	0.050	0.129	0.290	0.164	0.074	0.121	0.003	0.289	0.088	0.093	0.101	0.052	0.006
K	0.012	0.031	0.001	0.017	0.067	0.028	0.008	0.003	0.000	0.005	0.004	0.002	0.003	0.005	0.001
Total	15.055	15.261	15.051	15.146	15.357	15.192	15.083	15.124	15.003	15.294	15.092	15.095	15.105	15.056	15.007
X_{Mg}	0.825	0.778	0.491	0.469	0.725	0.748	0.689	0.637	0.600	0.508	0.726	0.737	0.645	0.337	0.613
Fe^{3+}/Fe	0.087	0.064	0.145	0.100	0.207	0.169	0.176	0.182	0.194	0.246	0.221	0.255	0.232	0.256	0.389
A-site	0.055	0.261	0.051	0.146	0.357	0.192	0.083	0.124	0.003	0.294	0.092	0.095	0.105	0.056	0.007
B: Ca/(Ca+Na)	0.884	0.813	0.012	0.090	0.659	0.689	0.104	0.123	0.016	0.445	0.017	0.034	0.055	0.010	0.007
C: Al/(Al+Fe^{3+})	0.720	0.881	0.863	0.901	0.696	0.704	0.868	0.830	0.852	0.282	0.868	0.843	0.803	0.639	0.632

Mineral abbriviations are: Act = actinolite; Bar = barroisite; Ed = edenite; Fba = ferro-barroisite; Fgl = ferro-glaucophane; Gln = glaucophane; Mhb = magnesio-hornblende; Mkt = magnesio-kataphorite; Mta = magnesio-taramite; Nyb = nyböite; Tr = tremolite; Win = winchite.

Table D.4. Amphibole continued

Sample	SY323	SY325					SY327			SY328	SY335		SY344		
Mineral Type	Fba II (in Grt)	Win rim III	Win rim II	Act rim I	Win core	Win core	Gln in Tur	Nyb in Tur	Mkt in Tur	Mta in Ep	Gln core	Gln rim	Gln	Act	Bar
SiO_2	43.21	56.62	55.60	56.52	55.50	55.68	54.16	50.83	45.84	43.34	58.44	58.06	58.99	56.06	52.83
TiO_2	0.02	0.01	0.04	0.03	0.00	0.07	0.12	0.19	0.35	0.46	0.05	0.00	0.00	0.03	0.14
Al_2O_3	20.12	0.52	1.56	0.76	1.73	1.50	11.43	11.49	14.29	14.91	10.36	9.07	11.54	1.14	7.32
Cr_2O_3	0.00	0.02	0.56	0.18	0.82	0.30	0.02	0.03	0.01	0.01	0.00	0.05	0.02	0.02	0.07
Fe_2O_3	4.46	2.79	3.77	2.52	3.64	3.23	2.21	1.69	3.32	3.96	2.45	4.67	0.78	1.56	1.93
FeO	18.52	5.12	4.78	4.29	4.81	4.90	10.99	12.42	13.47	12.88	7.09	6.76	7.24	7.19	7.92
MnO	1.95	0.22	0.30	0.40	0.27	0.35	0.06	0.07	0.18	0.15	0.00	0.02	0.07	0.10	0.22
MgO	1.19	19.80	18.32	20.23	18.52	19.20	9.31	9.12	8.43	8.25	11.21	11.30	11.22	18.63	14.92
CaO	4.79	8.92	7.73	10.22	8.50	9.73	1.22	2.55	4.80	5.70	7.46	7.44	0.51	12.27	9.28
Na_2O	3.93	2.93	3.41	1.92	2.98	2.40	7.70	7.43	6.83	6.54	0.34	0.20	7.36	0.55	2.68
K_2O	0.09	0.15	0.18	0.13	0.18	0.13	0.12	0.24	0.53	0.58	0.02	0.00	0.01	0.02	0.16
H_2O	2.03	2.15	2.13	2.16	2.14	2.15	2.14	2.08	2.06	2.03	2.21	2.20	2.23	2.15	2.14
Total	100.35	99.29	98.42	99.38	99.14	99.71	99.53	98.15	100.14	98.79	99.65	99.78	99.99	99.77	99.66

Formulas calculated to 22 oxygens + 2 OH; Fe^{2+}/Fe^{3+} calculated after Schumacher (1997)

T-site															
Si	6.418	7.954	7.889	7.911	7.832	7.814	7.641	7.384	6.710	6.464	7.991	7.980	7.993	7.894	7.474
Al	1.582	0.046	0.111	0.089	0.168	0.186	0.359	0.616	1.290	1.536	0.009	0.020	0.007	0.106	0.526
C-site															
Al	1.940	0.041	0.150	0.036	0.119	0.063	1.541	1.351	1.175	1.085	1.661	1.450	1.836	0.082	0.694
Ti	0.002	0.001	0.004	0.003	0.000	0.007	0.013	0.020	0.038	0.052	0.005	0.000	0.000	0.003	0.015
Fe^{3+}	0.498	0.295	0.403	0.265	0.386	0.342	0.188	0.184	0.317	0.444	0.252	0.483	0.079	0.165	0.206
Cr	0.000	0.002	0.063	0.020	0.091	0.034	0.002	0.004	0.001	0.001	0.000	0.005	0.002	0.002	0.007
Mg	0.263	4.148	3.875	4.220	3.896	4.018	1.959	1.976	1.840	1.834	2.286	2.315	2.266	3.911	3.146
Fe^{2+}	2.296	0.513	0.505	0.456	0.508	0.537	1.297	1.465	1.629	1.584	0.797	0.747	0.816	0.836	0.932
Mn	0.000	0.000	0.000	0.000	0.000	0.000	0.000	0.000	0.000	0.000	0.000	0.000	0.000	0.000	0.000
B-site															
Mg	0.000	0.000	0.000	0.000	0.000	0.000	0.000	0.000	0.000	0.000	0.000	0.000	0.000	0.000	0.000
Fe^{2+}	0.004	0.088	0.062	0.046	0.060	0.038	0.046	0.044	0.069	0.022	0.014	0.030	0.004	0.010	0.004
Mn	0.245	0.026	0.036	0.047	0.033	0.041	0.007	0.009	0.022	0.018	0.000	0.002	0.008	0.012	0.026
Ca	0.763	1.342	1.176	1.532	1.285	1.463	0.185	0.397	0.752	0.911	0.049	0.029	0.074	1.850	1.407
Na	0.989	0.544	0.727	0.375	0.623	0.457	1.762	1.550	1.157	1.049	1.937	1.939	1.915	0.127	0.563
A-site															
Na	0.144	0.255	0.212	0.145	0.193	0.197	0.344	0.542	0.780	0.841	0.042	0.042	0.019	0.022	0.173
K	0.016	0.026	0.033	0.023	0.032	0.024	0.021	0.045	0.098	0.110	0.003	0.000	0.002	0.004	0.029
Total	15.160	15.281	15.245	15.168	15.226	15.221	15.365	15.587	15.879	15.951	15.045	15.042	15.021	15.026	15.201
X_{Mg}	0.102	0.873	0.872	0.894	0.873	0.875	0.602	0.567	0.527	0.533	0.738	0.749	0.734	0.822	0.771
Fe^{3+}/Fe	0.178	0.330	0.415	0.346	0.405	0.373	0.153	0.109	0.181	0.217	0.237	0.383	0.088	0.163	0.180
A-site	0.160	0.281	0.245	0.168	0.226	0.221	0.359	0.587	0.873	0.951	0.045	0.042	0.021	0.026	0.201
B: Ca/(Ca+Na)	0.435	0.712	0.618	0.803	0.674	0.762	0.095	0.204	0.394	0.465	0.025	0.015	0.037	0.936	0.714
C: Al/(Al+Fe^{3+})	0.796	0.122	0.272	0.119	0.235	0.155	0.891	0.880	0.788	0.710	0.868	0.750	0.959	0.332	0.771

Table D.4. Amphibole continued

Sample	SY347			SY402A		SY403	SY406		SY412	SY413	SY425G	SY429			SY438
Mineral Type	Tr	Mhb	Ed	Gln core	Gln rim	Gln	Gln core	Gln rim	Gln	Gln	Gln	Tr	Mhb	Ed	Gln
SiO_2	58.09	52.16	46.66	57.52	58.16	57.98	58.03	55.92	56.48	56.87	58.09	58.50	51.27	45.17	58.95
TiO_2	0.01	0.24	0.73	0.08	0.06	0.20	0.08	0.03	0.05	0.04	0.00	0.01	0.19	0.68	0.03
Al_2O_3	0.13	4.44	8.96	10.89	11.18	11.65	9.76	7.95	9.47	9.34	10.61	0.07	4.05	10.83	11.52
Cr_2O_3	0.01	0.76	1.33	0.02	0.03	0.04	0.02	0.00	0.02	0.04	0.00	0.07	0.50	1.20	0.01
Fe_2O_3	0.77	1.61	1.62	1.79	1.32	0.61	2.17	4.61	5.95	4.14	1.48	1.72	1.62	0.58	0.95
FeO	1.91	3.37	5.17	7.61	7.08	8.53	7.97	12.87	8.49	9.27	10.12	1.28	3.72	5.00	7.02
MnO	0.13	0.13	0.03	0.12	0.09	0.13	0.12	0.12	0.18	0.11	0.04	0.30	0.23	0.17	0.09
MgO	23.09	20.33	17.94	11.49	11.59	10.60	11.41	8.14	9.28	9.21	9.88	22.87	19.84	17.24	11.36
CaO	12.30	11.62	11.60	0.88	0.52	0.96	0.74	0.36	0.96	0.51	0.42	11.58	11.68	11.86	0.31
Na_2O	0.44	2.36	3.52	7.27	7.44	6.97	7.06	7.23	7.06	7.14	7.10	1.21	2.06	3.53	7.47
K_2O	0.06	0.06	0.05	0.03	0.03	0.02	0.07	0.04	0.14	0.02	0.04	0.21	0.05	0.01	0.01
H_2O	2.19	2.14	2.11	2.21	2.22	2.21	2.20	2.12	2.16	2.14	2.20	2.21	2.10	2.08	2.23
Total	99.12	99.21	99.71	99.92	99.72	99.89	99.62	99.40	100.23	98.83	99.97	100.03	97.30	98.35	99.97

Formulas calculated to 22 oxygens + 2 OH: Fe^{2+}/Fe^{3+} calculated after Schumacher (1997)

T-site															
Si	7.997	7.349	6.682	7.871	7.926	7.920	7.975	7.960	7.846	7.971	7.992	7.994	7.378	6.545	7.984
Al	0.003	0.651	1.318	0.129	0.074	0.080	0.025	0.040	0.154	0.029	0.008	0.006	0.622	1.455	0.016
C-site															
Al	0.017	0.085	0.193	1.628	1.722	1.795	1.555	1.294	1.397	1.515	1.712	0.006	0.064	0.393	1.822
Ti	0.001	0.025	0.078	0.008	0.006	0.020	0.009	0.004	0.005	0.004	0.000	0.001	0.020	0.074	0.003
Fe^{3+}	0.080	0.170	0.175	0.184	0.135	0.063	0.224	0.494	0.622	0.436	0.154	0.177	0.175	0.063	0.097
Cr	0.001	0.085	0.150	0.002	0.003	0.004	0.002	0.000	0.003	0.004	0.000	0.008	0.057	0.137	0.001
Mg	4.739	4.271	3.831	2.345	2.354	2.158	2.337	1.727	1.922	1.925	2.026	4.660	4.257	3.723	2.294
Fe^{2+}	0.162	0.363	0.573	0.832	0.779	0.960	0.872	1.482	0.986	1.087	1.109	0.146	0.426	0.606	0.783
Mn	0.000	0.000	0.000	0.000	0.000	0.000	0.000	0.000	0.021	0.013	0.000	0.002	0.000	0.003	0.000
B-site															
Mg	0.000	0.000	0.000	0.000	0.000	0.000	0.000	0.000	0.000	0.000	0.000	0.000	0.000	0.000	0.000
Fe^{2+}	0.058	0.033	0.046	0.038	0.028	0.014	0.044	0.051	0.000	0.000	0.055	0.000	0.022	0.000	0.012
Mn	0.015	0.015	0.003	0.014	0.011	0.014	0.014	0.014	0.000	0.000	0.005	0.032	0.028	0.018	0.011
Ca	1.814	1.754	1.779	0.130	0.076	0.140	0.109	0.055	0.143	0.076	0.062	1.696	1.801	1.842	0.045
Na	0.113	0.197	0.171	1.818	1.885	1.831	1.833	1.879	1.857	1.924	1.878	0.272	0.149	0.140	1.932
A-site															
Na	0.005	0.446	0.806	0.110	0.081	0.015	0.047	0.117	0.045	0.015	0.015	0.049	0.425	0.852	0.029
K	0.011	0.011	0.009	0.006	0.005	0.003	0.012	0.007	0.024	0.004	0.006	0.036	0.009	0.002	0.001
Total	15.016	15.457	15.815	15.116	15.086	15.018	15.060	15.124	15.024	15.004	15.021	15.085	15.434	15.855	15.030
X_{Mg}	0.956	0.915	0.861	0.729	0.745	0.689	0.718	0.530	0.661	0.639	0.635	0.970	0.905	0.860	0.743
Fe^{3+}/Fe	0.266	0.300	0.220	0.175	0.143	0.060	0.197	0.244	0.387	0.286	0.117	0.548	0.281	0.094	0.109
A-site	0.016	0.457	0.815	0.116	0.086	0.018	0.060	0.124	0.024	0.004	0.021	0.085	0.434	0.855	0.030
B: Ca/(Ca+Na)	0.941	0.899	0.912	0.067	0.039	0.071	0.056	0.029	0.072	0.038	0.032	0.862	0.924	0.929	0.023
C: $Al/(Al+Fe^{3+})$	0.179	0.334	0.525	0.898	0.927	0.966	0.874	0.724	0.692	0.776	0.918	0.032	0.269	0.863	0.949

Table D.5. Chlorite

Sample	SY2	SY112	SY304	SY309B	SY323	SY325	SY327	SY328	SY347	SY403	SY404	SY406	SY412 Chl I	SY412 Chl II	SY413	SY420	SY441
Mineral Type	Chl	Chl	Chl	Chl	Chl	Chl	Chl	Chl	Chl	Chl	Chl	Chl	Chl	Chl	Chl	Chl	Chl
SiO_2	30.52	27.56	26.02	27.67	30.61	31.18	27.95	26.66	34.45	27.16	29.08	24.14	25.33	27.40	27.34	28.61	28.20
TiO_2	0.00	0.06	0.05	0.02	0.00	0.02	0.00	0.02	0.02	0.03	0.01	0.02	0.02	0.00	0.00	0.00	0.02
Al_2O_3	17.99	19.24	19.44	20.01	13.84	15.82	17.61	20.40	12.06	20.49	18.24	18.05	19.93	19.27	19.17	19.42	20.84
Cr_2O_3	0.27	0.00	0.00	0.14	0.00	0.91	0.00	0.00	0.47	0.05	0.00	0.03	0.02	0.00	0.06	0.03	0.02
FeO	11.22	19.51	26.18	15.70	17.96	10.79	17.12	19.81	6.72	17.55	13.63	35.27	28.34	21.31	21.59	15.96	10.28
MnO	0.21	0.25	0.41	0.28	2.93	0.14	0.30	0.16	0.06	0.10	0.13	1.30	0.75	0.50	0.44	0.52	0.28
CuO					3.07												
NiO									0.30								
MgO	25.68	20.65	15.32	22.91	14.93	27.54	22.02	19.73	32.73	21.23	25.22	8.37	13.04	19.32	19.09	23.04	25.97
CaO	0.15	0.03	0.08	0.01	0.48	0.03	0.03	0.00	0.03	0.01	0.02	0.08	0.02	0.05	0.02	0.00	0.01
Na_2O	0.01	0.00	0.01	0.01	0.06	0.01	0.01	0.02	0.00	0.02	0.00	0.03	0.01	0.01	0.00	0.00	0.02
K_2O	0.04	0.02	0.00	0.00	0.45	0.00	0.01	0.00	0.01	0.01	0.00	0.01	0.04	0.01	0.03	0.00	0.00
H_2O	12.10	11.70	11.28	11.86	11.02	12.14	16.13	11.61	12.47	11.74	11.96	10.57	11.12	11.65	11.61	11.97	12.07
Total	98.20	99.01	98.80	98.62	95.34	98.57	101.18	98.42	99.30	98.39	98.29	97.86	98.61	99.50	99.35	99.55	97.70

Formulas calculated to 14 oxygens + 4 OH; $Fe^{2+} = Fe^t$

Sample	SY2	SY112	SY304	SY309B	SY323	SY325	SY327	SY328	SY347	SY403	SY404	SY406	SY412 Chl I	SY412 Chl II	SY413	SY420	SY441
Si	3.026	2.825	2.767	2.798	3.332	3.081	2.910	2.753	3.314	2.774	2.918	2.738	2.733	2.821	2.823	2.866	2.803
Ti	0.000	0.004	0.004	0.001	0.000	0.001	0.000	0.002	0.001	0.002	0.001	0.001	0.002	0.000	0.000	0.000	0.001
Al	2.102	2.324	2.437	2.384	1.775	1.842	2.161	2.483	1.367	2.466	2.157	2.413	2.534	2.339	2.333	2.293	2.440
Cr	0.021	0.000	0.000	0.011	0.000	0.071	0.000	0.000	0.036	0.004	0.000	0.003	0.002	0.000	0.005	0.002	0.002
Fe^{2+}	0.930	1.672	2.328	1.328	1.635	0.892	1.490	1.711	0.540	1.499	1.144	3.345	2.557	1.835	1.864	1.338	0.854
Mn	0.017	0.022	0.037	0.024	0.270	0.011	0.026	0.014	0.005	0.009	0.011	0.125	0.068	0.043	0.038	0.044	0.023
Cu					0.252												
Ni									0.023								
Mg	3.796	3.156	2.428	3.453	2.423	4.057	3.418	3.037	4.694	3.232	3.772	1.414	2.097	2.966	2.939	3.442	3.848
Ca	0.016	0.003	0.009	0.001	0.056	0.003	0.003	0.000	0.003	0.001	0.002	0.010	0.003	0.005	0.002	0.000	0.001
Na	0.002	0.001	0.002	0.002	0.012	0.002	0.001	0.004	0.000	0.004	0.000	0.006	0.001	0.002	0.000	0.000	0.003
K	0.005	0.002	0.000	0.000	0.063	0.000	0.001	0.000	0.001	0.002	0.000	0.002	0.006	0.001	0.004	0.000	0.000
Total	9.916	10.010	10.011	10.004	9.818	9.962	10.011	10.005	9.984	9.992	10.004	10.057	10.002	10.011	10.010	9.986	9.976
X_{Mg}	0.803	0.654	0.510	0.722	0.597	0.820	0.696	0.640	0.897	0.683	0.767	0.297	0.451	0.618	0.612	0.720	0.818

Table D.6. Epidote and clinozoisite

Sample	SY2	SY109		SY112		SY304	SY308		SY309A	SY309B	SY323						SY328		SY335	
Mineral Type	Czo	Ep	Ep	Ep core	Ep rim	Ep	Ep	Ep	Ep	Ep	Ep 1	Ep 2	Ep 3	Ep 4	Ep 5	Ep 6	Ep	Ep	Ep	Ep
SiO_2	38.73	37.65	37.16	37.44	37.78	37.55	38.63	37.17	37.61	37.67	36.90	36.77	37.25	37.87	37.83	37.30	37.45	37.39	38.21	37.22
TiO_2	0.18	0.10	0.05	0.07	0.03	0.08	0.08	0.14	0.13	0.14	0.08	0.02	0.14	0.07	0.09	0.06	0.05	0.33	0.09	0.07
Al_2O_3	29.33	24.42	20.86	24.60	22.24	23.17	28.88	22.36	25.28	24.96	21.34	20.41	25.26	25.69	25.48	21.69	24.37	23.25	26.88	22.71
Cr_2O_3	0.16	0.01	0.00	0.05	0.00	0.00	0.00	0.04	0.00	0.93	0.07	0.00	0.01	0.06	0.07	0.01	0.00	0.00	0.03	0.10
Fe_2O_3	5.31	11.55	15.94	11.96	14.34	13.81	5.87	14.35	10.36	10.53	16.54	17.44	11.60	10.30	11.04	15.60	12.18	13.25	8.59	14.05
MnO	0.04	0.09	0.22	0.07	0.35	0.46	0.09	0.59	0.23	0.22	0.91	1.35	0.61	0.48	0.23	0.34	0.12	0.59	0.09	0.27
MgO	0.05	0.00	0.00	0.04	0.00	0.00	0.12	0.02	0.06	0.09	0.00	0.00	0.02	0.02	0.01	0.00	0.00	0.03	0.02	0.01
SrO											0.31	0.00	0.43	1.11	0.46	0.08				
CaO	23.68	23.02	22.91	23.36	23.04	22.53	24.00	22.91	23.13	22.81	22.44	21.97	22.78	22.67	22.90	23.23	23.58	22.36	23.68	22.82
Na_2O	0.01	0.01	0.00	0.01	0.00	0.00	0.00	0.03	0.02	0.00	0.00	0.00	0.00	0.02	0.02	0.00	0.00	0.03	0.02	0.00
K_2O	0.01	0.00	0.02	0.03	0.01	0.00	0.00	0.01	0.02	0.00	0.00	0.00	0.00	0.01	0.00	0.01	0.00	0.00	0.02	0.01
H_2O	1.93	1.88	1.85	1.89	1.87	1.87	1.93	1.86	1.88	1.89	1.86	1.85	1.89	1.90	1.90	1.87	1.89	1.87	1.91	1.86
Total	99.42	98.71	99.01	99.52	99.66	99.47	99.60	99.46	98.70	99.22	100.46	99.81	100.01	100.20	100.06	100.19	99.64	99.10	99.55	99.12

Formulas calculated to 12 oxygens + 1 OH; $Fe^{3+} = Fe^t$

Si	3.002	3.009	3.016	2.977	3.025	3.003	2.998	2.989	2.997	2.991	2.968	2.984	2.953	2.990	2.985	2.991	2.978	2.999	2.998	2.995
Ti	0.010	0.006	0.003	0.004	0.002	0.005	0.005	0.008	0.008	0.008	0.005	0.001	0.008	0.004	0.005	0.004	0.003	0.020	0.005	0.004
Al	2.680	2.300	1.995	2.305	2.099	2.184	2.642	2.120	2.374	2.336	2.023	1.953	2.360	2.391	2.369	2.050	2.284	2.197	2.485	2.153
Cr	0.010	0.001	0.000	0.003	0.000	0.000	0.000	0.002	0.000	0.058	0.004	0.000	0.001	0.004	0.004	0.001	0.000	0.000	0.002	0.006
Fe^{3+}	0.310	0.695	0.974	0.716	0.864	0.831	0.343	0.868	0.621	0.629	1.001	1.065	0.692	0.612	0.656	0.941	0.729	0.800	0.507	0.851
Mn	0.002	0.006	0.015	0.005	0.024	0.031	0.006	0.040	0.015	0.015	0.062	0.093	0.041	0.032	0.015	0.023	0.008	0.040	0.006	0.019
Mg	0.005	0.000	0.000	0.005	0.000	0.000	0.014	0.002	0.007	0.010	0.000	0.000	0.003	0.002	0.001	0.000	0.000	0.003	0.002	0.001
Sr											0.015	0.000	0.020	0.051	0.021	0.004				
Ca	1.967	1.971	1.992	1.990	1.976	1.931	1.996	1.974	1.974	1.941	1.934	1.911	1.935	1.917	1.936	1.996	2.009	1.921	1.990	1.967
Na	0.002	0.001	0.000	0.002	0.000	0.000	0.000	0.004	0.002	0.000	0.000	0.001	0.000	0.003	0.002	0.000	0.000	0.005	0.003	0.000
K	0.001	0.000	0.002	0.003	0.001	0.000	0.000	0.001	0.002	0.000	0.000	0.000	0.000	0.001	0.000	0.001	0.000	0.000	0.002	0.001
Total	7.990	7.988	7.998	8.010	7.992	7.985	8.004	8.009	8.000	7.989	8.013	8.007	8.013	8.005	7.996	8.010	8.012	7.985	8.002	7.997

Types in SY323 are: 1 = type-I inclusion in Grt; 2 = type-II inclusion in Grt; 3 = matrix Ep in direct contact to Grt; 4 = core of matrix Ep; 5 = rim of matrix Ep; 6 = Ep in stage-4 crack. Types in SY403 are: 1 = core of Ep in Qtz vein; 2 = rim of Ep in Qtz vein; 3 = core-1 of Ep-Czo in pseudomorphs after Lws; 4 = core-2 of Ep-Czo in pseudomorphs after Lws; 5 = rim of Ep-Czo in pseudomorphs after Lws. Types in SY438 are: 1 = core of Ep in Lws; 2 = rim of Ep in Lws; 3 = Czo intergrown with Ab from Lws breakdown.

Table D.6. Epidote and clinozoisite continued

Sample	SY344		SY403					SY412	SY413	SY415	SY420	SY425D		SY425G		SY432	SY438			
Mineral Type	Czo	Ep	Ep 1	Ep 2	Ep 3	Ep 4	Czo 5	Ep	Ep	Ep	Ep	Ep in Omp	Ep large crystal	Czo rim	Czo core	Ep	Ep 1	Ep 2	Czo 3	Czo 3
SiO_2	39.12	38.53	37.47	38.38	37.68	38.36	38.81	38.21	38.32	37.46	38.75	37.20	37.10	37.39	37.81	37.61	37.41	37.98	38.77	39.49
TiO_2	0.04	0.16	0.07	0.11	0.08	0.14	0.96	0.14	0.21	0.14	0.22	0.14	0.10	0.05	0.04	0.03	0.04	0.15	0.15	0.04
Al_2O_3	32.17	28.28	24.24	27.88	23.71	28.39	31.54	24.04	25.20	22.22	27.90	26.03	23.17	21.27	25.46	22.55	23.38	26.63	29.35	33.23
Cr_2O_3	0.05	0.00	0.00	0.00	0.04	0.00	0.03	0.01	0.04	0.02	0.07	0.00	0.03	0.00	0.03	0.01	0.00	0.00	0.04	0.00
Fe_2O_3	2.00	6.59	12.14	7.34	11.53	6.65	2.02	12.37	10.25	14.56	8.28	10.84	14.02	15.97	10.63	14.40	12.88	8.84	5.28	0.76
MnO	0.06	0.17	0.27	0.34	0.19	0.23	0.08	0.08	0.32	0.26	0.17	0.12	0.55	0.57	0.01	0.27	0.16	0.44	0.07	0.00
MgO	0.01	0.03	0.03	0.01	0.00	0.03	0.02	0.02	0.06	0.00	0.02	0.03	0.00	0.00	0.03	0.00	0.00	0.02	0.01	0.00
SrO																				
CaO	24.34	23.91	22.97	23.31	23.02	23.67	24.27	23.16	22.81	23.16	23.31	23.21	22.70	22.61	23.59	22.89	22.87	23.48	24.46	25.12
Na_2O	0.02	0.00	0.02	0.02	0.00	0.03	0.00	0.00	0.04	0.01	0.01	0.00	0.00	0.00	0.02	0.01	0.00	0.01	0.01	0.00
K_2O	0.00	0.00	0.01	0.00	0.00	0.01	0.00	0.00	0.01	0.05	0.00	0.02	0.01	0.01	0.01	0.00	0.00	0.00	0.01	0.01
H_2O	1.96	1.93	1.88	1.92	1.86	1.92	1.96	1.89	1.89	1.87	1.94	1.89	1.87	1.86	1.90	1.87	1.86	1.90	1.94	1.99
Total	99.76	99.59	99.09	99.31	98.11	99.43	99.69	99.91	99.14	99.73	100.68	99.48	99.53	99.74	99.54	99.63	98.61	99.44	100.08	100.63

Formulas calculated to 12 oxygens + 1 OH; $Fe^{3+} = Fe^t$

	Czo	Ep	Ep 1	Ep 2	Ep 3	Ep 4	Czo 5	Ep	Ep	Ep	Ep	Ep in Omp	Ep large crystal	Czo rim	Czo core	Ep	Ep 1	Ep 2	Czo 3	Czo 3
Si	2.988	3.000	2.993	3.002	3.033	2.992	2.972	3.023	3.033	3.003	2.995	2.945	2.974	3.012	2.989	3.011	3.009	2.990	2.992	2.981
Ti	0.002	0.009	0.004	0.007	0.005	0.008	0.055	0.008	0.012	0.008	0.013	0.008	0.006	0.003	0.002	0.002	0.002	0.009	0.009	0.002
Al	2.896	2.595	2.282	2.571	2.249	2.610	2.846	2.242	2.350	2.099	2.541	2.429	2.189	2.019	2.373	2.128	2.217	2.470	2.670	2.957
Cr	0.003	0.000	0.000	0.000	0.002	0.000	0.002	0.001	0.002	0.001	0.004	0.000	0.002	0.000	0.002	0.000	0.000	0.000	0.002	0.000
Fe^{3+}	0.115	0.386	0.730	0.432	0.698	0.390	0.117	0.736	0.610	0.879	0.482	0.646	0.846	0.968	0.633	0.868	0.780	0.524	0.307	0.043
Mn	0.004	0.011	0.018	0.022	0.013	0.015	0.005	0.005	0.021	0.017	0.011	0.008	0.037	0.039	0.001	0.018	0.011	0.029	0.005	0.000
Mg	0.001	0.004	0.003	0.001	0.000	0.003	0.002	0.002	0.007	0.000	0.003	0.003	0.000	0.000	0.003	0.000	0.000	0.002	0.001	0.000
Sr																				
Ca	1.992	1.994	1.966	1.954	1.986	1.978	1.991	1.963	1.934	1.989	1.930	1.969	1.949	1.951	1.999	1.963	1.971	1.980	2.023	2.032
Na	0.002	0.000	0.004	0.004	0.000	0.004	0.000	0.000	0.006	0.001	0.002	0.000	0.000	0.000	0.003	0.001	0.000	0.001	0.001	0.000
K	0.000	0.000	0.001	0.000	0.000	0.001	0.000	0.000	0.001	0.005	0.000	0.002	0.001	0.001	0.001	0.000	0.000	0.000	0.001	0.001
Total	8.004	8.000	8.000	7.992	7.987	8.002	7.990	7.980	7.977	8.002	7.980	8.011	8.003	7.993	8.007	7.991	7.990	8.005	8.011	8.017

Table D.7. Albite

Sample	SY109	SY309B	SY314	SY323	SY327	SY328	SY402A	SY403	SY406	SY412	SY413	SY415	SY420	SY425G	SY432	SY438	SY442
SiO_2	69.32	69.44	68.81	68.28	68.61	67.81	68.99	68.65	68.41	69.74	69.33	69.88	69.77	68.77	68.62	68.09	69.51
TiO_2	0.00	0.04	0.02	0.00	0.00	0.00	0.00	0.02	0.01	0.02	0.01	0.00	0.03	0.00	0.02	0.00	0.00
Al_2O_3	19.55	19.04	19.46	19.26	19.16	19.80	19.35	19.56	19.52	18.96	18.76	19.16	19.60	19.39	19.15	20.36	19.05
Cr_2O_3	0.00	0.00	0.00	0.00	0.00	0.00	0.03	0.00	0.03	0.00	0.00	0.03	0.00	0.02	0.05	0.00	0.02
Fe_2O_3	0.06	0.23	0.42	0.57	0.73	0.34	0.34	0.00	0.69	0.05	0.13	0.02	0.09	0.36	0.14	0.08	0.12
FeO	0.00	0.00	0.00	0.00	0.00	0.00	0.00	0.00	0.00	0.00	0.00	0.00	0.00	0.00	0.00	0.00	0.00
MnO	0.00	0.00	0.01	0.20	0.00	0.00	0.04	0.00	0.01	0.01	0.01	0.00	0.01	0.03	0.00	0.00	0.06
MgO	0.00	0.01	0.00	0.02	0.06	0.00	0.00	0.00	0.00	0.00	0.00	0.00	0.02	0.02	0.04	0.05	0.00
CaO	0.12	0.00	0.04	0.14	0.64	0.43	0.02	0.25	0.07	0.01	0.02	0.04	0.15	0.08	0.29	0.66	0.10
Na_2O	11.64	11.94	12.16	12.25	11.59	11.85	11.96	11.76	12.07	12.13	12.00	11.36	11.10	11.77	11.57	11.58	11.78
K_2O	0.01	0.04	0.05	0.04	0.06	0.02	0.05	0.01	0.03	0.03	0.03	0.03	0.04	0.00	0.19	0.18	0.05
Total	100.70	100.74	100.97	100.77	100.87	100.25	100.78	100.25	100.84	100.95	100.29	100.53	100.82	100.44	100.09	100.99	100.69

Formulas calculated to 8 oxygens; $Fe^{3+} = Fe^t$

	SY109	SY309B	SY314	SY323	SY327	SY328	SY402A	SY403	SY406	SY412	SY413	SY415	SY420	SY425G	SY432	SY438	SY442
Si	3.003	3.011	2.985	2.977	2.983	2.965	2.995	2.991	2.975	3.018	3.021	3.026	3.012	2.993	2.999	2.954	3.015
Ti	0.000	0.001	0.001	0.000	0.000	0.000	0.000	0.001	0.000	0.000	0.000	0.000	0.001	0.000	0.001	0.000	0.000
Al	0.998	0.973	0.995	0.989	0.982	1.020	0.990	1.005	1.000	0.967	0.963	0.978	0.997	0.995	0.986	1.041	0.974
Cr	0.000	0.000	0.000	0.000	0.000	0.000	0.001	0.000	0.001	0.000	0.000	0.001	0.000	0.001	0.002	0.000	0.001
Fe^{3+}	0.002	0.008	0.014	0.019	0.024	0.011	0.011	0.000	0.023	0.002	0.004	0.001	0.003	0.012	0.004	0.003	0.004
Mn	0.000	0.000	0.000	0.008	0.000	0.000	0.002	0.000	0.000	0.000	0.000	0.000	0.000	0.001	0.000	0.000	0.002
Mg	0.000	0.001	0.000	0.001	0.004	0.000	0.000	0.000	0.000	0.000	0.000	0.000	0.001	0.001	0.002	0.003	0.000
Ca	0.005	0.000	0.002	0.007	0.030	0.020	0.001	0.012	0.003	0.000	0.001	0.002	0.007	0.004	0.014	0.031	0.005
Na	0.978	1.004	1.023	1.035	0.977	1.005	1.007	0.993	1.018	1.017	1.014	0.954	0.929	0.993	0.981	0.974	0.990
K	0.001	0.002	0.003	0.002	0.003	0.001	0.003	0.001	0.002	0.002	0.002	0.002	0.002	0.000	0.011	0.010	0.002
Total	4.986	5.000	5.023	5.038	5.004	5.022	5.009	5.003	5.022	5.007	5.006	4.962	4.953	5.000	5.000	5.016	4.993
Ab	99.4	99.8	99.5	99.1	96.7	97.9	99.6	98.8	99.5	99.8	99.7	99.7	99.0	99.6	97.6	96.0	99.3
An	0.5	0.0	0.2	0.6	2.9	2.0	0.1	1.2	0.3	0.0	0.1	0.2	0.8	0.4	1.4	3.0	0.5
Or	0.1	0.2	0.3	0.2	0.3	0.1	0.3	0.1	0.2	0.2	0.2	0.2	0.2	0.0	1.0	1.0	0.2

Table D.8. Talc, antigorite, lawsonite and chloritoid

Sample	SY325	SY347	SY429		SY438		SY304
Mineral Type	Tlc	Atg	Tlc	Atg	Lws core	Lws rim	Cld
SiO_2	62.32	41.73	63.19	44.07	37.87	37.91	24.33
TiO_2	0.02	0.00	0.00	0.01			0.02
Al_2O_3	0.04	2.57	0.14	1.57	32.15	31.02	39.19
Cr_2O_3	0.00	0.44	0.01	0.31			0.00
Fe_2O_3					0.49	0.83	2.65
FeO	3.83	7.64	2.12	8.25			21.18
MnO	0.01	0.12	0.00	0.13			0.42
NiO		0.21	0.24	0.23			
MgO	28.60	34.59	29.66	32.90			4.12
BaO					0.01	0.01	
SrO					0.11	0.16	
CaO	0.00	0.02	0.02	0.02	17.11	16.90	0.00
Na_2O	0.02	0.00	0.00	0.01	0.00	0.00	0.03
K_2O	0.00	0.01	0.02	0.01	0.01	0.00	0.00
H_2O	4.65	12.57	4.71	12.64	11.36	11.23	7.26
Total	99.48	99.90	100.12	100.15	99.11	98.06	99.20
Si	4.018	3.980	4.021	4.181	1.999	2.025	2.010
Ti	0.001	0.000	0.000	0.001			0.001
Al	0.003	0.289	0.011	0.176	2.000	1.952	3.817
Cr	0.000	0.033	0.001	0.024			0.000
Fe^{3+}					0.020	0.033	0.165
Fe^{2+}	0.206	0.609	0.113	0.654			1.464
Mn	0.001	0.010	0.000	0.010			0.029
Ni		0.016	0.012	0.018			
Mg	2.749	4.918	2.814	4.652			0.508
Ba					0.000	0.000	
Sr					0.003	0.005	
Ca	0.000	0.002	0.001	0.002	0.968	0.967	0.000
Na	0.002	0.001	0.000	0.002	0.000	0.000	0.005
K	0.000	0.002	0.002	0.001	0.000	0.000	0.000
Total	6.981	9.860	6.974	9.721	4.991	4.983	8.000
X_{Mg}	0.930	0.890	0.962	0.877			0.258

Formulas calculated as follows: 10 oxygens + 2 OH and $Fe^{2+} = Fe^t$ for talc; 10 oxygens + 8 OH and $Fe^{2+} = Fe^t$ for antigorite; 7 oxygens + 2 OH + 1 H_2O and $Fe^{3+} = Fe^t$ for lawsonite; 10 oxygens + 4 OH and 8 cations for chloritoid.

Table D.9. Rutile

Sample	SY109	SY112	SY304	SY309A	SY323	SY325	SY328	SY402B	SY404	SY412	SY420	SY441
SiO_2	0.05	0.06	0.01	0.04	0.06	0.08	0.02	0.00	0.04	0.03	0.01	0.05
TiO_2	99.87	98.46	99.51	97.90	98.92	98.41	98.06	98.22	98.34	99.35	98.63	99.69
Al_2O_3	0.00	0.00	0.00	0.00	0.00	0.00	0.00	0.00	0.00	0.00	0.00	0.00
Cr_2O_3	0.00	0.10	0.04	0.00	0.05	0.84	0.03	0.05	0.00	0.02	0.07	0.00
Fe_2O_3	1.29	1.25	0.98	0.86	1.52	0.54	1.62	0.78	0.83	0.76	1.15	0.58
MnO	0.00	0.00	0.00	0.03	0.10	0.00	0.00	0.00	0.00	0.00	0.03	0.01
MgO	0.00	0.00	0.00	0.00	0.00	0.01	0.00	0.00	0.00	0.00	0.00	0.00
CaO	0.04	0.33	0.09	0.55	0.25	0.03	0.04	0.02	0.61	0.19	0.06	1.03
Na_2O	0.01	0.01	0.00	0.02	0.06	0.00	0.00	0.00	0.00	0.00	0.02	0.00
K_2O	0.06	0.00	0.01	0.00	0.00	0.00	0.00	0.00	0.00	0.00	0.01	0.00
Total	101.33	100.22	100.63	99.39	100.96	99.91	99.77	99.08	99.82	100.35	99.98	101.36

Formulas calculated to 2 oxygens; $Fe^{3+} = Fe^t$

	SY109	SY112	SY304	SY309A	SY323	SY325	SY328	SY402B	SY404	SY412	SY420	SY441
Si	0.001	0.001	0.000	0.000	0.001	0.001	0.000	0.000	0.000	0.000	0.000	0.001
Ti	0.989	0.987	0.992	0.989	0.985	0.988	0.987	0.993	0.989	0.992	0.990	0.988
Al	0.000	0.000	0.000	0.000	0.000	0.000	0.000	0.000	0.000	0.000	0.000	0.000
Cr	0.000	0.001	0.000	0.000	0.001	0.009	0.000	0.001	0.000	0.000	0.001	0.000
Fe^{3+}	0.013	0.013	0.010	0.009	0.015	0.005	0.016	0.008	0.008	0.008	0.012	0.006
Mn	0.000	0.000	0.000	0.000	0.001	0.000	0.000	0.000	0.000	0.000	0.000	0.000
Mg	0.000	0.000	0.000	0.000	0.000	0.000	0.000	0.000	0.000	0.000	0.000	0.000
Ca	0.001	0.005	0.001	0.008	0.003	0.000	0.001	0.000	0.009	0.003	0.001	0.014
Na	0.000	0.000	0.000	0.000	0.002	0.000	0.000	0.000	0.000	0.000	0.000	0.000
K	0.001	0.000	0.000	0.000	0.000	0.000	0.000	0.000	0.000	0.000	0.000	0.000
Total	1.005	1.006	1.003	1.007	1.007	1.004	1.004	1.002	1.007	1.003	1.004	1.009

Table D.10. Hematite, ilmenite and magnetite

Sample	SY323		SY328		SY335	SY429			SY432
Mineral	Hem	Ilm	Ilm	Mag	Hem	Mag	Ti-Hem	Ilm	Hem
SiO_2	0.03	0.03	0.00	0.00	0.02	0.00	0.02	0.01	0.04
TiO_2	0.38	48.63	49.73	2.30	1.76	0.02	13.92	49.02	1.37
Al_2O_3	0.06	0.00	0.00	0.01	0.06	0.00	0.00	0.00	0.04
Cr_2O_3	0.06	0.02	0.00	0.00	0.03	2.04	0.84	0.07	0.05
Fe_2O_3	98.89	8.58	6.25	65.50	95.58	67.38	72.29	7.20	97.36
FeO	0.00	40.04	42.27	33.51	0.95	31.07	11.32	39.01	0.73
MnO	0.49	3.28	1.92	0.02	0.01	0.04	0.81	4.38	0.06
MgO	0.01	0.06	0.24	0.01	0.00	0.05	0.09	0.33	0.01
CaO	0.16	0.23	0.02	0.00	0.43	0.00	0.01	0.01	0.33
Na_2O	0.00	0.00	0.01	0.01	0.02	0.00	0.05	0.00	0.01
K_2O	0.00	0.00	0.00	0.00	0.00	0.03	0.01	0.00	0.00
Total	100.08	100.87	100.44	101.36	98.87	100.63	99.34	100.05	100.00
Si	0.001	0.001	0.000	0.000	0.000	0.000	0.001	0.000	0.001
Ti	0.008	0.918	0.941	0.066	0.035	0.001	0.276	0.931	0.027
Al	0.002	0.000	0.000	0.000	0.002	0.000	0.000	0.000	0.001
Cr	0.001	0.000	0.000	0.000	0.001	0.062	0.017	0.001	0.001
Fe^{3+}	1.975	0.162	0.118	1.869	1.926	1.939	1.433	0.137	1.942
Fe^{2+}	0.000	0.841	0.889	1.063	0.021	0.993	0.249	0.824	0.016
Mn	0.011	0.070	0.041	0.000	0.000	0.001	0.018	0.094	0.001
Mg	0.000	0.002	0.009	0.000	0.000	0.003	0.003	0.012	0.000
Ca	0.005	0.000	0.001	0.000	0.012	0.000	0.000	0.000	0.009
Na	0.000	0.000	0.001	0.001	0.001	0.000	0.002	0.000	0.001
K	0.000	0.006	0.000	0.000	0.000	0.001	0.000	0.000	0.000

Formulas calculated as follows: 3 oxygens and 2 cations for hematite and ilmenite; 4 oxygens and 3 cations for magnetite.

Table D.11. Apatite

Sample	SY11	SY109	SY304	SY308	SY309B	SY314	SY328	SY400	SY401B	SY402A	SY403	SY404	SY405	SY406
P_2O_5	41.22	41.51	41.74	41.78	41.67	41.50	42.05	41.46	39.34	39.71	40.45	42.81	42.40	42.42
SiO_2	0.10	0.00	0.03	0.03	0.02	0.02	0.00	0.03	0.01	0.03	0.07	0.05	0.12	0.01
Al_2O_3	0.02	0.02	0.00	0.01	0.02	0.01	0.02	0.02	0.03	0.00	0.00	0.00	0.00	0.00
FeO	0.13	0.48	0.36	0.05	0.19	0.05	0.00	0.15	0.09	0.10	0.05	0.08	0.02	0.18
MnO	0.03	0.07	0.10	0.01	0.04	0.07	0.02	0.04	0.09	0.00	0.02	0.12	0.06	0.19
MgO	0.00	0.00	0.00	0.00	0.00	0.00	0.00	0.00	0.00	0.00	0.00	0.00	0.00	0.00
CaO	55.67	55.77	56.23	55.94	56.43	56.34	56.12	56.00	56.58	56.42	56.43	55.73	56.29	55.58
SrO	0.21	0.18	0.00	0.08	0.06	0.09	0.45	0.17	0.05	0.11	0.04	0.16	0.11	0.17
Na_2O	0.00	0.01	0.04	0.00	0.00	0.01	0.00	0.03	0.00	0.10	0.00	0.08	0.11	0.02
F	1.58	3.39	2.50	3.62	1.57	3.30	1.44	1.65	1.70	1.99	2.81	1.67	1.53	2.49
Cl	0.00	0.01	0.06	0.01	0.00	0.01	0.00	0.00	0.00	0.01	0.05	0.00	0.00	0.00
H_2O	1.06	0.23	0.64	0.10	1.09	0.24	1.14	1.03	0.95	0.83	0.45	1.04	1.11	0.64
Total	100.02	101.66	101.70	101.63	101.08	101.63	101.24	100.60	98.83	99.30	100.35	101.74	101.75	101.69

Formulas calculated to 12 oxygens +1 (OH+F+Cl); Fe^{2+} = Fe^t

	SY11	SY109	SY304	SY308	SY309B	SY314	SY328	SY400	SY401B	SY402A	SY403	SY404	SY405	SY406
P	2.960	2.964	2.963	2.976	2.960	2.959	2.978	2.962	2.888	2.903	2.926	3.005	2.981	2.998
Si	0.008	0.000	0.003	0.003	0.001	0.001	0.000	0.003	0.001	0.002	0.006	0.004	0.010	0.001
Al	0.002	0.001	0.000	0.001	0.002	0.001	0.001	0.002	0.003	0.000	0.000	0.000	0.000	0.000
Fe^{2+}	0.010	0.034	0.025	0.004	0.013	0.004	0.000	0.011	0.007	0.007	0.004	0.006	0.001	0.012
Mn	0.002	0.005	0.007	0.001	0.003	0.005	0.001	0.003	0.006	0.000	0.001	0.008	0.004	0.013
Mg	0.000	0.000	0.000	0.000	0.000	0.000	0.000	0.000	0.000	0.000	0.000	0.000	0.000	0.000
Ca	5.059	5.040	5.052	5.043	5.074	5.084	5.030	5.062	5.258	5.218	5.167	4.951	5.008	4.970
Sr	0.010	0.009	0.000	0.004	0.003	0.004	0.022	0.008	0.002	0.006	0.002	0.008	0.005	0.008
Na	0.000	0.001	0.007	0.000	0.000	0.001	0.000	0.005	0.001	0.016	0.000	0.013	0.018	0.003
Total	8.051	8.054	8.057	8.032	8.057	8.060	8.033	8.056	8.166	8.152	8.105	7.995	8.028	8.005
F	0.424	0.874	0.650	0.944	0.417	0.869	0.389	0.441	0.472	0.540	0.748	0.447	0.411	0.658
Cl	0.000	0.001	0.008	0.001	0.000	0.001	0.000	0.000	0.000	0.001	0.007	0.000	0.000	0.001
OH	0.576	0.125	0.342	0.055	0.583	0.130	0.611	0.559	0.528	0.459	0.245	0.552	0.589	0.341

Table D.12. Titanite

Sample	SY2	SY109	SY112	SY309A	SY314	SY323	SY328	SY335	SY344	SY402A	SY403	SY404	SY412	SY413	SY420	SY441
SiO_2	30.78	30.72	30.57	30.24	30.38	30.18	30.29	30.47	30.69	30.20	30.23	30.33	26.50	30.57	30.56	30.08
TiO_2	37.75	37.78	38.34	38.75	36.89	36.89	38.94	37.90	39.00	38.89	38.69	39.78	39.52	39.21	38.20	38.80
Al_2O_3	1.84	1.78	0.73	0.80	1.45	1.96	0.64	1.57	0.91	0.93	1.20	0.16	0.88	0.57	1.31	1.08
Cr_2O_3	0.03	0.00	0.00	0.00	0.01	0.00	0.00	0.00	0.00	0.01	0.00	0.00	0.02	0.00	0.05	0.00
Fe_2O_3	0.14	0.48	0.62	0.35	0.53	0.75	0.40	0.86	0.50	0.54	0.72	0.73	0.66	0.54	0.54	0.38
MnO	0.00	0.04	0.00	0.03	0.15	0.01	0.01	0.00	0.03	0.08	0.16	0.03	0.05	0.05	0.03	0.04
MgO	0.00	0.00	0.00	0.00	0.00	0.00	0.00	0.00	0.00	0.00	0.00	0.00	0.04	0.00	0.00	0.00
CaO	28.60	28.29	28.08	28.29	28.46	28.21	28.72	28.43	28.33	28.04	28.38	28.27	25.64	28.70	28.47	28.09
Na_2O	0.01	0.02	0.04	0.01	0.05	0.03	0.02	0.03	0.05	0.06	0.02	0.08	0.19	0.02	0.00	0.03
K_2O	0.01	0.01	0.02	0.02	0.04	0.00	0.00	0.03	0.00	0.00	0.02	0.01	0.00	0.00	0.01	0.00
Total	99.15	99.12	98.39	98.49	97.97	98.04	99.03	99.29	99.51	98.75	99.42	99.39	93.50	99.66	99.16	98.51

Formulas calculated to 5 oxygens; $Fe^{3+} = Fe^t$

	SY2	SY109	SY112	SY309A	SY314	SY323	SY328	SY335	SY344	SY402A	SY403	SY404	SY412	SY413	SY420	SY441
Si	1.010	1.008	1.013	1.002	1.012	1.003	0.999	1.001	1.005	0.998	0.993	0.998	0.930	1.002	1.005	0.996
Ti	0.931	0.933	0.955	0.965	0.924	0.922	0.966	0.936	0.961	0.966	0.956	0.984	1.043	0.967	0.944	0.966
Al	0.071	0.069	0.029	0.031	0.057	0.077	0.025	0.061	0.035	0.036	0.046	0.006	0.037	0.022	0.051	0.042
Cr	0.001	0.000	0.000	0.000	0.000	0.000	0.000	0.000	0.000	0.000	0.000	0.000	0.001	0.000	0.001	0.000
Fe^{3+}	0.003	0.012	0.016	0.009	0.013	0.019	0.010	0.021	0.012	0.013	0.018	0.018	0.017	0.013	0.013	0.010
Mn	0.000	0.001	0.000	0.001	0.004	0.000	0.000	0.000	0.001	0.002	0.005	0.001	0.002	0.001	0.001	0.001
Mg	0.000	0.000	0.000	0.000	0.000	0.000	0.000	0.000	0.000	0.000	0.000	0.000	0.002	0.000	0.000	0.000
Ca	1.005	0.995	0.997	1.004	1.016	1.005	1.015	1.001	0.994	0.993	0.999	0.996	0.964	1.008	1.003	0.996
Na	0.001	0.001	0.002	0.001	0.003	0.002	0.002	0.002	0.003	0.004	0.001	0.005	0.013	0.001	0.000	0.002
K	0.000	0.000	0.001	0.001	0.002	0.000	0.000	0.001	0.000	0.000	0.001	0.000	0.000	0.000	0.000	0.000
Total	3.022	3.020	3.012	3.014	3.031	3.028	3.018	3.023	3.012	3.013	3.019	3.008	3.007	3.015	3.018	3.013

E. Measured and corrected boron isotope analyses from SIMS and TIMS

The following tables include measured and corrected data on all boron isotope analyses performed during this study, including analyses of reference materials and samples. In detail the tables display:

Table E.1: Measured boron isotope ratios of reference materials and calculated instrumental correction factors (α_{inst}),

Table E.2: Comparison of boron isotope analyses of Syros dravite from TIMS and SIMS. These data are plotted graphically in Fig. 2.7,

Table E.3: Tourmaline type I and coexisting phengite and glaucophane,

Table E.4: Amphibole and antigorite from serpentinites,

Table E.5: Tourmaline type II and coexisting phengite and glaucophane.

Table E.1. Measured boron isotope ratios of reference materials and calculated instrumental correction factors (α_{inst})

Sample	Type	$^{11}B/^{10}B$ SIMS	$2\sigma_{mean}$ (%)	$\delta^{11}B$ reference	$^{11}B/^{10}B$ reference	α_{inst}	I_P (nA)	date
98144	elbaite	3.8397	1.020	-10.4	4.0016	1.0422	1	2003-01-03
98144	elbaite	3.8209	0.923	-10.4	4.0016	1.0473	1	2003-03-05
108796	dravite	3.8482	1.422	-6.6	4.0169	1.0438	1	2003-01-02
108796	dravite	3.8325	1.050	-6.6	4.0169	1.0481	1	2003-03-05
112566	schorl	3.8319	1.118	-12.5	3.9931	1.0421	1	2003-01-03
112566	schorl	3.8124	0.881	-12.5	3.9931	1.0474	1	2003-03-05
112566	schorl	3.8179	0.863	-12.5	3.9931	1.0459	1	2003-03-10
112566	schorl	3.7994	0.993	-12.5	3.9931	1.0510	1	2003-09-01
SRM 610	synth. glass	3.8422	0.797	-1.05	4.0394	1.0513	30	2003-03-11
SRM 610	synth. glass	3.8361	1.952	-1.05	4.0394	1.0530	30	2003-08-29
B4	schorl	3.8379	0.893	-8.6	4.0089	1.0446	1	2003-03-10
B6	obsidian	3.8515	0.795	-1.56	4.0373	1.0482	30	2003-03-11
Rocc-3	obsidian	3.8327	0.504	-5.88	4.0199	1.0488	30	2003-03-11
Phe-80-3	phengite	3.7932	2.302	-13.77	3.9879	1.0513	30	2003-03-05
Phe-80-3	phengite	3.8020	1.853	-13.77	3.9879	1.0489	30	2003-03-11

Table E.2. Comparison of boron isotope analyses of Syros dravite from TIMS and SIMS

Sample	Batch	Type					SIMS core		rim	
	No.		$^{11}B/^{10}B$	1σ	$\delta^{11}B$	1σ	$\delta^{11}B$	$2\sigma_{mean}$	$\delta^{11}B$	$2\sigma_{mean}$
SY309B	1	dravite	4.1361	0.0010	+22.87	0.24	+21.6	0.8	+21.6	1.0
SY309B		dravite	4.1363	0.0011	+22.92	0.27				
SY400	1*	dravite	4.1099	0.0013	+16.39	0.32				
SY400		dravite	4.1092	0.0007	+16.22	0.17				
SY400		dravite	4.1102	0.0014	+16.46	0.34				
SY400	2*	dravite	4.1141	0.0014	+17.43	0.34	+19.0	1.2	+20.3	0.8
SY400		dravite	4.1160	0.0018	+17.90	0.44				
SY441	1	dravite	4.1186	0.0011	+18.54	0.27	+18.8	0.9	+19.3	0.9
SY441		dravite	4.1183	0.0019	+18.47	0.46				

*Dravite batches No. 1 and 2 were taken from the same hand specimen. No. 2, however, was taken from the same crystal that was measured by SIMS before. The two different TIMS analyses of each dravite sample were processed by two differnt methods of chemical dissolution.

Table E.3. Tourmaline type I and coexisting phengite and glaucophane

Analysis	Sample	Type	I_P (nA)	n	$^{11}B/^{10}B$ measured	α_{inst}	$^{11}B/^{10}B$ corrected	$\delta^{11}B$ (‰)	$2\sigma_{mean}$ (‰)
1	SY314	9 core	1	50	3.870	1.0427	4.0352	-2.08	0.99
2		9 core	1	50	3.870		4.0352	-2.08	0.74
3		9 core	1	50	3.874		4.0394	-1.05	0.82
4		12 rim I	1	50	3.879		4.0446	+0.24	0.79
5		12 p.c.	1	50	3.864		4.0290	-3.63	0.79
6		12 p.c.	1	50	3.862		4.0269	-4.14	0.99
7		12 p.c.	1	50	3.872		4.0373	-1.56	0.74
8		12 p.c.	1	50	3.865		4.0300	-3.37	0.79
9		12 rim I	1	50	3.883		4.0488	+1.27	1.16
10		66 rim II	1	50	3.908		4.0748	+7.72	1.02
11		66 rim II	1	50	3.895		4.0613	+4.37	0.68
12		66 rim II	1	50	3.891		4.0571	+3.34	0.76
13		66 rim I	1	50	3.884		4.0498	+1.53	0.85
14		66 p.c.	1	50	3.866		4.0310	-3.11	0.99
15		66 core	1	50	3.874		4.0394	-1.05	1.05
16		53 rim II	1	50	3.902		4.0686	+6.17	0.85
17		53 rim I	1	50	3.877		4.0425	-0.27	0.74
18		53 core	1	50	3.871		4.0363	-1.82	0.82
19		53 core	1	50	3.869		4.0342	-2.34	0.88
20		53 p.c.	1	50	3.863		4.0279	-3.88	0.88
21		53 core	1	50	3.871		4.0363	-1.82	0.96
22		core (in Gln)	1	50	3.874		4.0394	-1.05	0.85
23		Gln core	50	200	3.857	1.0447	4.0294	-3.52	6.41
24		Gln rim	50	200	3.841		4.0127	-7.66	4.27
25		Gln	50	200	3.857		4.0294	-3.52	5.69
26		Gln rim	50	200	3.857		4.0294	-3.52	5.52
27		Phe	30	200	3.847		4.0189	-6.11	1.54
28		Phe	30	200	3.845		4.0168	-6.62	1.26
1	SY323	Tur (?)	1	50	3.918	1.0427	4.0853	+10.30	2.60
2		Tur core	1	100	3.882		4.0477	+1.01	1.06
3		Tur rim	1	100	3.889		4.0550	+2.82	0.96

Table E.3. Tourmaline type I, continued

Analysis	Sample	Type	I_P (nA)	n	$^{11}B/^{10}B$ measured	α_{inst}	$^{11}B/^{10}B$ corrected	$\delta^{11}B$ (‰)	$2\sigma_{mean}$ (‰)
1	SY432	rim	1	50	3.864	1.0476	4.0479	+1.06	0.91
2		core 1	1	50	3.849		4.0322	-2.82	1.19
3		core 1	1	50	3.846		4.0291	-3.60	0.91
4		core 1	1	50	3.852		4.0354	-2.04	0.93
5		rim	1	50	3.870		4.0542	+2.62	0.82
6		rim	1	50	3.867		4.0511	+1.84	0.91
7		rim	1	50	3.862		4.0458	+0.55	0.76
8		rim	1	50	3.865		4.0490	+1.32	0.93
9		rim	1	50	3.862		4.0458	+0.55	0.99
10		core 2	1	50	3.838		4.0207	-5.67	0.88
11		core 2	1	50	3.820		4.0018	-10.33	0.82
12		core 2	1	50	3.817		3.9987	-11.11	0.96
13		core 2	1	50	3.833		4.0155	-6.97	0.91
14		rim	1	50	3.860		4.0437	+0.03	0.93
15		rim	1	50	3.863		4.0469	+0.81	0.91
16		core 4	1	50	3.870		4.0542	+2.62	1.02
17		core 4	1	50	3.877		4.0616	+4.43	1.02
18		rim	1	50	3.865		4.0490	+1.32	0.85
19		core 4	1	50	3.874		4.0584	+3.66	0.85
20		rim	1	50	3.860		4.0437	+0.03	0.88
21		core 4	1	50	3.874		4.0584	+3.66	0.91
22		rim C	1	50	3.858		4.0416	-0.49	1.24
23		rim C	1	50	3.859		4.0427	-0.23	0.91
24		rim C	1	50	3.861		4.0448	+0.29	0.96
25		rim C	1	50	3.859		4.0427	-0.23	0.79
26		rim C	1	50	3.863		4.0469	+0.81	0.88
27		rim C	1	50	3.859		4.0427	-0.23	0.93
28		rim C	1	50	3.862		4.0458	+0.55	0.91
29		rim C	1	50	3.867		4.0511	+1.84	1.02
30		rim C	1	50	3.867		4.0511	+1.84	0.96
31		rim C	1	50	3.867		4.0511	+1.84	1.02
32		rim C	1	50	3.869		4.0532	+2.36	0.96
33		rim C	1	50	3.866		4.0500	+1.58	1.13
34		rim C	1	50	3.863		4.0469	+0.81	0.85
35		Phe	30	200	3.805	1.0513	4.0004	-10.70	1.22
36		Phe	30	200	3.806		4.0014	-10.44	1.44
37		Phe	30	200	3.801		3.9961	-11.74	1.22

Table E.4. Serpentinite

Analysis	Sample	Type	I_P (nA)	n	$^{11}B/^{10}B$ measured	α_{inst}	$^{11}B/^{10}B$ corrected	$\delta^{11}B$ (‰)	$2\sigma_{mean}$ (‰)
1	SY347	Srp clast	30	200	3.851	1.0479	4.0354	-2.04	5.63
2		Srp clast	30	200	3.828		4.0113	-8.00	5.71
3		Srp clast	30	200	3.865		4.0501	+1.59	5.40
4		Srp clast	30	200	3.866		4.0511	+1.85	5.29
5		Srp clast	30	200	3.852		4.0364	-1.78	5.46
6		Srp matrix	30	200	3.837		4.0207	-5.67	5.95
7		Srp matrix	30	200	3.834		4.0176	-6.44	5.77
1	SY429	Am core	30	200	3.905	1.0479	4.0920	+11.96	4.67
2		Am core	30	200	3.883		4.0689	+6.25	3.62
3		Am core	30	200	3.895		4.0815	+9.36	3.58

Table E.5. Tourmaline type II and coexisting phengite and glaucophane

Analysis	Sample	Type	d (μm)	I_P (nA)	n	$^{11}B/^{10}B$ measured	α_{inst}	$^{11}B/^{10}B$ corrected	$\delta^{11}B$ (‰)	$2\sigma_{mean}$ (‰)
1	SY309B	rim	55	1	68	3.959	1.0427	4.1280	+20.87	0.65
2		rim	45	1	50	3.962		4.1311	+21.64	0.88
3		rim	50	1	50	3.960		4.1291	+21.13	0.82
4		core	150	1	50	3.960		4.1291	+21.13	0.91
5		core	152	1	50	3.964		4.1332	+22.16	0.88
6		core	116	1	50	3.962		4.1311	+21.64	0.96
7		rim	10	1	50	3.963		4.1322	+21.90	0.93
8		rim	37	1	50	3.965		4.1343	+22.42	0.71
9		rim	63	1	50	3.961		4.1301	+21.39	0.91
10		core	91	1	50	3.965		4.1343	+22.42	0.93
11		core	182	1	50	3.959		4.1280	+20.87	0.74
12		core	220	1	50	3.963		4.1322	+21.90	0.74
13		core	260	1	50	3.963		4.1322	+21.90	0.71
14		rim	310	1	50	3.963		4.1322	+21.90	0.76
15		rim	347	1	50	3.962		4.1311	+21.64	0.85
16		rim	397	1	50	3.963		4.1322	+21.90	0.88
17		rim	459	1	50	3.962		4.1311	+21.64	0.79
18		rim	508	1	49	3.961		4.1301	+21.39	0.94
19		rim	550	1	50	3.963		4.1322	+21.90	0.88
20		core	155	1	50	3.960		4.1291	+21.13	0.91
21		core	160	1	50	3.961		4.1301	+21.39	0.91
22		rim	40	1	50	3.962		4.1311	+21.64	0.96
23		Gln		50	50	3.893	1.0447	4.0670	+5.78	1.73
24		Gln		30	100	3.892		4.0659	+5.52	1.48
25		Phe		50	200	3.915		4.0900	+11.46	3.55
26		Phe		30	200	3.913		4.0879	+10.94	3.61
1	SY327	rim	10	1	50	3.944	1.0476	4.1317	+21.79	0.85
2		rim	101	1	50	3.945		4.1328	+22.05	0.96
3		rim	385	1	50	3.940		4.1276	+20.75	0.96
4		rim	815	1	50	3.943		4.1307	+21.53	0.91
5		core	1203	1	50	3.943		4.1307	+21.53	1.24
6		core	1523	1	50	3.945		4.1328	+22.05	0.99
7		core	1933	1	50	3.942		4.1296	+21.27	0.85
8		core	2241	1	50	3.946		4.1338	+22.31	0.99
9		rim	2674	1	50	3.946		4.1338	+22.31	1.02
10		rim	3011	1	50	3.943		4.1307	+21.53	0.93
11		rim	3311	1	50	3.945		4.1328	+22.05	1.07

Table E.5. Tourmaline type II, continued

Analysis	Sample	Type	d (μm)	I_P (nA)	n	$^{11}B/^{10}B$ measured	α_{inst}	$^{11}B/^{10}B$ corrected	$\delta^{11}B$ (‰)	$2\sigma_{mean}$ (‰)	Comment
1	SY400	rim	10	1	50	3.937	1.0476	4.1244	+19.98	1.05	
2		rim	10	1	50	3.937		4.1244	+19.98	0.82	
3		rim	49	1	50	3.935		4.1223	+19.46	0.76	
4		rim	86	1	50	3.939		4.1265	+20.50	1.10	
5		rim	127	1	50	3.939		4.1265	+20.50	0.96	
6		core	233	1	50	3.940		4.1276	+20.75	0.96	
7		core	428	1	50	3.933		4.1202	+18.94	1.10	
8		core	564	1	50	3.932		4.1192	+18.68	0.93	
9		core	716	1	50	3.938		4.1255	+20.24	0.88	
10		core	790	1	50	3.933		4.1202	+18.94	0.99	next to point No. 11
11		core	815	1	50	3.927		4.1139	+17.39	0.96	count rate at 95% (inclusion)
12		core	936	1	50	3.932		4.1192	+18.68	0.68	
13		core	1022	1	50	3.932		4.1192	+18.68	1.07	
14		core	1096	1	50	3.930		4.1171	+18.16	1.05	
15		core	1169	1	50	3.933		4.1202	+18.94	0.93	
16		core	1260	1	50	3.929		4.1160	+17.90	1.13	
17		core	1434	1	50	3.930		4.1171	+18.16	0.93	
18		core	1540	1	50	3.924		4.1108	+16.61	1.02	count rate at 80% (inclusion)
19		core	1590	1	50	3.936		4.1234	+19.72	1.02	next to point No. 18
20		core	1600	1	50	3.934		4.1213	+19.20	0.85	
21		core	1610	1	50	3.932		4.1192	+18.68	1.13	
22		core	1680	1	50	3.935		4.1223	+19.46	1.02	
23		core	1740	1	50	3.934		4.1213	+19.20	1.10	
24		core	1829	1	50	3.936		4.1234	+19.72	0.93	
25		core	1922	1	50	3.934		4.1213	+19.20	0.96	
26		core	2093	1	50	3.932		4.1192	+18.68	0.82	
27		rim	2146	1	50	3.964		4.1527	+26.97	2.26	count rate at 50% (inclusion)
28		rim	2230	1	50	3.964		4.1527	+26.97	2.74	count rate at 50% (inclusion)
29		rim	2281	1	50	3.936		4.1234	+19.72	1.02	
30		rim	2434	1	50	3.940		4.1276	+20.75	0.82	
31		rim	2527	1	50	3.941		4.1286	+21.01	0.91	
32				1	50	3.933		4.1202	+18.94	0.88	section perpendicular to c-axis
33				1	50	3.938		4.1255	+20.24	0.93	
34		rim		1	50	3.940		4.1276	+20.75	0.96	paralell to c-axis, at Chl-vein
35		rim		1	49	3.936		4.1234	+19.72	0.91	not at Chl-vein
36		rim		1	50	3.936		4.1234	+19.72	1.13	not at Chl-vein
37		rim		1	50	3.938		4.1255	+20.24	1.19	not at Chl-vein
38		rim		1	50	3.937		4.1244	+19.98	0.88	paralell to c-axis, at Chl-vein
39		rim		1	50	3.936		4.1234	+19.72	0.93	paralell to c-axis, at Chl-vein
40		core		1	50	3.942		4.1296	+21.27	0.99	paralell to c-axis, at Chl-vein
1	SY412	rim	10	1	50	3.939	1.0476	4.1265	+20.50	0.91	
2		rim	89	1	50	3.942		4.1296	+21.27	0.91	
3		rim	183	1	50	3.936		4.1234	+19.72	1.16	
4		core	268	1	50	3.937		4.1244	+19.98	1.05	
5		core	380	1	50	3.941		4.1286	+21.01	0.96	
6		core		1	50	3.951		4.1391	+23.60	1.81	count rate at 80% (inclusion)
7		rim	480	1	50	3.941		4.1286	+21.01	0.79	next to point No. 6
8		rim	131	1	50	3.939		4.1265	+20.50	1.07	
9		rim	610	1	50	3.946		4.1338	+22.31	0.88	
10		core	271	1	50	3.944		4.1317	+21.79	1.10	
11		core	379	1	50	3.944		4.1317	+21.79	0.79	
12		rim	469	1	50	3.939		4.1265	+20.50	0.74	
13		rim	544	1	50	3.939		4.1265	+20.50	0.93	
14		rim	645	1	50	3.941		4.1286	+21.01	1.27	
15		Phe		30	200	3.887	1.0513	4.0866	+10.62	1.33	
16		Phe		30	200	3.877		4.0760	+8.02	1.46	
17		Phe		30	200	3.894		4.0939	+12.44	1.43	
18		Phe		30	200	3.894		4.0939	+12.44	1.23	
19		Phe		30	200	3.899		4.0992	+13.74	1.33	
20		Phe		30	198	3.894		4.0939	+12.44	1.31	
21		Phe		30	200	3.900		4.1002	+14.00	1.29	

Table E.5. Tourmaline type II, continued

Analysis	Sample	Type	d (μm)	I_P (nA)	n	$^{11}B/^{10}B$ measured	α_{inst}	$^{11}B/^{10}B$ corrected	$\delta^{11}B$ (‰)	$2\sigma_{mean}$ (‰)	Comment
1	SY413	rim		1	50	3.935	1.0476	4.1223	+19.46	1.13	rim of thin section
2		rim		1	50	3.940		4.1276	+20.75	0.85	rim of thin section
3		rim		1	50	3.944		4.1317	+21.79	1.10	rim of thin section
4		rim	10	1	50	3.939		4.1265	+20.50	0.82	
5		rim	89	1	50	3.947		4.1349	+22.57	0.99	
6		rim	187	1	50	3.945		4.1328	+22.05	0.88	
7		rim	282	1	50	3.941		4.1286	+21.01	0.82	
8		rim	388	1	50	3.939		4.1265	+20.50	0.91	
9		rim	496	1	50	3.949		4.1370	+23.09	0.91	
10		rim	610	1	50	3.947		4.1349	+22.57	0.99	
11		core	720	1	50	3.940		4.1276	+20.75	0.93	
12		core	829	1	50	3.945		4.1328	+22.05	0.88	
13		core	924	1	50	3.944		4.1317	+21.79	0.85	
14		core	1097	1	50	3.942		4.1296	+21.27	1.02	
15		core	1223	1	50	3.948		4.1359	+22.83	1.10	
16		core	1367	1	50	3.946		4.1338	+22.31	0.93	
17		core	1523	1	50	3.948		4.1359	+22.83	1.07	
18		core	1624	1	50	3.948		4.1359	+22.83	1.07	
19		core	1766	1	50	3.950		4.1380	+23.35	1.05	
20		core	1895	1	50	3.950		4.1380	+23.35	0.76	
21		core	2013	1	50	3.946		4.1338	+22.31	0.93	
22		core	2129	1	50	3.944		4.1317	+21.79	1.02	
23		core	2269	1	50	3.942		4.1296	+21.27	1.13	
24		core	2449	1	50	3.947		4.1349	+22.57	0.85	
25		core	2626	1	50	3.947		4.1349	+22.57	1.02	
26		core	2751	1	50	3.947		4.1349	+22.57	0.88	
27		core	2880	1	50	3.943		4.1307	+21.53	0.88	
28		rim	3027	1	50	3.942		4.1296	+21.27	1.10	
29		rim	3151	1	50	3.941		4.1286	+21.01	1.05	
30		rim	3282	1	50	3.946		4.1338	+22.31	0.99	
31		rim	3427	1	50	3.945		4.1328	+22.05	0.93	
32		rim	3552	1	50	3.942		4.1296	+21.27	0.88	
33		rim	3672	1	50	3.947		4.1349	+22.57	0.74	
34		rim	3780	1	50	3.946		4.1338	+22.31	0.99	
35		rim	3821	1	49	3.937		4.1244	+19.98	0.94	
36		rim	3846	1	50	3.940		4.1276	+20.75	0.82	
37		rim	3876	1	50	3.934		4.1213	+19.20	1.10	
38		Phe		30	200	3.885	1.0513	4.0845	+10.10	1.22	
39		Phe		30	200	3.881		4.0803	+9.06	1.29	
40		Phe		30	200	3.889		4.0887	+11.14	1.32	
41		Phe		30	200	3.887		4.0866	+10.62	1.23	
42		Phe		30	200	3.886		4.0855	+10.36	1.29	
1	SY420	rim	10	1	50	3.934	1.0476	4.1213	+19.20	0.91	
2		rim	38	1	50	3.939		4.1265	+20.50	0.93	
3		rim	65	1	50	3.936		4.1234	+19.72	0.96	
4		rim	105	1	50	3.937		4.1244	+19.98	0.76	
5		rim	137	1	50	3.938		4.1255	+20.24	0.88	
6		core	177	1	50	3.939		4.1265	+20.50	0.96	
7		core	240	1	50	3.939		4.1265	+20.50	0.82	
8		core	345	1	50	3.933		4.1202	+18.94	1.07	
9		rim	451	1	50	3.937		4.1244	+19.98	0.93	
10		rim	551	1	50	3.939		4.1265	+20.50	0.88	
11		Phe		30	200	3.874	1.0513	4.0729	+7.24	1.33	section paralell to c-axis
12		Phe		30	200	3.876		4.0750	+7.76	1.23	
13		Phe		30	200	3.860		4.0582	+3.60	1.15	
14		Phe		30	200	3.867		4.0655	+5.42	1.29	perpendicular to c-axis
15		Phe		30	200	3.867		4.0655	+5.42	1.15	
16		Phe		30	200	3.878		4.0771	+8.28	1.17	
17		Phe		30	200	3.876		4.0750	+7.76	1.17	
18		Phe		30	200	3.878		4.0771	+8.28	1.24	
19		Phe		30	200	3.876		4.0750	+7.76	1.20	

Table E.5. Tourmaline type II, continued

Analysis	Sample	Type	d (μm)	I_P (nA)	n	$^{11}B/^{10}B$ measured	α_{inst}	$^{11}B/^{10}B$ corrected	$\delta^{11}B$ (‰)	$2\sigma_{mean}$ (‰)	Comment
1	SY441	4 rim III		1	50	3.958	1.0427	4.1270	+20.61	0.82	
2		4 rim II		1	50	3.951		4.1197	+18.81	0.96	
3		4 core		1	50	3.949		4.1176	+18.29	0.85	
4		1 rim III		1	50	3.953		4.1218	+19.32	0.99	
5		1 core		1	50	3.949		4.1176	+18.29	0.85	
6		1 rim II		1	50	3.953		4.1218	+19.32	0.82	
7		2 core		1	50	3.952		4.1207	+19.06	0.76	
8		2 rim II		1	50	3.952		4.1207	+19.06	0.85	
9		2 rim III		1	50	3.951		4.1197	+18.81	0.82	
10		3 core		1	50	3.952		4.1207	+19.06	0.96	
11		3 rim II		1	50	3.952		4.1207	+19.06	0.85	
12		3 rim III		1	50	3.949		4.1176	+18.29	0.93	
13		Chl		50	200	3.865	1.0447	4.0377	-1.46	7.65	
1	SY442	rim III	10	1	50	3.940	1.0476	4.1276	+20.75	1.07	
2		rim III	10	1	50	3.937		4.1244	+19.98	0.85	
3		rim III	26	1	50	3.931		4.1181	+18.42	0.76	
4		rim III	46	1	50	3.939		4.1265	+20.50	1.07	
5		rim III	71	1	50	3.944		4.1317	+21.79	0.96	
6		rim III	88	1	50	3.952		4.1401	+23.86	1.13	
7		rim III	106	1	50	3.947		4.1349	+22.57	1.30	
8		rim III	127	1	50	3.947		4.1349	+22.57	1.10	
9		rim III	144	1	50	3.947		4.1349	+22.57	0.85	
10		rim III	173	1	50	3.950		4.1380	+23.35	0.93	
11		rim III	200	1	50	3.942		4.1296	+21.27	0.88	
12		rim II	228	1	50	3.960		4.1485	+25.94	0.91	
13		rim II	249	1	50	3.965		4.1537	+27.23	0.79	
14		rim II	285	1	50	3.968		4.1569	+28.01	1.05	
15		rim II	316	1	50	3.970		4.1590	+28.53	1.16	
16		rim II	348	1	50	3.966		4.1548	+27.49	0.88	
17		rim I	385	1	50	3.962		4.1506	+26.45	0.85	
18		rim I	419	1	50	3.962		4.1506	+26.45	0.88	
19		rim I	451	1	50	3.965		4.1537	+27.23	0.85	
20		rim I	476	1	50	3.972		4.1611	+29.05	0.99	
21		rim I	506	1	50	3.969		4.1579	+28.27	0.91	
22		rim I	533	1	50	3.969		4.1579	+28.27	0.93	
23		rim I	563	1	50	3.962		4.1506	+26.45	0.96	
24		rim I	588	1	50	3.966		4.1548	+27.49	0.91	
25		core	617	1	50	3.970		4.1590	+28.53	1.61	
26		core	651	1	50	3.970		4.1590	+28.53	0.99	
27		core	682	1	50	3.969		4.1579	+28.27	0.79	
28		core	721	1	50	3.968		4.1569	+28.01	1.10	
29		core	758	1	50	3.970		4.1590	+28.53	0.96	
30		core	802	1	50	3.968		4.1569	+28.01	1.02	
31		core	844	1	50	3.969		4.1579	+28.27	1.02	
32		core	887	1	50	3.968		4.1569	+28.01	0.96	
33		core	936	1	50	3.972		4.1611	+29.05	1.19	
34		rim I	980	1	50	3.971		4.1600	+28.79	0.99	
35		rim I	1028	1	49	3.978		4.1674	+30.60	1.11	
36		rim I	1083	1	50	3.968		4.1569	+28.01	1.07	
37		rim II	1136	1	50	3.968		4.1569	+28.01	0.99	
38		rim II	1187	1	50	3.973		4.1621	+29.30	1.02	
39		rim II	1227	1	50	3.972		4.1611	+29.05	1.02	
40		rim II	1273	1	50	3.969		4.1579	+28.27	0.93	
41		rim II	1301	1	50	3.970		4.1590	+28.53	1.02	
42		rim II	1336	1	50	3.965		4.1537	+27.23	0.93	
43		rim III	1365	1	50	3.944		4.1317	+21.79	0.93	
44		rim III	1394	1	50	3.949		4.1370	+23.09	0.91	
45		rim III	1417	1	50	3.953		4.1412	+24.12	1.19	
46		rim III	1444	1	50	3.951		4.1391	+23.60	0.93	
47		rim III	1460	1	50	3.930		4.1171	+18.16	3.42	low count rate (inclusion)
48		rim III	1467	1	50	3.945		4.1328	+22.05	1.02	next to 48
49		rim III	1488	1	50	3.941		4.1286	+21.01	0.79	
50		rim III	1508	1	50	3.939		4.1265	+20.50	0.96	

F. Lithium, beryllium and boron concentrations in minerals from ultramafic samples

Table F.1, displayed below, contains lithium, beryllium and boron SIMS analyses of different minerals in serpentinite samples SY347 and SY429 and from a serpentinite sample from the Pfulwe Pass (PF1) in the Zone of Zermatt-Saas Fee in the Central Alps (Switzerland) for comparison.

Analyses of all other samples from Syros are summarised in Tables 7.2, 7.3 and 7.4.

Table F.1. Li, Be and B concentrations in minerals from ultramafic samples

Sample	No.	Type	Li (μg/g)	$2\sigma_{mean}$ (%)	Be (μg/g)	$2\sigma_{mean}$ (%)	B (μg/g)	$2\sigma_{mean}$ (%)
SY347	1	Atg matrix	0.972	4.4	0.315	6.6	5.73	5.2
	2	Atg matrix	1.12	3.5	0.379	9.1	6.00	2.5
	3	Atg matrix	1.07	6.0	0.339	7.7	5.69	3.3
	4	Atg matrix	0.732	4.0	0.269	9.8	5.58	4.8
	5	Atg matrix	0.834	4.3	0.221	11.5	4.46	7.0
	6	Atg matrix	0.669	5.6	0.153	16.0	4.47	5.6
	16	Atg matrix	0.565	4.0	0.172	12.9	5.17	3.6
	17	Atg matrix	0.893	3.5	0.216	12.0	4.47	2.6
	18	Atg matrix	0.715	4.7	0.189	6.8	4.10	5.4
	19	Atg matrix	0.804	3.5	0.213	5.9	4.78	1.9
	7	Atg clast	0.753	4.6	0.247	13.5	5.66	4.6
	8	Atg clast	0.685	5.7	0.224	6.9	5.76	2.6
	9	Atg clast	0.747	7.4	0.268	4.9	5.52	5.8
	10	Atg clast	0.680	4.8	0.255	7.1	5.80	4.0
	11	Atg clast	0.685	6.0	0.242	4.6	5.96	3.4
	12	Atg clast	0.677	4.9	0.227	11.7	5.65	2.8
	13	Atg clast	0.595	8.6	0.195	13.0	5.30	5.6
	14	Atg clast	0.738	2.8	0.265	9.0	6.78	2.2
	15	Atg clast	0.727	3.6	0.235	13.7	5.56	5.6
	20	Atg clast	0.661	3.9	0.182	10.4	5.45	2.6
	21	Atg clast	0.670	5.1	0.263	6.0	5.73	3.0
SY429	15	Atg	3.55	1.3	0.194	7.1	3.90	5.7
	16	Atg	3.91	1.2	0.210	5.8	3.75	3.4
	17	Atg	4.32	1.2	0.215	5.8	4.80	2.9
	18	Atg	3.89	1.2	0.207	6.6	4.43	4.0
	19	Atg	3.72	1.8	0.198	6.8	4.35	2.4
	7	Am	0.357	4.8	2.01	2.4	10.5	1.8
	9	Am	0.473	3.7	1.94	2.4	11.5	1.4
	10	Am	0.555	2.3	3.95	1.3	13.6	1.9
	11	Am	0.568	3.9	4.55	1.6	16.1	1.6
	13	Am	0.554	3.1	4.06	1.7	13.8	1.9
	14	Am	0.319	4.5	1.45	3.2	13.5	2.5
	2	Tlc	0.915	2.0	0.076	11.3	2.37	9.7
	3	Tlc	1.09	2.9	0.090	9.9	3.87	9.0
	4	Tlc	1.24	4.1	0.085	22.5	3.84	13.5
	5	Tlc	0.657	5.1	0.051	14.2	1.83	7.1
	6	Tlc	0.940	3.3	0.098	10.0	2.36	5.3
	8	Tlc	0.808	3.8	0.100	11.7	1.59	2.9
	12	Tlc	0.624	4.5	0.140	9.0	1.70	5.6
PF1	1	Atg clast	0.673	4.4	0.196	6.4	4.60	2.5
	2	Atg clast	0.574	3.9	0.183	6.1	3.87	2.7
	3	Atg clast	0.423	5.2	0.166	5.4	5.65	2.6
	4	Atg clast	0.494	4.3	0.196	5.0	4.67	2.4
	14	Atg clast	0.541	3.4	0.177	8.1	3.95	3.0
	10	Atg clast	0.565	3.8	0.190	5.2	4.46	4.0
	11	Atg clast	0.441	2.7	0.173	6.7	4.94	3.1
	12	Atg matrix	0.672	3.9	0.222	6.2	8.82	2.2
	13	Atg matrix	0.724	3.8	0.291	6.1	13.1	1.7
	16	Atg matrix	0.601	2.0	0.096	5.6	3.24	6.4
	15	Atg matrix	0.752	1.7	0.292	4.7	6.11	2.8
	17	Atg matrix	0.939	3.1	0.104	7.1	2.75	4.2
	5	Atg matrix	0.720	3.6	0.230	9.6	4.55	3.1
	6	Am	0.075	14.9	0.258	4.5	3.73	2.5
	7	Am	0.052	12.5	0.201	7.3	4.40	1.6
	8	Am	0.034	16.0	0.233	4.7	3.19	2.5
	9	Am	0.046	15.2	0.219	7.9	3.80	2.5

G. Trace element mineral analyses determined by laser ablation ICP-MS

The analytical details on laser-ablation ICP-MS are given in Section 2.6 on page 32. In addition to average trace-element abundances of tourmaline given in Chapter 11, the following tables give all results of single analyses of different minerals in the tourmaline-bearing samples.

Analysed isotopes were: ^{29}Si, ^{49}Ti, ^{51}V, ^{55}Mn, ^{59}Co, ^{65}Cu, ^{71}Ga, ^{85}Rb, ^{88}Sr, ^{89}Y, ^{90}Zr, ^{93}Nb, ^{121}Sb, ^{133}Cs, ^{137}Ba, ^{139}La, ^{140}Ce, ^{141}Pr, ^{146}Nd, ^{147}Sm, ^{153}Eu, ^{157}Gd, ^{159}Tb, ^{163}Dy, ^{165}Ho, ^{166}Er, ^{169}Tm, ^{172}Yb, ^{175}Lu, ^{178}Hf, ^{181}Ta, ^{182}W, ^{208}Pb, ^{232}Th, ^{238}U.

Table G.1. Sample SY309

| Type | Aln | Ep | Chl | Chl | Chl | Gln | Gln | Omp | Omp | Omp | Omp |
No.	1	2	1	2	3	1	2	1	2	3	4
V	448	401	91	102	100	202	220	353	386	369	428
Mn	1,358	1,461	1,950	1,589	2,052	600	581	1,105	1,163	1,039	1,083
Co	11	13	87	63	85	43	41	14	16	20	15
Cu	8	20	28	37	24	18	13	14	17	17	12
Zn	177	19	371	259	374	121	124	54	49	42	43
Ga	75	43	26	17	25	10	10	9	10	9	11
Rb	13.7	1.1	< 0.15	< 0.15	0.3	13.8	11.9	0.7	0.7	1.1	0.6
Sr	805	1078	0.27	0.33	0.65	0.79	0.47	6.8	6.7	7.4	6.9
Y	876	32.3	< 0.02	< 0.02	0.42	0.09	0.08	0.99	0.79	0.22	0.45
Zr	1.88	5.27	1.18	< 0.09	0.26	0.56	0.18	1.59	1.56	1.68	1.43
Nb	< 0.01	0.11	< 0.01	< 0.01	1.02	0.20	0.05	0.04	0.10	0.11	0.03
Sb	< 0.26	< 0.26	< 0.26	< 0.26	< 0.26	< 0.26	< 0.26	< 0.26	< 0.26	< 0.26	< 0.26
Cs	0.21	0.34	< 0.05	< 0.03	0.09	0.45	0.30	0.27	0.21	0.26	0.12
Ba	8.3	5.1	3.9	2.6	3.0	14.4	7.7	0.84	1.42	1.10	0.22
La	2,550	14.1	0.07	< 0.01	0.02	0.03	< 0.01	< 0.01	0.02	0.04	< 0.01
Ce	8,279	27.0	0.12	< 0.01	0.04	0.00	< 0.01	0.03	0.01	0.01	< 0.01
Pr	1,251	3.05	< 0.01	< 0.01	< 0.01	< 0.01	< 0.01	0.02	< 0.01	0.02	0.02
Nd	4,982	13.6	< 0.03	0.05	< 0.03	< 0.03	< 0.03	< 0.05	< 0.03	< 0.03	0.20
Sm	1,453	3.77	< 0.03	< 0.03	< 0.03	0.11	< 0.03	0.16	< 0.03	0.19	0.16
Eu	82.0	4.46	< 0.01	< 0.01	0.02	< 0.02	0.03	0.02	0.02	0.05	0.00
Gd	762	3.30	< 0.05	< 0.05	< 0.05	0.10	< 0.05	0.09	0.11	0.13	< 0.05
Tb	87.7	0.77	< 0.01	< 0.01	< 0.01	0.02	< 0.01	0.01	0.02	0.02	0.02
Dy	340	4.39	< 0.02	< 0.04	0.09	0.05	< 0.02	0.16	0.13	0.21	0.08
Ho	44.6	0.91	< 0.01	< 0.01	0.02	< 0.02	< 0.01	0.03	0.05	0.02	0.03
Er	83.8	3.38	< 0.02	< 0.02	0.05	< 0.04	< 0.02	0.27	0.15	< 0.04	0.10
Tm	8.64	0.45	< 0.01	< 0.01	< 0.01	< 0.01	< 0.01	0.05	0.05	0.03	< 0.01
Yb	52.2	5.44	< 0.02	< 0.02	0.15	0.06	0.06	0.34	0.29	0.44	0.09
Lu	4.96	0.72	< 0.01	< 0.01	0.03	0.02	< 0.01	0.06	0.06	0.06	0.04
REE	19,981	85.4	0.19	0.05	0.42	0.40	0.08	1.25	0.93	1.22	0.74
Hf	< 0.06	0.19	0.11	< 0.04	< 0.04	< 0.06	0.08	0.23	0.26	0.15	0.23
Ta	< 0.01	< 0.01	< 0.01	< 0.01	0.03	0.02	0.02	< 0.01	0.03	0.02	< 0.01
W	< 0.05	0.24	< 0.03	< 0.03	< 0.03	< 0.05	< 0.03	< 0.05	0.06	0.09	0.07
Pb	16.5	12.8	1.59	1.78	1.50	1.81	1.57	1.55	9.8	4.3	2.7
Th	194	0.72	< 0.02	< 0.02	< 0.03	< 0.02	< 0.02	< 0.02	< 0.02	0.05	0.05
U	44.8	0.86	< 0.02	< 0.01	0.02	< 0.02	< 0.01	< 0.01	0.02	0.04	0.04

Table G.1. Sample SY309 continued

Type No.	Phe 1	Phe 2	Rt 1	Rt 2	Ttn 1	Ttn 2	Tur core3	Tur core4	Tur core5	Tur rim1	Tur rim2	Tur rim6
V	358	372	1194	1408	547	548	181	207	152	233	278	392
Mn	171	161	72	71	353	342	132	131	139	141	104	147
Co	23	21	36	40	16	11	40	39	46	41	37	42
Cu	31	26	77	89	33	28	16	10	20	21	55	13
Zn	105	133	53	61	41	38	70	72	63	54	58	60
Ga	30	31	3.0	4.1	1.7	1.6	13	13	11	14	15	16
Rb	200	216	3.3	2.7	1.3	0.8	1.0	0.4	1.0	1.2	1.0	0.5
Sr	4.7	3.9	8.0	10.0	50	44	92	101	99	234	85	234
Y	0.11	0.08	0.74	1.19	162	178	0.06	< 0.02	0.09	0.05	0.09	0.10
Zr	1.36	0.84	71	74	4.67	3.80	0.28	0.28	0.68	0.84	0.39	0.30
Nb	0.48	0.36	82	144	202	192	< 0.02	< 0.02	0.04	0.05	0.08	< 0.02
Sb	< 0.26	< 0.26	1.43	3.97	1.67	1.37	< 0.26	< 0.26	< 0.26	< 0.26	< 0.26	< 0.26
Cs	4.4	4.9	0.86	0.95	0.36	0.15	0.16	0.11	0.34	0.26	0.22	0.22
Ba	863	836	2.4	2.9	0.91	0.65	0.58	0.27	0.34	0.66	0.73	0.21
La	0.06	0.06	0.24	0.44	0.22	0.43	0.04	< 0.02	< 0.02	0.02	0.03	< 0.01
Ce	0.04	0.03	0.11	0.24	1.44	1.24	0.02	< 0.01	< 0.01	0.04	< 0.01	0.01
Pr	0.02	< 0.01	0.05	0.09	0.58	0.48	< 0.01	< 0.01	< 0.01	0.02	0.02	0.01
Nd	0.19	0.18	0.30	0.39	5.48	4.28	< 0.05	0.06	0.09	0.07	0.06	< 0.05
Sm	0.29	0.09	0.51	0.39	4.74	3.83	< 0.05	< 0.05	0.14	0.08	< 0.03	< 0.05
Eu	0.15	0.10	0.12	0.16	5.21	5.29	< 0.01	0.03	0.07	< 0.02	0.03	0.03
Gd	0.22	0.21	0.23	0.26	10.2	9.73	0.08	0.10	0.10	< 0.08	0.21	0.13
Tb	0.03	< 0.01	0.03	0.05	3.01	2.95	< 0.01	< 0.01	< 0.01	0.02	< 0.01	< 0.01
Dy	0.17	0.06	0.14	0.14	22.7	27.4	0.09	< 0.04	0.17	0.04	0.09	0.08
Ho	0.06	0.03	0.03	0.10	5.79	6.99	< 0.01	< 0.01	0.02	< 0.01	0.02	< 0.01
Er	0.07	0.11	0.15	0.09	18.7	23.0	< 0.04	< 0.02	0.08	0.04	< 0.02	0.05
Tm	0.02	0.04	0.05	0.05	3.44	4.08	0.02	< 0.01	< 0.01	0.02	< 0.01	0.02
Yb	0.13	0.11	0.22	0.18	27.8	32.2	0.10	0.08	0.05	0.09	0.10	0.06
Lu	0.03	0.03	0.03	0.07	4.74	4.93	0.02	< 0.01	< 0.01	0.03	0.02	< 0.01
REE	1.46	1.05	2.22	2.65	114	127	0.48	0.36	0.72	0.54	0.61	0.47
Hf	0.34	0.07	5.33	7.02	0.45	0.43	< 0.06	< 0.04	0.12	0.08	< 0.06	< 0.04
Ta	0.32	0.26	2.85	3.96	6.96	7.04	< 0.01	< 0.01	0.02	0.02	< 0.01	0.02
W	0.36	0.38	50.6	69.5	0.19	0.06	0.09	< 0.03	< 0.03	< 0.03	0.07	< 0.03
Pb	3.2	4.1	9.0	13.2	6.9	8.7	1.19	1.33	0.95	1.37	2.48	2.20
Th	0.06	< 0.03	0.27	1.16	< 0.02	0.96	0.03	< 0.02	0.06	< 0.02	0.05	< 0.02
U	< 0.01	0.03	0.26	0.51	0.38	0.24	< 0.02	0.02	0.03	0.02	0.03	0.03

Table G.2. Sample SY400

Type No.	Omp 1	Tur core4	Tur core5	Tur rim1	Tur rim2	Tur rim3
Ti	483	2693	2735	2463	2256	2551
V	190	70	63	88	73	70
Mn	961	129	137	135	143	113
Co	14.2	39	43	56	54	53
Cu	5.3	12.2	12.8	8.7	9.4	7.3
Zn	27	43	48	53	50	47
Ga	14	19	19	14	13	14
Rb	< 0.7	2.6	4.2	2.4	2.2	1.6
Sr	22	301	259	268	220	306
Y	1.84	0.16	0.22	0.14	0.22	0.17
Zr	6.23	1.40	2.24	1.12	0.99	0.97
Nb	< 0.04	0.06	0.26	0.10	0.14	0.10
Sb	< 0.54	< 0.54	3.38	< 0.54	< 0.54	< 0.54
Cs	< 0.16	0.88	0.81	0.66	0.65	0.27
Ba	0.43	1.33	1.37	0.79	0.60	0.77
La	< 0.04	0.11	0.09	0.07	0.13	0.07
Ce	0.03	0.04	0.03	0.03	< 0.01	< 0.02
Pr	< 0.02	0.03	0.09	0.04	< 0.01	< 0.01
Nd	0.16	0.17	0.35	0.24	0.19	0.19
Sm	< 0.08	0.60	0.44	0.20	0.20	< 0.13
Eu	0.10	< 0.02	< 0.04	0.06	0.04	0.05
Gd	< 0.10	0.29	0.49	< 0.10	0.39	0.37
Tb	< 0.01	0.03	0.14	0.05	< 0.01	< 0.01
Dy	0.39	0.27	0.33	< 0.07	0.16	< 0.04
Ho	0.11	0.03	0.05	0.04	< 0.01	< 0.01
Er	0.31	0.13	0.21	0.07	< 0.04	0.13
Tm	0.08	0.03	0.10	0.06	0.06	0.05
Yb	0.38	0.13	0.40	< 0.04	0.09	0.09
Lu	0.09	0.06	0.09	0.04	< 0.02	< 0.02
REE	1.63	1.94	2.84	1.07	1.28	1.11
Hf	0.71	< 0.05	0.38	< 0.05	0.16	0.09
Ta	< 0.03	0.07	0.06	< 0.02	< 0.03	< 0.03
W	< 0.05	0.20	0.21	0.12	< 0.09	< 0.09
Pb	1.41	3.00	2.41	6.60	4.93	4.38
Th	< 0.02	0.00	0.17	0.04	0.05	0.07
U	< 0.02	< 0.02	0.06	< 0.02	0.09	< 0.01

Table G.3. Sample SY401

Type No.	Ttn 1	Ttn 2	Ttn 3	Ttn 4	Tur core1	Tur core4	Tur rim2	Tur rim3	Tur rim5	Tur rim6	Tur rim7
Ti	190,000	173,200	215,900	212,300	819	950	3412	3182	3783	4095	3199
V	403	447	494	553	255	206	279	320	273	392	345
Mn	354	558	359	340	149	143	145	161	141	145	111
Co	11.4	13.1	10.6	3.4	31	43	35	41	39	39	37
Cu	18.8	13.3	28.3	23.2	16	12	13	14	12	9	10
Zn	34.4	54.7	35.1	32.0	45	61	64	49	63	65	72
Ga	3.7	3.7	4.2	1.5	15	15	17	17	19	18	20
Rb	2.2	< 0.7	2.7	< 1.2	2.8	1.7	2.3	3.2	1.6	1.2	< 1.2
Sr	55	51	66	70	42	38	96	90	107	243	81
Y	917	631	572	573	0.31	0.14	0.20	0.17	0.13	0.11	0.07
Zr	6.1	3.8	7.3	5.4	1.39	1.32	1.92	1.95	1.04	1.07	0.75
Nb	88	100	109	164	0.16	0.09	0.17	0.15	< 0.04	0.08	0.09
Sb	1.54	1.55	1.60	1.91	< 0.33	< 0.33	< 0.33	< 0.54	< 0.33	< 0.33	< 0.33
Cs	0.72	< 0.16	0.74	0.29	0.85	0.48	0.69	0.88	0.44	0.29	0.29
Ba	2.07	0.30	1.51	0.47	1.41	0.45	1.12	2.11	0.96	0.45	0.91
La	1.41	0.93	1.59	1.41	0.18	0.10	0.06	0.12	0.04	< 0.02	< 0.02
Ce	8.77	8.64	8.35	9.46	0.03	0.05	0.06	< 0.01	< 0.01	0.04	< 0.01
Pr	2.77	2.66	2.42	3.04	0.06	< 0.01	0.08	0.03	< 0.02	0.03	< 0.02
Nd	24.3	21.6	23.6	27.5	0.36	0.34	< 0.05	0.64	0.12	0.44	0.27
Sm	22.7	20.3	20.8	24.5	0.53	0.38	0.52	0.23	0.21	0.13	< 0.08
Eu	24.2	23.0	22.4	27.1	0.10	0.05	0.20	0.15	< 0.04	0.07	< 0.04
Gd	47.4	36.6	40.6	45.7	0.76	0.31	0.26	0.20	0.19	0.71	0.26
Tb	14.4	10.6	11.8	13.5	0.06	< 0.01	0.04	0.07	< 0.01	0.05	< 0.02
Dy	132.9	97.5	92.7	100.0	0.34	0.18	0.22	0.30	0.24	< 0.04	< 0.04
Ho	37.0	26.7	23.0	23.2	0.05	0.05	0.02	0.04	0.02	0.05	< 0.01
Er	128.1	90.7	69.7	70.2	0.18	< 0.04	0.21	< 0.06	0.11	0.12	0.08
Tm	23.7	17.0	12.5	10.6	0.03	< 0.02	0.03	0.08	0.05	< 0.02	0.09
Yb	208.2	137.7	88.5	76.2	0.14	< 0.04	0.16	0.28	< 0.04	0.17	< 0.04
Lu	24.5	16.1	11.6	9.8	0.10	0.04	0.06	0.10	< 0.03	0.08	0.10
REE	700	510	429	442	2.82	1.57	1.95	2.28	1.07	1.94	0.99
Hf	0.61	0.47	1.12	0.76	0.31	< 0.08	0.09	0.16	< 0.05	< 0.08	< 0.05
Ta	5.99	5.30	5.90	8.87	< 0.02	0.07	0.04	0.06	0.11	< 0.03	< 0.02
W	0.36	< 0.09	0.26	< 0.09	0.18	0.18	< 0.09	0.30	0.10	0.12	< 0.05
Pb	4.10	4.14	3.99	4.97	1.25	0.73	1.40	0.97	1.84	2.68	1.73
Th	0.43	0.18	0.74	1.03	0.19	0.12	< 0.02	0.20	0.13	0.06	< 0.02
U	1.54	1.57	1.42	2.15	0.05	0.07	0.07	0.04	< 0.02	0.06	< 0.01

Table G.4. Sample SY412

Type No.	Ep 1	Ep 2	Omp 1	Omp 2	Omp 3	Omp 4	Omp 5	Phe 1	Rt 1	Tur core2	Tur rim1	Tur rim3	Tur rim4
Ti	1,267	1,190	664	3,456	3,985	563	402	1,306	543,500	3,524	4,287	5,088	4,807
V	624	774	736	781	587	1,049	854	658	1,072	509	533	518	535
Mn	2,520	2,358	1,059	450	540	297	251	41	100	76	85	70	60
Co	4.1	6.0	16	20	23	25	20	15	26	41	43	38	39
Cu	7.2	8.6	16	14	19	23	19	5.2	48	17	19	13	13
Zn	16	14	47	55	50	57	51	88	48	85	84	82	81
Ga	68	65	20	24	17	21	18	52	4.0	27	21	21	22
Rb	1.3	1.5	3.0	2.7	3.8	3.4	2.8	97	3.1	3.5	5.8	3.0	2.6
Sr	3,478	1,804	19	26	7.8	24	7.4	10	17	48	54	52	41
Y	119	64	1.80	4.06	17.9	1.11	28.9	0.10	2.82	0.29	0.40	0.26	0.19
Zr	6.15	6.40	3.00	339	994	6.8	1.00	0.73	50	1.89	2.58	1.92	1.58
Nb	0.06	0.08	0.16	1.13	0.78	0.11	< 0.04	< 0.04	78	0.21	0.41	0.22	0.14
Sb	< 0.33	< 0.33	< 0.54	< 0.33	< 0.33	< 0.33	< 0.33	< 0.33	4.35	< 0.33	< 0.33	< 0.33	< 0.54
Cs	0.31	0.34	0.64	0.95	0.97	0.63	0.64	0.71	0.67	0.55	1.11	0.68	0.54
Ba	3.48	2.12	0.75	0.93	2.18	1.03	1.80	360	3.18	0.82	1.05	0.82	0.45
La	33.7	1.23	0.36	0.04	0.09	0.13	0.09	0.05	0.21	0.06	0.09	0.09	0.10
Ce	115	4.84	0.97	< 0.01	0.09	0.03	0.07	0.07	0.55	0.02	< 0.02	0.04	0.02
Pr	18.6	0.96	0.18	0.11	0.07	0.06	0.03	< 0.01	0.07	0.03	0.04	0.08	< 0.01
Nd	91.1	5.77	1.02	< 0.05	0.18	0.60	0.16	< 0.05	0.55	0.35	0.27	0.22	< 0.05
Sm	30.8	4.61	0.33	< 0.08	0.43	0.26	0.68	0.30	0.93	0.23	0.27	0.12	0.11
Eu	38.6	3.43	0.29	0.11	0.26	0.14	0.22	0.13	0.16	< 0.04	0.06	0.17	0.11
Gd	29.2	7.22	0.23	0.87	0.50	0.22	0.45	0.18	0.32	0.76	0.71	0.31	0.58
Tb	4.81	1.44	0.06	0.11	0.16	0.06	0.06	0.03	0.06	0.07	0.08	0.08	0.05
Dy	28.5	12.3	0.31	0.37	1.47	0.46	0.15	< 0.04	0.93	< 0.07	0.44	0.15	0.19
Ho	5.13	2.38	0.10	0.08	0.63	0.10	0.06	< 0.01	0.12	0.07	0.04	0.07	< 0.01
Er	10.4	7.30	0.31	0.56	3.43	0.54	0.40	< 0.06	0.40	0.19	< 0.04	0.17	0.13
Tm	1.15	1.15	0.06	0.19	0.99	0.02	0.04	< 0.02	0.10	0.08	< 0.02	0.03	0.04
Yb	7.24	10.01	0.42	1.61	9.09	0.31	0.33	< 0.07	0.69	0.26	0.28	0.09	0.17
Lu	0.88	1.24	0.09	0.32	1.44	0.15	0.04	0.07	0.08	0.08	0.05	0.05	0.08
REE	415	63.9	4.70	4.35	18.8	3.10	2.76	0.83	5.16	2.28	2.36	1.68	1.60
Hf	0.09	0.25	0.52	10.1	24.0	0.32	1.62	0.54	4.86	0.26	0.21	0.40	< 0.08
Ta	0.03	0.05	0.12	0.10	0.05	0.12	0.13	1.16	7.78	< 0.03	< 0.02	0.08	0.05
W	0.09	< 0.05	0.19	0.18	0.25	< 0.09	0.15	< 0.09	6.40	0.10	0.23	0.25	0.15
Pb	68.1	42.9	2.29	1.15	2.43	3.55	2.06	7.33	2.88	1.69	1.03	1.97	2.30
Th	3.43	0.11	0.12	< 0.02	0.76	0.08	0.09	< 0.04	2.15	0.05	0.17	< 0.02	< 0.02
U	1.87	0.18	0.10	0.12	0.52	0.08	< 0.02	0.05	0.46	0.05	0.11	0.11	0.03

Table G.5. Sample SY413

Type No.	Ep 1	Gln 1	Omp 1	Omp 2	Omp 3	Omp 4	Omp 5	Phe 1	Phe 2	Phe 3	Ttn 1	Ttn 3	Tur core3	Tur core4	Tur core5	Tur rim1	Tur rim2
Ti	554	622	533	451	751	679	563	1188	1240	1201	204100	212700	4446	3817	3716	4118	5059
V	525	235	464	552	595	544	427	287	285	507	498	531	282	219	347	432	471
Mn	785	708	1321	1189	1254	1383	1430	68	76	44	263	178	188	177	89	182	158
Co	7.4	68	17	18	22	21	26	19	19	11	15	3	63	64	46	48	48
Cu	8.1	25	11	16	12	14	18	20	11	8	25	22	43	38	15	14	16
Zn	8.7	103	44	38	42	48	46	45	43	38	34	30	109	78	66	78	61
Ga	49	16	18	18	19	20	19	33	35	36	3.1	1.3	17	16	21	17	20
Rb	1.9	4.7	1.6	1.9	2.1	2.6	3.6	91	74	72	3.9	1.0	6.4	5.3	1.8	1.8	1.8
Sr	1501	7.0	17	31	12	16	31	7.8	12.0	8.5	114	43	108	81	83	327	607
Y	34	1.4	2.9	3.0	3.4	4.2	4.5	0.3	0.1	< 0.03	396	222	1.72	2.67	0.54	0.38	0.21
Zr	91	5.9	2.3	14.6	117	5.0	17.4	2.6	2.1	4.2	310	5.0	4.20	11.6	2.15	1.83	5.81
Nb	0.19	0.24	0.09	0.10	0.28	0.22	0.16	0.17	0.13	0.07	25	22	0.40	0.65	0.18	< 0.04	0.12
Sb	< 0.33	< 0.33	< 0.54	< 0.33	< 0.33	< 0.33	< 0.33	< 0.33	< 0.33	< 0.33	0.43	0.63	< 0.33	< 0.33	< 0.33	< 0.33	< 0.33
Cs	< 0.27	< 0.04	0.47	0.50	0.44	0.54	0.60	1.44	1.18	0.81	0.72	< 0.27	1.63	2.22	0.60	0.38	0.44
Ba	2.88	2.96	0.62	0.65	0.54	1.09	1.34	214	220	199	1.08	2.24	4.04	4.76	0.50	0.69	1.00
La	2.28	0.88	0.07	0.07	0.10	0.18	0.06	0.10	0.13	0.05	0.69	0.12	0.19	0.21	0.15	0.75	0.13
Ce	5.43	0.39	0.02	< 0.01	0.06	0.12	< 0.01	0.09	< 0.01	0.04	6.84	1.03	< 0.01	0.11	0.21	2.26	< 0.01
Pr	0.93	0.18	0.02	0.02	0.05	0.02	< 0.01	0.05	0.11	< 0.01	3.02	0.43	0.12	< 0.01	0.02	0.44	0.02
Nd	5.17	0.34	0.19	< 0.05	0.31	0.39	0.38	0.39	0.11	0.33	33.5	4.23	0.40	1.72	0.19	1.81	0.19
Sm	2.97	0.51	0.31	0.75	0.51	0.24	0.29	< 0.13	0.45	0.19	21.9	3.20	< 0.08	< 0.08	< 0.13	0.21	0.20
Eu	0.87	< 0.02	0.07	0.04	0.11	0.18	0.13	0.10	< 0.04	0.12	8.54	1.37	0.09	0.26	0.10	0.16	0.16
Gd	2.86	0.43	0.73	< 0.17	0.20	0.31	0.39	0.33	< 0.10	< 0.10	38.0	8.19	0.57	4.60	0.42	0.37	0.34
Tb	0.71	0.21	0.05	< 0.01	0.08	0.06	0.11	< 0.02	0.08	< 0.01	9.24	2.18	0.15	0.16	0.08	< 0.01	0.03
Dy	5.87	< 0.07	0.51	0.34	0.48	0.58	0.33	0.33	0.24	0.04	60.6	22.3	0.65	0.91	0.29	0.14	0.16
Ho	1.28	0.26	0.25	0.17	0.21	0.17	0.18	0.07	0.15	< 0.01	14.7	7.56	< 0.01	0.21	< 0.01	0.03	0.05
Er	4.54	0.23	0.59	0.70	0.67	0.76	0.63	0.07	< 0.06	< 0.04	46.2	33.3	0.89	< 0.04	0.25	0.23	< 0.04
Tm	0.76	< 0.02	0.15	0.13	0.10	0.20	0.15	0.04	0.03	0.02	7.61	7.25	< 0.02	0.24	0.04	0.05	0.02
Yb	5.53	< 0.04	1.55	0.39	1.53	1.71	1.59	0.52	0.34	< 0.04	58.5	74.7	0.75	< 0.04	0.23	0.10	0.04
Lu	0.85	0.30	0.17	0.14	0.30	0.18	0.34	0.09	0.07	< 0.02	9.19	11.10	0.45	0.18	0.08	0.11	0.11
REE	40.0	3.71	4.70	2.75	4.69	5.09	4.60	2.17	1.66	0.75	318	177	4.33	8.72	2.18	6.64	1.46
Hf	2.40	< 0.05	0.40	0.26	3.64	0.39	0.88	0.18	< 0.08	0.60	7.45	0.30	< 0.05	< 0.05	0.12	0.23	< 0.05
Ta	0.07	0.09	0.04	< 0.02	0.08	0.10	< 0.03	0.79	0.43	0.62	3.40	3.65	0.08	0.10	0.04	< 0.02	0.05
W	0.08	0.89	0.08	< 0.05	0.13	< 0.09	< 0.05	< 0.05	< 0.05	0.18	< 0.05	0.07	0.23	0.28	0.23	0.12	0.07
Pb	19.2	1.42	4.14	3.52	2.83	1.32	4.49	1.60	2.06	3.06	7.81	9.09	3.38	2.20	3.22	3.93	5.91
Th	0.14	< 0.02	0.04	< 0.02	0.22	0.07	0.09	0.08	0.06	< 0.02	0.20	< 0.04	0.64	0.42	0.11	0.20	< 0.02
U	0.28	0.03	0.05	< 0.02	0.07	0.04	0.06	0.07	< 0.01	< 0.01	0.20	0.03	0.09	0.22	0.04	0.04	0.06

Table G.6. Sample SY420

Type No.	Ep 1	Ep 2	Grt 1	Grt 2	Grt 3	Grt 4	Phe 1	Tur core3	Tur rim4	Tur rim5	Tur rim6
Ti	762	740	1,238	962	1,385	1,316	1,148	1,155	3,343	3,342	1,896
V	337	216	74	72	55	53	176	116	189	214	165
Mn	1,017	1,575	16,610	20,430	7,770	6,486	770	299	296	275	275
Co	< 0.98	17	74	63	52	47	36	74	71	69	69
Cu	< 1.15	16	29	25	35	28	20	4.4	17	4.9	3.8
Zn	28	30	88	66	61	64	69	101	77	77	85
Ga	67	41	11	7.3	11	10	39	20	26	31	28
Rb	< 0.6	3.2	7.7	5.2	6.5	5.4	238	< 1.2	3.6	1.2	< 1.2
Sr	1,346	2,137	3.3	2.0	2.5	2.0	15.2	134	348	301	134
Y	52	171	112	91	59	106	0.85	< 0.06	0.51	0.12	< 0.03
Zr	3.1	5.3	10.8	6.0	9.0	7.6	3.2	0.55	2.52	3.41	3.32
Nb	0.18	0.31	0.52	0.46	0.96	0.69	2.54	< 0.03	0.23	0.12	0.06
Sb	< 0.33	< 0.33	< 0.54	< 0.33	< 0.33	< 0.33	< 0.33	< 0.33	< 0.33	< 0.33	< 0.33
Cs	< 0.12	1.27	1.71	1.23	1.18	1.52	2.56	< 0.16	0.79	< 0.27	< 0.16
Ba	2.81	3.19	2.53	1.50	3.30	1.56	2,313	1.17	1.77	2.20	3.26
La	227	133	< 0.04	< 0.02	< 0.02	< 0.04	< 0.02	< 0.02	< 0.02	< 0.02	< 0.02
Ce	522	310	< 0.01	< 0.01	< 0.01	< 0.01	< 0.01	< 0.01	< 0.01	< 0.01	< 0.01
Pr	56.2	35.3	< 0.02	< 0.02	0.14	0.10	< 0.01	< 0.01	< 0.01	< 0.01	< 0.01
Nd	198	128	0.85	0.66	1.09	0.73	< 0.08	< 0.05	< 0.05	< 0.08	< 0.05
Sm	35.5	25.4	0.93	0.77	0.69	1.47	0.51	0.21	0.41	0.16	< 0.08
Eu	12.9	12.3	0.47	0.18	0.29	0.18	0.10	0.07	0.12	0.03	0.04
Gd	20.3	22.6	3.25	1.88	1.12	2.73	0.62	0.47	1.14	0.30	0.33
Tb	3.21	4.05	0.68	0.56	0.54	1.31	0.04	0.05	0.13	< 0.02	< 0.01
Dy	14.1	22.4	9.99	6.72	6.70	11.55	0.22	< 0.04	0.28	< 0.07	0.12
Ho	2.15	11.8	3.77	2.88	2.20	3.83	0.08	< 0.01	0.11	< 0.01	< 0.01
Er	4.31	25.5	17.75	12.36	6.19	9.64	0.22	< 0.04	0.34	< 0.06	0.09
Tm	0.38	1.19	3.46	2.81	0.73	1.81	0.08	< 0.02	0.13	0.03	< 0.02
Yb	1.71	7.28	33.15	25.87	8.13	10.75	0.97	0.17	< 0.07	0.21	< 0.04
Lu	0.05	0.93	5.42	4.22	1.03	1.25	0.12	< 0.02	0.07	< 0.03	< 0.02
REE	1,097	739	79.7	58.9	28.8	45.4	2.95	1.11	2.82	0.96	0.74
Hf	0.19	2.99	0.56	0.26	0.81	0.43	0.58	< 0.05	0.15	< 0.05	0.25
Ta	< 0.02	< 0.02	0.19	0.09	0.22	0.13	1.25	< 0.03	0.06	< 0.03	0.03
W	< 0.04	0.13	0.28	0.23	0.19	0.39	0.36	< 0.05	0.10	< 0.09	< 0.05
Pb	153	155	1.64	3.60	1.63	1.07	5.55	5.08	11.4	10.1	7.56
Th	24.1	27.1	0.63	0.21	0.23	< 0.02	0.20	0.22	< 0.04	< 0.02	0.36
U	14.2	13.1	0.06	0.09	0.02	0.10	0.08	< 0.01	0.16	0.02	0.09

H. Mass balance calculations for trace element partitioning and isotope fractionation

H.1. Trace element partitioning (Chapter 8)

For the calculation of light element concentrations in rocks and released fluids in the model presented in chapter 8 on page 153, the following equation was used:

$$c_i^{\mathrm{f}} = \frac{c_i^{\mathrm{r}_{n-1}}}{(\mathrm{D}_n - 1)\frac{m_{\mathrm{r}_n}}{m_{\mathrm{r}_{n-1}}} + 1} \tag{H.1}$$

where

- c_i^{f} is the concentration of element i in the fluid,

- $c_i^{\mathrm{r}_{n-1}}$ is the concentration of element i in the rock before dehydration step n,

- D_n is the partition coefficient between dehydrated rock at step n and fluid,

- $m_{\mathrm{r}_{n-1}}$ is the mass of the rock before dehydration step n,

- m_{r_n} is the mass of the rock after dehydration step n.

Furthermore, the following definitions are used:

- m_{f_n} is the mass of fluid released during dehydration step n,

- $c_i^{\mathrm{r}_n}$ is the concentration of element i in the rock after dehydration step n,

- $m_i^{\mathrm{r}_{n-1}}$ is the mass of element i in the rock before dehydration step n,

- $m_i^{\mathrm{r}_n}$ is the mass of element i in the rock after dehydration step n,

- $m_i^{\mathrm{f}_n}$ is the mass of element i in the fluid released during dehydration step n.

395

Equation H.1 is derived from

1. mass balance between the masses of fluid and rock before and after dehydration

$$m_{r_{n-1}} = m_{r_n} + m_{f_n} \Leftrightarrow m_{r_n} = m_{r_{n-1}} - m_{f_n} \tag{H.2}$$

2. mass balance between the masses of trace element i in fluid and rock before and after dehydration

$$m_i^{r_{n-1}} = m_i^{r_n} + m_i^{f_n} \tag{H.3}$$

3. the definition of the partition coefficient

$$D_n = \frac{c_i^{r_n}}{c_i^f} \tag{H.4}$$

4. the definition of the concentration of element i in rocks and fluid

$$c_i^{r_n} = \frac{m_i^{r_n}}{m_{r_n}} \tag{H.5}$$

$$c_i^{r_{n-1}} = \frac{m_i^{r_{n-1}}}{m_{r_{n-1}}} \Leftrightarrow m_i^{r_{n-1}} = c_i^{r_{n-1}} \cdot m_{r_{n-1}} \tag{H.6}$$

and

$$c_i^{f_n} = \frac{m_i^{f_n}}{m_{f_n}} \Leftrightarrow m_i^{f_n} = c_i^{f_n} \cdot m_{f_n} \tag{H.7}$$

The combination of equations H.4, H.5 and H.7 results in

$$D_n = \frac{m_i^{r_n}}{m_i^{f_n}} \cdot \frac{m_{f_n}}{m_{r_n}} \tag{H.8}$$

Combing this equation with equation H.2 and solving it for $m_i^{f_n}$, results in

$$m_i^{f_n} = \frac{m_i^{r_{n-1}}}{D_n \cdot \frac{m_{r_{n-1}}}{m_{f_n}} + 1} \tag{H.9}$$

Replacing the mass of element i in the fluid by its concentration, using equation H.7 results in

$$c_i^{\mathrm{f}} = \frac{m_i^{\mathrm{r}_{n-1}}}{\mathrm{D}_n m_{\mathrm{r}_n} m_{\mathrm{f}_n}} \tag{H.10}$$

Replacing the mass of element i in the rock by its concentration, using equation H.6, and the mass of the fluid by the mass difference between the rock before and after dehydration (equation H.2) results in euqation H.1.

H.2. Isotope fractionation (Chapter 8)

For the calculation of B isotopic ratios of fluids and rocks during dehydration, the mass balance calculations were extended by using

1. mass balance between the two isotopes of B in fluid and rock

$$m_{10}^{\mathrm{f}_n} + m_{11}^{\mathrm{f}_n} = m_{\mathrm{B}}^{\mathrm{f}_n} \tag{H.11}$$

$$m_{10}^{\mathrm{r}_n} + m_{11}^{\mathrm{r}_n} = m_{\mathrm{B}}^{\mathrm{r}_n} \tag{H.12}$$

2. mass balance of the B isotopes in fluid and rock before and after dehydration

$$m_{10}^{\mathrm{r}_n} + m_{10}^{\mathrm{f}_n} = m_{10}^{\mathrm{r}_{n-1}} \tag{H.13}$$

$$m_{11}^{\mathrm{r}_n} + m_{11}^{\mathrm{f}_n} = m_{11}^{\mathrm{r}_{n-1}} \tag{H.14}$$

3. the defenition of $\delta^{11}\mathrm{B}$, for both fluid and rock

$$\delta^{11}\mathrm{B}_{\mathrm{f}_n} = \left(\frac{\frac{m_{11}^{\mathrm{f}_n}}{m_{10}^{\mathrm{f}_n}}}{\frac{m_{11}^{Std}}{m_{10}^{Std}}} - 1 \right) \cdot 1000 \tag{H.15}$$

$$\delta^{11}\mathrm{B}_{\mathrm{r}_n} = \left(\frac{\frac{m_{11}^{\mathrm{r}_n}}{m_{10}^{\mathrm{r}_n}}}{\frac{m_{11}^{Std}}{m_{10}^{Std}}} - 1 \right) \cdot 1000 \tag{H.16}$$

4. the definition of the isotopic fractionation between fluid and rock

$$\Delta^{11}\mathrm{B} = \delta^{11}\mathrm{B}_{\mathrm{f}_n} - \delta^{11}\mathrm{B}_{\mathrm{r}_n} \tag{H.17}$$

where

- $m_{\mathrm{B}}^{\mathrm{f}_n}$ is the mass of boron solved in the fluid at dehydration step n

- $m_{\mathrm{B}}^{\mathrm{r}_n}$ is the mass of boron in the rock after dehydration step n

- $m_{10}^{\mathrm{f}_n}$ is the mass of ^{10}B solved in the fluid at dehydration step n

- $m_{11}^{\mathrm{f}_n}$ is the mass of ^{11}B solved in the fluid at dehydration step n

- $m_{10}^{\mathrm{r}_n}$ is the mass of ^{10}B in the rock after dehydration step n

- $m_{11}^{\mathrm{r}_n}$ is the mass of ^{11}B in the rock after dehydration step n

- $m_{10}^{\mathrm{r}_{n-1}}$ is the mass of ^{10}B in the rock before dehydration step n

- $m_{11}^{\mathrm{r}_{n-1}}$ is the mass of ^{11}B in the rock before dehydration step n

- $\frac{m_{11}^{Std}}{m_{10}^{Std}}$ is the B isotope ratio in standard material SRM951

- $\delta^{11}\mathrm{B}_{\mathrm{f}_n}$ is the B isotope ratio of the fluid released at dehydration step n, in δ-notation relative to SRM951

- $\delta^{11}\mathrm{B}_{\mathrm{r}_n}$ is the B isotope ratio of the rock after dehydration step n, in δ-notation relative to SRM951

- $\Delta^{11}\mathrm{B}$ is the difference in the B isotopic ratio (in δ-notation) between rock and fluid

The masses of boron in fluid ($m_{\mathrm{B}}^{\mathrm{f}_n}$) and rock ($m_{\mathrm{B}}^{\mathrm{r}_n}$) are calculated as demonstrated in section H.1. The B isotope ratio and concentrations ($m_{10}^{\mathrm{r}_{n-1}}$, $m_{11}^{\mathrm{r}_{n-1}}$) in the rock before dehydration are known. The B isotopic fractionation is temperature dependent and is calculated using the formula given by Hervig *et al.* (2002). The following mass balance calculation is used to determine the δ^{11}B values of the rock after dehydration step n and of the released fluid. Values for standard reference material SRM951 are taken from Catanzaro *et al.* (1970).

Combining equations H.15, H.16 and H.17 results in

$$\frac{m_{11}^{f_n}}{m_{10}^{f_n}} - \frac{m_{11}^{r_n}}{m_{10}^{r_n}} = \frac{\Delta^{11}B}{1000} \cdot \frac{m_{11}^{Std}}{m_{10}^{Std}} \tag{H.18}$$

Combining equation H.18 with equations H.13 and H.14 results in

$$\frac{m_{11}^{r_{n-1}} - m_{11}^{r_n}}{m_{10}^{r_{n-1}} - m_{10}^{r_n}} - \frac{m_{11}^{r_n}}{m_{10}^{r_n}} = \frac{\Delta^{11}B}{1000} \cdot \frac{m_{11}^{Std}}{m_{10}^{Std}} \tag{H.19}$$

or

$$\frac{m_{10}^{r_n}m_{11}^{r_{n-1}} - m_{10}^{r_{n-1}}m_{11}^{r_n}}{m_{10}^{r_n}m_{10}^{r_{n-1}} - \left(m_{10}^{r_n}\right)^2} = \frac{\Delta^{11}B}{1000} \cdot \frac{m_{11}^{Std}}{m_{10}^{Std}} \tag{H.20}$$

The right side of equation H.20 is a temperature-dependent constant, which is substituted by the variable φ, in order to keep the equation readable. Combining equation H.20 with equation H.12 than results in

$$\frac{m_{10}^{r_n}m_{11}^{r_{n-1}} - m_{10}^{r_{n-1}}\left(m_B^{r_n} - m_{10}^{r_n}\right)}{m_{10}^{r_n}m_{10}^{r_{n-1}} - \left(m_{10}^{r_n}\right)^2} = \varphi \tag{H.21}$$

which is a quadratic equation with $m_{10}^{r_n}$ being the only unknown variable. It can be written in the form

$$\left(m_{10}^{r_n}\right)^2 + m_{10}^{r_n} \cdot \frac{(1-\varphi)m_{10}^{r_{n-1}} + m_{11}^{r_{n-1}}}{\varphi} - \frac{m_{10}^{r_{n-1}}m_B^{r_n}}{\varphi} = 0 \tag{H.22}$$

The positive solution of quadratic equation H.22 for $m_{10}^{r_n}$ results in the mass of ^{10}B in the rock after dehydration step n. All other parameters are calculated by using the simple equations H.12 to H.16.

H.3. Evolution of B concentrations (Chapter 10)

B concentrations in a fluid migrating from the dehydrating slab towards the site of tourmaline-formation within the exhumation channel are modelled in Chapter 10. The model is based on mass balance calculations, similar those used in Section H.1.

The following definitions are used:

- f/r is the fluid/rock mass ratio during each step of interaction,

- D_B is the partition coefficient of B between rock and fluid,

- $c_B^{f_n}$ is the concentration of B in the fluid after interaction step n,

- $c_B^{f_{n-1}}$ is the concentration of B in the fluid before interaction step n,

- $c_B^{r_n}$ is the concentration of B in the rock after interaction step n,

- $c_B^{r_{n-1}}$ is the concentration of B in the rock before interaction step n,

- m_{f_n} is the mass fluid after interaction step n,

- $m_{f_{n-1}}$ is the mass fluid before interaction step n,

- m_{r_n} is the mass rock after interaction step n,

- $m_{r_{n-1}}$ is the mass rock before interaction step n,

- $m_B^{f_n}$ is the mass B in the fluid after interaction step n,

- $m_B^{f_{n-1}}$ is the mass B in the fluid before interaction step n,

- $m_B^{r_n}$ is the mass B in the rock after interaction step n,

- $m_B^{r_{n-1}}$ is the mass B in the rock before interaction step n.

No hydration or dehydration of the rock is suggested, and therefore the masses of fluid and rock are constant

$$m_{r_{n-1}} = m_{r_n} \tag{H.23}$$

and

$$m_{f_{n-1}} = m_{f_n} \tag{H.24}$$

The fluid/rock ratio (f/r) is the mass ratio of fluid to rock:

$$f/r = \frac{m_f}{m_r} \tag{H.25}$$

Mass balance of B in fluid and rock before and after interaction:

$$m_B^{r_{n-1}} + m_B^{f_{n-1}} = m_B^{r_n} + m_B^{f_n} \tag{H.26}$$

The partition coefficient D_B is defined as the concetration ratio of B in fluid and rock after interaction:

$$D_B = \frac{c_B^{f_n}}{c_B^{r_n}} \tag{H.27}$$

The concentration of B is defined by the mass of B devided by the mass of rock or fluid, respectively:

$$c_B^{r_n} = \frac{m_B^{r_n}}{m_{r_n}} \tag{H.28}$$

and

$$c_B^{f_n} = \frac{m_B^{f_n}}{m_{f_n}} \tag{H.29}$$

Combining Equations H.27, H.28 and H.29 results in:

$$D_B = \frac{m_B^{f_n} \cdot m_{r_n}}{m_B^{r_n} \cdot m_{f_n}} \tag{H.30}$$

or

$$m_B^{r_n} = \frac{m_B^{f_n}}{D_B \cdot \frac{m_{f_n}}{m_{r_n}}} \tag{H.31}$$

Combining Equations H.25, H.26 and H.31 results in:

$$m_B^{r_{n-1}} + m_B^{f_{n-1}} = m_B^{f_n} + \frac{m_B^{f_n}}{D_B \cdot (f/r)} \tag{H.32}$$

This equation can be solved for the mass of B in the fluid after interaction:

$$m_B^{f_n} = \frac{m_B^{r_{n-1}} + m_B^{f_{n-1}}}{D_B \cdot (f/r) + 1} \tag{H.33}$$

Concentrations of B in fluid and rock after interaction can be calculated by using Equations H.28 and H.29, after calculating the masses of B in fluid and rock using Equations H.33 and H.30.

H.4. Evolution of B isotope ratios (Chapter 10)

Boron isotope ratios were calculated based on Equation H.22. However, the mass balance used in this equation has to take in account the amount of ^{10}B and ^{11}B contributed by the fluid before interaction with the rock. Therefore, $m_{10}^{r_{n-1}}$ was replaced by $(m_{10}^{r_{n-1}} + m_{10}^{f_{n-1}})$ and $m_{11}^{r_{n-1}}$ by $(m_{11}^{r_{n-1}} + m_{11}^{f_{n-1}})$, resulting in:

$$\left(m_{10}^{r_n}\right)^2 + m_{10}^{r_n} \cdot \frac{(1-\varphi) \cdot \left(m_{10}^{r_{n-1}} + m_{10}^{f_{n-1}}\right) + \left(m_{11}^{r_{n-1}} + m_{11}^{f_{n-1}}\right)}{\varphi}$$
$$-\frac{\left(m_{10}^{r_{n-1}} + m_{10}^{f_{n-1}}\right) \cdot m_{B}^{r_n}}{\varphi} = 0 \qquad \text{(H.34)}$$

The positive solution of quadratic equation H.34 for $m_{10}^{r_n}$ results in the mass of ^{10}B in the rock after interaction step n. All other parameters are calculated by using the simple Equations H.11, H.12, H.16 and the expansions of Equations H.13 and H.14 displayed below.

Equation H.13 is expanded to:

$$m_{10}^{r_n} + m_{10}^{f_n} = m_{10}^{r_{n-1}} + m_{10}^{f_{n-1}} \qquad \text{(H.35)}$$

and Equation H.13 is expanded to:

$$m_{11}^{r_n} + m_{11}^{f_n} = m_{11}^{r_{n-1}} + m_{11}^{f_{n-1}} \qquad \text{(H.36)}$$

I. Author's publications related to this thesis

I.1. Papers in peer-review journals

Marschall HR, Ludwig T (2004) The Low-Boron contest: minimising surface contamination and analysing boron concentrations at the ng/g-level by secondary ion mass spectrometry. *Mineralogy and Petrology* 81: 265-278

Marschall HR, Ertl A, Hughes JM, McCammon C (2004) Metamorphic Na- and OH-rich disordered dravite with tetrahedral boron, associated with omphacite, from Syros, Greece: chemistry and structure. *European Journal of Mineralogy* 16: 817-823

Marschall HR, Kasztovszky Zs, Gméling K, Altherr R (2005) Chemical analysis of high-pressure metamorphic rocks by PGNAA - comparison with results from XRF and solution-ICP-MS. *Journal of Radioanalytical and Nuclear Chemistry*, 265 (2): in press

Woodland AB, Seitz HM, Altherr R, Olker B, Marschall H, Ludwig T (2002) Li abundances in eclogite minerals: a clue to a crustal or mantle origin? *Contributions to Mineralogy and Petrology* 143: 587-601. Erratum: 144: 128-129

I.2. Papers in preparation

Marschall HR, Altherr R, Ludwig T, Kalt A, Tonarini, S Syros tourmaline: evidence for very high-δ^{11}B fluids in subduction zones. To be submitted to *Journal of Petrology*

Marschall HR, Altherr R, Ludwig T, Kalt A, Kasztovszky Zs, Gméling K Partitioning of Li, Be and B between high-pressure metamorphic minerals. To be submitted to *Geochimica et Cosmochimica Acta*

Marschall HR, Rüpke L, Altherr R Squeezing out the slab – modeling light element release and B isotope fractionation during high-pressure metamorphism. To be submitted to *Earth and Planetary Science Letters*

I.3. Abstracts

Ludwig T, Marschall HR, Altherr R (2004)   Is there a matrix effect in SIMS boron isotope analysis? *Supplement issue of Geochimica et Cosmochimica Acta* 68: A54

Marschall H, Altherr R, Ludwig T, Kalt A (2001)   Li-Be-B budgets of high-pressure metamorphic rocks from Syros, Cyclades, Greece. *Berichte der DMG, Beiheft 1 zu European Journal of Mineralogy* 13: 117

Marschall H, Altherr R, Ludwig T, Kalt A (2002)   Li-Be-B partitioning between high-pressure metamorphic minerals and implications for transfer of these elements in subduction zones. *Abstract Volume of the 18th General Meeting of the IMA 2002, Edinburgh*, 206-207

Marschall H, Nasdala L (2002)   Andradite inclusions in almandine garnet in an eclogite from Syros (Greece). *Berichte der DMG, Beiheft 1 zu European Journal of Mineralogy* 14: 107

Marschall H, Altherr R, Ludwig T, Kalt A (2002)   On the occurence and characterization of Tourmaline in high-pressure metamorphic rocks from Syros (Greece). *Schriftenreihe der Deutschen Geologischen Gesellschaft* 21: 233

Marschall H, Altherr R, Ludwig T, Kalt A (2003)   Boron isotope study of high-pressure metamorphic rocks from Syros (Greece) by secondary ion mass spectrometry (SIMS). *Geophysical Research Abstracts* 5: 05068

Marschall H, Altherr R, Ludwig T, Kalt A (2003)   Syros tourmaline: evidence for very high-δ^{11}B fluids in subduction zones. *Berichte der DMG, Beiheft 1 zu European Journal of Mineralogy* 15: 127

Marschall H, Ludwig T, Altherr R (2003)   The Low-Boron-Contest: eliminating surface contamination and analysing B concentrations at the ppb-level by Secondary Ion Mass Spectrometry. *Symposium LERM 2003, Nové Mesto na Morave, Czech Republic, Book of abstracts*: 51-52

Marschall H, Altherr R, Ludwig T, Kalt A (2004)   Evidence for subduction related fluids and their boron isotopic composition from metasomatic zones in high-pressure metamorphic rocks from Syros (Greece). *Geophysical Research Abstracts* 6: 03865

Marschall H, Ludwig T (2004) The Low-Boron-Contest: minimising surface contamination and analysing boron concentrations at the ng/g-level by SIMS. *Supplement issue 1-2 to Lithos* 73: S74

Marschall HR, Altherr R, Gméling K, Kasztovszky Zs (2004) Trace element systematics of high-pressure metamorphic rocks from Syros (Greece). *Supplement issue of Geochimica et Cosmochimica Acta* 68: A42

Marschall H, Rüpke L, Altherr R (2004) Squeezing out the slab – modelling trace element transfer in subduction zones by using information deduced from HP-rocks. *Berichte der DMG, Beiheft 1 zu European Journal of Mineralogy* 16: 85

Zack T, Marschall H (2003) Isotope fractionation during subduction: The case for Li and B. *Supplement issue of Geochimica et Cosmochimica Acta* 67: A573

Acknowledgements

I would like to express my sincere gratitude to my supervisor Prof. Dr. Rainer Altherr from the Mineralogisches Institut, Universität Heidelberg whose support, stimulating suggestions and encouragement helped me in all the time of research for and writing of this thesis. Initiating the light-element project at the Mineralogisches Institut by him and Prof. Dr. Angelika Kalt brought a number of interesting sub-projects with different young researchers together in a lively and constructive atmosphere. This initiative by Rainer and Angelika is gratefully appreciated.

Especially, I would like to give my thanks to Angela who is the principal performer of our most important projects (Helbling & Marschall, 2002, 2005).

I also want to thank my parents Erich and Winnie Marschall for years of constructive support. The family is, and always was, one of my most important footholds.

Budapest, Hungary I am very grateful to the group of people from Budapest Research Reactor, who were very cooperative during my stay in Budapest in November/December 2003 and truely interested in the details of my project. I especially remember head of department, Gábor Molnár, who was very interested in the details of geological research. Very sadly, he died unexpectedly a month after my stay. Katalin Gméling and Zsolt Kasztovszky are thanked for cooperation and intense co-work on the project and dealing with the samples and the spectras. They put a lot of their time and effort on the PGNAA analysis of my samples.

Bristol, United Kingdom People from the University of Bristol were helpful and cooperative during my two stays at Bristol in March and September 2002. Bruce Paterson assisted during Laser-ablation ICP-MS work and Chung Choi and Tony Kemp (the Older) performed the solution-ICP-MS and solution-ICP-AES analysis at Bristol. John Dalton managed my stays in Bristol and organised the details. I especially remember the fruitful discussions with John Schumacher on the topic of metamorphic rocks from Syros and all other aspects of live in general. I'm thankful to him and other people from Bristol for sharing their after-work pint with me, which gave me hope and anchor in that foreign city.

Pisa, Italy I am thankful to Sonia Tonarini, who performed boron isotope analyses of Syros tourmaline by TIMS which was essential to monitor the accuracy of the Heidelberg SIMS. She also analysed phengite sample Phe-80-3 and provided samples Rocc-3 and B4.

of the XRF analysis and was very helpful in the discussion of analytical details. During electron microprobe work at the Mineralogisches Institut over the last seven years, he was very cooperative and provided most of the formula calculation programs. Maike Hillers is thanked for assistance during whole-rock sample preparation. Stefan Hepp provided sample SY406. Ilona Fin and Oliver Wienand for preparing high-quality thin sections for electron and ion microprobe investigation, and especially for cooperation and support in our fight against boron contamination.

All participants of the Heidelberg Low-Boron-Contest are acknowledged for the contribution of silicate samples, namely: Rainer Altherr, Ralf Bernhard, Marc Bornefeld, Miriam Ebert, Angela Helbling, Stefan Hepp, Dominik Hezel, Jens Hopp, Melanie Kaliwoda, Stephan Klemme, Emily W. Lowe, Hans-Peter Meyer, Jörn Ogiermann, Bettina Olker, Jens Paquin, Georg Partzsch, Stefan Prowatke, Mario Trieloff and Thomas Zack.

Eidesstattliche Erklärung

Hiermit erkläre ich, Horst Reinhold Marschall, geboren am 26.12.1974 in Mainz, an Eides statt, dass ich die vorliegende Dissertation selbst verfasst und mich dabei keiner anderen als der von mir ausdrücklich bezeichneten Quellen und Hilfen bedient habe.

Ich, Horst Reinhold Marschall, geboren am 26.12.1974 in Mainz, erkläre zudem an Eides statt, dass ich an keiner anderen Stelle ein Prüfungsverfahren beantragt habe, dass ich die Dissertation nicht in dieser oder anderer Form bereits anderweitig als Prüfungsarbeit verwendet habe und dass ich sie an keiner anderen Fakultät als Dissertation vorgelegt habe.

Heidelberg, den 26. April 2005